



2017

## Investigating Novel Methods of Interaction with Pharmaceutically Relevant Enzymes

Cory T. Reidl  
*Loyola University Chicago*

Follow this and additional works at: [https://ecommons.luc.edu/luc\\_diss](https://ecommons.luc.edu/luc_diss)

 Part of the [Medical Biochemistry Commons](#)

---

### Recommended Citation

Reidl, Cory T., "Investigating Novel Methods of Interaction with Pharmaceutically Relevant Enzymes" (2017). *Dissertations*. 2601.  
[https://ecommons.luc.edu/luc\\_diss/2601](https://ecommons.luc.edu/luc_diss/2601)

This Dissertation is brought to you for free and open access by the Theses and Dissertations at Loyola eCommons. It has been accepted for inclusion in Dissertations by an authorized administrator of Loyola eCommons. For more information, please contact [ecommons@luc.edu](mailto:ecommons@luc.edu).



This work is licensed under a [Creative Commons Attribution-Noncommercial-No Derivative Works 3.0 License](#).  
Copyright © 2017 Cory T. Reidl

LOYOLA UNIVERSITY CHICAGO

INVESTIGATING NOVEL METHODS OF INTERACTION  
WITH PHARMACEUTICALLY RELEVANT ENZYMES

A DISSERTATION SUBMITTED TO  
THE FACULTY OF THE GRADUATE SCHOOL  
IN CANDIDACY FOR THE DEGREE OF  
DOCTOR OF PHILOSOPHY

PROGRAM IN CHEMISTRY

BY  
CORY T. REIDL  
CHICAGO, IL  
MAY 2017

Copyright by Cory T. Reidl, 2017  
All rights reserved.

## ACKNOWLEDGEMENTS

Thank you to every individual who provided me with guidance, encouragement, friendship, and support on my long journey to complete this dissertation.

I would like to send a heartfelt thank you to my advisor, Daniel P. Becker, Ph. D. for all his guidance throughout my tenure as a doctorate student. I have the utmost respect for his wisdom, expertise, and commitment to education. The lessons and wealth of knowledge I have learned from him is a gift that I will treasure for a lifetime.

To the Department of Chemistry and Biochemistry at Loyola University Chicago for giving me the opportunity to further advance my career in chemistry.

To my progress and dissertation committee members for their advice, cognizance and willingness to help me during this process. Dr. Liu, for always giving me constructive and detailed feedback during my progress committee presentations. Dr. Crumrine, for being a genuinely awesome person and a first-rate professor. Dr. Misty Kuhn, for allowing me to collaborate on her acetyltransferase projects and helping me set up and run the GNAT discontinuous assay; that data was incredibly crucial to my work.

To Dr. Olsen, for helping me get started with in silico molecular modeling and allowing me to access his computation lab.

To my fellow group members and the undergraduate researchers (past and present) I have had the great fortune to work with. Their immense help will always be remembered and appreciated.



Finally, thank you to my family member who have grounded me in the stressful times and celebrated the triumphs. I am extremely grateful to have them in my life.

To my partner, Kiwi, for the unwavering love and support she has shown me through the peaks and valleys of this whole process.

To my Grandpa Wayne and Grandma Arlene, thank you for teaching me that wisdom is not a product of schooling, but of the lifelong attempt to acquire it.

To my Mother, thank you for teaching me that genius is perseverance in disguise.

To my Grandpa Wayne and Grandma Arlene  
and to  
my mother Becky Henson

Make no little plans. They have no magic to stir men's blood.... Make big plans; aim high in hope and work.

— Daniel H. Burnham

## TABLE OF CONTENTS

|  |      |
|--|------|
| ACKNOWLEDGEMENTS   | iii  |
| LIST OF TABLES   | xi   |
| LIST OF FIGURES  | xiii |
| LIST OF SCHEMES  | xx   |
| LIST OF EQUATIONS  | xxi  |
| LIST OF ABBREVIATIONS  | xxii |
| ABSTRACT   | xxvi |
| CHAPTER ONE: INTRODUCTION TO METALLOENZYMES  | 1    |
| Overview   | 1    |
| Challenges in Targeting Di-metalloenzymes  | 4    |
| Metal Promiscuity and the Presents of Multiple Isoforms  | 4    |
| Conformational Dynamics  | 6    |
| Catalytic Center   | 7    |
| Metalloenzymes in Focus  | 7    |
| N-succinyl-L,L-diaminopimelic Acid Desuccinylase (DapE)  | 9    |
| New Delhi Metallo- $\beta$ -lactamase-1 (NDM-1)  | 10   |
| AHL-lactonase (AiiA/AidC)  | 12   |
| CHAPTER TWO: INSIGHT INTO LARGE CONFORMATIONAL CHANGES,<br>SUBSTRATE AND PRODUCTS BINDING AND RELEASE IN N-SUCCINYLL,L-<br>DIAMINOPIMELIC ACID DESUCCINYLAZE | 14   |
| DapE's Structural Background   | 14   |
| Product Bound DapE   | 22   |
| Experimental   | 24   |
| Protein Expression and Purification  | 24   |
| Crystallization  | 24   |
| Structure Determination  | 25   |
| Product-Based Transition-State Modeling (PDTSM)  | 25   |
| Molecular Dynamics for Analysis of Product Release   | 32   |
| Results and Discussion   | 32   |
| HiDapE in the Closed Conformation  | 32   |
| Succinic Acid & LL-Diaminopimelic Acid Binding Unveiled  | 34   |
| Product-Based Transition-State Modeling Analysis   | 35   |
| Hypothetical Conformational Changes Drive Catalysis  | 39   |
| Substrate Specificity Regulates Formation of Transient Oxyanion Hole   | 40   |
| Updated Catalytic Mechanism of DapE  | 43   |

|  |    |
|--|----|
| Conclusions  | 45 |
| Chapter Acknowledgements   | 45 |
| <b>CHAPTER THREE: SUBSTRATE ANALOG SYNTHESIS AND NINHYDRIN-BASED ENZYME ASSAY FOR THE BACTERIAL ENZYME DIAMINOPIMELATE DESUCCINYLA</b> |    |
| DIAMINOPIMELATE DESUCCINYLA  | 47 |
| Introduction   | 47 |
| DapE Molecular Modeling to Assess Mono- Vs. Dimethyl-SDAP Analogs  | 50 |
| Synthetic Protocol   | 53 |
| Results and Discussion   | 55 |
| Primary Amine Detection with Ninhydrin   | 55 |
| DapE Ninhydrin-based Enzymatic Assay and IC <sub>50</sub> Determination  | 56 |
| Conclusion   | 57 |
| Experimental Section   | 57 |
| Materials  | 57 |
| Chemistry  | 58 |
| DapE Molecular Modeling  | 59 |
| Modified SDAP as Potential Substrates  | 61 |
| Ninhydrin-based Assay for DapE Enzymatic Activity  | 61 |
| IC <sub>50</sub> Determinations  | 61 |
| Chapter Acknowledgments  | 62 |
| <b>CHAPTER FOUR: DESIGN, MODELING AND SYNTHESIS OF DI-METALLOENZYME INHIBITORS</b>   |    |
| DI-METALLOENZYME INHIBITORS  | 63 |
| Inhibiting Di-nuclear Metalloenzymes   | 63 |
| Inhibition of DapE   | 64 |
| Inhibition of NDM-1  | 67 |
| Original 225nm DapE Assay.   | 70 |
| High-Throughput Screen & Early Docking Results.  | 71 |
| Material and Methods   | 72 |
| Metalloenzyme Inhibition Assays.   | 72 |
| DapE Assay Description   | 72 |
| NDM-1 Assay Description  | 73 |
| <i>In Silico</i> Docking Protocols with DapE.  | 74 |
| Early SWISSDOCK <i>In Silico</i> Docking Protocol  | 74 |
| Later <i>In Silico</i> Docking Protocol with DapE  | 75 |
| HiTS Hit Ligand Library Dock to NmDapE_OC  | 75 |
| Standardized Substrate & Ligand Library Dock to NmDapE_OC.   | 81 |
| 6- & 7-Substituted Sulfonamide Indoline Series.  | 83 |
| N-Cbz-indoline-7-(N-acyl-sulfonamide) Series.  | 86 |
| Simple N-Acetyl Sulfonamide Series.  | 88 |
| Sulfonyl Azide-Derivatization Series.  | 90 |
| N-Acetyl Indoline-6-Sulfonyl Azide Synthesis.  | 90 |
| N-Cbz-Indoline Protected Sulfonyl Azide Synthesis  | 92 |
| Three-component-copper-coupling Reaction Overview.   | 95 |

|  |     |
|--|-----|
| Sulfonyl Triazoles.  | 96  |
| Sulfonyl Imidates and N-Ac Sulfonylamides                                      | 97  |
| Sulfonyl Amidines (1°, 2°, 3°).  | 97  |
| Results  | 100 |
| SWISSDOCK Results.   | 100 |
| HiTS Hit Docking Results.  | 103 |
| Standardized Substrate and Inhibitor Docking Results.                          | 107 |
| Enzyme Assay Inhibition Results  | 110 |
| Sulfonyl Azide-Derived Analog Inhibition Results                               | 114 |
| Purification Procedure to Remove Copper Contamination for DapE Inhibition.     | 120 |
| Conclusion   | 122 |
| Chapter Acknowledgments  | 122 |
| Experimental Section   | 123 |
| Procedure for Continuous Flow Synthesis of N-Acetyl-5-chloroindoline.          | 126 |
| General Procedure for Preparing N-acetyl-5-haloindolines-6-sulfonylamides      | 131 |
| General Synthesis Procedure for N-acylation of N-Cbz-indoline-7-sulfonylamides | 152 |
| General Synthesis Procedure for Simple N-Ac-sulfonylamides                     | 153 |
| General Synthesis Procedure for N-acetyl-5-haloindoline-6-sulfonylamides.      | 157 |
| General Synthesis Procedure for N-Acetyl-5-Haloindoline-6-Sulfonyl Azide from  |     |
| Sulfonyl Chloride  | 161 |
| General Synthesis Procedure for Sulfonyl Azides Via Azide Transfer             | 164 |
| General Synthesis Procedure for Sulfonyl Triazole Via CuAAC                    | 168 |
| General Synthesis Procedure [A] for Sulfonyl Imidates Via CuAAC                | 174 |
| General Synthesis Procedure [A] for N-Acyl-Sulfonylamides Via CuAAC            | 175 |
| General Synthesis Procedure [B] for N-Acyl-Sulfonylamides Via CuAAC            | 176 |
| General Synthesis Procedure [A] for Sulfonyl Amidines.                         | 179 |
| General Synthesis Procedure [B] for Sulfonyl Amidines                          | 180 |
| <br>   |     |
| CHAPTER FIVE: CYCLOBUTANONE BINDING IN COBALT                                  |     |
| FUNCTIONALIZED HOMOSERINE METALLO- $\gamma$ -LACTONASE AiiA                    | 194 |
| Abstract   | 194 |
| Introduction   | 195 |
| Materials and Methods  | 199 |
| Materials  | 199 |
| Synthesis  | 199 |
| Discontinuous HPLC analysis  | 200 |
| Chemically-Induced Radical-Mediated Cyclobutanone Ring-opening                 | 201 |
| X-ray Exposure Cyclobutanone Digestion   | 201 |
| Product-Based Transition-State Modeling (PBTS) of AiiA_Co                      | 203 |
| Results and Discussion   | 210 |
| Design of substrate analogs  | 210 |
| Ring-opened Analog Formation Via Enzyme-mediated Mechanism                     | 211 |
| Ring-opened Analog Formation Via Radical-mediated Mechanism                    | 213 |
| Product-Based Transition-State Modeling Analysis                               | 214 |
| Conclusion   | 217 |

|   |         |
|---|---------|
| Chapter Acknowledgements  | 218     |
| Experimental Section  | 218     |
| <b>CHAPTER SIX: GCN-5-RELATED N-ACETYLTRANSFERASE (GNAT)<br/>BISUBSTRATE INHIBITORS AND INSIGHT INTO KINETIC AND CHEMICAL<br/>MECHANISM</b> | 224     |
| Abstract  | 224     |
| Introduction  | 225     |
| Results   | 229     |
| Design of substrate analogs   | 229     |
| PA4794 does not O-acetylate the alcohol substrate analog  | 230     |
| Bisubstrate formation in crystals via an enzyme-mediated mechanism  | 232     |
| Bisubstrate formation in crystals via a radical-mediated mechanism  | 232     |
| Two substrate analog binding modes reveal functionally important interactions   | 235     |
| Importance of Arg49 and Arg141 residues of PA4794   | 236     |
| Product-Based Transition-State Modeling Approach  | 238     |
| Active site regions important along the reaction trajectory   | 240     |
| Kinetic mechanism of PA4794 toward NPAcGK   | 242     |
| Overall PA4794 reaction sequence  | 242     |
| Discussion  | 243     |
| Conclusions   | 246     |
| Experimental Section  | 247     |
| Materials   | 247     |
| Chemistry   | 247     |
| Determination of kinetic mechanism  | 260     |
| Substrate analog test   | 260     |
| Enzyme-mediated formation of bisubstrate with alkene  | 261     |
| HPLC analysis of enzyme-mediated formation of bisubstrate with alkene   | 261     |
| HPLC analysis of radical-mediated AIBN formation of bisubstrate with alkene   | 262     |
| AIBN mediated bisubstrate sample purification & LC MS/MS analysis   | 262     |
| Protein Crystallization   | 263     |
| Data collection, structure determination and refinement   | 263     |
| <i>In Silico</i> Modeling   | 264     |
| Chapter Acknowledgements  | 266     |
| <br>APPENDIX A:   | <br>267 |
| <br>APPENDIX B:   | <br>269 |
| <br>REFERENCES  | <br>271 |
| <br>VITA  | <br>291 |

## LIST OF TABLES

|  |     |
|--|-----|
| Table 1. GBVI/WSA $\Delta G$ Binding Affinity Calculations for PBTSM-Generated Structures.   | 38  |
| Table 2. Sulfonamide Ligand Library for SWISSDOCK.   | 75  |
| Table 3. High Throughput Screen Ligand Docking Library.  | 76  |
| Table 4. HiTS-hits_NmDapE_OC Docking Parameters.   | 80  |
| Table 5. Standardized Substrate & Ligand Library.  | 81  |
| Table 6. Sulfonamide Indoline Inhibitor Data Table.  | 103 |
| Table 7. N-Acetyl-5-alo indoline-6-Sulfonamides Inhibition Results.  | 111 |
| Table 8. N-Cbz indoline-7-(N-acyl-sulfonamide) Inhibition Results.   | 111 |
| Table 9. Simple N-Acetyl Sulfonamide Inhibition Results.   | 112 |
| Table 10. Miscellaneous Structure Analog Inhibition Results.   | 112 |
| Table 11. Side by Side comparison of sulfonyl azide-derived analog batches.  | 115 |
| Table 12. Copper-Assayed Sulfonyl Amidine Inhibition Results Against DapE.   | 120 |
| Table 13. Copper Assay Results.  | 121 |
| Table 14. X-ray Exposure Cyclobutanone Digestion Sample Conditions.  | 203 |
| Table 15. HPLC Results of discontinuous enzyme assay with cyclobutanone <b>2</b> exposure to AiiA_Co. A) Standard HPLC of 4-decanamideobutanoic acid <b>3</b> . B) Control HPLC of N-(2-oxocyclobutyl)decanamide <b>2</b> in Buffer only. C) HPLC Assay with 2.0 mM cyclobutanone <b>2</b> + 0.05 mM AiiA_Co in Buffer incubated over 2 hours, D) HPLC Assay with 2.0 mM cyclobutanone <b>2</b> + 0.01 mM AiiA_Co in Buffer incubated over 2 hours, E) HPLC Assay with 2.0 mM cyclobutanone <b>2</b> + 0.05 mM AiiA_Co in Buffer incubated over 2.5 d. | 211 |



|  |     |
|--|-----|
| Table 16. HPLC Analysis of radical-mediated cyclobutanone ring opening under various conditions. | 214 |
| Table 17. GBVI/WSA $\Delta G$ Binding Affinity Calculations for PBTSM-Generated AiiA Structures. | 217 |

## LIST OF FIGURES

- Figure 1. The 1960 crystal structure of Myoglobin (PDB ID: 1mbn). Depicted is the Myoglobin ribbon structure consisting of an eight  $\alpha$ -helical backbone domain (blue) that wrap around a central heme-binding domain containing a heme group (green) coordinating a single iron atom (rust-red). The Fe atom is flanked by His93 on one side and bound O2 which further interacts with His64. 2
- Figure 2. Effect of divalent cations on DapE\_Mn-catalyzed hydrolysis of Asp-Leu. An activity level of 100 % is 222 mol/min/mg. Divalent cations (as chloride salts) were present at 1 mM. B) Substrate specificity of DapE\_Mn for aspartyl peptides. The activity for Asp-Leu is set as 100 %. C) Structure Comparison of known DapE Substrates. 6
- Figure 3. Timeline of antibiotic discovery through medicinal chemistry. 8
- Figure 4. Enzyme active sites for A) N-succinyl-L,L-diaminopimelic Acid Desuccinylase (DapE), B) New Delhi Metallo- $\beta$ -lactamase-1 (NDM-1), C) AHL-lactonase (AiiA/AidC). 9
- Figure 5. Crystal structure of NDM-1 (B-factor ribbon model) bound to the hydrolyzed form of the common antibiotic meropenem seen in orange (PDB ID: 4EYL). 11
- Figure 6. Modeled structure of AiiA\_Co AHL metallo-lactonase bound to N-(2-oxocyclobutyl)decanamide as the tetrahedral transitions state mimetic. 13
- Figure 7. Biosynthetic Pathways of meso-diaminopimelic acid and lysine in bacteria. DapE is indicated in red. 15
- Figure 8. A) Ribbon diagram of HiDapE dimer and monomer, B) di-zinc active site, C) mono-zinc active site. 16
- Figure 9. The active site of WT-HiDapE showing loop V in orange. T325 resides on loop V directly over the dinuclear active site. 17
- Figure 10. Previously proposed mechanism of DapE (a) monozinc DapE and (b) dizinc DapE. 19

|  |    |
|--|----|
| Figure 11. Ribbon diagrams showing DapE's truncated catalytic domain from <i>Haemophilus influenzae</i> (Green) in comparison to Aminopeptidase from <i>Aeromonas proteolytica</i> (Teal).   | 20 |
| Figure 12. ZnZn_NmDapE complex with L-captopril. A) Ribbon diagram of NmDapE homodimer, subunits in blue and orange; B) active site with L-captopril, key residues, and water molecule (red sphere).   | 22 |
| Figure 13. Structures of dimetaleted HiDapE in ligand free form (A: open conformation) and HiDapE product bound form (B: closed-conformation) (C). Active site of HiDapE showing binding interactions of succinic acid and diaminopimelic acid.  | 23 |
| Figure 14. PBTSM Protocol.   | 26 |
| Figure 15. A) Solvent Box of LLSDAP transition state intermediate DapE model. B) Solvate Function. C) QuickPrep Function.  | 27 |
| Figure 16. Molecular Dynamic Protocol Window in MOE.   | 30 |
| Figure 17. A series of snapshots of one of the dimers of DapE from a 40 ps steered molecular dynamics experiment. The total simulation was 36 frames visualized in VMD with a stride of 100 frames.  | 32 |
| Figure 18. Shown is a surface structure cross-section of the closed product conformation of DapE with products succinate and DAP bound in the active site.   | 34 |
| Figure 19. Model results as each stage of Product-Base Transition-State Modeling. A) Succinate & DAP products bound to the closed conformation of DapE, generated from crystal structure obtained from Dr. Nocek. B) L,L-SDAP transition state intermediate bound to the closed conformation of DapE, generated through PBTSM. C) L,L-SDAP and activated cat. hydroxyl group bound to the closed conformation of DapE, generated through PBTSM. D) L,L-SDAP and unactivated cat. water bound to the closed conformation of DapE, generated through PBTSM. Atoms associated with succinate and DAP are colored cyan and yellow while protein chains A and B are colored dark green and orange respectively. | 37 |
| Figure 20. Shown are four major zones of ligand-enzyme interaction as seen in LLSDAP-TS_DapE_PC. A) Bond distance of transition state intermediate bound to metal center. Binding analysis of transition state intermediate after molecular dynamics and minimization: B) Distal carboxylate of succinyl segment, C) Proximal carboxylate of TS bound DAP segment, D) Distal end of DAP segment.   | 39 |
| Figure 21. Hypothesized transient oxyanion hole in the (A) catalytically active form, (B) catalytically inactive form.   | 41 |

|   |    |
|---|----|
| Figure 22. Trapped product bound conformation of Human Carnosinase-2 (CN2) (PDB I.D. 4RUH) trapped in the closed conformation by inhibitor bestatin interacting with metal center and a highly-conserved histidine.   | 42 |
| Figure 23. NDM-1 active site cleft with a modeled meropenem transition state intermediate bound at the metal center. Enzyme represented in B-factor with ribbon diagram shown as wire except for the hairpin loop and binding loop I.   | 43 |
| Figure 24. Generic diagram of Ninhydrin Assay implementation.   | 50 |
| Figure 25. Minimized substrate/analogs docked and modeled in the DapE active site; a) native substrate L,L-SDAP (yellow), b) monomethyl-LL-SAP (brown), c) dimethyl-L,L-SDAP (turquoise). Note*Chain A (catalytic domain, green), Chain B (dimerization domain, purple).              | 51 |
| Figure 26. Enzymatic action for cleavage of L,L-SDAP by DapE.   | 64 |
| Figure 27. A) Cartoon representation of the Gram-positive (left) and Gram-negative (right) bacteria cell wall. B) Primary structures of Lys-type and DAP-type peptidoglycan.  | 65 |
| Figure 28. Succinylase Biosynthesis Pathway with DapE Metallohydrolase highlighted in red.  | 66 |
| Figure 29. Core structures of the common $\beta$ -lactam antibiotics. (Side chains omitted for clarity). (A) Monobactam core, (B) Penam core, (C) Oxapenam core, (D) Carbapenam core, (E) Penem core, (F) Carbapenem core, (G) Cephem core, (H) Oxacephem core, (I) Carbacephem core. | 67 |
| Figure 30. Coupled assay for HiTS screen.   | 71 |
| Figure 31. Five inhibitors identified through the HiTS screen.  | 72 |
| Figure 32. Structure of Chromacef, a chromogenic cephalosprin used in the detection and assay of $\beta$ -lactamases.   | 73 |
| Figure 33. Database Wash utility function in MOE used to quickly prepare large database set for further analysis in MOE.  | 76 |
| Figure 34. MOE docking receptor preparation of NmDapE_OC model (PDB = 5UEJ).  | 78 |
| Figure 35. Site Finder operating window in MOE used for calculating the probable ligand binding sites for NmDapE_OC docking model.  | 79 |
| Figure 36. Site Directed Docking Metal Center Site for NmDapE_OC Receptor Model.  | 80 |

|   |     |
|---|-----|
| Figure 37. a) Synthesis of indoline-6-sulfonamides, b) Borrow-adapted synthesis of 7-sulfonamides.  | 84  |
| Figure 38. Continuous Flow Chlorination Setup for 5-chloro-N-acetyl indoline. A) Schematic representation, B) Laboratory apparatus configuration.   | 85  |
| Figure 39: Docking and minimization of the simple N-succinyl-benzylsulfonamide with NDM-1 using MOE. A) mono-anionic state B) di-anionic state.   | 89  |
| Figure 40. Reaction Setup for Sulfonyl Chloride Azidation with Sodium Azide.  | 91  |
| Figure 41. Synthesis Versatility of CuAAC-Sulfonyl Azide Chemistry.   | 95  |
| Figure 42. Sulfonyl Amidine Bioisosteric Relationship to N-acetyl-sulfonamides.   | 98  |
| Figure 43. First Iteration of Purification Protocol for Preparing Sulfonyl Azide-derived Inhibitor.   | 99  |
| Figure 44. HiTS Sulfonamide Indoline Derivative Docking to DapE's open conformation (PDB = 3IC1). A) Lead compound <b>5d</b> , B) simplified pyrrolidinyl derivative <b>12b</b> of HiTS hit <b>4</b> . C) Surface representation and D) ligand interaction map of <b>12b</b> .  | 102 |
| Figure 45. Line Graph Representation (LGR) of HiTS Hit Ligand Database Docking Results Against NmDapE Receptor. The Y-axis (bottom) represents $\Delta G$ scoring values in kcal/mol. The X-axis (right-hand) represents ligand pose sequence sorted by two tier organization. Intervals of 15 data points represent docking results of a single ligand entry (1-21) organized in ascending $\Delta G$ scoring values. Horizontal graph lines denote ligand entry transitions. Refer to Table 3 for ligand entry identities. A) Docking Results for HiTS-hits_NmDapE_OC-SF-dock; B) Docking Result for HiTS-hits_NmDapE_OC-SD-dock. | 105 |
| Figure 46. HiTS hit docking pose selection. A) 6-sulfonamide, B) 7-sulfonamide, C) HiTS hit <b>7</b> , pose 1 D) HiTS hit <b>7</b> , pose 1, E) HiTS hit <b>6</b> , pose 1, F) HiTS hit <b>6</b> , pose 2, G) $\beta$ -sulfone <b>8</b> .   | 106 |
| Figure 47. Line Graph Representation (LGR) of Standardized Substrate and Inhibitor Database Docking Results Against NmDapE Receptor. Y-axis (bottom) represents $\Delta G$ scoring values in kcal/mol. X-axis (right-hand) represents ligand pose sequence sorted by two tier organization. Intervals of 15 data points represent docking results of a single ligand entry (1-21) organized in ascending $\Delta G$ scoring values. Horizontal graph lines denote ligand entry transitions. Refer to Table 4 for ligand   | 109 |
| Figure 48. Selection of substrate docking pose into NmDapE open structure. A) L,L-SDAP, B) N-Methyl-L,L-SDAP assay substrate.   | 110 |

|   |     |
|---|-----|
| Figure 49. HPLC and LC-MS analytical comparison between NDM-1 inhibitors with identical structures. A) CTR-D-28-FS 6/6/16 batch v. MM-80. B) 6/6/16 batch IYD-B-75-FSRCW v. MM-64a. C) 6/6/16 batch CTR-D-17-FSRCW v. CTR-C-8-FS. D) 6/6/16 batch IYD-B-75-FSRCW v. MM-64a. E) 6/6/16 batch IYD-B-75-FSRCW LC-MS analysis. F) MM-64a LC-MS analysis.  | 117 |
| Figure 50, A) CuI + Sat. NH <sub>4</sub> Cl. B) CuI + Sat. NH <sub>4</sub> Cl + 30% NH <sub>4</sub> OH buffer solution with pH ~ 10. C) CuI + Sat. NH <sub>4</sub> Cl + TEA. D) CuI + TEA/AcOH buffer solution with pH ~ 7. E) CuI + sat. EDTA solution. F) CuI + Sat. Sodium thiosulfate. Conditions A, D and E all had CuI remain in solid phase while B, C and F conditions fully dissolved the CuI.     | 119 |
| Figure 51. HPLC analysis, Fractions collected at 7 min intervals: A) tube 2, B) tube 3, C) tube 4, D) tube 5, E) tube 6, F) tube 7, G) tube 8, H) tube 9. Peaks at 8.8 mins and 10.3 mins correspond to starting material and products, respectively.   | 127 |
| Figure 52: Comparing flow vs. batch synthetic protocols. A) NAc-Indoline starting material, B) filtered products from 1st flow reaction 1, C) filtered products from 2nd Flow reaction after optimization, D) batch reaction 1, run at rt for 2 h), batch reaction 2, ran at 70 °C for 2 h).  | 128 |
| Figure 53. A) Structure of Oxa-10 complexed with Cyclobutanone derivative of penicillin as serine-bound hemiketal (PDB ID: 3LCE), B) Structure of a serine hydrolase from <i>Francisella tularensis</i> complexed as a serine-bound hemiketal with N-Cyclobutanone sulfonamide inhibitor (PDB ID: 4F21). The tosylamide was not observed in the crystal structure, but has been modeled in for this Figure. | 196 |
| Figure 54. N-acyl-L-homoserine metallo- $\gamma$ -lactonase (AiiA, AHL lactonase) catalyzes the hydrolysis of N-acyl-L-homoserine lactones to the corresponding ring-opened products, the corresponding N-acyl-L-homoserines.   | 195 |
| Figure 55. Depiction of AiiA_Co AHL metallo-lactonase structure bound to: A) Hypothesized N-(2-oxocyclobutyl)decanamide as the tetrahedral transition state mimetic (PBTSM Generated Model), B) Observed ring-opened byproduct 4-decanamideobutanoic acid (PDB ID: TBD). We hypothesize that the opening is mediated by hydroxyl radicals generated during X-ray irradiation.                               | 198 |
| Figure 56. X-ray exposure cyclobutanone digestion setup. A) sample mounting setup, B) X-ray etched glass inserts.   | 202 |
| Figure 57. PBTSM Protocol for AiiA_Co.  | 204 |
| Figure 58. Distorted cyclobutanone transition state mimetic before minimization.  | 206 |

|  |     |
|--|-----|
| Figure 59. Molecular geometry differences of the active site resulting from transformations in steps 4 to 5 of the PBTSM protocol.   | 207 |
| Figure 60. Molecular geometry differences of the active site resulting from transformations in steps 4 to 5 of the PBTSM protocol.   | 209 |
| Figure 61. Final ligand binding geometry generated through PBTSM protocol.   | 210 |
| Figure 62. Transition state mimetic stabilization by cobalt, Tyr194 and Asp108.  | 216 |
| Figure 63. Gen5-related N-Acetyltransferase (4L8A).  | 228 |
| Figure 64. Experimental HPLC Assay Data. A) Discontinuous assay design to determine source of C-S bond formation. Assay result HPLC Chromatogram for B) Control: Mix + Buffer, C) Trial 1: HSCoA + Mix + Buffer, D) Trial 2: HSCoA + Mix + AIBN + Buffer.  | 233 |
| Figure 65. A) MS and B) MS-MS Fragmentation Analysis of Trial 2 After Solid Phase Extraction (SPE) Preparation.  | 234 |
| Figure 66. Comparison of binding products and bisubstrate <b>3</b> and <b>6</b> analogs. PA4794 is shown in orange atoms with B-Factor ribbon diagram. Residues 19-37 are shown as wire-ribbons for clarity. Ligand atoms represented as followed: CoA; dark green, NPAcGK from pdb:4L8A; light green, inhibitor atoms attributed to bisubstrate <b>3</b> and <b>6</b> ; cyan & salmon respectively. (A) PA4794 in complex with bisubstrate analog <b>6</b> synthesized from CoA and alcohol/alkene mixture <b>4/5</b> determined at 1.2 Å. (B) PA4794 in complex with bisubstrate analog <b>3</b> synthesized in the active site from CoA and compound <b>2a</b> determined at 1.4 Å. (C) Ternary complex structure of PA4794 with the bound reaction products CoA and Nε-acetylated NPAcGAcK. (D) 2Fo-Fc electron density map of the bound bisubstrate analog <b>6</b> ( $\sigma=1.0$ ) (E) 2Fo-Fc electron density map of the bound bisubstrate analog <b>3</b> ( $\sigma=1.0$ ). | 236 |
| Figure 67. Substrate saturation curves for wild-type and R49 and R141 mutants. Steady-state enzyme kinetic experiments were performed by holding AcCoA concentration constant at 0.5 mM and varying NPAcGK peptide concentration. Standard deviations for all proteins are shown. See Experimental procedures for details.   | 238 |
| Figure 68. Product-Based Transition-State Modeling (PBTSM). Protocol for systematic remodeling of tetrahedral intermediate and substrate binding modes from product or bisubstrate bound crystal structures. Molecular Minimization (MM) and Molecular Dynamics (MD) stages in the protocol are shown.   | 239 |
| Figure 69. Product-Based Transition-State Modeling Analysis. A) Schematic diagram of tetrahedral transition state intermediate indicating major regions of substrate-  | 241 |

enzyme interactions in the active site, including substrate C-terminal carboxylate stabilizing interactions (black square), oxyanion hole (blue circle), and stabilizing interactions for substrate amine approach (red circle). PBTSM generated transition state models are shown in panels B and C. B) Transition state model based on PA4794 co-crystal structure with products bound (PDB ID: 4L8A) shown in light green. C) Transition state model based on PA4794 structure in complex with bisubstrate **3** shown in cyan. The CoA moiety of the tetrahedral intermediate is shown in dark green and protein side chains are in orange. Amino groups are in dark blue, oxygens in red, sulfurs in yellow, and waters as red and white spheres.

- Figure 70. Proposed chemical mechanism for PA4794 acetyl transfer. 243
- Figure 71.: Spectral data for N6-(2-chloroacetyl)-N2-((2-phenylacetyl)glycyl)-L-lysine (2a). A) predicted 1H NMD, B) unprocessed 1H NMR, C) Mnova-processed 1H NMR, D) & COSY NMR, E) HRMS. 251
- Figure 72. Spectral data for N6-(2-chloroacetyl)-N2-((2-phenylacetyl)glycyl)-L-lysine (2a). A) predicted 1H NMD, B) unprocessed 1H NMR, C) Mnova-processed 1H NMR, D) 13C NMR, E) COSY NMR. 253
- Figure 73. HPLC and LC-MS Data for **4** & **5** Sample Mixture. 258
- Figure 74. NMR Trituration Experiment on **4** / **5** Product Mixture. 260



## LIST OF SCHEMES

|   |     |
|---|-----|
| Scheme 1. Conversion of SDAP substrate by DapE.   | 48  |
| Scheme 2. Synthesis of N <sup>6</sup> -acetyl-L,L/D,D-SDAP substrate <b>1d</b> .  | 53  |
| Scheme 3. Synthesis of N <sup>6</sup> -Methyl-L,L-SDAP substrate <b>1b</b> .  | 54  |
| Scheme 4. General Synthesis of 6-substituted Sulfonamide Indoline Inhibitors.   | 86  |
| Scheme 5. Synthesis of 7-substituted N-Cbz-indoline -7-(N-acyl-sulfonamide).  | 87  |
| Scheme 6. Synthesis of Simple Aryl N-Succinyl and N-Glutamyl Sulfonamides.  | 88  |
| Scheme 7. Synthesis of N-Cbz-Indoline Protected Sulfonyl Azides.  | 93  |
| Scheme 8. An example of “Click” Chemistry.  | 96  |
| Scheme 9. Synthesis of Sulfonyl Triazole analogs  | 96  |
| Scheme 10. Synthesis of Sulfonyl Imidate and N-Ac Sulfonamide Analogs.  | 97  |
| Scheme 11. Synthesis of 1°, 2°, and 3° Sulfonyl Amidine Derivatives.  | 98  |
| Scheme 12: Synthesis of $\alpha$ -amido cyclobutanones <b>1</b> ; n=4 & <b>2</b> ; n=7, under anhydrous acidic conditions with primary amides. B) Synthesis of ring-opened analog 4-decanamideobutanoic acid <b>3</b> . | 200 |
| Scheme 13. Synthesis of $\alpha$ -haloacetyl derivatives of NPACGK <b>2a</b> (X = Cl) and <b>2b</b> (X = Br) and enzyme-mediated formation of bisubstrate <b>3</b> .  | 230 |
| Scheme 14. Formation of the alcohol/alkene mixture ( <b>4</b> and <b>5</b> ) from NPACGK, and radical-mediated reaction of CoA with alkene <b>5</b> to form the covalent bisubstrate <b>6</b> .                         | 231 |
| Scheme 15. Mechanistic hypothesis for the formation of bisubstrate <b>6</b> from CoA and alkene <b>5</b> .  | 245 |
| Scheme 16. Synthesis of (S)-6-hydroxy-2-(2-(2-phenylacetamido)acetamido)hexanoic acid ( <b>4</b> ) and (S)-2-(2-(2-phenylacetamido)acetamido)hex-5-enoic acid ( <b>5</b> ).   | 255 |

## LIST OF EQUATIONS

Eq. (1)  $\Delta G \approx c + \alpha \left[ \frac{2}{3} (\Delta E_{\text{Coul}} + \Delta E_{\text{sol}}) + \Delta E_{\text{vdW}} + \beta \Delta S A_{\text{weighted}} \right]$  38

## LIST OF ABBREVIATIONS

|            |  |
|------------|--|
| $\alpha$   | alpha  |
| $\beta$    | beta   |
| $\gamma$   | gamma  |
| $\delta$   | delta  |
| $\epsilon$ | epsilon  |
| AiiA       | N-acyl homoserine lactonase                        |
| Boc        | t-butyloxycarbonyl                                 |
| Cbz        | carboxybenzyl                                      |
| CoA        | coenzyme A   |
| DapE       | diaminopimelate desuccinylase,                     |
| L,L-SDAP   | N-Succinyl-L,L-diaminopimelic acid                 |
| MRSA       | methicillin-resistant <i>Staphylococcus aureus</i> |
| $\nu$      | Wavenumber; cm <sup>-1</sup>                       |
| °C         | Degree Celsius                                     |
| Å          | Ångström   |
| Abs        | absorbance   |
| Ac         | acetyl   |
| ACN        | Acetonitrile                                       |
| AHL        | acyl-homoserine lactonase                          |

|                               |  |
|-------------------------------|--|
| AiiA_Co                       | Cobalt metalloisoform of the AiiA lactonase      |
| Ar                            | Aryl peak (NMR)                                  |
| Au                            | absorbance units                                 |
| Bn                            | Benzyl   |
| CA                            | Carbonic anhydrase                               |
| Calc.                         | Calculated                                       |
| CD                            | circular dichroism                               |
| CuTC                          | Copper(I)-thiophene-2-carboxylate                |
| d                             | Doublet (NMR)                                    |
| DAP                           | diaminopimelate                                  |
| DapE                          | N-succinyl-L,L-diaminopimelic acid Desuccinylase |
| DCM                           | dichloromethane                                  |
| DMF                           | Dimethylformamide                                |
| DMSO                          | Dimethyl sulfoxide                               |
| EA                            | ethyl acetate                                    |
| EDTA                          | Ethylenediaminetetraacetic acid                  |
| equiv.                        | Equivalent                                       |
| ESI-MS                        | Electrospray ionization mass spectrometry        |
| Et <sub>3</sub> N             | Triethylamine                                    |
| EtOAc                         | ethyl acetate                                    |
| Ev                            | electronvolts                                    |
| Fe                            | Iron   |
| H <sub>2</sub> O <sub>2</sub> | Hydrogen peroxide                                |

|           |   |
|-----------|---|
| HEPES     | 4-(2-hydroxyethyl)-1-piperazineethanesulfonic acid) |
| HO        | hydroxyl  |
| OH        | hydroxyl  |
| HPLC      | High performance liquid chromatography              |
| HRMS      | High resolution mass spectrometry                   |
| HiTS      | High Throughput Screen                              |
| Hz        | Hertz   |
| IPA       | isopropyl alcohol                                   |
| J         | Coupling constant                                   |
| K         | Kelvin  |
| MALDI-TOF | Matrix-assisted laser desorption time-of-flight     |
| MBG       | Metal Binding Group                                 |
| m-DAP     | meso-diaminopimelate                                |
| MeOH      | Methanol  |
| min       | minutes   |
| MOE       | Molecular Operating Environment                     |
| MP        | Metalloprotein                                      |
| mp        | experimental melting point                          |
| MS        | Mass spectrometry                                   |
| NDM-1     | New Dahli Metallo-beta-lactamase                    |
| NMR       | Nuclear magnetic resonance spectroscopy             |
| PDB       | Protein Data Bank                                   |
| pKa       | Acid dissociation constant                          |

|      |  |
|------|--|
| RBF  | round bottom flask                       |
| RT   | Room temperature                         |
| Rev  | revolutions                              |
| s    | Singlet (NMR)                            |
| SAR  | Structure-activity relationship          |
| SDAP | N-Succinyl diaminopimelic acid           |
| SOD  | Superoxide dismutase                     |
| T    | Temperature                              |
| TFA  | trifluoroacetate or trifluoroacetic acid |
| THF  | Tetrahydrofuran                          |
| TLC  | thin layer chromatography                |
| TMS  | tetramethylsilane                        |
| ZBG  | Zinc-binding group                       |

## ABSTRACT

Metalloproteins requiring one or more metal ions for normal function make up 30 % of all known proteins, and many critical biological pathways contain at least one metallo-enzyme. Di-nuclear metallo-proteins constitute a large class of these proteins yet we currently lack effective methods of inhibiting these enzymes for the development of new medical therapies, particularly for the discovery of new antibiotics. Our work has focused on developing novel functionalities that selectively interact with di-nuclear catalytic centers, and we are targeting three separate di-zinc-metallo-enzymes that are unique to bacteria and play key roles in their growth and development. These enzymes are DapE, AiiA, and NDM-1. DapE is involved in biosynthesis of lysine and meso-diaminopimelic acid, essential precursors in the production of bacterial cell walls. AiiA is a di-Zn-dependent lactonase involved in bacterial cell-cell communication, and NDM-1 is a di-metallo-beta-lactamase capable of deactivating the most commonly administered antibiotics, gaining international attention for this enzyme as a clinically-relevant pharmaceutical target, yet drug development efforts have proven ineffective due to a lack of effective inhibitors.

As part of our ongoing studies to functionally annotate the Gcn5-related N-acetyltransferase (GNAT) PA4794 from *Pseudomonas aeruginosa* with unknown functions, we have used PA4794 as a model system for exploring efficient formation of bisubstrate complexes to enhance our success rate in obtaining co-crystal structures of GNATs with ligands bound in their acceptor sites. We have synthesized and tested substrate analogs of the previously identified

N-phenylacetyl glycine lysine (NPAcGK) enabling two separate three-dimensional structures of PA4794 with NPAcGK analog-derived bisubstrates formed through direct reaction with CoA—the first through direct alkylation with a reactive substrate, and the second through X-ray induced radical-mediated process. We have also performed docking and molecular dynamics simulations of the reverse reaction pathway from the NPAcGK product back to formation of the tetrahedral intermediate/transition state to complement our structural work and to explore the key ligand-protein interactions within the active site of PA4794, guiding mutant synthesis and kinetics to explore the role of key residues in the active site.



CHAPTER ONE  
INTRODUCTION TO METALLOENZYMES

**Overview**

The metallome, described as the collection of transcriptome, proteome, and metabolome, is the assemblage of biological macromolecules that share the common characteristic of complexing metal ions into their protein tertiary structure to fulfill a given biological task.<sup>1,2</sup> The themes expressed in this work can be, in large part, applied over the entire metallome. However, the focus of this work pertains to the interaction of metals with proteins, referred to as the metalloproteome.

Metalloproteins include any protein that is coordinated to a metal ion cofactor. Metalloproteins (MP) have fascinated chemists and biochemists since 1960, when John Kendrew and coworkers reported the first X-ray crystal structure of sperm whale myoglobin (PDB ID: 1mbn) bound to a single iron atom (Figure 1).<sup>3</sup>

Much is now known about metalloproteins, including how metal clusters are assembled and introduced into target proteins and which metal ions are commonly found in metalloproteins. Moreover, it has been estimated that such proteins make up more than 30% of the known proteome.<sup>4</sup> In fact, the majority of biological pathways contain at least one metalloprotein that requires one or more metals in order to express its given biological function. Although metalloproteins are known to participate in a wide range of biological functions, when a metalloprotein is involved in catalyzing a biochemical transformation we refer to the class of

proteins as metalloenzymes.<sup>2</sup>

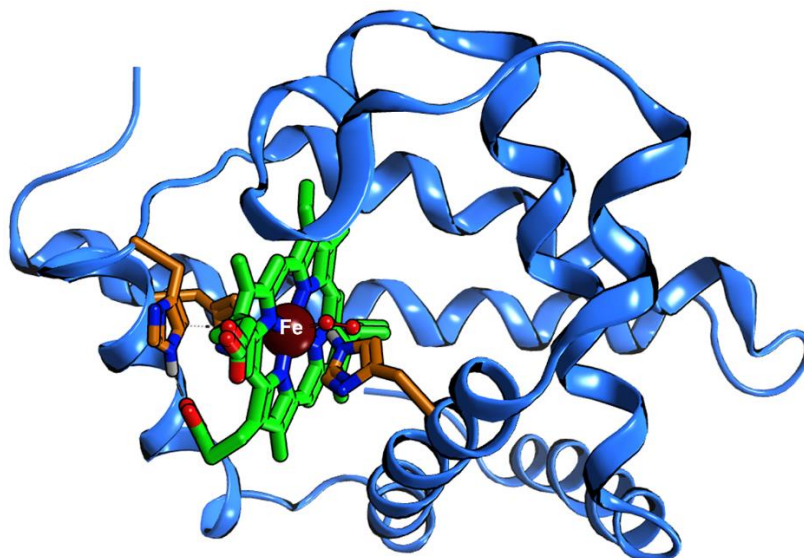


Figure 1. The 1960 crystal structure of Myoglobin (PDB ID: 1mbn). Depicted is the Myoglobin ribbon structure consisting of an eight  $\alpha$ -helical backbone domain (blue) that wrap around a central heme-binding domain containing a heme group (green) coordinating a single iron atom (rust-red). The Fe atom is flanked by His93 on one side and bound O<sub>2</sub> which further interacts with His64.

The field of metalloenzyme studies has made substantial progress toward the understanding of these interesting molecules. We are much closer to understanding the mechanisms by which metalloenzymes catalyze a vast array of complex chemical reactions as well as how we can use traditional chemical techniques to manipulate the metalloenzymatic functions. However, despite more than half a century of research by chemists, biochemists, and cell biologists, there is still much to learn about metalloenzymes. The work described herein is our contribution to the understanding of metalloproteins through the investigation of novel methods of small molecules interacting with pharmaceutically relevant metalloenzymes, and in understanding their mechanism of action through computational methods.

Naturally occurring metalloenzymes utilize trace micronutrients found in the cellular microenvironment. These micronutrient metal cofactors play a crucial role as Lewis acids for

the host metalloenzyme in their biological catalytic function. Metalloproteins are coordinated to metal cofactors in the protein's active site referred to as the metal center through interactions with nitrogen, oxygen or sulfur atoms belonging to amino acids in the protein chain, or a through a porphyrin ring incorporated into the protein as in the case of myoglobin.<sup>3</sup> All amino acid residues have been shown to have the ability to coordinate metal centers. These metal cofactors are most commonly  $Mg^{+2}$ ,  $K^{+1}$ ,  $Ca^{+2}$ ,  $Na^{+1}$ ,  $Fe^{+2/+3}$ ,  $Mn^{+2}$ ,  $Co^{+2}$ , and  $Zn^{+2}$  but can also be other less common trace metals such as  $Cu^{+2}$ ,  $Ni^{+2}$ ,  $Se^{+2}$ ,  $W^{+4}$ ,  $Mo^{+4}$ , etc., and even occasionally uranium.<sup>5-7</sup> Metalloenzymes have evolved to coordinate a particular metal cofactor to enable finely tuned catalytic transformations.<sup>8</sup>

Metalloenzymes are considered amongst the most proficient catalysts in terms of their activity, selectivity, and ability to operate under mild conditions.<sup>8</sup> Additionally, metalloenzymes can express more than one biological functions' depending upon metal cofactor composition while maintaining a conserved protein sequence to create a new metalloisoform. When the metal cofactor of a metalloenzyme is changed, subtle changes in the metal coordination sphere manifest themselves as altered biological functions. This phenomenon is referred to as metal promiscuity, metal plasticity and/or metal moonlighting, allows this class of proteins to change its purpose through simply swapping one metal for another.

An excellent example of such metal promiscuity was reported recently by a team of researchers from Northwestern University who found that at the moment of egg fertilization by the sperm, organelles in the germocyte cells release a significant amount of  $Zn^{+2}$  ions from specialized vesicles, dramatically increasing the  $Zn^{+2}$  concentrations within the zygote. Upon the  $Zn^{+2}$  ion concentration spike, the  $Cu^{+2}$  ions coordinated in membrane-bound metalloenzymes are displaced by  $Zn^{+2}$  ions, turning off the enzyme's original function, thus resulting in the entire

surface of the zygote becoming impervious to other sperm cell entry.<sup>9</sup> Understanding the plasticity of metalloenzymes is an important factor when designing methods to manipulate and utilize metalloenzymes toward therapeutic strategies.

Therefore, absolute metal ion concentrations are tightly regulated in biological systems through a system of metal uptake and extrusion protein complexes which maintain metallo-homeostasis in the organism. A variety of metal transport molecules ranging in size from simple peptides like glutathione, to large proteins like serum albumin, and compartmentalization that create metal ion gradients across membranes all for the expressed purpose of maintaining organism homeostasis.<sup>10-13</sup> Taken together, metalloenzymes have evolved over most of Earth's geologic past to be ideal biological tools for the maintenance and proliferation of all life.<sup>4</sup>

### **Challenges in Targeting Di-metalloenzymes**

Di-nuclear metalloenzymes constitute a large class of proteins in the metalloproteome yet we currently lack effective methods of inhibiting these enzymes for the development of new medical therapies, particularly for the discovery of new antibiotics. The research herein is focused on the investigation of novel methods of interacting with di-metalloenzymes of pharmaceutical relevance, such as unexplored metal-binding functional groups that selectively interact with di-nuclear catalytic centers and also on unique *in silico* analytical techniques to probe enzymatic structure/function relationships. The task of finding new inhibitor strategies that selectively interact with di-metallo catalytic centers is a challenging proposition. Towards this aim, we have targeted three separate di-nuclear metalloenzymes that are unique to bacteria and play key roles in their growth and development.

### **Metal Promiscuity and the Presence of Multiple Isoforms.**

Metal promiscuity and the presence of multiple isoforms (closely-related enzymes) within biological systems is a common feature among di-metalloenzymes that adds an additional challenge to targeted inhibition. This is due to Zn1-Zn2 and Zn1-[M]2 enzyme variants comprising essentially two separate targets that may possess differing active site geometries and enzymatic functionalities.<sup>14-17</sup> Multiple X-ray crystal structures of di-Zn-MP have shown a common catalytic site geometry, with two Zn(II) atoms bound in the active site  $\sim 3.30$  Å apart and bridged by a catalytic water molecule. The coordination sphere of the catalytic Zn metals adopts a distorted tetrahedral geometry in the active site. One metal ion, Zn1, is bound more tightly than the second metal site which can exchange a second Zn (II) for an alternative metal ion *in vivo* or can function with only one Zn(I).<sup>14</sup>

Recent studies indicate the active site metal composition of the di-metallopeptidase DapE may regulate the enzyme's roles between mDAP and lysine biosynthesis and aspartate peptidase activity. Broder and Miller have investigated the promiscuity of DapE acting as an aspartyl peptidase in the presence of different metals by activating DapE with MnCl<sub>2</sub>, which replaces the weaker bound Zn2 metal in the active site, and have shown the enzyme to catalytically cleave the amide bonds of small dipeptide molecules with the general formula of Asp-X, most notably Asp-Ser, Asp-Gly, and Asp-Leu dipeptides (Figure 2). It is also important to mention that Asp-Pro was found to have absolutely no detectable binding with Mn-activated DapE.<sup>14, 15</sup> Their results revealed that DapE's catalytic activity as a peptidase is up to 15x greater when the enzyme is bound to manganese and zinc instead of two zinc ions and that in the Zn/Mn isoform the native substrate N-succinyl-L,L-diaminopimelic acid (L,L-SDAP) and dipeptide Asp-X substrates compete against one another for active site binding.

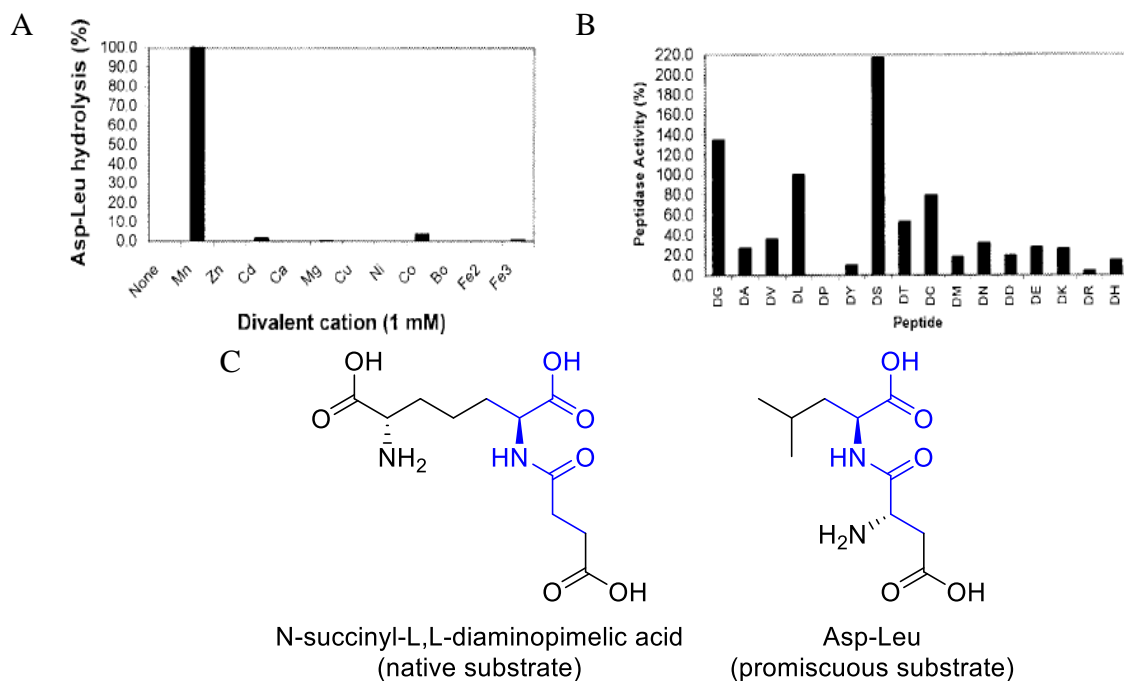


Figure 2. Effect of divalent cations on DapE\_Mn-catalyzed hydrolysis of Asp-Leu. An activity level of 100 % is 222 mol/min/mg. Divalent cations (as chloride salts) were present at 1 mM.<sup>15</sup> B) Substrate specificity of DapE\_Mn for aspartyl peptides with Asp-Leu activity at 100 %.<sup>15</sup> C) Structure Comparison of known DapE Substrates.<sup>14</sup>

The native substrate of the di-Zn isoform of DapE, L,L-SDAP shows similarity with the Mn-activated dipeptide Asp-X specificity and most likely shares key protein/substrate interactions.<sup>15</sup> However, the subtle changes in active site geometries coupled with the differing binding properties of zinc and manganese shed light on the challenge of targeting differing Zn/Zn, Zn/-, and/or Zn/Mn isoforms *in vivo* with a single broad-spectrum inhibitor class.<sup>14</sup>

### Conformational Dynamics.

Major protein conformational changes play a key role in enzymatic activity in this class of enzymes. Metalloenzymes are not static structures but rather are dynamic entities that are in constant motion, therefore, addressing the dynamic nature of the proteins is critical.<sup>18</sup> Any successful inhibitory interaction may involve simultaneous interaction with two separate metallo-centers at once while altering the dynamic movements of the proteins macrostructure.

**Catalytic Center.**

A crucial issue pertaining to the synthesis of novel inhibitor classes for MPs containing dinuclear metal centers stems from the nature of the catalyst itself. The dinuclear metal catalytic centers activate simple water molecules in the strongly basic and potentially nucleophilic hydroxyl form that can cleave peptides or labile functionalities. Any inhibitor selective enough to bind to the active site of a dinuclear metal active site must also be chemically stable enough to survive this environment.

**Metalloenzymes in Focus**

Antimicrobial therapy has saved millions of lives over the past 80 years, yet our arsenal of effective antibiotics is increasingly diminished by the alarming rise of bacteria that are resistant to all currently available antibiotics.<sup>19</sup> Over two million people annually in the United States acquire infections that are resistant to antibiotics, and at least 23,000 people die as a result, according to a report issued by the Centers for Disease Control and Prevention.<sup>20</sup> In the U.S., antibiotic resistance adds \$20 billion in additional direct health care costs, with cost productivity as high as an additional \$35 billion annually.<sup>21</sup> According to the Infectious Disease Society of America, at least ten new synthetic antibacterial drugs need to enter the market by the year 2020 in order to maintain the current quality of healthcare.<sup>22</sup>

There is an urgent need for antibacterial agents with new cellular mechanisms of action, yet the pharmaceutical industry shows little interest in antibiotic research and development even though bacterial infections are a global medical problem.<sup>23</sup> Since the discovery of penicillin in 1928, and the Golden Age of Discovery (Figure 3), antibiotics have been a major tool in fighting infections and saving and extending the lives of millions globally.

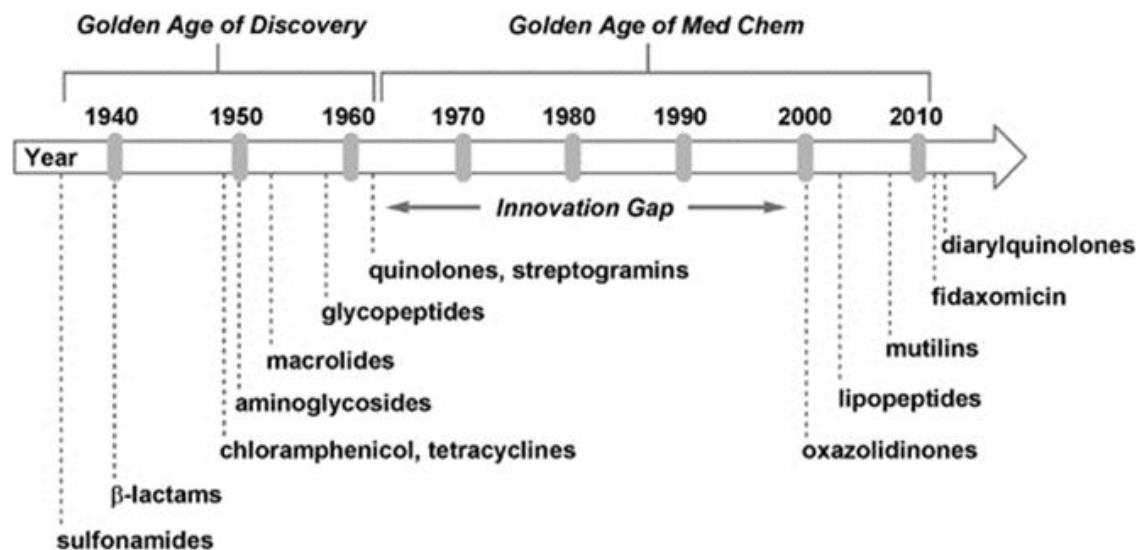


Figure 3. Timeline of antibiotic discovery through medicinal chemistry.

Yet, the emergence of drug resistance in bacteria is reversing the advancements of the past nine decades, with the treatment choices for many bacterial infections becoming increasingly limited, expensive, and, in some cases, nonexistent. The Centers for Disease Control and Prevention has recently reported that there are now several strains of *Staphylococcus aureus* that are resistant to all known antibiotics including vancomycin, underlying the need for research of new antimicrobial targets with previously unexplored mechanisms of action. Thus, researchers have the arduous challenge of developing new methods for combating the spread of infectious bacterial diseases.

The study of MPs has become a growing area of research with the rise of antibiotic resistance in bacteria and the persistent problem of metallo- $\beta$ -lactamases (MBL) that deactivate our most important antibiotics. The impending dilemma of how to manage antibiotic resistant superbugs and the need to discover novel mechanisms of action to block bacterial proliferation has sparked our interest in the study of bacterial metalloenzymes, such as N-succinyl-L,L-diaminopimelic Acid Desuccinylase (DapE), New Delhi Metallo- $\beta$ -lactamase-1 (NDM-1), and



AHL-lactonase (AiiA/AidC) (Figure 4), each of which possesses the unique dinuclear metal center motif. Our strategies and efforts for addressing this dilemma are thus presented herein.

Efforts in our lab to selectively target di-metal specific catalytic sites in metalloproteins have already led to the discovery of separate compound classes that can target each of these three enzymes. These include N-acetyl-5-halo-indoline-6-sulfonamide, N-Cbz-indoline-7-(N-acyl-sulfonamides), simplified N-succinyl- and N-glutamyl aryl sulfonamides, and a series of novel sulfonyl azide-derived sulfonyl triazoles, sulfonyl amidines, sulfonyl imidates and N-acyl-sulfonamides that show potential as di-metalloenzyme inhibitors and a small series of cyclobutanones that have been shown to function as tetrahedral transition state mimics at the catalytic metal center. We have developed robust chemical methods for making these new inhibitors, enabling preparation of analogs to optimize activity. Preliminary docking results suggest that these novel compounds may function as inhibitors over a broad class of di-metalloenzymes.

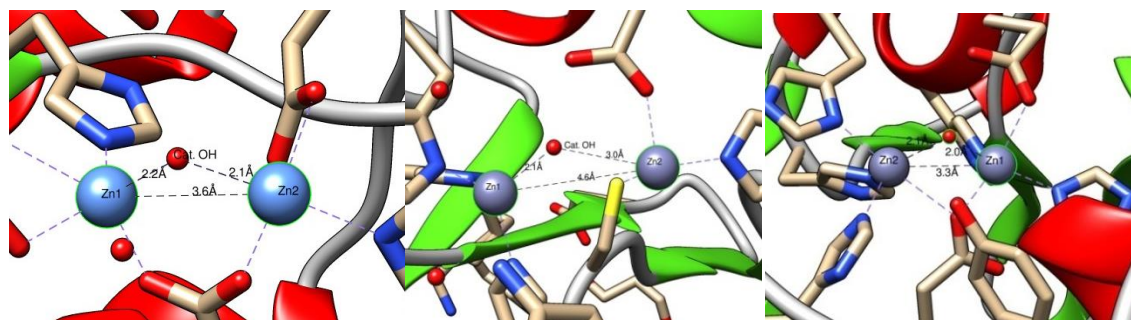


Figure 4. Enzyme active sites for A) N-succinyl-L,L-diaminopimelic Acid Desuccinylase (DapE), B) New Delhi Metallo- $\beta$ -lactamase-1 (NDM-1), C) AHL-lactonase (AiiA/AidC).

#### **N-succinyl-L,L-diaminopimelic Acid Desuccinylase (DapE).**

The bacterial enzyme N-succinyl-L,L-diaminopimelic acid desuccinylase (DapE) offers an excellent target for the development of new antibiotics.<sup>24</sup> DapE is one of the crucial enzymes in the meso-diaminopimelate (mDAP)/lysine biosynthetic pathway utilized by most bacteria,

some archaea, some fungi, some algae, and plants.<sup>25-28</sup> The products of this pathway, mDAP and lysine, are essential components for the synthesis of the peptidoglycan cell wall in Gram-negative and most Gram-positive bacteria, hence inhibitors of enzymes within this pathway should provide a new class of antibiotics. Since there are no analogous pathways in mammals, inhibitors of enzymes in the mDAP/lysine pathway should exert selective toxicity against bacteria without mechanism-related toxicity in mammals. Furthermore, it has been shown that deletion of the DapE gene that encodes the DapE enzyme is lethal to *Helicobacter pylori* and *Mycobacterium smegmatis*<sup>29, 30</sup> and only in the presence of mDAP supplemented media was the *H. pylori* deletion mutant able to grow, and not in the presence of only lysine supplemented medium. Therefore, DapE is essential for prokaryotic growth and proliferation but is absent in mammals, thus providing a very attractive antibiotic target with a new mechanism of action.<sup>24</sup>

Therefore, it is important to study this enzyme in the mDAP/Lys pathway, and enhance the structural and mechanistic understanding of DapE through crystallographic studies of wild type and selected mutants. It is of equal importance to synthesize potent and ultimately druggable inhibitors toward a new generation of antibiotics.

### **New Delhi Metallo- $\beta$ -lactamase-1 (NDM-1).**

Multidrug-resistant *Mycobacterium tuberculosis*, methicillin-resistant and vancomycin-resistant *Staphylococcus aureus*, and *bla*<sub>NDM-1</sub>/*bla*<sub>KPC</sub> *Klebsiella pneumoniae* are significant global threats.<sup>31</sup>  $\beta$ -Lactam antibiotics penicillin, cephalosporin and carbapenems represent more than 50 % of antibiotic usage worldwide, and are among the cheapest and most effective antibacterial agents available, but growing resistance to these drugs is a major concern.<sup>17</sup>

Metallo- $\beta$ -lactamases (MBLs) are a diverse set of enzymes that catalyze the hydrolysis of a broad range of  $\beta$ -lactam drugs conferring resistance to the bacteria. New Delhi metallo- $\beta$ -

lactamase 1 (NDM-1), shown in Figure 5, is a zinc-dependent metallohydrolase belonging to the B1 family found in bacteria that confers resistance to commonly administered antibiotics, including penicillins, cephalosporins, and carbapenems.<sup>17, 32, 33</sup>

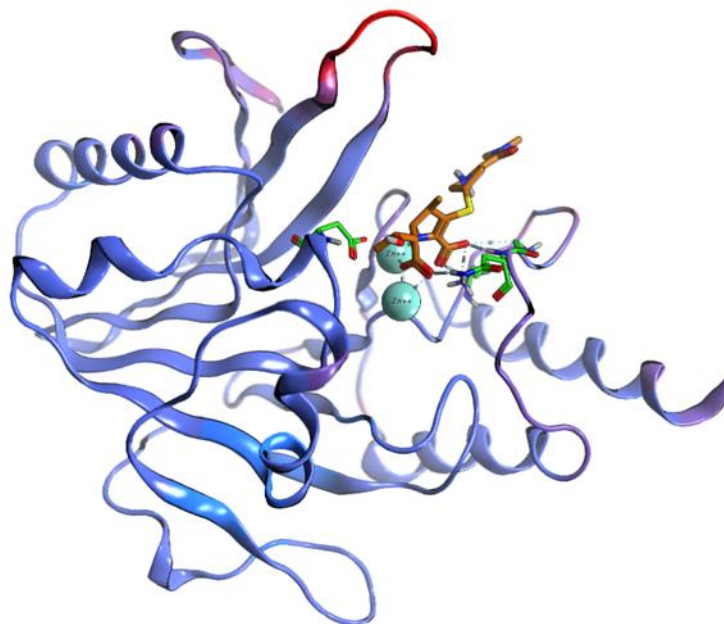


Figure 5. Crystal structure of NDM-1 (B-factor ribbon model) bound to the hydrolyzed form of the common antibiotic meropenem seen in orange (PDB ID: 4EYL).

Horizontal gene transfer has enabled the *bla*<sub>NDM-1</sub> gene encoding NDM-1 to spread between species, facilitating the development of multi-drug resistant bacterial strains.<sup>17, 34</sup> Bacteria carrying the *bla*<sub>NDM-1</sub> gene have been found on all continents, and consequently, NDM-1 has gained international attention as a clinically relevant pharmaceutical target.<sup>32, 35-54</sup> Known inhibitors of MBLs, such as thiol-containing inhibitors, are prone to oxidation and challenges with selectivity due to the thiol moiety.<sup>55</sup> As such, drug development efforts of NDM-1 have proven ineffective due to a lack of effective inhibitors.

**AHL-lactonase (AiiA/AidC).**

AiiA-related metalloenzymes utilize a di-Zn metallo center to catalyze the hydrolysis of important N-acyl homoserine lactones (AHLs) important for cell-to-cell communication between bacteria.<sup>56-59</sup> Development of drug-like molecules that are capable of targeting metal centers in AiiA and related enzymes are predicted to disrupt the quorum sensing/quenching mechanism between bacterial communities and provide another chemical tool for studying these systems. Since each species of bacteria has specific and unique molecules for quorum sensing, tailor-made inhibitors may modulate the risk of specific bacterial proliferation.<sup>59</sup> Our collaborative work with Dr. Liu's crystallography research group to target AiiA di-Zn-dependent lactonase with a small series of  $\alpha$ -amido cyclobutanones possessing a C6 and C10 hydrocarbon tails, synthesized using chemistry pioneered in the Becker research lab, has resulted in co-crystal structures of our inhibitors bound to the metallo active site of AiiA-cobalt (AiiA\_Co). The electron density of the C6 cyclobutanone co-crystal was not resolved enough to make an accurate atom placement. Surprisingly, because the extra length of the C10 alkyl chain was able to interact with the hydrophobic phenylalanine clamp region of AiiA adjacent to the active site,<sup>60</sup> atomic placement of the C10 alkyl chain and cyclobutanone functionality of N-(2-oxocyclobutyl)decanamide was assigned. However, the determination of the co-crystalized cyclobutanone did not show the presence of the trapped tetrahedral transition-state mimetic of cyclobutanone (Figure 6), as hypothesized, but rather the ring-opened product 4-decanamidebutanoic acid. The ring-opened product was synthesized and confirmed by NMR.

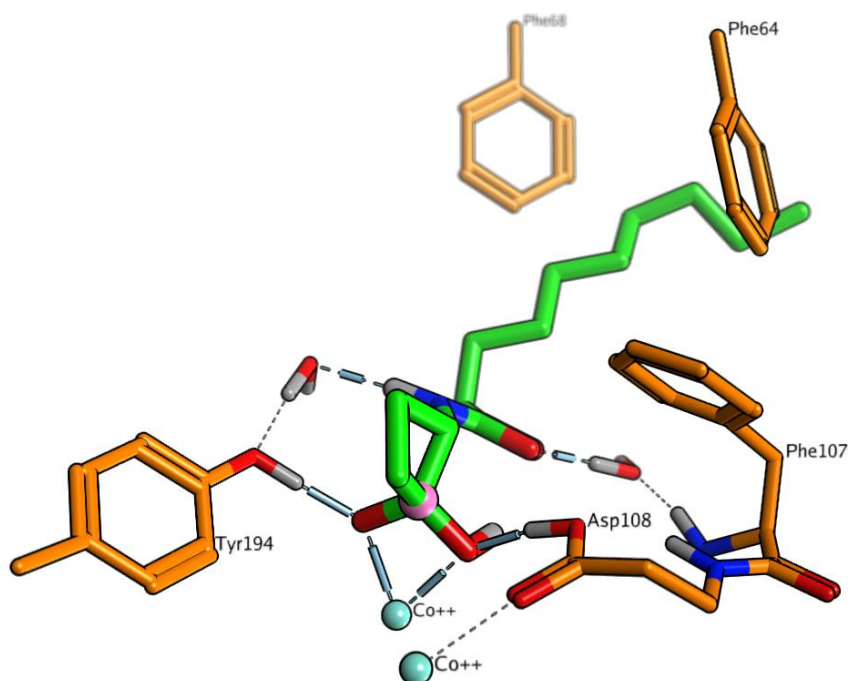


Figure 6. Modeled structure of AiiA\_Co AHL metallo-lactonase bound to N-(2-oxocyclobutyl)decanamide as the tetrahedral transition state mimetic.

Follow-up experiments were performed to determine whether the presence of the observed ring-opened product originated from enzymatic catalysis or radiation damage during crystallographic data collection. A discontinuous assay experiment was performed in conjunction with radical catalyzed organic reaction screening with AIBN,  $H_2O_2$ , and  $H_2O_2$  in the presence of various metal salts. A series of radical-mediated synthetic experiments, including an X-ray exposure assay performed at Argonne National Laboratory, were also carried out to assay the ability of the cyclobutanone to be opened under chemical means. These experiments are in progress and the results will be disclosed in due course.

CHAPTER TWO

INSIGHT INTO LARGE CONFORMATIONAL CHANGES, SUBSTRATE AND  
PRODUCTS BINDING AND RELEASE IN N-SUCCINYL-L,L-DIAMINOPIMELIC ACID  
DESUCCINYLAASE

**DapE's Structural Background**

The *dapE*-encoded N-succinyl-L,L-diaminopimelic acid desuccinylase (DapE) is a late-stage dinuclear zinc(II) dependent M20 metallopeptidase in the lysine biosynthetic pathway.<sup>25-27</sup> Most bacteria, plants, and algae use this pathway to synthesize mDAP and lysine from aspartic acid through three related pathways that diverge after the production of L-tetrahydrodipicolinate (Figure 7). In bacteria, lysine biosynthesis is required for protein synthesis and is also used in the peptidoglycan layer of Gram-positive bacterial cell walls. The amino acid meso-diaminopimelate (mDAP), is also an essential component of the peptidoglycan cell wall for Gram-negative bacteria.

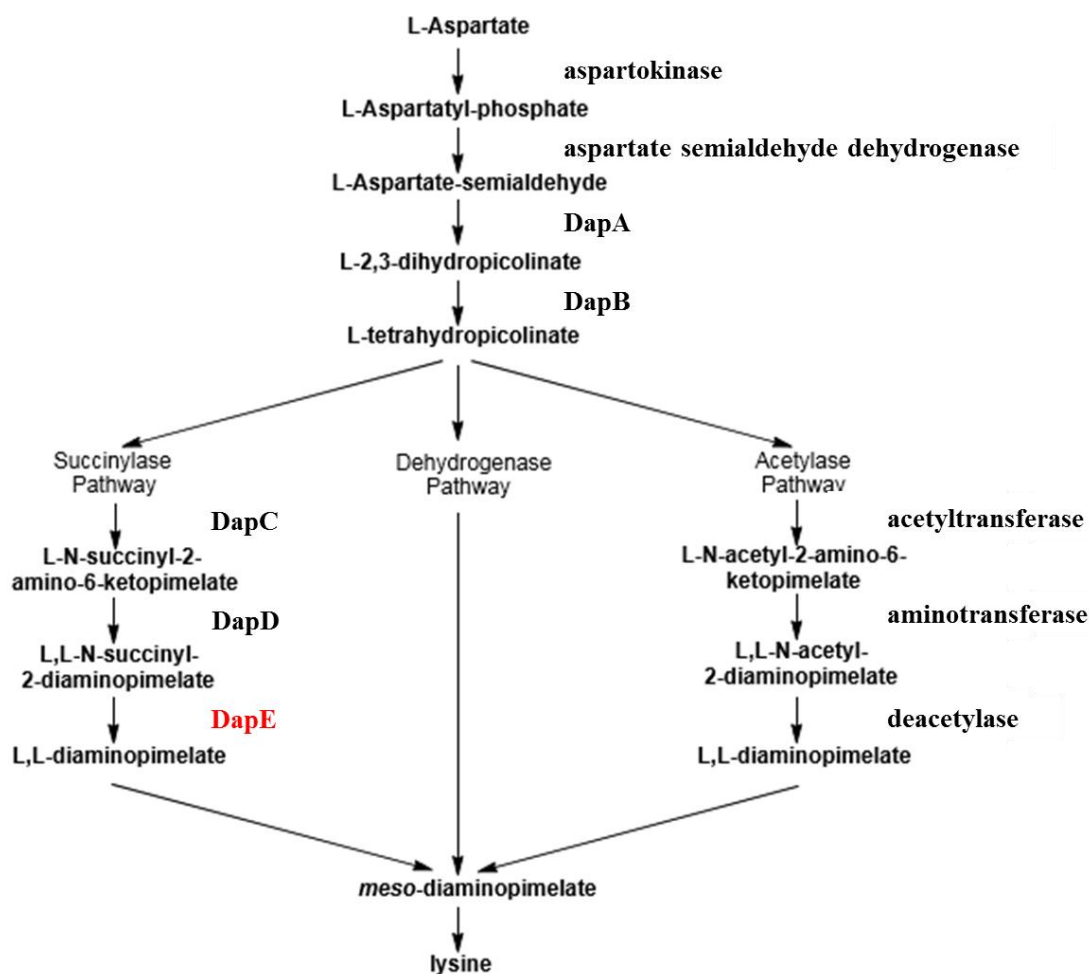


Figure 7. Biosynthetic Pathways of meso-diaminopimelic acid and lysine in bacteria. DapE is indicated in red.<sup>61</sup>

The gene responsible for encoding the bacterial metalloenzyme DapE have been identified in many pathogenic Gram-positive and Gram-negative bacteria and purified from multiple sources. Furthermore, it has been shown that deletion of the *dapE* gene that encodes DapE is lethal to *Helicobacter pylori* and *Mycobacterium smegmatis*<sup>29, 62</sup> Only in the presence of mDAP supplemented media was *H. pylori* able to grow, but not in the presence of Lys supplemented medium. Therefore, DapE is essential for bacterial cell growth and proliferation but is absent in mammals, thus providing a very attractive antibiotic target with a new mechanism of action.<sup>24</sup>

Much of the biochemical and structural work on DapE enzyme has come from studies performed by our collaborators Dr. Richard Holz and Dr. Boguslaw Nocek on model organisms *Neisseria meningitidis* (NmDapE) and *Haemophilus influenzae* (HiDapE). X-ray structures<sup>63</sup> of DapEs from NmDapE and HiDapE revealed almost identical homodimeric architectures, as expected given a high degree (57 %) of sequence identity. HiDapE has an elongated shape as shown in Figure 8.

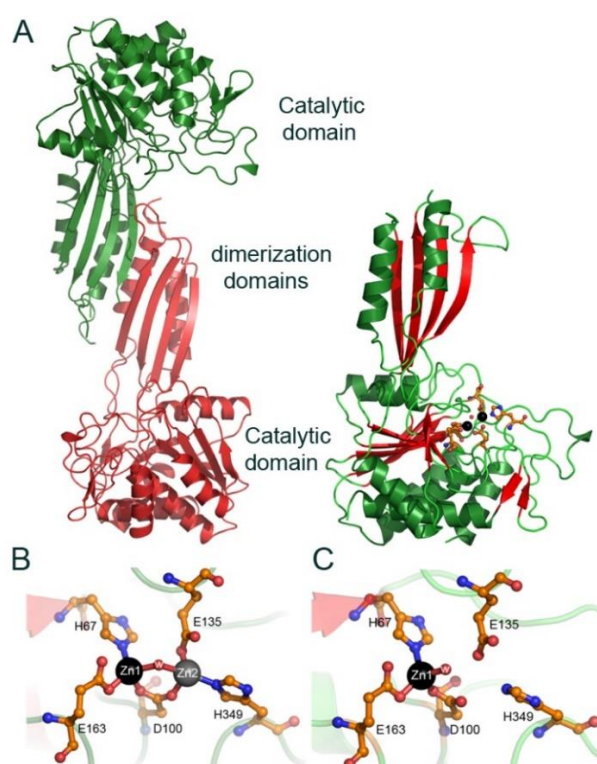


Figure 8. A) Ribbon diagram of HiDapE dimer and monomer, B) di-zinc active site, C) mono-zinc active site.

Each subunit of the dimer consists of two functional domains: an  $\alpha/\beta$  catalytic domain, which houses the active site, and the dimerization domain attached to the catalytic domain via flexible linkers. The catalytic domains are enclosed by several functionally important loops, most notably loop V seen in Figure 9.



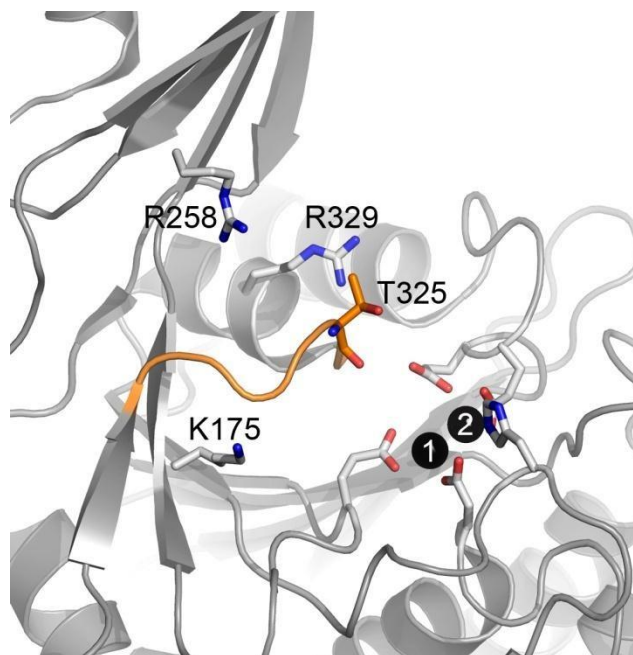


Figure 9. The active site of WT-HiDapE showing loop V in orange. T325 resides on loop V directly over the dinuclear active site.

The location and architecture of the active sites are strikingly similar to the dinuclear active sites of other members of M20 and M28 family of dinuclear Zn(II)-dependent metalloproteases such as the leucine aminopeptidase AAP from *Aeromonas proteolytica* and the carboxypeptidase CPG2 from *Pseudomonas sp* strain-RS-16.<sup>64, 65</sup> The active site of DapE (Figure 8B) contains two Zn(II) ions at a distance of  $\sim 3.3$  Å. Each of the Zn(II) ions adopts a distorted tetrahedral geometry and is coordinated by one imidazole group (H67 for Zn1 and H349 for Zn2) and one carboxylate group (E163 for Zn1 and E135 for Zn2). Both Zn(II) ions are bridged by additional carboxylate groups (D100) on one side and water/hydroxide on the opposite side, forming a ( $\mu$ -aquo)( $\mu$ - carboxylato)dizinc(II) core with one terminal carboxylate and one histidine residue at each metal site. By limiting the amount of divalent metal ions present during crystallization our group obtained both the mono- and dinuclear forms of the active site. In the active site of mono-Zn(DapE), Zn1 resides in a distorted tetrahedral geometry coordinated by the carboxylate oxygens (OD1) of D100 and (OE1) of E163 as well as one nitrogen atom (NE2) of

H67 and an oxygen atom provided by a water molecule.<sup>63</sup>

Analysis of mono and dimethylated DapE structures and previously reported kinetic and spectroscopic studies on DapE enzymes allowed a refined mechanism of the catalysis for DapE enzymes to be proposed (Figure 10).<sup>63, 66-68</sup> It was proposed that the first step in catalysis for DapEs is likely recognition of the L,L-SDAP side chain by the cavity adjacent to Zn1. Next, the peptide carbonyl oxygen of L,L-SDAP coordinates to Zn1, expanding its coordination number from four to five, and activating the carbonyl for nucleophilic attack. Deprotonation of the metal-bound water molecule by E134 to form a nucleophilic hydroxide moiety is consistent with the postulated pKa of the zinc-bound water molecule.<sup>25</sup> Once the zinc-bound hydroxide is formed, it could attack the activated carbonyl carbon of the substrate, forming a  $\eta$ -1- $\mu$ -transition-state complex. Steady-state kinetic experiments verified a metal-dependent mechanism, with a  $K_m$  for N-succinyl-L,L-diaminopimelic acid of 1.3 mM and a turnover number of 200 s<sup>-1</sup> in the presence of zinc. Solvent kinetic isotope effect studies yielded an inverse kinetic isotope effect, that was explained by the attack of a zinc-bound hydroxide on the amide carbonyl.<sup>25</sup> E134 may provide a proton to the penultimate amino nitrogen, similar to that observed for AAP, returning it to its ionized state and facilitating product release.

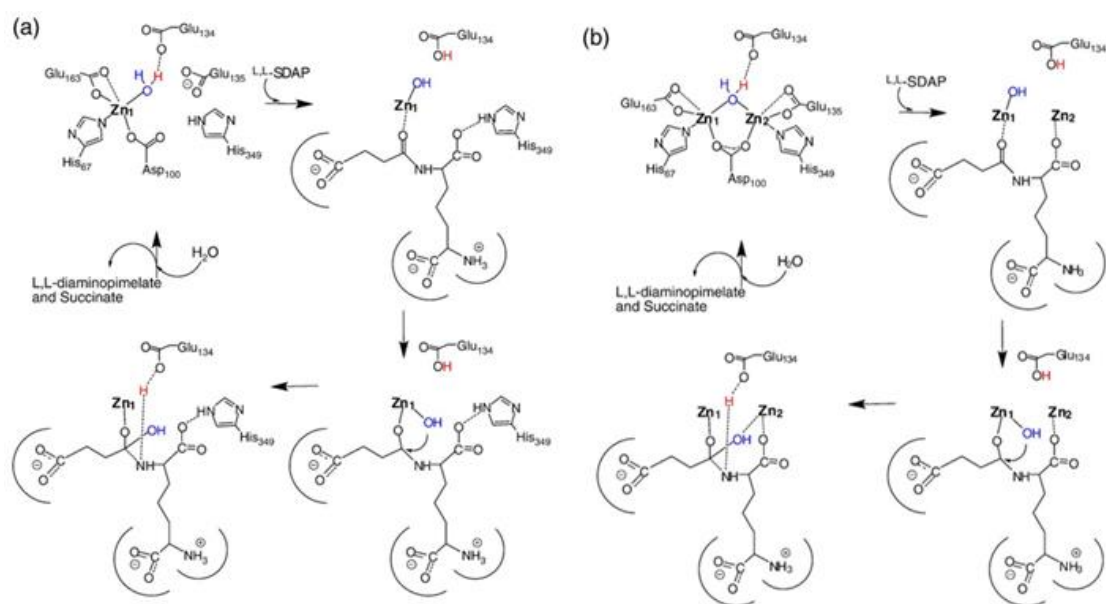


Figure 10. Previously proposed mechanism of DapE (a) mono zinc DapE and (b) dizinc DapE.<sup>63</sup>

Once the products are released, the water molecule bridging the two metal ions is replaced. In the absence of a second metal ion, the catalytic mechanism does not likely change markedly as H349 is in position to assist in orienting the substrate properly in the active site through the formation of a hydrogen bond with a carboxylate side chain of the substrate, thereby stabilizing the transition-state intermediate reminiscent to proposals for the mono-metallated forms of AAP and EcMetAP.<sup>69-71</sup> In the presence of a dinuclear site, it was proposed that the second metal ion coordinates either the peptide carbonyl oxygen in a bridging fashion or a carboxylate side chain of the substrate.

Structural analysis of M20 metalloproteases showed that these enzymes exist either as dimers with both catalytic and dimerization domains, or as monomers having a single catalytic domain, yet the substrate specificity of these enzymes remains poorly understood. To understand the specific role of each domain of DapE, truncated versions of DapE were previously engineered that possessed only the catalytic domain, are monomeric in solution, and closely resemble AAP (Figure 11). It was found that removal of the dimerization domain in DapE

rendered the enzyme inactive, suggesting that the dimerization domain function is critical in catalysis.<sup>72</sup>

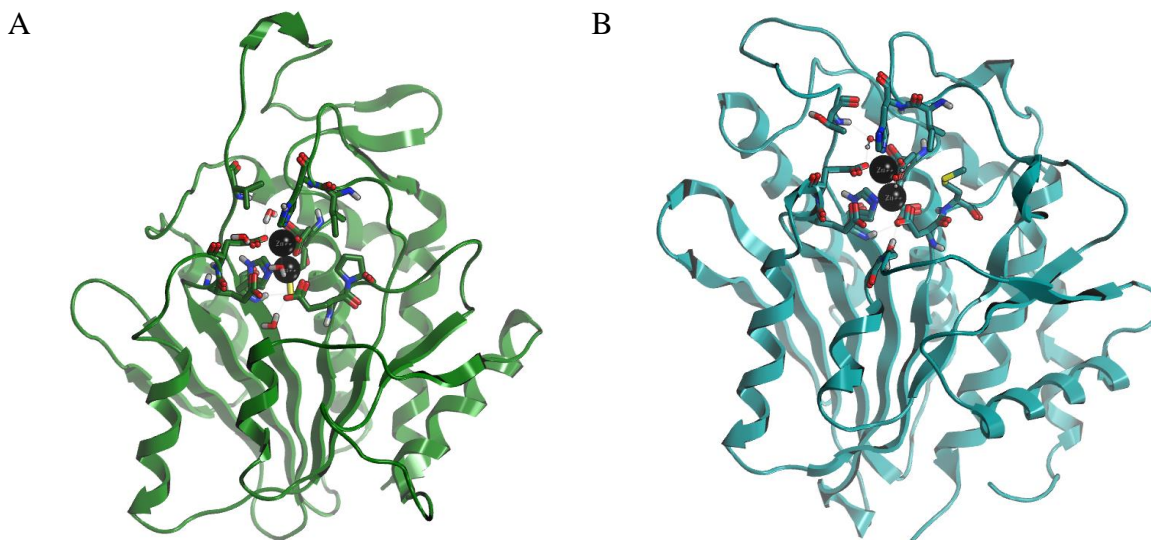


Figure 11. Ribbon diagrams showing DapE's truncated catalytic domain from *Haemophilus influenzae* (Green) in comparison to Aminopeptidase from *Aeromonas proteolytica* (Teal).

It was concluded that the dimerization domain likely restricts the conformational freedom of the active site and contributes several residues to the active site environment (H194, R179, R258, T325) that are important for substrate recognition and binding. Recent molecular dynamics studies of DapE by Mishra<sup>73</sup> further confirmed the results, suggesting plasticity of the architecture of DapE, and suggested that the enzyme undergoes significant conformational changes upon SDAP binding. Additionally, Mishra proposed a list of residues (K175, R178, N345, K350) involved in binding.<sup>73</sup>

The binding mode of the DapE inhibitor L-captopril was revealed by 1.8 Å resolution complex structure of NmDapE with L-captopril showing clear electron density corresponding to L-captopril inside a positively charged binding groove formed between the catalytic and the dimerization domains (Figure 12).<sup>74</sup> The structural work revealed that the sulfhydryl group of L-captopril bridges the two active site Zn(II) ions while displacing the bridging water molecule

(Figure 12B) The carboxylate of the proline moiety of L-captopril forms a hydrogen bond with N346 (ND2–O3, 3.0 Å) and the amide of G325 (N–O2, 2.9 Å). It also makes a strong hydrogen bond with the hydroxyl of Y198 (OH–O3, 2.5 Å), which reaches over from the second subunit of the dimer. The significant interaction with the residues from the opposite dimerization subunit of the dimer was certainly unexpected and indicates that both domains play a functional role in substrate binding. The O1 peptide carbonyl oxygen of L-captopril forms a hydrogen bond with a well-ordered water molecule (2.8 Å) that is stabilized by its interaction with R179 (NH2–O, 3.1 Å) and P165 (2.6 Å). Thiols are commonly used as inhibitors of Zn(II) metalloproteins because Zn(II) is a relatively soft acid and thiols are soft bases, however, organosulfur compounds have a higher potential for drug-induced toxicity and off-target interactions.

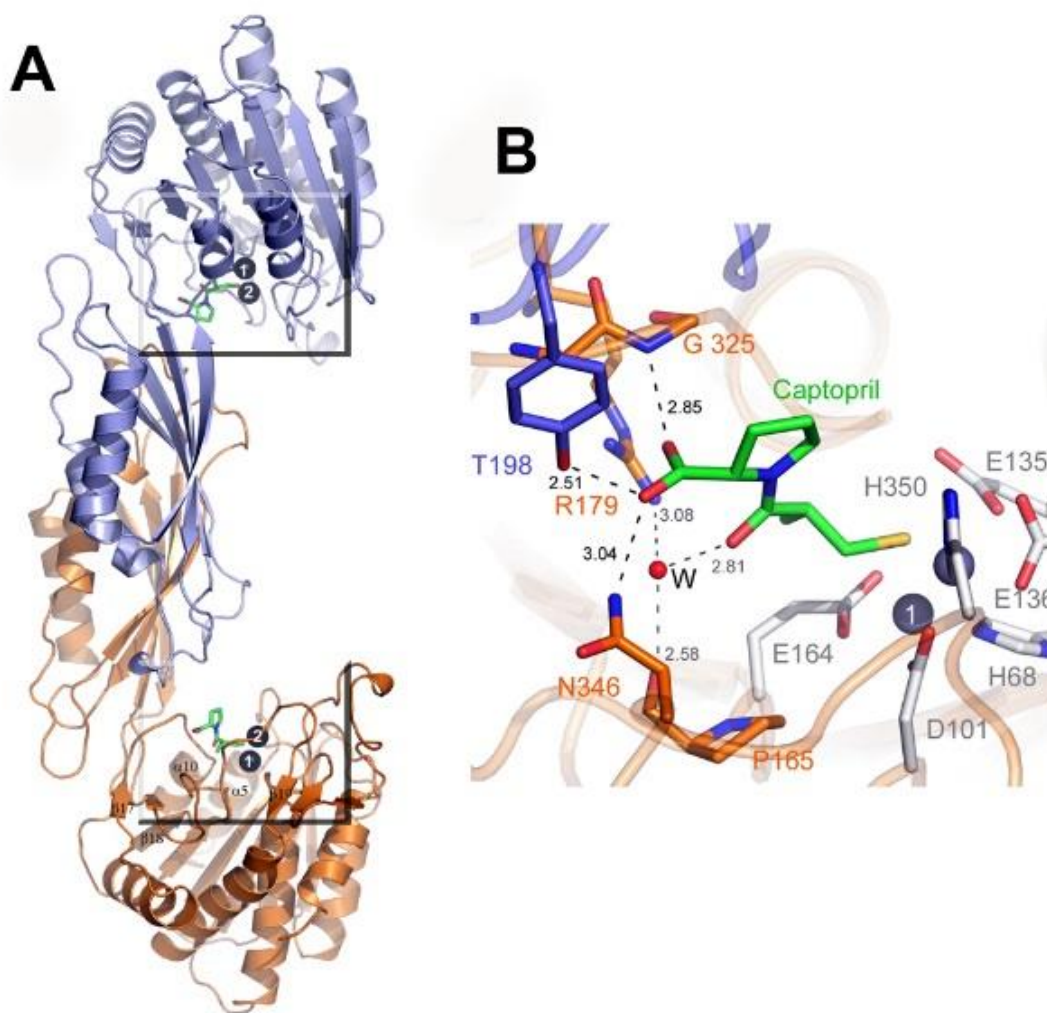


Figure 12. ZnZn\_NmDapE complex with L-captopril. A) Ribbon diagram of NmDapE homodimer, subunits in blue and orange; B) active site with L-captopril, key residues, and a water molecule (red sphere).

### Product Bound DapE

We have characterized a new crystal form of DapE that was grown in the presence of the substrate (L,L-SDAP). This structure unveiled HiDapE with the significantly changed dimensions  $47 \times 45 \times 111 \text{ \AA}$  (Figure 13B), with the active sites completely enclosed and inaccessible, and where the enzymatic reaction has occurred producing a remarkable product-bound complex. An overlay of the product-bound HiDapE and apo-HiDapE structures reveals large domain shifts, with the catalytic domains rotated approximately 50 degrees and moved

closer to the dimerization domains by  $\sim 11$  Å. These results show that HiDapE enzyme undergoes dynamic modulation between the open and closed states, likely induced by substrate binding.

The overall movement is consistent with a hinge domain mechanism, which enables both domains to interact with the substrate. The HiDapE product-bound structure reveals the surprisingly flexible nature of DapE's active site and identifies several new protein-ligand interactions which have not been predicted either by docking attempts or molecular dynamics.<sup>75</sup> The HiDapE-product structure shows that the active site can be divided into succinic acid and diaminopimelic acid binding pockets and that both domains play a key role in recognition and catalysis. Furthermore, this structure has enabled application of our new computational analysis to explore the enzymatic mechanism.

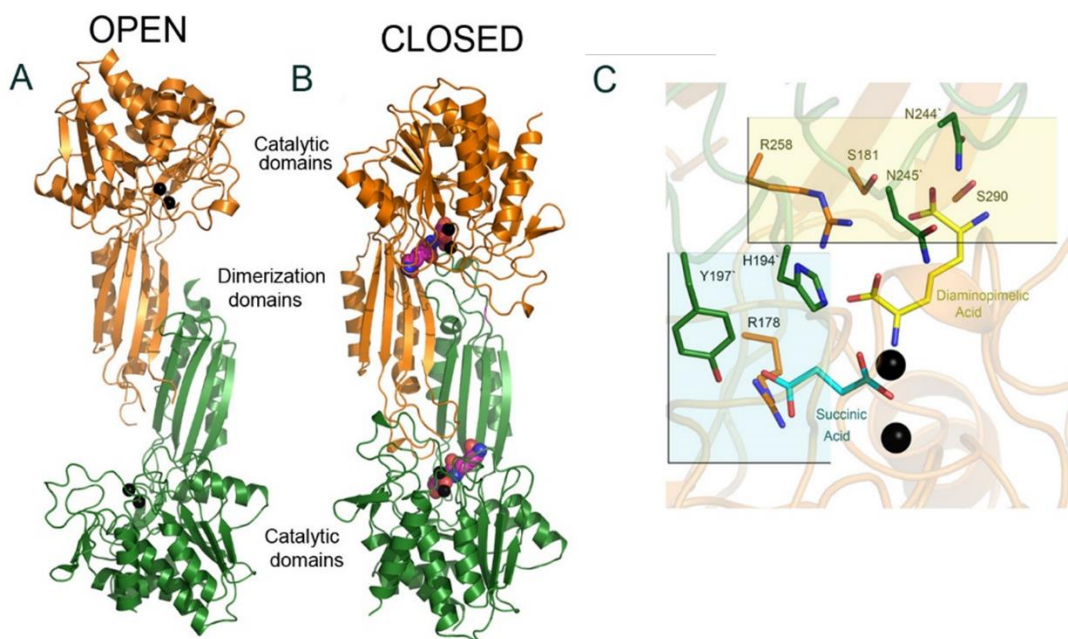


Figure 13. Structures of dimetaleted HiDapE in ligand free form (A: open conformation) and HiDapE product bound form (B: closed-conformation) (C). Active site of HiDapE showing binding interactions of succinic acid and diaminopimelic acid.



## Experimental Procedures

### Protein Expression, Purification, Crystallization, & Structure Determination.

Detail cloning, expression and purification of HiDapE enzyme was performed by our collaborator Dr. Boguslaw Nocek at Argonne national laboratory according to the standard protocol described previously.<sup>72</sup> Specifically, prior to crystallization 50 mM N-succinyl-L-lysine dihydrochloride (SDAP) was added to HiDapE protein and equilibrated on ice for 30 min. Almost three hundred commercially available conditions were used for screening by the sitting-drop vapor-diffusion method at 16 °C using a Mosquito liquid handling robot with 96 well plates. Crystals grew in 10-different conditions within 3 weeks. The best crystals were obtained using 400 nl of a precipitant solution (0.05 M HEPES pH 7.3, 10.7 % (w/v) PEG MME 2000, and 8.6 % (w/v) PEG 2000) and 400 nl of 18 mg/ml solution of HiDapE. The crystals belonged to the orthorhombic space group I222 with unit cell parameters  $a = 56.6 \text{ \AA}$ ,  $b = 135.5 \text{ \AA}$ ,  $c = 149.6 \text{ \AA}$ , and  $\alpha = \beta = \gamma = 90^\circ$ , and one molecule within the asymmetric unit.

The presence of Zn ions in the protein crystals of HiDapE was confirmed by the X-ray fluorescence spectrum. Data was collected on the 19-ID beam line of the Structural Biology Center at the Advanced Photon Source using SBC-Collect software at a wavelength of  $0.9795 \text{ \AA}$  from the single crystals and were processed using HKL3000. The structure of the complex of HiDapE was determined by molecular replacement using the catalytic and dimerization domains separately (PDB ID 4H2K and 3ISZ)<sup>63, 72</sup> as search models. Analysis and validation of the structures were performed with the aid of MOLPROBITY and COOT validation tools. Figures were prepared using Pymol. The atomic coordinates and structure factor file for the complexed structure of HiDapE have been deposited in the RCSB Protein Bank with PDB ID: (TBD).



**Product-Based Transition-State Modeling (PDTSM).**

We employed the HiDapE product-bound structure as a starting point to model in reverse chronological time back through a model of the tetrahedral intermediate and further back to a hypothetical model of the bound substrate and the catalytic water in the active site of DapE. This method, which we refer to as “Product-Based Transition State Modeling” (PBTSM), is intended to provide a hypothetical model of the substrate binding geometry before initiation of the catalytic cycle. This modeling technique was performed using the Chemical Computing Group’s Molecular Operating Environment (MOE).<sup>76</sup> A step-by-step description of the PBTSM protocol is outline in Figure 14 below, which hereafter will be referred to as Figure14-Step# in the following text to refer to steps 1 through 7.

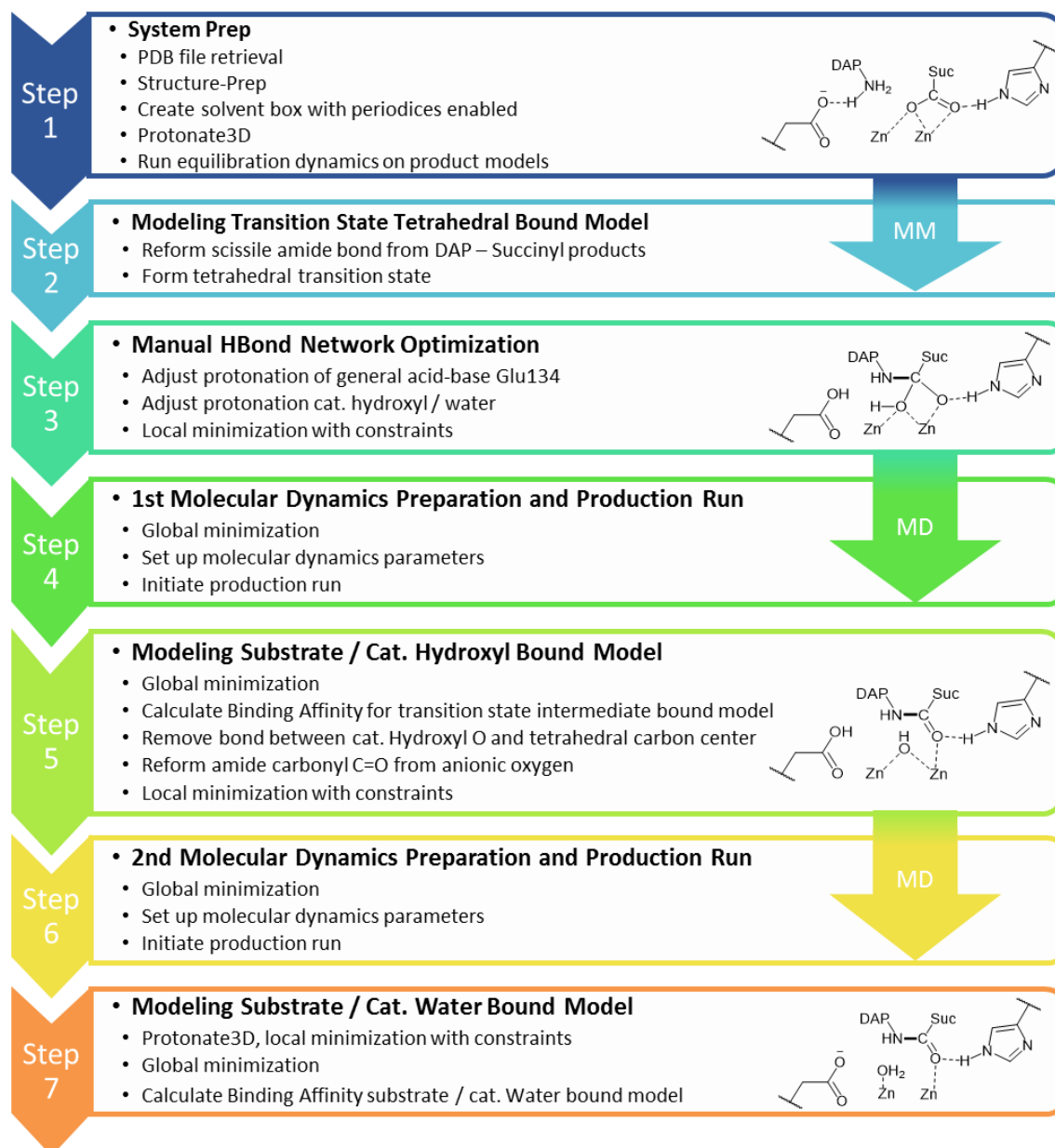
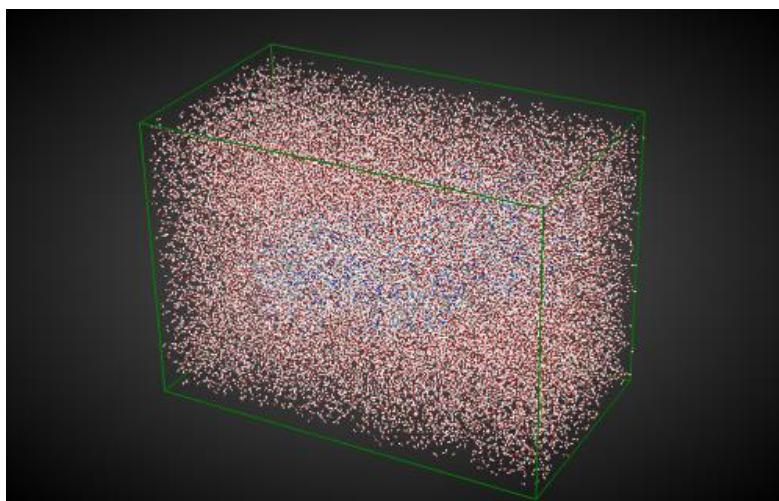


Figure 14. PBTSM Protocol.

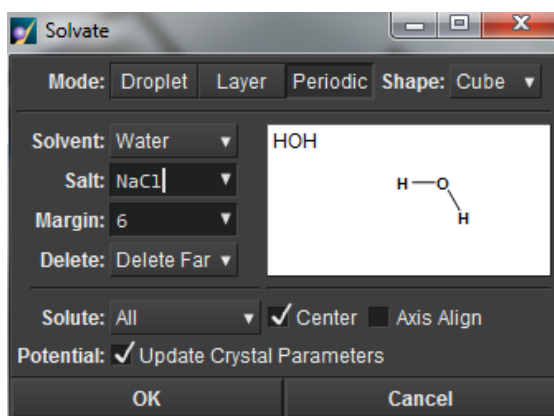
After upload of the crystallographic data of the product-bound structure, the system was prepared using MOE's utility Structure-Prep to correct problems encountered in crystallographic data such as missing loops, empty residues, chain termini or breaks, missing disulfide bonds or atom names, picking alternate conformations, and other potential artifacts.<sup>76</sup> The model was then solvated in a simple water box at pH of 7.4 (Figure 15A) which was treated with NaCl counter

ions to balance the charge (Figure 15B). Periodic boundary conditions were enabled, and the hydrogen bonding network of the model was optimized by automatic sampling different tautomer/protomer states using Protonate3D.<sup>77</sup> Protonate3D is employed to calculate optimal protonation states, including titration, rotamer and “flips” using a large-scale combinatorial search.<sup>78</sup> A localized energy minimization was run on the solvated system using the MOE function QuickPrep (Figure 15C) followed by a short global minimization to equilibrate the system for further modeling. After structural preparation, solvation and energy optimization using MOE, the product bound HiDapE molecular model is referred to as the model Suc\_DAP\_DapE\_PC (Figure 14-Step1).

A



B



C

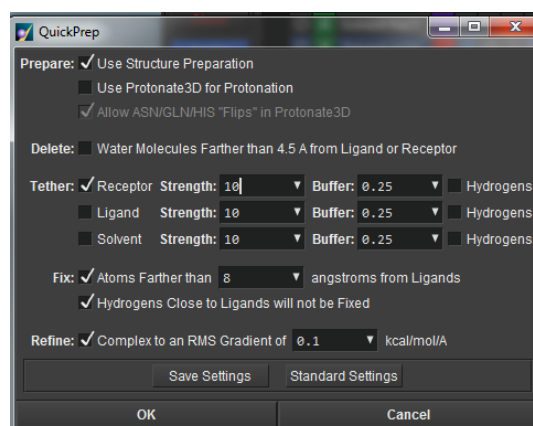


Figure 15. A) Solvent Box of LLSDAP transition state intermediate DapE model. B) Solvate Function. C) QuickPrep Function.

Upon completion of system equilibration, product atom coordinates were used to model the tetrahedral transition state intermediate of the substrate-catalytic hydroxyl bound structure. This model was referred to as the LLSDAP-TS\_DapE\_PC model and reflects the moment just after nucleophilic attack by the activated hydroxyl group at the amide carbonyl of the substrate which forms the tetrahedral transition state intermediate but just before cleavage of the scissile amide bond. The double bond of the succinyl carbonyl, proximal to di-Zn metal center, were converted to a single bond using the Builder utility in MOE. The scissile amide bond was then reformed by creating a bond between the ammonium nitrogen of DAP to the carbonyl carbon of succinate atoms proximal to the metal cofactors. The results of the remodeling are the creation of a distorted tetrahedral transition state intermediate of the substrate and catalytic hydroxyl group possessing distorted bond distance/angles (Figure 14-Step2). It should be noted here that a transition state by definition is an energy maximum whereas the tetrahedral intermediate is a local energy minimum, yet given that formation of the tetrahedral intermediate is an endothermic process, Hammond postulate states that the tetrahedral intermediate is a good approximation of the transition state. In medicinal chemistry, a mimetic of the tetrahedral intermediate is a transition state mimetic, and the language herein reflects this convention.

At this point, the hydrogen bonding network was manually optimized, and charge adjustment of the tetrahedral atoms in the transition state was applied to the formal charges of the ammonium nitrogen and the alkoxide oxygen associated with the amide carbonyl of the substrate, resulting in a neutral and negative charge respectively. This was followed by hydrogen bond network optimization of the important active site residues critical for catalysis and transition state intermediate stabilization. These residues were manually adjusted so that active site formal charges kept the overall net charge of the system balanced throughout the

process and conservation of matter was strictly adhered to. In total, these minor, but critical system adjustments most heavily affected the ionization states and hydrogen bonding motifs of the general acid-base Glu134, the amide associated nitrogen and oxygen atoms, and the catalytic water/hydroxyl group atoms. At this stage in the protocol, a localized minimization was conducted to normalize the bond distances/angles of the L,L-SDAP-OH transition state intermediate to reasonable values as well as balance the net charges of ligand/receptor system (Figure 14-Step3).

Following preparation of the *in silico* generated substrate transition state intermediate model, a relatively short 1.0 ns molecular dynamics equilibration was performed using an NPA algorithm with a Amber12:EHT force field (Figure 16). The MD experiment was initiated with parameters as followed: initial heating from 0 K to 300 K over 100 ps followed by equilibration for 100 ps at 300 K, followed by a 700 ps production run, and finally a 100 ps cooling from 300 K to 0 K (Figure 14-Step4). After completion of the dynamics equilibration run, two major changes were observed in the transition state intermediate bound model. The hydrogen bond network strengthened, as indicated by swelling hydrogen bond and vdW contact-cylinder representations between ligand and receptor, and an increase in atom distance of the catalytic Zn metals from 3.3 Å to 3.97 Å was observed.

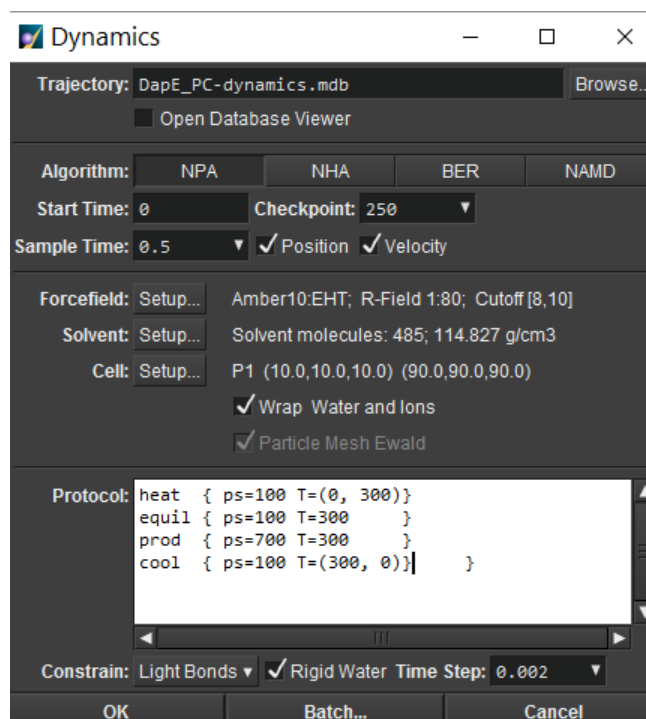


Figure 16. Molecular Dynamics Protocol Window in MOE.

Step 5 in the PBTSM protocol used the final transition state intermediate model from the previous step to estimate the atomic coordinates of the catalytic hydroxyl group and native substrate bound to the metal center of the product binding conformation of DapE. This following model was referred to as the LLSdap\_OH\_DapE\_PC model and reflected the moment just after deprotonation of the catalytic water by general acid-base Glu134 but just before nucleophilic attack by the activated hydroxyl group at the amide carbonyl of the substrate. MOE's Builder utility was again utilized to first remove the bond between the tetrahedral carbon center and the oxygen closest to the Zn ion and Glu134 followed by a ionization state adjustment of the newly formed catalytic water/hydroxide oxygen to a negative ( $\text{O}^-\text{C}---\text{X}---\text{OH}$  to  $\text{O}^-\text{C}^-\text{OH}$ ). Thus, the catalytic hydroxyl group, coordinated to the metallo-center, was modelled into the system in the approximate area observed in other known crystal structures of DapE. Next, a double bond was reestablished between the tetrahedral carbon center and the anionic oxygen of

the transitional state (  $\text{O}^-$ -C-NH to  $\text{O}=\text{C}$ -NH) to reform the amide carbonyl. Finally, a local minimization with constraints was initiated to correct for distorted molecular bond angles and distances resulting from the Builder manipulations (Figure 14-Step5).

After the *in silico* generated substrate and catalytic hydroxide model was prepared, a second 1.0 ns molecular dynamics equilibration was performed using an NPA algorithm with a Amber12:EHT force field. The MD experiment was initiated with parameters as followed: initial system heating from 0 K to 300 K over 100 ps followed by an equilibration stage at 300 K over 100 ps before an 800 ps production run at constant temperature. The dynamics experiment was concluded with a final 100 ps cooling stage from 300 K to 0 K (Figure 14-Step6).

The last step in the PBTSM protocol was a continuation of the previously generated model which was used to estimate the atomic coordinates of the catalytic water group and native substrate bound to the metal center of the product binding conformation of DapE. This last model was referred to as the LLSRAP\_HOH\_DapE\_PC model and reflected the moment just after substrate complexation to the metallo active site, displacement of the metal-bridging catalytic water to a single Zn ion closest to the general acid-base Glu134 and subsequent conformational closure of the active site by the dimerization domain thus forming the product binding conformation of DapE. This model's point in time also falls just before activation of the catalytic water by Glu134 deprotonation. The final model was generated using Protonate3D followed by QuickPrep to reoptimize the hydrogen bonding network and perform a localized energy minimization before a final global energy minimization. The final steps in the PBTSM modeling protocol results in deprotonation of the neutralized carboxylic acid side chain of Glu134 along with a simultaneous protonation of the catalytic hydroxyl group (Figure 14-Step7).

## Molecular Dynamics for Analysis of Product Release.

Former undergraduate researcher Kaitlyn Lovato, in collaboration with Dr. Ken Olsen, employed NAMD to gain insight into the structural dynamics of DapE. Using our previously reported open conformation of DapE and guided by the newly-obtained structure of DapE with the cleaved substrate products, L,L-DAP and succinate were modeled into both active sites of DapE in Visual Molecular Dynamics (VMD). In a computer generated solvent box, a 50 ns molecular dynamics (MD) experiment was run using NAMD. The reaction products did not move in the 50 ns experiment, so this was followed by a series of 8 steered molecular dynamics (SMD) experiments, each of 40 ps duration (Figure 17). In these simulations, an additional unit vector force was directed from one of the nitrogen atoms in L,L-SDAP out of the active site towards a water molecule in the solvent box at different angles out the active site. One SMD simulation resulted in succinate, which is deeper in the active site, moving out of the active site in addition to the movement of L,L-DAP into the solvent. These SMD experiments provide insight into the favorable and unfavorable exit trajectories for the DapE reaction products.

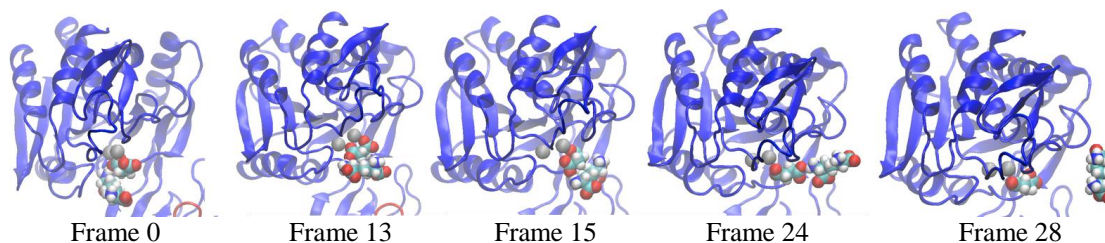


Figure 17. A series of snapshots of one of the dimers of DapE from a 40 ps steered molecular dynamics experiment. The total simulation was 36 frames visualized in VMD with a stride of 100 frames.

## Results and Discussion

### HiDapE in the Closed Conformation

In our previous studies, we reported the apo-structure of HiDapE, which revealed the



structure of the DapE enzyme in the open conformation (DapE\_OC).<sup>63</sup> In this conformation, the catalytic and dimerization domains adopt an extended conformation with dimensions  $50 \times 44 \times 121$  Å. The active site clefts, which are located between the two domains in the center of the catalytic domains that coordinate the metal ions, are broadly open. The open conformation allows easy access to the di-zinc centers (Figure 13A). Addition of the substrate (SDAP) to the protein prior to crystallization yielded a new crystal form that has not been observed previously. In this crystal form, Dr. Nocek was able to capture the enzyme in the products-bound state, with succinate and L,L-diaminopimelic acid as both products are clearly observed and modeled into the Fo-Fc omit electron density map.

The 1.95 Å resolution product-bound structure unveiled the HiDapE enzyme in the significantly changed conformation with the dimensions  $47 \times 45 \times 111$  Å (Figure 13B) and close comparison of the product-bound HiDapE (DapE\_PC) structure to its previously determined apo-HiDapE structure revealed a large domain movement of the catalytic domains. The overlay of the open and closed conformations reveals that in the product bound-conformation the catalytic domains rotated and shifted approximately 50 degrees and 11 Å (as measured at the position of Zn atoms) relatively to the dimerization domain, effectively closing the access to the active site. The extent of movement is shown in Figure 13A and 13B. These two states clearly show that HiDapE enzyme undergoes dynamics modulation between the different catalytic states presumably to bind and activate the substrate in the active site. The overall characteristic of the closure movement is consistent with the hinge domain movement mechanism reported for Allantoate Amidohydrolase from *Escherichia coli*, beta-alanine synthase from the yeast *Saccharomyces kluyveri*, and the antibiotic resistance factor HmrA from methicillin-resistant *Staphylococcus aureus*,<sup>79-81</sup> which allows a twist and turn movement at the inter-domain linker.

### Succinic Acid & LL-Diaminopimelic Acid Binding Revealed.

The HiDapE product-bound structure unveiled the surprising flexible nature of DapE's active site and identified several new protein-ligand interactions which have not been predicted either by docking attempts or molecular dynamics studies.<sup>75</sup> The HiDapE-product complex show that the active site can be segmented into two distinct binding pockets for succinic acid and for diaminopimelic acid (Figure 18). The succinic acid binding pocket is positioned adjacent to the Zn metal center as highlighted in the cyan box, in Figure 13C. The succinic acid is bound in such way that one of the carboxylate moieties bridges between two Zn ions while simultaneously interacting with the hydrogen bond donor His194.B located on the dimerization domain of the opposing chain. The other carboxylate forms the salt bridge interaction with Arg178, and forms H-bonding interactions with Tyr197.B also from the opposing dimerization domain.

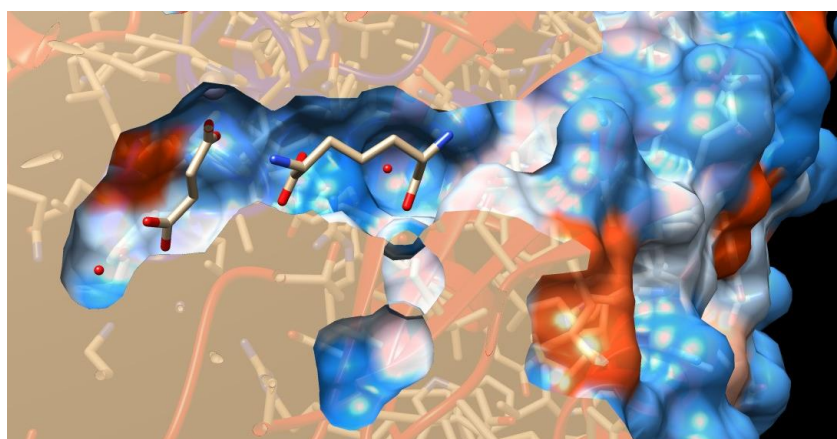


Figure 18. Shown is a surface structure cross-section of the closed product conformation of DapE with products succinate and DAP bound in the active site.

The interactions with diaminopimelic acid are shown in the yellow box in Figure 13C. Similar to succinic acid, the diaminopimelic acid interacts with HiDapE through the interaction of its carboxylate groups with the side chains of following residues: Ser181, Asn244.B, Asn245.B, Ser290, Arg258. The results clearly show that residues supplied by both domains play a key role in catalysis, and it is noteworthy that many of these residues are highly conserved in

DapE protein sequences.

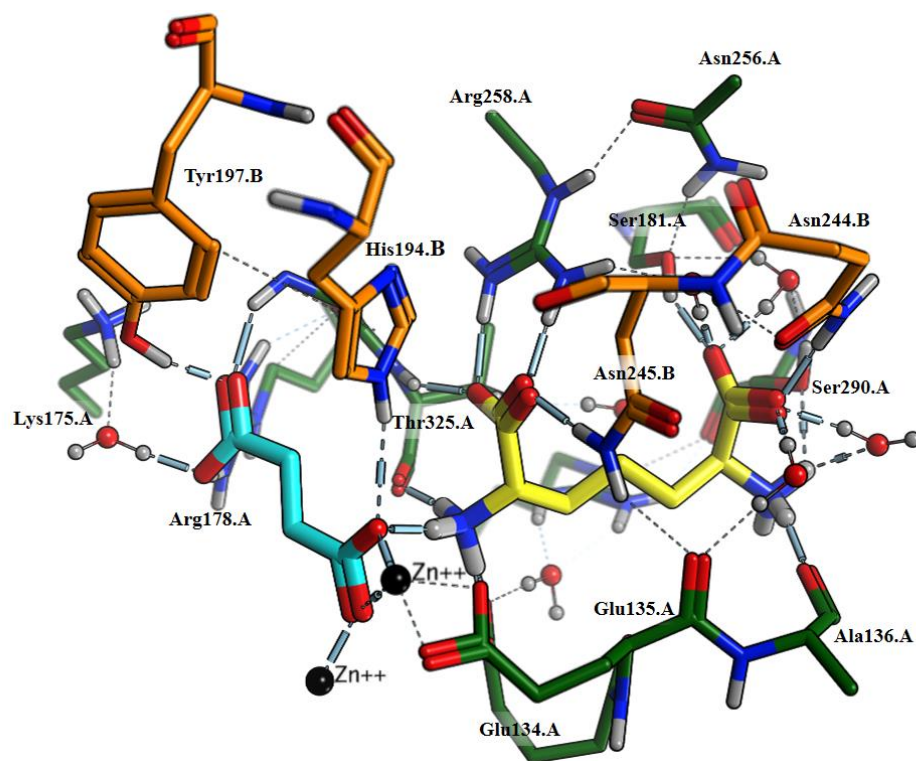
### **Product-Based Transition-State Modeling Analysis**

The structure of the catalytically-generated products of L,L-SDAP in the active site of DapE reveals important protein-ligand interactions and implicates previously unidentified residues in the stabilization of the L,L-SDAP tetrahedral intermediate/transition state complex of DapE. We have employed the *in silico* modeling technique that we refer to as “Product-Based Transition State Modeling” (PBTSM), to model hypothetical native substrate and the catalytic water/hydroxide bound to DapE as well as the substrate transition state intermediate-bound DapE model, and could also be applied to non-substrate studies in the future. This technique, described in Figure 14, employed the product-bound crystal structure as a starting point to generate these models in reverse chronology back through the substrate tetrahedral intermediate and two native substrate-catalytic water/hydroxyl binding modes.

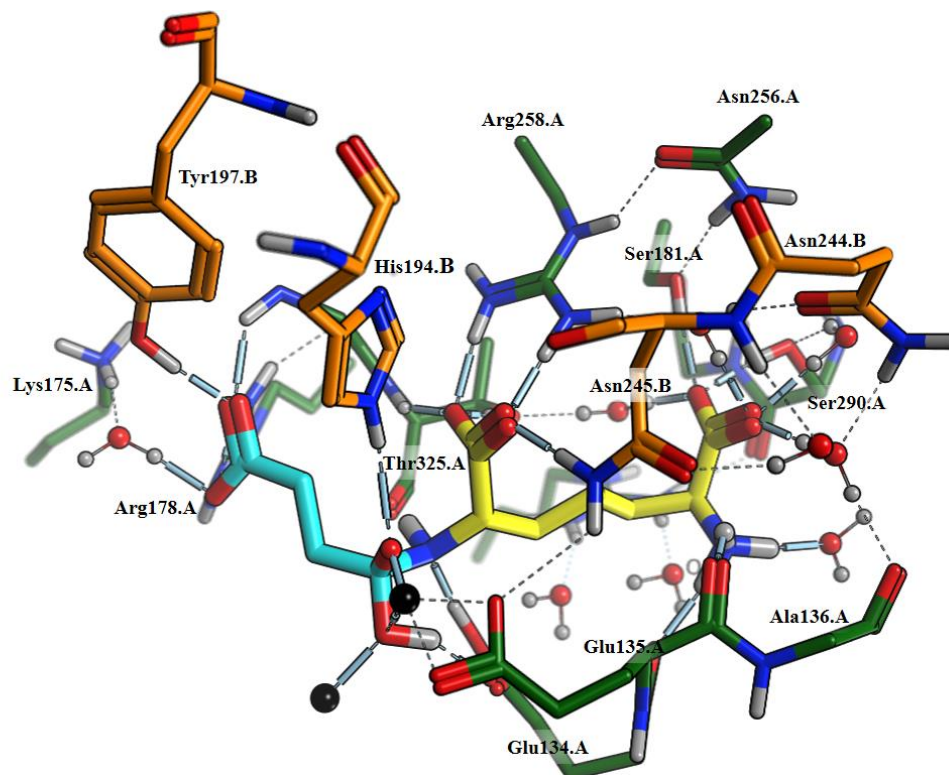
The atomic coordinates of the structurally prepared model of the original product bound DapE crystal structure, Suc\_DAP\_DapE\_PC were used to generate three additional DapE molecular models of substrate species at key stages along the enzyme’s catalytic trajectory. That being the LLSRAP\_HOH\_DapE\_PC substrate bound with unactivated catalytic water model (Figure 19D), LLSRAP\_OH\_DapE\_PC substrate bound with activated catalytic hydroxide model (Figure 19C), and the LLSRAP-TS\_DapE\_PC transition state intermediate bound model after nucleophilic attack of the amide by the catalytic hydroxide (Figure 19B). The free energy of binding was calculated by the Generalized Born Volume Integral Weighed Surface Area (GBVI/WSA)  $\Delta G$  method using MOE. The GBVI/WSA is a forcefield-based scoring function which estimates the free energy of binding of the ligand from a given pose and is reported in units of kcal/mol. It has been trained using the MMFF94x and AMBER99 forcefield on the 99

protein-ligand complexes of the solvated interaction energy (SIE) training set.<sup>82, 83</sup>

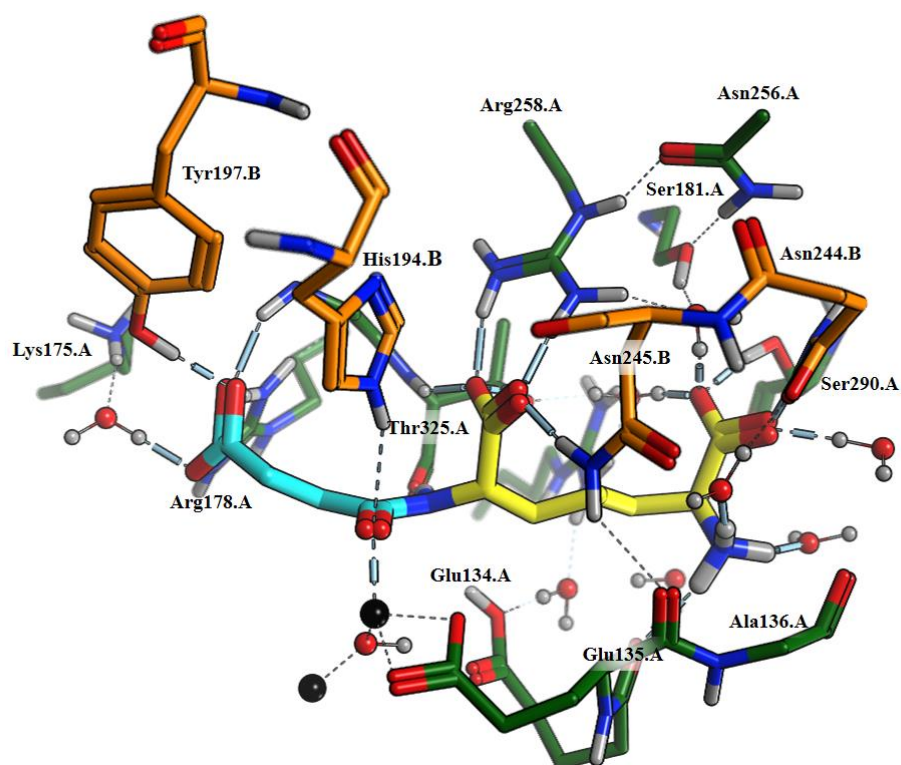
A



B



C



D

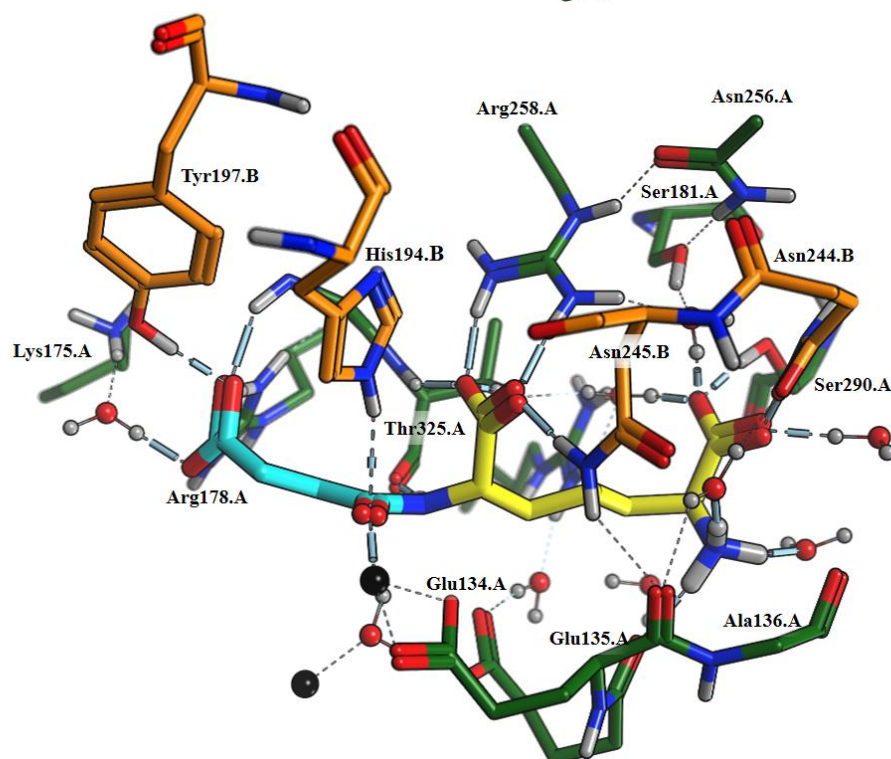


Figure 19. Model results as each stage of Product-Base Transition-State Modeling. A) Succinate & DAP products bound to the closed conformation of DapE, generated from crystal structure obtained from Dr. Nocek. B) L,L-SDAP transition state intermediate bound to the closed conformation of DapE, generated through PBTSM. C) L,L-SDAP and activated cat. hydroxyl

group bound to the closed conformation of DapE, generated through PBTSM. D) L,L-SDAP and unactivated cat. water bound to the closed conformation of DapE, generated through PBTSM. Atoms associated with succinate and DAP are colored cyan and yellow while protein chains A and B are colored dark green and orange respectively.

In the GBVI/WSA method, the free energy of substrate binding to the DapE enzyme is obtained as the sum of the contributions from average gain/loss of rotational and translational entropy, Coulombic electrostatic free energy, the free energy of solvation, van der Waals contributions to binding, and the free energy contribution of surface area, weighed by exposure which penalizes exposed surface area, whereas the alpha and beta terms refer to constants which are determined during training. This calculation is expressed in Eq. (1) below.

$$\Delta G \approx c + \alpha \left[ \frac{2}{3} (\Delta E_{\text{Coul}} + \Delta E_{\text{sol}}) + \Delta E_{\text{vdW}} + \beta \Delta SA_{\text{weighted}} \right] \quad \text{Eq. (1)}$$

Binding Affinities found for all four molecular models in the PBTSM series are summarized in Table 1. The free energy trends are in agreement with expected energy profile for enzyme catalyzed hydrolysis.

Table 1. GBVI/WSA  $\Delta G$  Binding Affinity Calculations for PBTSM-Generated Structures.

| Model ID           | Figure Ref.  | GBVI/WSA $\Delta G$ |
|--------------------|--------------|---------------------|
| LLSDAP_HOH_DapE_PC | (Figure 19D) | -21.58 kcal/mol     |
| LLSDAP_OH_DapE_PC  | (Figure 19C) | -20.68 kcal/mol     |
| LLSDAP-TS_DapE_PC  | (Figure 19B) | -34.86 kcal/mol     |
| Suc_DAP_DapE_PC    | (Figure 19A) | -30.79 kcal/mol     |

Super positioning of the models and analysis of the binding interaction reveals four main ligand-enzyme interaction zones as described in Figure 20 below. These zones are the catalytic metallo-center, the distal carboxylate of the succinyl subunit, the proximal carboxylate of the DAP subunit, and the distal amino acid end of the DAP segment. These zones of substrate-ligand interaction work together to orient the scissile bond of the native substrate optimally over the catalytic metal center while simultaneously creating Coulombic and van der Waals interactions along the active site cleft between the opposing catalytic and dimerization domains.



The interaction at this interface by the substrate functions as the glue that stabilizes the interfacial interaction between the two opposing enzyme domains which keeps DapE in the closed conformation.

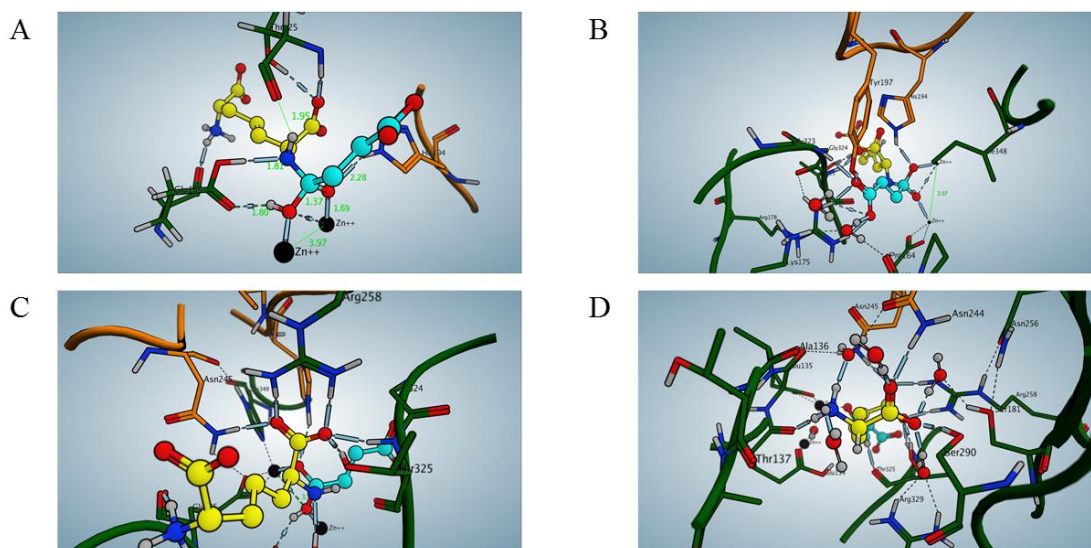


Figure 20. Shown are four major zones of ligand-enzyme interaction as seen in LLS-DAP-TS\_DapE\_PC. A) Bond distance of transition state intermediate bound to metal center. Binding analysis of transition state intermediate after molecular dynamics and minimization: B) Distal carboxylate of succinyl segment, C) Proximal carboxylate of TS bound DAP segment, D) Distal end of DAP segment.

### Hypothetical Conformational Changes Drive Catalysis.

It has become clear that major conformational changes in the structure of DapE are a critical component in the function of the enzyme. In the open conformation of DapE the metallo active site is open to solvent and the dimerization domains of the opposing chain are situated above. The initial open conformation of DapE, as seen in the previously reported crystal structures 3IC1 & 5UEJ, facilitates an open binding site for the succinyl portion of the substrate to fill the hydrophobic binding pocket with a positive charge at the bottom of the pocket while the terminal mDAP carboxyl group can interact with the two arginine residues, Arg244 and Arg258, located in or near the hinge region of DapE. The Coulombic interactions formed by the

distal end of the substrate also lie in close proximity to Tyr197.B and His194.B. Once interactions are made with DAP by the opposing dimerization residues a contraction of the dimer superstructure flexes and twists the hinge region. The enzyme conformational movement leads directly to closure of substrate binding pocket by the dimerization domain residues and orientation of the scissile peptide bond onto Zn1, displacement of the bridging catalytic water on Zn2, deprotonation by general acid base Glu134 and subsequent catalytic hydrolysis of the substrate. Upon catalytic turnover and cleavage of the scissile bond, the tethering interaction between the two domains holding the active site closed is interrupted. The subsequent increase in entropy leads to the release of the products and reformation of the open conformation of DapE.

### **Substrate Specificity Regulates Formation of Transient Oxyanion Hole.**

The concept of an oxyanion hole is a well-established enzyme characteristic in biochemistry, specifically when referring to serine or serine-like hydrolase/peptidase enzymatic functions. The oxyanion hole refers to a pocket in the active site of an enzyme that stabilizes the tetrahedral transition state negative charge on a deprotonated oxygen or alkoxide. This residue motif typically consists of backbone amides or positively charged side chain residues. This functions to stabilize the transition state while lowering the activation energy necessary for the reaction, and so promotes catalysis.<sup>84, 85</sup>

Analysis of the models described herein suggests a transient oxyanion hole that is utilized by the enzyme to modulate both catalytic turnover and substrate specificity for DapE (Figure 21). One of the two H-bond donors of the transient oxyanion hole provided by His194 from the dimerization domain and the other through a single Zn cofactor from the opposing catalytic domain.



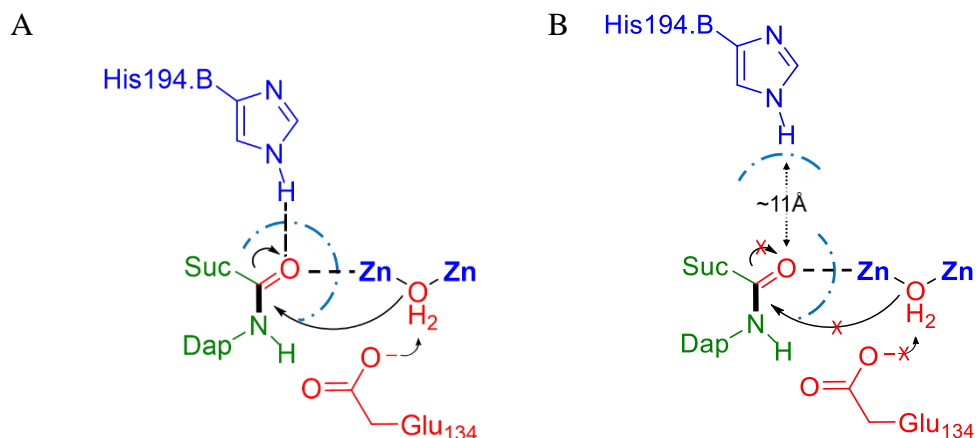


Figure 21. Hypothesized transient oxyanion hole in the (A) catalytically active form, (B) catalytically inactive form.

The concept of a transient oxyanion hole gating and its role in substrate specificity is, to my knowledge, an unidentified enzymatic characteristic shared among many different di-metalloenzymes to regulate catalytic turnover. Information about substrate shape is incorporated into an enzyme catalytic feedback loop which imparts a conformational response by the enzyme to accommodate the substrate. As seen with many M20 metallopeptidase such as, Human Carnosinase-2 (CN2) (Figure 22), Dug1p from *Saccharomyces cerevisiae*, *Staphylococcus aureus* metallopeptidase (Sapep) and now DapE, enzymes possessing a high degree of substrate specificity often require an equally high degree of conformation dynamics in the enzyme's macrostructure to facilitate catalytic turnover. If a potential substrate cannot activate the requisite conformational change needed to create a full residue-metallocofactor oxyanion hole and thus activate it for transitions-state stabilization, then catalytic turnover will not proceed.

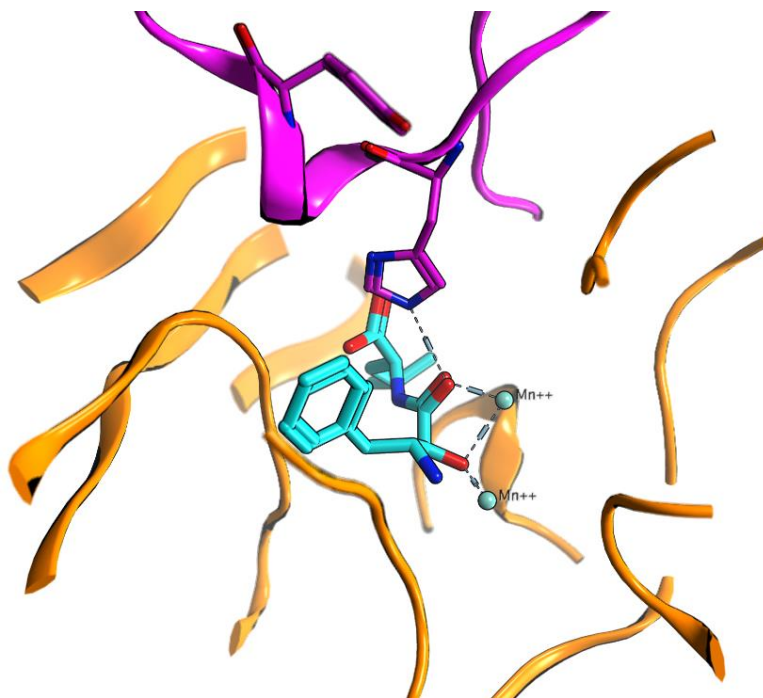


Figure 22. Trapped product bound conformation of Human Carnosinase-2 (CN2) (PDB I.D. 4RUH) trapped in the closed conformation by inhibitor bestatin interacting with metal center and a highly-conserved histidine.

Conversely, in the notoriously un-specific metallo- $\beta$ -lactamase NDM-1, catalytic turnover is facilitated by a similar transient oxyanion hole that is formed by Asn220 and the Zn1 of the di-Zn system (Figure 23). However, the loop associated Asn220 is much smaller and is conformationally stabilized closer to the metallo active site, thus leading to less specific activation of the oxyanion components and leading to more flexible and promiscuous  $\beta$ -lactamase activity.<sup>18, 47, 86-88</sup>

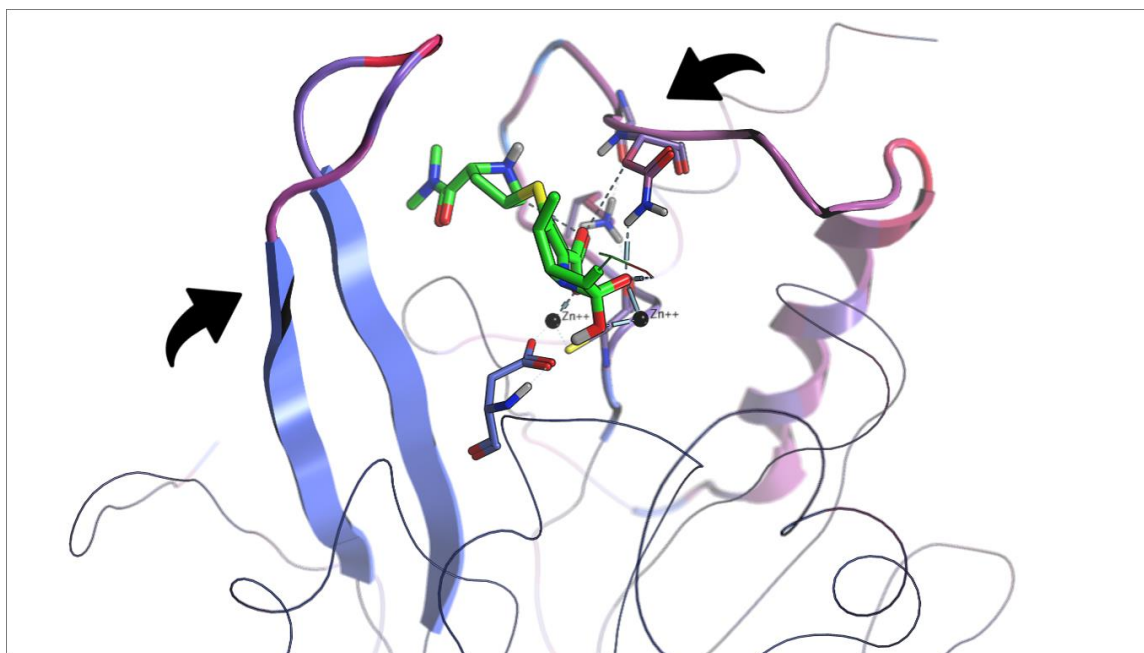


Figure 23. NDM-1 active site cleft with a modeled meropenem transition state intermediate bound at the metal center. Enzyme represented in B-factor with ribbon diagram shown as wire except for the hairpin loop and binding loop I.<sup>18, 47, 86-88</sup>

### Updated Catalytic Mechanism of DapE.

The product bound X-ray structures of DapE prompted us to reconsider the catalytic mechanism previously proposed. The first step in the updated catalysis for DapE remains initial recognition of the L,L-SDAP by the solvent accessible crescent-shaped cavity residues in the open conformation. Subsequent induced conformational change in DapE's structure induces interfacial interaction between the catalytic and dimerization domains facilitating stabilization of the substrate transition state interaction. During the conformational change, the peptide carbonyl oxygen of L,L-SDAP coordinates to Zn1 which is followed by formation of an activated transient oxyanion hole by alignment of His194.B from the dimerization domain. Strong interactions made by the Zn and His194.B to the carbonyl oxygen leads to polarization of the carbonyl oxygen and activation the carbonyl for nucleophilic attack at the carbon center. Carbonyl coordination to Zn1 by L,L-SDAP simultaneously leads to displacement of the

bridging catalytic water group onto Zn<sup>2+</sup>. Movement of the catalytic water onto Zn<sup>2+</sup> brings it in optimal proximity to the general acid base Glu134 where deprotonation of the metal-bound water molecule by Glu134 forms the nucleophilic hydroxide moiety. This is consistent with the postulated pK<sub>a</sub> of the zinc-bound water molecule.<sup>25</sup> Once the zinc-bound hydroxide is formed, it can attack the activated carbonyl carbon of the substrate, forming a transition-state complex.<sup>25</sup> Solvent kinetic isotope effect studies yielded an inverse isotope effect that was explained by the attack of a zinc-bound hydroxide on the amide carbonyl.<sup>25</sup> As seen with similar M20 metalloenzymes such as AAP and elucidated further by PBTSM evidence described herein, Glu134 then provides a proton to the penultimate amino nitrogen, returning it to its ionized state thus facilitating product release.<sup>69</sup> Once the products are released, a water molecule bridging the two metal ions is replaced.

In the absence of a second metal ion, the catalytic mechanism does not likely change markedly as H349 is in position to assist in orienting the substrate properly in the active site through the formation of a hydrogen bond with a carboxylate side chain of the substrate, thereby stabilizing the transition-state intermediate reminiscent to proposals for the mono-metalated forms of AAP and the methionine aminopeptidase from *E. coli*.<sup>69-71</sup> However, the product bound crystallographic data presented here suggest that in the presence of a dinuclear site, the second metal ion likely does not coordinate the proximal carboxylate side chain of the substrate's DAP subunit. More likely, the proximal carboxylate participates in bifurcated H-bonds with the side chains of Arg258.A, Thr325.A and Asn245.B which is more reminiscent of what is known about substrate binding in Metallo-B-lactamase NMD-1.<sup>39, 89, 90</sup>

## Conclusions

We have presented a previously unidentified product bound crystal structure of DapE in complex with products succinate and DAP which were generated through co-crystallization of DapE with the native substrate L,L-SDAP. This new crystal structure shows clear conformational changes in the overall enzyme structure that we believe to be critical in structure/function relationship for DapE. The single turnover catalytic hydrolysis of the substrate observed in the solid-state crystal structure of DapE allowed for modeling of key steps in the mechanistic process that lead to the observed products bound in the active site by utilization of the *in silico* modeling technique that we refer to as “Product-Based Transition-State Modeling” (PBTSM). The results of these models, in combination with previously reported DapE crystal structures and molecular dynamics publications, help to form a more complete story of how DapE catalyzes the hydrolysis of L,L-SDAP. In summary, the results obtained from the studies described herein have provided new insight into the structure and function of DapE enzymes and additional insight into the catalytic mechanism of DapE. Determination and understanding of substrate binding will be critical for the rational design of future selective DapE inhibitors that may function as a new class of antimicrobial agents.

## Chapter Acknowledgements

I would like to thank Bogousli (Bogi) Nocek, Ph.D., Anna Starus, Ph.D. and Rick Hotz, Ph.D., for all their previous work on DapE. I cannot overstate the importance of your contributions to my understanding of DapE’s structure and function. I would also like to thank Ken Olsen, Ph.D. and Kaitlyn Lovato for their work on steered dynamics simulations with DapE featured in this chapter.

Finally, I would like to sincerely thank my advisor Daniel P. Becker, Ph.D., and the Loyola U. Chicago Chemistry & Biochemistry Department for providing me with the computational suite Molecular Operating Environment (MOE) which made possible all the *in silico* analytical technique described herein.

## CHAPTER THREE

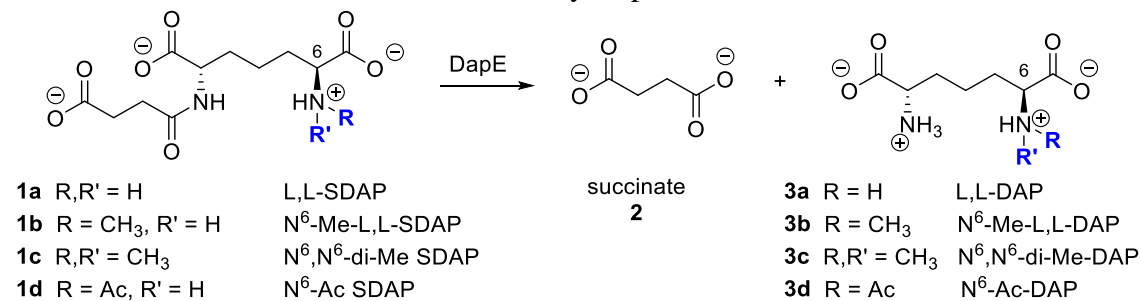
### SUBSTRATE ANALOG SYNTHESIS AND NINHYDRIN-BASED ENZYME ASSAY FOR THE BACTERIAL ENZYME DIAMINOPIMELATE DESUCCINYLAZE

#### **Introduction**

The sharp increase in mortality and morbidity due to rising general infections caused by antibiotic-resistant bacteria underlines the need to discover previously unexplored enzymatic mechanisms as novel antibiotic targets with the goal of developing new molecular leads. For example, invasive methicillin-resistant *Staphylococcus aureus* (MRSA) is a serious and growing health problem.<sup>91</sup> Several newly discovered strains of MRSA show antibiotic resistance even to vancomycin, which has been considered for decades as the standard for the treatment of systemic infections.<sup>92</sup> An attractive bacterial target is the dapE-encoded N-succinyl-L,L-diaminopimelic acid desuccinylase (DapE, E.C. 3.5.1.18)) enzyme which is a member of the succinylase pathway in bacteria that provides both lysine and m-DAP,<sup>24</sup> since these metabolites are essential in bacteria both for protein production and for bacterial peptidoglycan cell-wall synthesis. DapE catalyzes the hydrolysis of N-succinyl-L,L-diaminopimelic acid (SDAP) to succinate and L,L-diaminopimelic acid (Scheme 1). Deletion of the dapE gene is lethal to *Helicobacter pylori* and *Mycobacterium smegmatis* demonstrating the indispensable role of this bacterial enzyme in most pathogens.<sup>29, 62</sup> Furthermore, lack of a similar pathway in humans suggests that selective inhibition of DapE may be toxic to bacteria but not to human hosts, making it a promising pathway to exploit for antibiotics with a new mechanism of action.<sup>24</sup>

It had been demonstrated by Cospér *et al.* that DapE is a dinuclear metallohydrolase,<sup>67</sup> but later it was shown with high-resolution X-ray crystal structures that functionally relevant DapE enzymes may have either one or two zinc ions bound in the active site. These structures have enabled further refinement of a mechanistic hypothesis of peptide bond cleavage by DapE enzymes which have facilitated inhibitor identification.<sup>63</sup> A small, focused screen of compounds containing zinc-binding groups identified the thiol-containing ACE inhibitor captopril as a low micromolar competitive inhibitor of DapE from *Haemophilus influenzae* ( $IC_{50} = 3.3 \mu\text{M}$ ) along with several other small molecule inhibitors including 3-mercaptobenzoic acid ( $IC_{50} = 35 \mu\text{M}$ ), phenylboronic acid ( $IC_{50} = 107 \mu\text{M}$ ) and 2-thiopheneboronic acid ( $IC_{50} = 92 \mu\text{M}$ ).<sup>93</sup> A high-resolution (1.8 Å) X-ray crystal structure of captopril bound to DapE from *Neisseria meningitidis* revealed a thiolate-bridged dinuclear Zn(II) active site complex and provided a model for in silico approaches to identify potential inhibitors of DapE.<sup>94</sup>

Scheme 1. Conversion of SDAP substrate by DapE.



SDAP (**1a**) and analogs N<sup>6</sup>-methyl SDAP (**1b**), N<sup>6</sup>,N<sup>6</sup>-dimethyl-SDAP (**1c**), and N<sup>6</sup>-acetyl-SDAP (**1d**) with corresponding hydrolysis products succinate (**2**) and L,L-diaminopimelic acid derivatives (**3a-d**).

Gelb first isolated the DapE enzyme from *Escherichia coli* and characterized it with its natural substrate SDAP, which exhibited a  $K_m$  value of 0.4 mM and a turnover rate of 16,000  $\text{min}^{-1}$ , as well as several substrate analogs.<sup>95</sup> Further work on substrate analogs was taken up by Holz, in addition to investigating the differences in activities of the zinc and cobalt metal



isozymes of DapE, and it was revealed that DapE is inactive toward the substrate analog lacking the free N<sup>6</sup>-amino group.<sup>96</sup> Several assays have been developed for examining inhibitors of DapE. The original assay<sup>97</sup> for DapE took advantage of the fact that DAP reacts somewhat faster with ninhydrin than with SDAP, but this assay suffered from a lack of reproducibility. Gelb then developed two new assays for DapE. The first employed <sup>14</sup>C-labeled SDAP followed by scintillation counting of liberated <sup>14</sup>C-succinate. The second was a coupled assay utilizing porcine succinate thiokinase and inositol triphosphate to convert liberated succinate to succinyl-CoA and inositol diphosphate. The inositol diphosphate was then detected by its reaction with phosphoenolpyruvate to yield liberated pyruvate, itself being detected spectrophotometrically using lactate dehydrogenase. Finally, in our own earlier work, inhibitors of DapE were assayed against zinc-reconstituted DapE by monitoring amide bond cleavage of L,L-SDAP at 225 nm utilizing L,L-SDAP as a substrate ( $225 \text{ nm} = 304 \text{ M}^{-1}\text{cm}^{-1}$ ).<sup>93</sup> All of these assays suffered serious limitations. The original ninhydrin assay employing native or racemic SDAP, as noted, had very poor reproducibility. The <sup>14</sup>C-labeled substrate assay required working with radioactivity with extra safety protocols and waste disposal issues. We employed Gelb's coupled assay with some success, but found it to be technically troublesome and therefore unreliable. Finally, the assay measuring cleavage of the simple amide bond of the substrate at 225 nm is simple and reliable, but precludes the testing of inhibitors that absorb strongly in the ultraviolet region, thus ruling out testing of many preferred medicinal chemistry leads and analogs.

The desire for a robust and higher throughput assay for supporting our medicinal chemistry efforts toward the discovery of DapE inhibitors as new antibiotics led us to consider developing a new assay. Gelb's and Holz's work demonstrated strict structural requirements for the substrate in order to be cleaved by the enzyme: The free amino group of SDAP is important

for substrate recognition as SDAP lacking the basic 6-amino group (at the non-succinylated end) was hydrolyzed at only 0.036 % of the rate of the natural SDAP substrate.<sup>95</sup> Recognizing the ease and reliability of a ninhydrin-based assay to detect the release of the primary amino group upon cleavage of the succinate amide, we explored whether we could block the reactivity of the free amino group of the substrate to prevent interference caused by its reaction with ninhydrin. We prepared both N<sup>6</sup>-acetylated and N<sup>6</sup>-methylated derivatives of SDAP, and deprioritized the contemplated N,N-dimethyl SDAP analog based on molecular docking and modeling.

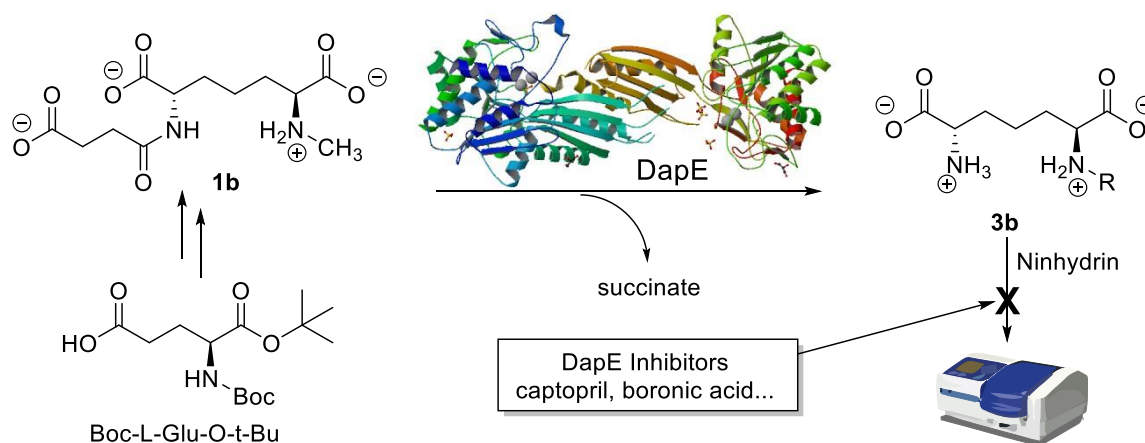


Figure 24. Generic diagram of Ninhydrin Assay implementation.

### DapE Molecular Modeling to Assess Mono- Vs. Dimethyl-SDAP Analogs.

Ligand models of L,L-SDAP, mono-methyl-L,L-SDAP and di-methyl-L,L-SDAP were built using the Molecular Operating Environment (MOE) computational suite's Builder utility followed by minimization in the gas phase using the force field MMFF94X. An X-ray crystal structure of the product-bound DapE crystal structure in the closed conformation was obtained.<sup>98</sup> Following receptor preparation, molecular docking was performed using ligand conformation databases. Docking poses of the substrate SDAP (**1a**) and analogs **1b** and **1c** were assessed as

judged by their similarity to the product binding interactions seen in the original product-bound crystal structure. The three ligand/enzyme models were then solvated in a simple water box at pH of 7.4. The system atoms were then optimized with a short, localized molecular minimization process. Molecular Dynamics parameters were set to globally minimize the protein, ligand and solvent atoms with a typical heating and cooling protocol. Simulation results were then minimized once again before the final binding poses were obtained for comparison. The final solvated and minimized substrate-bound DapE models are shown in Figure 25a-c.

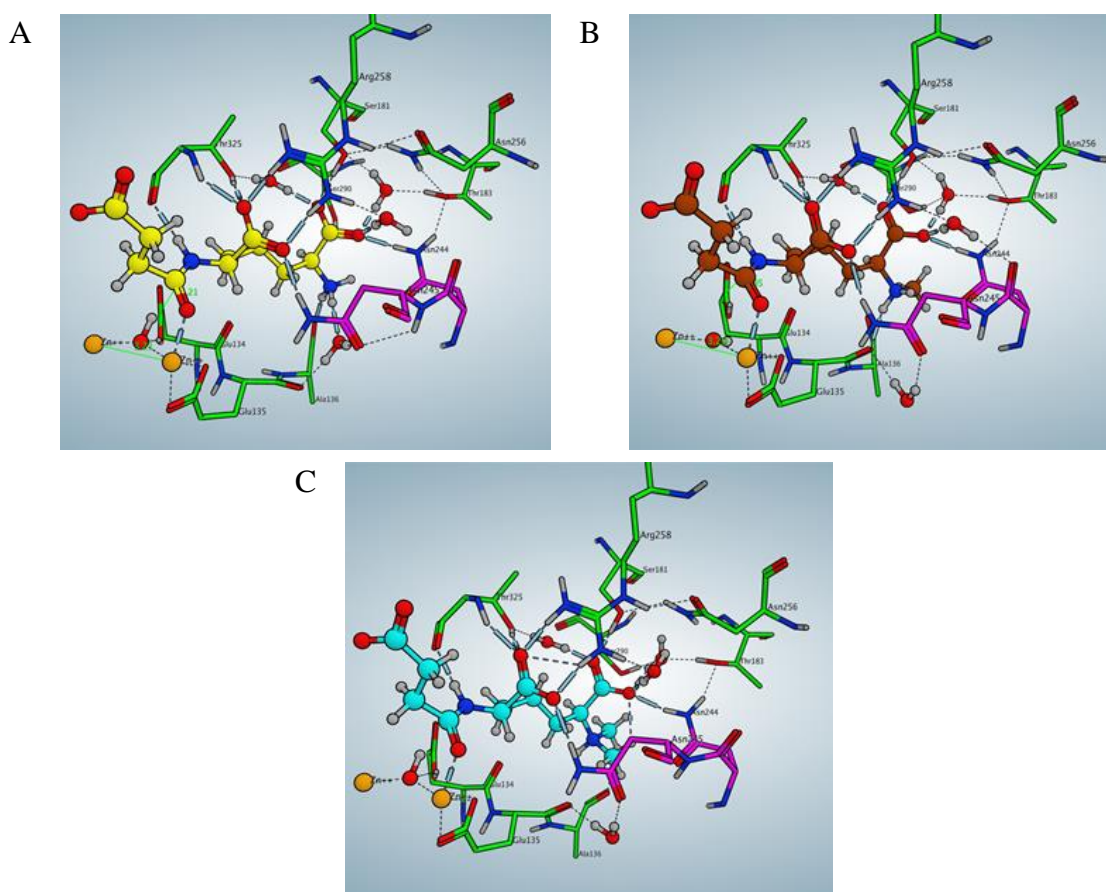


Figure 25. Minimized substrate/analogs docked and modeled in the DapE active site; A) native substrate L,L-SDAP (yellow), B) monomethyl-LL-SAP (brown), C) dimethyl-L,L-SDAP (turquoise). Note\*Chain A (catalytic domain, green), Chain B (dimerization domain, purple).

As seen in Figure 25, the docked and modeled endogenous substrate SDAP amide carbonyl is bound to one of the zinc atoms while the amide N-H acts as an H-bond donor to the

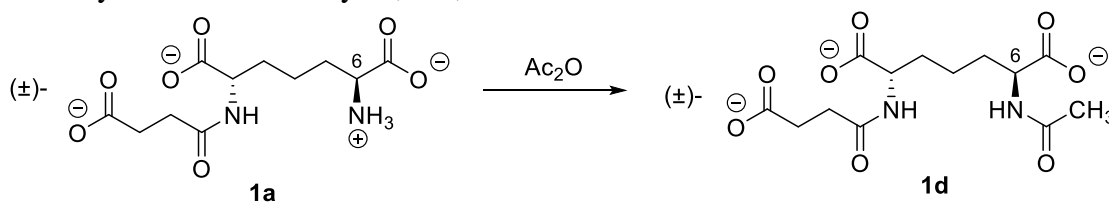
backbone carbonyl of Thr325.A. The proximal carboxylate participates in bifurcated H-bonds with the side chains of Arg258.A, Thr325.A and Asn245.B. The free primary amino group acts as an H-bond donor to the backbone carbonyl of Ala136.A and a water molecule, which in turn participates in H-bond donation to the backbone carbonyl of Glu135.A and to the side chain carbonyl of Asn245.B. The terminal carboxylate of the pimelic acid moiety is H-bonded to the N-H of Asn244.B, the side chain hydroxyl of Ser181.A, and Ser290.A, and a water molecule, which in turn H-bond donates to the side chain hydroxyls of Thr183.A and Thr325.A. We observe by comparing the enzyme-substrate interactions in the crystal-bound L,L-SDAP product(s) and the docked & modeled L,L-SDAP structures, that the substrate links the catalytic domain of chain A to the dimerization/cap domain of chain B. We propose that the presence of the substrate induces a conformational change in the enzyme structure that facilitates catalytic activation within the active site, and without the substrate the enzyme remains in the open, inactive conformation. In effect, the substrate is the conduit that links the catalytic domain of chain A to the dimerization/cap domain of chain B. The interactions of the monomethyl-L,L-SDAP analog **1b** are identical to those of the endogenous substrate, except for the added methyl group on the primary amino group that eliminates the H-bond interaction to the backbone carbonyl of Ala-136.A. The presence of the N-methyl group also leads to perturbations of the water interaction at the ammonium N-H. However, H-bond bridging between the backbone carbonyl of Glu135.A and the side chain carbonyl of Asn245.B by the ammonium N-H(s) are maintained, while the N-methyl forms a new hydrophobic interaction with the adjacent alanine-136.A residue. In contrast, the dimethyl-L,L-SDAP dimethyl substrate **1c** is quite distinct from the natural L,L-SDAP substrate's binding due to the presence of the two additional methyl groups. Loss of the interfacial domain interaction between the backbone carbonyl of Glu135.A

and the side chain carbonyl of Asn245.B by the ammonium N-H species, due to interference of the additional methyl groups, appear to be the key difference to the endogenous L,L-SDAP substrate binding mode. The additional bulk of the two methyl groups also leads to the migration of the N-H bond from the ammonium species of the potential substrate from Glu135.A to the backbone carbonyl of Glu134.A. Significantly, Glu134 (E134) is proposed to act as the general acid/base during the hydrolysis reaction catalyzed by DapE<sup>99</sup> and this residue is shifted further away from the active site. Thus, it is concluded that the mono-methyl-L,L-SDAP substrate analog **1b** retains overall similar binding to the endogenous L,L-SDAP **1a**, while the dimethyl-L,L-SDAP analog **1c** would likely suffer loss of significant binding interactions due to the presence of the second methyl group. N-Acetyl-SDAP analog **1d** was found not to act as a substrate.

### Synthetic Protocol

The mixture of N-succinyl-N<sup>6</sup>-acetyl-L,L/D,D-diaminopimelic acid (**1d**) was prepared by exposing a mixture of L,L/D,D- N-succinyl-diaminopimelic acid, previously synthesized by Dinuta Gilner, Ph.D., to acetic anhydride in the presence of NaOAc in glacial acetic acid (Scheme 2). The acetylated substrate **1d** was obtained as a colorless powder in quantitative yield. However, this analog was not cleaved by the enzyme, either due to the need for a charged cationic species at that position, or due to negative steric interactions or a combination of those two factors.

Scheme 2. Synthesis of N<sup>6</sup>-acetyl-L,L/D,D-SDAP substrate **1d**.

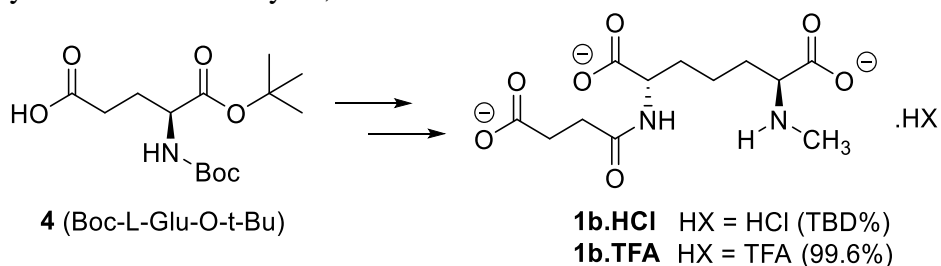


Reaction Conditions: Ac<sub>2</sub>O, NaOAc·3H<sub>2</sub>O, glacial AcOH, 30 °C for 10 min-rt for 1h.

In contrast, considering the more conservative change of adding a single methyl group involving minimal steric bulk and still maintaining a positively charged ammonium species at physiological pH suggested preparation of the monomethyl-L,L-SDAP acid (**1b**) analog for study. Cleavage of monomethyl-SDAP substrate **1b** would yield succinate (**2**) and the monomethyl L,L-diaminopimelic acid, a secondary amine which may be differentiated from primary amines in reactivity with ninhydrin. The dimethyl-SDAP substrate **1c** is more sterically encumbered at the critical cationic ammonium moiety, but as a tertiary amine it is inert to reaction with ninhydrin. We selected the more conservative monomethyl derivative, consistent with modeling that suggests that the tertiary N,N-dimethylamine substrate **1c** would be a very poor substrate.

The N-succinyl-N<sup>6</sup>-methyl-L,L-diaminopimelic acid substrate **1b** was prepared enantioselectively by Marlon Lutz as summarized in Scheme 3, beginning with commercially available BOC-L-glutamic acid t-butyl ester **4** to afford the trifluoroacetate salt **1b.TFA** in nearly quantitative yield.

Scheme 3. Synthesis of N<sup>6</sup>-Methyl-L,L-SDAP substrate **1b**.



Summarized synthesis route for preparation of monomethyl substrate analog as the hydrochloride salt (**1b**) via the methyl ester, or the trifluoroacetate salt (**1b**) via the benzyl ester.

## Results and Discussion

### Primary Amine Detection with Ninhydrin.

With the monomethyl SDAP substrate **1b** in hand, we demonstrated that it functions as a substrate by observing hydrolysis of the amide bond at 225 nm in the presence of DapE. Since **1b** can function as a substrate we set out to design a robust and operationally straightforward enzymatic assay that would be amenable to inhibition studies for drug discovery. While ninhydrin reacts with both primary and secondary amines, only primary amines (that bear an alpha-hydrogen) can form the Schiff base known as Ruhemann's purple, which has a longer wavelength absorptions with  $\lambda_{\text{max}}$  at 570 nm and 450 nm. In contrast, ninhydrin reacts with secondary amines such as proline to form an iminium salt that is yellow-orange in color, with  $\lambda_{\text{max}}$  at 440 and 405 nm.<sup>100</sup>

Therefore, control reactions of standard enzyme activity were carried out in triplicate as follows: to a buffered DapE solution at 30 °C was added the N-methyl SDAP TFA salt **1b**. The reaction was allowed to proceed for 10 min after which a 2 % ninhydrin reagent in 100 % DMSO was added and subsequently heated to 80 °C for 15 min. The ninhydrin reaction was quenched by placing the mixture in ice for 2 min after which the absorbance was read at 570 nm. This control reaction was set as 100 % standard enzymatic activity of DapE.

DapE was incubated with DMSO prior to addition of N-methyl-SDAP substrate under various times to show the effects of DMSO on the hydrolytic activity of DapE. The DMSO incubation reactions were carried out with the exchange of buffered solution with DMSO. The enzyme was allowed to incubate for the desired time between 0 and 10 min. After the allotted incubation time, N-methyl-SDAP TFA salt **1b** was added and the reaction was allowed to proceed for 10 min. The enzymatic reaction was quenched by addition of 2 % ninhydrin solution

and was subsequently heated to 80 °C for 15 min. The ninhydrin reaction was quenched by placing in ice for 2 min and the absorbance was read at 570 nm. Comparison of 100 % standard enzymatic activity versus rates obtained in the presence of DMSO indicate a ca. 50 % decrease in enzymatic activity over the 10 min time period in the presence of ninhydrin/DMSO, but enzymatic activity is not abolished even after 10 min. This demonstrates that the addition of the ninhydrin/DMSO solution does not fully quench the catalytic activity of DapE.

#### **DapE Ninhydrin-based Enzymatic Assay and IC<sub>50</sub> Determination.**

It was found that the optimal DapE assay conditions using the trifluoroacetate (TFA) salt of monomethyl-L,L-SDAP **1b** as the substrate and with ninhydrin as the colorimetric probe are 8 nM DapE in 50 mM HEPES buffer at pH 7.5 at 30°C followed by the addition of 2 mM N-methyl SDAP. After 10 min the reaction is quenched by heating at 100 °C for 1 min. followed by cooling on ice. A 2 % ninhydrin solution in 100 % DMSO (100 µL) is added and heated at 80 °C for 15 min followed by cooling on ice. Once the sample is cooled to 30 °C the absorbance at 570 nm is determined.

In order to test N-methyl SDAP as a substrate for screening potential inhibitors of DapE, the potency of several previously-identified inhibitors were examined and found to be comparable with results from the previous assay. Specifically, captopril was found to have an IC<sub>50</sub> value of 3.3 µM which is identical to that reported using SDAP.<sup>93</sup> Likewise, the IC<sub>50</sub> values for 3-mercaptopbenzoic acid (IC<sub>50</sub> = 25 µM), phenylboronic acid (IC<sub>50</sub> = 319 µM), and thiophene boronic acid (IC<sub>50</sub> = 166 µM) were found to be in agreement with the literature values of 35 µM, 107 µM, and 92 µM, respectively.<sup>93</sup>



## Conclusion

In summary, a new spectrophotometric assay for DapE is described, amenable to identification and optimization of DapE inhibitors as potential antimicrobial agents. Ultimately, it will be imperative to screen different metalloisozymes of DapE, in particular the Mn<sup>2+</sup> enzyme in addition to the Zn<sup>2+</sup> form, as captopril was found to be a moderately potent inhibitor of the Zn<sup>2+</sup> enzyme but not of the Mn<sup>2+</sup> enzyme. Indeed captopril displayed modest antibiotic activity against *Escherichia coli* and *Salmonella enterica*<sup>101</sup> confirming our own observation of antibiotic activity,<sup>93</sup> but Udo found that captopril does not inhibit the Mn<sup>2+</sup> enzyme,<sup>14</sup> and that, surprisingly, the antibiotic activity of captopril was independent of DapE inhibition in bacteria.<sup>101</sup> Even within the divalent zinc enzyme, mono- and di-zinc enzymes were determined to show different activities, and their crystal structures have been determined with structural insights that impact rational design of inhibitors.<sup>63</sup> In summary, utilizing N-methyl SDAP **1b** as the modified substrate enables a ninhydrin-based assay for measuring inhibition of the bacterial enzyme DapE should support both new lead discovery as well as lead optimization toward the discovery of new antibiotics with a new mechanism of action to treat bacterial infections.

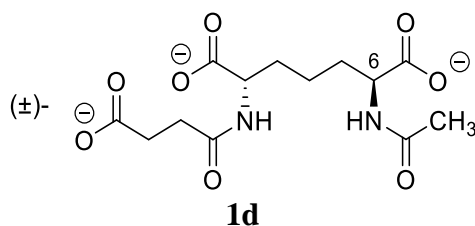
## Experimental Section

### Materials.

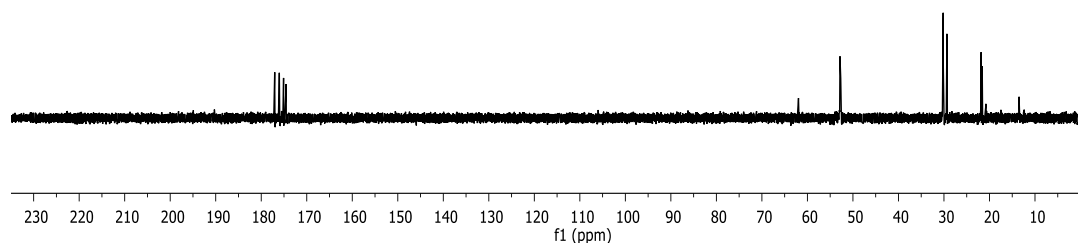
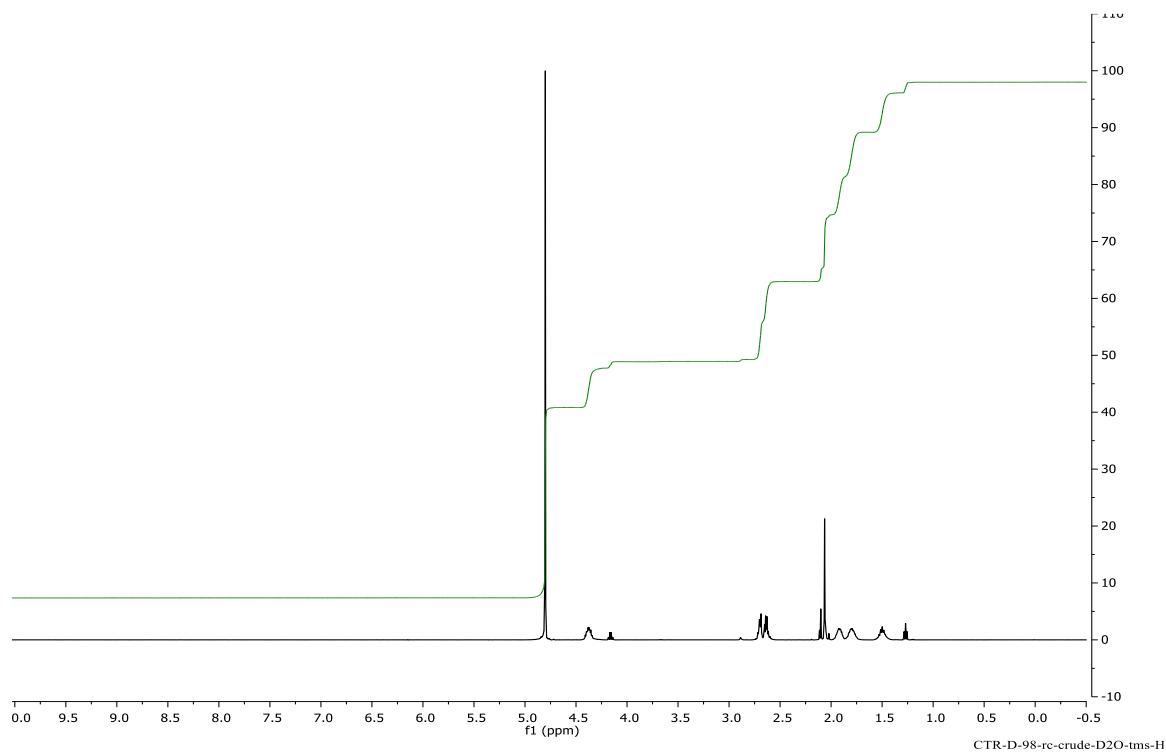
All solvents were distilled prior to use, and all reagents were used without further purification unless otherwise noted. Ninhydrin solution was purchased as a 2 % solution in 100 % DMSO with a lithium acetate buffer at pH 4.5. All synthetic reactions were conducted under a nitrogen atmosphere. Silica gel 60A, 40–75  $\mu\text{m}$  (200  $\times$  400 mesh), was used for column chromatography. Aluminum-backed silica gel 200  $\mu\text{m}$  plates were used for TLC. All <sup>1</sup>H NMR spectra were obtained using either a 300 MHz spectrometer or a 500 MHz spectrometer with

trimethylsilane (TMS) as the internal standard. All  $^{13}\text{C}$  NMR spectra were obtained using a 75 MHz spectrometer or a 125 MHz spectrometer. HRMS spectra were measured on a TOF instrument by electrospray ionization (ESI).

### Chemistry.



(±)-(2S,6S/2R,6R)-2-Acetamido-6-(3-carboxylatopropanamido) heptanedioic acid (**1d**). To a racemic mixture of D,D/L,L-SDAP (22.8 mg, 0.079 mmol) was added glacial acetic acid (100 uL), acetic anhydride (17.3 uL, 0.236 mmol) and NaOAc·3H<sub>2</sub>O (24.0 mg, 0.079 mmol). The reaction was degassed and agitated with mechanical stirring (200 rpm) at 30 °C for 10 min, then 1h at room temperature after which time TLC using 30:1:69 H<sub>2</sub>O-AcOH-CH<sub>3</sub>CN on reverse phase TLC indicated consumption of starting material. The resulting reaction mixture was quenched with HCl and concentrated to dryness under reduced pressure and the resulting oil was placed under high vacuum overnight where it became an off-white foam/solid. The racemic product mixture was collected to afford the N-acetylated SDAP derivative **1d** as a colorless powder (38.5 mg, 99 %).  $^1\text{H}$  NMR (500 MHz, D<sub>2</sub>O):  $\delta$  4.68 (bs, ammonium ion), 4.07-4.02 (m, 2H), 2.55-2.43 (m, 4H), 1.92 (s, 3H), 1.75-1.65 (m, 2H), 1.63-1.53 (m, 2H), 1.29 (p, J = 8Hz, 2H).  $^{13}\text{C}$  NMR (500 MHz, D<sub>2</sub>O):  $\delta$  179.2, 179.1, 178.9, 174.9, 174.0, 55.1, 55.0, 31.4, 31.3, 31.1, 22.2, 22.1, 21.8. HRMS (IT-TOF) m/z calcd. for C<sub>13</sub>H<sub>20</sub>N<sub>2</sub>O<sub>8</sub> [M]<sup>+</sup>:332.1232, found: 332.1220.



### DapE Molecular Modeling.

Ligand models of L,L-SDAP, mono-methyl-L,L-SDAP and di-methyl-L,L-SDAP were built using the Molecular Operating Environment (MOE) computational suite's Builder utility followed by minimization in the gas phase using the force field MMFF94X. The minimized ligands were the subjected to the Conformational Search protocol to generate structural-conformation-databases populated with as many as 10,000 individual conformations.

Conformational databases were generated for all three ligands of interest for use in the following docking experiments.

An X-ray crystal structure of the product-bound DapE crystal structure in the closed conformation was obtained<sup>98</sup> and the molecular system was uploaded into MOE. Following receptor preparation, molecular docking was performed using the previously-generated ligand conformation databases. Ligand docking was carried out in the prepared DapE enzyme model with product structures and solvent atoms inactivated and the docking site specified at the catalytic metal atoms. Ligand placement employed the Proxy Triangle method with London  $\Delta G$  scoring generated 50 data points which were further refined using the induced fit method with GBVI/WSA  $\Delta G$  scoring to obtain the top 30 docking results. The docking protocol was repeated for all three ligand models and analyzed for selection of the best docking pose. Docking poses of the substrate SDAP (**1a**) and analogs **1b** and **1c** were assessed as judged by their similarity to the product binding interactions seen in the original product-bound crystal structure. A single ligand docking pose was selected for each of the three ligand models providing initial substrate-bound ligand/enzyme models.

The three ligand/enzyme models were then solvated in a simple water box at pH of 7.4 which was treated with NaCl counterions to balance the charge. Periodic boundary conditions were enabled, and the hydrogen bonding network of the model was optimized by automatic sampling different tautomer/protomer states using Protonate3D<sup>102</sup> which calculates optimal protonation states, including titration, rotamer and “flips” using a large-scale combinatorial search.<sup>103</sup> The system atoms were then optimized with a short, localized molecular minimization process with atoms further than 8 Å from the ligand fixed and system refinement continued until a RMS Gradient of 0.1 kcal/mol/Å was attained. Molecular Dynamics parameters were set to

globally minimize the protein, ligand and solvent atoms in the system using an NPA algorithm with a Amber12:EHT force field, with a typical heating and cooling protocol. Simulation results were then minimized once again before the final binding poses were obtained for comparison.

#### **Modified SDAP as Potential Substrates.**

The hydrolytic activity of DapE with modified SDAP analogs was monitored by the decrease in absorbance at 225 nm via Shimadzu UV-2450 UV/Visible Spectrophotometer. All reaction volumes were 1 mL with 8 nM DapE and 5 mM of N-Methyl-SDAP **1b** or 5 mM N-Ac-SDAP **1d** in 50 mM HEPES buffer pH 7.5. Spectra were recorded over 35 min with one scan per minute. Enzyme dilutions were made directly before each trial from the concentrated stock solution at -80 °C.

#### **Ninhydrin-based Assay for DapE Enzymatic Activity.**

The enzymatic activity of DapE is measured in triplicate as follows: To 50 mM HEPES at pH 7.5 buffered solution with 8 nM DapE at 30 °C was added 2 mM N-methyl SDAP **1b** (final volume 200  $\mu$ L). The reaction was allowed to proceed for 10 min and quenched by heating at 100 °C for 1 minute and subsequent cooling on ice for 1 minute. To the cooled reaction was added the 2 % ninhydrin solution, and the reaction vortexed and subsequently heated at 80 °C for 15 min for the ninhydrin reaction. This reaction was quenched by placing in ice 2 min and the absorbance of 80  $\mu$ L was read at 570 nm. These reactions were set as 100 % standard enzymatic activity of DapE. Glutamic acid concentrations of 0 mM, 0.1 mM, 0.2 mM, 0.3 mM, 0.4 M, and 0.5 mM were used as a standard control of the measurement of primary amine.

#### **IC<sub>50</sub> Determinations.**

All inhibition assays were conducted with a reaction volume of 200  $\mu$ L, 2 mM N-methyl SDAP **1b** and 8 nM DapE unless otherwise stated. Glutamic acid standards of 0 to 0.5 mM were

used in every trial. To a 50 mM HEPES pH 7.5 buffered solution was added desired inhibitor concentration at 30 °C followed by DapE and allowed to incubate for 10 min. N-methyl SDAP **1b** was added and allowed to react for an additional 10 min and quenched by heating at 100 °C for 1 minute and cooled on ice to 30 °C. The 2 % ninhydrin solution (100 µL) was added, the reaction vortexed and heated at 80 °C for 15 min. after which the reaction was quenched by cooling on ice to 30 °C and the absorbance was examined at 570 nm. IC<sub>50</sub> values were obtained through GraphPad Prism software.

### **Chapter Acknowledgments**

I would like to thank my group members Tahirah Heath and Marlon Lutz for all their work they put into developing this DapE assay. I would also like to thank Dr. Miguel Ballicora for all the guidance he provided our group during the development of this assay. Finally, I would like to thank Dr. Danuta Gilner for providing the Becker Group and I with the L,L/D,D-SDAP substrate starting materials used to synthesize the N<sup>6</sup>-acetyl-L,L/D,D-SDAP analog.

## CHAPTER FOUR

### DESIGN, MODELING AND SYNTHESIS OF DI-METALLOENZYME INHIBITORS

#### **Inhibiting Di-nuclear Metalloenzymes**

Antibiotics rank as some of the most commonly used therapeutic agents prescribed by doctors today. The study of metalloproteins (MPs) and how to modulate their activity to stem the rise of the antibiotic resistance in bacteria has become a growing area of research. The impending dilemma of how to manage antibiotic resistance superbugs and the need to discover novel mechanisms of action to block bacterial proliferation has sparked our interest in the bacterial metalloenzymes DapE and NDM-1. The two enzymes possess the unique di-nuclear metal center motifs, but represent very different enzyme characteristics, with DapE possessing extraordinarily specific catalytic activity and NDM-1 demonstrating substrate promiscuity. These two pharmaceutically relevant enzyme targets account for unique challenges to medicinal chemistry, have still retained many of their secrets. However, our small molecular inhibitory strategies and *in silico* analyses efforts towards DapE and NDM-1 are thus presented in the following in hopes that one day our scientific understanding in the field may grow enough to develop methods of control over this elusive class of proteins.

## Inhibition of DapE.

The di-Zn metalloenzyme DapE, has been shown to cleave L,L-diaminopimelate (L,L-SDAP) into succinate and L,L-diaminopimelic acid (Figure 26).

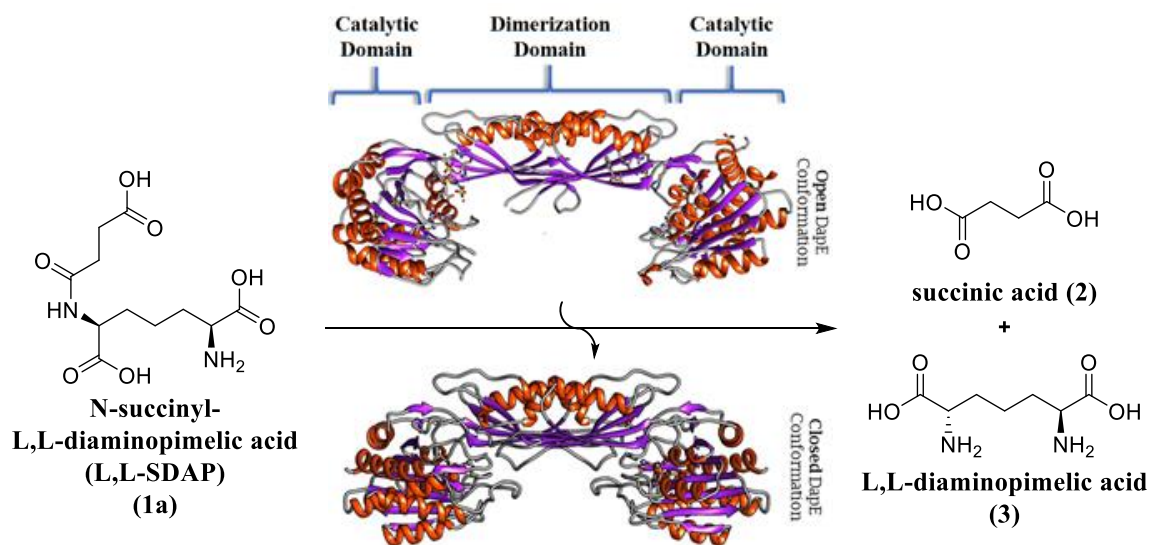


Figure 26. Enzymatic action for cleavage of L,L-SDAP by DapE.

DapE is ultimately responsible for synthesizing lysine for bacterial peptide synthesis, and for providing both mDAP and lysine for peptidoglycan cell wall formation in both Gram-negative and most Gram-positive bacteria (Figure 27A).<sup>28</sup> Peptidoglycan (PGN) is a major component of the cell wall of bacteria, and it is covalently linked to other biomolecular polymers, such as lipoprotein-peptides (LP) and lipoteichoic acids (LTA).<sup>104</sup> The PGN structure of both Gram-positive and Gram-negative bacteria contains repeating disaccharide backbones of N-acetylglucosamine (NAG) and  $\beta$ -(1-4)-N-acetylmuramic acid (NAM) that are cross-linked by peptide stem chains attached to the NAM residues. The first two residues of the stem peptide are generally L-alanine and D-glutamine or isoglutamine, while the last residue is typically D-alanine (Figure 27B) while the third peptide residue is a lysine in Gram-positive bacteria or



meso-diaminopimelate (mDAP) residue in Gram-negative bacteria as well as in many rod shaped Gram-positive bacteria such as *Listeria* and *Bacillus* species.<sup>105</sup> These two peptide-linking motifs are commonly referred to as the Lys-type PGN and DAP-type PGN, respectively.<sup>105</sup>

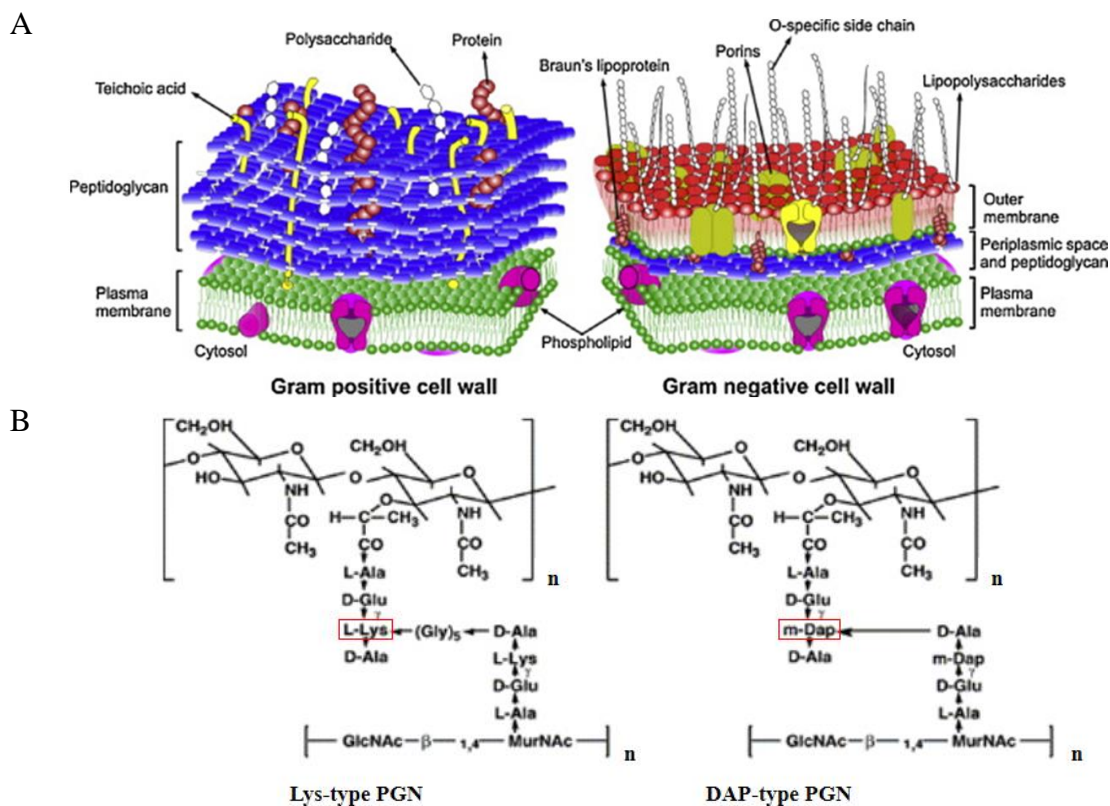


Figure 27. A) Cartoon representation of the Gram-positive (left) and Gram-negative (right) bacteria cell wall. B) Primary structures of Lys-type and DAP-type peptidoglycan.<sup>105</sup>

Therefore, enzymes involved in the critical mDAP/lysine biosynthetic pathway are all potential antibiotic targets. The bacterial biosynthesis of lysine utilizes L-aspartate and a series of four enzymes, aspartokinase, aspartate semialdehyde dehydrogenase, DapA, and DapB, to produce L-tetrahydropicolinate. The biosynthesis then diverges into three separate pathways: the acetylase pathway, the dehydrogenase pathway, and the succinylase pathway (see Chapter 2, Figure 7). The dehydrogenase pathway forms mDAP directly from L-tetrahydrodipicolinate, but this is a high-energy transformation and is limited to certain *Bacillus* species.<sup>28</sup> The acetylase

pathway is also a minor biosynthetic pathway for mDAP production and appears to also be limited to only a few *Bacillus* species.<sup>26</sup> The four-step succinylase biosynthetic branch is believed to be the major biosynthetic pathway for production of mDAP and ultimately lysine in most bacterial strains (Figure 28).<sup>24</sup>

### Succinylase Pathway

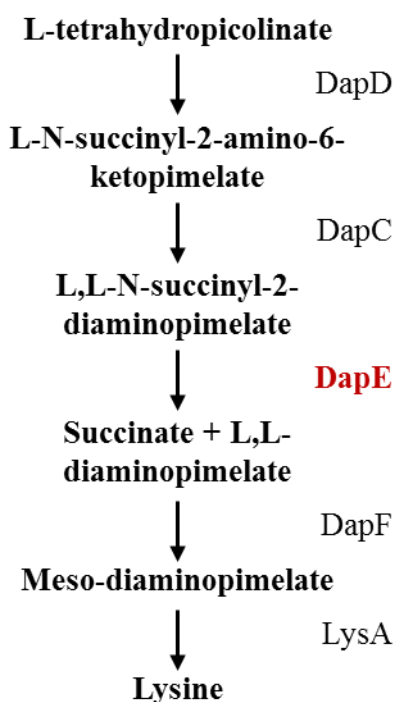


Figure 28. Succinylase Biosynthesis Pathway with DapE Metallohydrolase highlighted in red.<sup>24</sup>

Furthermore, it has been shown that deletion of the gene encoding DapE is lethal to *H. pylori* and *M. smegmatis*.<sup>29, 62</sup> Even in the presence of lysine-supplemented media, the *dapE* *H. pylori* knockout mutant was unable to grow, and only in the presence of supplemented mDAP could the mutant survive. The succinylase biosynthetic pathway is the predominate source for lysine in bacteria, making DapE essential for cell growth and proliferation. Inhibitors of peptidoglycan biosynthesis (vancomycin and  $\beta$ -lactams, to name a few) have proven to be very potent antibiotics, providing evidence that interfering with cell wall synthesis has deleterious

effects on bacterial cell survival. Since there are no similar biosynthetic pathways in mammals, inhibitors that target an enzyme in the succinylase pathway should exhibit selective toxicity against bacteria and not the human patient.<sup>28</sup> Moreover, the fact that the *dapE* gene has been discovered in *M. tuberculosis*, *Escherichia coli* (O157:H7), *Vibrio cholerae*, *Pseudomonas aeruginosa*, and *Staphylococcus aureus* (strain MRSA252) suggests that inhibitors of DapE may provide new broad-spectrum antibiotics.<sup>24</sup>

### Inhibition of NDM-1.

Because of their safety and efficacy,  $\beta$ -lactam antibiotics comprise one of the most popular categories of antibiotics utilized in medicine. Beta-lactam antibiotics, including the commonly prescribed drug penicillin, function by targeting cell wall development in bacteria (Figure 29). Altogether, the  $\beta$ -lactam classes including penicillin, cephalosporin and carbapenems represent more than 50% of antibiotic usage worldwide, and are the cheapest and among the most effective antibacterial agents available.<sup>106</sup>

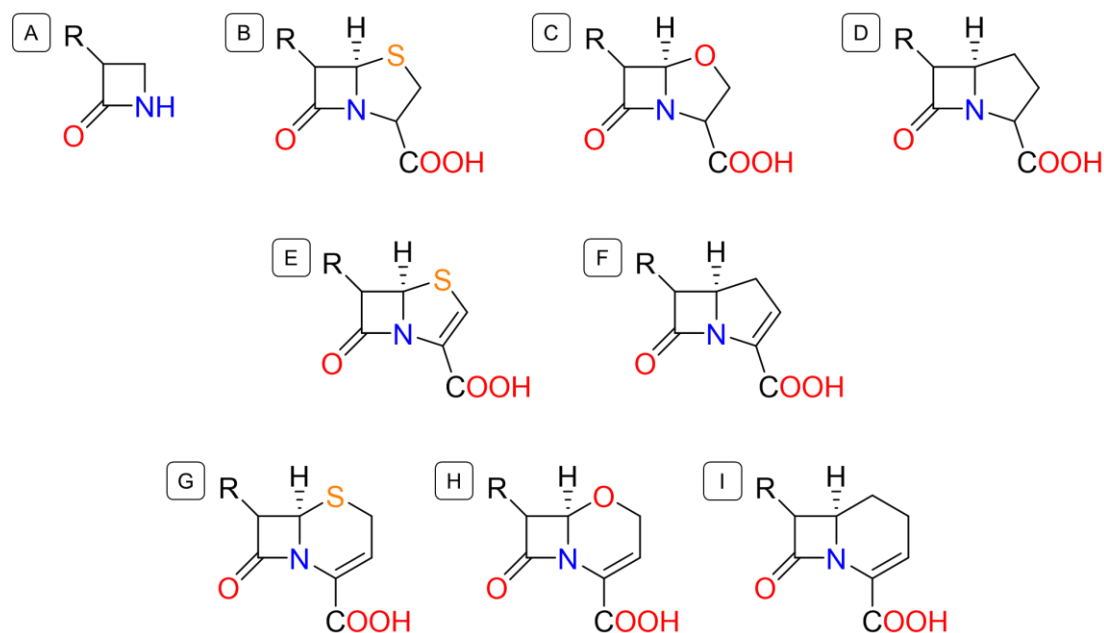


Figure 29. Core structures of the common  $\beta$ -lactam antibiotics. (Side chains omitted for clarity).

(A) Monobactam core, (B) Penam core, (C) Oxapenam core, (D) Carbapenam core, (E) Penem core, (F) Carbapenem core, (G) Cephem core, (H) Oxacephem core, (I) Carbacephem core.<sup>107</sup>

Fully functional bacterial cell walls are supported by interconnections of neighboring peptidoglycan monomers, and it is the formation of these interconnections that  $\beta$ -lactam antibiotics target. The polymerization of bacterial cell wall peptidoglycan (a NAG-NAM disaccharide bearing a pentapeptide) consists of a transglycosylation reaction and followed by a transpeptidation reaction, the latter of which is inhibited by  $\beta$ -lactam antibiotics through formation of irreversibly reacting with the reactive serine residues of these transpeptidases. This action blocks peptidoglycans from connecting to each other, leading to impeded cell wall synthesis resulting in bacterial cell death.

Unfortunately,  $\beta$ -lactam antibiotic efficacy has dropped tremendously in recent years because of the increased spread of antibiotic resistance, and the effects have been devastating. In the U.S. alone, antibiotic resistant bacteria have caused over 20,000 deaths and two million infections annually. Resistant bacteria contribute to surgical complications, resulting in the deaths of countless more individuals. Antibiotic resistance has thus been called one of our most serious public health threats. To combat the increasingly urgent problem of antibiotic resistance, we have collaborated with Dr. Walter Fast of UT Austin to assay our series of novel non-covalent metalloenzyme inhibitors against New Delhi Metallo- $\beta$ -lactamase-1 (NDM-1).

The recently-discovered bacterial enzyme New Delhi Metallo- $\beta$ -lactamase-1 (NDM-1) is a di-nuclear metallo- $\beta$ -lactamase (MBL) belonging to the B1 family. NDM-1 is capable deactivating commonly administered  $\beta$ -lactam antibiotics by hydrolyzing the amide bond of the four-membered  $\beta$ -lactam ring (Figure 29).<sup>108</sup>

The gene responsible for encoding NDM-1 (*bla*<sub>NDM-1</sub>) was first isolated in 2009 from

*Klebsiella pneumoniae* from a UK patient who had attended a hospital in India. The plasmid encoded NDM-1 is one of a number of metallo- $\beta$ -lactamase genes that are capable of horizontal gene transfer which has contributed to the rapid global spread of resistant superbugs.<sup>32, 34, 48, 51, 55,</sup>

108-148

There are more than 1000  $\beta$ -lactamases identified and isolated to date that populate four classes of  $\beta$ -lactamases, A, B, C and D, which can hydrolyze all  $\beta$ -lactam drugs except the monobactams.<sup>106</sup> Classes C and D represent the serine  $\beta$ -lactamases. Serine- $\beta$ -lactamases utilize active site residues including a nucleophilic serine residue to catalyze the hydrolysis of the lactam. However, while serine- $\beta$ -lactamases are sensitive to an array of mechanism-based inhibitors such as clavulanic acid, sulbactams and tazobactams, the B1 class of metallo- $\beta$ -lactamases remains insensitive to known serine- $\beta$ -lactamases due to the utilization of active-site metal ions. There are currently no clinical inhibitors in use that are capable of targeting these enzymes.<sup>106</sup>

The search for new antibiotics that target enzymes is essential for humans' continued standard of healthcare and lifestyle. Targeting the succinylase biosynthetic pathway is an advantageous approach for medicinal chemistry as DapE has potential to provide science and the healthcare system with a much-needed new class of antibacterial inhibitors. In addition, developing strategies to reinvigorate the potency of existing antibiotics is of great interest to society. Targeted inhibition of NDM-1 has the potential to reset the clock on  $\beta$ -lactam antibiotic resistance. Furthermore, these two pharmaceutically relevant di-nuclear metalloenzyme targets represent very useful model systems to aid in developing novel metalloenzyme inhibition strategies.

**Original 225nm DapE Assay.**

There have been a paucity of medicinal chemistry leads to serve as starting points for the development of DapE inhibitors, exacerbated by the critical need for a robust assay to monitor the SAR of inhibition. Mandal recently reported a small molecule docking and fragment-based in silico screening approach based on the known substrate (L,L-SDAP) that yielded three simple peptide derivatives (Gly-Gly, N-formyl-Lysine, and a Gly-(nor)Ile derivative)<sup>149</sup> that are of limited utility as starting points to launch a medicinal chemistry effort.

The original assay for DapE activity and inhibition was to monitor the cleavage of the SDAP substrate at 225 nm.<sup>66</sup> The very low wavelength of monitoring amide bond cleavage precludes using this assay for many drug-like molecules with chromophores that would interfere with monitoring at 225 nm. Nonetheless, our group employed this assay to screen a targeted library of potential inhibitors containing zinc-binding groups including thiols and boronic acids, and identified captopril as a fairly potent lead molecule ( $IC_{50} = 3.3 \mu M$ ,  $K_i = 1.8 \mu M$ , competitive).<sup>93</sup> While captopril might be considered to be a good lead molecule for medicinal chemistry optimization, given its use as an ACE inhibitor for hypertension, its thiol moiety is generally considered to be a liability in the ultimate quest for druggability, given concerns about selectivity, as thiols can bind tightly to zinc in a variety of metalloenzymes. The sensitivity of thiols toward oxidation also complicates synthesis and analysis. Furthermore, while captopril both inhibits DapE and exhibits antibiotic activity, its antibiotic activity is independent of DapE inhibition<sup>150</sup>, suggesting that inhibition of multiple targets may give rise to its antibacterial efficacy.

To further understand the catalytic and structural features of DapE enzymes we have determined the structure of HiDapE in complex with the bound products. The product-bound

structure of HiDapE reveals conformational changes induced upon substrate binding and provides significant insight into how this enzyme coordinates hydrolysis, while molecular dynamics simulation provides insight of the substrate and product release.

### High-Throughput Screen & Early Docking Results.

Thus, while captopril serves as a standard DapE inhibitor and ligand for co-crystallization, given the paucity of DapE inhibitor leads, a high-throughput screen (HiTS) was performed to provide new starting points for medicinal chemistry. This was supported by an earlier NIH R15 by our collaborator Richard Holz (NIAID 1R15AI085559-01A1), and was accomplished by screening 33,000 compounds from ChemBridge using the coupled assay shown in Figure 30 with a cut-off of at least 20 % inhibition at 12  $\mu$ M concentration of inhibitors.

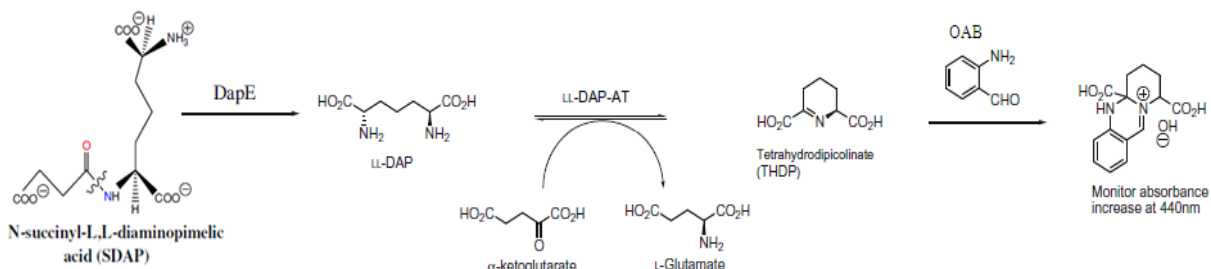


Figure 30. Coupled assay for HiTS screen.

The successful HiTS screen provided five inhibitors (1-5, Figure 31) belonging to four distinct chemical classes; two simple indoline sulfonamides, a functionally rich thio-tetrazoyl-thiazole, a di-fluorinated sulfonamide, and a flexible but hydrophobic  $\beta$ -sulfone. We hypothesized the leads identified by our previous HiTS screen could ultimately be optimized to nanomolar potency inhibitors with antibiotic activity. To accomplish this goal, we have focused synthetic efforts on four different synthetic series possessing 6- and 7-sulfonyl indolines and/or phenylsulfonamide core structural motifs.

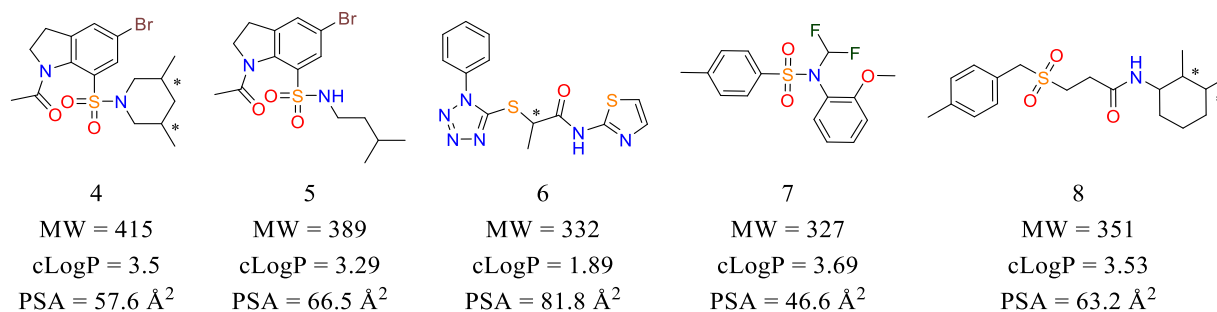


Figure 31. Five inhibitors identified through the HiTS screen.

## Material and Methods

### Metalloenzyme Inhibition Assays.

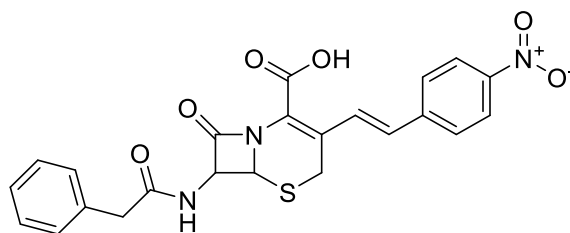
**DapE Assay Description.** All DapE inhibition and activity assays were conducted in the Becker lab by Tahirah Heath. The enzymatic activity of DapE was measured in triplicate at 570 nm by the Ruhemann's purple complex formed through the reaction of the cleaved primary amine and ninhydrin at 30 °C. To 175 μL of 50 mM HEPES buffer at pH 7.5 with 5 μL of 1μM DapE stock solution at 30°C was added 20 μL of 10 mM monomethyl SDAP ((2*S*,6*S*)-2-(3-carboxypropanamido)-6-(methylamino)heptanedioic acid) TFA salt. The reaction was allowed to proceed for 10 min and quenched by heating at 100 °C for 1 minute and subsequently cooling on ice for 1 minute. To the cooled reaction was added 2 % ninhydrin reagent in 100 % DMSO (final volume 300 μL) and subsequently heated to 80 °C for 15 min. This was quenched by placing in ice water for 2 min, and the absorbance of 80 μL was read at 570 nm via a microplate reader. These reactions were set as 100 % standard enzyme activity of DapE. Glutamic acid of concentrations 0 mM, 0.02 mM, 0.04 mM, 0.06 mM, 0.08 mM, 0.1 mM, 0.2 mM, 0.4 mM, 0.6 mM, 0.8 mM, 1.0 mM were used as a standard control of primary amine to compare enzyme activity.

The IC<sub>50</sub> of the inhibitors described herein can be determined using captopril as the positive control. To a reaction mixture in 50 mM at pH 7.5 HEPES buffer, containing DapE



(0.25  $\mu\text{M}$ ), a solution of the inhibitor is added. Next, the reaction mixture is allowed to incubate for 10 min. Thereafter, 1 mM of alpha-N-monomethylated SDAP substrate, initially prepared by reductive amination of the SDAP substrate with aqueous formaldehyde and sodium cyanoborohydride, was added, and reaction was allowed to incubate for 40 min. Next, 0.33 mL of the reaction solution was transferred into another 1.7 mL Eppendorf tube, 0.166 mL of 2 % Ninhydrin reagent was added to the reaction mixture, and the mixture was heated in a boiling water bath for 15 min. The water bath was cooled. The mixture was vigorously agitated and the absorbance was measured at 570 nm. The  $\text{IC}_{50}$  for the captopril standard is ca. 3.0  $\mu\text{M}$ .

**NDM-1 Assay Description.** All NDM-1 inhibition and activity assays were conducted by the Fast Lab at the University of Texas Austin. The ability of the compounds described herein to inhibit NDM-1 was determined in the following way. A Substrate Working Solution was prepared from Chromacef (6  $\mu\text{M}$ ) and Tween-20 (0.02 % v/v) in water. An Enzyme Working Solution was prepared with NDM-1 (0.5  $\mu\text{g}/\text{mL}$ ), HEPES (0.1 M), pH 7 and Tween-20 (0.02 % v/v). An Inhibitor Working Solution was prepared from 50 mM of the inhibitor in DMSO. The final assay conditions were 1 mL, HEPES (50 mM), pH 7, Tween-20 (0.02 % v/v), Chromacef (3  $\mu\text{M}$ ),  $\Delta 35$  NDM-1 (0.25  $\mu\text{g}/\text{mL}$ ). Extra zinc was omitted from these assays because extra  $\text{ZnSO}_4$  interferes with the metal binding groups in inhibitors.



Chromacef

Figure 32. Structure of Chromacef, a chromogenic cephalosprin used in the detection and assay of  $\beta$ -lactamases.<sup>151</sup>

An aliquot of the Inhibitor Working Solution was added to a polystyrene disposable

cuvette to achieve a final concentration of 0-50  $\mu\text{M}$  (in 1 mL final). Supplemental DMSO was added to reach a final volume of 4  $\mu\text{L}$ . NDM-1 Working Solution (0.05 mL) was added to the cuvette and the inhibitor and enzyme were allowed to incubate for about 20 min. The reaction was initiated by added 0.5 mL Substrate Working Solution. The solution was mixed quickly, but gently to avoid bubble formation after Chromacef 6 M addition to start the reaction. The reaction was mixed fast, but gently. The change in absorbance  $\Delta\text{Abs}_{442\text{nm}/\text{min}}$  was measured for each inhibitor from the linear slope from each inhibitor concentration.

### ***In Silico* Docking Protocols with DapE.**

Molecular modeling and docking simulations were performed using the open source web service SWISSDOCK and the Chemical Computing Group's Molecular Operating Environment (MOE) computation suites.<sup>76</sup> We have docked three separate ligand library databases into the open conformation of DapE (PDB ID: 3IC1 or 5UEJ) using the protocol described herein. In silico screening techniques are instrumental in helping us understand how the native substrate, standardized compounds from assay development, or compounds found during high throughput screening experiments can interact with the enzyme at resting state and before the dynamic enzyme conformational changes leading to mechanistic turnover have occurred.

**Early SWISSDOCK *In Silico* Docking Protocol.** Analysis of the hits through docking suggests a di-Zn binding motif for all four structural types identified. A library of 6- and 7-substituted N-acetylundoline sulfonamides with various alkyl group substituted to the sulfonamide nitrogen were prepared based on the two N-acetylundoline sulfonamides hit core structures (Table 2). Early docking studies using SwissDock were performed with this library using the open conformational HiDapE crystal structure (PDB ID: 3IC1) as the docking receptor.

Table 2. Sulfonamide Ligand Library for SWISSDOCK.

| Ligand Entry  |               | R                                  | X  |
|---------------|---------------|------------------------------------|----|
| 6 Substituted | 7 Substituted |                                    |    |
| <b>5a</b>     | <b>5c</b>     | -NH-isoPentyl                      | Cl |
| <b>5b</b>     | <b>5d</b>     |                                    | Br |
| <b>9a</b>     | <b>9b</b>     | -NH-cylcohexyl                     | Cl |
| <b>10a</b>    | <b>10b</b>    |                                    | Br |
| <b>11a</b>    | <b>11b</b>    | -N-Pyrrolidinyl                    | Cl |
| <b>12a</b>    | <b>12b</b>    |                                    | Br |
| <b>13a</b>    | <b>13b</b>    | -N-Piperidinyl                     | Cl |
| <b>14a</b>    | <b>14b</b>    |                                    | Br |
| <b>15a</b>    | <b>15b</b>    | -N(2-methoxyethan-yl) <sub>2</sub> | Cl |
| <b>16a</b>    | <b>16b</b>    |                                    | Br |
| <b>17a</b>    | <b>17b</b>    | -N(ethyl) <sub>2</sub>             | Br |
| <b>18a</b>    | <b>18b</b>    | -N(propyl) <sub>2</sub>            | Cl |
| <b>19a</b>    | <b>19b</b>    |                                    | Br |
| <b>20a</b>    | <b>20b</b>    | -NH-isoPropyl                      | Cl |
| <b>21a</b>    | <b>21b</b>    |                                    | Br |
| <b>22a</b>    | <b>22b</b>    | -PheOMe                            | Cl |
| <b>23a</b>    | <b>23b</b>    |                                    | Br |
| <b>24a</b>    | <b>24b</b>    | -MetOMe                            | Br |
| <b>25a</b>    | <b>25b</b>    | -ProOBz                            | Br |
| <b>26a</b>    | <b>26b</b>    | -GlyOMe                            | Cl |
| <b>27a</b>    | <b>27b</b>    |                                    | Br |
| <b>28a</b>    | <b>28b</b>    | -βAlaOMe                           | Br |
| <b>29a</b>    | <b>29b</b>    | -ValOMe                            | Cl |
| <b>30a</b>    | <b>30b</b>    |                                    | Br |

### Later MOE *In Silico* Docking Protocols with DapE.

**HiTS Hit Ligand Library Dock to NmDapE\_OC.** The five high throughput screen hits and two simplified 6- and 7-substituted piperidinyl analogs of HiTS hit **4** were built using ChemDraw and included in an MOE ligand database. Structures containing stereocenters were separated into individual enantiomers or diastereomeric analogs and included in the database.

The nineteen original ligand structures were minimized in the gas phase using the force field MMFF94X followed by protonation states enumeration at pH = 7.4 using the Wash function in MOE (Figure 33).

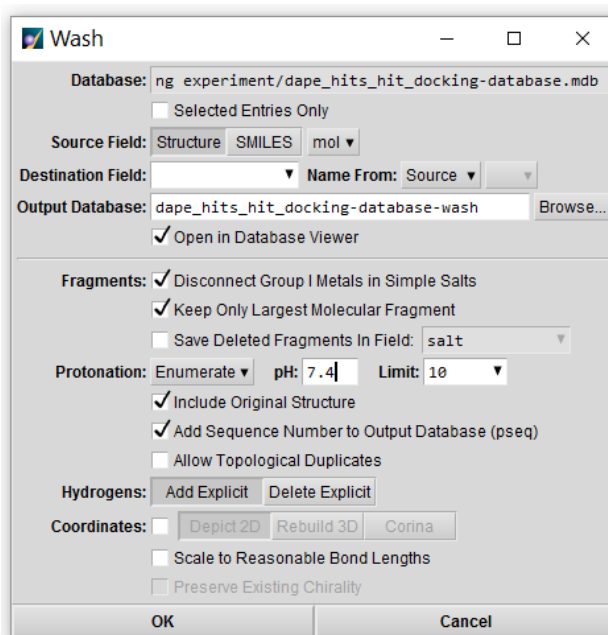


Figure 33. Database Wash utility function in MOE used to quickly prepare large database set for further analysis in MOE.

The database preparation protocol brought to total number of docking ligands to twenty-one and are presented in Table 3 below.

Table 3. High Throughput Screen Ligand Docking Library.<sup>a</sup>

| Seq      | IUPAC Name  | #          | MW     | cLogP | TPSA | HB acc | HB don | B rot. |
|----------|---|------------|--------|-------|------|--------|--------|--------|
| <b>1</b> | 1-(5-bromo-6-(piperidin-1-ylsulfonyl)indolin-1-yl)ethan-1-one                       | <b>14a</b> | 387.30 | 1.9   | 57.7 | 3      | 0      | 3      |
| <b>2</b> | 1-(5-bromo-7-(piperidin-1-ylsulfonyl)indolin-1-yl)ethan-1-one                       | <b>14b</b> | 387.30 | 1.9   | 57.7 | 3      | 0      | 3      |
| <b>3</b> | 1-(5-bromo-6-(((3R,5S)-3,5-dimethylpiperidin-1-yl)sulfonyl)indolin-1-yl)ethan-1-one | <b>4a</b>  | 415.35 | 2.6   | 57.7 | 3      | 0      | 3      |
| <b>4</b> | 1-(5-bromo-6-(((3S,5S)-3,5-dimethylpiperidin-1-yl)sulfonyl)indolin-1-yl)ethan-1-one | <b>4b</b>  | 415.35 | 2.6   | 57.7 | 3      | 0      | 3      |

|           |   |           |         |     |       |   |     |   |
|-----------|---|-----------|---------|-----|-------|---|-----|---|
| <b>5</b>  | 1-(5-bromo-6-(((3R,5R)-3,5-dimethylpiperidin-1-yl)sulfonyl)indolin-1-yl)ethan-1-one | <b>4c</b> | 415.35  | 2.6 | 57.7  | 3 | 0   | 3 |
| <b>6</b>  | 1-(5-bromo-6-(((3S,5R)-3,5-dimethylpiperidin-1-yl)sulfonyl)indolin-1-yl)ethan-1-one | <b>4d</b> | 415.35  | 2.6 | 57.7  | 3 | 0   | 3 |
| <b>7</b>  | 1-(5-bromo-7-(((3S,5R)-3,5-dimethylpiperidin-1-yl)sulfonyl)indolin-1-yl)ethan-1-one | <b>4e</b> | 415.35  | 2.6 | 57.7  | 3 | 0   | 3 |
| <b>8</b>  | 1-(5-bromo-7-(((3R,5S)-3,5-dimethylpiperidin-1-yl)sulfonyl)indolin-1-yl)ethan-1-one | <b>4f</b> | 415.35  | 2.6 | 57.7  | 3 | 0   | 3 |
| <b>9</b>  | 1-(5-bromo-7-(((3S,5S)-3,5-dimethylpiperidin-1-yl)sulfonyl)indolin-1-yl)ethan-1-one | <b>4g</b> | 415.35  | 2.6 | 57.7  | 3 | 0   | 3 |
| <b>10</b> | 1-(5-bromo-7-(((3R,5R)-3,5-dimethylpiperidin-1-yl)sulfonyl)indolin-1-yl)ethan-1-one | <b>4h</b> | 415.35  | 2.6 | 57.7  | 3 | 0   | 3 |
| <b>11</b> | 1-acetyl-5-bromo-N-isopentylindoline-6-sulfonamide                                  | <b>5a</b> | 389.31  | 3.0 | 66.5  | 3 | "1" | 6 |
| <b>12</b> | 1-acetyl-5-bromo-N-isopentylindoline-7-sulfonamide                                  | <b>5b</b> | 389.31  | 3.0 | 66.5  | 3 | "1" | 6 |
| <b>13</b> | N-(difluoromethyl)-N-(2-methoxyphenyl)-4-methylbenzenesulfonamide                   | <b>6</b>  | 327.35  | 3.2 | 46.6  | 3 | "0" | 5 |
| <b>14</b> | (R)-2-((1-phenyl-1H-tetrazol-5-yl)thio)-N-(thiazol-2-yl)propanamide                 | <b>7a</b> | 332.412 | 1.7 | 85.66 | 5 | 1   | 6 |
| <b>15</b> | (R)-2-((1-phenyl-1H-tetrazol-5-yl)thio)-N-(thiazol-2-yl)propanamide                 | <b>7b</b> | 333.42  | 2.2 | 86.8  | 4 | 0   | 6 |
| <b>16</b> | (S)-2-((1-phenyl-1H-tetrazol-5-yl)thio)-N-(thiazol-2-yl)propanamide                 | <b>7c</b> | 332.41  | 1.7 | 85.6  | 5 | 1   | 6 |
| <b>17</b> | (S)-2-((1-phenyl-1H-tetrazol-5-yl)thio)-N-(thiazol-2-yl)propanamide                 | <b>7d</b> | 333.42  | 2.2 | 86.8  | 4 | 0   | 6 |
| <b>18</b> | N-((2R,3R)-2,3-dimethylcyclohexyl)-3-((4-methylbenzyl)sulfonyl)propanamide          | <b>8a</b> | 351.51  | 3.4 | 63.2  | 3 | 1   | 7 |
| <b>19</b> | N-((2S,3S)-2,3-dimethylcyclohexyl)-3-((4-methylbenzyl)sulfonyl)propanamide          | <b>8b</b> | 351.51  | 3.4 | 63.2  | 3 | 1   | 7 |
| <b>20</b> | N-((2R,3S)-2,3-dimethylcyclohexyl)-3-((4-methylbenzyl)sulfonyl)propanamide          | <b>8c</b> | 351.51  | 3.4 | 63.2  | 3 | 1   | 7 |
| <b>21</b> | N-((2S,3R)-2,3-dimethylcyclohexyl)-3-((4-methylbenzyl)sulfonyl)propanamide          | <b>8d</b> | 351.51  | 3.4 | 63.2  | 3 | 1   | 7 |

<sup>a</sup>Table Legend: cLogP = calculated octanol/water partition coefficient. HBacc = number of hydrogen bond acceptors. TPSA = total polar surface area. HBdon = number of hydrogen bond donors. B-rot. = number of rotatable single bonds.

The next step in the docking process is to prepare the docking receptor model. The recent Apo DapE structure from *Neisseria meningitidis* (PDB ID: 5UEJ, 1.30 Å resolution) reported by our collaborator Dr. Nocek of Argonne National Laboratory was used due to the high quality of refinement at the dimerization loops discussed in Chapter 2 to play a role in substrate binding. The .pdb file was retrieved from the protein databank and loaded into MOE. Then the structure was prepared in MOE using the Structure Preparation utility to model in any missing loops and fix format translational errors between different computational platforms (Figure 34). Structure Preparation was followed by Protonate3D to optimize the protonation network of the system.

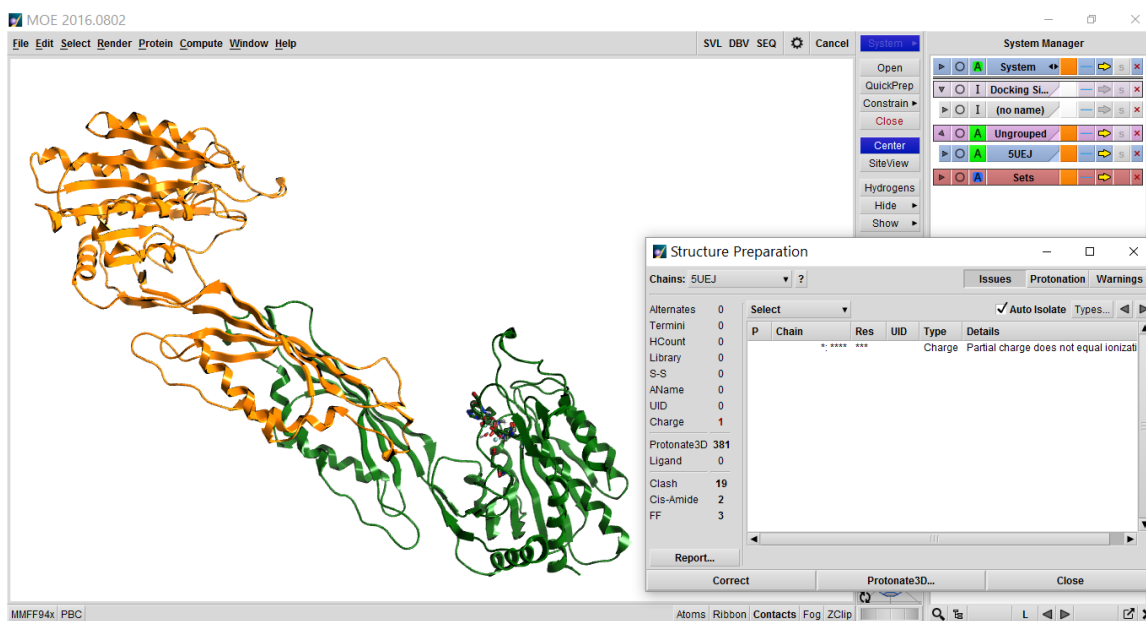


Figure 34. MOE docking receptor preparation of NmDapE\_OC model (PDB ID: 5UEJ, 1.30 Å resolution).

We then determined potential binding pockets which were mapped out using the 'SiteFinder' MOE utility (Figure 35). The SiteFinder calculation can then be used to generate

dummy atoms that populate empty pocket space which can be used to direct molecular docking in later steps.

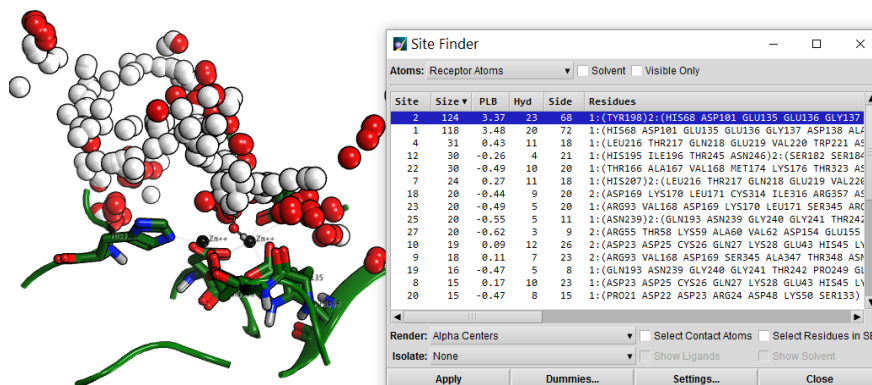


Figure 35. Site Finder operating window in MOE used for calculating the probable ligand binding sites for NmDapE\_OC docking model.

Upon completion of our receptor preparation, the model was reviewed for consistency and saved as the default DapE\_OC docking receptor (Figure 36). The previously generated ligand database and the prepared receptor model was used to perform the molecular docking protocol in two separate stages; first, a global induced-fit docking which incorporated the Site Finder dummy atoms as docking sites, the second, a site-directed induced-fit docking at the Zn metallo center.

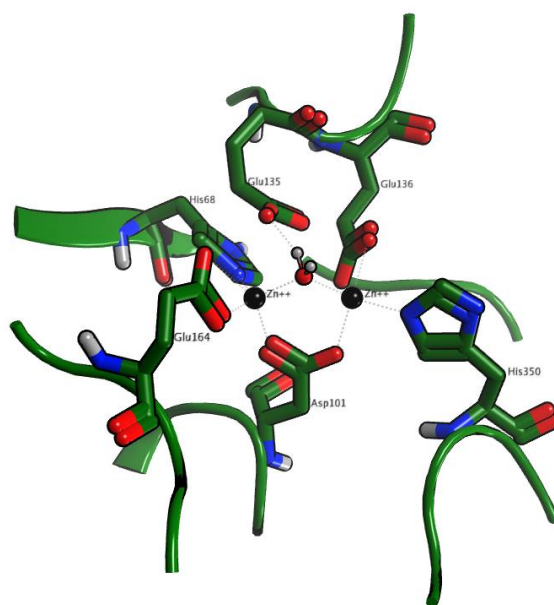


Figure 36. Site-Directed Docking Metal Center Site for NmDapE\_OC Receptor Model.

The placement and scoring functions were identical between the two docking stages enabling our docking results to be merged together. Docking Parameters for both stages are presented in Table 4.

Table 4. HiTS-hits\_NmDapE\_OC Docking Parameters.<sup>a</sup>

| Global Site Finder Docking Parameters  | Site Directed Docking Parameters   |
|--|--|
| <b>Receptor:</b> MOE; Receptor Atoms   | <b>Receptor:</b> MOE; Receptor Atoms   |
| <b>Site:</b> Dummy Atoms   | <b>Site:</b> Di-Zn Metal Site  |
| <b>Pharmacophore:</b> NA   | <b>Pharmacophore:</b> NA   |
| <b>Density:</b> NA   | <b>Density:</b> NA   |
| <b>Ligand:</b> MDB File;<br>DapE_HiTS_hit_docking_database_wash  | <b>Ligand:</b> MDB File;<br>DapE_HiTS_hit_docking_database_wash  |
| <b>Method Placement=</b><br>Alpha Triangle; Score: Affinity $\Delta G$<br>-50 Poses Generated / ligand entry | <b>Method Placement=</b><br>Alpha Triangle; Score: Affinity $\Delta G$<br>-50 Poses Generated / ligand entry |
| <b>Method Refinement =</b><br>Induced Fit Receptor; Score: GBVI/WSA dG<br>-15 Poses Kept / ligand entry      | <b>Method Refinement =</b><br>Induced Fit Receptor; Score: GBVI/WSA dG<br>-15 Poses Kept / ligand entry      |
| <b>Output:</b> HiTS-hits_NmDapE_OC-SF-dock.mdb   | <b>Output:</b> HiTS-hits_NmDapE_OC-SD-dock.mdb   |

<sup>a</sup>See appendix A for in silico file naming paradigm. Table Legend: MDB = molecular database. HiTS = high throughput screen. NmDapE\_OC = apo DapE from *Neisseria meningitidis* in the open conformation possessing 1.30 Å resolution. GBVI/WSA = Generalized Born Volume Integer Weight Surface Area. SF = Site Finder docking. SD = site directed docking.



Docking Parameters were carried out into the prepared NmDapE\_OC enzyme model with solvent atoms inactivated. The docking Site was specified at the Site Finder dummy atoms or at the catalytic metal atoms (Figure 35). Ligand placement employing Alpha Triangle method with Affinity  $\Delta G$  scoring generated 50 data points which were further refined using the induced fit method with GBVI/WSA  $\Delta G$  scoring to obtain the top 15 docked poses per ligand entry.

**Standardized Substrate & Ligand Library Dock to NmDapE\_OC.** The default NmDapE\_OC docking receptor was used to perform a site-directed induced-fit docking at the di-Zn metallo center with a database of standardized substrate and inhibitor ligands known for DapE in enumerated protonation states. The ligand database entries are summarized in Table 5 below.

Table 5. Standardized Substrate & Ligand Library.<sup>a</sup>

| Seq.     | IUPAC  | Formal Charge | MW     | cLogP | HB acc | HB don | B-rot |
|----------|--|---------------|--------|-------|--------|--------|-------|
| <b>1</b> | (2S,6R)-2-amino-6-(3-carboxypropanamido) heptanedioic acid | 0             | 290.27 | -3.64 | 8      | 8      | 8     |
| <b>2</b> | (2S,6R)-2-amino-6-(3-carboxypropanamido) heptanedioic acid | -2            | 288.26 | -0.88 | 1      | 1      | 1     |
| <b>3</b> | (2R,6S)-2-amino-6-(3-carboxypropanamido) heptanedioic acid | 0             | 290.27 | -3.64 | 8      | 8      | 8     |
| <b>4</b> | (2R,6S)-2-amino-6-(3-carboxypropanamido) heptanedioic acid | -2            | 288.26 | -0.88 | 1      | 1      | 1     |
| <b>5</b> | (2R,6R)-2-amino-6-(3-carboxypropanamido) heptanedioic acid | 0             | 290.27 | -3.64 | 8      | 8      | 8     |
| <b>6</b> | (2R,6R)-2-amino-6-(3-carboxypropanamido) heptanedioic acid | -2            | 288.26 | -0.88 | 1      | 1      | 1     |
| <b>7</b> | (2S,6S)-2-amino-6-(3-carboxypropanamido) heptanedioic acid | 0             | 290.27 | -3.64 | 8      | 8      | 8     |

|           |   |    |        |       |   |   |   |
|-----------|---|----|--------|-------|---|---|---|
| <b>8</b>  | (2S,6S)-2-amino-6-(3-carboxypropanamido)heptanedioic acid         | -2 | 288.26 | -0.88 | 1 | 1 | 1 |
| <b>9</b>  | (2S,6S)-2-(3-carboxypropanamido)-6-(methylamino)heptanedioic acid | 0  | 304.30 | -0.71 | 8 | 8 | 8 |
| <b>10</b> | (2S,6S)-2-(3-carboxypropanamido)-6-(methylamino)heptanedioic acid | -2 | 302.28 | -0.35 | 1 | 1 | 1 |
| <b>11</b> | (2S,6S)-2-acetamido-6-(3-carboxypropanamido)heptanedioic acid     | 0  | 332.31 | -1.07 | 8 | 8 | 8 |
| <b>12</b> | (2S,6S)-2-acetamido-6-(3-carboxypropanamido)heptanedioic acid     | -3 | 329.29 | -0.71 | 2 | 2 | 2 |
| <b>13</b> | (2R,6S)-2-acetamido-6-(3-carboxypropanamido)heptanedioic acid     | 0  | 332.31 | -1.07 | 8 | 8 | 8 |
| <b>14</b> | (2R,6S)-2-acetamido-6-(3-carboxypropanamido)heptanedioic acid     | -3 | 329.29 | -0.71 | 2 | 2 | 2 |
| <b>15</b> | phenylboronic acid  | 0  | 121.93 | 0.92  | 2 | 2 | 2 |
| <b>16</b> | phenylboronic acid  | -1 | 120.92 | 1.40  | 2 | 1 | 2 |
| <b>17</b> | 3-mercaptopbenzoic acid   | 0  | 154.19 | 2.11  | 2 | 2 | 2 |
| <b>18</b> | 3-mercaptopbenzoic acid   | -1 | 153.18 | 2.23  | 0 | 0 | 0 |
| <b>19</b> | 3-mercaptopbenzoic acid   | -2 | 152.17 | 2.23  | 0 | 0 | 0 |
| <b>20</b> | thiopheneboronic acid   | 0  | 127.96 | 0.78  | 2 | 2 | 2 |
| <b>21</b> | thiopheneboronic acid   | -1 | 126.95 | 1.26  | 2 | 1 | 2 |
| <b>22</b> | L-Captopril   | 0  | 217.29 | 0.68  | 3 | 2 | 3 |
| <b>23</b> | L-Captopril carboxylate   | -1 | 216.28 | 0.80  | 1 | 0 | 1 |
| <b>24</b> | L-Captopril di-anion  | -2 | 215.27 | 0.80  | 1 | 0 | 1 |
| <b>25</b> | L-Captopril thiol anion   | -1 | 216.28 | 0.80  | 1 | 0 | 1 |

<sup>a</sup>Table Legend: cLogP = calculated octanol/water partition coefficient. HB acc = number of hydrogen bond acceptors. HB don = number of hydrogen bond donors. B-rot. = number of rotatable single bonds.

Docking Parameters were carried for the prepared NmDapE\_OC enzyme model with solvent atoms inactivated. The docking site was specified at the catalytic binding pocket.

Ligand placement employing Alpha Triangle method with Affinity  $\Delta G$  scoring generated 500

data points which were further refined using the induced-fit method with GBVI/WSA  $\Delta G$  scoring to obtain the top 50 docked poses per ligand entry.

### **6- & 7-Substituted Sulfonamide Indoline Series.**

We have followed up to varying degrees on all five hits from the high-throughput screen (Figure 31) but the synthetic work discussed herein has focused on the first two indoline sulfonamide HiTS hits. We have chosen to focus on the indoline scaffold as the top priority, first because two of the independent hits were indoline sulfonamides, thus providing an internal confirmation, and also the indoline scaffold is important in natural products as well as in drug molecules.<sup>152</sup> Further, the indoline structure provides a divergent scaffold toward analogs that may be readily functionalized at different positions including on the indoline nitrogen, the 5-position (bromo in the two hits), and the 6- and 7-positions (7-sulfonamide depicted in the hits). Regarding the actual location of the sulfonamide in hits **4** and **5**, Borrer has previously shown<sup>153</sup> that chlorosulfonylation attacks the 6-position of the indoline, (Figure 37a) correcting a still-persistent error in the literature that had assumed that electrophilic aromatic substitution would attack the 7-position, ortho to the *o*-, *p*-directly indoline nitrogen. Thus, though encouraged by initial docking of 7-sulfonamides, we realized that the given structures for the library hits were probably incorrectly labeled as 7-sulfonamides, since the structures given could not be synthesized by existing literature methods and should be represented as 6-sulfonamides. ChemBridge was not able to provide samples for further analysis, nor could they produce a synthetic protocol for the preparation of those hits, nonetheless, docking of 6- and 7-sulfonamides reveals the potential for binding of both isomers. Interestingly there is a preference for binding of the less-accessible 7-sulfonamides. The only reported synthesis of indoline-7-sulfonamides was again by Borrer<sup>153</sup> who employed a reaction of chlorosulfonyl isocyanate with

5-bromoindoline to deliver the sulfonyl intramolecularly to the 7-position, then oxidizing the indoline to the known indole-7-N-methylsulfonamide for structure confirmation. Borrer's chemistry has been adapted by us to prepare the indoline-7-sulfonamido derivatives via  $S_N2$  alkylation of the cyclic sulfonyl urea followed by hydrolysis. (Figure 37b).

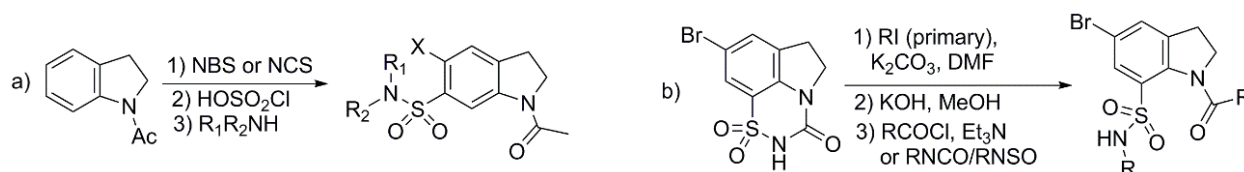


Figure 37. a) Synthesis of indoline-6-sulfonamides, b) Borrer-adapted synthesis of 7-sulfonamides.

Our research team has successfully designed and synthesized 6- and -7 sulfonamide indolines by the following methods. Batch synthesis of N-acetyl indoline (**31**) was conducted per conditions described by Wu *et al.*<sup>154</sup> Indoline in methylene chloride was exposed to acetyl chloride in the presence of base at low temperatures to afford the N-acetyl indoline product after recrystallization from DMF.

Halogenation of the N-acetyl indoline at the 5-position was achieved through batch synthesis conditions described by Borrer *et al.*<sup>153, 155, 156</sup> and later through continuous flow synthesis conditions<sup>157, 158</sup> worked out in our lab.

Batch conditions were carried out by exposure of N-acetyl indoline **31** with N-chlorosuccinimide and N-bromosuccinimide, respectively, in the presence of catalytic amounts of ammonium acetate to afford **32a** and **32b** analogs in 83 % and 61 % yields, respectively. Alternatively, continuous flow synthesis using conditions adapted from Pelleter *et al.*<sup>158</sup> afforded **32a** in superior reaction rates and product purity with moderate yields around 50 % after recrystallization (Figure 34).

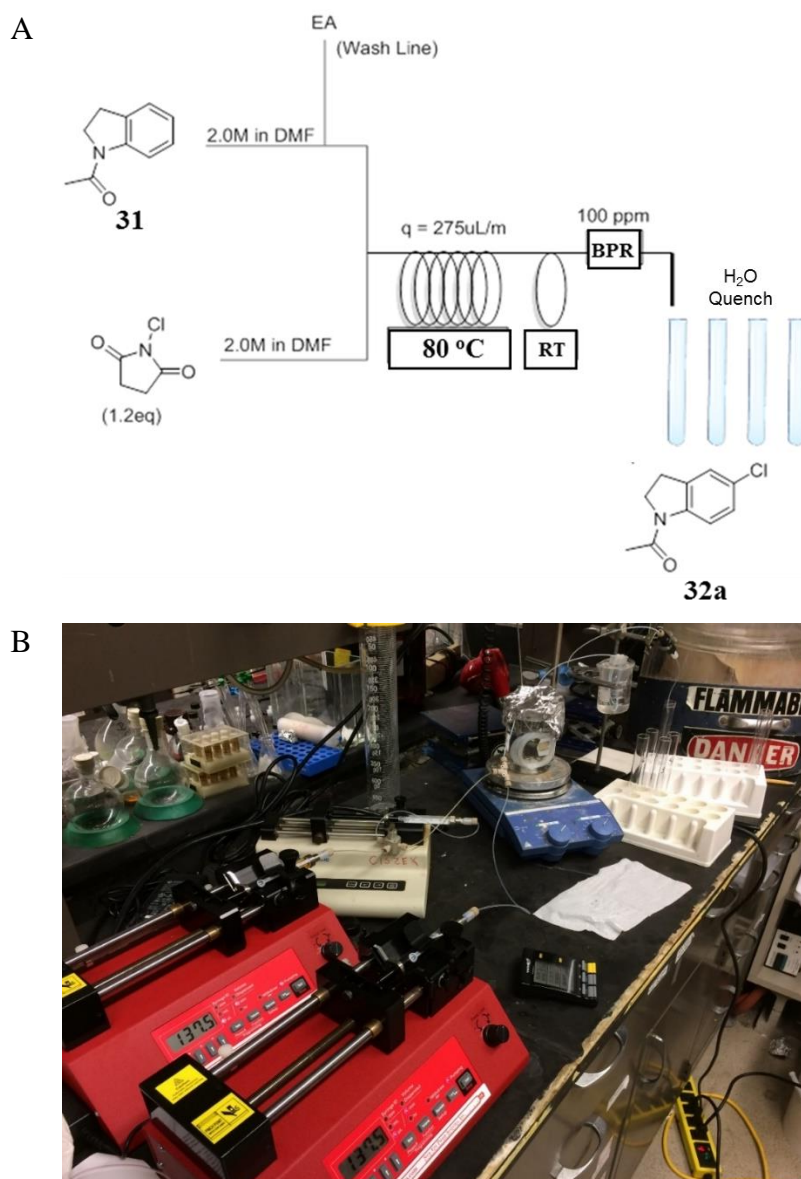


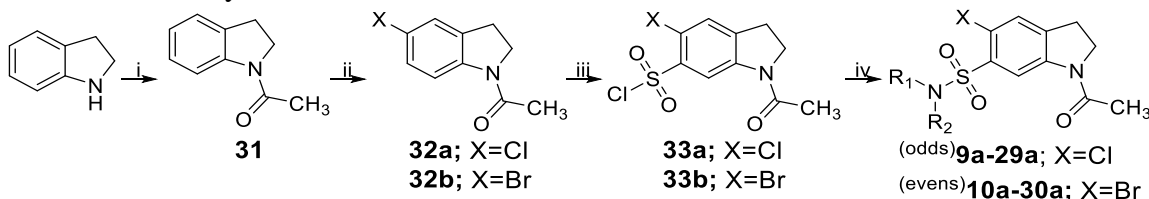
Figure 38. Continuous Flow Chlorination Setup for 5-chloro-N-acetyl indoline. A) Schematic representation, B) Laboratory apparatus configuration.

The 5-chloro and 5-bromo N-acetyl indoline analogs were each subjected to chlorosulfonation at the 6-position through heating at 65-70 °C in neat chlorosulfonic acid, at a 7.0 mL/g starting material loading ratio, over a 3 h period. The reaction mixture was then quenched over ice to afford the desired products as beige colored precipitates that were collected via vacuum filtration on a water aspirator to allow toxic fumes to be neutralized.<sup>153, 156</sup> This

method produced yields between 75 – 91 %, and NMR analysis shows that the products are pure enough to be taken to the next step without further purification.

A library of primary and secondary alkyl amines was reacted with chloro and the bromo analogs of the 6-substituted sulfonyl chloride derivative, respectively, in the presence of triethylamine base to afford a series of sulfonamide inhibitors according to literature precedent.<sup>153, 159</sup> In the instances where the reacting amine was secondary, a catalytic amount of DMAP was added to the reaction solution. The sulfonamide products were isolated through a simple liquid-liquid extraction under acidic condition followed by passing through activated carbon plug and recrystallization from chloroform-ethyl acetate to afford the final inhibitors in high purity. Each inhibitor sample was characterized and submitted for enzyme inhibition. A full description of the synthesis of 6-substituted sulfonamide inhibitors is summarized in Scheme 4 below.

Scheme 4. General Synthesis of 6-substituted Sulfonamide Indoline Inhibitors.



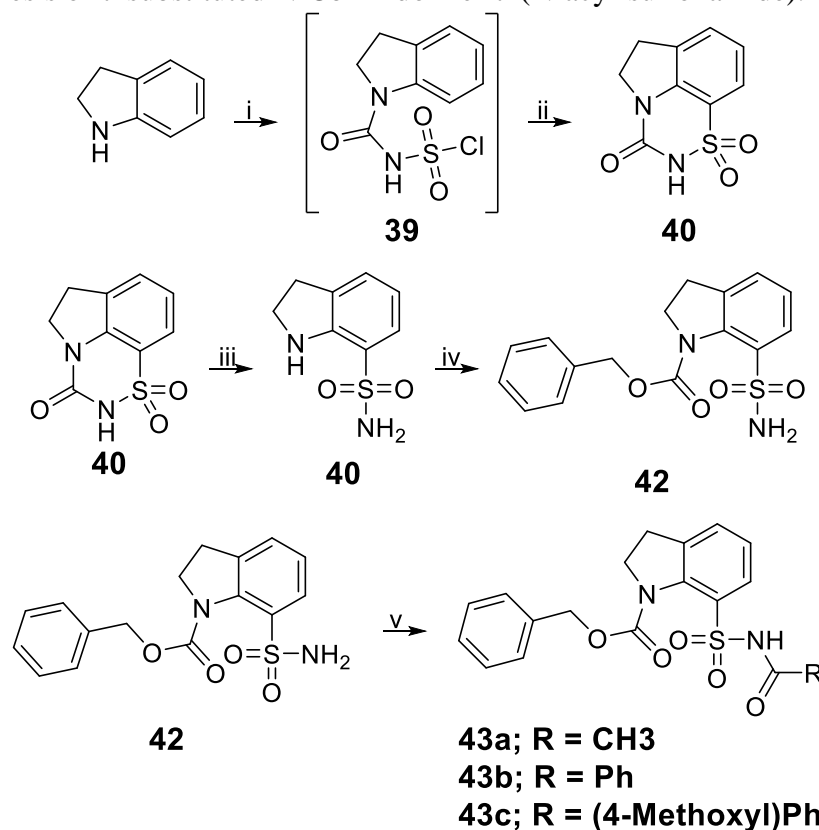
Reaction Conditions: i) AcCl, Et<sub>3</sub>N, CH<sub>2</sub>Cl<sub>2</sub>, 0 °C-RT, 3h. ii) N-halo-succinimide, NH<sub>4</sub>Cl cat., MeCN, RT, 3.5-4h. iii) 1) neat chlorosulfonic acid, 65-70 °C, 3h. 2) quench over ice, filter product. iv) CH<sub>2</sub>Cl<sub>2</sub>, Et<sub>3</sub>N, RT, 2-3h (cat. DMAP for 2° amines). 2) Acid workup with CH<sub>2</sub>Cl<sub>2</sub>. 3) Pass through activated carbon and recrystallize from chloroform-EA.<sup>153, 154, 156</sup>

### N-Cbz-indoline-7-(N-acyl-sulfonamide) Series.

Synthesis of N-Cbz-indoline-7-(N-acyl-sulfonamide) derivatives was carried out under different reaction conditions to the 6-substituted sulfonamide isomers as described by Borrer *et al.*<sup>153</sup> In order to facilitate directed installation of the sulfonyl moiety selectively at the 7-position of the indoline core structure we employed synthetic conditions (Scheme 5) with modifications

of literature protocols.<sup>153</sup>

Scheme 5. Synthesis of 7-substituted N-Cbz-indoline-7-(N-acyl-sulfonamide).<sup>a</sup>



<sup>a</sup>Reagents and Conditions: (i) chlorosulfonyl isocyanate, nitroethane, -42 °C, (ii) AlCl<sub>3</sub>, rt-110 °C 2 h; (iii) 50 % H<sub>2</sub>SO<sub>4</sub>, 135 °C 2h; (iv) benzyl chloroformate, sodium bicarbonate in 1:1 THF-H<sub>2</sub>O, rt overnight; (v) acyl chloride, Et<sub>3</sub>N, DMAP, CH<sub>2</sub>Cl<sub>2</sub>.

Synthesis of the N-Cbz-indoline-7-(N-acyl-sulfonamide) derivatives was achieved by first reacting indoline, or the 5-halogenated indoline analog, with chlorosulfonyl isocyanate at cryogenic temperature to form the corresponding N-urinic sulfonyl chloride intermediate **39** in situ. The reaction was then subjected to Friedel-Craft acylation-like reaction conditions upon the addition of aluminum chloride with heating to afford the corresponding tricyclic sulfonamide indoline product **40** in moderate yields.

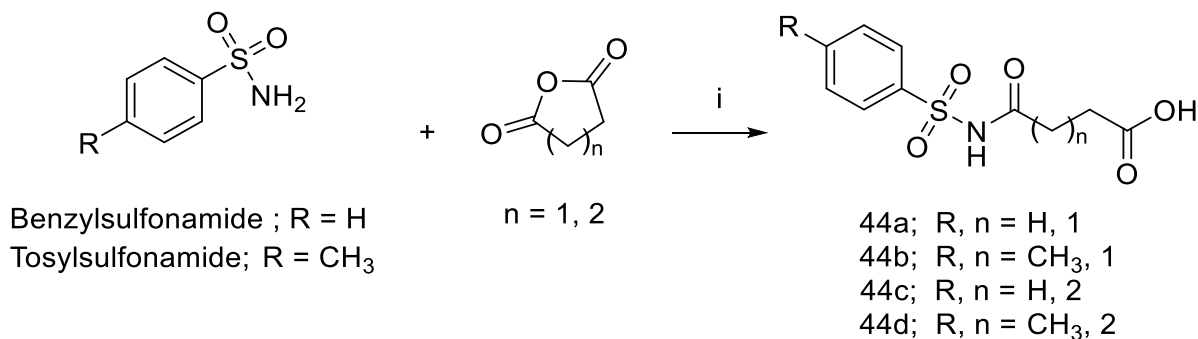
The tricyclic sulfonamide moiety was hydrolyzed open under acidic conditions to afford the analogous 7-substituted sulfonamide **41**. Benzyl carbonylation of the exposed aniline

nitrogen in the presence of sodium bicarbonate afforded the N-Cbz-indoline-7-sulfonamide **42** derivative in up to 62 % yield and high purity. Acid chloride acylation of the N-Cbz-indoline-7-sulfonamide analog at the sulfonamide nitrogen using acetyl chloride (**43a**), phenylacetyl chloride (**43b**) and the 4-methoxybenzoyl chloride (**43c**) in the presence of base afforded the N-acyl sulfonamide derivatives in high yield and purity.

### Simple N-Acetyl Sulfonamide Series.

We have also produced a small series of N-Ac-sulfonamides containing succinyl like moieties through a non-copper catalyzed synthetic route. In 2014, Morkunaite *et al.* reported a class of sulfonyl substituted saccharin compounds and their ability to bind to Zn metal centers of Carbonic Anhydrase, a mono-Zn metalloenzyme.<sup>160</sup> This paper inspired up to pursue the design and synthesis of a series of N-acetyl aryl sulfonamide derivatives using conditions described by Liu *et al.*, with modification (Scheme 6).<sup>161</sup>

Scheme 6. Synthesis of Simple Aryl N-Succinyl and N-Glutamyl Sulfonamides.



Reagents and Conditions: (i) MeOH, DIPEA, catalytic DMAP, rt overnight.<sup>161</sup>

These compounds were designed with DapE's native substrate binding mode in mind. DapE, as previously discussed, can recognize succinyl-like functionality in DapE's known metallo-isoforms. It was hypothesized that the succinylate functionality of the compound would enable binding to DapE's succinyl binding pocket while the N-Ac sulfonamide moiety, which is



a carboxylic acid mimetic, could interact with the positive ionic metal center and form a stable complex. However, there is a possibility that the activated hydroxide could hydrolyze one of the S-N-C bonds of the N-Ac sulfonamide group leading to deactivation of the inhibitor. If these bonds are stable enough to survive the hydrolytic conditions of the Zn-(HO<sup>-</sup>)-Zn active site, the compounds may chelate one or both metal centers to form a stable complex as was shown in the molecular docking data of the simple N-succinyl-benzylsulfonamide docked into NDM-1's active site (Figure 39). To our knowledge, the N-Ac sulfonamide moiety has never been tested against a di-nuclear metalloenzyme.

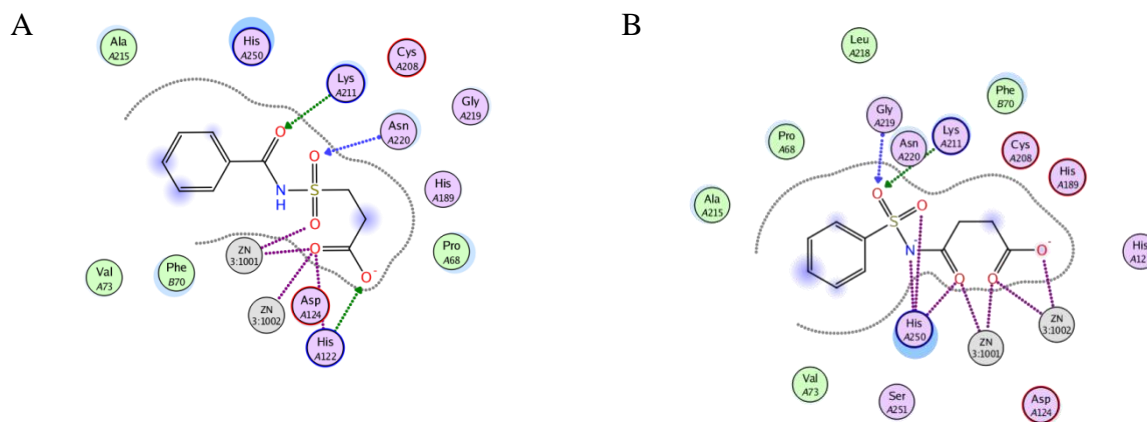


Figure 39. Docking and minimization of the N-succinyl analog **44a** with NDM-1 using MOE. A) mono-anionic state B) di-anionic state.

Synthesis of the simple aryl N-Ac-sulfonamides was achieved as per literature precedent. The N-Ac-sulfonamide moiety was installed on primary aryl sulfonamides, benzenesulfonamide and tosylsulfonamide, through exposure to succinic or glutamic anhydride in the presence of DIPEA base. The desired products were isolated in moderate yields after quenching over saturated aqueous H<sub>2</sub>CO<sub>3</sub>, washing twice with CH<sub>2</sub>Cl<sub>2</sub>, before acidification and extraction with CH<sub>2</sub>Cl<sub>2</sub>. For the two N-succinyl analogs (**44a**, **44b**), upon concentrating to minimal solvent, a white precipitate was readily formed and found to be pure product after NMR analysis resulting

in yields of 50 % and 39 % yields, respectively. Both succinyl containing N-Ac sulfonamide derivatives were submitted to the Walter Fast group for biological testing against NMD-1 and to Tahirah Heath for testing against DapE.

The N-glutamyl analog purification was slightly more involved, requiring normal phase column chromatography purification using 40:1:59 Ea-AcOH-Petroleum Ether elution. Desired glutamyl products **44c** & **44d** were isolated as clear oils that solidified as off-white semisolids after a week in moderate yields of 52 % and 44 %, respectively. Samples of each glutaryl derivative were also included for biological testing with NDM-1 by the Fast group and prep is currently underway to assay against DapE.

### **Sulfonyl Azide-Derivatization Series.**

Inspired by evidence that the N-acetyl indoline sulfonamides may be able to interact with both active site zinc atoms, and encouraged that X-ray confirmation that 8-hydroxyquinolines interact with both active site zinc atoms in NDM-1<sup>162</sup>, we proposed the installation of sulfonyl-containing functionality bearing a second ligand atom distal to the sulfonyl group via a variation on the popular copper-catalyzed azide-alkyne cycloaddition (CuAAC) reaction.

**N-Acetyl Indoline-6-Sulfonyl Azide Synthesis.** We have utilized the product stream from the sulfonamide series as a source of starting materials for synthesizing sulfonyl azide possessing the familiar indoline core structure. We have optimized the chemistry for installing the azide functionality from the sulfonyl chloride. Synthesis of the N-acetyl-5-haloindoline-6-sulfonyl azides **45a**, **45b**, and **45c** were achieved after exposure of the corresponding sulfonyl chloride to sodium azide in dry diglyme with slow addition of water and elevated temperatures (Scheme 7A). As azide compounds are potentially explosive, all precautions were taken to ensure safety including mandatory use of a blast shield (Figure 40).

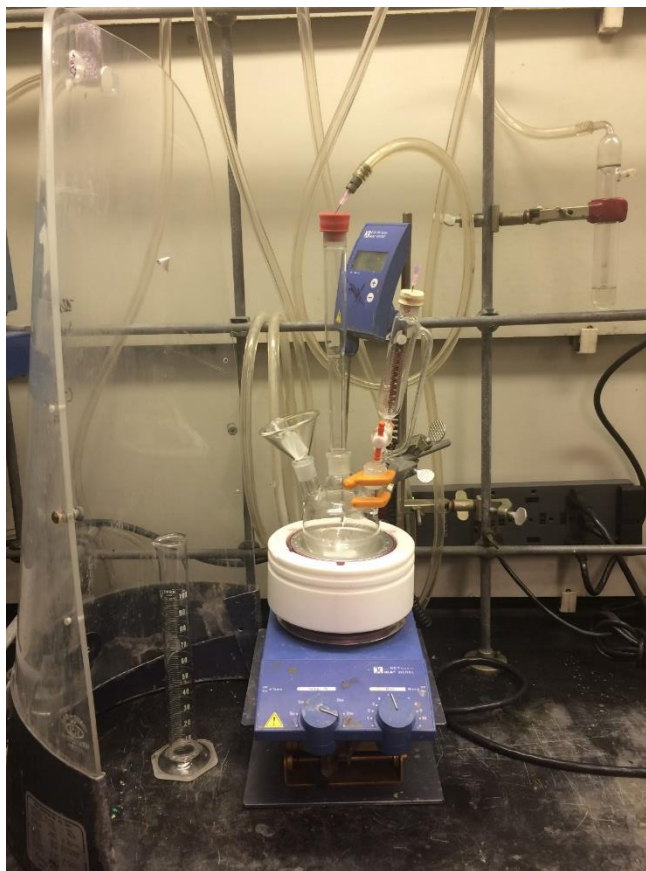


Figure 40. Reaction Setup for Sulfonyl Chloride Azidation with Sodium Azide.

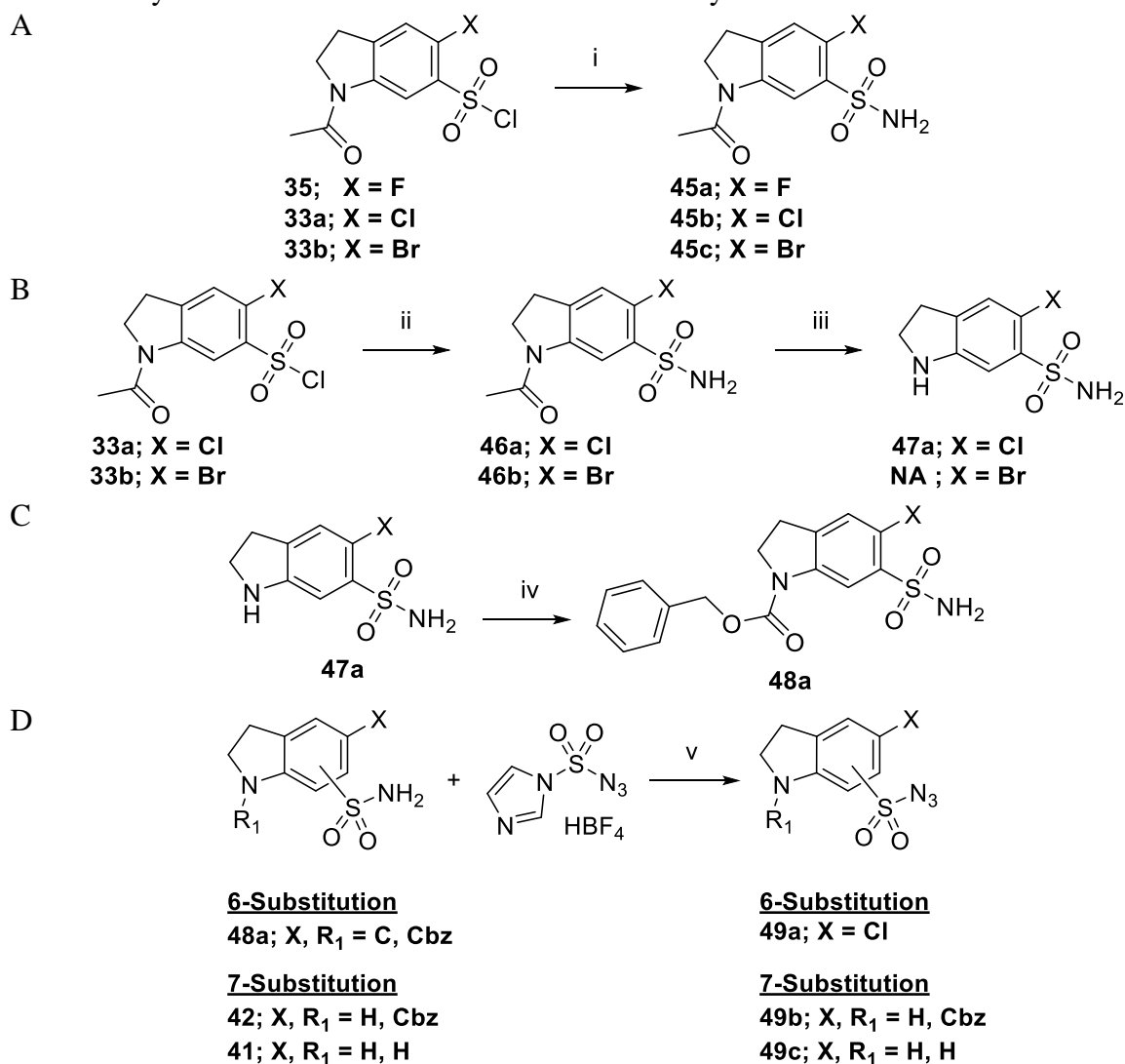
The freshly prepared sulfonyl chloride was added to a three-neck round bottom flask, purged with argon, and fitted with a 50 mL glass addition funnel on the right neck, an elongated glass neck extender on the middle neck and a glass stopper on the left neck. Rubber septa were fitted at the middle elongated-neck and the right-hand addition funnel as a gas inlet and outlet respectively. The reaction RBF module is fitted to a IKA thermocouple magnetic stirring/heating mantle for precise temperature control and the entire apparatus is barricaded with a blast shield for safety as shown in Figure 40 above. The left neck serves as the addition point for sulfonyl chloride, sodium azide, and dry diglyme. It was found that use of old diglyme in this reaction results in failure of the reaction as the dissolved water in the diglyme outcompetes sodium azide reactivity with the sulfonyl chloride. After addition of the dry starting materials, the sulfonyl

chloride and sodium azide were added through the left-hand flask neck, the dry diglyme is measured in a flame dried glass graduated cylinder and used to rinse the ground glass joint of static-clung azide solids to prevent friction or impaction of the azide when the glass stopper is applied. A heavy magnetic stir bar used to suspend the sodium azide in dry diglyme allows us to control reactivity of the sulfonyl azide until reaction temperature can reach an optimal range. The previously-used graduated cylinder was used to measure and add DI water, in a 3:2 diglyme-water volume ratio, to the 50 mL addition funnel is closed. The RBF reaction mixture was then heated to 100 °C with stirring, which results in dissolving of the sulfonyl chloride, before a gradient-temperature increase to 130 °C and slow addition of water over 10-15 min. After the water addition is complete the reaction was heated for one hour at 130 °C before being left to stir overnight at rt. The reaction is then quenched by slowly pouring the mixture over cooled saturated sodium bicarbonate with stirring behind a blast shield. If the reaction is observed to vigorously effervesce during the pour, it is an indication that sodium azide was unconsumed. We found this to be the case when wet diglyme was used in the reaction. When successful, the sodium bicarbonate quench results in a tan solid to precipitate from the solution which is dissolved during liquid-liquid partitioning with ethyl acetate. The product is isolated with 3-4 extractions of ethyl acetate and the combined organic fractions were washed once with brine before drying over sodium sulfate and concentration on a rotary evaporator to minimal volume, still containing some diglyme. The resulting diglyme-ethyl acetate-sulfonyl azide syrup is slowly triturated with hexane or petroleum ether to crash out desired product which was collected via vacuum filtration in 70-80 % yield and in high purity according to HPLC. Isolated sulfonyl azide products were carried into later synthetic steps without further purification.

**N-Cbz-Indoline Protected Sulfonyl Azide Synthesis.** In addition to synthesis of the N-

acetyl indoline-6-sulfonyl azide starting materials, we have also synthesized a series of 6- and 7-substituted N-Cbz-indoline-protected sulfonyl azides from the corresponding primary sulfonamides using the azide transfer reagent as described by Wang (Scheme 7).

Scheme 7. Synthesis of N-Cbz-Indoline Protected Sulfonyl Azides.<sup>a</sup>



<sup>a</sup>Reaction Conditions: i) NaN<sub>3</sub>, 3:2 Diglyme-H<sub>2</sub>O, 130 °C 1h to rt overnight. ii) NH<sub>3</sub> sat. MeOH, CH<sub>2</sub>Cl<sub>2</sub>, heat 1 h; iii) 6N HCl, 2 h 110 °C; iv) benzyl chloroformate, NaHCO<sub>3</sub>, 1:1 H<sub>2</sub>O-THF, rt overnight; v) imidazole-1-sulfonyl azide hydrochloride, K<sub>2</sub>CO<sub>3</sub>, 1:1 iPrOH-H<sub>2</sub>O, 2h rt.<sup>163</sup>

While we could utilize the product stream from the N-Cbz-indoline-7-(Nac-sulfonamide) synthetic series for the source of the N-Cbz-indoline-7-sulfonamide starting material, synthesis of the N-Cbz-indoline-6-sulfonamide was more involved. We utilized the 6-sulfonyl chlorides

**33a** & **33b** from the simple N-acetyl-5-halo indoline-6-sulfonamide series to synthesize the corresponding 6-sulfonamide products **46a** & **46b** in high purity and yields in two steps (Scheme 7B). Nucleophilic acyl substitution of the sulfonyl chloride in methanolic ammonium-methylene chloride solution was followed by acid hydrolysis of the N-acetyl group at 110 °C in 6N HCl for 2.5 h. The cooled hydrolysis reaction was triturated with ether-IPA to isolate the corresponding **47a** as the HCl salt.

Benzyl carbonylation selectively at the aniline nitrogen of the indoline core structure for the 6- and 7-sulfonamides **48a** & **42** was achieved by combining the primary sulfonamide products with benzyl chloroformate in the presence of sodium bicarbonate base and stirring at room temperatures overnight (Scheme 7C). Crude products were isolated in moderate to good yields (**48a**; 52 %, **42**; 91 %) and high purity (**48a**; 90 %, **42**; 99.7 %) after liquid-liquid partitioning with ethyl acetate and recrystallization.

Sulfonyl azide transfer onto the primary sulfonamide was facilitated by the azide transfer reagent, imidazole-1-sulfonyl azide • HBF<sub>4</sub> for the two N-Cbz indoline analogs **48a** and **42** as well as the NH indoline derivative **41** as shown in Scheme 7D. Reaction conditions were identical and a blast shield was used with all precautions taken when handling azide. The sulfonamide starting material was exposed to the azide transfer reagent in the presence of potassium carbonate in a 1:1 mix of i-PrOH-H<sub>2</sub>O at rt. The reaction was then stirred vigorously with rapid heating until the reaction became homogeneous and allowed to cool to room temp and stir overnight. The reaction mixture was quenched with saturated NH<sub>4</sub>Cl<sub>(aq.)</sub> and products were extracted with methylene chloride. Pure sulfonyl azide products were isolated from the crude extracts through flash column chromatography to afford desired sulfonyl azides **49a**, **49b**, and **49c** in good to moderate yields of 79 % and 51 % and 73 %, respectively. HPLC purities of the

isolated N-Cbz-5-chloroindoline-6-sulfonyl azide and N-Cbz-indoline-7-sulfonyl azide products were found to be 93 % (product eluting at 15.0 min) and 98 % (product eluting at 11.3 min), respectively.

### Three-component-copper-coupling Reaction Overview.

Once the scaled up syntheses of indoline sulfonyl azide starting materials were optimized we moved onto derivatizing the indoline scaffold under CuI-catalyzed conditions with a small library of alkyne and oxygen or nitrogen nucleophiles.

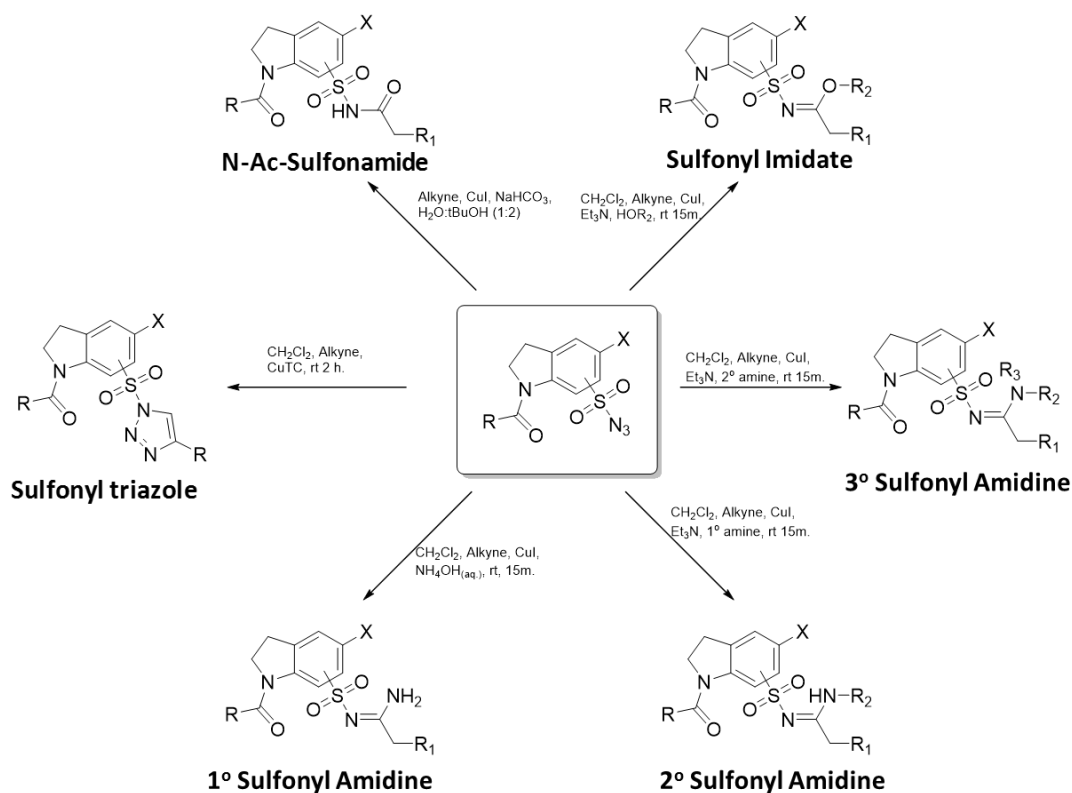
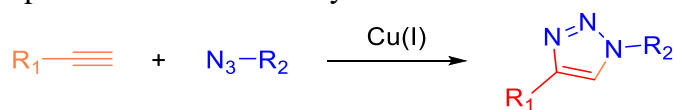


Figure 41. Synthesis Versatility of CuAAC-Sulfonyl Azide Chemistry.

A series of sulfonyl azide derived analogs, which include: sulfonyl triazoles, amidines (1°, 2°, and 3°), imidates, and N-acyl sulfonamides (Figure 41), were prepared directly from the N-Acetyl-5-halo indoline-6-sulfonyl azides through a three-component-copper-coupling reaction adapted from the general procedure described by Chang *et al.*<sup>164-167</sup>

One example of “Click” chemistry refers the ability of the azide-containing functional group to undergo copper-catalyzed azide-alkyne cycloaddition (CuAAC) (Scheme 8), which results in 1,4-disubstituted 1,2,3-triazoles.<sup>168-170</sup>

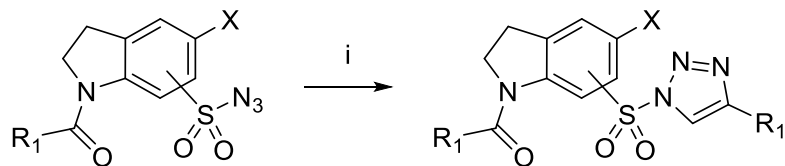
Scheme 8. An example of “Click” Chemistry.<sup>168-170</sup>



“Click” chemistry describes reactions which are modular, highly selective, and proceed under easily attainable conditions, and therefore provide great potential in medicinal chemistry.<sup>171, 172</sup> Mirroring the remarkable capabilities of “Click” chemistry is the chemistry of sulfonyl azide catalyzed by transition metals such as copper, which promises new routes to biologically relevant functionality yet to be accessed.

**Sulfonyl Triazoles.** We have synthesized a library of sulfonyl triazoles using the general procedure described by Bock in 2005.<sup>168</sup> A solution of sulfonyl azide, copper(I) thiophene-2-carboxylate (CuTC), and alkyne in CH<sub>2</sub>Cl<sub>2</sub> was stirred at room temperature over 2 hours before diluting with a 1:1 mixture of CH<sub>2</sub>Cl<sub>2</sub> and saturated aqueous NH<sub>4</sub>Cl and isolation of precipitate via vacuum filtration. The synthetic schemes for these reactions are presented below.

Scheme 9. Synthesis of Sulfonyl Triazole analogs



**45b;** X = Cl  
**45c;** X = Br

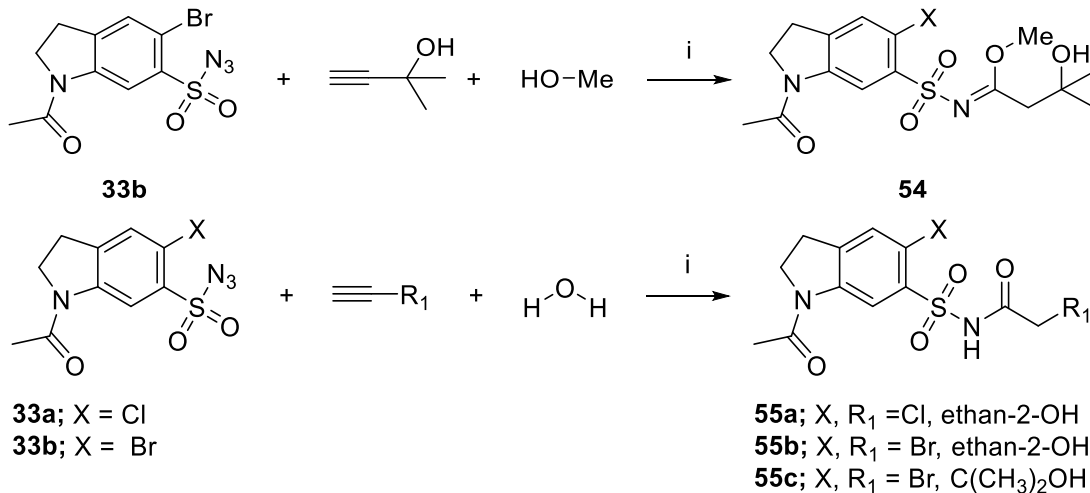
**50a;** X, R<sub>1</sub> = Br, Bn  
**51a;** X, R<sub>1</sub> = Cl, -C(CH<sub>3</sub>)<sub>2</sub>OH  
**51b;** X, R<sub>1</sub> = Br, -C(CH<sub>3</sub>)<sub>2</sub>OH  
**52a;** X, R<sub>1</sub> = Br, -1-cyclohexan-1-ol  
**53a;** X, R<sub>1</sub> = Cl, -1-propan-2-OH  
**53b;** X, R<sub>1</sub> = Br, -1-propan-2-OH

Reagents and Conditions: (i) CH<sub>2</sub>Cl<sub>2</sub>, Alkyne, CuTC, rt 2 h.



**Sulfonyl Imidates and N-Ac Sulfonamides.** A small series of sulfonyl imidates and N-Ac sulfonamides were synthesized from the N-acetyl-5-halo-indoline-6-sulfonyl azide under identical conditions as the sulfonyl amidines, but with alcohol or water acting as the nucleophile, respectively, instead of an amine (Scheme 10).

Scheme 10. Synthesis of Sulfonyl Imidate and N-Ac Sulfonamide Analogs.



Reagents and Conditions: (i) CH<sub>2</sub>Cl<sub>2</sub>, CuI, Et<sub>3</sub>N, rt 3h.<sup>173-175</sup>

**Sulfonyl Amidines (1°, 2°, 3°).** Sulfonyl amidines are a direct structural bioisostere of the N-acetyl-sulfonamide derivatives in terms of atom coordinates (Figure 42), with an amine replacing the oxygen in the carbonyl. However, it is expected that the sulfonyl amidine moiety may have improved stability over the N-acetyl sulfonamides, and should be able to avoid hydrolysis by di-Zn metal center of the enzyme. Due to the lower pK<sub>a</sub> of the sulfonyl amidine, once the neutral species enters into proximity of the activated catalytic hydroxide group of the di-Zn metal center, we expect the hydroxide nucleophile to deprotonate the amidine NH moiety which will result in a negatively charged resonance stabilization throughout the O-S-N-C-NH atoms. This is in direct contrast to the N-acetyl sulfonamide moiety which is already deprotonated at physiological pH and would be attacked by the activated hydroxide leading to

possible cleavage of the N-C=O bond and deactivation of the inhibitor. The pKa for the primary sulfonyl amidine functional group has not been reported and further pKa experiments will be conducted in the future to determine the acidity of the group.

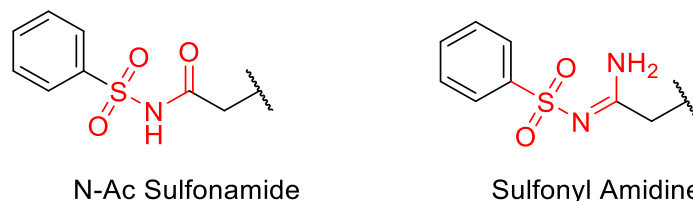
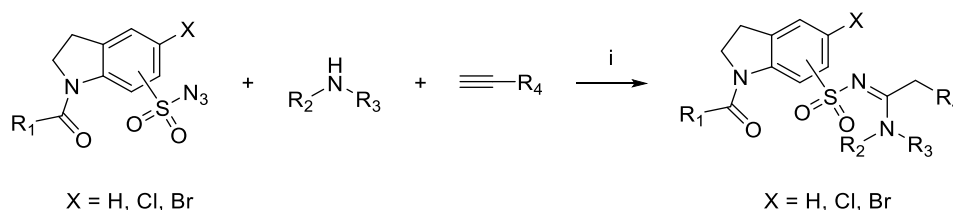


Figure 42. Sulfonyl Amidine Bioisosteric Relationship to N-acetyl-sulfonamides.

Optimization of the synthetic protocol for production of a series of N-acetyl-5-halo-indoline-6-sulfonyl amidines and a single N-Cbz-5-chloro-indoline-6-sulfonyl amidine were established and reported as follows. All reactants and reagents were used at the highest possible quality. To a solution of N-Cbz-5-halo-indoline-6-sulfonyl azide,  $\text{NH}_4\text{Cl}_{(s)}$  (1° sulfonyl amidine) or an amine nucleophile (2° & 3° sulfonyl amidines), and CuI catalyst in methylene chloride was added  $\text{Et}_3\text{N}$  base followed immediately by alkyne addition under inert atmosphere (Scheme 11).

Scheme 11. Synthesis of 1°, 2°, and 3° Sulfonyl Amidine Derivatives.



Reagents and Conditions: (i)  $\text{CH}_2\text{Cl}_2$ , CuI,  $\text{Et}_3\text{N}$ , rt 3-4 h.<sup>165, 166, 176, 177</sup>

The reaction proceeds under positive inert gas pressure that was maintained using a gas bubbler to allow for rapid liberation of nitrogen gas which drives the reaction. The reactions is agitated over several hours at standard temperatures and pressure until consumption of the sulfonyl azide by TLC and HPLC. Following literature precedent described for sulfonyl amidine

reaction workup and purification, we diluted reaction mixtures with a 1:1 mixture of methylene chloride or chloroform and saturated aqueous  $\text{NH}_4\text{Cl}$  for 30 min. If biphasic system became emulsified, then the layers were allowed to separate and products were isolated with liquid-liquid extractions with methylene chloride and purified by flash column chromatography. However, products were collected via vacuum filtration when found to precipitate during biphasic dilution. The compounds isolated through precipitation and collection via filtration were initially submitted for enzyme assay with NDM-1 without further purification as NMR analysis showed good purity in general. Later purification protocols were optimized to take into account copper contamination carried over in the precipitated products by applying a rigorous purification process on each compound. The process is summarized in Figure 43 below.

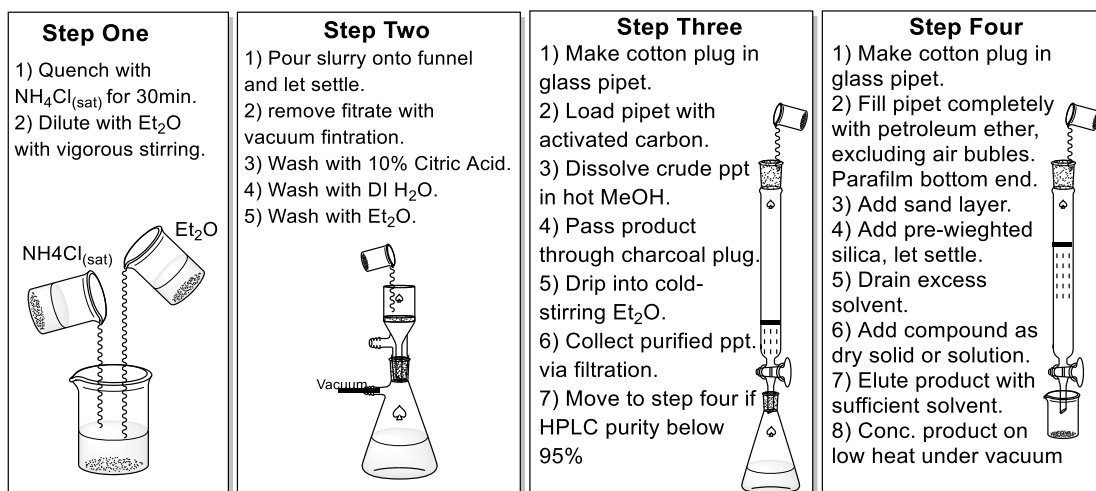


Figure 43. First Iteration of Purification Protocol for Preparing Sulfonyl Azide-derived Inhibitor.

The final iteration of sulfonyl azide-derived analog purification was to completely replace the saturated ammonium chloride aqueous quench step with a 1:1 saturated sodium thiosulfate and water mixture followed by dilution with methylene chloride. Products were isolated via filtration or through liquid-liquid extraction. Copper removal was facilitated by passing through a plug of activated carbon after dissolving the crude product in a mixture of hot

acetonitrile-methanol-DMF, followed by recrystallization. Spectral data comparison with previous product batches show a marked improvement in purity. Enzyme inhibition analysis and copper content analysis were determined and discussed later in this chapter.

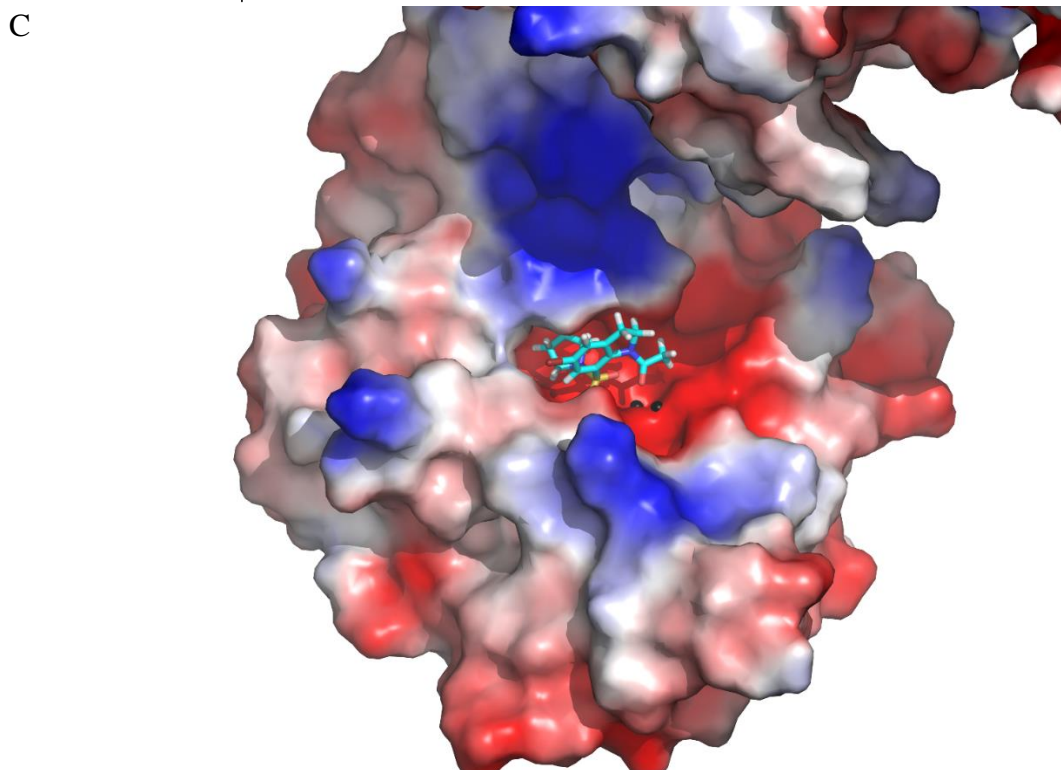
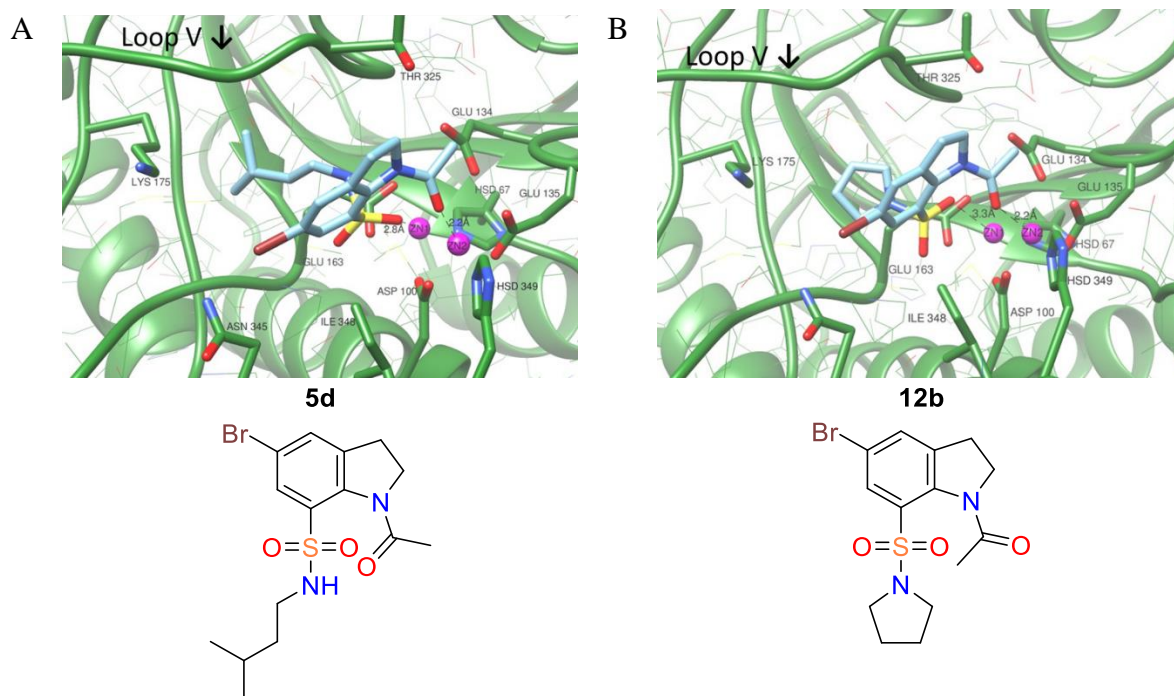
## Results

### SWISSDOCK Results.

A number of both 6- and 7-substituted sulfonamide indoline derivatives have been docked into the active site of DapE using Autodock Vina, SwissDOCK, and MOE over the course of the project. There is agreement between these separate molecular docking algorithms as to the orientation of the inhibitors, in that the 7-substituted indolines are expected to bind to the di-metal centers of DapE while the 6-substituted indoline derivatives are expected to be poor metal binders due to the suboptimal distance between the sulfonyl and amide oxygen atoms. However, the 7-substituted analogs are expected to possess an optimal distance and simultaneously bind both Zn metals which orients the N-alkyl groups to fill the hydrophobic succinate binding pocket, formed by DapE's flexible loop V. This ring orientation simultaneously positions the halo functionality into the pocket which would be filled by an incoming tyrosine residue from the opposite dimer chain in the dimerization domain. The tyrosine hydroxyl group may then engage in pseudo-hydrogen bonding with the halo group, increasing the binding. The expected inhibitor binding mode also orients the indoline directly over the di-metal center with the N-acetyl carbon situated in the cleft, which would accept the mDAP product during native substrate binding to DapE. This suggests there is room for functionalization off the N-acetyl group, which could improve structure activity and binding.

Docking suggested that both 6-sulfonamides and 7-sulfonamides can bind to the active site of DapE, but showed a calculated preference for the 7-sulfonamides as illustrated by the

docked N-acetyl-5-bromoindoline-7-pyrrolidinyl sulfonamide analog (Figure 44 B-D). The results suggested that for the 7 sulfonamides, one of the sulfonamide oxygens acts as a ligand for one active site zinc, while the N-acetyl oxygen acts as a ligand for the second zinc (Figure 44C).



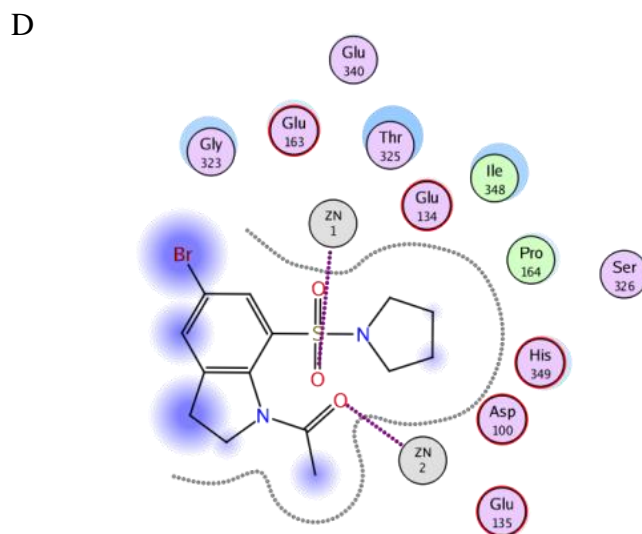
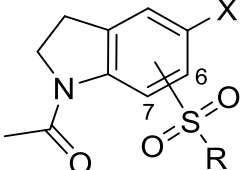


Figure 44. HiTS Sulfonamide Indoline Derivative Docking to DapE's open conformation (PDB ID: 3IC1). A) Lead compound **5d**, B) simplified pyrrolidinyl derivative **12b** of HiTS hit **4**. C) Surface representation and D) ligand interaction map of **12b**.

While there are many single zinc-binding groups (ZBGs) that have been reported and reviewed,<sup>178, 179</sup> the structural motif of ligands bridging two active site metals in metalloenzyme inhibitors is rare, and was exemplified recently for 8-quinolinol binding to the di-Zn active site of aminopeptidase (AAP) reported by Hanaya.<sup>162</sup> A structural assessment was done using docking to compare the library of 5-bromo-N-acetyl-indolines-6- & 7-sulfonamides bearing a variety of substituents on the sulfonamide nitrogen with 7-sulfonamides. While both regioisomers showed active site binding with  $\Delta G$  values of -7.7 to -10.2 kcal/mol, 18 of 24 matched pairs examined showed a calculated preference for the 7-sulfonamide (Table 6). These results also suggest the N-acyl indoline scaffold incorporates a sulfonamide moiety adjacent to the N-acetyl group can bridge the di-Zn metal center and form a stable bis-metal complex leading to inhibition.

Table 6. Sulfonamide Indoline Inhibitor Data Table.

|  |        |                                    |    |             |        |
|---|--------|------------------------------------|----|-------------|--------|
| Ligand Entry  |        | R                                  | X  | ΔG Affinity |        |
| 6 Sub.  | 7 Sub. |                                    |    | 6 Sub.      | 7 Sub. |
| 5a  | 5c     | -NH-isoPentyl                      | Cl | -7.2        | -10.24 |
| 5b  | 5d     |                                    | Br | -8.96       | -9.46  |
| 9a  | 9b     | -NH-cylcohexyl                     | Cl | -8.44       | -8.51  |
| 10a   | 10b    |                                    | Br | -7.44       | -10.21 |
| 11a   | 11b    | -N-Pyrrolidinyl                    | Cl | -8.35       | 9.14   |
| 12a   | 12b    |                                    | Br | -8.52       | -9.58  |
| 13a   | 13b    | -N-Piperidinyl                     | Cl | -8.14       | -9.14  |
| 14a   | 14b    |                                    | Br | -8.43       | -9.08  |
| 15a   | 15b    | -N(2-methoxyethan-yl) <sub>2</sub> | Cl | -8.58       | -10.29 |
| 16a   | 16b    |                                    | Br | -7.75       | -7.53  |
| 17a   | 17b    | -N(ethyl) <sub>2</sub>             | Br | -8.67       | -9.47  |
| 18a   | 18b    | -N(propyl) <sub>2</sub>            | Cl | -8.58       | -9.38  |
| 19a   | 19b    |                                    | Br | -8.66       | -7.53  |
| 20a   | 20b    | -NH-isoPropyl                      | Cl | -8.46       | -9.29  |
| 21a   | 21b    |                                    | Br | -8.33       | -10.19 |
| 22a   | 22b    | -PheOMe                            | Cl | -8.34       | -9.75  |
| 23a   | 23b    |                                    | Br | 7.94        | -8.66  |
| 24a   | 24b    | -MetOMe                            | Br | -9.41       | -8.51  |
| 25a   | 25b    | -ProOBz                            | Br | -9.01       | -7.44  |
| 26a   | 26b    | -GlyOMe                            | Cl | -8.82       | --     |
| 27a   | 27b    |                                    | Br | -8.45       | -9.85  |
| 28a   | 28b    | -βAlaOMe                           | Br | -9.54       | -10.39 |
| 29a   | 29b    | -ValOMe                            | Cl | -8.39       | -8.99  |
| 30a   | 30b    |                                    | Br | -9.25       | -8.68  |

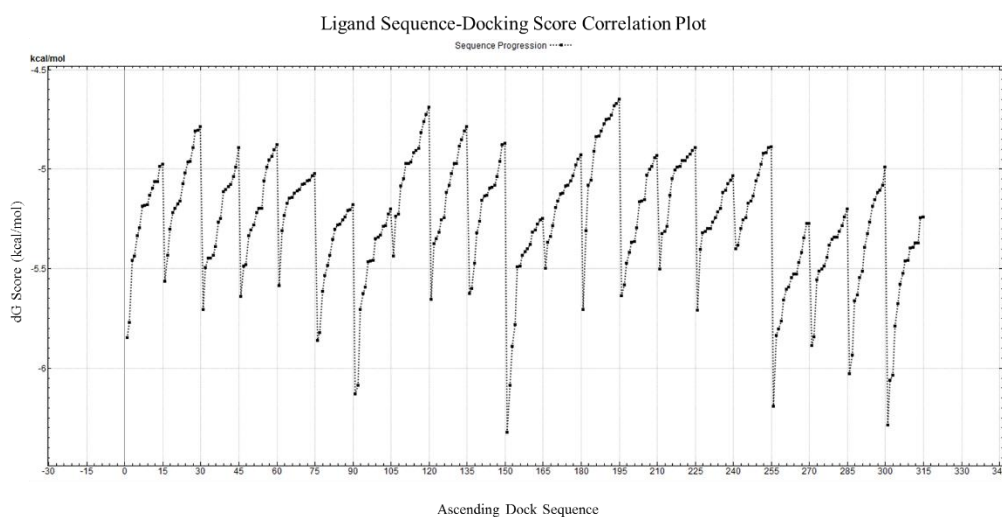
<sup>a</sup>Generic N-acetyl-5-halo indoline-6- & 7-sulfonamide structural scaffold (Top). Docking results for N-acetyl-5-halo indoline-6- & 7-sulfonamide with *in silico* ΔG calculations (Bottom).

### HiTS Hit Docking Results.

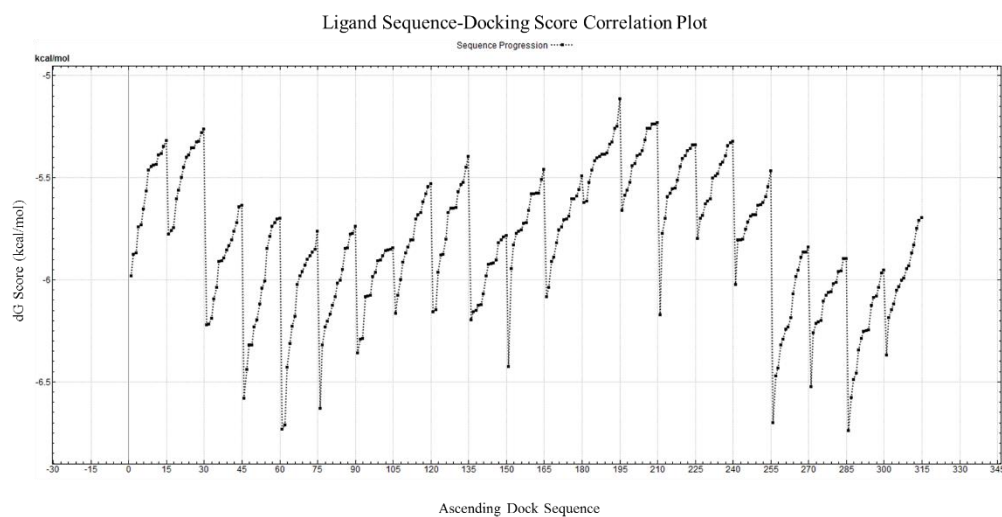
Docking results for the High Throughput Screen hit database against the open conformation NmDapE crystal structure were obtained, analyzed in MOE's database view window, and sorted into groups of ascending ΔG docking scores with respect to each ligand

database entry. The  $\Delta G$  score values were plotted against the overall pose sequence number. The processed database docking results for the global and site-directed docking experiments were analyzed and presented as the Line Graph Representation (LGR) plot shown in Figure 45A & B respectively, as well as a third LGR plot of the combined data sets with identical data plotting method (Figure 45C). The data points plotted at lower Y-axis values correspond to more stable docking poses with tighter binding.

A



B





C

Compiled Dock Results HiTS Hit Database Against NmDapE\_OC

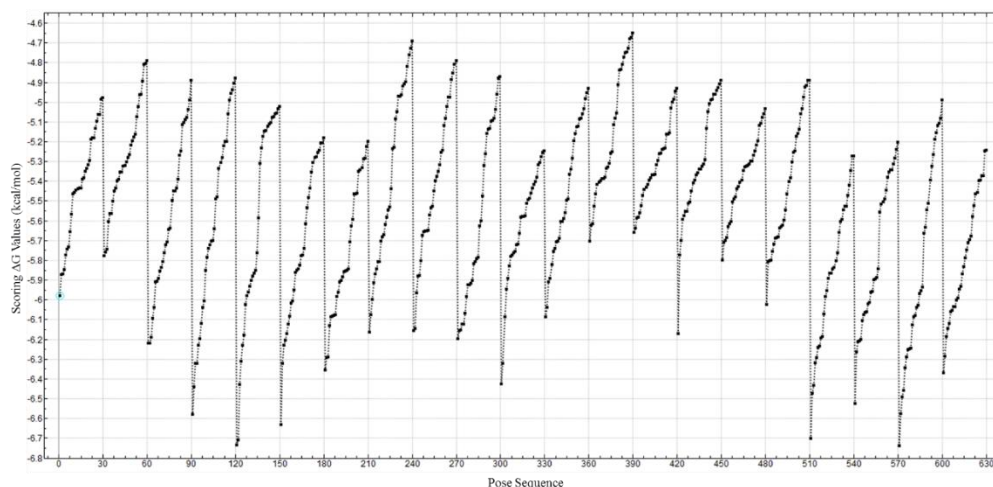
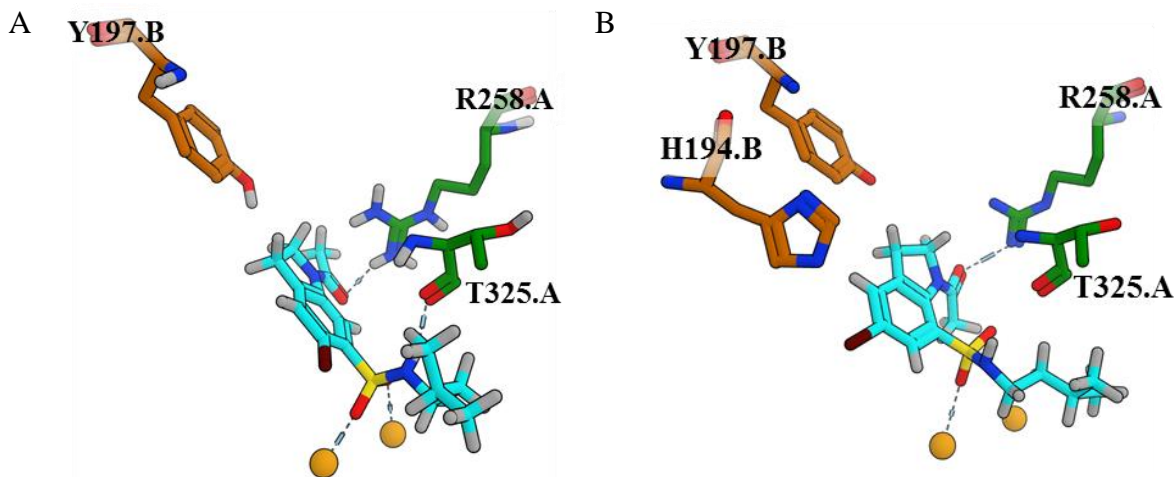


Figure 45. Line Graph Representation (LGR) of HiTS Hit Ligand Database Docking Results Against NmDapE Receptor. The Y-axis (bottom) represents  $\Delta G$  scoring values in kcal/mol. The X-axis (right-hand) represents ligand pose sequence sorted by two tier organization. Intervals of 15 data points represent docking results of a single ligand entry (1-21) organized in ascending  $\Delta G$  scoring values. Horizontal graph lines denote ligand entry transitions. Refer to Table 3 for ligand entry identities. A) Docking Results for HiTS-hits\_NmDapE\_OC-SF-dock; B) Docking Result for HiTS-hits\_NmDapE\_OC-SD-dock. \* Sharp connecting lines at interval transitions may be ignored.

Analysis of the docking poses in the MOE working window reveals interesting ligand-receptor interactions that might be responsible for inhibition in the original screen. A selection of HiTS hit docking poses are presented in the following Figure.



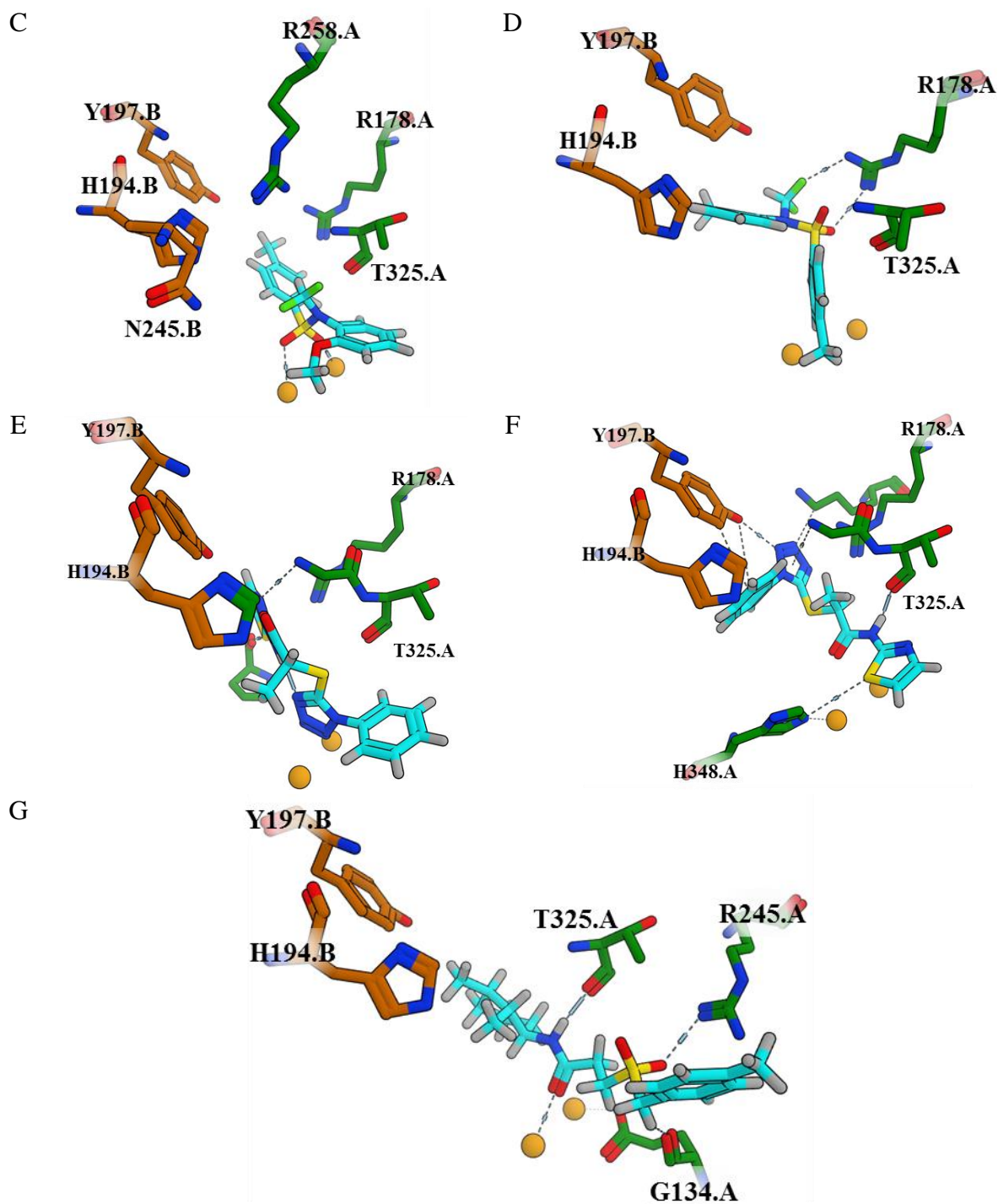


Figure 46. HiTS hit docking pose selection. A) 6-sulfonamide, B) 7-sulfonamide, C) HiTS hit **7**, pose 1 D) HiTS hit **7**, pose 1, E) HiTS hit **6**, pose 1, F) HiTS hit **6**, pose 2, G)  $\beta$ -sulfone **8**.

A common zone of interaction between docking ligands and receptor seems to be the pocket made by the junction of R178.A, Gly324.A, Th325.A, Y197.B, and sometimes H194.B,

where the propensity to coordinate hydrogen bond donors is evident (Figure 46A, B, D, F). When DapE is in the open conformation we commonly refer to this zone of interaction as the succinyl-binding patch. It is worth noting that docking of one of the direct HiTS analog hits (Figure 46A) provided evidence of coordination to this site via hydrogen bond accepting from the oxygen of the N-acetyl group while the sulfonamide's oxygen atoms bridge the Zn metals and NH form hydrogen bond donating interaction with the backbone T325.A. Moreover, this binding pocket seems to facilitate tetrahedral sulfate-like species more readily as shown in one of the poses found for the difluoromethyl sulfonamide hit (Figure 46D). The docking pose was found to incorporate a pseudo-H-bond to R178.A and one of the fluorines of the difluoromethyl, suggesting that the fluorines may yield enhanced potency toward DapE. Figure 46E and Figure 46F represent the thiazole compound in opposite binding configurations while Figure 46G represents the sulfone analog hit in a pose reminiscent of what we see in the product bound substrate hydrogen bonding network as the sulfone oxygen make interaction with the same arginine residue as the proximal (to the amide) carboxylate of the L,L-SDAP structure. These docking results lead us to believe we are on the right path with pursuing analogs of the original HiTS. However, the analogs described herein mostly represent SAR relating to succinic interaction sites on the enzyme and synthetic efforts should be refocused to pursuing SAR interaction with the DAP binding sites as well.

### **Standardized Substrate and Inhibitor Docking Results.**

Docking results for the standardized substrate and inhibitor database against the open conformation NmDapE crystal structure were obtained and analyzed in MOE's database view window. The data set was processed in a similar manor to the HiTS docking results, with the data sets being sorted into groups of ascending  $\Delta G$  docking scores with respect to each ligand

database entry. The  $\Delta G$  score values were plotted against the overall pose sequence number ending at 1250. The processed database docking results were analyzed and are presented as a LGR plot in Figure 47 below.

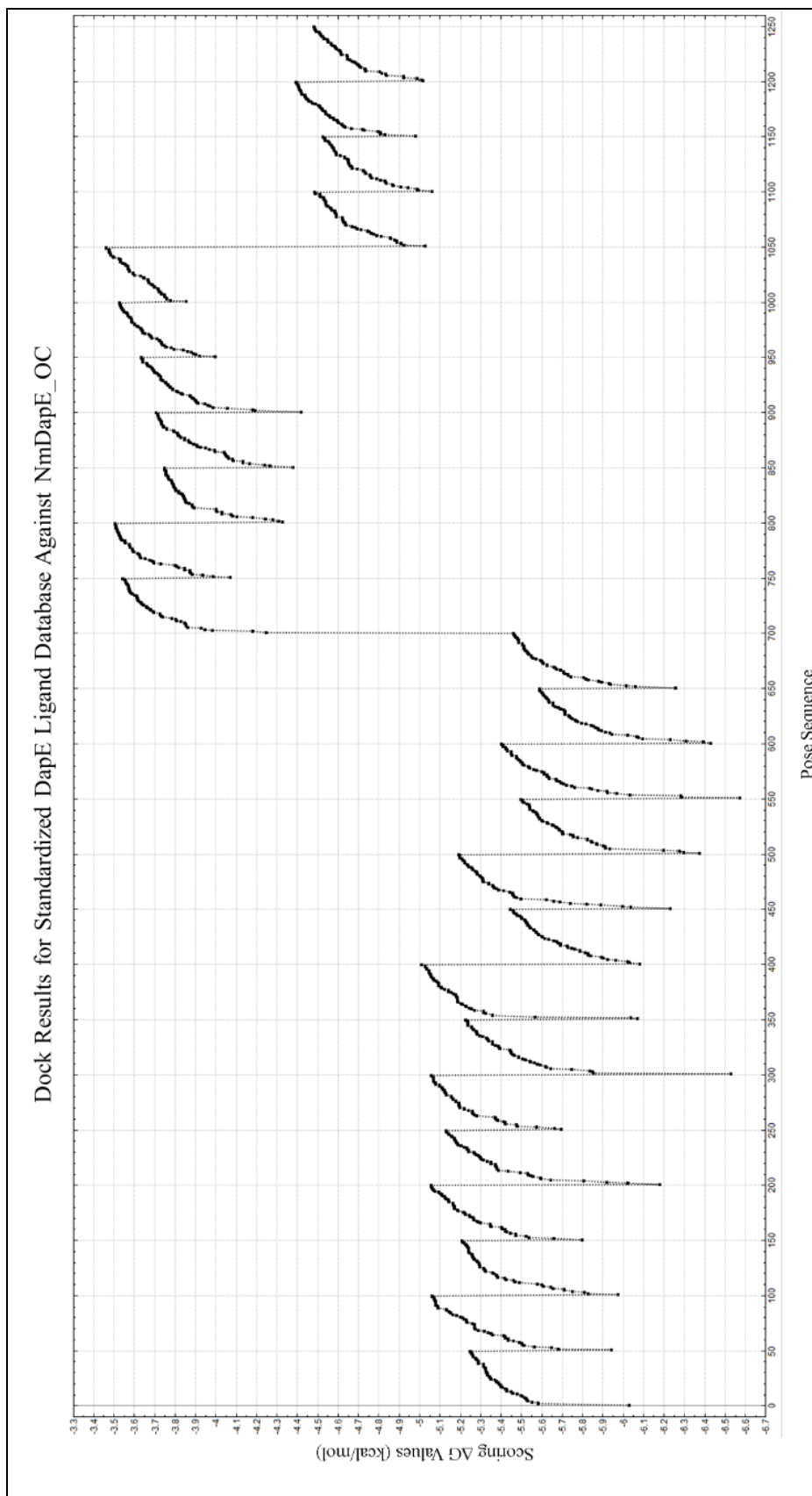


Figure 47. Line Graph Representation (LGR) of Standardized Substrate and Inhibitor Database Docking Results Against NmDapE Receptor. Y-axis (bottom) represents  $\Delta G$  scoring values in kcal/mol. X-axis (right-hand) represents ligand pose sequence sorted by two tier organization. Intervals of 15 data points represent docking results of a single ligand entry (1-21) organized in ascending  $\Delta G$  scoring values. Horizontal graph lines denote ligand entry transitions. Refer to Table 4 for ligand entry identities.

Analysis of the docking poses in the MOE working window reveals interesting ligand-receptor interactions that may shed light on the transition from the open to the closed conformations of DapE during substrate binding. A selection of L,L-SDAP docking poses are presented in Figure 48.

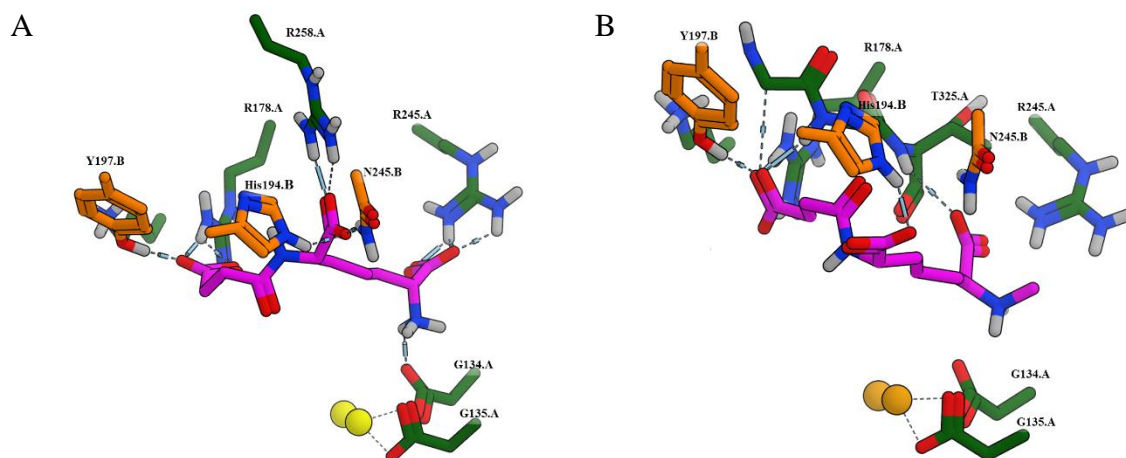


Figure 48. Selection of substrate docking pose into NmDapE open structure. A) L,L-SDAP, B) N-methyl-L,L-SDAP assay substrate.

Docking analysis of the native L,L-SDAP and the synthesized assay substrate N-methyl-L,L-SDAP show common binding interactions. The results seem to suggest that substrates bind to the dimerization interface through interaction at the succinyl carbonate, proximal carboxylate and distal DAP carboxylate. The ammonium moiety is observed to form a hydrogen bonding interaction with the general acid base E134.A while the methylated analog appears to locate the methyl along the binding groove as described in chapter 3 of this work.

### Enzyme Assay Inhibition Results.

Enzyme inhibition was determined under the described method for the library of 6 substituted N-Ac sulfonamide inhibitions that were synthesized. Sample screening concentrations of 200  $\mu\text{M}$  and 20  $\mu\text{M}$  were used to determine the percent inhibition for DapE and NDM-1. The results are summarized in Table 7 below.

Table 7. N-Acetyl-5-halo indoline-6-Sulfonamides Inhibition Results.<sup>a</sup>

| Compounds  | DapE Inhibition |       |                       | NDM-1 % Inhibitions |      |
|------------|-----------------|-------|-----------------------|---------------------|------|
|            | 200 uM          | 20 uM | Est. IC <sub>50</sub> | 200uM               | 20uM |
| <b>5b</b>  | P               | P     | P                     | 42                  | 8    |
| <b>9a</b>  | 58.2            | 21.5  | 163 uM                | --                  | 6    |
| <b>10a</b> | 40.3            | 18.9  | 279 uM                | --                  | 0    |
| <b>11a</b> | 56.7            | 33.7  | 145 uM                | --                  | 0    |
| <b>12a</b> | 72.5            | 29.8  | 104 uM                | 20                  | --   |
| <b>13a</b> | 97.7            | 38.6  | 54 uM                 | --                  | 9    |
| <b>14a</b> | 97.5            | 14.4  | 97 uM                 | --                  | 3    |
| <b>15a</b> | 90.4            | 31.9  | 75 uM                 | --                  | 13   |
| <b>16a</b> | P               | P     | P                     | 3                   | --   |
| <b>17a</b> | 80.3            | 10.2  | 122 uM                | --                  | --   |
| <b>18a</b> | P               | P     | P                     | --                  | 5    |
| <b>21a</b> | 18.9            | -1.78 | 492 uM                | --                  | 57   |
| <b>22a</b> | 92.9            | 31.8  | 74 uM                 | 13                  | --   |
| <b>23a</b> | P               | P     | P                     | 61                  | 6    |
| <b>28a</b> | 87.1            | 26.2  | 90 uM                 | 17                  | --   |
| <b>37</b>  | P               | P     | P                     | 50                  | 20   |
| <b>38</b>  | 55.9            | 9     | 178 uM                | --                  | 31   |

<sup>a</sup>Table Legend: P = Pending Results, -- = no data collected at given concentration.

Our early inhibition results for the N-acetyl-5-halo indoline-6-sulfonamides towards NDM-1 suggests virtually no inhibition, with **21a** performing the best. However, this series performed better towards inhibition of DapE as expected.

Inhibition data of the N-Cbz indoline-7-(N-acyl-sulfonamide) series toward DapE and NDM-1 are summarized in Table 8.

Table 8. N-Cbz indoline-7-(N-acyl-sulfonamide) Inhibition Results.

| Compounds  | DapE % Inhibition |       |                       | NDM-1 % Activity |
|------------|-------------------|-------|-----------------------|------------------|
|            | 200 uM            | 20 uM | Est. IC <sub>50</sub> | 500 uM           |
| <b>43a</b> | 95.7              | 47.5  | 29 $\mu$ M            | 0                |
| <b>43b</b> | 98.7              | 36.8  | 59 $\mu$ M            | 0                |
| <b>43c</b> | P                 | P     | P                     | 0                |

<sup>a</sup>Table Legend: P = pending results.

This series of inhibitors performed poorly against NDM-1, but resulted in modest

inhibition of 47.5 and 36.8 % at 20  $\mu$ M towards DapE for the two compounds tested. Inhibition of the simple N-acetyl sulfonamide series towards DapE and NDM-1 are summarized in Table 8.

Table 9. Simple N-Acetyl Sulfonamide Inhibition Results.<sup>a</sup>

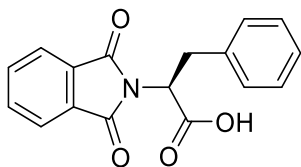
| # | Compounds  | DapE % Inhibition |             |            | NDM-1 % Inhibition |             |
|---|------------|-------------------|-------------|------------|--------------------|-------------|
|   |            | 500 $\mu$ M       | 200 $\mu$ M | 20 $\mu$ M | 500 $\mu$ M        | 200 $\mu$ M |
| 1 | <b>44a</b> | 97.4              | 92.4        | 36.7       | 5                  | --          |
| 2 | <b>44b</b> | 97.4              | 85.7        | 31.2       | 4                  | --          |
| 3 | <b>44c</b> | P                 | P           | P          | --                 | 3           |
| 4 | <b>44d</b> | P                 | P           | P          | --                 | 2           |

<sup>a</sup>Table Legend: P = pending results, -- = no data collected at given concentration.

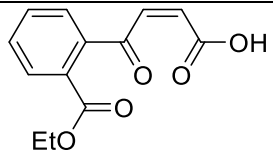
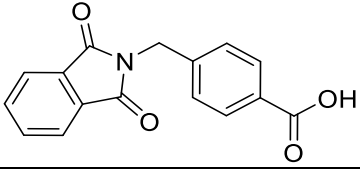
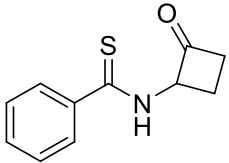
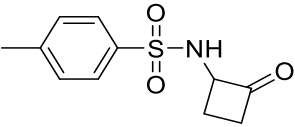
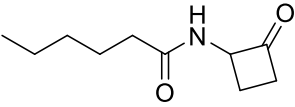
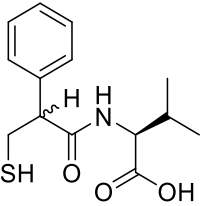
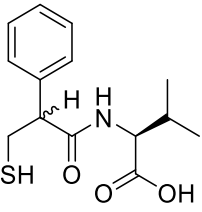
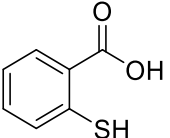
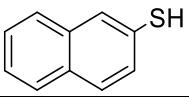
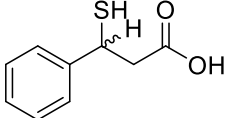
Inhibition results of the simple sulfonamide series towards NDM-1 indicates virtually no inhibition. However, inhibition of the N-succinyl sulfonamides, **44a** and **44b** resulted in nearly complete inhibition of DapE at 500  $\mu$ M, modest inhibition at 200  $\mu$ M and a respectable inhibition at 20  $\mu$ M. Assay results are pending for the two N-glutamyl sulfonamides possessing an extra  $\text{CH}_2$ , but docking study suggests this extra  $\text{CH}_2$  may facilitate better interactions between the positively charged succinyl binding patch and the catalytic metal center in the open form of DapE, thus hopefully resulting in better inhibition performance.

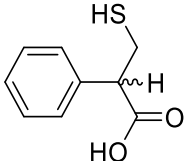
A series of miscellaneous commercially available analogs, or made in short, simple syntheses in an attempt to identify new inhibitor scaffolds were included in assays against DapE and NDM-1. Inhibition results for the compounds are summarized in Table 9.<sup>a</sup>

Table 10. Miscellaneous Structure Analog Inhibition Results.

| #          | Miscellaneous Compounds   | DapE % Inhibition |            | NDM-1 % Inhibition |                       |
|------------|---|-------------------|------------|--------------------|-----------------------|
|            |   | 200 $\mu$ M       | 20 $\mu$ M | 200 $\mu$ M        | 20 $\mu$ M            |
| <b>66a</b> |  | 78.6              | 21.8       | --                 | (at 500 $\mu$ M)<br>2 |



|            |   |      |      |     |   |
|------------|---|------|------|-----|---|
| <b>66b</b> |                      | 42.7 | 20.2 | 13  | --  |
| <b>66c</b> |                      | 27   | 24.7 | 62  | (at 100uM) 46<br>IC <sub>50</sub> = 120 ± 10<br>Hill = 0.4 ± 0.03 |
| <b>66d</b> |                      | 93.7 | 15.4 | NA  | --  |
| <b>66e</b> |                      | --   | --   | --  | (at 500uM)<br>2   |
| <b>66f</b> |                      | --   | --   | 0   | --  |
| <b>66g</b> | <br>CTR-a-22 (R,S)  | --   | --   | 84  | 48  |
| <b>66h</b> | <br>CTR-a-16 (S,S) | --   | --   | 81% | 59%   |
| <b>66i</b> |                    | --   | --   | 40% | 3%  |
| <b>66j</b> |                    | --   | --   | --  | 3   |
| <b>66k</b> |                    | --   | --   | 37  | 0   |

|            |   |    |    |    |    |
|------------|---|----|----|----|----|
| <b>66l</b> |  | -- | -- | 59 | 16 |
|------------|---|----|----|----|----|

aTable Legend: P = pending results, -- = no data collected at given concentration.

We have only assayed a small selection these miscellaneous analogs toward DapE inhibition, with carboxylic acid **66c** showing the most potency. The results from docking suggests that this compound can interact with the succinyl-sulfonyl interaction patch with one or both imidine carbonyl oxygens while the benzoic acid moiety can interact with the catalytic metal center. The inhibitor **66c** showed sufficient inhibitory potency to warrant obtaining  $IC_{50}$  and Hill coefficient values which were  $120 \mu\text{M} \pm 10$  and  $0.4 \pm 0.03$ , respectively.

The series of thiol containing compounds have only been assayed with NDM-1 to date, showing modest potency overall, with thiol compound **66h** inhibiting NDM-1 59 % suggesting an  $IC_{50}$  just under  $20 \mu\text{M}$ . However, we decided not to pursue this thiol-containing inhibitor series due to many possible off-target side effects common to thiol-containing drug classes.

### Sulfonyl Azide-Derived Analog Inhibition Results.

A series of potential MBL inhibitors which included sulfonyl triazoles, sulfonyl amidines ( $1^\circ$ ,  $2^\circ$ , and  $3^\circ$ ), sulfonyl imidates, and N-acyl sulfonamides were submitted to our NDM-1 project collaborator, Dr. Walter Fast, for inhibitor screening against the metallo- $\beta$ -lactamase NDM-1. The Fast group started by treating the NDM-1 enzyme with inhibitors at  $100 \mu\text{M}$  to see if substrate (at near  $K_m$  concentrations) turnover was inhibited. If any compounds looked promising, assay conditions (incubation time, fix solubility issues, etc) were optimized. The initial inhibition results were very promising and we moved to scale up compounds for  $IC_{50}$  and Hill coefficient determination.

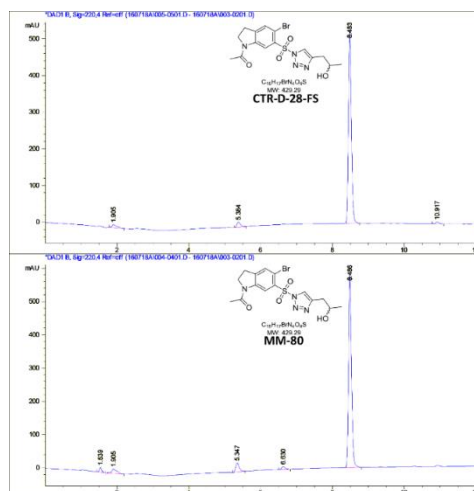
The first iteration of sulfonyl azide-derived analog purification yielded high-purity samples of 95% purity or better. Table 11 represents the inhibitory results of those samples that were re-prepped with side-by-side comparisons of the original batch of inhibitors. However, we found disturbing discrepancies in NDM-1 inhibitory potency between the old and new inhibitor batches, with the older, less pure batches possessing greater inhibitory potency. Enzyme inhibition assays were repeated and performed in unison for all the compounds in Table 11.

Table 11. Side by Side comparison of sulfonyl azide-derived analog batches.

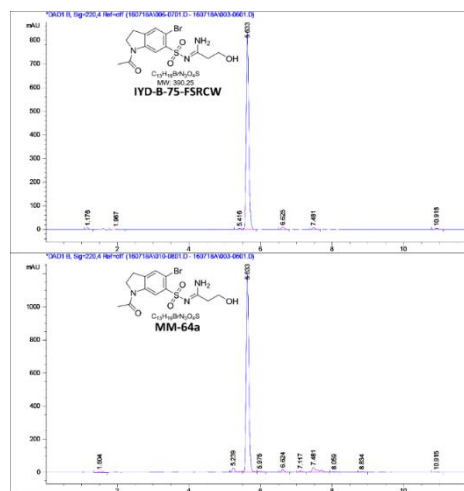
| Structure  | Sample Data<br>% Purity  | IC50 (uM)  | Hill Coefficient |
|------------|--|------------|------------------|
| <b>53b</b> | <b>(6/6/16 batch)</b><br>97% pure by HPLC.<br>Light grey powder. | 3.0 ± 0.5  | 0.65 ± 0.07      |
|            | <b>(4/2/15 batch)</b><br>Light green/blue<br>Powder.             | 1.7 ± 0.5  | 0.6 ± 0.1        |
| <b>55c</b> | <b>(6/6/16 batch)</b><br>95% pure by HPLC<br>White powder.       | > 100      | N/A              |
|            | <b>(4/2/15 batch)</b><br>Off-white/ tan<br>powder.               | 2.4 ± 0.4  | 0.60 ± 0.06      |
| <b>57a</b> | <b>(6/6/16 batch)</b><br>95.5% pure by HPLC.<br>A White Powder.  | > 100      | N/A              |
|            | <b>(7/10/15 batch)</b><br>Light green powder.                    | 0.45 ± .06 | 0.71 ± 0.06      |
| <b>57b</b> | <b>(6/6/16 batch)</b><br>94.5% pure by HPLC.<br>White Powder.    | 29.8 ± 3.5 | 0.9 ± 0.1        |
|            | <b>(4/2/15 batch)</b><br>Light green powder                      | 3.8 ± 0.8  | 0.8 ± 0.1        |

HPLC analysis of the early and later compound batches show identical retention times as seen in Figure 49A-D. Compounds **57b** from both batches were subjected to further LC-MS analysis and show identical chromatograms and mass spectra (Figure 49E-F).

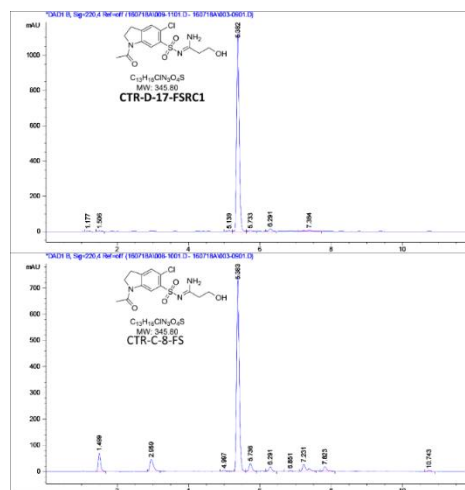
A



B



C



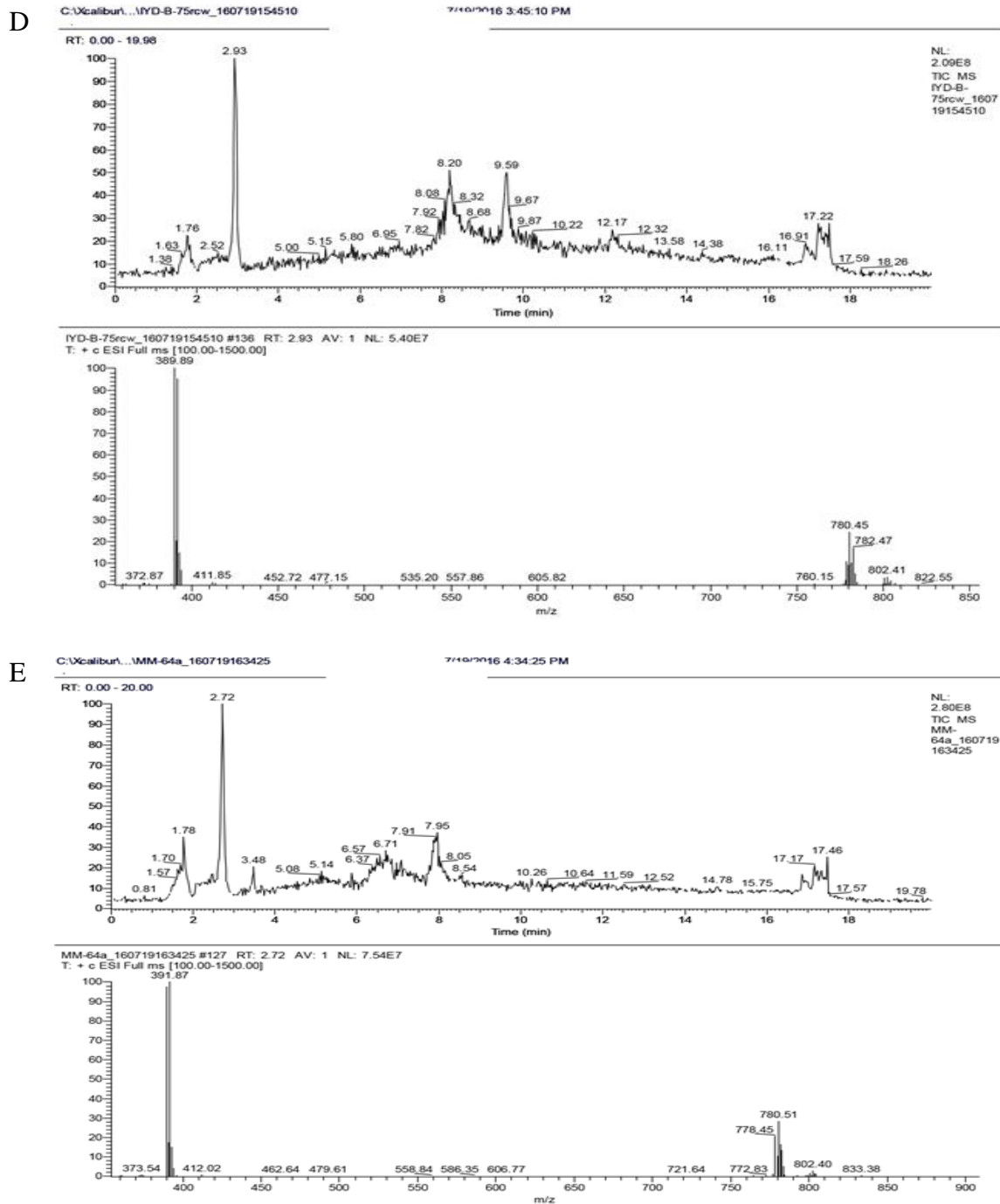


Figure 49. HPLC and LC-MS analytical comparison between NDM-1 inhibitors with identical structures. A) **53b** 6/6/16 batch v. 4/2/15 batch. B) **57b** 6/6/16 batch v. 4/2/15 batch C) **57a** 6/6/16 batch v. 4/2/15 batch. LC-MS analysis: D) **57b** batch 6/6/16, E) **57b** batch 4-2-15.

Unfortunately, copper (II) was found to potently inhibit NMD-1 with nanomolar potency after the discovery of discrepancies in inhibition data between the original, less pure sulfonyl

azide-derived inhibitors and recent higher purity resubmissions of structurally identical inhibitors (Results Section). Our sulfonyl azide-derived inhibitors were designed to be strong metal coordinators and we rationalized the inhibition discrepancy between batches as the presence of copper in the original samples which were not subjected to re-crystallization protocols to remove copper ions. This hypothesis was confirmed with follow-up enzyme studies of NDM-1 in the presence of various Cu(II) salts conducted by the Fast group.

The question of improving the removal of copper ions from our copper-catalyzed reaction caused us to take a closer look at our quenching workup. The traditional method of removing copper catalyst from organic reactions is with copper-absorbing resins or quenching with saturated ammonium chloride solution, which creates a blue aqueous color indicating copper ions in solution. When we employed saturated  $\text{NH}_4\text{Cl}$  in the CuI catalyzed reaction workup we observe a blue aqueous layer.

However, the question remaining was whether this method was completely removing all the copper metal from the sulfonyl azide reactions during the workup procedures. A simple control experiment was set up to probe this question. A 10 mg sample of the reaction-grade CuI catalyst was added to a dram vial and mixed with a number of different quenching conditions as depicted in Figure 50.

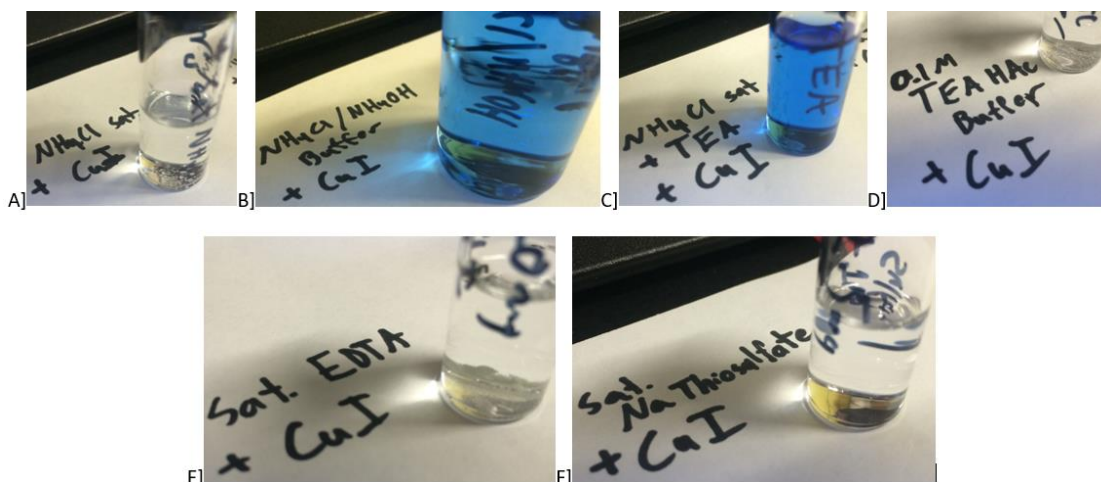


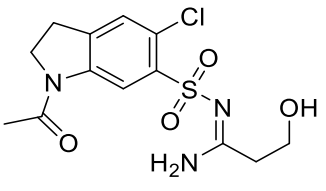
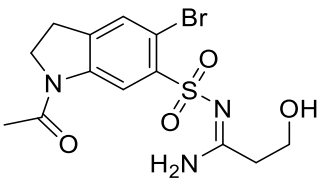
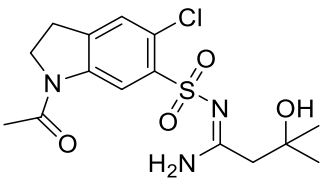
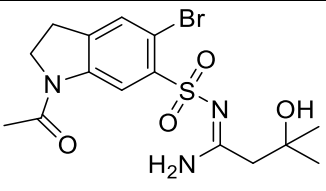
Figure 50, A] CuI + Sat.  $\text{NH}_4\text{Cl}$ . B] CuI + Sat.  $\text{NH}_4\text{Cl}$  + 30%  $\text{NH}_4\text{OH}$  buffer solution with pH ~ 10. C] CuI + Sat.  $\text{NH}_4\text{Cl}$  + TEA. D] CuI + TEA/ $\text{AcOH}$  buffer solution with pH ~ 7. E] CuI + sat. EDTA solution. F] CuI + Sat. Sodium thiosulfate. Conditions A, D and E all had CuI remain in solid phase while B, C and F conditions fully dissolved the CuI.

It was found that  $\text{CuI(s)}$  does not fully dissolve in the absence of a sufficient amount of base present. The sulfonyl azide reactions are run with a 1.5 eq excess of TEA which could be the source of the dissolved copper ions observed, but we do not know if this completely removes the catalyst. Cuprisorb resin was also assayed for effectiveness of removing copper. However, the resin was found to require extended periods of time to absorb copper ions and quickly reaches its upper limit of copper capacity after only a few milligrams of copper per gram of resin. We also cannot use EDTA reliably to remove CuI from our reaction as it does not effectively coordinate to  $\text{Cu}^+$  species. We demonstrated that  $\text{NH}_4\text{OH}$  solution was good for fully dissolving copper, but the basic pH of the quenching media can also lead to unwanted side products as well as product dissolution into the aqueous washes where acidification would just lead to copper precipitation with protonated products. It seemed that sodium thiosulfate is a good candidate for removing copper from the reaction as it can dissolve  $\text{Cu}^{+2}$  ions, reducing them to  $\text{Cu}^+$  and then forming very soluble  $\text{Cu}^+$  complexes. The saturated sodium thiosulfate also has a pH range of 6-8 making it ideal for inhibitors with acidic functional groups.

### Purification Procedure to Remove Copper Contamination for DapE Inhibition.

The final iteration of sulfonyl azide-derived analog purification was used to synthesize a series of highly purified and recrystallized sulfonyl amidine analogs which have been assayed against DapE (Table 12) to replace the ammonium chloride quenching step with a 1:1 saturated sodium thiosulfate and water mixture that yielded high-purity sample, 95 % pure or better.

Table 12. Copper-Assayed Sulfonyl Amidine Inhibition Results Against DapE.

| Compounds<br>Entry  | % Inhibition of DapE at: |       |
|---|--------------------------|-------|
|   | 200 uM                   | 20 uM |
| <br><b>57a</b>   | 76.8                     | 24.4  |
| <br><b>57b</b>  | 72.1                     | 27.9  |
| <br><b>58a</b> | 79.1                     | 22.7  |
| <br><b>58b</b> | 98.3                     | 36.6  |

The realization of copper contamination in some of our samples has influenced our group to adapt a commercially-available copper assay kit for fish tanks to developing a standardized UV-Vis copper assay using a commercially available aquarium testin kit to quantify the amount



of copper contamination in each inhibitor sample.<sup>180</sup> A screening library of synthesized compounds produced via of copper catalysis which possessing differing amounts of copper was used as our pilot experiment. The results of our pilot experiment are summarized in Table 13.

Table 13. Copper Assay Results.<sup>a</sup>

| #   | Copper Purifications Protocols |    |    |    | Est. Eq. Cu (3-0) | Assay Determined Eq. Cu |
|-----|--------------------------------|----|----|----|-------------------|-------------------------|
|     | FS                             | RC | CA | AC |                   |                         |
| 50a | X                              |    |    |    | 2                 | 7.5                     |
| 51b | X                              |    |    |    | 2                 | 0.1                     |
| 52b | X                              |    |    |    | 2                 | 2                       |
| 53b | X                              |    |    |    | 2                 | 2.5                     |
| 55a | X                              | X  | X  |    | 0                 | 0.03                    |
| 55b | X                              |    |    |    | 2                 | 1.8                     |
| 55b | X                              | X  | X  |    | 0                 | 1.7                     |
| 55c | X                              | X  |    |    | 1                 | 0.065                   |
| 55c | X                              | X  | X  |    | 0                 | 0.025                   |
| 57a | X                              | X  |    | X  | 0                 | 0.2                     |
| 57a | X                              |    |    |    | 3                 | 2.4                     |
| 57b | X                              |    |    |    | 2                 | 0.4                     |
| 57b | X                              | X  |    | X  | 0                 | 0.037                   |
| 57b | X                              |    |    |    | 3                 | 2.2                     |
| 58a | X                              | X  |    |    | 1                 | 6                       |
| 58a | X                              | X  | X  |    | 0                 | 0.22                    |
| 58a | X                              | X  |    | X  | 0                 | 0.01                    |
| 58b | X                              | X  |    |    | 1                 | 0.01                    |
| 58b | X                              | X  |    | X  | 0                 | 0.125                   |
| 64a | X                              |    |    |    | 3                 | 1.4                     |

<sup>a</sup>Table Legend; FS = quench, precipitate and filtrate products, RC=recrystallized, CA=10% citric acid wash, AC=passed through activated carbon plug. Est. Eq. Cu= degree of expected copper in sample on a scale of 3 (Highest) - 0 (Lowest).

Enzyme inhibition assays with NDM-1 and later with DapE looked promising. The results confirm that the final iteration of copper purification protocol applied to the sulfonyl azide-derived analogs results in a substantial drop in copper composition of the samples as compared to the earlier batches. However, our copper assay tests still showed detectable levels of copper in the samples even after rigorous purification protocols were applied. Since copper is a nanomolar inhibitor against NDM-1, the inhibition values initially obtained were rendered

unreliable and discarded. We have made the in-house copper assay standard in our enzyme inhibition assay workflow to ensure that our future inhibitor samples will be copper free.

### **Conclusion**

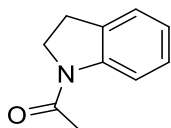
We have validated the synthesis of indoline-6-sulfonamides, and have made significant progress in the development of new chemistry to access the 7-sulfonamide derivatives, which will provide synthetic accessibility to new derivatives of this medicinally important scaffold to the scientific community.<sup>152</sup> The route to the 7-sulfonamides has utilized Borrer's procedure to afford the cyclic sulfonyl urea **40** which was hydrolyzed with sulfuric acid and selectively protected with Cbz on the indoline nitrogen. N-Acylation on the primary sulfonamide of the Cbz-protected indoline-7-sulfonamides afforded a small library of N-Cbz-indoline-7-(N-acyl-sulfonamide) which has been assayed against DapE and NDM-1. Synthesis of a small library of simple N-succinyl and N-glutamyl sulfonamides was also carried out and included with a library of miscellaneous compounds which were assayed for inhibition against our two model metalloenzymes. Finally, we have also pursued sulfonyl azide chemistry to access new sulfonyl triazoles, sulfonyl amidines (1°, 2°, and 3°), sulfonyl imidates, and N-acyl sulfonamides using a Cu(I)-catalyzed three-component. The information compiled in the work represents a strong foundation on which to build our understanding of how metalloenzymes function and how to interact with them using traditional and cutting edge medicinal chemistry techniques.

### **Chapter Acknowledgements**

I am extremely grateful to all the undergraduate researchers who have worked on synthetic projects. I would like to thank Max Moore and Iman Darwish for all their hard work on the sulfonyl azide synthetic series and I would also like to thank J.R. Godlewski for working on the synthesis of the N-Cbz-Indoline-7-(N-acyl-sulfonamide) series.

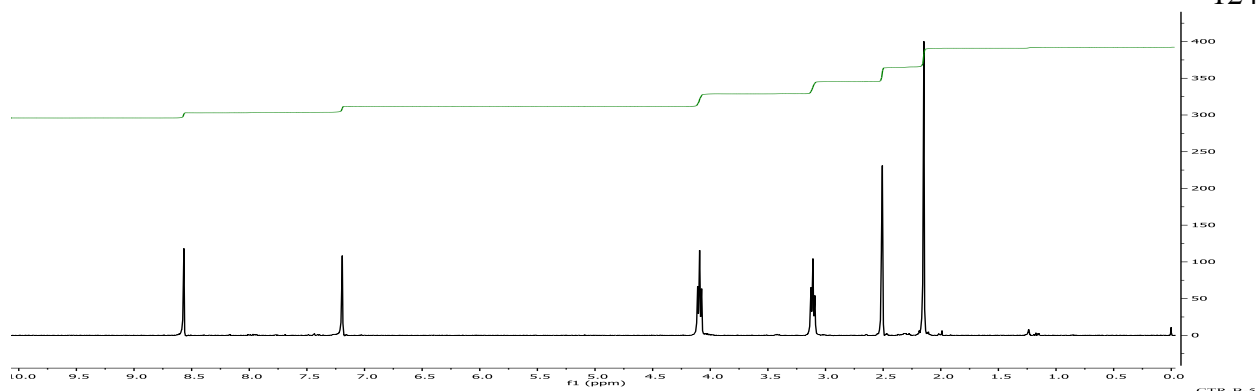
A special thanks to Tahirah Heath for working out conditions for and running both the DapE assay and the copper assays. Finally, I would like to thank Walter Fast, Ph.D. and his lab for collaborating with us and screening our compounds against NDM-1.

### Experimental Section

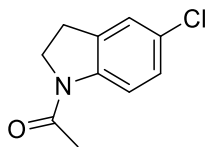


**31**

**1-(Indolin-1-yl)ethan-1-one (31).** To a RBF was added 0.850 mL (8.42 mmol, 1eq.) indoline into 9 mL of CH<sub>2</sub>Cl<sub>2</sub> and stirred over an ice bath for 5 min. Then 3.87 mL of TEA was added and the reaction was left to stir for 5m after which 0.852 mL of acetyl chloride was added to the stirred reaction mixture over 5 min then left to stir for 2 h. The reaction mixture was quenched with 15 mL of water and extracted 3x with DCM to yield a brown tar. The crude product was then purified through flash column using 50:49:1 EA-Petroleum Ether-AcOH solvent system as eluent to yield the desired product. Product collected (1.10 g, 80 %) as an orange solid: mp 96–99 °C; <sup>1</sup>H NMR (500 MHz, CDCl<sub>3</sub>): δ 2.22 (s, 3H), 3.20 (t, J = 6.8 Hz, 2H), 4.05 (t, J = 6.8 Hz, 2H), 7.00 (d, J= 6.0 Hz, 1H), 7.03–7.18 (m, 2H), 8.20 (d, J= 6.4 Hz, 1H); <sup>13</sup>C NMR(125 MHz, CDCl<sub>3</sub>): δ 24.4, 28.1, 48.9, 117.1, 123.7, 124.6, 127.7, 131.2,143.0, 168.9; MS ESI<sup>m/z</sup> 184 ([M + Na]<sup>+</sup>, 100); HRMS EI (DFA) m/z calcd. for C<sub>10</sub>H<sub>11</sub>NO [M<sup>+</sup>] 161.0841, found 161.0840.<sup>154, 159</sup>

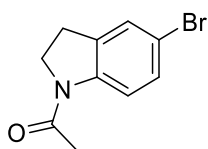
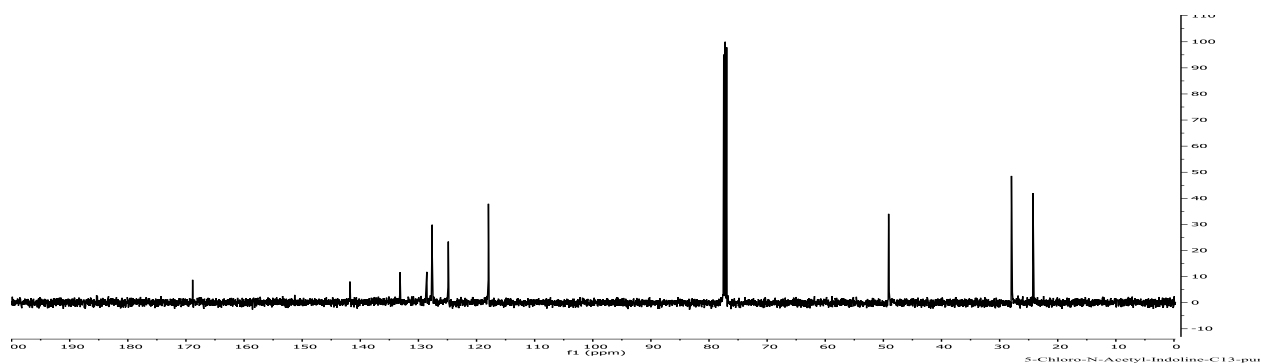
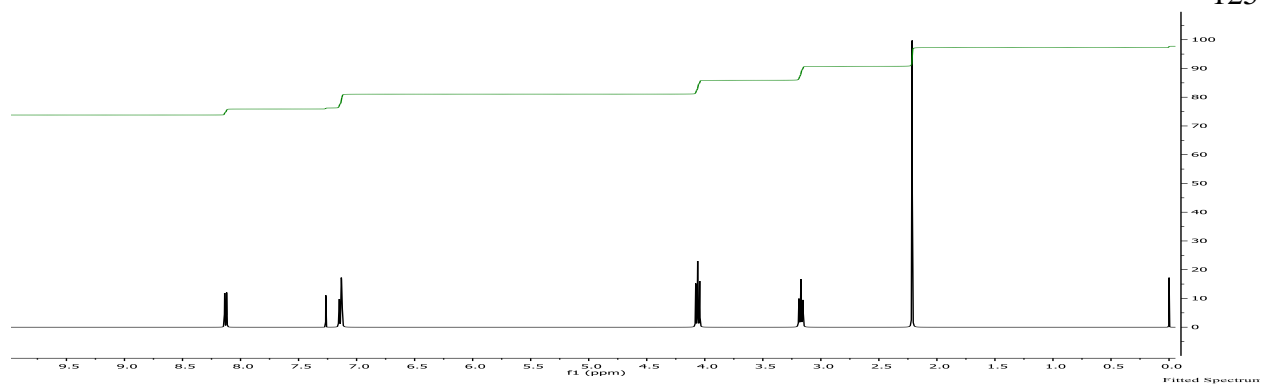


**General Batch Synthesis Procedure for Halogenation of N-Acetylindolines.** A mixture of 1-acetylindoline (2.01 g, 12.47 mmol) and NCS (1.748 g, 13.09 mmol) or NBS (2.33 g, 13.09 mmol) in 60 mL of acetonitrile was left to stir at room temperature for 3.5 hrs. After the solvent was removed under vacuum and the residue diluted with water and extracted 3x with  $\text{CH}_2\text{Cl}_2$  and concentrated to dryness. The collected crude product was then purified by flash chromatography on silica gel eluting with 1:1 EtOAc/hexane.<sup>181</sup>

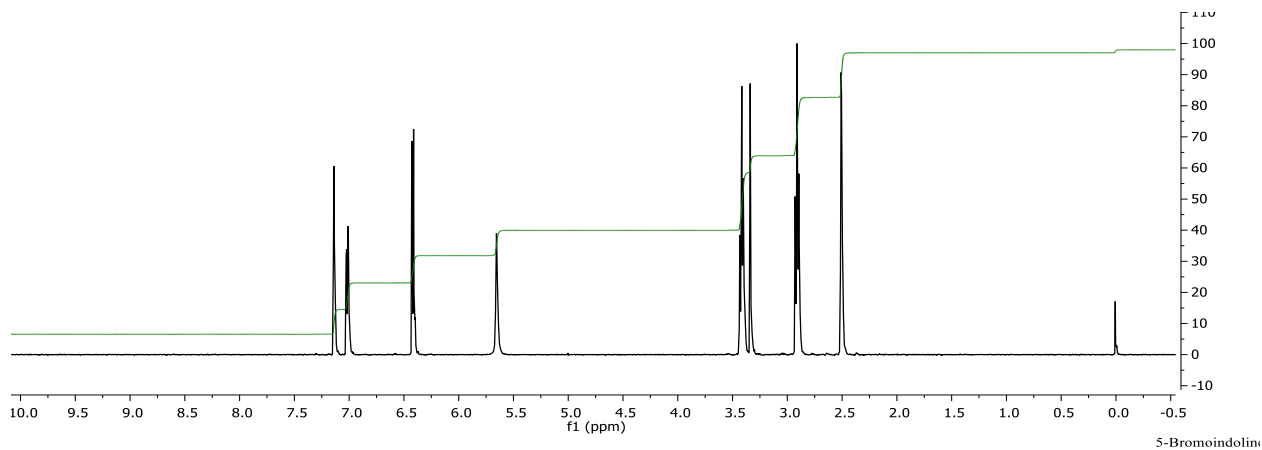


**32a**

**1-(5-Chloroindolin-1-yl)ethan-1-one (32a).** Product collected (2.02 g, 83%) as an orange solid;  $^1\text{H}$  NMR (500 MHz,  $\text{CDCl}_3$ ):  $\delta$  8.13 (d,  $J = 8.5$  Hz, 1H), 7.14 (d,  $J = 9.5$  Hz, 1H), 7.13 (s, 1H), 4.06 (t,  $J = 8.0$  Hz, 2H), 3.17 (t,  $J = 8.5$  Hz, 2H), 2.21 (s, 3H).  $^{13}\text{C}$  NMR (500 MHz,  $\text{CDCl}_3$ ):  $\delta$  168.9, 141.8, 133.2, 128.6, 127.6, 124.7, 124.8, 1187.0, 49.1, 28.0, 24.3.

**32b**

**1-(5-Bromoindolin-1-yl)ethan-1-one (32b).** Product collected (1.81 g, 61 %) as an orange crystalline solid: mp 122-124 °C;  $^1\text{H}$  NMR (500 MHz,  $\text{CDCl}_3$ ):  $\delta$  8.05 (d,  $J = 8.5$  Hz, 1H), 7.26 (d,  $J = 9.5$  Hz, 1H), 7.24 (s, 1H), 4.01 (t,  $J = 8.5$  Hz, 1H), 3.14 (t,  $J = 8.5$  Hz, 2H), 2.19 (s, 3H).



5-Bromoindolin

**Procedure for Continuous Flow Synthesis of N-Acetyl-5-chloroindoline.**

Continuous flow synthesis was carried out with a 7 min residence time and reactor heating at 80 °C. Two 2.0 M DMF solutions of N-Acetylindoline and N-Chlorosuccinimide, line A and B respectively, were freshly prepared and filtered immediately before loading into separate 5 mL syringes which were fitted to syringe pumps. A third syringe pump loaded with an ethyl acetate wash syringe was also prepared (line C) and attached to a three-way solvent valve spliced into solvent line A. Line C was used to pump ethyl acetate through the system in order to remove air from the reactor headspace before reaction initiation. The solvent flow rates for line A and line B were set to 137.5  $\mu\text{L}/\text{min}$  which were combined at a mixing T-joint into the reactor loop for a final reaction flow rate of 275  $\mu\text{L}/\text{min}$ . The reactor loop, possessing a volume of 1.9 mL, was heated in an 80 °C water bath and fitted with a 100 psi back pressure regulator. This reactor setup was able to process 5 mL of 2.0M N-Ac-indoline in the initial reaction run and 10 mL in a followup reaction run. The product stream was immediately quenched into H<sub>2</sub>O by dripping directly into test tube filled with 4.0 mL H<sub>2</sub>O at 7.0 min collection intervals whereupon fluffy white product crystals crash out of solution. Once the syringe volume from line A reached zero the three-way valve was switched allowing for the EA syringe pump to clear the remaining 1.9 mL reaction volume still left in the reactor headspace. The test tubes were combined into one filter funnel and rinsed with DI H<sub>2</sub>O followed by petroleum ether and left to dry under high vac. Recovered products for the first and second optimized reactions were found to be 1.002 g and 1.920 g of an off-white fluffy crystalline solid in a yield of 51 %. HPLC analysis was performed on each fraction collected during the second reaction run in order to determine the product stream composition at each time point (Figure 51). The results of the product stream HPLC analysis are given below with the first and last fractions omitted due to EA contamination.

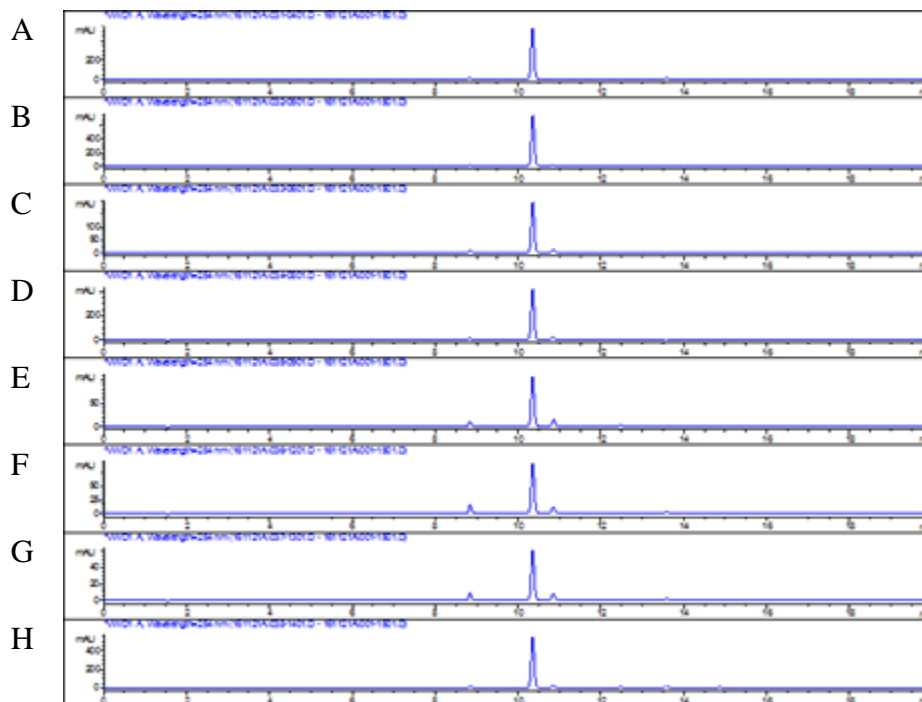


Figure 51. HPLC analysis, Fractions collected at 7 min intervals: A) tube 2, B) tube 3, C) tube 4, D) tube 5, E) tube 6, F) tube 7, G) tube 8, H) tube 9. Peaks at 8.8 mins and 10.3 mins correspond to starting material and products, respectively.

The batch reaction was carried out to simultaneously with flow protocols to compare the two different routes to halogenation or the N-acetyl indoline. The procedures were as followed: N-Ac-indoline (1.0 g) was added to a small RBF and dissolved in DMF (2.0 M, 3.1 mL). Then a 2.4 M solution of freshly prepared NCS in DMF (3.1 mL) was slowly added to the reaction vessel at rt (batch reaction 1), or 70 °C (batch reaction 2) at a flow rate of 137.5  $\mu\text{L}/\text{min}$  with stirring. Upon completion of the NCS addition the reaction was allowed to stir for 2 hrs and quenched with water, forming the precipitate. product was collected via filtration while the rt reaction remained incomplete and allowed to stir overnight. The reactions were then analysed by HPLC and results summarized in Figure 52.

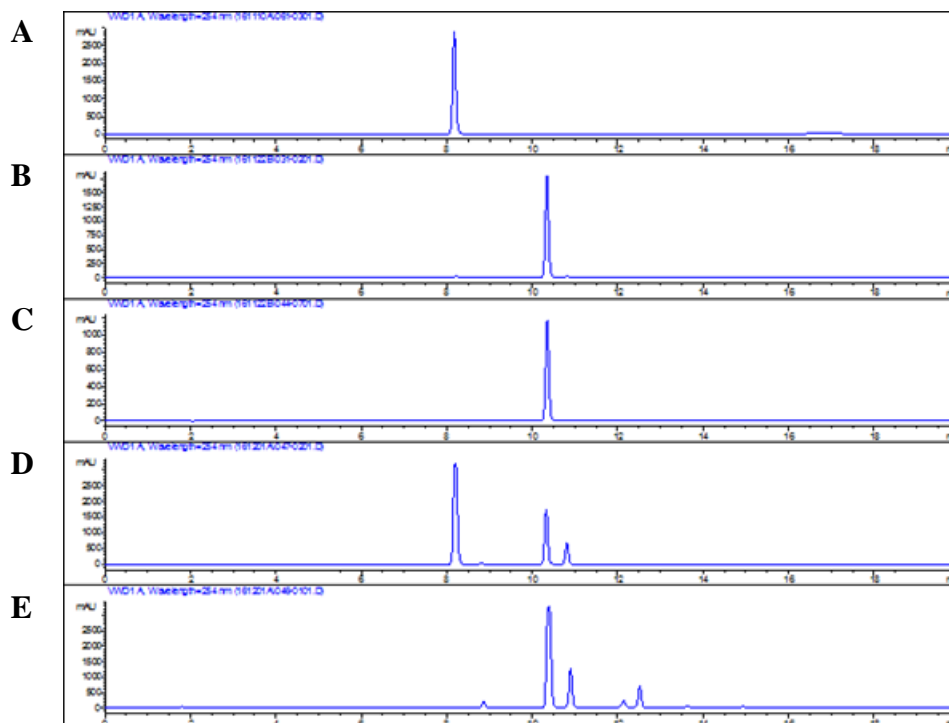
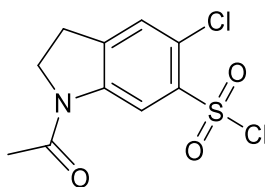


Figure 52: Comparing flow vs. batch synthetic protocols. A) NAc-indoline starting material, B) filtered products from 1st flow reaction 1, C) filtered products from 2nd Flow reaction after optimization, D) batch reaction 1, run at rt for 2 h), batch reaction 2, ran at 70 °C for 2 h).

The optimized flow reaction only took 30 min for a 1.0 g scale reaction to go to completion with high purity conversion while the batch reactions either produces multiple products after heating or does not finish in under two hours on the same scale as flow. These results illustrate the benefits to using continuous flow synthesis to prepare the 5-chloro-NAc-indoline product.

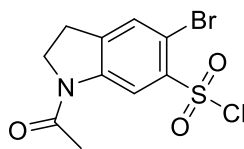


**33a**

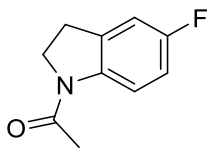
**1-Acetyl-5-chloroindoline-6-sulfonyl chloride (33a).** To 1-acetyl-5-chloroindoline (300 mg) was added to chlorosulfonic acid (2.25 M, 7 mL/g of sm) in small portions with intensive stirring and cooling (ice). The mixture was heated at 60 °C, stirred for 3.5 hrs and TLC was taken using



60:1:39 EA-petroleum ether-AcOH solvent ratio to confirm reaction completion. The reaction mixture was quenched over ice in a large earlenmeyer flask by pouring down the sides of the flask. The precipitate was filtered and re-crystallized from methyl ethyl ketone to yield 341 mg of an off white solid. Exp mp = 190-195 °C; <sup>1</sup>H NMR (500 MHz, CDCl<sub>3</sub>): δ 8.98 (s, 1H), 7.42 (s, 1H), 4.02 (t, J = 9.0 Hz, 2H), 3.33 (t, J = 8.0 Hz, 2H), 2.09 (s, 3H).

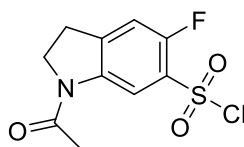
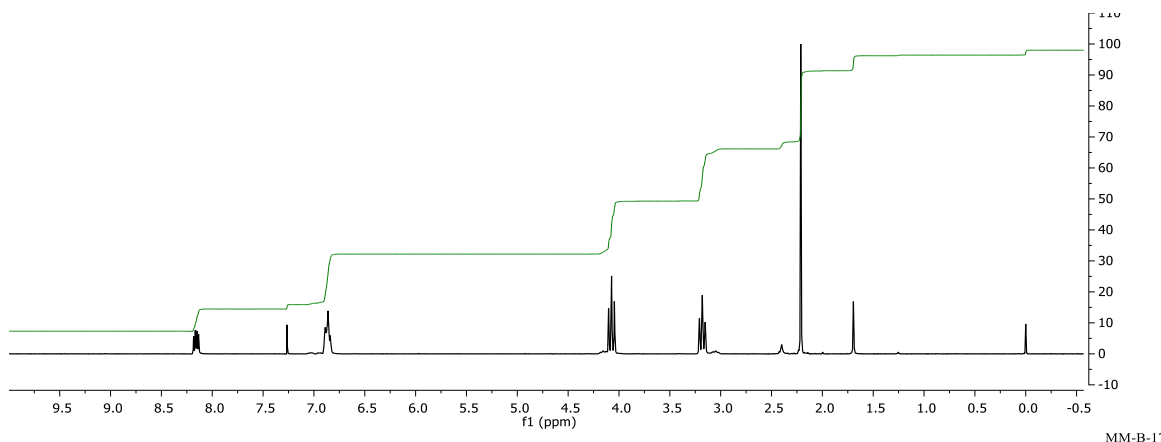
**33b**

**1-Acetyl-5-bromoindoline-6-sulfonyl chloride (33b).** To 1-acetyl-5-bromoindoline (1.20 g, 5.0 mmol) was added to chlorosulfonic acid (8.5 mL) in small portions with intensive stirring and cooling(ice).<sup>156</sup> The mixture was heated at 60 °C, stirred for 3 hrs and TLC was taken using 60:1:39 EA-petroleum ether-AcOH to confirm reaction completion. Reaction mixture was quenched over ice in a large earlenmeyer flask by pouring down the sides of the flask with stirring. The precipitate was filtered and re-crystallized from methyl ethyl ketone to yield 1.69 g of a white solid. Exp. mp = 211-212 °C; <sup>1</sup>H NMR (300 MHz, CDCl<sub>3</sub>): δ 9.03 (s, 1H), 7.63 (s, 1H), 4.20 (t, J = 8.5 Hz, 2H), 3.12 (t, J = 8.0 Hz, 2H), 2.28 (s, 3H).

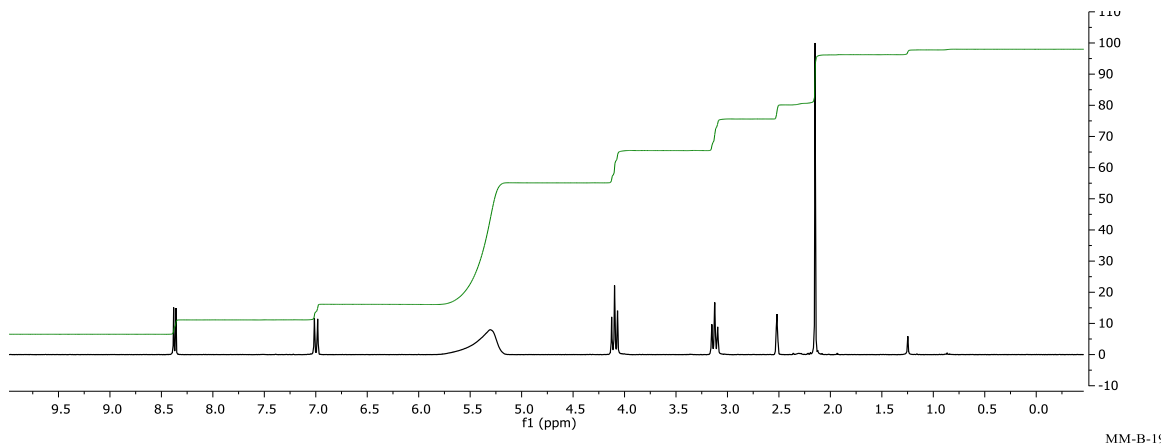
**34**

**1-(5-Fluoroindolin-1-yl)ethan-1-one (34).** To neat acetic anhydride (2 mL, 21.2 mmol) was added 5-fluoroindoline portionwise (427 μL, 3.65 mmol) with stirring. After 15 min stirring at room temperature under N<sub>2</sub>, reaction mixture was dripped over ice, stirred for 30 min, and the precipitate was collected by vacuum filtration, washing with 100 mL H<sub>2</sub>O, to yield a light pink

solid (543.3 mg, 83%).  $^1\text{H NMR}$  (300 MHz,  $\text{CDCl}_3$ ):  $\delta$  8.16 (dd, 1H,  $J_{\text{F,H}} = 9.75$  Hz,  $J_{\text{H,H}} = 4.95$  Hz), 6.89-6.84 (m, 2H), 4.07 (t, 2H,  $J = 8.55$  Hz), 3.18 (t, 2H,  $J = 8.4$  Hz), 2.21 (s, 3H).

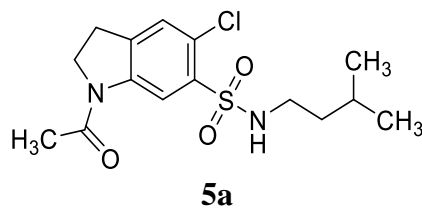
**35**

**1-Acetyl-5-fluoroindoline-6-sulfonyl chloride (35).** The fluoro analog 1-(5-fluoroindolin-1-yl)ethan-1-one (500 mg, 2.79 mmol) was dissolved in chlorosulfonic acid (5.0 mL, 75 mmol) under  $\text{N}_2$  at  $0^\circ\text{C}$ , and the reaction mixture was gradually heated to  $50^\circ\text{C}$  and stirred for 2 h. Temperature was then increased to  $65^\circ\text{C}$  and reaction mixture was stirred for an additional 1 h, then cooled to room temperature. The reaction mixture was slowly dripped over ice, stirred for 10 min, and precipitate was collected by vacuum filtration, washing with 100 mL  $\text{H}_2\text{O}$ , to afford 723 mg of a white solid at a 93 % yield. mp =  $163.8$ - $175.2$  (decomp).  $^1\text{H NMR}$  (300 MHz,  $\text{DMSO-d}_6$ ):  $\delta$  8.35 (d, 1H,  $J = 6.6$  Hz), 6.97 (d, 1H,  $J = 9.6$  Hz), 4.08 (t, 2H,  $J = 8.55$  Hz), 3.10 (t, 2H,  $J = 8.55$  Hz), 2.13 (s, 3H).



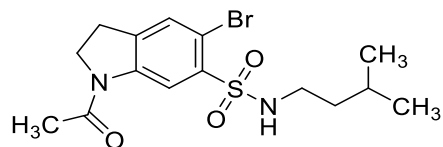
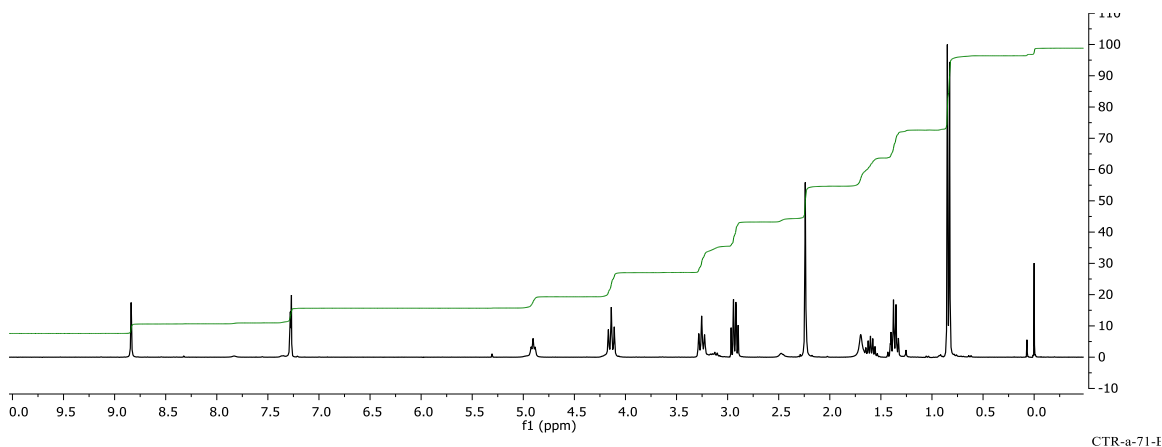
### General Procedure for Preparing N-Acetyl-5-haloindolines-6-sulfonamides.<sup>159</sup>

In a reaction vial was added 100 mg of N-acetyl-5-chlorindoline-6-sulfonyl chloride (0.340 mmol, 1 eq.) or N-acetyl-5-bromoindoline-6-sulfochloride (0.295 mmol, 1 eq.) along with a stir bar and a 5 mol% amount of DMAP if the procedure employs a 2° amine. This is followed by addition of methylene chloride (3 mL), Et<sub>3</sub>N (1.5 eq.) and the respective amine (1.25 eq.) to the reaction vial. The reaction is then left to stir at room temperature for 2 to 3 hours or until TLC indicated complete reaction. Upon completion, the reaction is diluted with dichloromethane followed by 1N HCl. The aqueous layers then extracted three times with methylene chloride to remove the product from the aqueous layer, the fractions were then combined and washed once more with brine, then dried over sodium sulfate and condensed to dryness on the vacuum. The crude product is the taken up in chloroform and passed through a plug of activated carbon, concentrating, and recrystallized from 1:2 chloroform-EA.<sup>159</sup>



**1-Acetyl-5-chloro-N-isopentylindoline-6-sulfonamide (5a).** Product collected (117 mg, 99 %)

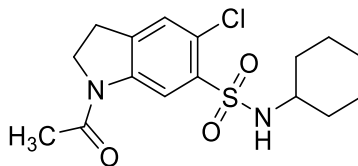
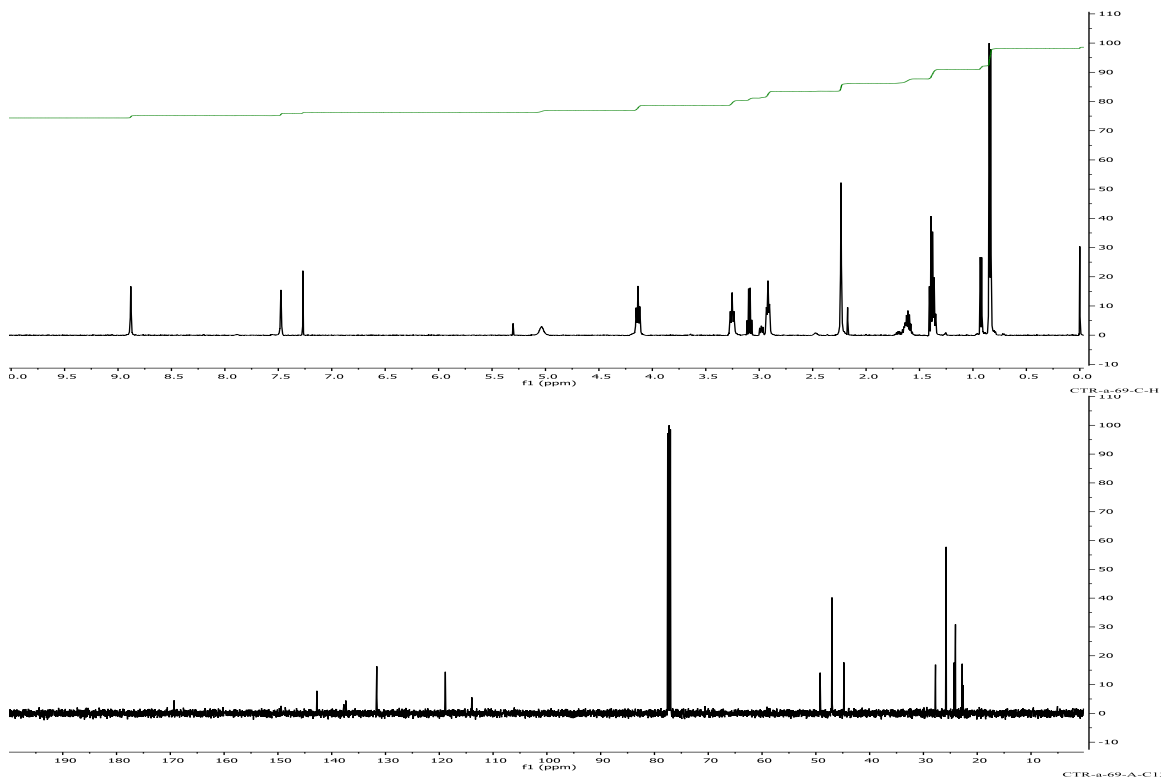
as a tan solid: mp = 174-180 °C;  $^1\text{H NMR}$  (300 MHz,  $\text{CDCl}_3$ ):  $\delta$  8.89 (s, 1H), 7.28 (s, 1H), 4.90 (t,  $J = 6.0$  Hz, 2H), 4.14 (t,  $J = 8.7$  Hz, 2H), 3.25 (t,  $J = 8.7$  Hz, 2H), 2.93 (dd,  $J = 13.7, 7.2$  Hz, 2H), 2.24 (s, 3H), 1.36 (dd,  $J = 14.4, 6.9$  Hz, 2H), 1.60 (m, 1H), 0.84 (d,  $J = 6.6$  Hz, 6H).



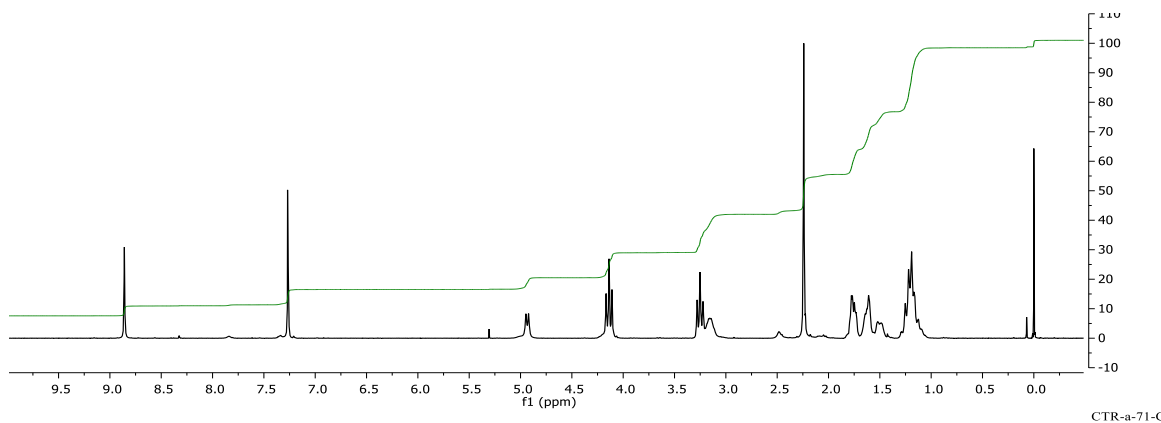
**5b**

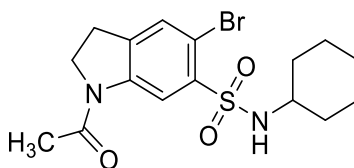
**1-Acetyl-5-bromo-N-isopentylindoline-6-sulfonamide (5b).** Product collected (0.114g, 99 %)

as a orange tacky solid: mp 190-191 °C;  $^1\text{H NMR}$  (500 MHz,  $\text{CDCl}_3$ ):  $\delta$  8.88 (s, 1H), 7.48 (s, 1H), 5.04 (bs, 1H), 4.14 (t,  $J = 8.5$  Hz, 2H), 3.25 (t,  $J = 9.0$  Hz, 2H), 2.92 (t,  $J = 7.5$  Hz, 2H), 2.24 (s, 3H), 1.67 (m, 1H), 1.38 (s, 2H), 0.84 (d,  $J = 7.0$  Hz, 6H),

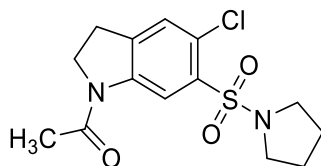
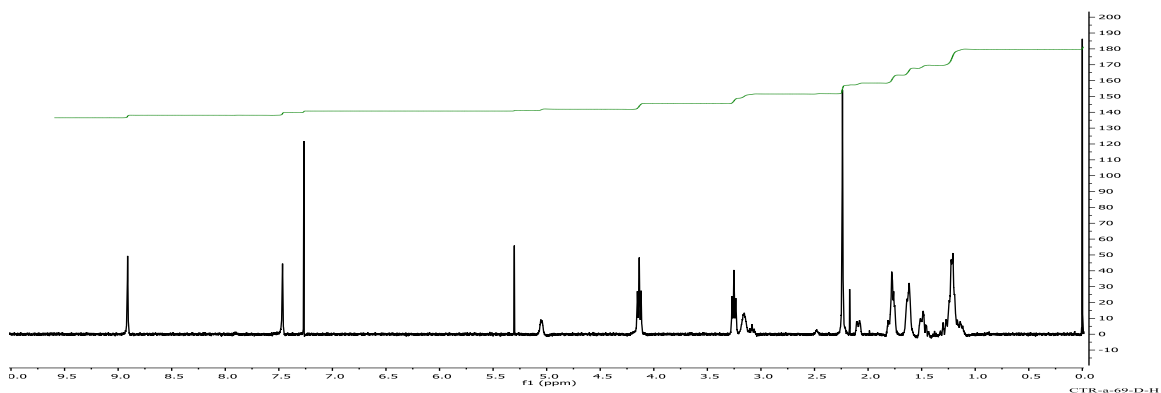
**9a**

**1-Acetyl-5-chloro-N-cyclohexylindoline-6-sulfonamide (9a).** Product collected (95.3 mg, 79 %) as a white solid: mp 224-232 °C;  $^1\text{H NMR}$  (300 MHz,  $\text{CDCl}_3$ ):  $\delta$  8.9 (s, 1H), 7.28 (s, 1H), 4.90 (t,  $J = 6.0$  Hz, 1H), 4.14 (t,  $J = 8.7$  Hz, 2H), 3.25 (t,  $J = 8.7$  Hz, 2H), 2.93 (dd,  $J = 13.7, 7.2$  Hz, 2H), 2.24 (s, 3H), 1.36 (dd,  $J = 14.4, 6.9$  Hz, 2H), 1.6 (m, 1H), 0.84 (d,  $J = 6.6$  Hz, 6H).

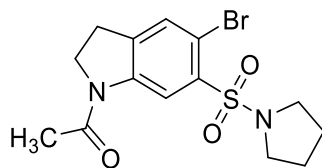
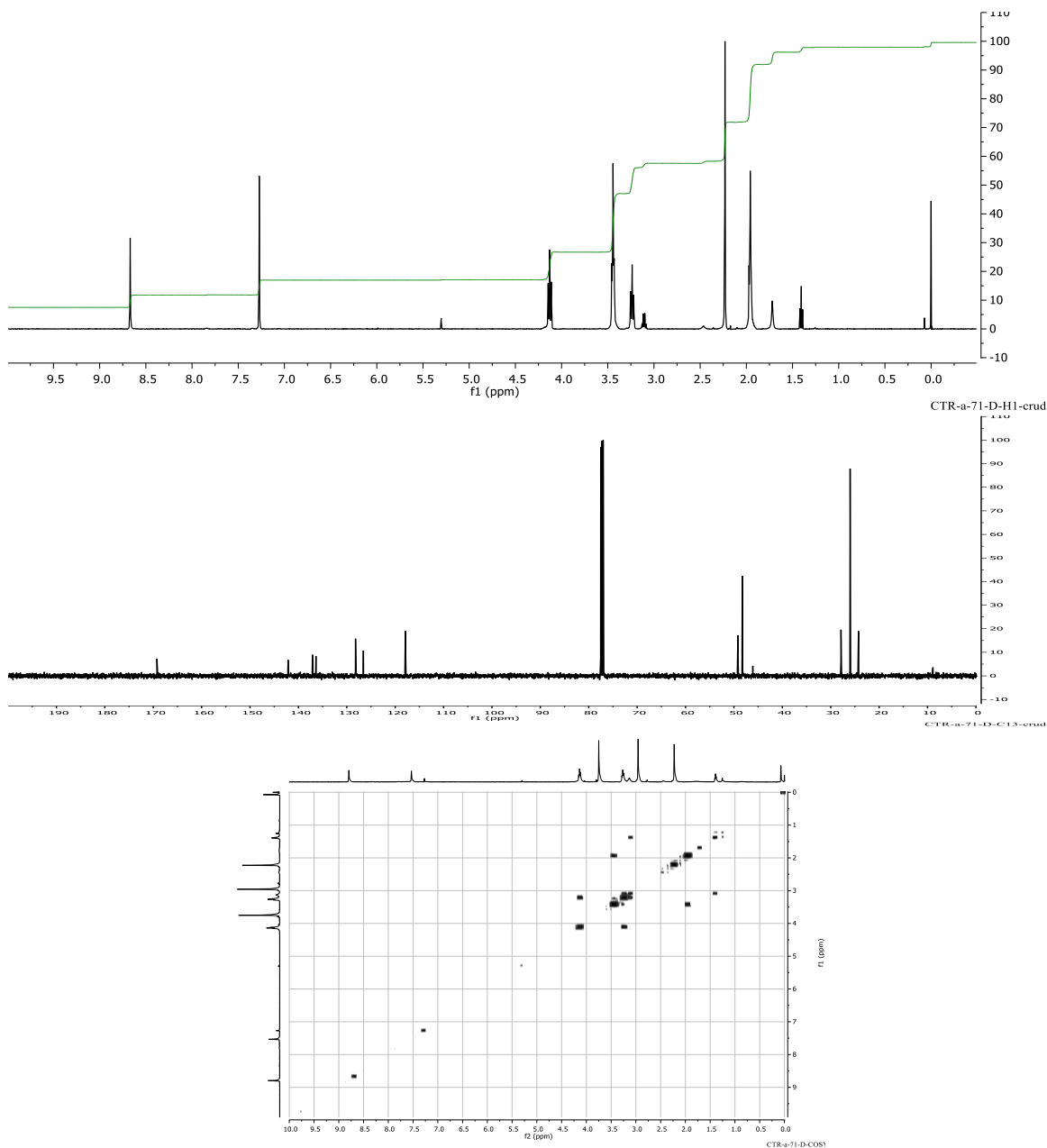


**10a**

**1-Acetyl-5-bromo-N-cyclohexylindoline-6-sulfonamide (10a).** Product collected (92.6 mg, 78 %) as a white crystalline solid: mp 226-228 °C; <sup>1</sup>H NMR (300 MHz, CDCl<sub>3</sub>): δ 8.91 (s, 1H), 7.47 (s, 1H), 5.55 (d, J = 7.5 Hz, 1H), 4.14 (t, J = 8.5 Hz, 2H), 3.25 (t, J = 9 Hz, 2H), 3.16 (m, 1H), 2.24 (s, 3H), 1.82-1.14 (m, 10H).

**11a**

**1-(5-Chloro-6-(pyrrolidin-1-ylsulfonyl)indolin-1-yl)ethan-1-one (11a).** Product collected (103 mg, 92 %) as a yellowish tan solid: mp 197-201 °C; <sup>1</sup>H NMR (500 MHz, CDCl<sub>3</sub>): δ 8.67 (s, 1H), 7.27 (s, 1H), 4.13 (t, J = 8.6 Hz, 2H), 3.44 (td, J = 6.7, 5.4, 2.9 Hz, 4H), 3.24 (t, J = 8.5 Hz, 2H), 2.23 (s, 3H), 2.04 – 1.89 (m, 4H). <sup>13</sup>C NMR (500 MHz, CDCl<sub>3</sub>): δ 169.3, 142.1, 137.1, 136.4, 128.2, 126.6, 117.4, 49.2, 48.3, 27.9, 26.0, 24.3.

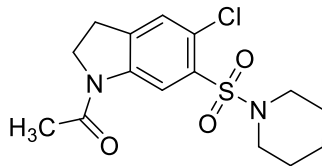
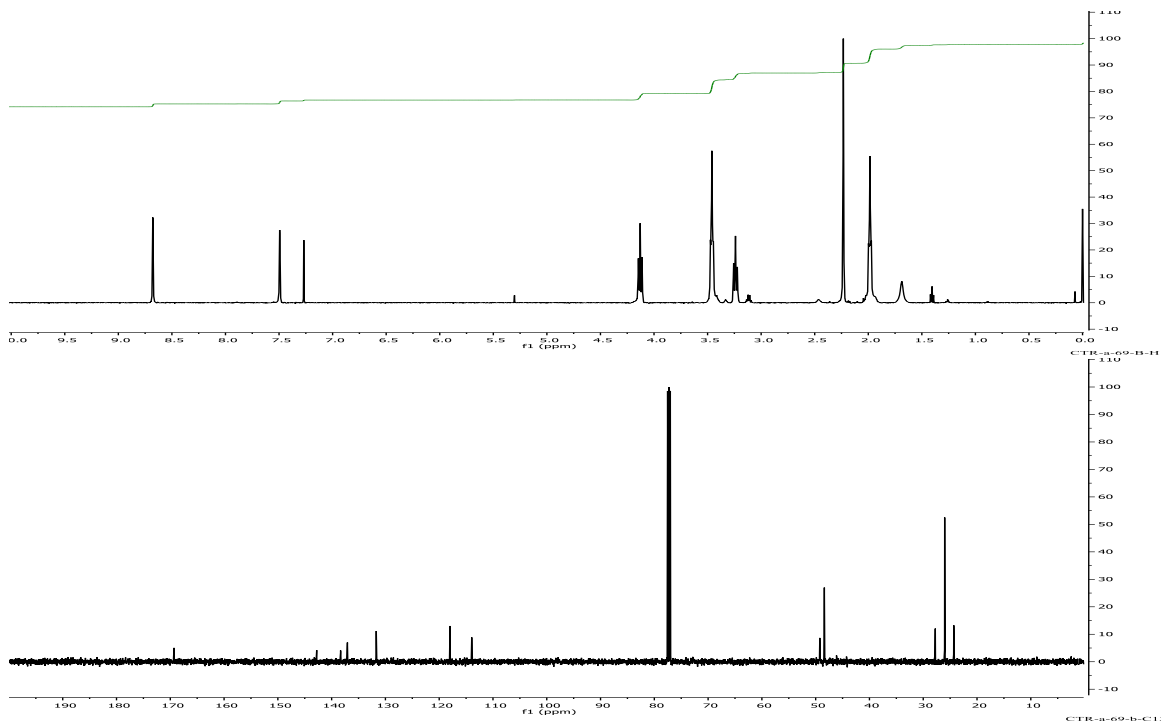
**12a**

**1-(5-Bromo-6-(pyrrolidin-1-ylsulfonyl)indolin-1-yl)ethan-1-one (12a).** Product collected

(98.8 mg, 90 %) as a light brown crystalline solid: mp 238-240 °C;  $^1\text{H}$  NMR (500 MHz,  $\text{CDCl}_3$ ):

$\delta$  8.68 (s, 1H), 7.50 (s, 1H), 4.13 (t,  $J = 9.0$  Hz, 2H), 3.46 (t,  $J = 6.5$  Hz, 4H), 3.24 (t,  $J = 6.0$  Hz,

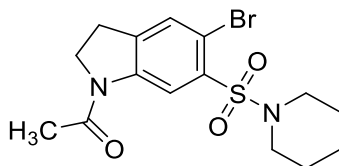
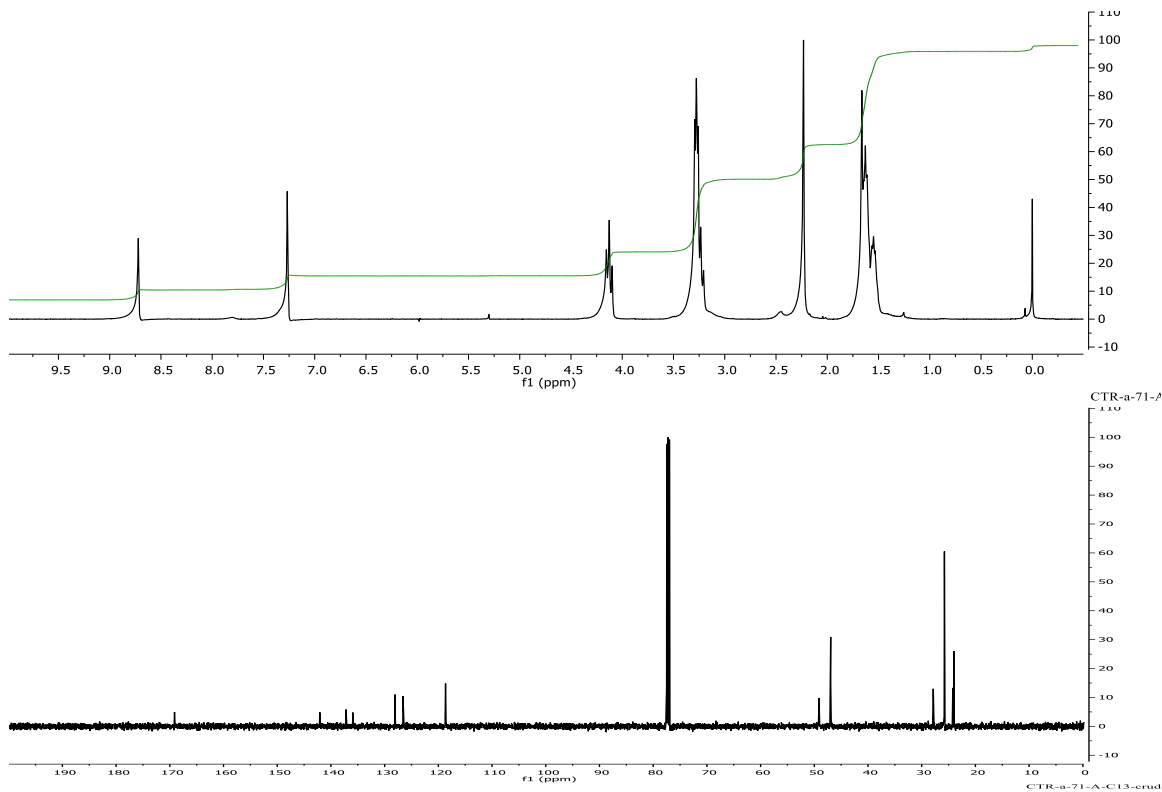
2H), 2.23 (s, 3H), 1.98 (t,  $J = 7.0$  Hz, 2H);  $^{13}\text{C}$  NMR (500 MHz,  $\text{CDCl}_3$ ):  $\delta$  169.3, 142.9, 138.3, 137.1, 131.7, 118.0, 114.0, 49.2, 48.4, 27.8, 26.0, 24.3.



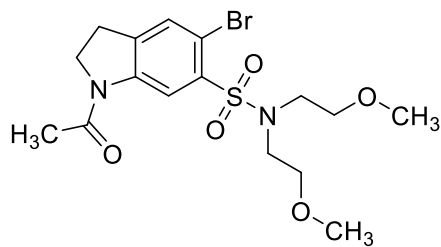
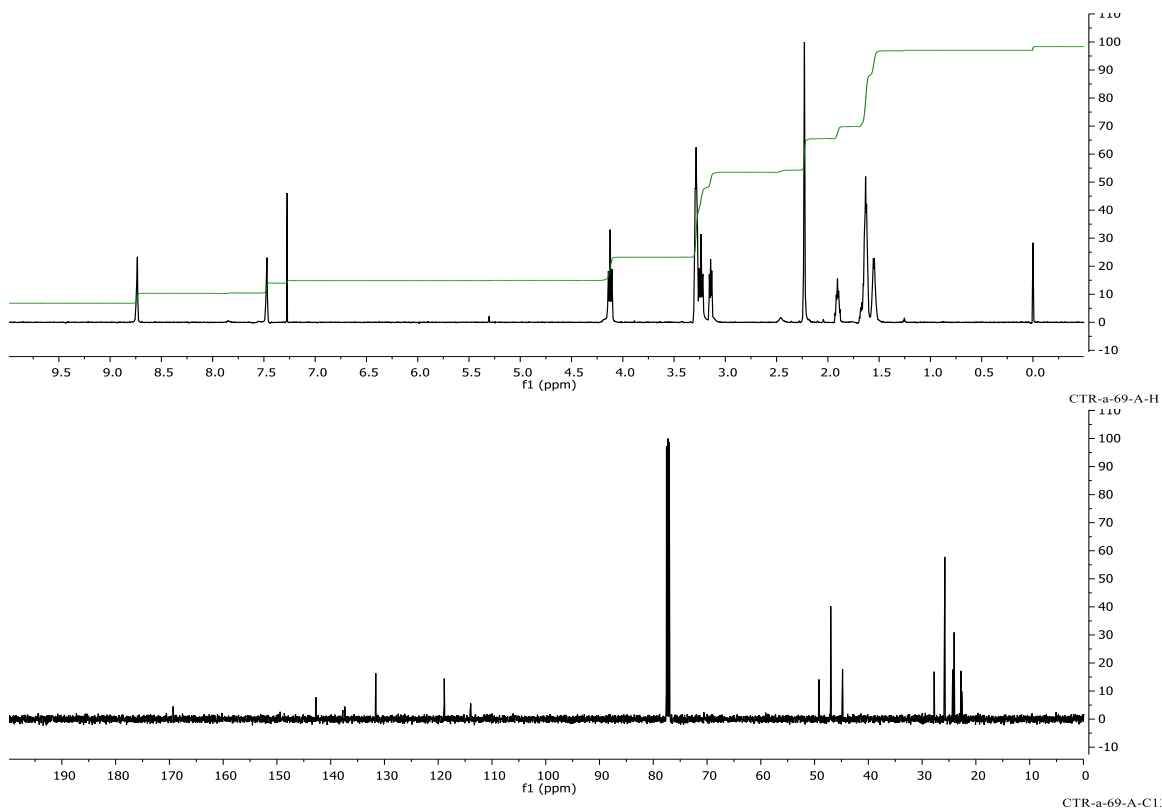
**13a**

**1-(5-chloro-6-(piperidin-1-ylsulfonyl)indolin-1-yl)ethan-1-one (13a).** Product collected (104 mg, 79 %) as a tan crystalline solid:  $^1\text{H}$  NMR (500 MHz,  $\text{CDCl}_3$ ):  $\delta$  8.72 (s, 1H), 7.27 (s, 1H), 4.13 (t,  $J = 9.0$  Hz, 2H), 3.28 (t,  $J = 66.5$  Hz, 4H), 3.24 (t,  $J = 9.0$  Hz, 2H), 2.23 (s, 3H), 1.66-1.61 (m, 4H), 1.54 (dd,  $J = 11.0, 6.0$  Hz, 2H);  $^{13}\text{C}$  NMR (500 MHz,  $\text{CDCl}_3$ ):  $\delta$  169.1, 142.1, 137.2, 135.9, 128.1, 126.6, 118.7, 49.1, 47.0, 27.9, 25.8, 24.2, 24.0.



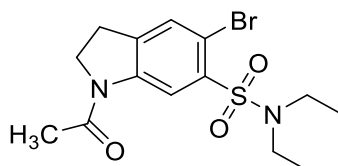
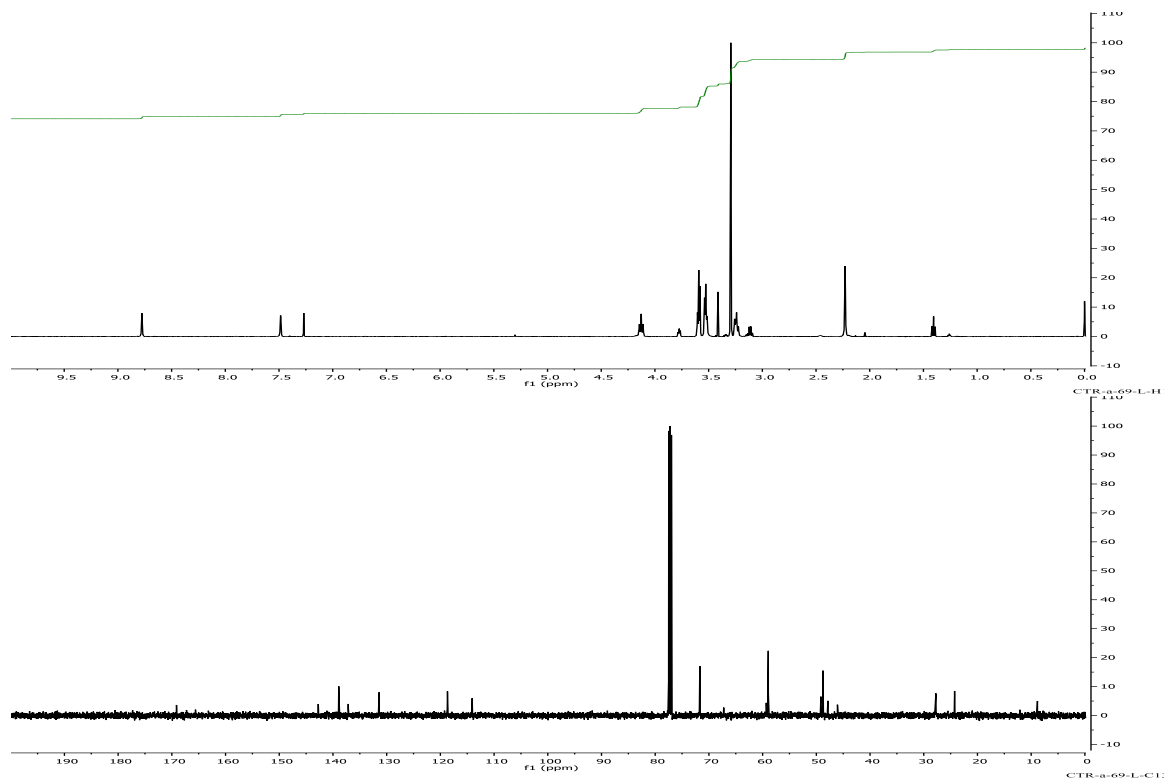
**14a**

**1-(5-Bromo-6-(piperidin-1-ylsulfonyl)indolin-1-yl)ethan-1-one (14a).** Product collected (114 mg, 70 %) as a off white crystalline solid: mp 212-214°C;  $^1\text{H}$  NMR (500 MHz,  $\text{CDCl}_3$ ):  $\delta$  8.73 (s, 1H), 7.47 (s, 1H), 4.12 (t,  $J = 8.0$  Hz, 2H), 3.29 (t,  $J = 4.5$  Hz, 4H), 3.24 (t,  $J = 8.5$  Hz, 2H), 2.23 (s, 3H), 1.63 (m, 4H), 1.552 (m, 2H);  $^{13}\text{C}$  NMR (500 MHz,  $\text{CDCl}_3$ ):  $\delta$  169.3, 142.8, 137.7, 137.4, 131.6, 118.9, 114.0, 49.2, 47.0, 44.8, 27.8, 25.8, 24.3, 24.0.

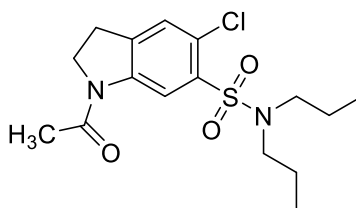
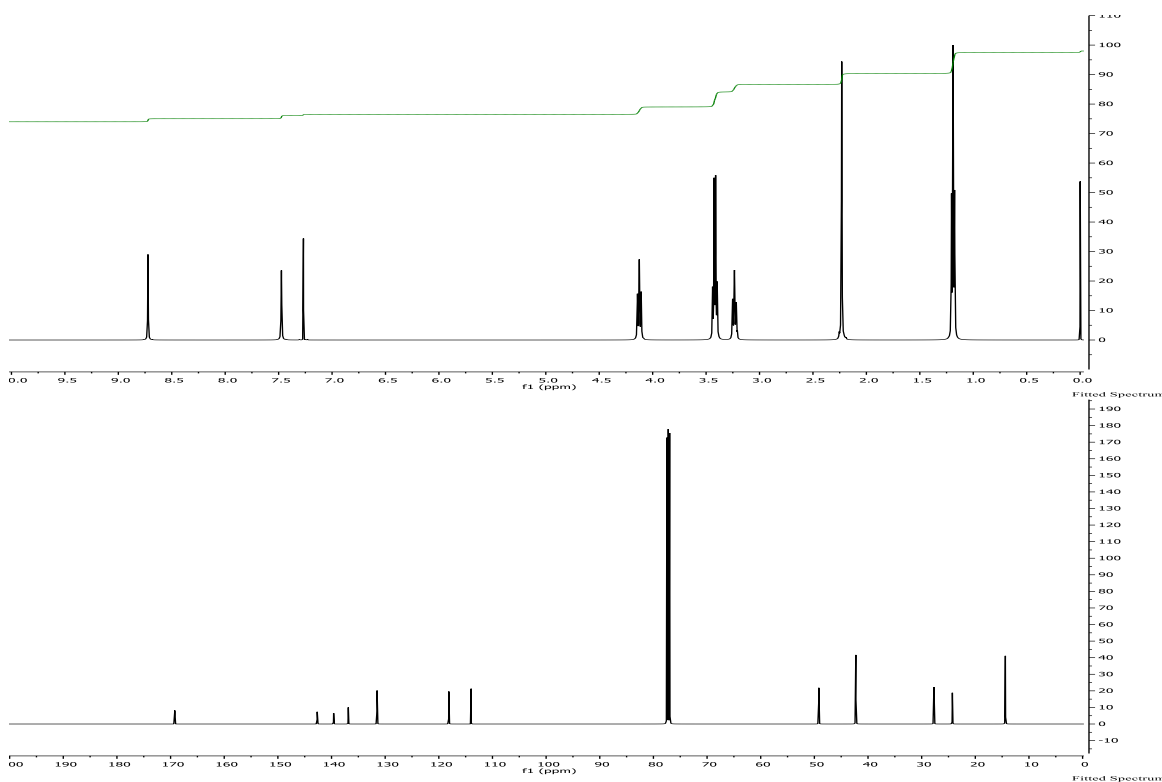


**16a**

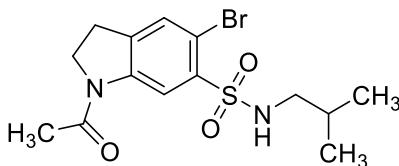
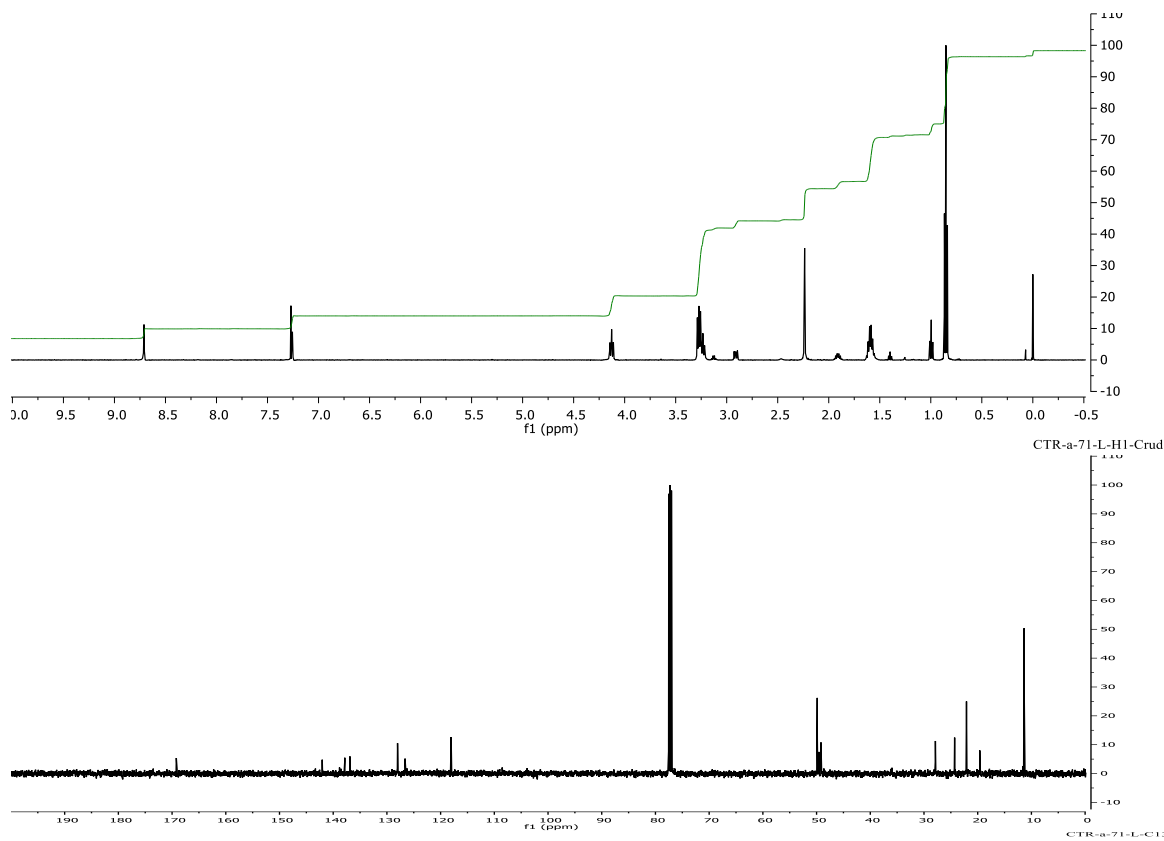
**1-Acetyl-5-bromo-N,N-bis(2-methoxyethyl)indoline-6-sulfonamide (16a).** Product collected (125 mg, 97 %) as a yellowish tan solid: mp 110-111 °C;  $^1\text{H}$  NMR (500 MHz,  $\text{CDCl}_3$ ):  $\delta$  8.78 (s, 1H), 7.49 (s, 1H), 4.23 (t,  $J = 8.5$  Hz, 2H), 3.40 (t,  $J = 6.0$  Hz, 4H), 3.53 (t,  $J = 5.5$  Hz, 4H), 3.30 (s, 6H), 3.24 (t,  $J = 9.0$  Hz, 2H), 2.23 (s, 3H);  $^{13}\text{C}$  NMR (500 MHz,  $\text{CDCl}_3$ ):  $\delta$  169.2, 142.8, 139.0, 137.2, 131.5, 118.7, 114.2, 71.7, 59.0, 48.8, 27.8, 24.3, 8.9.

**17a**

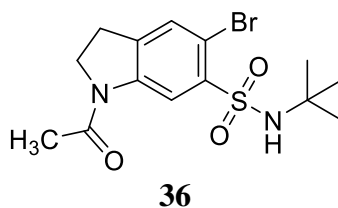
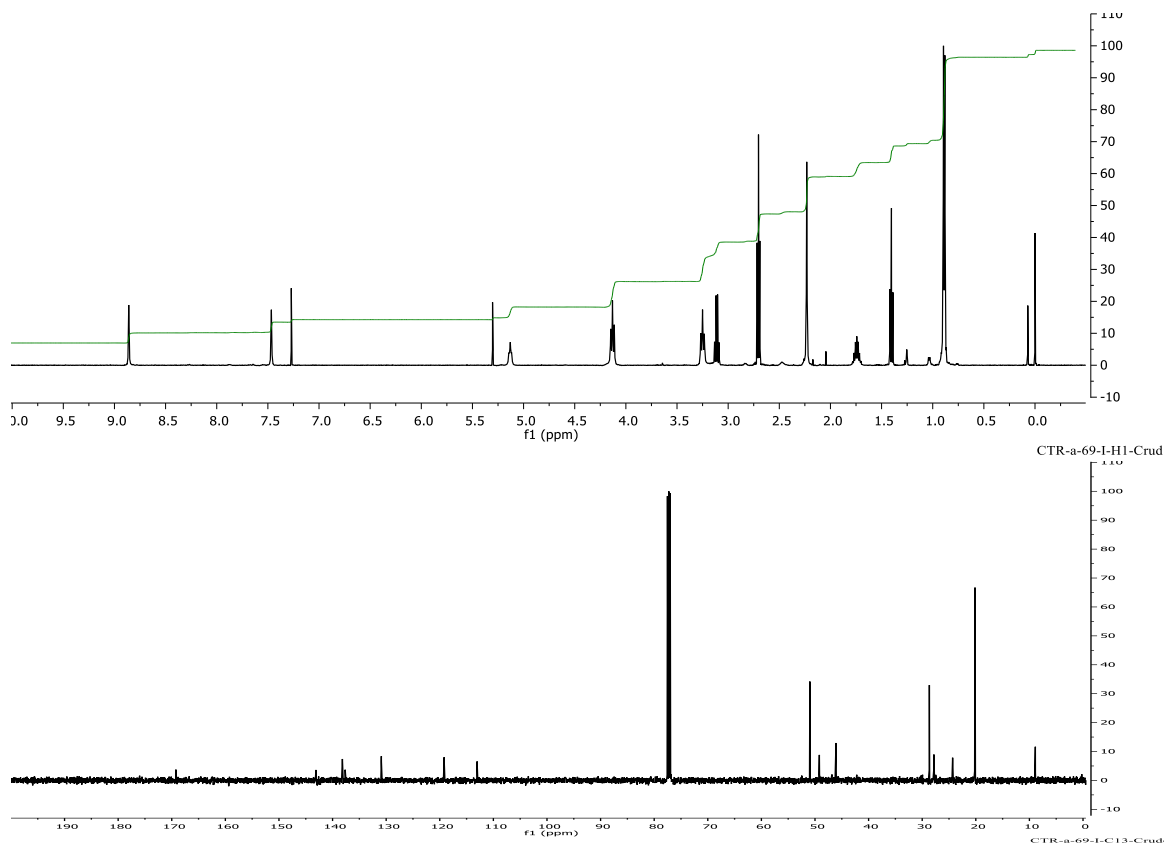
**1-Acetyl-5-bromo-N,N-diethylindoline-6-sulfonamide (17a).** Product collected (110 mg, 99%) as an off white solid: mp 195-196 °C;  $^1\text{H}$  NMR (500 MHz,  $\text{CDCl}_3$ ):  $\delta$  8.72 (s, 1H), 7.47 (s, 1H), 4.13 (t,  $J = 8.5$  Hz, 2H), 3.42 (q,  $J = 7.0$  Hz, 4H), 3.23 (t,  $J = 8.0$  Hz, 2H), 2.23 (s, 3H), 1.19 (t,  $J = 7.5$  Hz, 6H);  $^{13}\text{C}$  NMR (126 MHz,  $\text{CDCl}_3$ ):  $\delta$  169.2, 142.7, 139.6, 136.9, 131.5, 118.1, 114.0, 77.5, 77.2, 77.0, 49.2, 42.3, 27.7, 24.3, 14.4.

**18a**

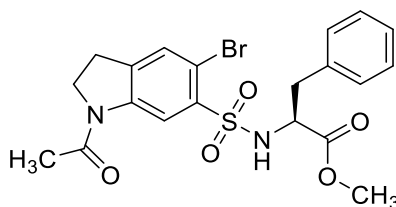
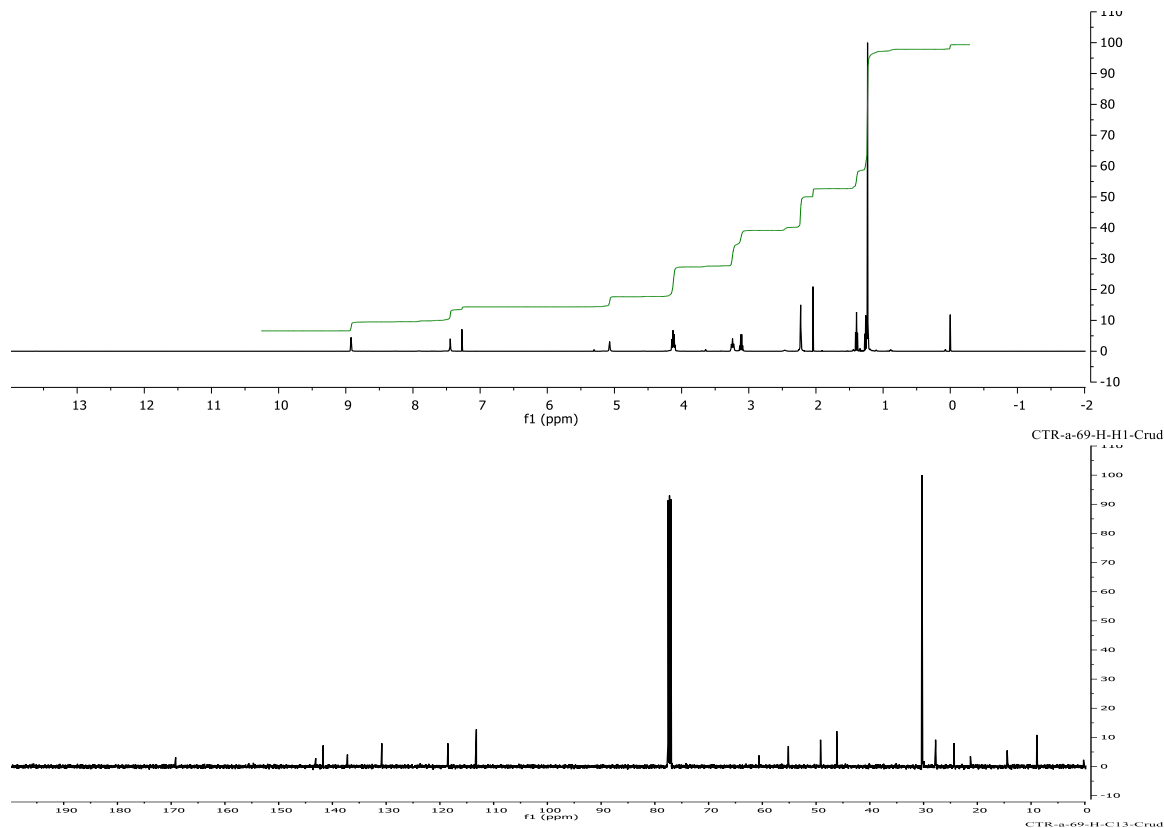
**1-Acetyl-5-chloro-N,N-dipropylindoline-6-sulfonamide (18a).** Product collected (104 mg, 85 %) as a light brown solid: mp 118-120 °C;  $^1\text{H}$  NMR (500 MHz,  $\text{CDCl}_3$ ):  $\delta$  8.78 (s, 1H), 7.49 (s, 1H), 4.23 (t,  $J = 8.5$  Hz, 2H), 3.59 (t,  $J = 6.0$  Hz, 4H), 3.53 (t,  $J = 5.5$  Hz, 4H), 3.29 (s, 6H), 3.24 (t,  $J = 9.0$  Hz, 2H), 2.23 (s, 3H);  $^{13}\text{C}$  NMR (500 MHz,  $\text{CDCl}_3$ ):  $\delta$  169.2, 142.1, 137.9, 136.9, 128.0, 126.6, 118.1, 49.9, 49.6, 49.2, 27.9, 24.3, 22.1, 19.6, 11.5, 11.4.

**21a**

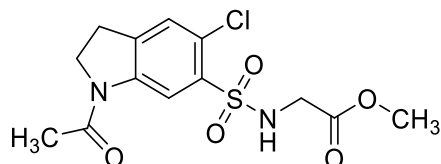
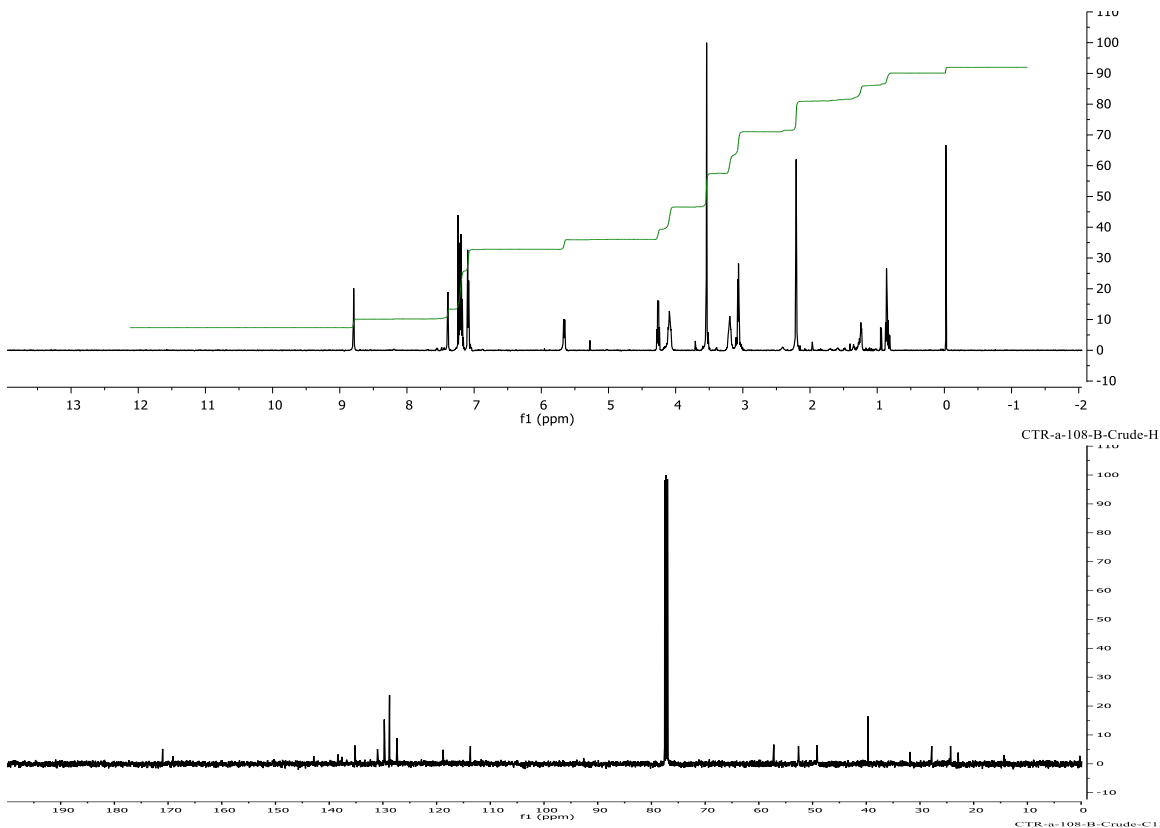
**1-Acetyl-5-bromo-N-isobutylindoline-6-sulfonamide (21a).** Product collected (93 mg, 84 %) as white crystal: mp 215-220 °C;  $^1\text{H}$  NMR (500 MHz,  $\text{CDCl}_3$ ):  $\delta$  8.87 (s, 1H), 7.47 (s, 1H), 5.13 (t,  $J = 6.5$  Hz, 1H), 4.13 (t,  $J = 8.5$  Hz, 2H), 3.25 (t,  $J = 9.0$  Hz, 2H), 2.70 (t,  $J = 6.5$  Hz, 2H), 2.23 (s, 3H), 1.74 (m, 1H), 0.89 (d,  $J = 8.5$  Hz, 6H),  $^{13}\text{C}$  NMR (500 MHz,  $\text{CDCl}_3$ ):  $\delta$  169.2, 143.1, 138.2, 137.7, 130.9, 119.2, 113.1, 50.9, 649.2, 46.1, 28.7, 27.8, 24.3, 8.9.



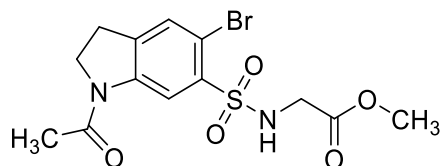
**1-Acetyl-5-bromo-N-(tert-butyl)indoline-6-sulfonamide (36).** Product collected (44.2 mg, 40 %) as an off-white solid: mp 225-230 °C; <sup>1</sup>H NMR (500 MHz, CDCl<sub>3</sub>): δ 8.82 (s, 1H), 7.45 (s, 1H), 5.07 (s, 1H), 4.23 (t, J = 9.0 Hz, 2H), 3.24 (t, J = 8.5 Hz, 2H), 2.23 (s, 3H), 1.23 (s, 9H); <sup>13</sup>C NMR (500 MHz, CDCl<sub>3</sub>): δ 169.2, 143.1, 141.7, 137.2, 130.8, 118.5, 113.2, 55.2, 49.2, 46.2, 30.3, 27.8, 24.4, 8.9.

**23a**

**Methyl ((1-acetyl-5-bromoindolin-6-yl)sulfonyl)-L-phenylalaninate (23a).** Product collected (127 mg, 90%) as a tan solid: mp 178-183 °C;  $^1\text{H}$  NMR (500 MHz,  $\text{CDCl}_3$ ):  $\delta$  8.79 (s, 1H), 7.39 (s, 1H), 7.21–7.08 (m, 5H), 5.66 (d,  $J = 8.0$  Hz, 1H), 4.26 (dt,  $J = 8.0, 5.8$  Hz, 1H), 4.09 (m, 2H), 3.54 (s, 3H), 3.20 (t,  $J = 1.0$  Hz, 2H), 3.06 (t,  $J = 4.8$  Hz, 2H), 2.21 (m, 3H);  $^{13}\text{C}$  NMR (500 MHz,  $\text{CDCl}_3$ ):  $\delta$  171.0, 169.1, 142.9, 138.4, 137.6, 135.2, 131.0, 129.8, 128.8, 127.4, 118.8, 113.7, 57.2, 52.6, 49.2, 39.7, 27.8, 24.3.

**26a**

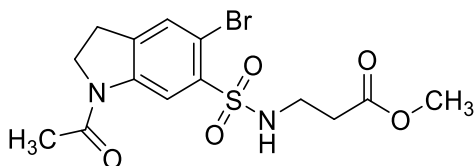
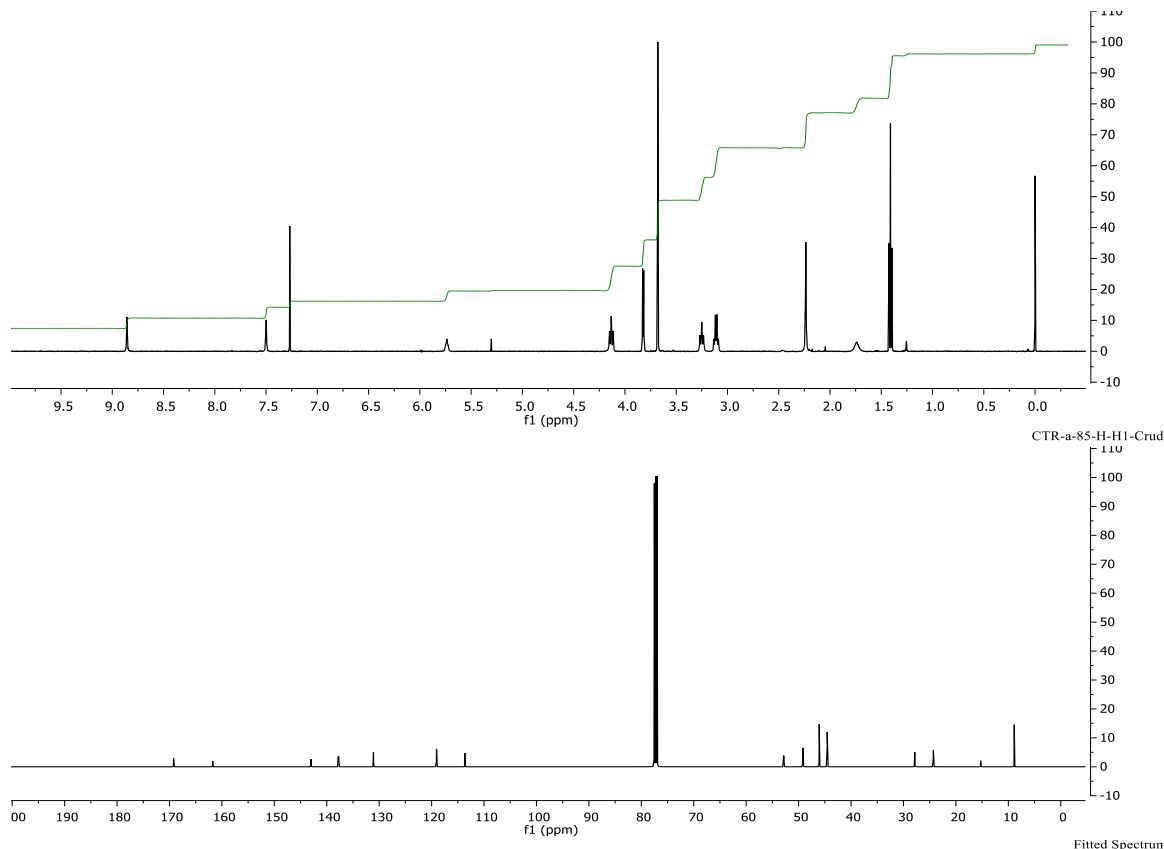
**Methyl ((1-acetyl-5-chloroindolin-6-yl)sulfonyl)glycinate (26a).** Crude product collected (26.4 mg, 22 %) as a tan solid.

**27a**

**Methyl ((1-acetyl-5-bromoindolin-6-yl)sulfonyl)glycinate (27a).** Product collected (105 mg, 93 %) as a tan solid: mp 176-182 °C; <sup>1</sup>H NMR (500 MHz, CDCl<sub>3</sub>): δ 8.86 (s, 1H), 7.49 (s, 1H), 5.74 (bs, 1H), 4.13 (t, J = 8.5 Hz, 2H), 3.82 (d, J = 5.5 Hz, 2H), 3.68 (s, 3H), 3.25 (t, J = 8.5 Hz,

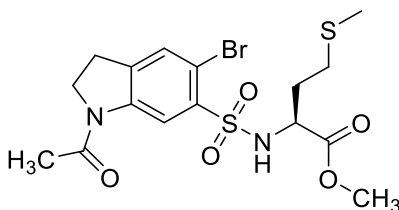
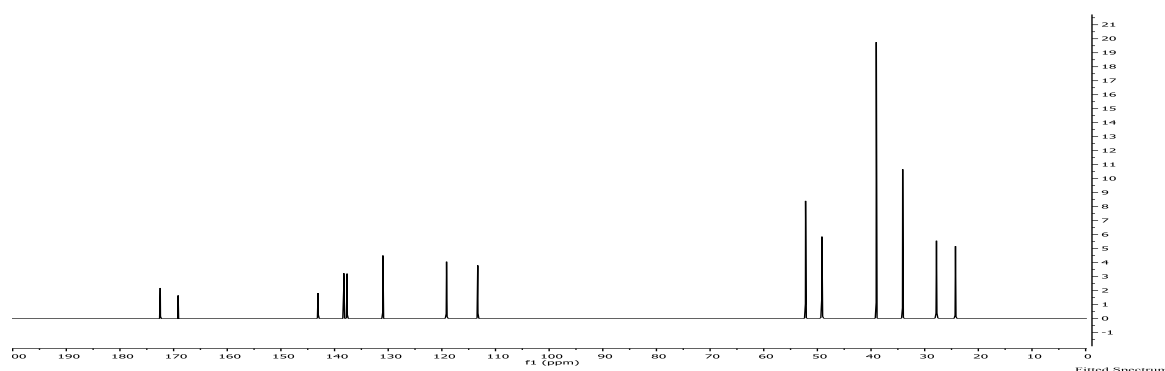
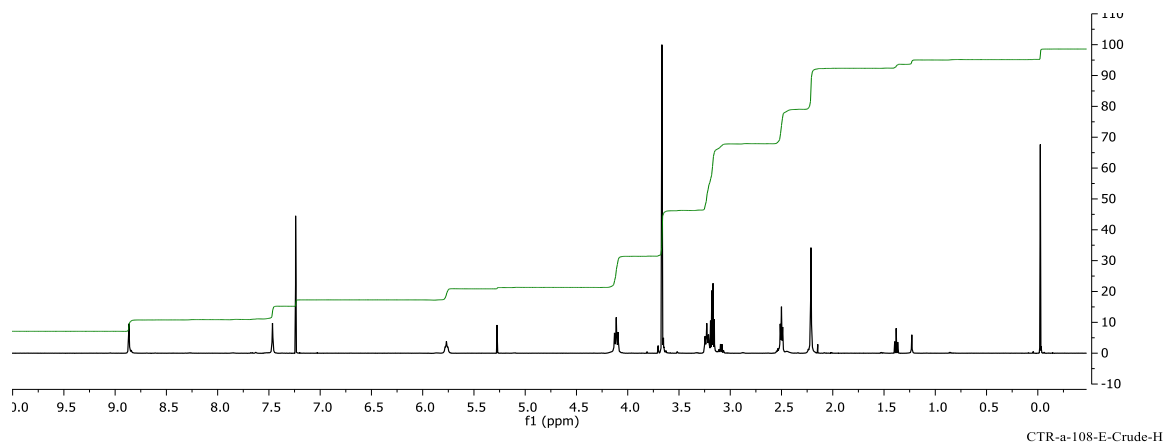


2H), 2.24 (s, 3H);  $^{13}\text{C}$  NMR (500 MHz,  $\text{CDCl}_3$ ):  $\delta$  169.2, 161.8, 143.0, 137.9, 137.7, 131.1, 119.1, 113.7, 49.2, 46.1, 44.6, 24.3, 8.9.

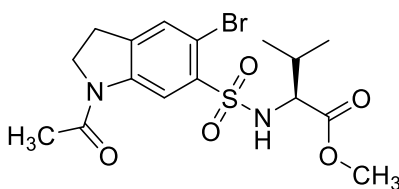
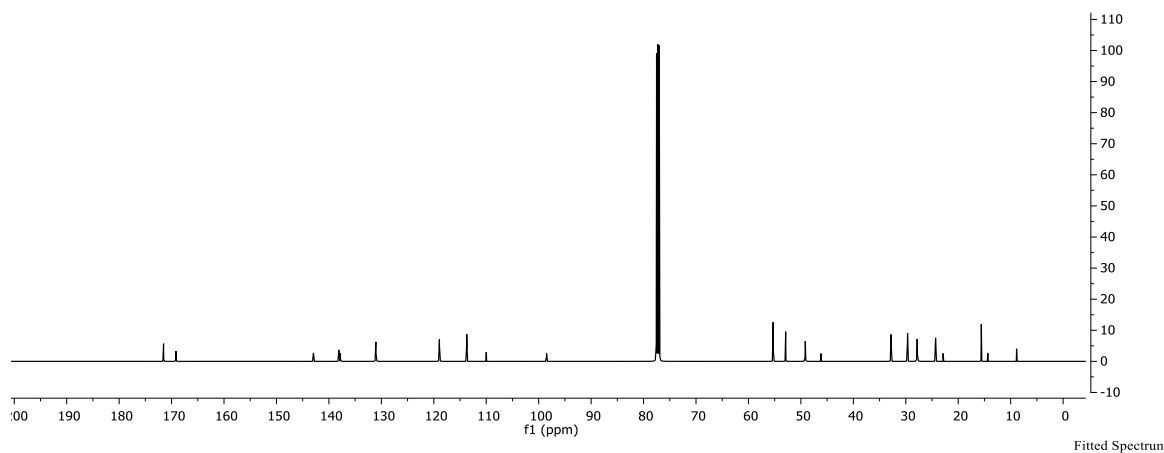
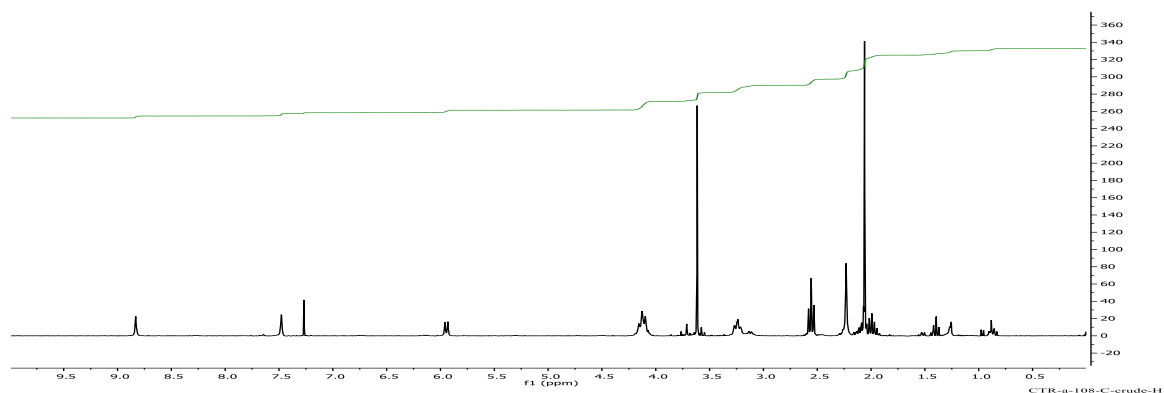


**28a**

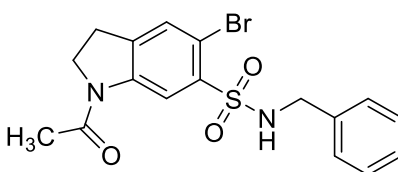
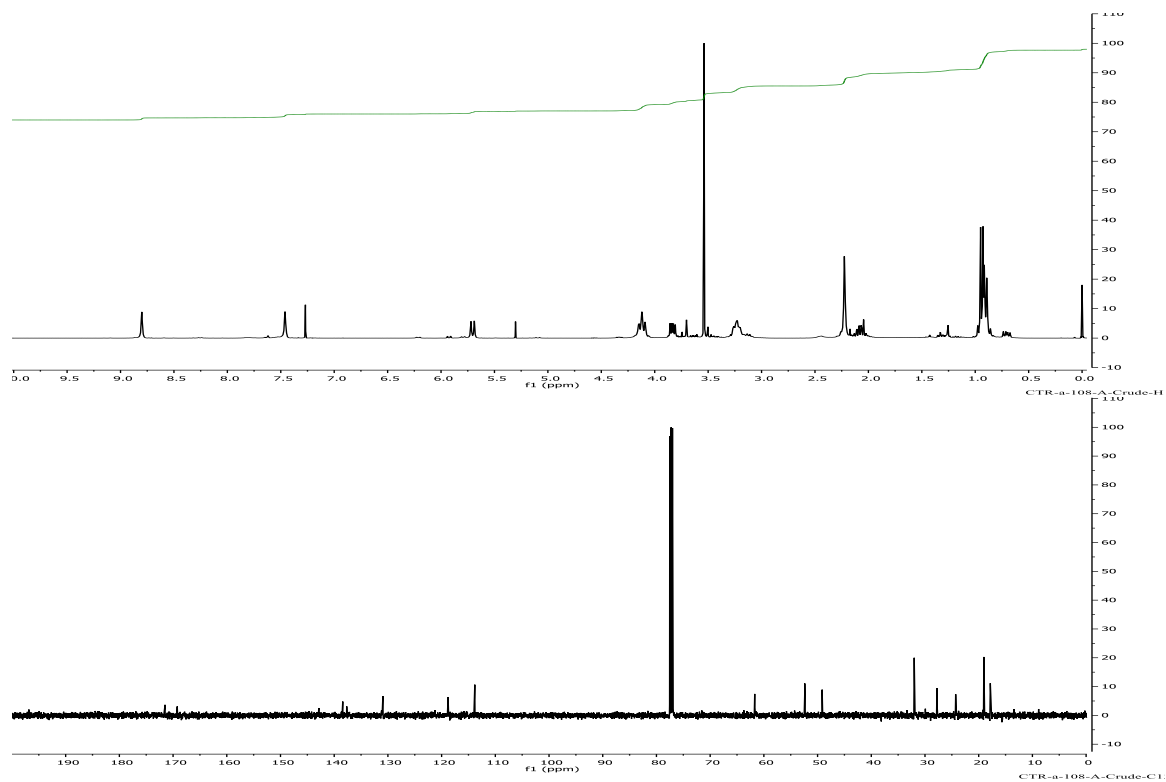
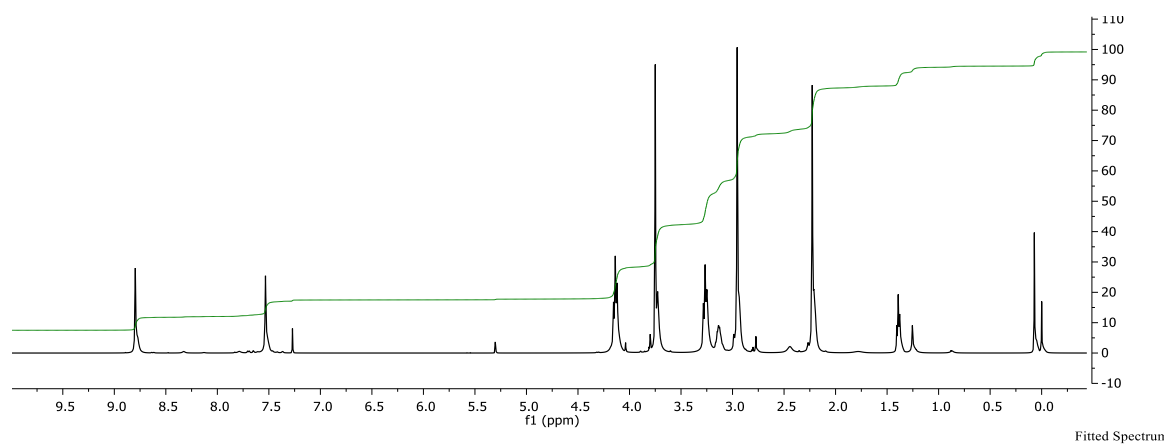
**Methyl 3-((1-acetyl-5-bromoindoline)-6-sulfonamido)propanoate (28a).** Product collected (117 mg, 97 %) as an off white solid: mp 190-193 °C;  $^1\text{H}$  NMR (500 MHz,  $\text{CDCl}_3$ ):  $\delta$  8.87 (s, 1H), 7.47 (s, 1H), 5.77 (t,  $J = 6.0$  Hz, 1H), 4.11 (t,  $J = 8.5$  Hz, 2H), 3.67 (s, 3H), 3.23 (t,  $J = 8.5$  Hz, 2H), 3.17 (dd,  $J = 12.0, 6.5$  Hz, 2H), 2.50 (t,  $J = 5.5$  Hz, 2H), 2.21 (s, 3H);  $^{13}\text{C}$  NMR (500 MHz,  $\text{CDCl}_3$ ):  $\delta$  172.5, 169.2, 143.1, 138.3, 137.7, 131.0, 119.1, 113.3, 52.2, 49.2, 39.0, 34.1, 27.8, 24.3.

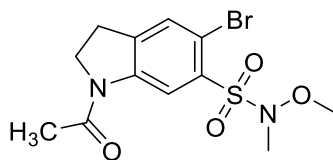
**24a**

**Methyl ((1-acetyl-5-bromoindolin-6-yl)sulfonyl)-L-methioninate (24a).** Product collected (114 mg, 83%) as a light tan solid: mp 117-119 °C;  $^1\text{H}$  NMR (500 MHz,  $\text{CDCl}_3$ ):  $\delta$  8.83 (s, 1H), 7.47 (s, 1H), 5.94 (d,  $J = 8.1$  Hz, 1H), 4.13 (t,  $J = 8.5$  Hz, 2H), 3.62 (s, 3H), 3.24 (t,  $J = 7.2$  Hz, 2H), 2.23 (s, 3H), 2.06 (s, 3H);  $^{13}\text{C}$  NMR (500 MHz,  $\text{CDCl}_3$ ):  $\delta$  171.6, 169.2, 143.0, 138.1, 131.1, 118.9, 113.7, 55.3, 52.9, 49.2, 32.8, 29.7, 27.8, 24.3, 15.6, 8.9.

**30a**

**Methyl ((1-acetyl-5-bromoindolin-6-yl)sulfonyl)-L-valinate (30a.** Product collected (111 mg, 87 %) as a tan solid: mp 178-182 °C;  $^1\text{H}$  NMR (500 MHz,  $\text{CDCl}_3$ ):  $\delta$  8.50 (s, 1H), 7.46 (s, 1H), 5.70 (d,  $J = 9.6$  Hz, 1H), 4.12 (t,  $J = 7.8$  Hz, 2H), 3.83 (dd,  $J = 9.3, 5.1$  Hz, 1H), 3.54 (s, 3H), 3.23 (t,  $J = 9.0$  Hz, 2H), 2.23 (s, 3H), 2.08 (m, 1H), 0.92 (m, 6H);  $^{13}\text{C}$  NMR (500 MHz,  $\text{CDCl}_3$ ):  $\delta$  171.5, 169.2, 142.9, 138.4, 137.7, 130.95, 118.8, 113.8, 61.7, 52.4, 49.2, 32.0, 27.8, 24.3, 19.0, 17.8.

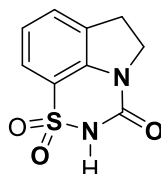
**37****1-Acetyl-N-benzyl-5-bromoindoline-6-sulfonamide (37).**



38

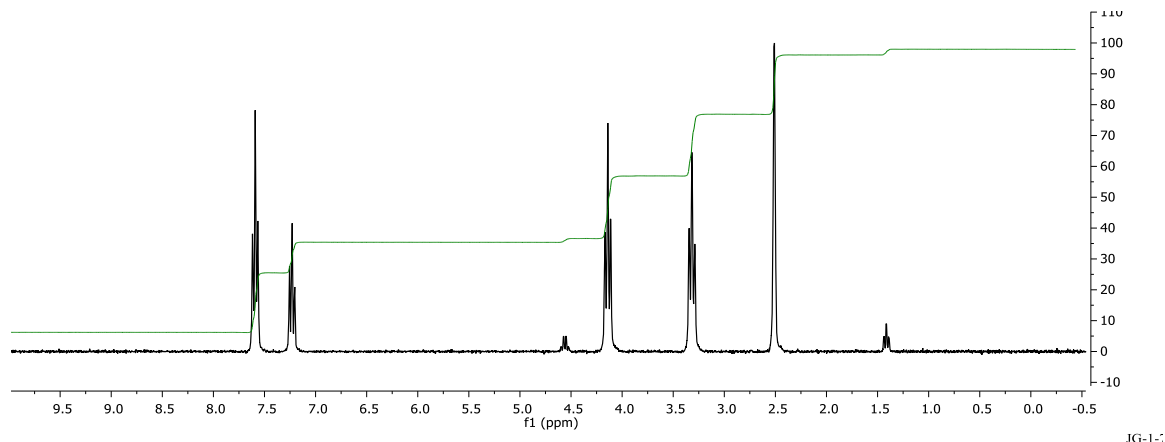
**1-Acetyl-5-bromo-N-methoxy-N-methylindoline-6-sulfonamide (38).**

**N-Cbz-Indoline Protected Sulfonyl Azide Synthesis.**

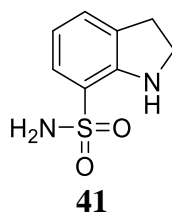


40

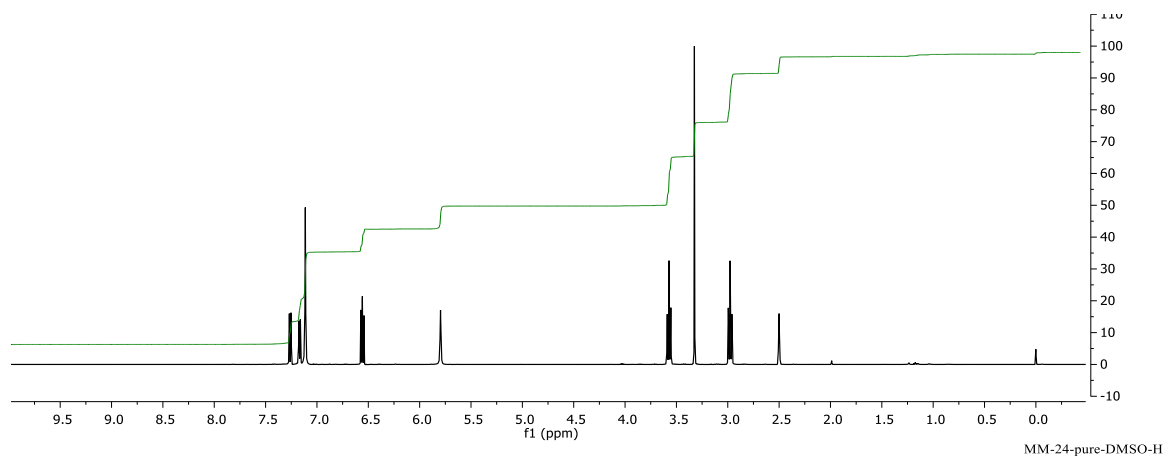
**5,6-Dihydro-[1,2,4]thiadiazino[6,5,4-hi]indol-3(2H)-one 1,1-dioxide (40).** To a solution of chlorosulfonyl isocyanate (1.80 mL, 18.4 mmol) in nitroethane (32 mL) cooled to  $-42^{\circ}\text{C}$  was added indoline slowly drop wise with stirring. The intermediate precipitated and turned cloudy and white, and the mixture was slowly warmed to room temperature over one hour with continued stirring. Aluminum chloride (2.45 g, 18.4 mmol) was added in one portion and allowed to stir for 15 min at room temperature. The solution went from cloudy and white to a clear, pale yellow solution to a light purple to a dark purple over this time period. The reaction was then heated to  $110^{\circ}\text{C}$  for one hour. The mixture was cooled to room temperature and quenched by pouring into ice water slowly where a black precipitate formed. The solid was isolated by filtering via vacuum filtration. A dark gray clay-like substance was obtained and dried overnight via vacuum yielding the cyclic sulfonyl urea indoline **3** (58-83 %) as a dark gray solid compound. The crude product is recrystallized from a warm 1:3 DMF- $\text{H}_2\text{O}$  mixture.  $^1\text{H}$  NMR (300 MHz,  $\text{DMSO } \text{D}_6$ ):  $\delta$  7.55 (t, 2H), 7.22 (t, 1H), 4.18 (2H, t), 3.35 (2H, t).<sup>182</sup>



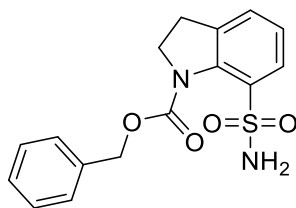
JG-1-7



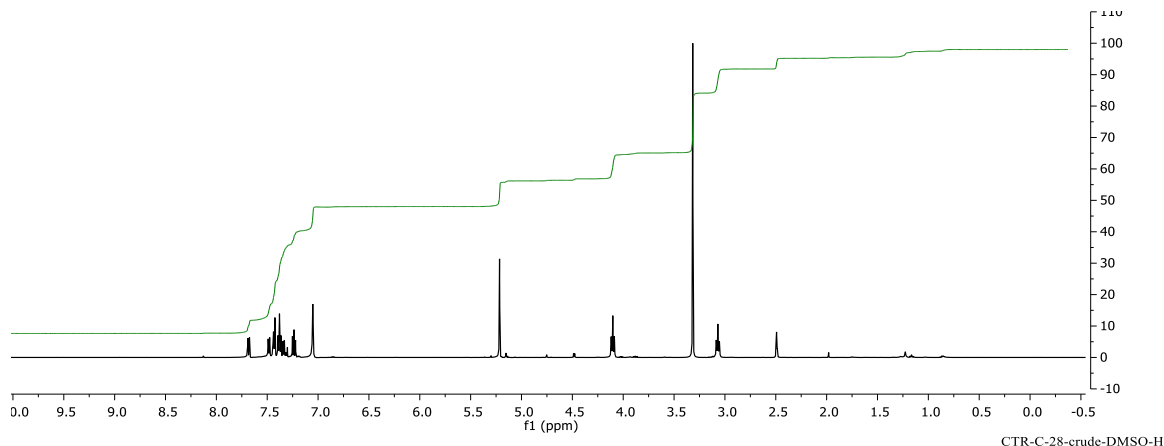
**Indoline-7-sulfonamide (41).** A solution of the cyclic sulfonfyl urea indoline **3** in 50 % sulfuric acid was heated to 135 °C for two hours. The reaction was cooled to room temperature and then neutralized carefully with a 10 N NaOH solution while over ice. The aqueous layer was extracted with ethyl acetate three times and the organic fractions were combined and dried over magnesium sulfate and concentrated in vacuum yielding the hydrolyzed 7-sulfonamide indoline **41** as a light brown needle like solid (50 %).



MM-24-pure-DMSO-H

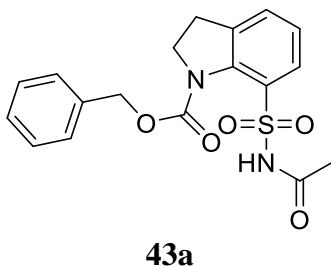


**Benzyl 7-sulfamoylindoline-1-carboxylate (42).** To a round bottom flask was added 7-sulfonamide indoline **41** (1.0 g, 5.0 mmol, 1 eq.) in THF (23 mL), followed by NaHCO<sub>3</sub> (4.66 g, 55.5 mmol, 11 eq.) and water (2.9 mL). The round bottom flask was sealed and flushed with N<sub>2</sub> gas. To this sealed mixture was added benzyl chloroformate (2.7 mL, 19.2 mmol, 3.8 eq.) slowly over a few minutes by syringe. After complete addition, the reaction was allowed to stir at room temperature overnight. The reaction was diluted with ethyl acetate and filtered to remove undissolved excess NaHCO<sub>3</sub>. The organic portion was acidified with 6M HCl to pH 3. The aqueous portions were further extracted with ethyl acetate three times, and organic fractions were combined and washed with brine and dried over NaSO<sub>4</sub> and concentrated giving a tacky off-white solid. The crude product was taken up in a minimal amount of ethyl acetate then Et<sub>2</sub>O was added to precipitate a white solid which was collected via vacuum filtration and further washed with petroleum ether and placed on high vac to fully dry. This reaction afforded 1.52 g of a white fluffy solid at 91 % yield and found to be 99.7 % pure by HPLC. <sup>1</sup>H NMR (500 MHz, d<sub>6</sub>-DMSO): δ 7.69 (d, J=7.5Hz, 1H), 7.49 (d, J=7.5Hz, 1H), 7.45-7.31 (m, 4H), 7.25 (t, J=7.5Hz, 1H), 7.06 (d, 2H), 5.22 (s, 2H), 4.11 (t, J=8Hz, 2H), 3.08 (t, J=7.5Hz, 2H). <sup>13</sup>C NMR (500 MHz, CDCl<sub>3</sub>): δ 154.9, 138.6, 136.7, 136.1, 132.4, 128.4, 128.4, 128.1, 127.9, 127.2, 124.5, 67.3, 50.8, 28.6.



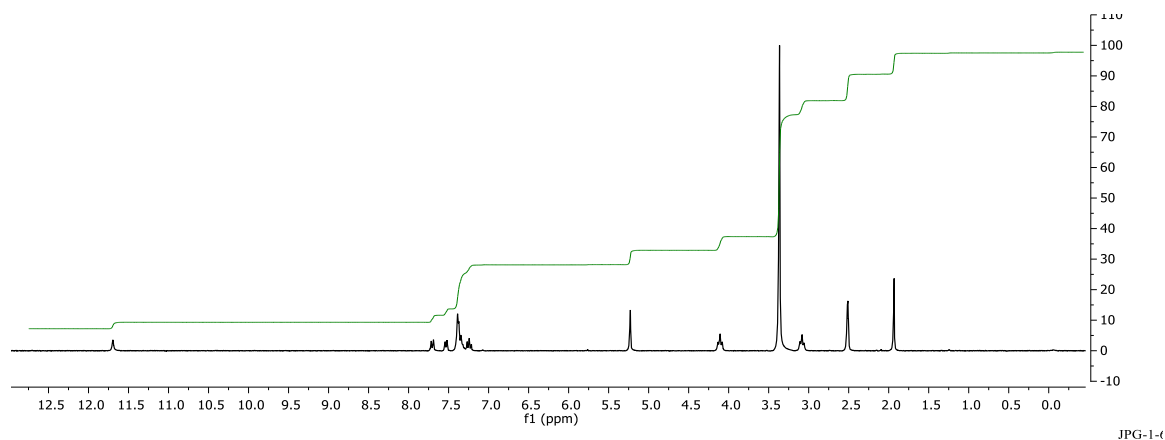
### General Synthesis Procedure for N-acylation of N-Cbz-indoline-7-sulfonamides.

A solution of acetyl chloride (1.25 eq. acid chloride) dissolved in dichloromethane was cooled to 0 °C. To a separate solution of dichloromethane and trimethylamine (1.5 eq.) was added the N-Cbz-indoline-7-sulfonamide **42**. The sulfonamide remained suspended in the solution until 10 % mol of DMAP was added. The mixture was heated until all materials dissolved and then placed on ice to cool to 0 °C. The first solution of the acid chloride was added to the sulfonamide solution slowly dropwise with stirring over 10 min making sure to keep the solution cool. After complete addition, the reaction was allowed to warm to room temperature and stir until completion as determined by HPLC. The solution was then quenched with water and extracted with dichloromethane. The organic portions were washed one time with 1M HCl, once with water and once with brine. The solution was then dried over Na<sub>2</sub>SO<sub>4</sub> and solvent was removed via rotovap and crude product was recrystallized from MeOH.

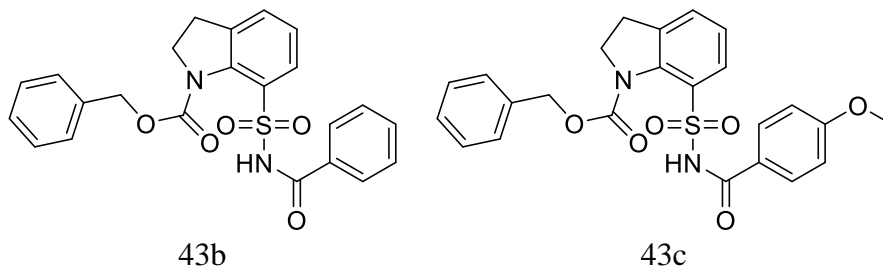




**Benzyl 7-(N-acetylsulfamoyl)indoline-1-carboxylate (43a).** Recrystallization afforded 106.1 mg of an off white solid at 94 % yield found to be 97 % purit by HPLC.  $^1\text{H}$  NMR (300 MHz,  $\text{d}_6$ -DMSO):  $\delta$  11.69 (s, 1H), 7.70 (d,  $J = 6.6$  Hz, 1H), 7.53 (d,  $J = 7.3$  Hz, 1H), 7.41-7.32 (m, 6H), 7.24 (t,  $J = 15$  Hz, 1H), 5.23 (s, 2H), 4.11 (t,  $J = 8.0$  Hz, 2H), 3.08 (t,  $J = 8.5$  Hz, 2H), 1.94 (s, 3H).



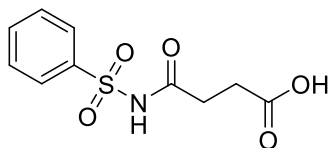
JPG-1-c



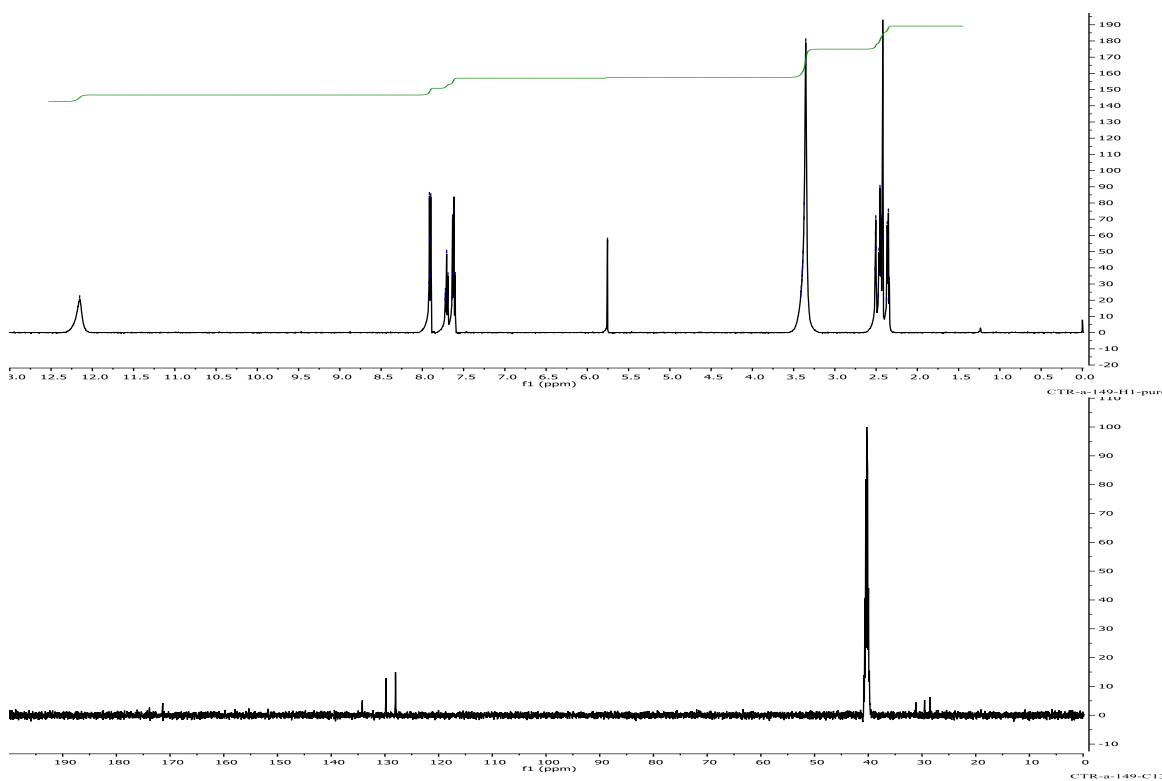
### General Synthesis Procedure for Simple N-Ac-sulfonamides.

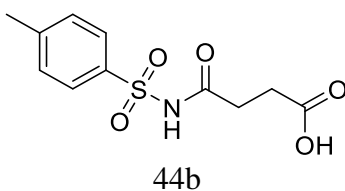
In a round bottom flask was suspended a 1.1 eq. of anhydride in methylene chloride or MeOH and an equal amount of DIPEA. An equivalent of aromatic primary sulfonamide was added to the anhydride suspension leading to reaction homogeneity. After 3.5 h reaction time at rt the reaction was worked up by quenching with saturated  $\text{NaHCO}_3$  and was then washed twice with methylene chloride. The Aq. layer is acidified to pH 3 followed by extraction three times

with methylene chloride, dried with sodium sulfate and concentrated to dryness. Reaction is purified by column chromatography or recrystallization as per lit.

**44a**

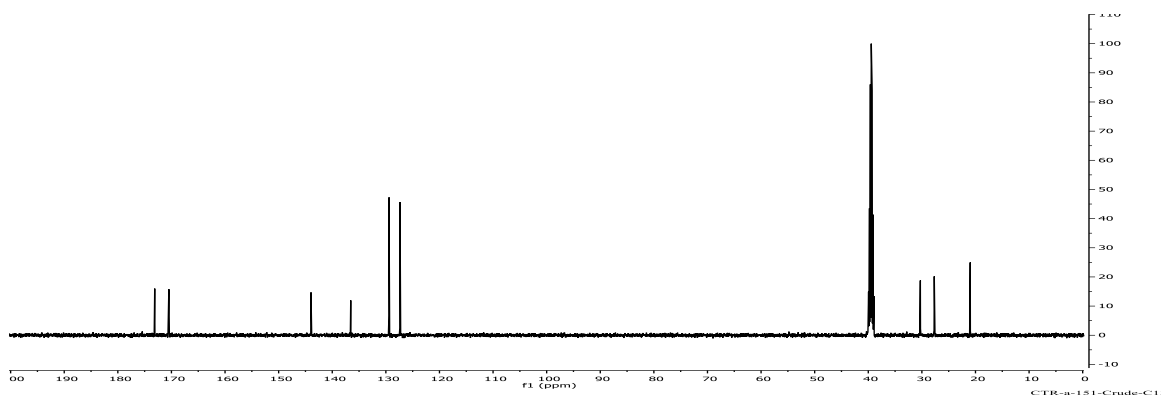
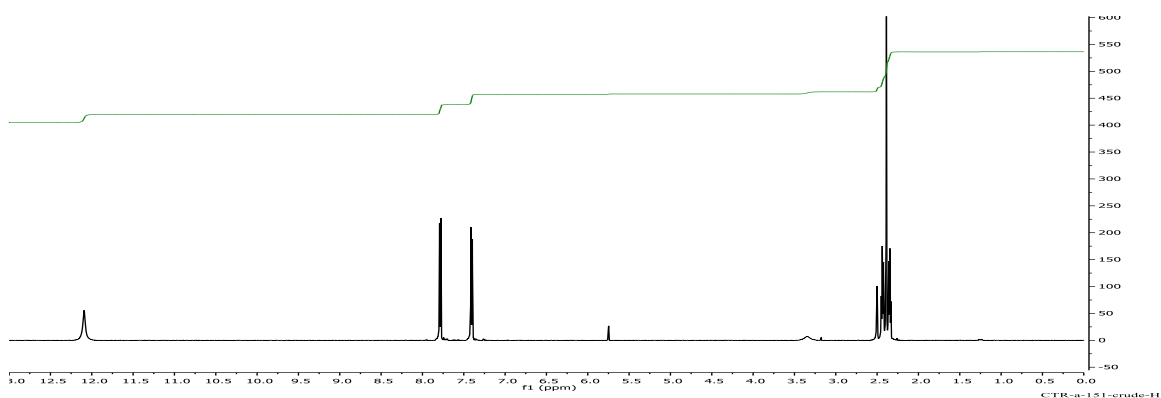
**4-Oxo-4-(phenylsulfonamido)butanoic acid.** Product collected (413 mg, 50 % yield); white precipitate.  $^1\text{H}$  NMR (500 MHz,  $\text{DMSO-}d_6$ ):  $\delta$  12.16 (s, 2H), 7.93 – 7.87 (m, 2H), 7.74 – 7.67 (m, 1H), 7.62 (dd,  $J = 8.4, 7.2$  Hz, 2H), 2.44 – 2.32 (m, 4H).  $^{13}\text{C}$  NMR (500 MHz,  $\text{DMSO-}d_6$ ):  $\delta$  173.8, 171.4, 134.2, 129.8, 128.0, 31.2, 29.5, 28.5.

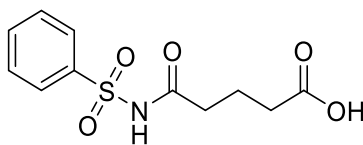




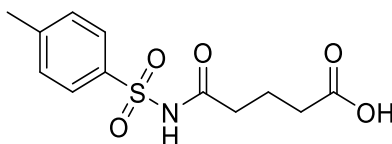
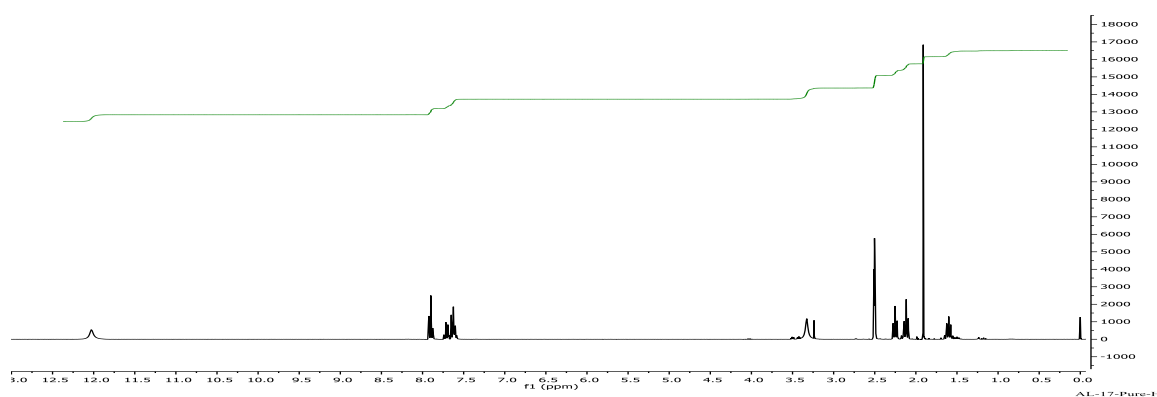
**4-((4-Methylphenyl)sulfonamido)-4-oxobutanoic acid.** Product collected (312 mg, 39 % yield)

off white solid. mp = 173-175 °C,  $^1\text{H}$  NMR (500 MHz,  $\text{DMSO-}d_6$ ):  $\delta$  12.09 (s, 2H), 7.78 (d,  $J = 8.1$  Hz, 2H), 7.40 (d,  $J = 8.0$  Hz, 2H), 2.48 – 2.35 (m, 7H).  $^{13}\text{C}$  NMR (500 MHz,  $\text{DMSO-}d_6$ ):  $\delta$  173.9, 171.2, 144.8, 137.3, 130.2, 128.2, 31.1, 28.5, 21.8.

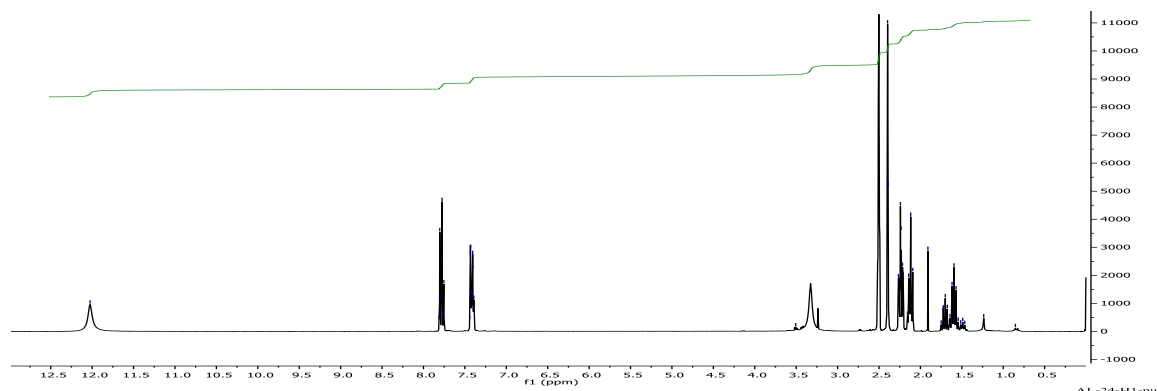


**44c**

**5-Oxo-5-(phenylsulfonamido)pentanoic acid (44c).** Product collected (446 mg, 52 % yield) off white solid.  $^1\text{H NMR}$  (300 MHz,  $\text{DMSO-}d_6$ ):  $\delta$  12.03 (s, 2H), 7.94 – 7.86 (m, 2H), 7.77 – 7.67 (m, 1H), 7.67 – 7.57 (m, 2H), 2.25 (t,  $J = 7.4$  Hz, 2H), 2.12 (t,  $J = 7.4$  Hz, 2H), 1.60 (p,  $J = 7.5$  Hz, 2H).

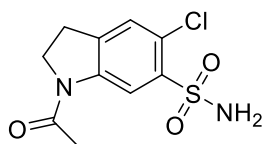
**44d**

**5-((4-Methylphenyl)sulfonamido)-5-oxopentanoic acid (44d).** Product collected (365.6 mg, 44 % yield) off-white gel.  $^1\text{H NMR}$  (300 MHz,  $\text{DMSO-}d_6$ ):  $\delta$  12.03 (s, 2H), 7.84 – 7.71 (m, 2H), 7.47 – 7.36 (m, 2H), 2.39 (d,  $J = 1.8$  Hz, 2H), 2.24 (td,  $J = 7.4, 2.5$  Hz, 2H), 2.12 (td,  $J = 7.4, 4.2$  Hz, 2H).



### General Synthesis Procedure for N-acetyl-5-haloindoline-6-sulfonamides.

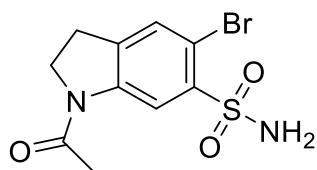
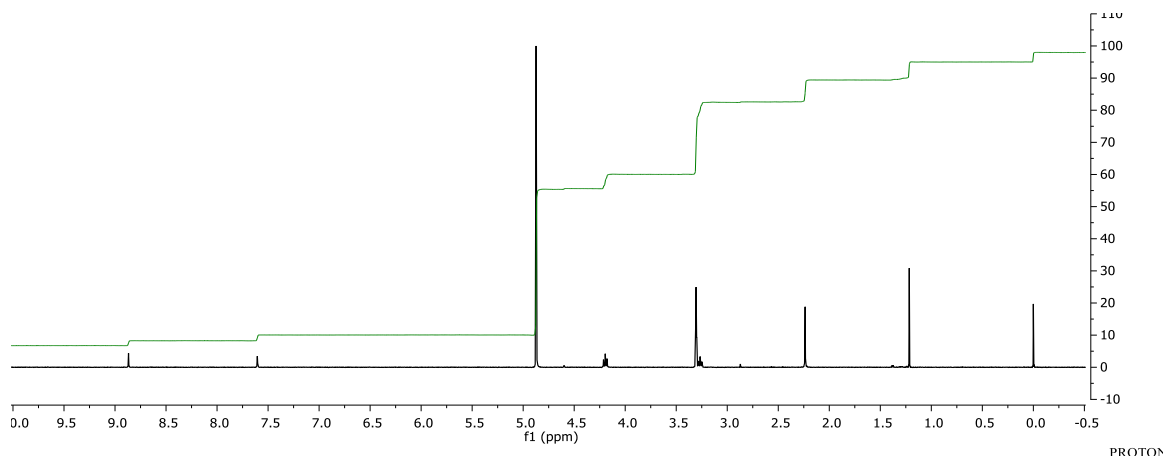
The sulfonyl chloride was added to a RBF with a long neck followed by addition of MeOH and methylene chloride in a 1:3 ratio. The reaction suspension was then heated to reflux until all the starting material was dissolved. Then anhydrous ammonium gas was bubbled into the hot solution until ppt formation. The reaction was allowed to stir vigorously for 10 min or until TLC indicated consumption of sulfonyl chloride starting material. The reaction was allowed to cool to rt and the ppt was filtered off. Not allowing to cool will lead to ppt formation inside filtrate. Alternatively, the reaction can be diluted with EA before filtration to increase ppt. HPLC indicate ppt collected as a pure compound.



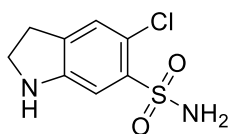
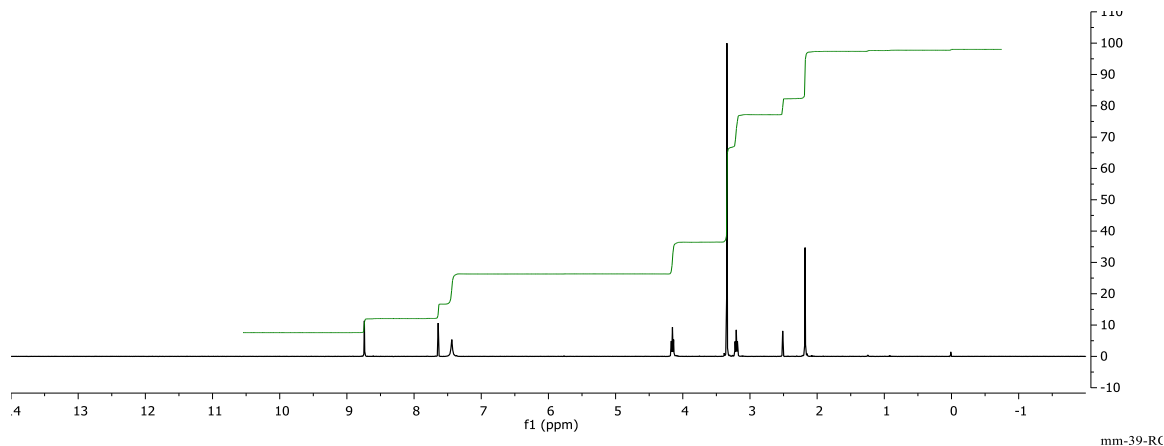
**46a**

**1-Acetyl-5-chloroindoline-6-sulfonamide (46a).** Prepared according to general procedure.

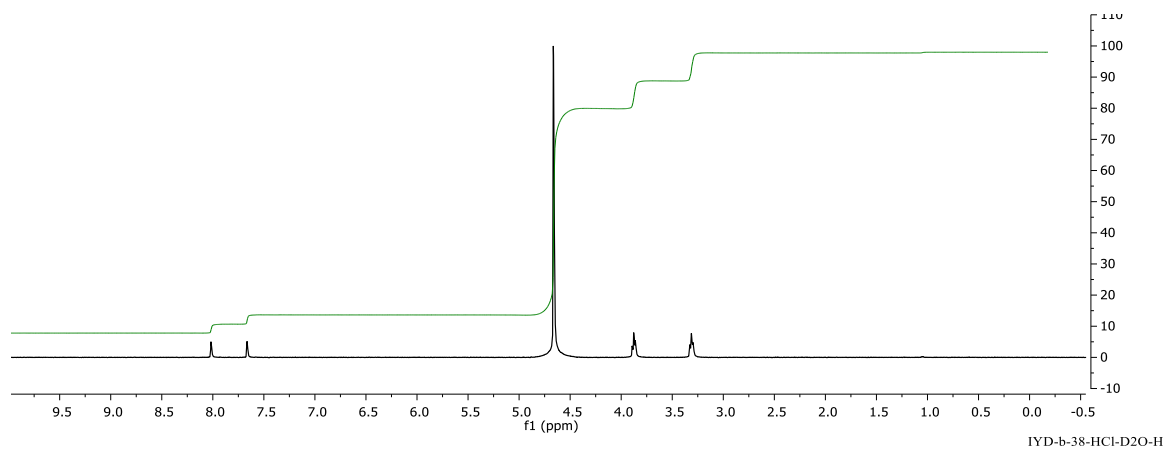
Collected product afforded 154.7 mg of a grey powder at 82 % yield found to be 92 % pure by HPLC with product eluting at 5.762 min (HPLC Method: CTV1, see Appendix B).  $^1\text{H}$  NMR (500 MHz, Methanol- $d_4$ ):  $\delta$  8.87 (s, 1H), 7.60 (s, 1H), 4.20 (t,  $J = 8.6$  Hz, 3H), 3.27 (t,  $J = 8.6$  Hz, 2H), 2.24 (s, 3H)

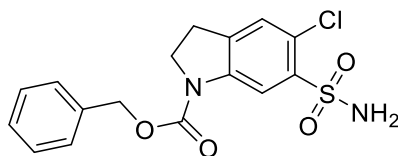
**46b**

**1-Acetyl-5-bromoindoline-6-sulfonamide (46b).** A stirred solution of sulfonyl chloride (500 mg, 1.7 mmol) in methylene chloride (15 mL) and saturated methanolic ammonia (5.0 mL, approx. 35 mmol) was heated until all solids dissolved, then allowed to return to room temperature. After 30 min, solids were precipitated out by the addition of EtOAc (5 mL) and collected by vacuum filtration, washing with methylene chloride, ethyl acetate, and petroleum ether to yield a white solid (313 mg, 66 %). mp = 231 °C-deflagration at 254 °C. <sup>1</sup>H NMR (500 MHz, DMSO-d<sub>6</sub>): δ 8.74 (s, 1H), 7.64 (s, 1H), 7.44 (s, 2H), 4.15 (t, *J* = 8.5 Hz, 2H), 3.20 (t, *J* = 8.8 Hz, 2H), 2.18 (s, 3H). R<sub>f</sub> = 0.36 (20:80 EtOAc-CH<sub>2</sub>Cl<sub>2</sub>).

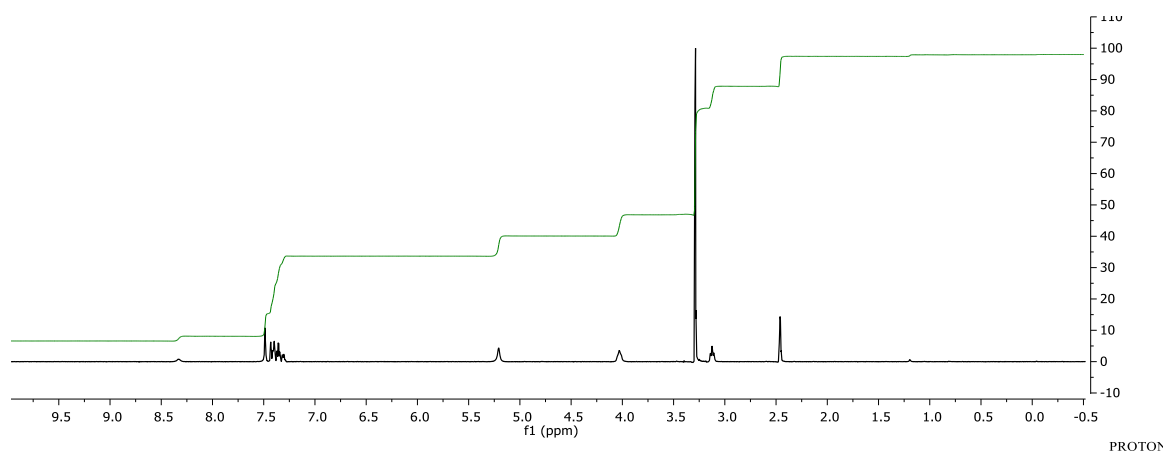
**47a**

**5-Chloroindoline-6-sulfonamide (47a).** The sulfonamide starting material N-acetyl-5-chloroindoline-6-sulfonamide (397 mg) was combined with 6M HCl (3.5 mL) and heated to reflux for 2.5 hrs. Reaction was cooled and triturated with Et<sub>2</sub>O and IPA, and the precipitated product was vacuum filtered to afford 239 mg of a fluffy white solid at 61 % yield found to be at 95 % pure by HPLC with product peak eluting at 6.590 min (HPLC Method: CTV1). mp = 177.9-180.0 °C. <sup>1</sup>H NMR (500 MHz, D<sub>2</sub>O): δ 8.02 (s, 1H) 7.66 (s, 1H), 3.88, (t, J = 7.5 Hz, 2H), 3.31 (t, J = 7.5 Hz, 2H).



**48a**

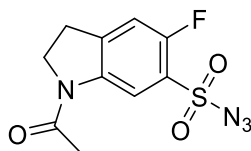
**Benzyl 5-chloro-6-sulfamoylindoline-1-carboxylate (48a).** To a three-neck round bottom flask charged with 5-chloroindoline-6-sulfonamide (51 mg, 0.2 mmol) in THF (1.2 mL) and H<sub>2</sub>O (0.1 mL) followed by 11 equivalents of sodium bicarbonate. The reaction vessel was degassed using a septum can after which benzyl chloroformate (89  $\mu$ L, 0.75 mmol) was added via syringe over 7 min. The reaction was then left to stir overnight and the monitored using HPLC. The reaction was acidified and water was added to dissolve bicarbonate salt. Reaction was extracted three times with ethyl acetate, and the organic layer was washed once with brine and dried with magnesium sulfate. Organic layer was concentrated to dryness on the rotary evaporator and triturated with ethyl ether to afford 613 mg of a white solid at 45 % yield found to be 99 % pure by HPLC with product peak eluting at 12.610 min (Method CTV1), mp =161.3-162.0 °C. <sup>1</sup>H NMR (500 MHz, d<sub>6</sub>-DMSO):  $\delta$  8.37 (s, 1H), 7.53-7.33 (m, 8H), 5.25, (s, 2H), 4.07 (t, 2H), 3.17 (t, J= 8.5 Hz, 2H) <sup>13</sup>C NMR (500 MHz, CDCl<sub>3</sub>):  $\delta$  152.9, 140.6, 138.2, 137.0, 129.2, 128.8, 128.5, 128.4, 124.4, 114.7, 67.4, 48.5, 27.4.





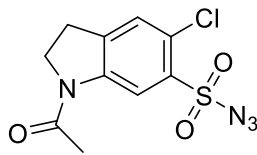
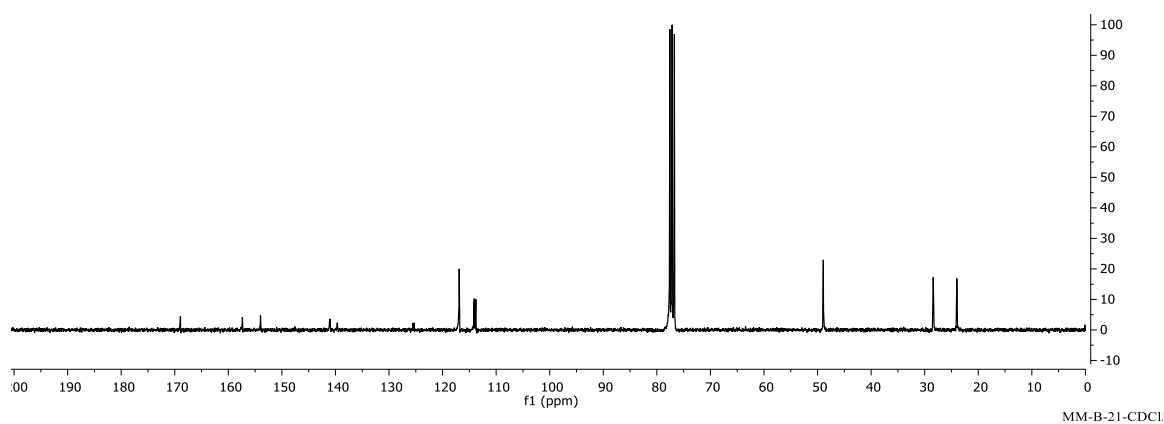
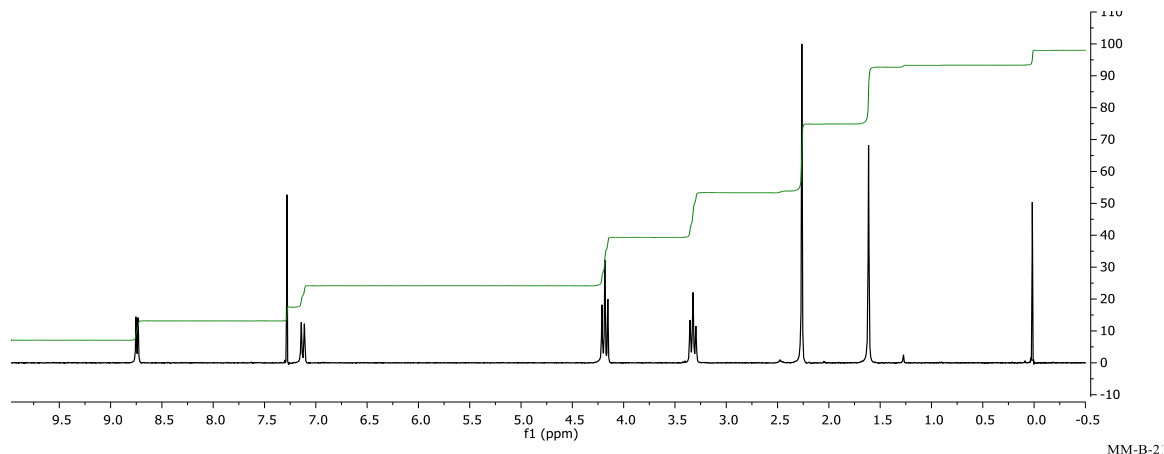
**General Synthesis Procedure for N-Acetyl-5-Haloindoline-6-Sulfonyl Azide from Sulfonyl Chloride.**

To a stirred solution of sulfonyl chloride in diglyme (0.1 M) at 110 °C was added sodium azide (5.5 eq.), followed by slow addition of H<sub>2</sub>O (0.15 M) over 10 min with heating to 130 °C. The reaction was allowed to stir at temperature for 1 h before leaving to stir at rt overnight. After overnight stirring under N<sub>2</sub>, mixture was diluted with saturated aqueous sodium bicarbonate and extracted with ethyl acetate. The combined organics were washed with brine (200 mL x 1) and dried over Na<sub>2</sub>SO<sub>4</sub>, followed by concentration to a diglyme rich product-syrup. The crude syrup is triturated with petroleum ether causing the pure product to crash out which is collected via vacuum filtration.



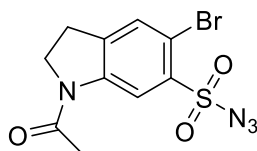
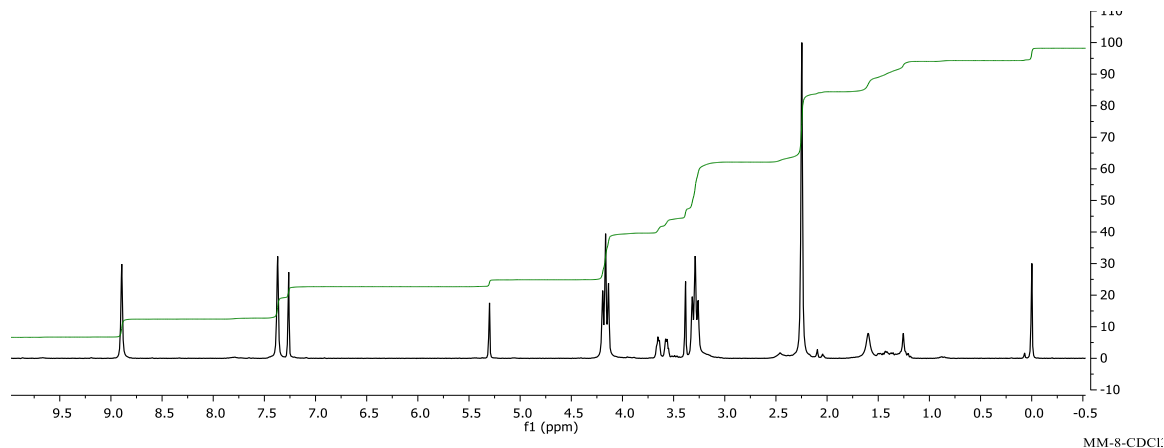
**45a**

**1-Acetyl-5-fluoroindoline-6-sulfonyl azide (45a).** To a stirred solution of sulfonyl chloride (500 mg, 1.8 mmol) in diglyme (5 mL) at 100 °C was added sodium azide (585 mg, 9.0 mmol) followed by H<sub>2</sub>O (2 mL). Reaction mixture was cooled to room temperature and stirred overnight, then poured over 50 mL H<sub>2</sub>O at 0 °C and stirred for 30 min. The precipitate was collected by vacuum filtration, washing with H<sub>2</sub>O (50 mL), to yield a white solid. Yield: 221.1 mg (43.2 %). <sup>1</sup>H NMR (300 MHz, CDCl<sub>3</sub>): δ 8.725 (d, 1H, *J* = 6.0 Hz), 7.110 (d, 1H, *J* = 9.0 Hz), 4.167 (t, 2H, *J* = 8.7 Hz), 3.307 (t, 2H, *J* = 8.7 Hz), 2.247 (s, 3H). <sup>13</sup>C NMR (75 MHz, CDCl<sub>3</sub>): δ 168.953, 155.697 (d, *J* = 253.35 Hz), 141.0495 (d, *J* = 8.325 Hz), 139.670, 125.4445 (d, *J* = 14.625 Hz), 116.914, 113.9555 (d, *J* = 23.475 Hz), 48.930, 28.404, 24.003. MP: 107.0-112.7 °C.

**45b**

**1-Acetyl-5-chloroindoline-6-sulfonyl azide (45b).** To a stirred solution of sulfonyl chloride (1 g, 3.4 mmol) in THF (30 mL) at 50°C was added sodium azide (1.2 g, 18.7 mmol) followed by H<sub>2</sub>O (20 mL). After 2 hrs stirring at 55 °C under N<sub>2</sub>, reaction mixture was poured over saturated aqueous sodium bicarbonate (200 mL). The reaction flask was washed with additional diglyme (30 mL heated to dissolve solids) and this was combined with the same aqueous sodium bicarbonate mixture. Precipitate was collected by vacuum filtration to yield a yellow solid (786 mg, 77% yield). mp = 93.1-95.4 °C <sup>1</sup>H NMR (300 MHz, CDCl<sub>3</sub>): δ 8.89 (s, 1H), 7.37 (s, 1H),

4.16 (t, 2H,  $J = 8.7$  Hz), 3.29 (t, 2H,  $J = 8.7$  Hz), 2.25 (s, 3H). HRMS (method)  $m/z$  calcd. for  $C_{10}H_{10}ClN_4O_3S$   $[M+H]^+$ : 301.0162, found: 301.0159.

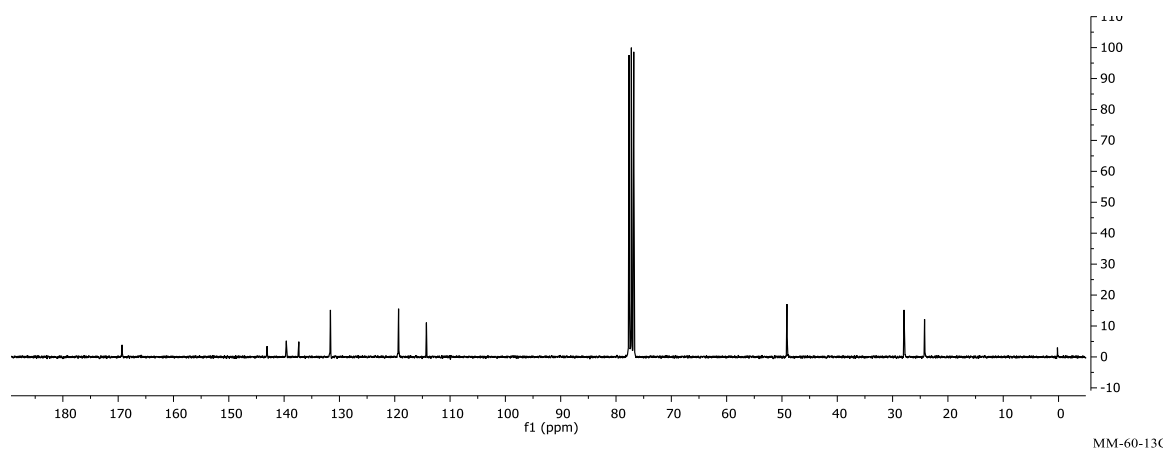
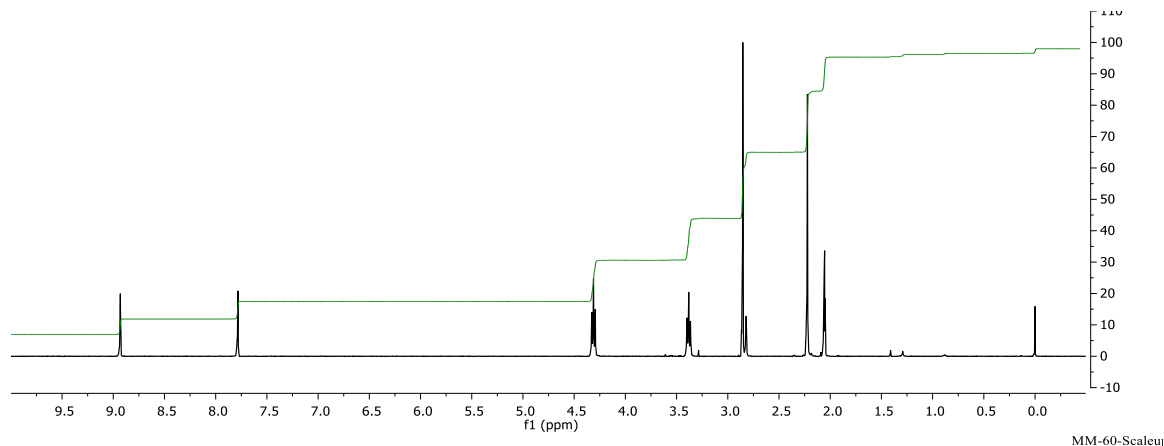


**45c**

**1-Acetyl-5-bromoindoline-6-sulfonyl azide (45c).** To a stirred solution of sulfonyl chloride (1.0 g, 2.95 mmol) in diglyme (30 mL, 0.1 M) at 110 °C was added sodium azide (1.1 g, 16.2 mmol, 5.5 eq.), followed by slow addition of H<sub>2</sub>O (20 mL, 0.15 M) over 10 min with heating to 130 °C. The reaction was allowed to stir at temperature for 1 h before leaving to stir at rt overnight. After overnight stirring under N<sub>2</sub>, mixture was diluted with saturated aqueous sodium bicarbonate (250 mL) and extracted with ethyl acetate (250 mL x3). The combined organics were washed with brine (100 mL x 1) and dried over Na<sub>2</sub>SO<sub>4</sub>, followed by concentration to a diglyme rich product-syrup. The crude syrup is diluted with petroleum ether causing the pure product to crash out which is collected via vacuum filtration. Product collected (790 mg, 77 %) as a beige solid at 99% purity.  $R_f = 0.36$  (20:80 EtOAc- CH<sub>2</sub>Cl<sub>2</sub>), mp = 110-125 °C, <sup>1</sup>H NMR (500 MHz, acetone-d<sub>6</sub>):  $\delta$  2.22 (s, 3H), 3.38 (t, 2H,  $J = 8.75$  Hz), 4.31 (t, 2H,  $J = 8.75$  Hz), 7.78 (s, 1H), 8.93 (s, 1H).

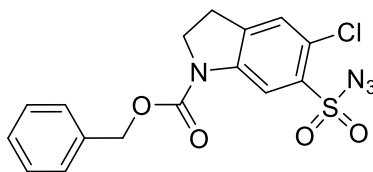
$^{13}\text{C}$  NMR (500 MHz,  $\text{CDCl}_3$ ):  $\delta$  169.3, 143.1, 139.6, 137.3, 131.6, 119.3, 114.3, 49.1, 27.9,

24.2. HRMS (ESI-MS)  $m/z$  calcd. for  $\text{C}_{10}\text{H}_{10}\text{BrN}_4\text{O}_3\text{S}$   $[M+H]^+$ : 346.9638, found: 346.9634.

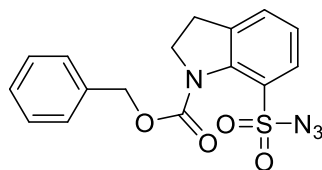
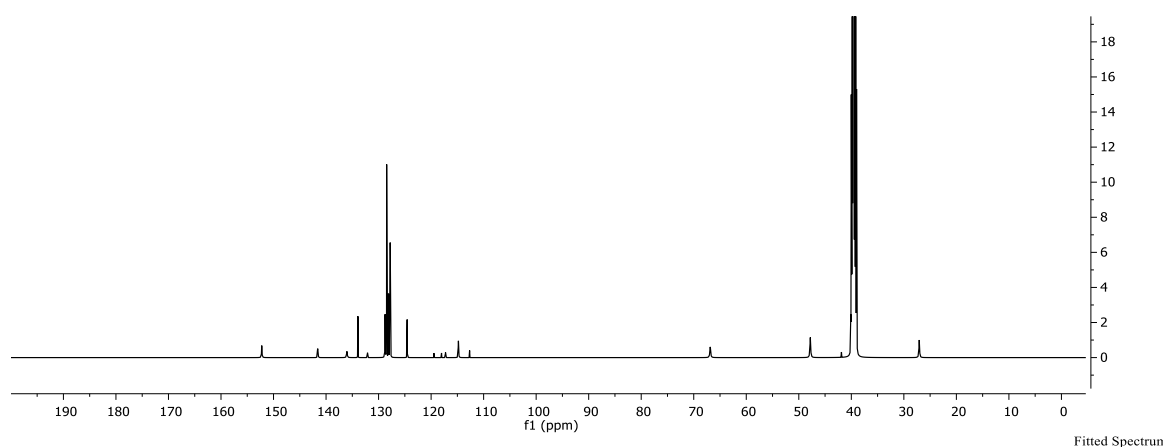
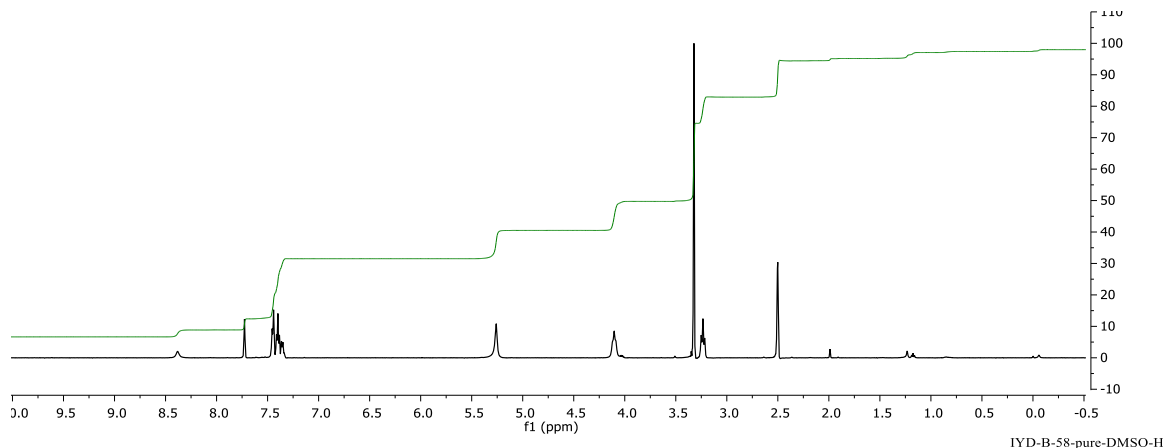


### General Synthesis Procedure for Sulfonyl Azides Via Azide Transfer.

To a solution of sulfonamide in 1:1 isopropanol-water mixture (0.04M) was added potassium carbonate (4.0 eq.), and imidazole-1-sulfonyl azide  $\text{HBF}_4$  salt (1.5 eq.) which was stirred at room temperature for 18h. The reaction was then diluted with saturated aqueous sodium bicarbonate and extracted with ethyl acetate and organic fractions were combined was washed once with brine, dried over  $\text{Na}_2\text{SO}_4$ , and concentrated. Purified products were isolated by flash column chromatography or recrystallization.

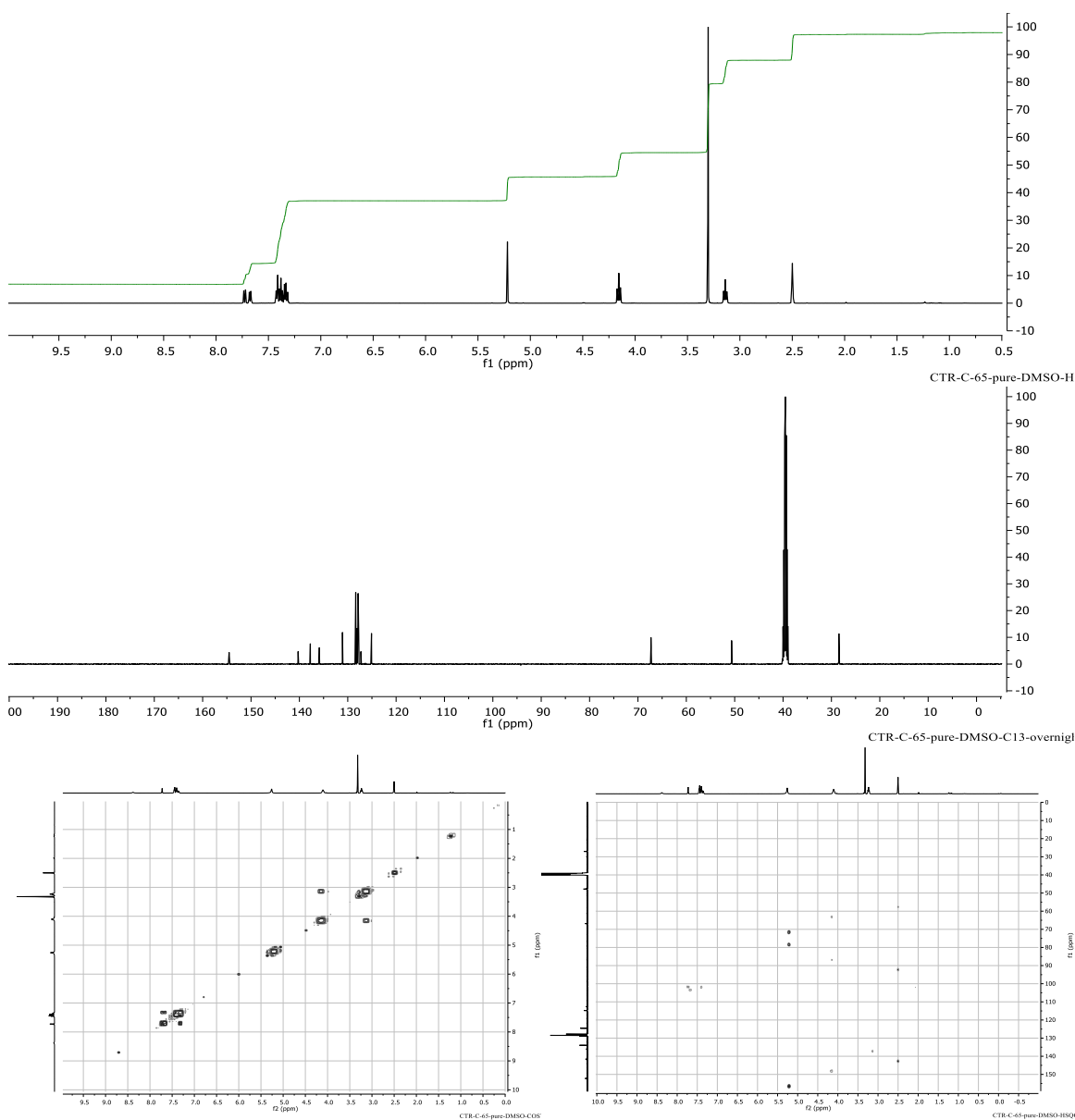
**49a**

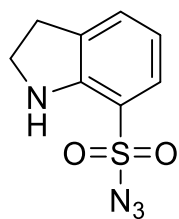
**Benzyl-6-(azidosulfonyl)-5-chloroindoline-1-carboxylate (49a).** Benzyl 5-chloro-6-sulfamoylindoline-1-carboxylate and potassium carbonate were added to a 50 mL 2-neck round bottom flask with a stir bar. Then imidazole-1-sulfonyl azide transfer reagent was added behind a blast shield, followed by a 1:1 mixture of isopropanol-water. Reaction was stirred vigorously while rapid heating with the heat gun was applied. After allowing reaction to boil for 5 min, the reaction mixture becomes dark orange and homogeneous and is allowed to cool overnight while stirring. The reaction is diluted with sodium bicarbonate solution and extracted with ethyl acetate three times. Organic layer is washed with brine, and concentrated to dryness on the rotary evaporator. Solid is transferred to a vial, where it is recrystallized in EA and dried to yield 210 mg of a beige sparkly precipitate yielding 79 % which was found to be 93 % pure by HPLC with product elution at 15.0 min. mp = 124.8-127.6 °C. <sup>1</sup>H NMR (500 MHz, DMSO): δ8.38 (s, 1H), 7.73 (s, 1H), 7.45-7.34 (m, 5H), 5.26 (s, 2H), 4.18 (broadened triplet, 2H), 3.23 (t, J = 8.7 Hz, 2H). <sup>13</sup>C NMR (500MHz, d<sub>6</sub>-DMSO): δ152.3, 141.6, 134.0,126.8, 28.5,128.1, 127.8, 124.6, 114.8, 66.9, 47.8, 40.1, 39.0, 27.1. HPLC purity = 93 % pure at 220 nm.

**49b**

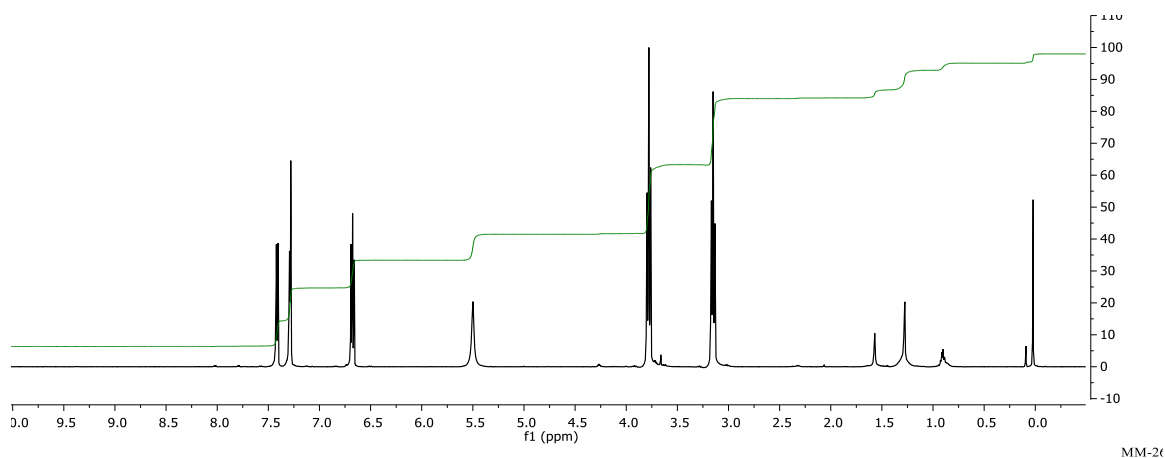
**Benzyl-7-(azidosulfonyl)indoline-1-carboxylate (49b)**. To a solution of benzyl 7-sulfamoylindoline-1-carboxylate (350 mg, 1.1 mmol) in 1:1 isopropanol-water mixture (26.3 mL, 0.04 M) was added potassium carbonate (582 mg, 4.2 mmol, 4.0 eq.), and imidazole-1-sulfonyl azide HBF<sub>4</sub> salt (412 mg, 1.6 mmol, 1.5 eq.) which was stirred at room temperature for 18h. Product was isolated using flash column purification. Two 4 g flash columns were pre-equilibrated with Pet-E using a Gilson fraction collector. The crude product was loaded onto the column using an Ether-CHCl<sub>3</sub>-EA mixture. The product was eluted using a 1:1 Et<sub>2</sub>O-Petroleum

Ether and product was collected and concentrated to a white crystalline solid to yield 193.7 mg at 51 % yield, and HPLC purity was found to be 98 % at 220nm. Exp mp = 99.0-102.7 °C, White crystalline solid.  $^1\text{H}$  NMR (500 MHz,  $d_6$ -DMSO):  $\delta$  7.73 (d,  $J$  = 8 Hz, 1H), 7.68 (d,  $J$  = 7.5 Hz, 1H), 7.43-7.37 (m, 5H), 7.33 (t,  $J$  = 7.7 Hz, 1H), 5.22 (s, 2H), 4.16 (t,  $J$  = 7.5 Hz, 2H), 3.14 (t,  $J$  = 7.5 Hz, 2H).  $^{13}\text{C}$  NMR (500 MHz,  $d_6$ -DMSO):  $\delta$  154.6, 140.3, 137.8, 135.9, 131.1, 128.4, 128.1, 127.9, 127.7, 127.3, 125.1, 67.3, 50.7, 28.5.



**49c**

**Indoline-7-Sulfonyl Azide (49c).** To a stirred solution of indoline-7-sulfonamide (170 mg, 0.86 mmol) and  $K_2CO_3$  (474 mg, 3.43 mmol) in 1:1 iPrOH:H<sub>2</sub>O (11 mL) was added imidazole-1-sulfonyl azide hydrochloride (270 mg, 1.29 mmol). After 1.5 h, reaction mixture was diluted with saturated aqueous sodium bicarbonate (25 mL) and extracted with ethyl acetate (50 mL x 4). Combined extracts were dried over  $MgSO_4$  and concentrated to give a dark red oil. Flash column chromatography (silica gel, 20:80 ethyl acetate:petroleum ether) yielded a yellow oil (140.5 mg, 73%). <sup>1</sup>H NMR (500 MHz, CDCl<sub>3</sub>): δ 7.413 (d, 1H, *J* = 8.5 Hz), 7.288 (d, 2H, *J* = 6.5 Hz), 6.675 (t, 1H, *J* = 7.5 Hz), 5.499 (s, 1H), 3.778 (t, 2H, *J* = 8.5 Hz), 3.151 (t, 2H, *J* = 8.5 Hz). RF = .3 (20:80 EtOAc:petroleum ether).

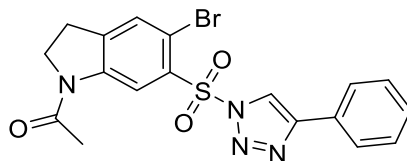


### General Synthesis Procedure for Sulfonyl Triazole Via CuAAC.

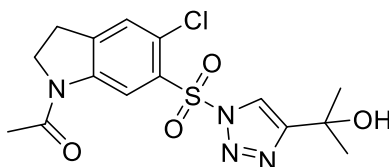
To a solution of sulfonyl azide and CuTC (10 mol%), in  $CH_2Cl_2$  (0.3M) was added the respective alkyne (1.1 eq.) at room temperature under inert atmosphere. The reaction was stirred at rt for 2-3 hrs before being diluted with  $CH_2Cl_2$  and saturated  $NH_4Cl_{(aq)}$ , stirred for 30 min, and



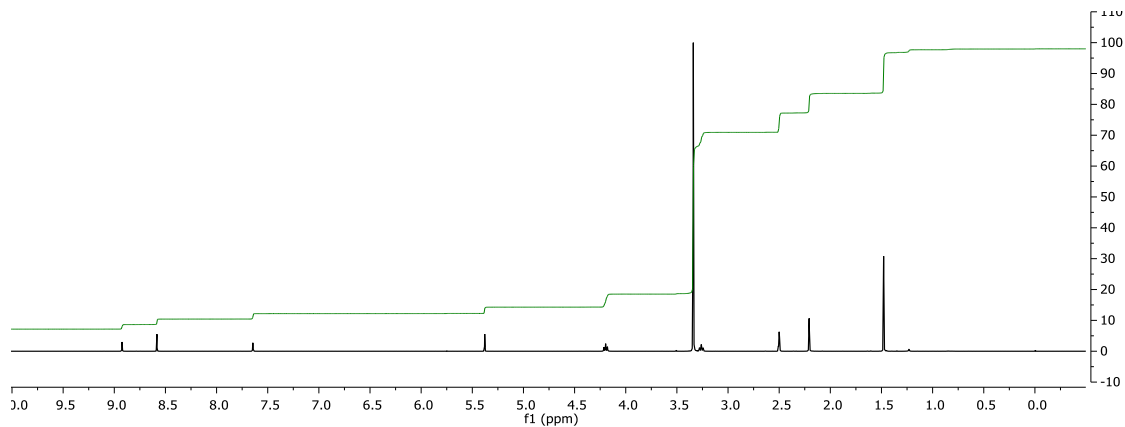
the precipitate was collected by vacuum filtration. The collected solids were washed with H<sub>2</sub>O, CH<sub>2</sub>Cl<sub>2</sub> and petroleum ether before drying under reduced pressure. Product isolation was achieved through flash column chromatography or recrystallization.

**50a**

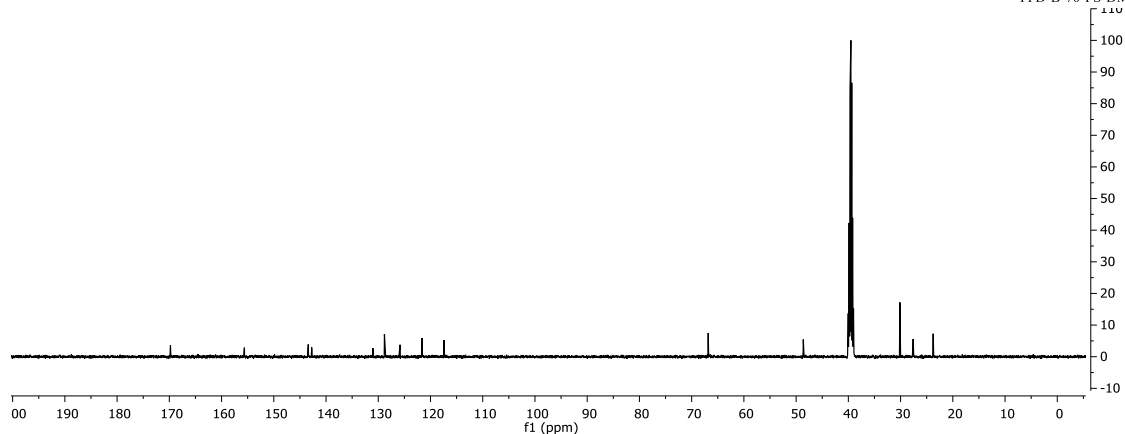
**1-(5-Bromo-6-((4-phenyl-1H-1,2,3-triazol-1-yl)sulfonyl)indolin-1-yl)ethan-1-one (50a).** A solution of CuTC (5.5 mg, 0.029 mmol), phenyl acetylene (33  $\mu$ L, 0.30 mmol), and sulfonyl azide (100 mg, 0.29 mmol) in CH<sub>2</sub>Cl<sub>2</sub> (2 mL) was stirred at room temperature under N<sub>2</sub> for 5 h. Precipitate was collected by vacuum filtration washing with CH<sub>2</sub>Cl<sub>2</sub>, H<sub>2</sub>O, and petroleum ether to give an off-white solid (27.4 mg, 21% yield). R<sub>f</sub> = 0.4 (10:1:89 EtOAc-AcOH-petroleum ether). mp = 104-110 °C. <sup>1</sup>H NMR (500 MHz, DMSO-d<sub>6</sub>):  $\delta$  2.22 (s, 3H), 3.28 (t, 2H, *J* = 8.5 Hz), 4.21 (t, 2H, *J* = 8.75 Hz), 7.42 (t, 1H, *J* = 7.25 Hz), 7.50 (t, 2H, *J* = 7.5 Hz), 7.83 (s, 1H), 8.00 (d, 2H, *J* = 7.5 Hz), 9.02 (s, 1H), 9.54 (s, 1H).

**51a**

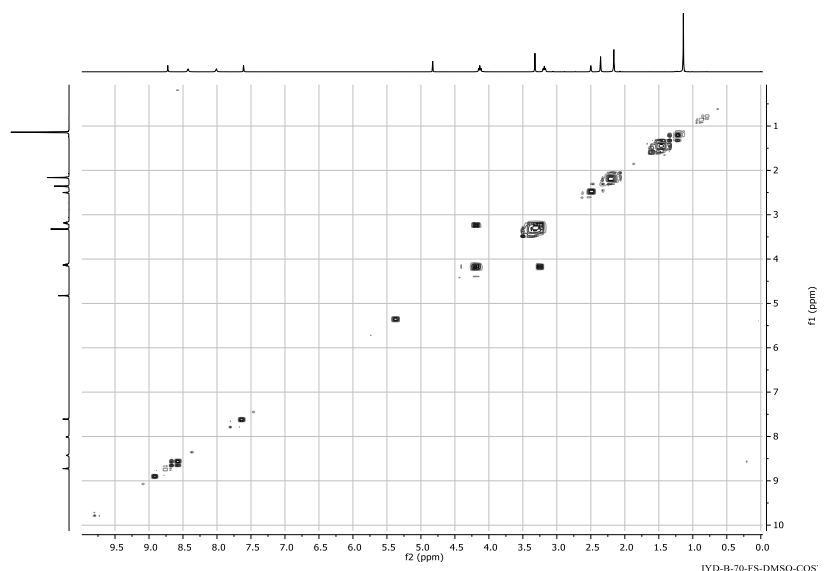
**1-(5-Chloro-6-((4-(2-hydroxypropan-2-yl)-1H-1,2,3-triazol-1-yl)sulfonyl)indolin-1-yl)ethan-1-one (51a).** Prepared according to general procedure. <sup>1</sup>H NMR (500 MHz, d<sub>6</sub>-DMSO):  $\delta$  8.92 (s, 1H), 8.58 (s, 1H), 7.65 (s, 1H), 5.38 (s, 1H), 4.20 (t, *J* = 9.0 Hz, 2H), 3.26 (t, *J* = 8.5 Hz, 2H), 2.21 (s, 2H), 1.48 (s, 2H). <sup>13</sup>C NMR (500 MHz, d<sub>6</sub>-DMSO):  $\delta$  169.8, 155.6, 143.4, 142.8, 131.0, 128.8, 125.8, 121.6, 117.4, 66.8, 48.6, 30.1, 27.6, 23.8.



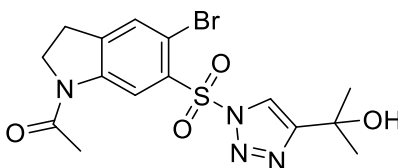
IYD-B-70-FS-DMSO-H



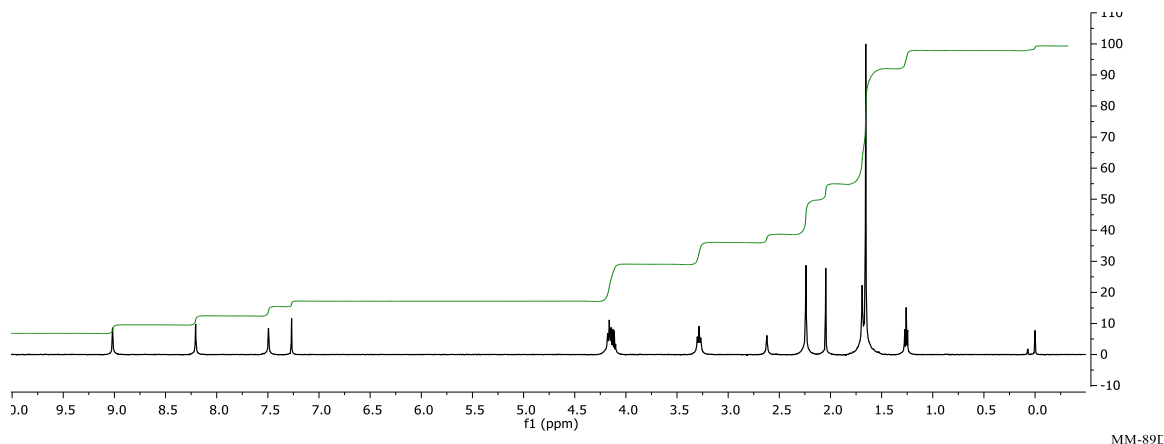
IYD-B-70-FS-DMSO-C1



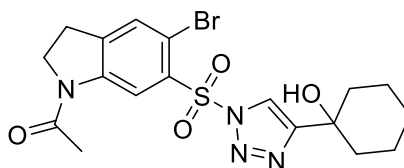
IYD-B-70-FS-DMSO-COS

**51b**

**1-(5-Bromo-6-((4-(2-hydroxypropan-2-yl)-1H-1,2,3-triazol-1-yl)sulfonyl)indolin-1-yl)ethan-1-one (51b).** Prepared according to general procedure. A solution of CuTC (5.5 mg, 0.029 mmol), 2-methylbut-3-yn-2-ol (37 mg, 0.44 mmol), and sulfonyl azide (100 mg, 0.29 mmol) in CH<sub>2</sub>Cl<sub>2</sub> (1 mL) was stirred for 5h, then diluted with CH<sub>2</sub>Cl<sub>2</sub> (5 mL) and saturated aqueous NH<sub>4</sub>Cl (5 mL) and the aqueous was extracted with CH<sub>2</sub>Cl<sub>2</sub> (10 mL x 2). Combined extracts were dried over MgSO<sub>4</sub> and concentrated. Recrystallization from ethyl acetate afforded 88.8 mg of colorless needles at a 71 % yield. mp = 120-130 °C with decomposition. <sup>1</sup>H NMR (500 MHz, CDCl<sub>3</sub>): δ 9.02 (s, 1H), 8.21 (s, 1H), 7.5 (s, 1H), 4.11 (t, 2H, *J* = 7.0), 3.29 (t, 2H, *J* = 8.5), 2.62 (s, 1H), 2.24 (s, 3H), 1.69 (s, 6H).

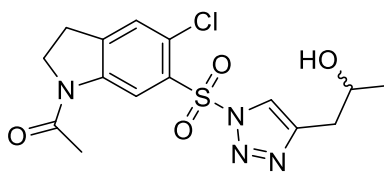
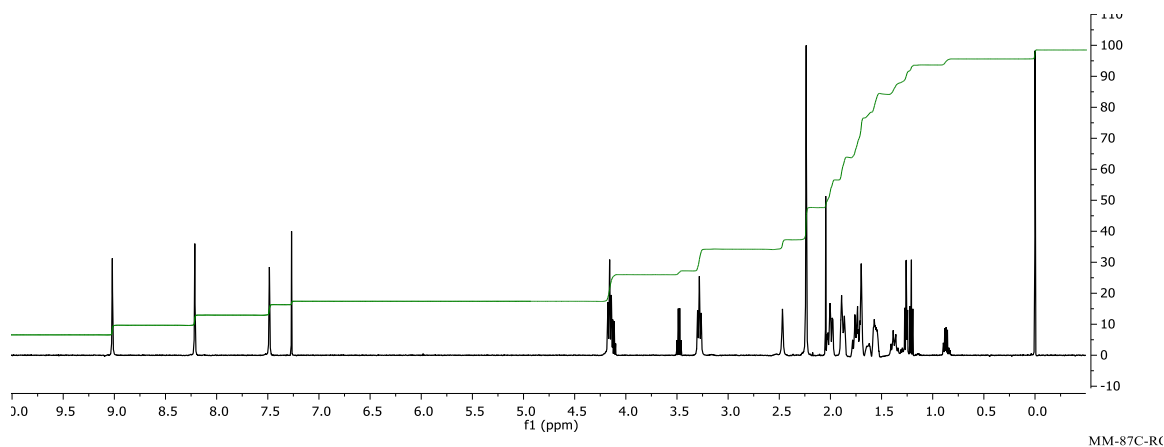


MM-89E

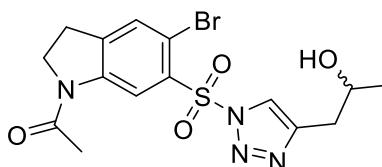
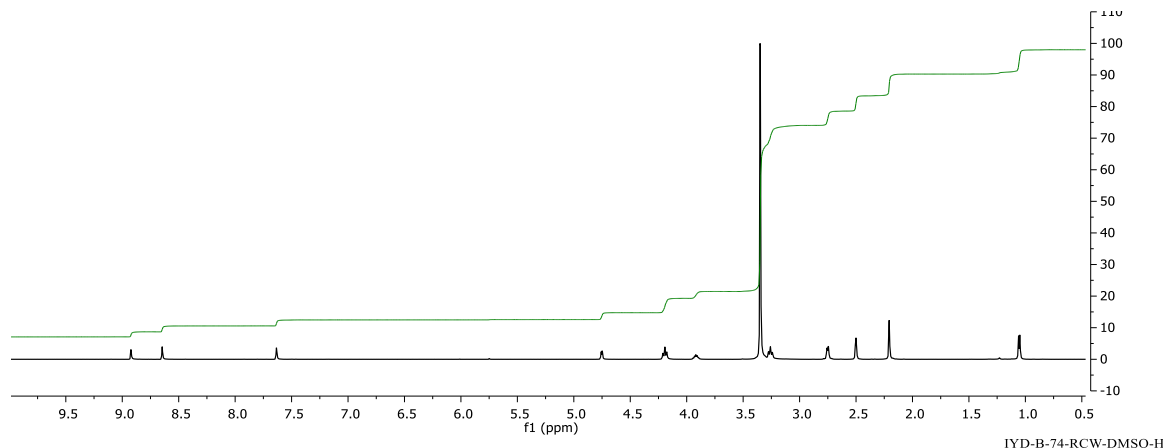
**52a**

**1-(5-Bromo-6-((4-(1-hydroxycyclohexyl)-1H-1,2,3-triazol-1-yl)sulfonyl)indolin-1-yl)ethan-1-one (52a).** Prepared according to general procedure. A solution of CuTC (5.5 mg, 0.029 mmol),

1-ethynylcyclohexan-1-ol (65 mg, 0.52 mmol), and sulfonyl azide (100 mg, 0.29 mmol) in  $\text{CH}_2\text{Cl}_2$  (1 mL) was stirred under  $\text{N}_2$  for 22 h, then diluted with  $\text{CH}_2\text{Cl}_2$  (5 mL) and saturated aqueous  $\text{NH}_4\text{Cl}$  (5 mL). Aqueous was extracted with  $\text{CH}_2\text{Cl}_2$  (5 mL x 3). The organic layers were combined, dried over  $\text{MgSO}_4$ , and concentrated to yield a foam, which was redissolved in minimal  $\text{CH}_2\text{Cl}_2$  and diluted with 8:2  $\text{Et}_2\text{O}$ -petroleum ether. Precipitate was collected by vacuum filtration and washed with  $\text{H}_2\text{O}$  and  $\text{Et}_2\text{O}$  to afford 72.4 mg of a white powder at an 53 % yield. mp = 112.4-130 °C (decomposes at 130 °C).  $^1\text{H}$  NMR (500 MHz,  $\text{CDCl}_3$ ):  $\delta$  9.02 (s, 1H), 8.21 (s, 1H), 7.48 (s, 1H), 4.16 (t, 2H,  $J = 8.25$  Hz), 3.28 (t, 2H,  $J = 8.5$  Hz), 2.47 (s, 1H), 2.24 (s, 3H), 2.0-1.2 (m, 10H).

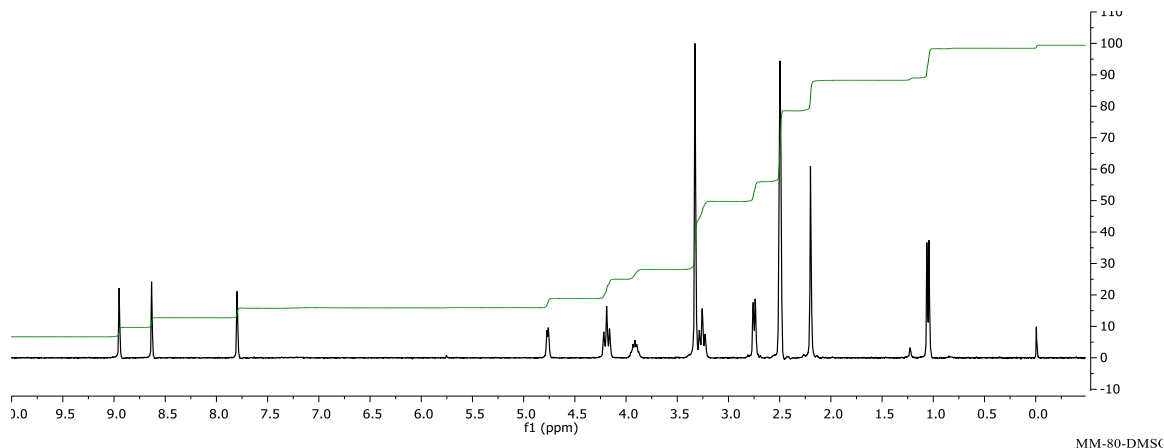
**53a**

**1-(5-Chloro-6-((4-(2-hydroxypropyl)-1H-1,2,3-triazol-1-yl)sulfonyl)indolin-1-yl)ethan-1-one (53a).** Prepared according to general procedure.  $^1\text{H}$  NMR (500 MHz,  $d_6$ -DMSO):  $\delta$  8.92 (s, 1H), 8.65 (s, 1H), 7.63 (s, 1H), 4.75 (d,  $J = 3.5$  Hz, 1H), 4.19 (t,  $J = 9$  Hz, 2H), 3.92 (m, 1H), 3.26 (t,  $J = 8$  Hz, 2H), 2.75 (d,  $J = 6$  Hz, 2H), 2.51 (s, 3H), 1.06 (d,  $J = 5$  Hz, 3H).

**53b**

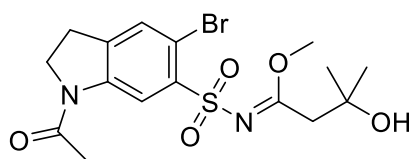
**1-(5-Bromo-6-((4-(2-hydroxypropyl)-1H-1,2,3-triazol-1-yl)sulfonyl)indolin-1-yl)ethan-1-one**

**(53b).** Prepared according to general procedure. A solution of CuTC (5.5 mg, .029 mmol), 4-pentyn-2-ol (33  $\mu$ L, .36 mmol), and sulfonyl azide (100 mg, .29 mmol) in  $\text{CH}_2\text{Cl}_2$  (1 mL) was stirred at room temperature under  $\text{N}_2$  for 2 h, then diluted with 3 mL  $\text{CH}_2\text{Cl}_2$  and 3 mL saturated aqueous  $\text{NH}_4\text{Cl}$ , stirred for 30 seconds, and the precipitate was collected by vacuum filtration washing with  $\text{CH}_2\text{Cl}_2$ , saturated aqueous  $\text{NH}_4\text{Cl}$ , and  $\text{H}_2\text{O}$  to afford 32.5 mg of a white solid at an 26 % yield. mp = Decomposes at 142.2  $^\circ\text{C}$ .  $^1\text{H}$  NMR (300 MHz,  $\text{DMSO-d}_6$ ):  $\delta$  8.95 (s, 1H), 8.63 (s, 1H), 7.80 (s, 1H), 4.77 (d,  $J = 4.2$  Hz, 1H), 4.161 (t, 2H,  $J = 8.7$  Hz), 3.91 (m, 1H), 3.26 (t,  $J = 8.6$  Hz, 2H), 2.75 (d,  $J = 6.0$  Hz, 2H), 2.20 (s, 3H), 1.05 (d,  $J = 6.0$  Hz, 3H).



### General Synthesis Procedure [A] for Sulfoyl Imidates Via CuAAC.

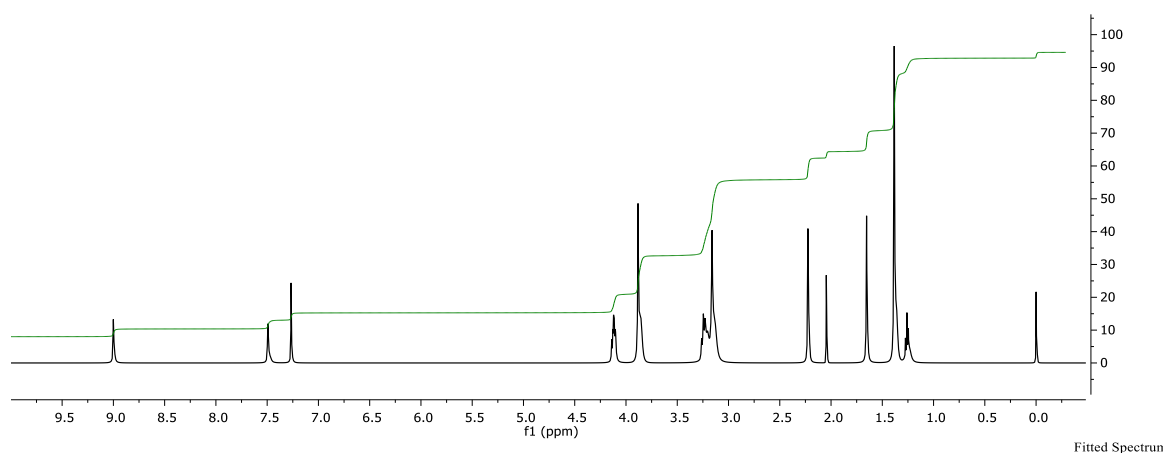
To a stirred solution of sulfonyl azide, copper iodide (15 mol%), and Et<sub>3</sub>N (1.5 eq.) in methanol (1.2 M, 20 eq.) was slowly added the respective alkyne (1.5 eq.) at room temperature under positive pressure inert gas. After 1-3 h of stirring the reaction mixture is diluted with CH<sub>2</sub>Cl<sub>2</sub> and a solution of 1:1 saturated aqueous Na<sub>2</sub>S<sub>2</sub>O<sub>3</sub>-H<sub>2</sub>O and stirred for 30 min. The layers were allowed to separate and product was extraction from aqueous with CH<sub>2</sub>Cl<sub>2</sub>, and the combined extracts were dried over MgSO<sub>4</sub>, filtered through activated carbon, concentrated in vacuo followed by recrystallization from ethyl acetate.



**54**

**Methyl (Z)-N-((1-acetyl-5-bromoindolin-6-yl)sulfonyl)-3-hydroxy-3-methylbutanimidate (54).** Prepared according to general procedure. To a stirred solution of sulfonyl azide (100 mg, 0.29 mmol), copper iodide (5.5 mg, 0.029 mmol), and Et<sub>3</sub>N (150 μL, 0.36 mmol) in methanol (235 μL, 5.8 mmol) was slowly added the 2-methylbut-3-yn-2-ol (35 μL, 0.36 mmol) at room temperature under positive pressure inert gas. After 30 min of stirring under N<sub>2</sub> at room temperature, reaction mixture was diluted with CH<sub>2</sub>Cl<sub>2</sub> (2 mL) and saturated aqueous NH<sub>4</sub>Cl (3

mL) and stirred for 15 min, and the layers were allowed to separate and product was extraction from aqueous with  $\text{CH}_2\text{Cl}_2$ , and the combined extracts were dried over  $\text{MgSO}_4$ , and recrystallized from ethyl acetate to afford 41.2 mg of clear crystals at 33 % yield.  $R_f = 0.47$  (5:95 MeOH- $\text{CH}_2\text{Cl}_2$ ). mp = 151.6-171.2  $^\circ\text{C}$ .  $^1\text{H NMR}$  (500 MHz,  $\text{CDCl}_3$ ):  $\delta$  9.00 (s, 1H), 7.49 (s, 1H), 4.12 (t,  $J = 8.5$  Hz, 2H), 3.88 (s, 3H), 3.25 (t,  $J = 8.5$  Hz, 2H), 3.16 (s, 2H), 2.23 (s, 3H), 2.05 (s, 1H), 1.38 (s, 6H).



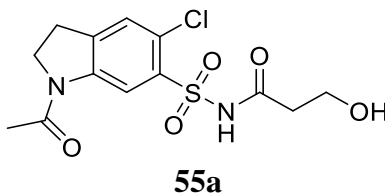
### General Synthesis Procedure [A] for N-Acyl-Sulfonamides Via CuAAC.

To a mixture of sulfonyl azide (100 mg, 0.29 mmol), copper iodide (15 mol%), and  $\text{Et}_3\text{N}$  (1.5 eq.) in 2:1 t-BuOH- $\text{H}_2\text{O}$  (0.1 M) was added the respective alkyne (1.5 eq.) slowly at room temperature under positive pressure inert gas. Reaction mixture was stirred under  $\text{N}_2$  for 3-4 h, then diluted with  $\text{CH}_2\text{Cl}_2$  and saturated aqueous  $\text{NH}_4\text{Cl}$ , stirred for 30 min and extracted with  $\text{CH}_2\text{Cl}_2$ . Combined organics were dried over  $\text{Na}_2\text{SO}_4$ , concentrated on rotavap, and purified with flash column chromatography. Alternatively, if precipitate forms during quenching stage then the biphasic system was diluted with  $\text{Et}_2\text{O}$  and solids collected via vacuum filtration. Solids were washed with cold 10 % citric acid,  $\text{H}_2\text{O}$ , and petroleum ether. Product isolation achieved by

taking up in a warm solution of 2:1:1 MeOH-AN-H<sub>2</sub>O, passed through activated carbon/cotton plug into 40 mL cold ether and collected by vacuum filtration.

### General Synthesis Procedure [B] for N-Acyl-Sulfonamides Via CuAAC.

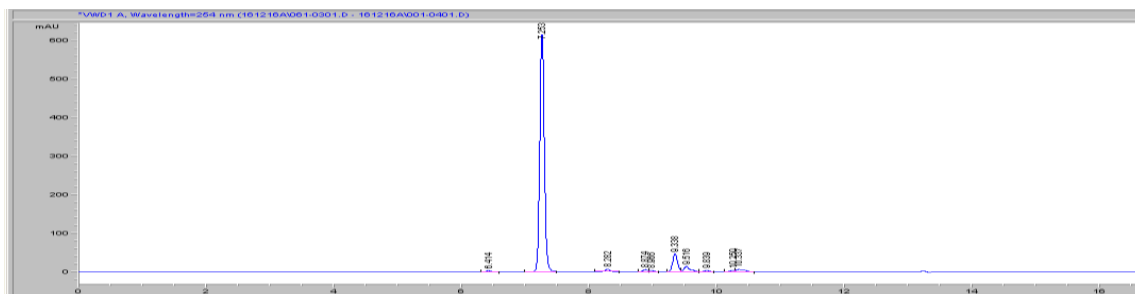
To a stirred solution of sulfonyl azide, copper iodide (15 mol%), and Et<sub>3</sub>N (1.5 eq.) in CH<sub>2</sub>Cl<sub>2</sub> (0.3M) was added H<sub>2</sub>O (1.5 eq.) followed by the respective alkyne (1.5 eq.) slowly at room temperature under positive pressure inert gas. After 1-3 h of stirring the reaction mixture is diluted with CH<sub>2</sub>Cl<sub>2</sub> (2 mL) and a 1:1 solution of saturated aqueous Na<sub>2</sub>S<sub>2</sub>O<sub>3</sub>-H<sub>2</sub>O and stirred for 30 minutes. The layers were allowed to separate and product was extraction from aqueous with CH<sub>2</sub>Cl<sub>2</sub>, and the combined extracts were dried over MgSO<sub>4</sub>, filtered through activated carbon, concentrated in vacuo followed by recrystallization.



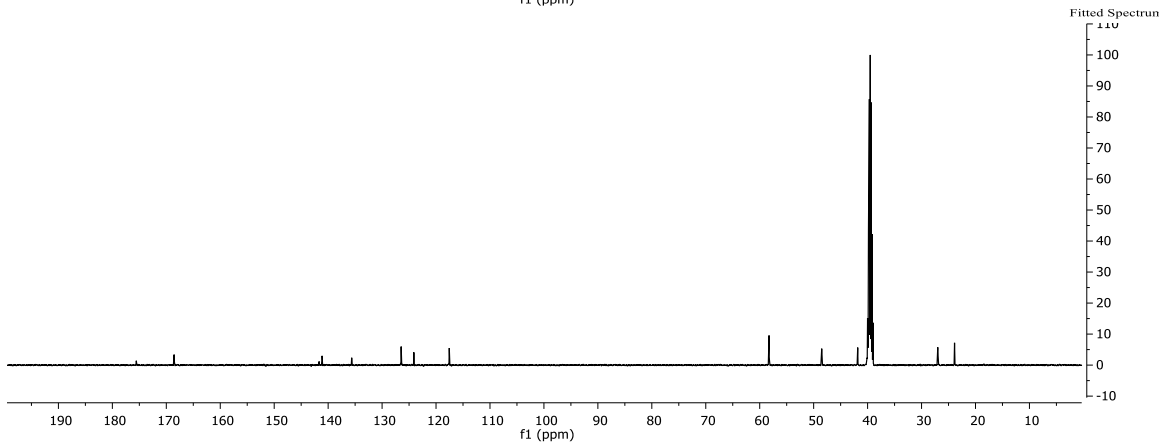
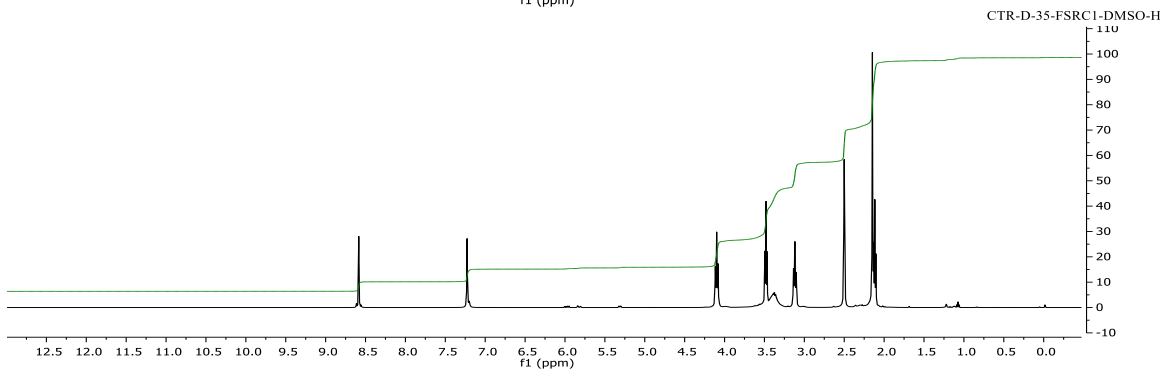
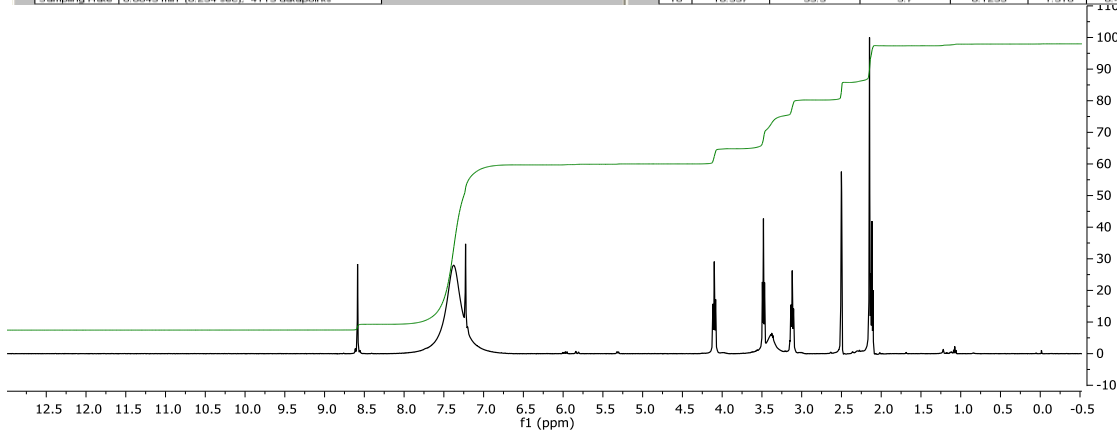
**N-((1-Acetyl-5-chloroindolin-6-yl)sulfonyl)-3-hydroxypropanamide (55a).** Prepared

according to general procedure [A]. Product collected as a white powder and found to be 95 % pure by HPLC. \*nmr broadened by paramagnetic interference [Cu]. <sup>1</sup>H NMR (500 MHz, d<sub>6</sub>-DMSO): δ 8.58 (s, 1H), 7.23 (s, 1H), (7.43 bs = NH<sub>4</sub>Cl contaminant), 4.10 (t, J = 8.5 Hz, 2H), 3.48 (t, J = 6.8 Hz, 2H), 3.12 (t, J = 8.4 Hz, 2H), 2.15 (s, 3H), 2.12 (t, J = 6.7 Hz, 2H). <sup>13</sup>C NMR (500 MHz, d<sub>6</sub>-DMSO): δ 175.6, 168.6, 141.7, 141.1, 135.7, 126.5, 124.1, 117.6, 58.3, 48.5, 41.8, 27.0, 23.9.

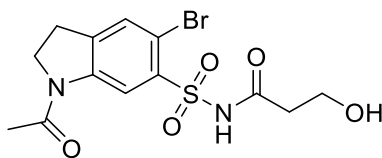




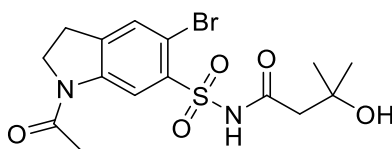
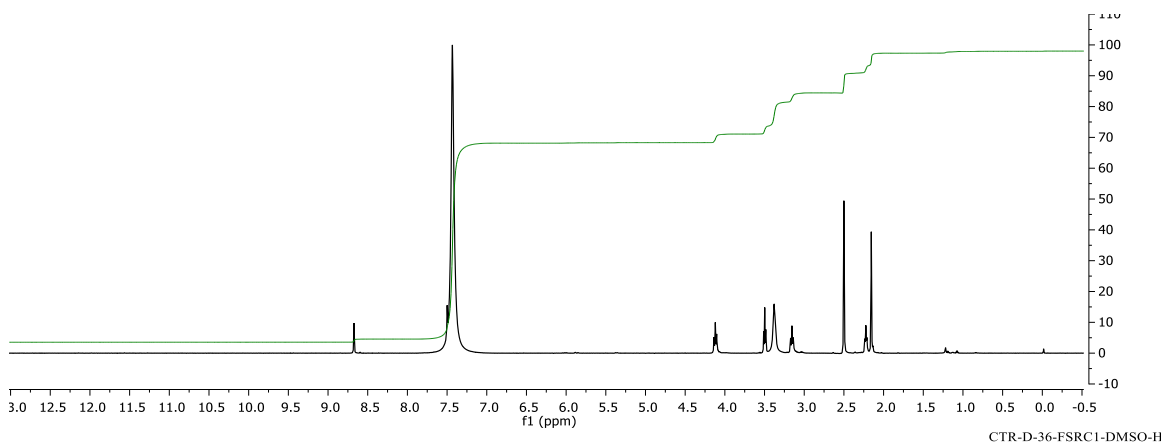
| File Information |   | #  | Time   | Area   | Height | Width  | Area%  | Symmetry |
|------------------|---|----|--------|--------|--------|--------|--------|----------|
| LC-File          | D01-0301.D                              | 1  | 0.414  | 14.0   | 3      | 0.0742 | 0.410  | 0.006    |
| File Path        | C:\MSDCHEM\MSDCHEM\DATA\161216A\        | 2  | 2.253  | 3019.1 | 615.4  | 0.0747 | 85.204 | 0.907    |
| Date             | 16-Dec-18, 16:50:51                     | 3  | 0.262  | 33.3   | 6.2    | 0.0801 | 0.342  | 1.04     |
| Sample           | CTR-D-35-FS2                            | 4  | 0.674  | 27.7   | 5.6    | 0.0757 | 0.783  | 0.952    |
| Barcode          |   | 5  | 0.966  | 14.7   | 3.1    | 0.0706 | 0.414  | 0.593    |
| Operator         | Corv                                    | 6  | 9.340  | 247.7  | 46     | 0.0011 | 5.996  | 0.916    |
| Method           | CE-254.M                                | 7  | 9.516  | 91.9   | 13.6   | 0.0961 | 2.595  | 0.570    |
| Analysis Time    | 19.906 min                              | 8  | 9.679  | 19.4   | 3.3    | 0.0897 | 0.547  | 1.269    |
| Sampling Rate    | 0.0049 min (0.294 sec), 4119 datapoints | 9  | 10.26  | 18.1   | 3.8    | 0.0704 | 0.510  | 2.152    |
|                  |   | 10 | 10.337 | 63.6   | 6.7    | 0.1235 | 1.610  | 0.418    |



CTR-D-35-FS2C1-DMSO-C1

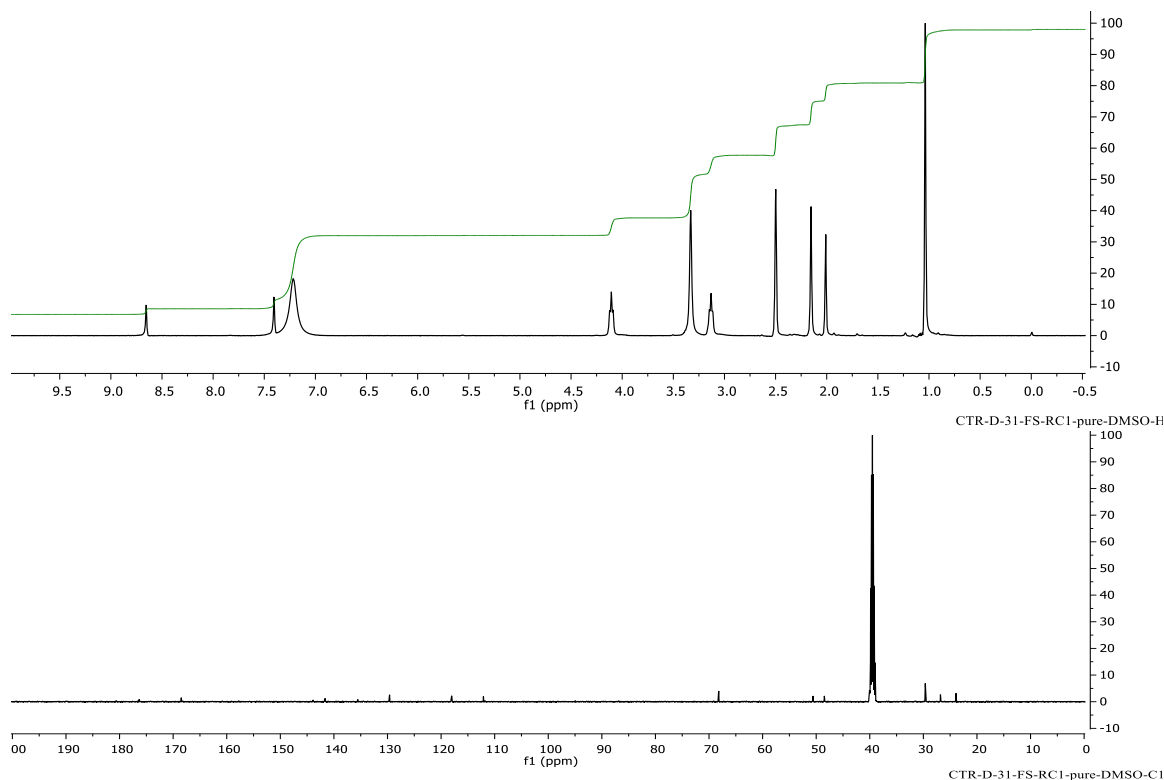
**55b**

**N-((1-Acetyl-5-bromoindolin-6-yl)sulfonyl)-3-hydroxypropanamide (55b).** Prepared according to general procedure [A]. Product collected as a white fluffy powder found to be 95% pure by HPLC. \*nmr broadened by paramagnetic interference [Cu].  $^1\text{H}$  NMR (500 MHz,  $\text{d}_6$ -DMSO):  $\delta$  8.68 (s, 1H), 7.50 (s, 1H), (7.43 bs =  $\text{NH}_4\text{Cl}$  contamination), 4.11 (t,  $J = 9.0\text{Hz}$ , 2H), 4.50 (t,  $J = 4.5\text{Hz}$ , 2H), 3.15 (t,  $J = 8.0\text{Hz}$ , 2H), 2.21(t,  $J = 1.5\text{Hz}$ , 1H), 2.15 (s, 3H).

**55c**

**N-((1-Acetyl-5-bromoindolin-6-yl)sulfonyl)-3-hydroxy-3-methylbutanamide (55c).** Prepared according to general procedure [A]. Product collected to afford 213.4 mg of an off-white powder at an 88 % yield that was found to be 96 % pure by HPLC.  $^1\text{H}$  NMR (300 MHz,  $\text{DMSO-d}_6$ ):  $\delta$  8.67 (s, 1H), 7.43 (s, 1H), 7.07 (br s, 1H), 4.11 (t,  $J = 8.4\text{ Hz}$ , 2H), 3.14 (t,  $J = 8.25\text{ Hz}$ , 2H), 2.16 (s, 3H), 2.04 (s, 2H), 1.05 (s, 6H).  $^{13}\text{C}$  NMR (126 MHz,  $\text{d}_6$ -DMSO):  $\delta$  176.34, 176.31, 168.47, 143.90, 141.66, 135.54, 135.52, 129.62, 118.03, 112.10, 68.19, 50.58, 48.47, 40.11, 40.01, 39.93,

39.84, 39.76, 39.67, 39.59, 39.53, 39.50, 39.34, 39.17, 39.03, 39.00, 29.64, 26.81. HRMS (ESI-MS)  $m/z$  calcd. for  $C_{15}H_{20}BrN_2O_5S$   $[M+H]^+$ : 421.0257, found: 421.0255. MP: 219-234°C (decomp.)



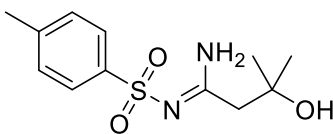
### General Synthesis Procedure [A] for Sulfonyl Amidines.

To a stirred solution of sulfonyl azide, copper iodide (15 mol%),  $Et_3N$  (1.5 eq.) and 28 %  $NH_4OH_{(aq)}$  (1.5 eq.) or alkyl amine (1.5 eq.), in  $CH_2Cl_2$  or THF (0.3 M) was added the respective alkyne (1.5 eq.) slowly at room temperature under positive pressure inert gas. After 3-4 h of stirring the reaction mixture diluted with  $CH_2Cl_2$  and saturated  $NH_4Cl_{(aq)}$ , stirred for 30 min and extracted with  $CH_2Cl_2$ . Combined organics were dried over  $Na_2SO_4$ , concentrated on rotavap, and purified with flash column chromatography. Alternatively, if precipitate forms during quenching stage, the biphasic slurry was diluted with  $Et_2O$  and solids collected via vacuum filtration. Crude solids were washed with cold 10 % citric acid,  $H_2O$ ,  $CH_2Cl_2$ , ether and

petroleum ether before drying under reduced pressure. Product isolation achieved by taking up in a warm solution of 5:5:1 MeOH-AN-DMF, passed through activated carbon/cotton plug and dripping into large amount of stirred cold ether, forming white precipitate which was collected by vacuum filtration.

### General Synthesis Procedure [B], Optimized for Sulfonyl Amidines.

To a stirred solution of sulfonyl azide, copper iodide (15 mol%), Et<sub>3</sub>N (1.5 eq.), and NH<sub>4</sub>Cl<sub>(s)</sub> (1.5 eq.) in CH<sub>2</sub>Cl<sub>2</sub> or THF (0.3M) was added the respective alkyne (1.5 eq.) slowly at room temperature under positive pressure inert gas. After 1-3 h of stirring the reaction mixture is diluted with CH<sub>2</sub>Cl<sub>2</sub> (2 mL) and a 1:1 solution of saturated aqueous Na<sub>2</sub>S<sub>2</sub>O<sub>3</sub>-H<sub>2</sub>O and stirred for 30 min. The layers were allowed to separate and product was extraction from aqueous with CH<sub>2</sub>Cl<sub>2</sub>, and the combined extracts were dried over NaSO<sub>4</sub>, filtered through activated carbon, concentrated in vacuo. Alternatively, if precipitate formed during quenching stage then the biphasic slurry was diluted with Et<sub>2</sub>O and solids collected via vacuum filtration. Solids were washed with cold 10% citric acid, H<sub>2</sub>O, CH<sub>2</sub>Cl<sub>2</sub>, ether and petroleum ether before drying under reduced pressure. Product isolation was achieved by taking up in a warm solution of 5:5:1 MeOH-AN-DMF, passed through activated carbon/cotton plug, and re-crystallized upon cooling.

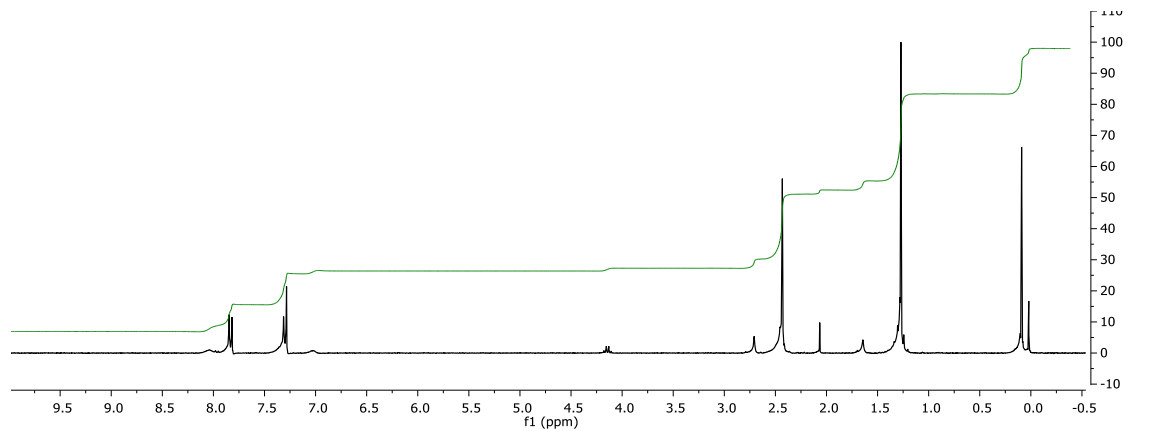


**56**

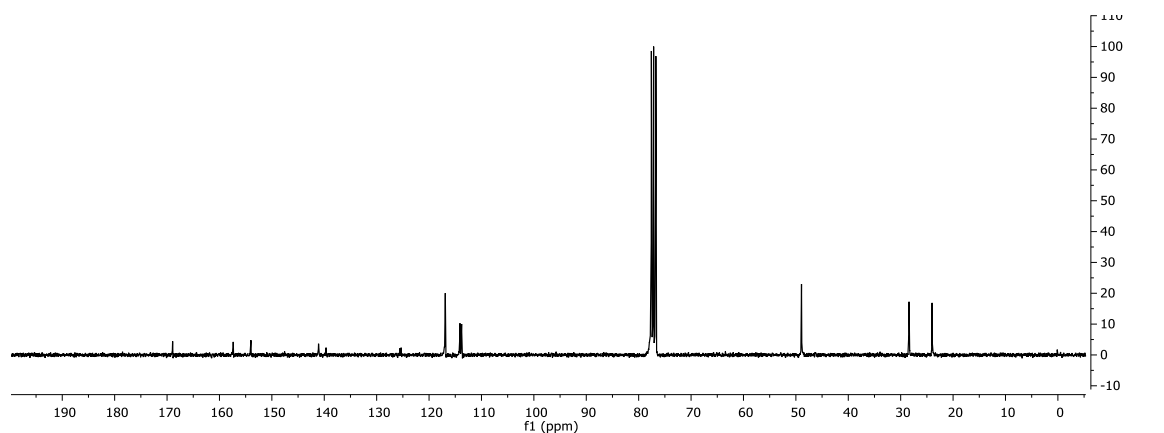
**(Z)-3-Hydroxy-3-methyl-N'-tosylbutanimidamide (56).** Prepared according to general procedure [A]. Flash column chromatography (silica gel, 4g, 1:1 EA-Pet. E.) afforded 52 mg of a yellow oil at 38 % yield. <sup>1</sup>H NMR (300 MHz, CDCl<sub>3</sub>): δ 8.01 (br s, 1H), 7.81 (d, *J* = 8.1 Hz, 2H), 7.28 (d, *J* = 8.1 Hz, 2H), 7.00 (br s, 1H), 2.69 (s, 1H), 2.44-2.41 (m, 5H), 1.25 (s, 6H). <sup>13</sup>C

NMR (75 MHz, CDCl<sub>3</sub>):  $\delta$  167.2, 143.3, 139.2, 129.6, 126.6, 70.7, 48.9, 29.5, 21.7. HRMS (ESI-

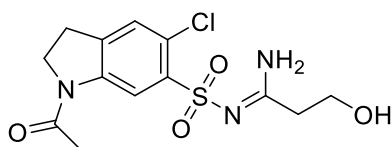
MS)  $m/z$  calcd. for C<sub>12</sub>H<sub>19</sub>N<sub>2</sub>O<sub>3</sub>S [ $M+H$ ]<sup>+</sup>: 271.1116, found: 271.1106.



MM-6



MM-B-21-CDCl

**57a**

**N'-((1-Acetyl-5-chloroindolin-6-yl)sulfonyl)-3-hydroxypropanimidamide (57a).** Prepared

according to general procedure [B]. Recrystallization from 5:5:1 MeOH-AN-DMF afforded

152.3 mg of a colorless crystals at 66 % yield found to be 97 % pure by HPLC. mp = 230-232

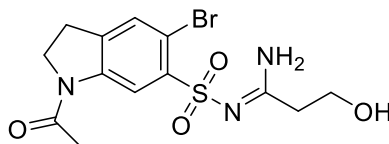
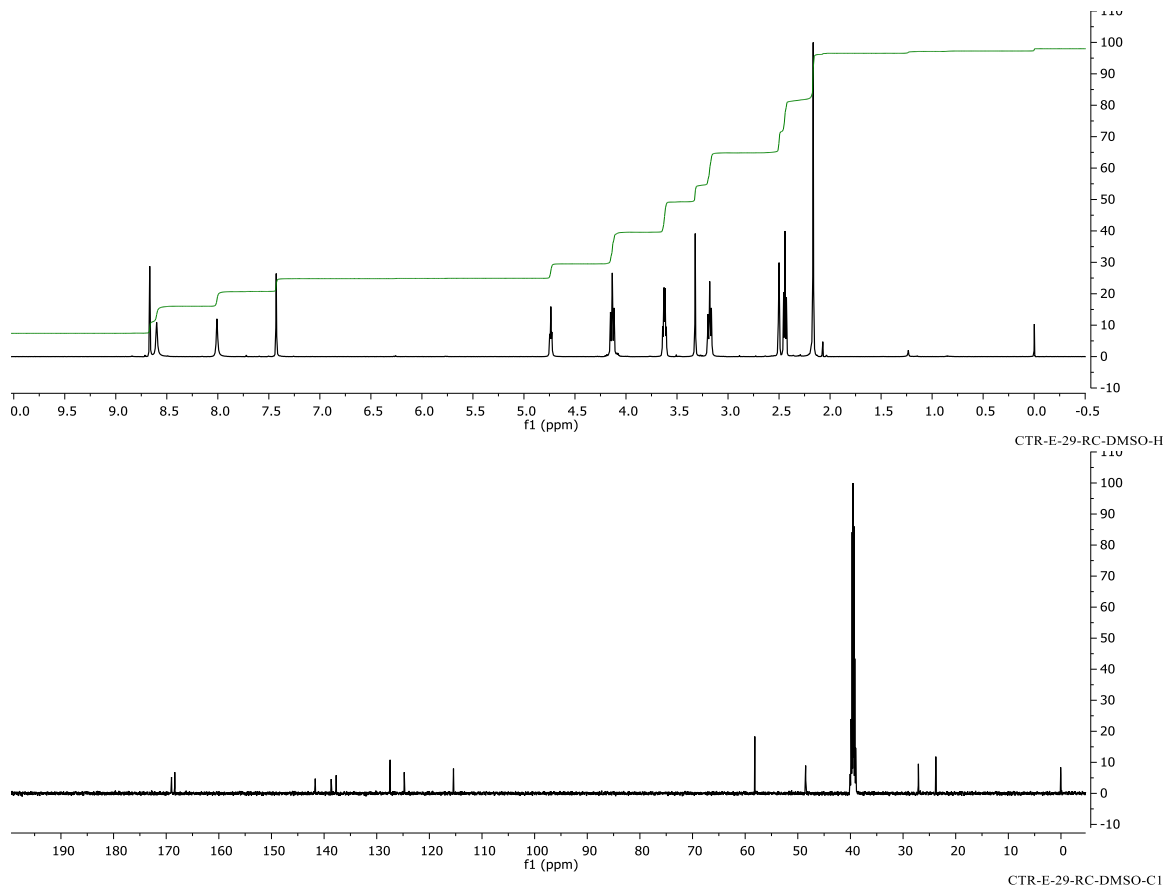
°C. <sup>1</sup>H NMR (500 MHz, d<sub>6</sub>-DMSO):  $\delta$  8.67 (s, 1H), 8.60 (s, 1H), 8.01 (s, 1H), 7.43 (s, 1H), 4.74

(t, J = 5.5 Hz, 1H), 4.14 (t, J = 8.0 Hz, 2H), 3.62 (q, J = 11.0, 6.0 Hz, 2H), 3.18 (t, J = 9.0 Hz,

2H), 2.44 (t, J = 7.0 Hz, 2H), 2.17 (s, 3H). <sup>13</sup>C NMR (500 MHz, d<sub>6</sub>-DMSO):  $\delta$  169.0, 168.4,

141.7, 138.7, 137.7, 127.5, 124.8, 115.4, 58.2, 48.5, 39.4, 27.1, 23.8. HRMS (IT-TOF)  $m/z$

calcd. for  $C_{13}H_{16}ClN_3O_4S$   $[M-]^+$ : 345.0533, found: 345.0550

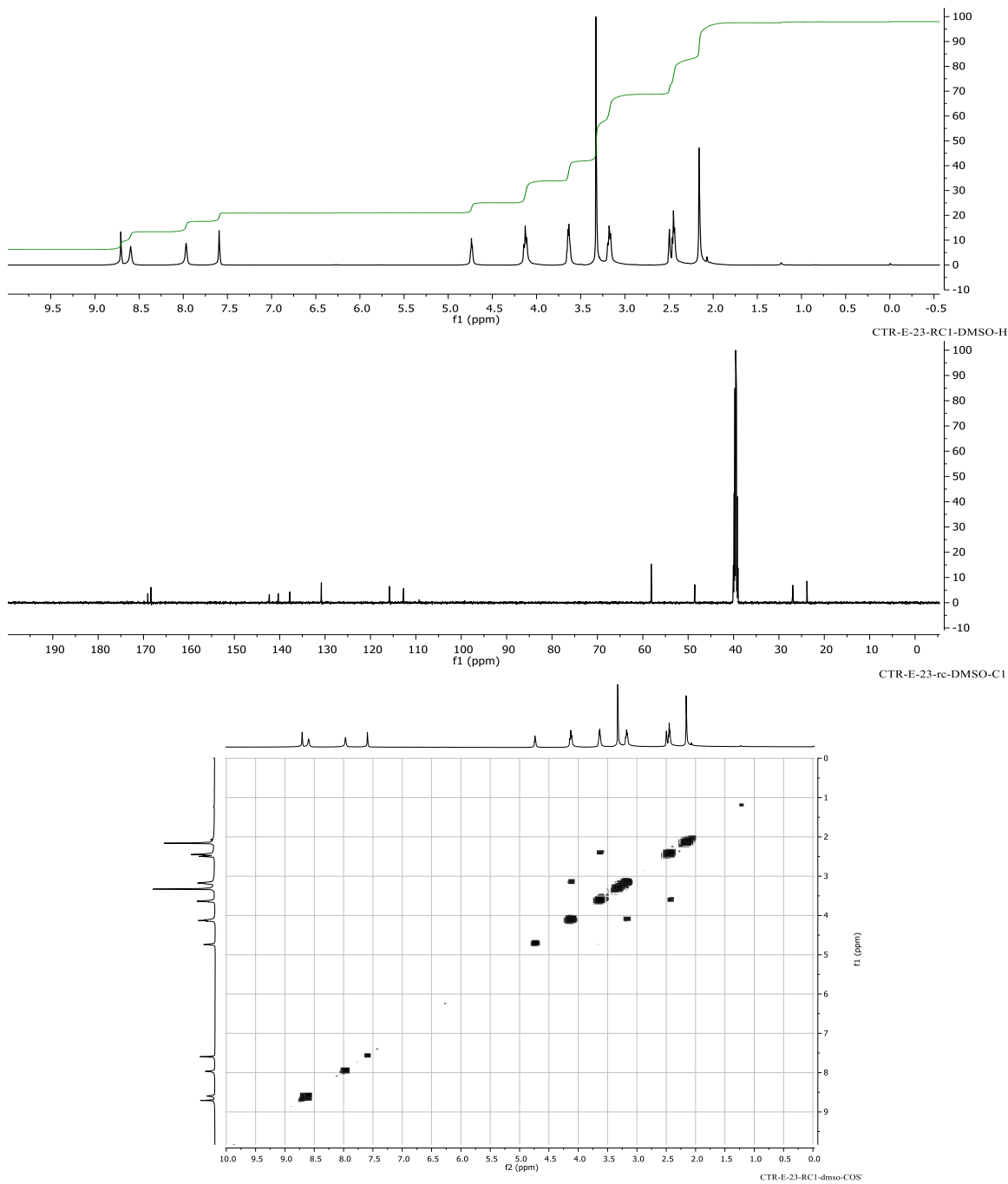


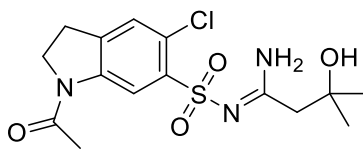
**57b**

**N'-((1-Acetyl-5-bromoindolin-6-yl)sulfonyl)-3-hydroxypropanimidamide (57b).** Prepared according to general procedure [B]. Recrystallization from 5:5:1 MeOH-AN-DMF afforded 38.8 mg of a colorless needle crystal at 18 % yield (loss to spill) found to be 97 % pure by HPLC. mp = 230-235 °C.  $^1H$  NMR (300 MHz, DMSO- $d_6$ ):  $\delta$  8.71 (s, 1H), 8.40 (br s, 1H), 7.97 (br s, 1H), 7.60 (s, 1H), 4.74 (t, 1H,  $J = 4.8$  Hz), 4.14 (t, 2H,  $J = 8.4$  Hz), 3.63 (td,  $J_{H,H} = 6.6$  Hz,  $J_{O,H} = 5.1$  Hz), 3.18 (t,  $J = 7.95$  Hz, 2H), 2.446 (t, 2H,  $J = 6.6$  Hz), 2.164 (s, 1H).  $^{13}C$  NMR (500 MHz,  $d_6$ -

DMSO):  $\delta$  169.1, 168.4, 142.3, 140.3, 137.8, 130.8, 115.8, 112.7, 58.2, 48.6, 39.5, 27.0, 23.8.

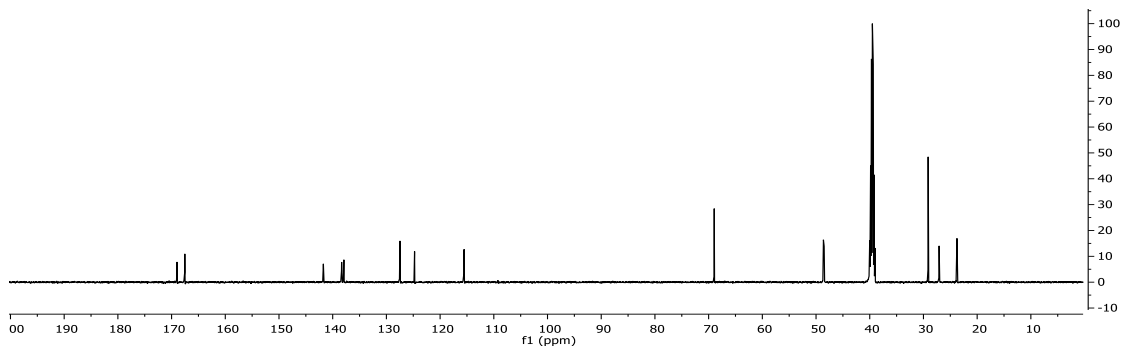
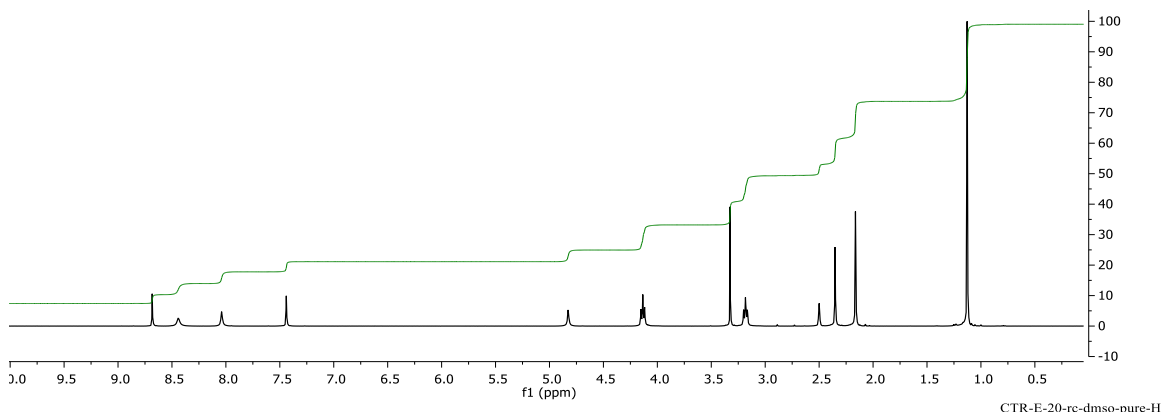
HRMS (ESI-MS)  $m/z$  calcd. for  $C_{13}H_{17}BrN_3O_4S$   $[M+H]^+$ : 392.0104, found: 392.0094.



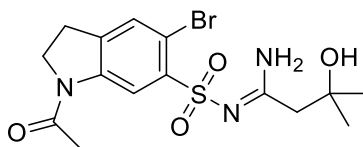
**58a**

**((Z)-N'-((1-Acetyl-5-chloroindolin-6-yl)sulfonyl)-3-hydroxy-3-methylbutanimidamide (58a).**

Prepared according to representative procedure [B]. Recrystallization from 5:5:1 AN-MeOH-DMF afforded 77.3 mg of colorless needle crystals at 30 % yield found to be 97 % pure by HPLC. mp = 210-222 °C.  $^1\text{H}$  NMR (300 MHz,  $d_6$ -DMSO):  $\delta$  8.69 (s, 1H), 8.57 (br s, 1H), 8.03 (br s, 1H), 7.46 (s, 1H), 4.89 (br s, 1H), 4.15 (t,  $J$  = 8.4 Hz, 2H), 3.20 (t,  $J$  = 8.55 Hz, 2H), 2.38 (s, 2H), 2.18 (s, 3H), 1.13 (s, 6H).  $^{13}\text{C}$  NMR (500 MHz,  $d_6$ -DMSO):  $\delta$  169.0, 167.5, 141.7, 138.4, 137.9, 127.5, 124.8, 115.5, 69.0, 48.6, 48.5, 29.1, 27.1, 23.8. HRMS (ESI-MS)  $m/z$  calcd. for  $\text{C}_{15}\text{H}_{21}\text{ClN}_3\text{O}_4\text{S}$  [ $M+\text{H}$ ] $^+$ : 374.0941, found: 374.0930.

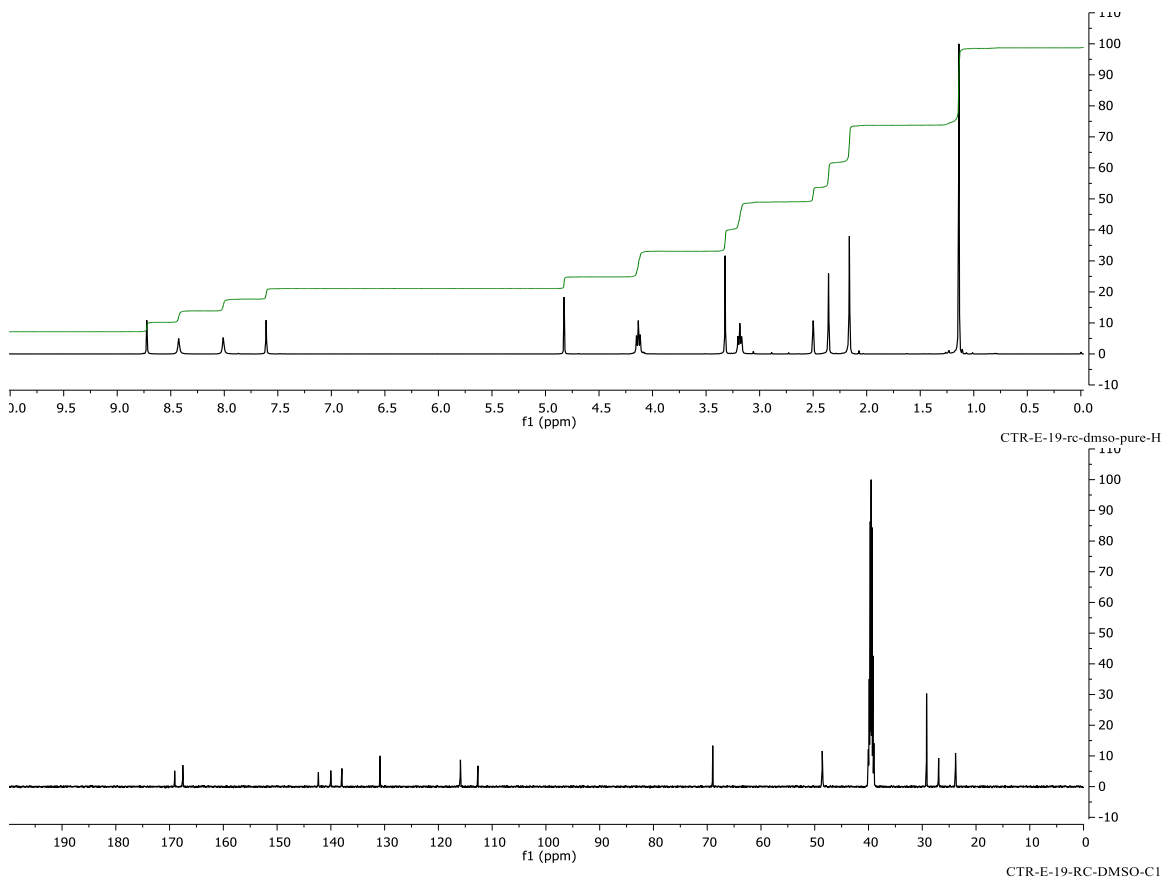


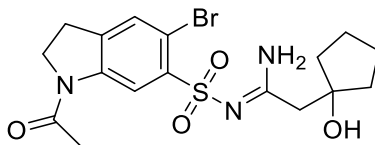


**58b**

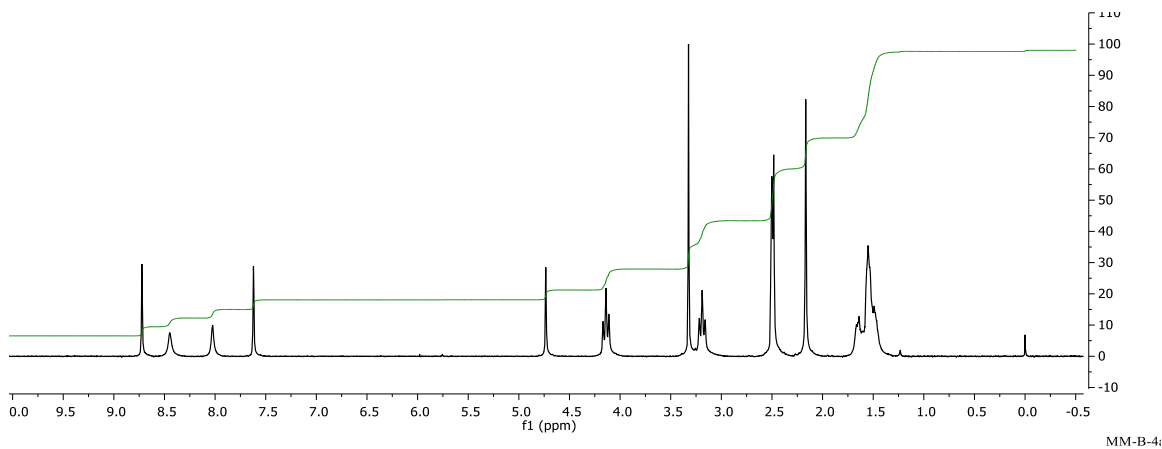
**((Z)-N'-((1-Acetyl-5-bromoindolin-6-yl)sulfonyl)-3-hydroxy-3-methylbutanimidamide**

**(58b)**. Prepared according to representative procedure [B]. Recrystallization from 5:5:1 AN-MeOH-DMF afforded 84.5 mg of colorless needle crystals at 34 % yield found to be 98 % pure by HPLC. mp = 240-245 °C  $^1\text{H}$  NMR (500 MHz,  $d_6$ -DMSO):  $\delta$  1.03 (s, 6H), 2.07 (s, 3H), 2.26 (s, 2H), 3.09 (t,  $J = 8.0$  Hz, 2H), 4.04 (t,  $J = 8.0$  Hz, 2H), 4.75 (s, 1H), 7.52 (s, 1H), 7.92 (s, 1H), 8.34 (s, 1H), 8.63 (s, 1H).  $^{13}\text{C}$  NMR (500 MHz,  $d_6$ -DMSO):  $\delta$  169.1, 167.6, 142.3, 140.0, 138.0, 130.9, 115.9, 112.7, 69.0, 48.6, 48.5, 29.2, 27.0, 23.8. HRMS (ESI-MS)  $m/z$  calcd. for  $\text{C}_{15}\text{H}_{21}\text{BrN}_3\text{O}_4\text{S}$   $[\text{M}+\text{H}]^+$ : 420.0417, found: 420.0403.  $R_f = 0.18$  (1:9 EtOAc- $\text{CH}_2\text{Cl}_2$ ).

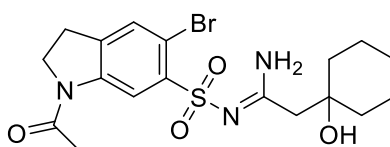
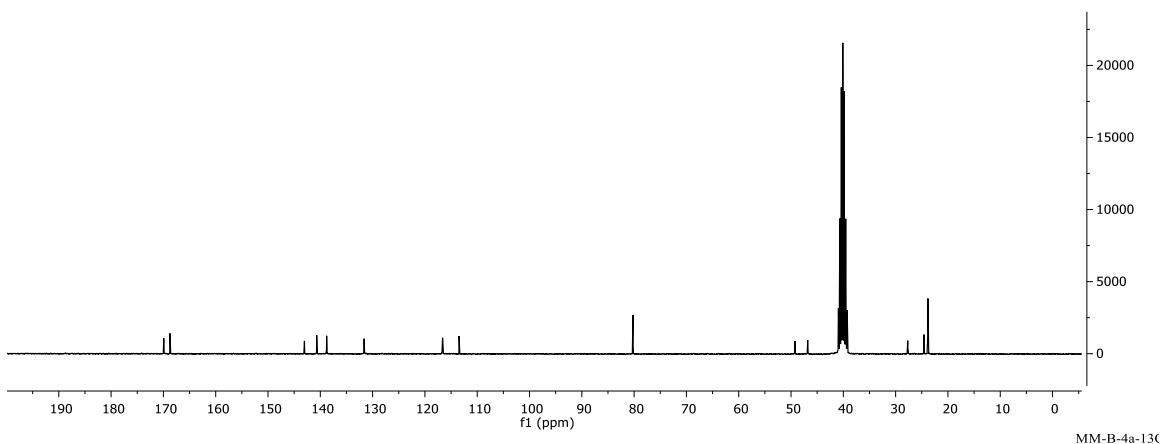


**59a****(Z)-N'-((1-Acetyl-5-bromoindolin-6-yl)sulfonyl)-2-(1-hydroxycyclopentyl)acetimidamide**

**(59a).** Prepared according to general procedure [A]. Flash column chromatography afforded 61.8 mg of a white solid at a 48 % yield. mp = 194.6-199.5 °C. <sup>1</sup>H NMR (300 MHz, d<sub>6</sub>-DMSO): δ 8.723 (s, 1H), 8.45 (br s, 1H), 8.03 (br s, 1H), 7.62 (s, 1H), 4.73 (s, 1H), 4.14 (t, *J* = 8.7 Hz, 2H), 3.19 (t, *J* = 8.6 Hz, 2H), 2.48 (s, 2H), 2.17 (s, 3H), 1.67-1.49 (m, 8H). <sup>13</sup>C NMR (300 MHz, d<sub>6</sub>-DMSO): δ 169.9, 168.7, 143.0, 140.7, 138.8, 131.6, 116.6, 113.5, 80.2, 49.3, 46.8, 27.7, 24.6, 23.8. HRMS (ESI-MS) *m/z* calcd. for C<sub>17</sub>H<sub>23</sub>BrN<sub>3</sub>O<sub>4</sub>S: 446.0573, found: 446.0558.

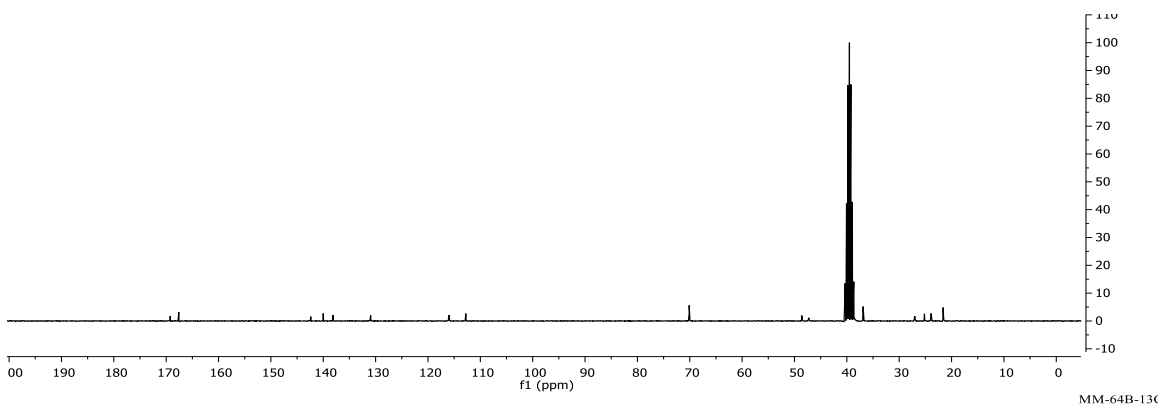


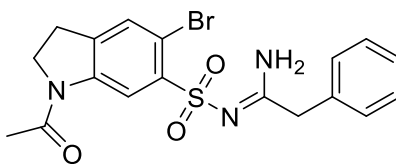
MM-B-4i

**60a**

**(Z)-N'-((1-Acetyl-5-bromoindolin-6-yl)sulfonyl)-2-(1-hydroxycyclohexyl)acetimidamide**

**(60a).** Prepared according to general procedure [A]. Yield: 49.3 mg white solid (37.1%). mp = 196.8-201°C (decomp). <sup>1</sup>H NMR (300 MHz, DMSO-d<sub>6</sub>): δ 8.72 (s, 1H), 8.43 (br s, 1H), 8.02 (br s, 1H), 7.62 (s, 1H), 4.62 (s, 1H), 4.14 (t, *J* = 8.55 Hz, 2H), 3.19 (t, *J* = 8.7 Hz, 2H), 2.35 (s, 2H), 2.16 (s, 3H), 1.50-1.15 (m, 10H). <sup>13</sup>C NMR NMR (300 MHz, d<sub>6</sub>-DMSO): δ 169.2, 167.6, 142.4, 140.0, 138.1, 131.0, 116.0, 112.8, 70.1, 48.6, 47.3, 36.9, 27.0, 25.2, 23.9, 21.6. HRMS (ESI-MS) *m/z* calcd. for C<sub>18</sub>H<sub>25</sub>BrN<sub>3</sub>O<sub>4</sub>S [*M*+*H*]: 460.0730, found: 460.0701.

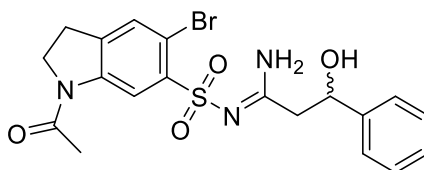
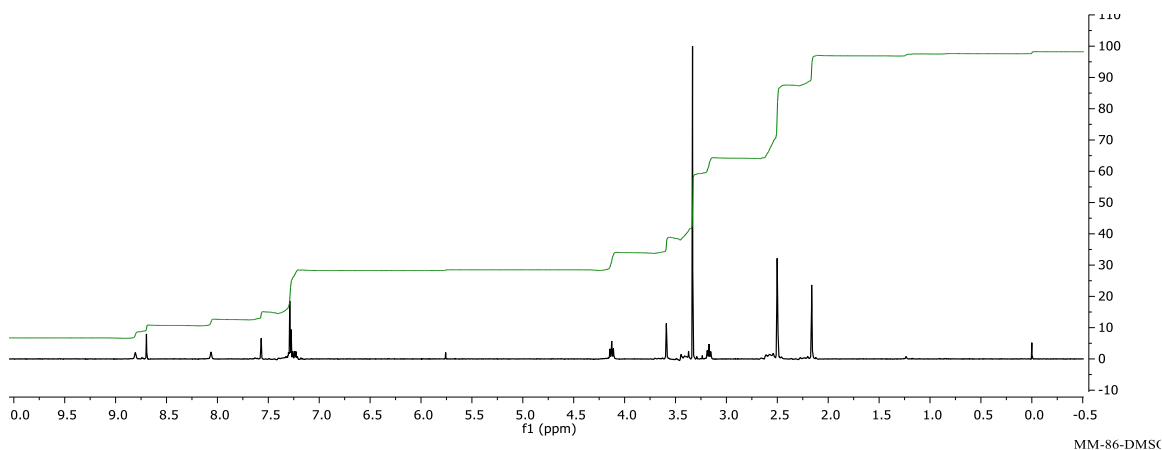


**61a**

**(Z)-N'-((1-Acetyl-5-bromoindolin-6-yl)sulfonyl)-2-phenylacetimidamide (61a).**

Prepared according to general procedure [A]. Flash column chromatography (silica gel, with 1:99 MeOH (sat. NH<sub>3</sub>)-CH<sub>2</sub>Cl<sub>2</sub> as eluent) for afford 54.1 mg of a yellow solid at 43 % yield.

R<sub>f</sub>=0.4 (5:95 MeOH sat. NH<sub>3</sub>-CH<sub>2</sub>Cl<sub>2</sub>). <sup>1</sup>H NMR (500 MHz, DMSO-d<sub>6</sub>): δ 2.16 (s, 3H), 3.17 (t, *J* = 8.25 Hz, 2H), 3.59 (s, 2H), 4.13 (t, *J* = 8.75 Hz, 2H), 7.24 (m, 5H), 7.57 (s, 1H), 8.70 (s, 1H), 8.81 (s, 1H). HRMS (ESI-MS) *m/z* calcd. for C<sub>18</sub>H<sub>19</sub>BrN<sub>3</sub>O<sub>3</sub>S: 438.0311, found: 438.0296.

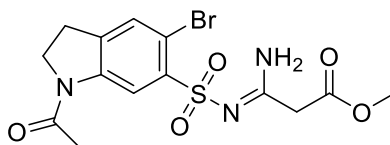
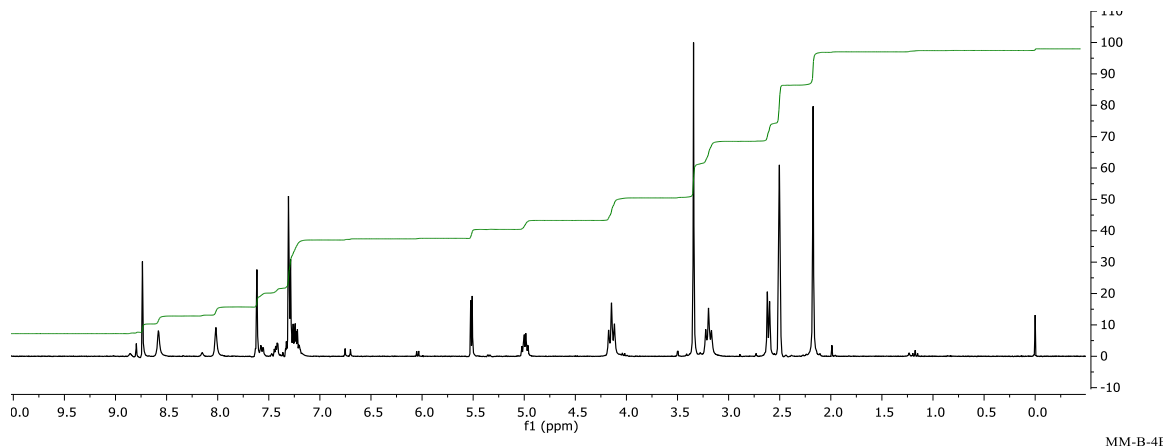
**62a**

**(Z)-N'-((1-Acetyl-5-bromoindolin-6-yl)sulfonyl)-3-hydroxy-3-phenylpropanimidamide (62a).**

Prepared according to general procedure [A]. Flash column chromatography afforded 90.3 mg of a green solid at 67 % yield. mp = 198.3 - 201 °C (decomposition at 201). <sup>1</sup>H NMR (300 MHz, DMSO-d<sub>6</sub>): δ 8.74 (s, 1H), 8.58 (br s, 1H), 8.02 (br s, 1H), 7.62 (s, 1H), 7.34-7.20 (m, 5H), 5.52 (d, *J* = 4.5 Hz, 1H), 4.99 (dd, *J*<sub>H,H</sub> = 6.9 Hz, *J*<sub>O,H</sub> = 4.5 Hz, 1H), 4.15 (t, *J* = 8.7 Hz, 2H),

3.20 (t,  $J = 8.25$  Hz, 2H), 2.61 (d,  $J = 6.6$  Hz, 2H), 2.17 (s, 3H). HRMS (ESI-MS)  $m/z$  calcd. for

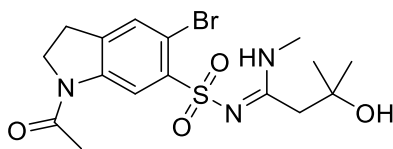
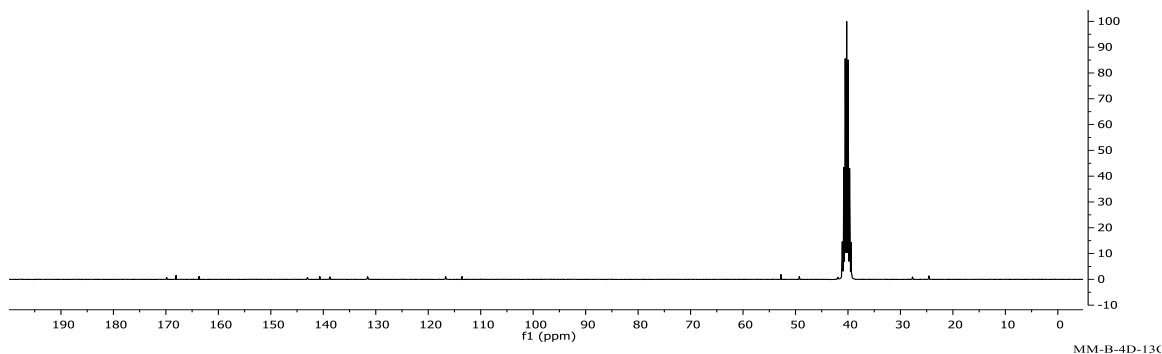
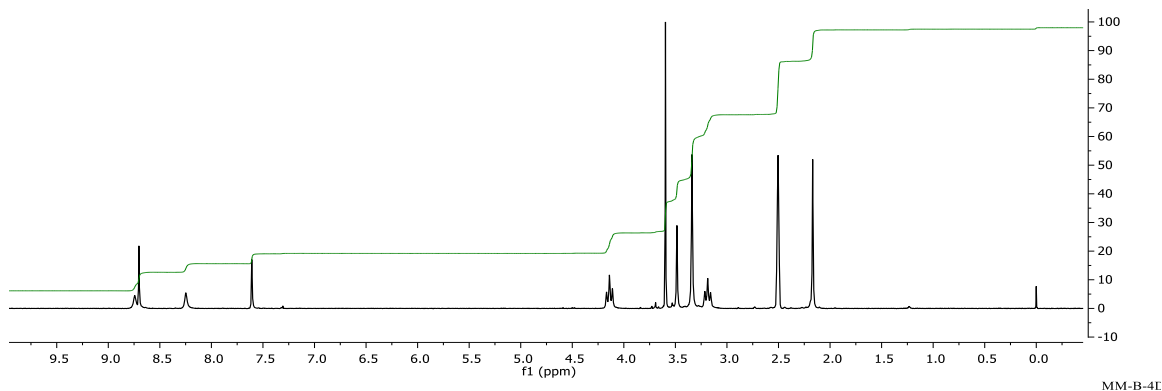
$C_{19}H_{21}BrN_3O_4S$  [ $M+H$ ] $^+$ : 468.0417, found: 468.0406.



**63a**

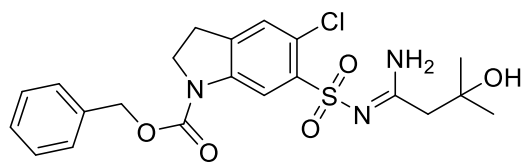
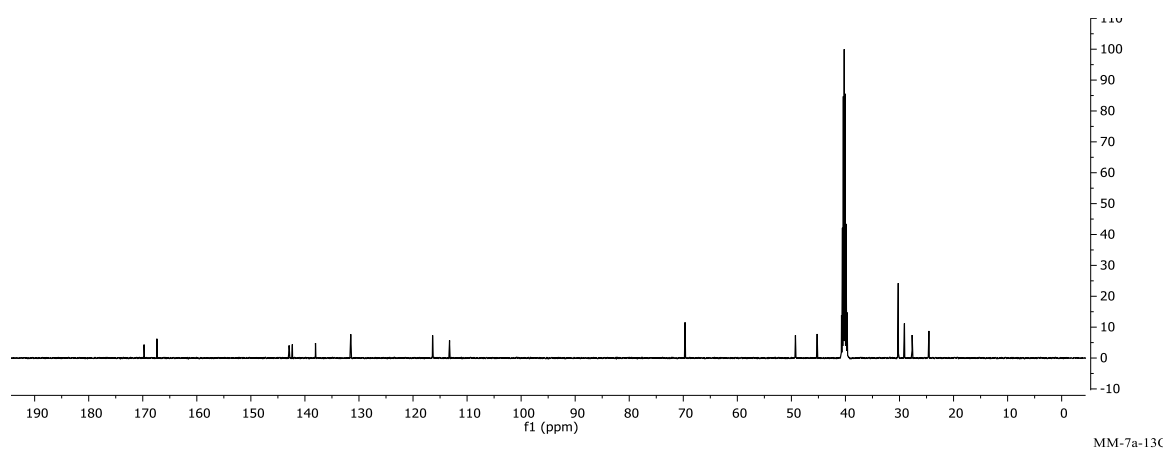
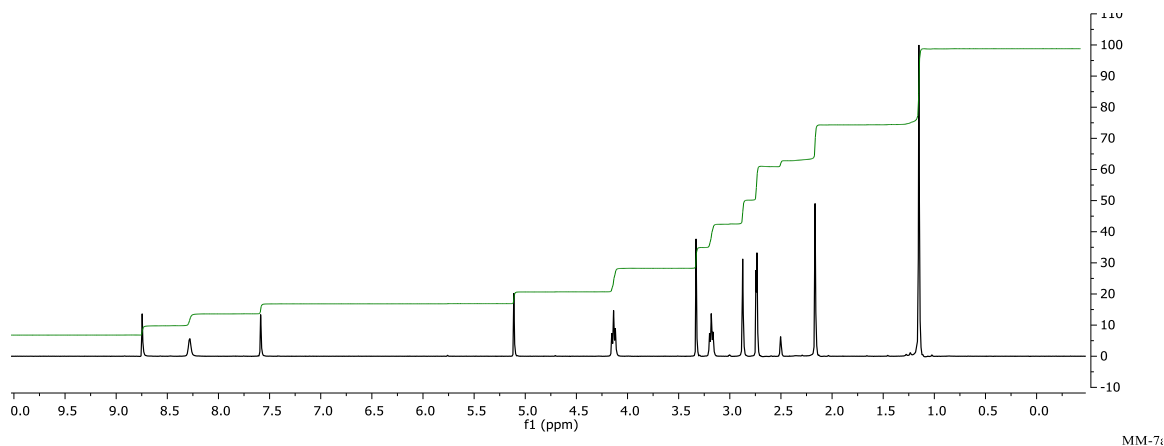
**Methyl (Z)-3-(((1-acetyl-5-bromoindolin-6-yl)sulfonyl)imino)-3-aminopropanoate (63a).**

Prepared according to representative procedure [A]. Flash chromatography afforded 39.7 mg of an off-white solid at 32 % yield. mp = 183.4 - 191.4 °C.  $^1H$  NMR (300 MHz, DMSO- $d_6$ ):  $\delta$  8.742 (br s, 1H), 8.703 (s, 1H), 8.248 (br s, 1H), 7.608 (s, 1H), 4.140 (t, 2H,  $J = 8.55$  Hz), 3.596 (s, 3H), 3.485 (s, 2H), 3.187 (t, 2H,  $J = 8.4$  Hz), 2.169 (s, 3H). HRMS (ESI-MS)  $m/z$  calcd. for  $C_{14}H_{17}BrN_3O_5S$  [ $M+H$ ] $^+$ : 420.0053, found: 420.0040.

**64a**

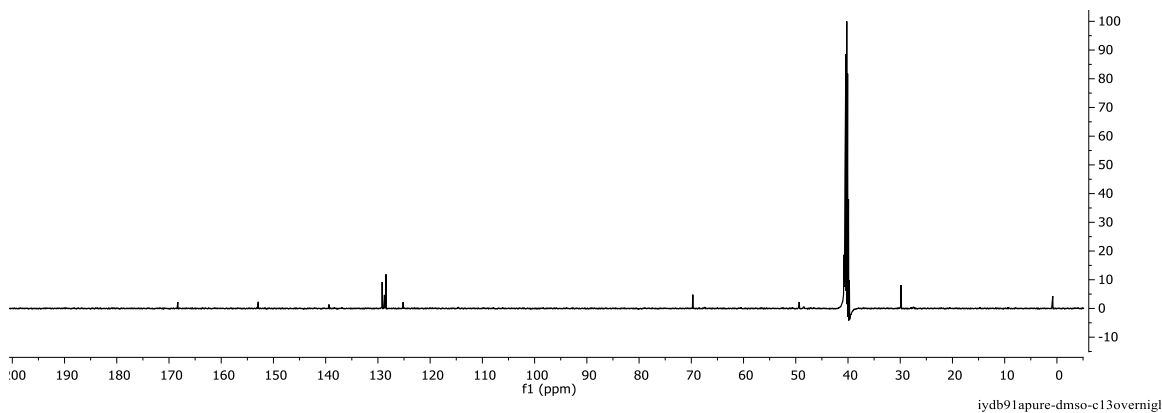
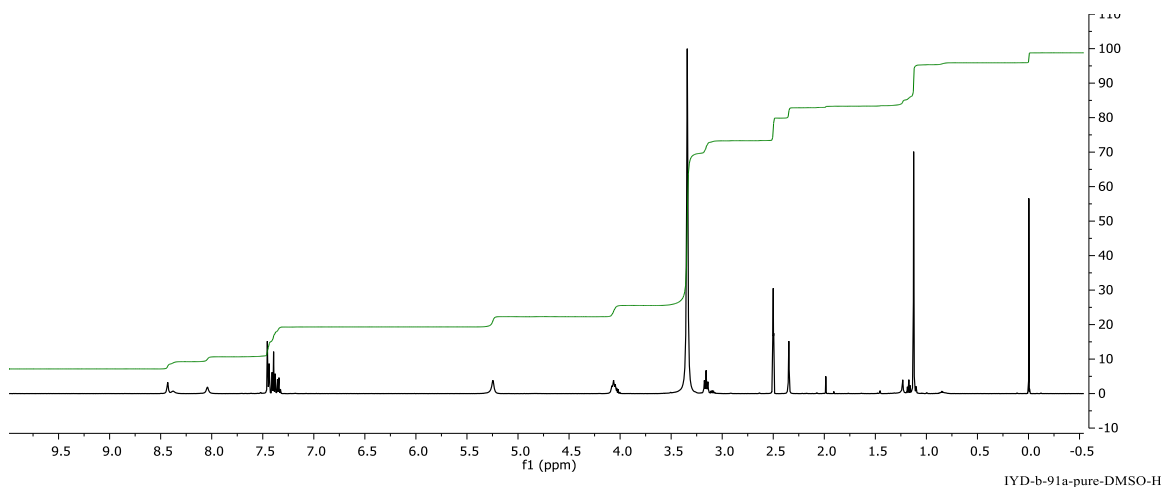
**(Z)-N'-((1-Acetyl-5-bromoindolin-6-yl)sulfonyl)-3-hydroxy-N,3-dimethylbutanimidamide**

**(64a).** Prepared according to general procedure [A]. Flash column chromatography (silica gel, with 1:99 MeOH (sat. NH<sub>3</sub>)-CH<sub>2</sub>Cl<sub>2</sub> as eluent) for afford 52.6 mg of a white solid at 42 % yield. mp = decomposes at 218 °C. <sup>1</sup>H NMR (500 MHz, DMSO-d<sub>6</sub>): δ 8.74 (s, 1H), 8.28 (br s, 1H), 7.59 (s, 1H), 5.11 (s, 1H), 4.14 (t, *J* = 8.75 Hz, 2H), 3.18 (t, *J* = 8.5 Hz, 2H), 2.87 (s, 2H), 2.74 (d, *J* = 4.5 Hz, 3H), 2.17 (s, 3H), 1.15 (s, 6H). <sup>13</sup>C NMR (500 MHz, DMSO-d<sub>6</sub>): δ 170.0, 167., 142.9, 142.3, 138.1, 131.5, 116.4, 113.3, 69.7, 49.2, 45.2, 30.2, 29.1, 27.7, 24.6.

**65a**

**Benzyl (Z)-6-(N-(1-amino-3-hydroxy-3-methylbutylidene)sulfamoyl)-5-chloroindoline-1-carboxylate (65a).** To  $\text{NH}_4\text{Cl}_{(s)}$ ,  $\text{CH}_2\text{Cl}_2$ , and triethylamine were added to 1-Cbz-5-chloroindoline-6-sulfonyl azide starting material at room temperature, followed by addition of copper iodide and the alkyne. Reaction was left to react at room temperature for 3.5 hours and monitored by TLC and HPLC. At 3.5 hours, a TLC was taken in 80-20 EA-PE, which indicated consumption of starting material. Then the reaction was diluted with  $\text{CH}_2\text{Cl}_2$  (804  $\mu\text{L}$ ) followed by 500  $\mu\text{L}$   $\text{NH}_4\text{Cl}$ . Reaction was allowed to stir at room temperature for 30 min. Reaction was

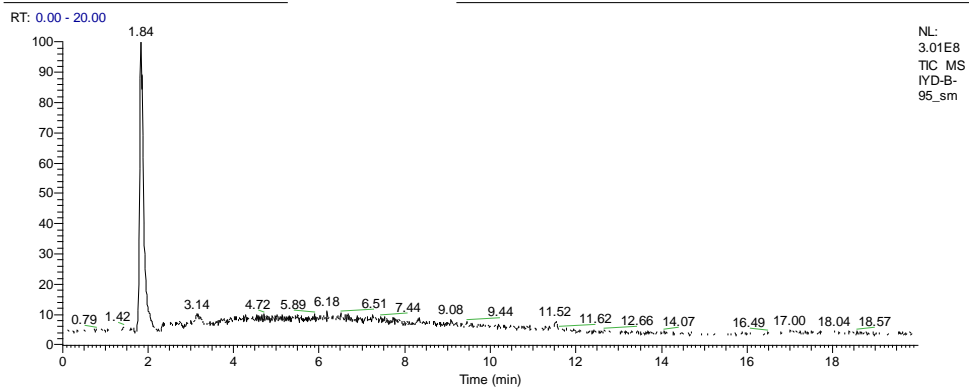
then concentrated to dryness on the rotary evaporator (not heated more than 40 °C) and left to dry overnight under vacuum. The crude product was dissolved in EA and pipetted from  $\text{NH}_4\text{Cl}_{(s)}$ . Gravity column chromatography (334 mg silica gel, 80-20 EA-Pet. E.) afforded 28 mg of a dark yellow solid at 47 % yield found to be 96 % pure by HPLC. mp = 165.4 -168.8 °C.  $^1\text{H}$  NMR (500MHz,  $d_6$ -DMSO):  $\delta$  8.40 (d, J = 28.5 Hz, 2H), 8.04(s, 1H). 7.45-7.33 (m, 6H), 5.25 (s, 2H), 5.25 (s, 2H), 4.87 (s, 1H), 4.06-4.02 (m, 2H), 3.16 (t, J = 8.5 Hz, 2H), 2.35 (s, 2H), 1.23-1.10 (m, 6H).  $^{13}\text{C}$  NMR (500MHz,  $d_6$ -DMSO):  $\delta$ 168.3, 152.9, 139.4, 129.2, 128.8, 128.5, 125.2, 69.7, 49.4, 40.7, 40.6, 40.4, 29.9. HRMS (ESI/APCI on IT-TOF) m/z calcd. for  $\text{C}_{21}\text{H}_{24}\text{N}_3\text{O}_5\text{SCl}$  [M] $^+$ : 465.1102, found: 465.1125.



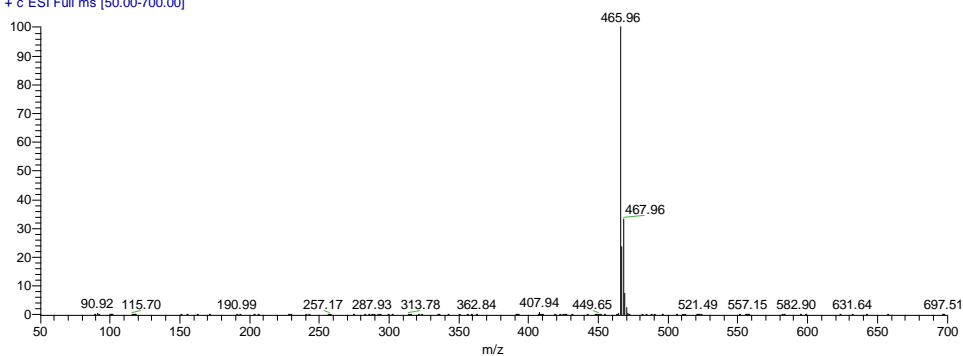


C:\XcaliburA...IYD-B-95\_sm

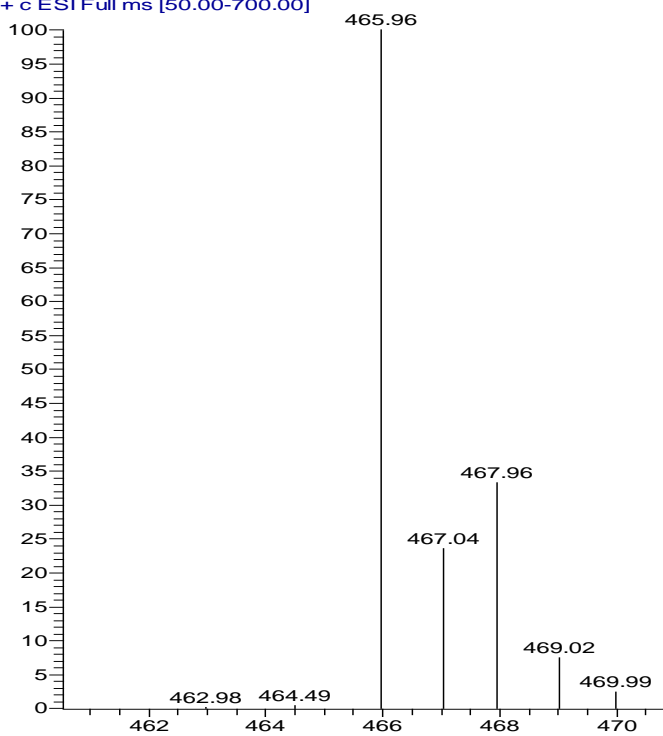
8/12/2016 7:20:43 PM



IYD-B-95\_sm #125 RT: 1.83 AV: 1 NL: 1.51E8  
T: + c ESI Full ms [50.00-700.00]



IYD-B-95\_sm #125 RT: 1.83 AV: 1 NL: 1.51E8  
T: + c ESI Full ms [50.00-700.00]



CHAPTER FIVE  
CYCLOBUTANONE BINDING IN COBALT FUNCTIONALIZED  
HOMOSERINE METALLO- $\gamma$ -LACTONASE AiiA

**Abstract**

We have synthesized and tested several  $\alpha$ -amido cyclobutanones possessing a C6 or C10 hydrocarbon tail which exhibit binding to AiiA related di-Zn-dependent lactonase metallo centers, enabling determination of two separate three-dimensional structures of N-(2-oxocyclobutyl)hexanamide (**1**) and N-(2-oxocyclobutyl)decanamide (**2**), bound to AiiA-Cobalt active site, respectively. The electron density of the C6 analog (**1**) co-crystal was not resolved enough to make an accurate ligand atom placement. However, the extra length of the C10 alkyl chain of compound **2** enabling interaction with the hydrophobic phenylalanine clamp region of AiiA, adjacent to the active site,<sup>60</sup> resulted in higher resolution structure enabling atomic placement of the ligand atoms including the C10 alkyl chain. The determination of the co-crystalized cyclobutanone did not show the presence of the trapped tetrahedral transition-state mimetic of cyclobutanone, as expected, but rather the ring-opened byproduct 4-decanamidebutanoic acid (**3**). Follow-up experiments were performed to determine whether the presence of the observed ring-opened product originated from

enzymatic catalysis or radiation damage during crystallographic data collect. A discontinuous assay experiment was performed in conjunction with radical-catalyzed organic reaction screening with AIBN,  $\text{H}_2\text{O}_2$ , and  $\text{H}_2\text{O}_2$  in the presence of various metal salts. A series of radical-mediated synthetic experiments were also carried out to assess the ability the cyclobutanone to be opened under chemical means.

### Introduction

Bacterial infections are a growing global medical problem, and there is an urgent need for antibacterial agents with new cellular mechanisms of action. There has been increasing attention surrounding cyclobutanones and their specific inhibitory properties towards serine hydrolases, serine- $\beta$ -lactamases and metallo- $\beta$ -lactamases. The restricted nature of a four-membered cyclobutanone ring causes the carbonyl carbon to become much more electrophilic.<sup>183, 184</sup> Thus, this increased strain associated with the four-membered cyclic ketone is partially released upon hydration, with the hydrated form of cyclobutanone closely resembling transition state of a wide-range of metalloenzyme classes.

OXA-10, KPC-2, and CG1 are broad spectrum serine- $\beta$ -lactamases that have been shown to be susceptible to inhibition by cyclobutanones. Recent studies have reported crystal structure showing a cyclobutanone analog of penicillin covalently bound to the catalytic serine in OXA-10's active site (Figure 53A).<sup>185</sup>

A recent crystal structures of FTT258, a serine hydrolase with broad substrate specificity that binds to bacterial membranes in the Gram-negative bacterium *F. tularensis*, shows a cyclobutanone inhibitor covalently bound to Ser116 was also reported by our research group (Figure 53B). Large conformational changes were observed in the protein structure when in the

presence of this cyclobutanone ligand, presumably interfering with regulating membrane binding and catalytic activity of acyl protein thioesterases.<sup>186</sup>

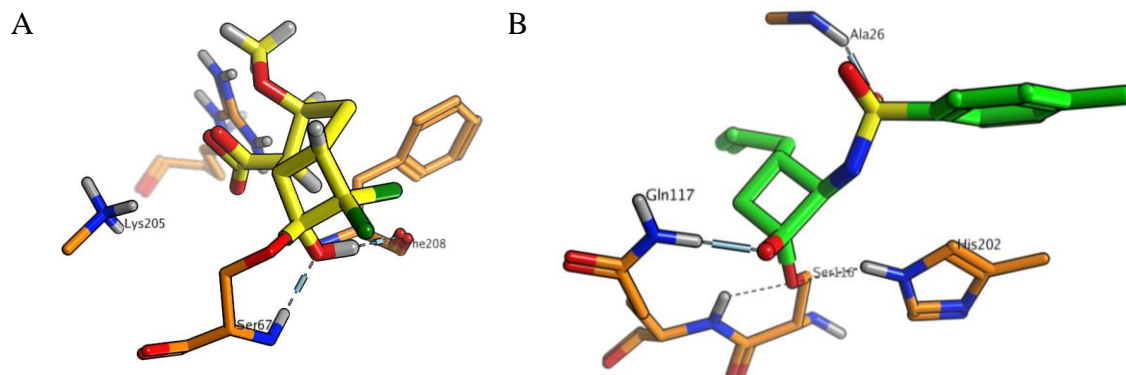


Figure 53. A) Structure of Oxa-10 complexed with Cyclobutanone derivative of penicillin as serine-bound hemiketal (PDB ID: 3LCE), B) Structure of a serine hydrolase from *Francisella tularensis* complexed as a serine-bound hemiketal with N-Cyclobutanone sulfonamide inhibitor (PDB ID: 4F21). The tosylamide was not observed in the crystal structure, but has been modeled in for this Figure.

Continuing our investigation toward developing new methods of interacting with pharmaceutically relevant metalloenzymes, we explored the ability for cyclobutanone functionalities to interact at the di-metallo site of metalloenzyme. We chose to investigate co-crystallization experiments with the wildtype di-cobalt functionalized metalloenzyme Autoinducer inactivator A (AiiA) provided by our collaborators in the Walter Fast group at UT-Austin. AiiA is a metal-dependent N-acyl homoserine lactone (AHL) hydrolase that displays broad substrate specificity, but shows a preference for substrates with long, hydrophobic N-acyl substituents (Figure 54).<sup>60, 187</sup>

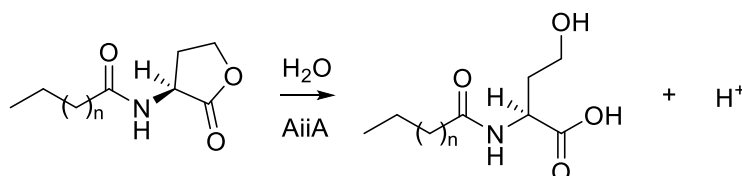


Figure 54. N-acyl-L-homoserine metallo- $\gamma$ -lactonase (AiiA, AHL lactonase) catalyzes the hydrolysis of N-acyl-L-homoserine lactones to the corresponding ring-opened products, the corresponding N-acyl-L-homoserines.<sup>187</sup>

AiiA and related metallo-lactonase AidC utilize a di-Zn metallo center to catalyze the hydrolysis of important N-acyl homoserine lactones that are important for cell to cell communication between bacteria.<sup>56, 58, 59, 188</sup> Development of drug-like molecules that are capable of targeting metal centers in AiiA and related enzymes is predicted to disrupt the quorum sensing/quenching mechanism between bacterial communities and provide another chemical tool for studying these systems. Since each species of bacteria has specific and unique molecules for quorum sensing, tailor-made inhibitors may modulate the risk of specific bacterial proliferation<sup>59</sup> Recently, we have made efforts to target AiiA related di-Zn-dependent lactonase with a small series of  $\alpha$ -amido cyclobutanones possessing a C6 and C10 hydrocarbon tail, synthesized using chemistry pioneered in our laboratory,<sup>189</sup> and our collaborators in Dr. Liu's lab here at Loyola were able to obtain and solve the crystal structures of AiiA complexed to a cyclobutanone analog bearing a 10-carbon hydrophobic tail.

The electron density of the C6 cyclobutanone co-crystal was not resolved enough to make an accurate atom placement. However, because the extra length, the C10 alkyl chain derivative was able to interact with the hydrophobic phenylalanine clamp region of AiiA adjacent to the active site<sup>60</sup> enabling atomic placement of the C10 alkyl chain and cyclobutanone-derived functionality of N-(2-oxocyclobutyl)decanamide (**2**). However, the determination of the co-crystalized cyclobutanone did not show the presence of the hypothesized tetrahedral transition-state mimetic of cyclobutanone as depicted in Figure 55A, but rather a ring-opened byproduct 4-decanamidebutanoic acid (**3**) shown in Figure 55B. The ring-opened byproduct **3** was synthesized, and the structure was confirmed with NMR.

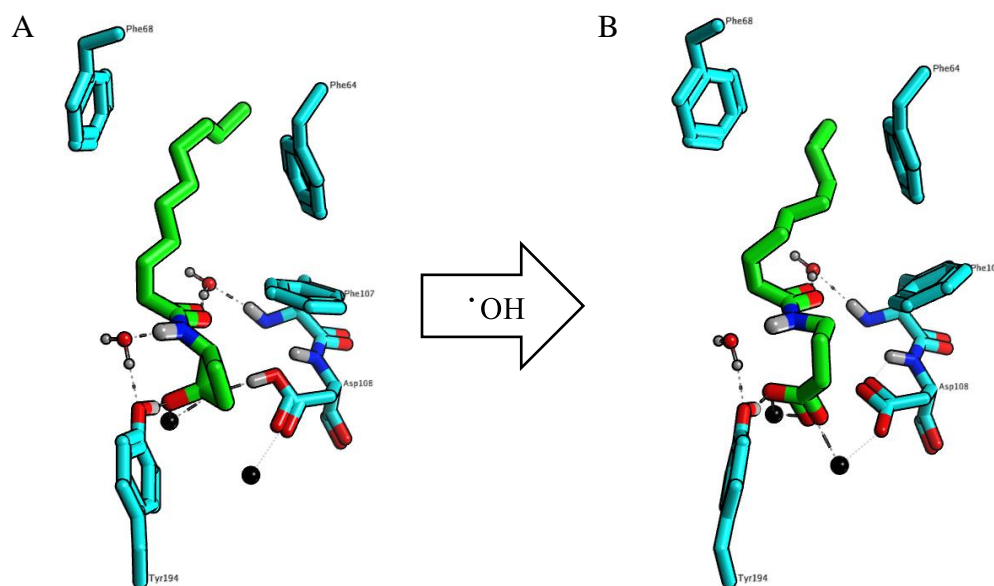


Figure 55. Depiction of AiiA\_Co AHL metallo-lactonase structure bound to: A) Hypothesized N-(2-oxocyclobutyl)decanamide as the tetrahedral transition state mimetic (PBTSM Generated Model), B) Observed ring-opened byproduct 4-decanamideobutanoic acid (PDB ID: TBD). We hypothesize that the opening is mediated by hydroxyl radicals generated during X-ray irradiation.

Our working hypothesis is that the C-C bond breakage was catalyzed by either bulk solvent radical hydroxides or by a radical induced tyrosine in close proximity to the metal active site. Follow-up experiments were performed to determine whether the presence of the observed ring-opened GABA product originated from enzymatic catalysis, radicals in the presence of enzymes, or purely through radiation damage during crystallographic data collect. We performed a series of cyclobutanone digestion experiments to test our hypothesis. A discontinuous HPLC assay experiment was performed with cyclobutanone **2** with varied incubation times and concentrations of AiiA\_Co enzyme. We also attempted a series of radical-mediated synthetic cyclobutanone digestions experiments to assay the ability the cyclobutanone to be opened under chemical means. Reaction screenings with our **2** in the presence AIBN,  $\text{H}_2\text{O}_2$ , or  $\text{H}_2\text{O}_2$  in the presence of various metal salts to chemically generate radicals *in situ*. Recently we have conducted experiments at Argonne National Lab using the X-ray beamline to

perform X-ray induced cyclobutanone digestion experiments in the presence or absence of AiiA\_Co. The cyclobutanone in buffer was exposed to X-rays under varying concentrations of enzyme and exposure times followed by analysis using LC-MS.

Supplemental *in silico* modeling was performed in order to gain further understanding of the pre-ring opened binding mode of the bounding dynamics of cyclobutanone analog. We employed the *in silico* Product-Based Transition-State Modeling (PBTSM) technique using the Molecular Operating Environment (MOE) computation suite provided through Loyola's Department of Chemistry and Biochemistry, to reconstruct the hypothetical intact cyclobutanone ring inside the active site of AiiA\_Co.

## Materials and Methods

### Materials.

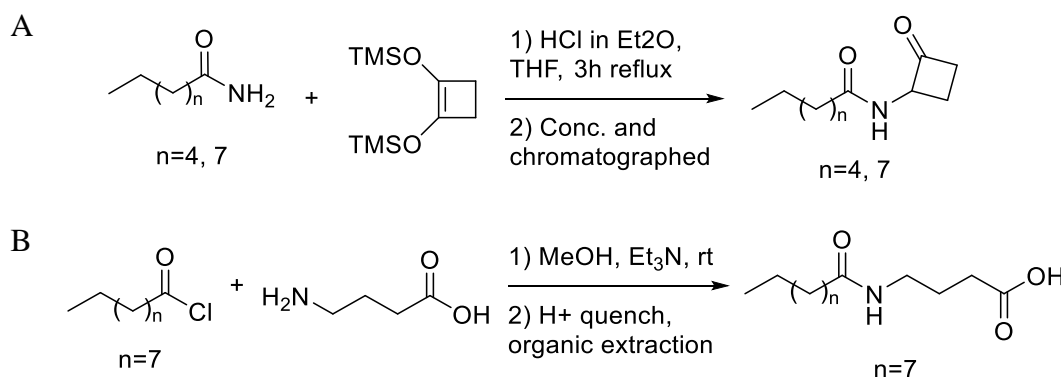
All solvents were distilled prior to use, and all reagents were used without further purification unless otherwise noted. All synthetic reactions were conducted under a nitrogen or argon atmosphere. Silica gel 60A, 40–75  $\mu\text{m}$  (200  $\times$  400 mesh), was used for column chromatography. Aluminum-backed silica gel 200  $\mu\text{m}$  plates were used for TLC.  $^1\text{H}$  NMR spectra were obtained using either a 300 MHz spectrometer or a 500 MHz spectrometer with trimethylsilane (TMS) as the internal standard.  $^{13}\text{C}$  NMR spectra were obtained using a 500 MHz spectrometer. HRMS spectra were measured on a TOF instrument by electrospray ionization (ESI). All other reagents for biochemical assays were purchased at the highest quality available.

### Synthesis.

Installation of the alpha-amidocyclobutanones were carried out per protocol described by Becker *et al.*<sup>189</sup> 1,2-Bis(trimethylsilyloxy)cyclobutene was reacted with hexanamide, and also with decanamide, affording the  $\alpha$ -amido cyclobutanone derivatives **1** and **2**, respectively. As

detailed below, **1** and **2** were included in co-crystallization efforts with AiiA-Cobalt metallolactonase. Compounds **1** and **2** yielded electron density with only the latter possessing sufficient resolution for structural determination. As per literature precedent,<sup>190</sup>  $\gamma$ -aminobutyric was reacted with decanoic acid in the presence of triethylamine to afford the ring-opened GABA derivative **3**, as observed in the aforementioned crystal structure. The desired products were isolated in high purity and synthetic routes summarized in Scheme 12 below.

Scheme 12: Synthesis of  $\alpha$ -amido cyclobutanones **1**;  $n=4$  & **2**;  $n=7$ , under anhydrous acidic conditions with primary amides.<sup>191, 192</sup> B) Synthesis of ring-opened analog 4-decanamideobutanoic acid **3**.<sup>190</sup>



### Discontinuous HPLC analysis.

High-performance liquid chromatography (HPLC) analysis was performed according to previously described method, with modifications.<sup>193</sup> To analyze the possible carbon-carbon bond cleavage catalyzed by AiiA-Cobalt, Romilla Mascarenhas and I set up a several enzyme incubation experiments with the C10 cyclobutanone in the presence of AiiA<sub>Co</sub> (in 50 mM HEPES pH7.5) at 37 °C. Reaction trials were quenched with acetonitrile at 10 sec, 30 sec, 1 min, 5 min, 2 hours, and 2.5 days. Final concentrations were set for C10 cyclobutanone = 0.5mM and AiiA<sub>Co</sub> = 0.04 mg/mL with blanks having all of the above except for the AiiA<sub>Co</sub>. Samples were chromatographed on an HPLC system Hewlett Packard 1050 series with a diode array detector (DAD) set to monitor at 205 nm by use of a Regis Little Champ II ODS guard column



coupled to a SymmetryShield RP18, 3.3  $\mu\text{m}$ , 100A. Pre-incubated and filtered samples were loaded into standard sized VWR autosampler HPLC vials fitted with 300  $\mu\text{L}$  conical glass insert. Samples were eluted on a 5 % AN (0.1v/v TFA)-H<sub>2</sub>O [A]/ 5 % AN (0.1v/v TFA) [B] at 1 mL/min flow rate. The analysis method employed a solvent gradient from 90 % A / 10 % B at time 0 to 10 % A / 90 % B at time 15 mins. At time 15.1 mins the gradient switch to 90 % A / 10 % B for a re-equilibration period until the end of the method at time = 25 mins.

### **Chemically-Induced Radical-Mediated Cyclobutanone Ring-opening.**

Along with the discontinuous HPLC enzyme assay analysis we also set up a series of experiments where cyclobutanone **2** was incubated in the presence of various radical forming reagents which include, AIBN in MeOH at 60 °C for 2-8 h, low concentrations of H<sub>2</sub>O<sub>2</sub> in H<sub>2</sub>O at 60 °C for 2 hours, high concentration of H<sub>2</sub>O<sub>2</sub> in acetone at room temperature over 3 hours, low concentrations of H<sub>2</sub>O<sub>2</sub> and catalytic amounts of FeCl<sub>2</sub> at room temperature of 2 hours. HPLC samples were collected from the incubated reactions and analyzed against standards of **2** and **3**.

### **X-ray Exposure Cyclobutanone Digestion.**

We have synthesized a C10 cyclobutanone for AiiA for our collaboration with the Liu crystallography lab and have obtained a structure. However, the we observe the ring-opened C10-GABA derivative in the active site which begs the interesting question of how this C-C bond in the cyclobutanone structure was broken. Whether the enzyme caused or somehow participates in the opening, or whether a hydroxyl radical from X-ray irradiated H<sub>2</sub>O molecules in the crystal sample are generated around the active site and subsequently abstracts a hydrogen atom from the cyclobutanone bound tetrahedral structure is still under debate. To test the contribution of high energy X-ray irradiation in the mechanism that led to the opening of the cyclobutanone ring in the active site of AiiA\_Co, we have conducted series of X-ray exposure

experiments at Argonne National laboratory's X-ray beamline. The experiment was conducted by preparing a series of buffered solutions charged with the C10-cyclobutanone derivative **2** in the presence of varying concentrations of AiiA\_Co. The samples were loaded into 150  $\mu\text{L}$  glass HPLC insert with 50  $\mu\text{L}$  reaction solution and mounted to the crystal holding apparatus of station 19BM using green hobby clay (Figure 56A). The mounted samples were capped with a plug with clay and then rotated along the glass tubes axis and irradiated with a continuous X-ray flux =  $1.7 \times 10^{11}$  eV, rotating every  $2^\circ$  for  $360^\circ$  with 1 or 10 second X-ray exposures per intervals per degree. The X-ray exposures were observed to create visible glass etching rings on the sample vial inserts for every complete revolution around the radial axis (Figure 56B).

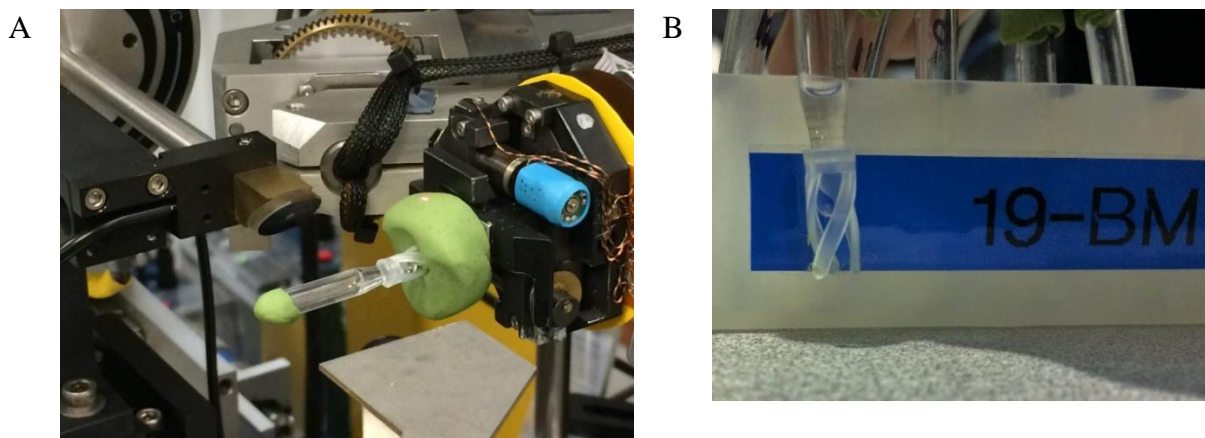


Figure 56. X-ray exposure cyclobutanone digestion setup. A) sample mounting setup, B) X-ray etched glass inserts.

A total of 11 samples were collected over two visits to Argonne. Conditions for the 11 samples are summarized in Table 14 below. The processed samples were further analyzed for

ring-opened GABA derivative peak development through LC-MS by Marlon Lutz of Regis LLC.

Results are still pending.

Table 14. X-ray Exposure Cyclobutanone Digestion Sample Conditions.<sup>a</sup>

| #         | Exposure   | Revolution | AiiA_Co Conc.                   | C10-CB Conc. | HEPES Conc.                      |
|-----------|------------|------------|---------------------------------|--------------|----------------------------------|
| <b>C1</b> | 10.0 s / ° | 2rev       | NA                              | NA           | 100.0 mM                         |
| <b>C2</b> | 10.0 s / ° | 2rev       | NA                              | 50.0 mM      | NA<br>(CH <sub>3</sub> CN Blank) |
| <b>1</b>  | 1.0 s / °  | 4rev       | NA                              | 1.0 mM       | 50.0 mM                          |
| <b>2</b>  | 10.0 s / ° | 3rev       | NA                              | 1.0 mM       | 50.0 mM                          |
| <b>3</b>  | 1.0 s / °  | 4rev       | 1.0 µL 1.2 mg/mL<br>of AiiA_Co  | 1.0 mM       | 50.0 mM                          |
| <b>4</b>  | 10.0 s / ° | 3rev       | 1.0 µL 1.2 mg/mL<br>of AiiA_Co  | 1.0 mM       | 50.0 mM                          |
| <b>5</b>  | 1.0 s / °  | 4rev       | 5.0 µL 1.2 mg/mL<br>of AiiA_Co  | 2.5 mM       | 50.0 mM                          |
| <b>6</b>  | 10.0 s / ° | 2rev       | 5.0 µL 1.2 mg/mL<br>of AiiA_Co  | 2.5 mM       | 50.0 mM                          |
| <b>7</b>  | 10.0 s / ° | 2rev       | 10.0 µL 1.0 mg/mL<br>of AiiA_Co | 2.5 mM       | 10.0 mM                          |
| <b>8</b>  | 10.0 s / ° | 2rev       | 10.0 µL 1.0 mg/mL<br>of AiiA_Co | 1.0 mM       | 10.0 mM                          |
| <b>9</b>  | 10.0 s / ° | 2rev       | 10.0 µL 1.0 mg/mL<br>of AiiA_Co | 5.0 mM       | 10.0 mM                          |

<sup>a</sup>Table Legend: C1 & C2 = control sample 1 & 2. rev = revolutions around sample vial radial axis.

### Product-Based Transition-State Modeling (PBTS) of AiiA\_Co.

We employed the ring-opening C10-GABA derivative bound co-crystal structure as a starting point to model in reverse chronology the hypothesized cyclobutanone tetrahedral transition state intermediate structure, as well as the cyclobutanone inhibitor-bound AiiA models containing metal bound catalytic hydroxyl or catalytic water respectively. This method, which we refer to as “Product-Based Transition State Modeling” (PBTS or PBTS modeling), is intended to provide a hypothetical model of the cyclobutanone’s tetrahedral transition state mimetic binding geometry in AiiA’s active site before the presumed X-ray induced ring opening

event. This modeling technique was performed using the Chemical Computing Group's Molecular Operating Environment (MOE).<sup>76</sup> A step by step description of the PBTSM protocol is outline in Figure 57 below, which for hereafter will be referred to as Figure 57-Step# in the following text to reference steps 1 through 7.

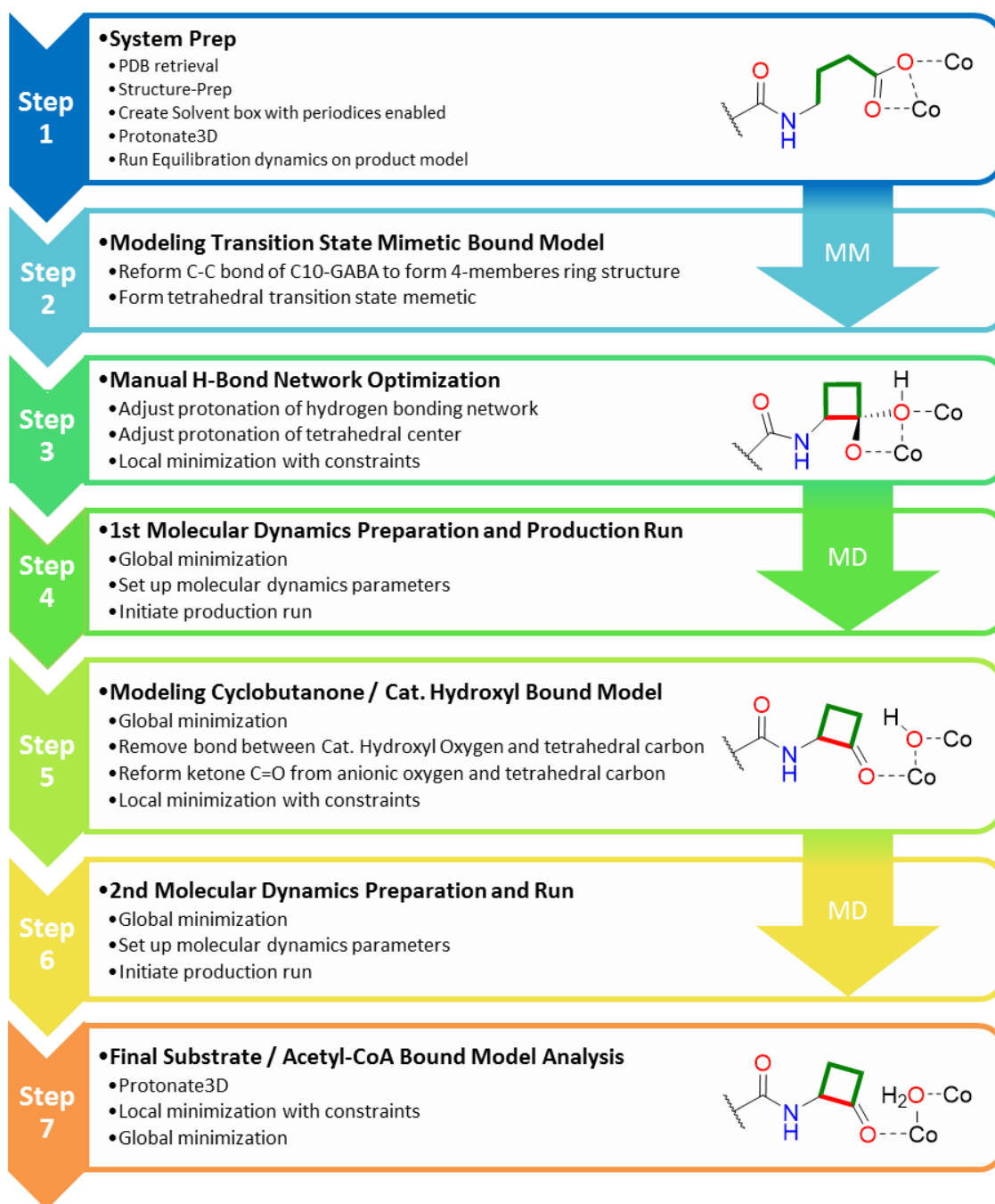


Figure 57. PBTSM Protocol for AiiA\_Co.

After upload of the crystallographic data, the system was prepared using MOE's utility Structure-Prep to correct problems encountered in crystallographic data such as missing loops, empty residues, chain termini or breaks, missing disulfide bonds or atom names, picking alternate conformations, and other potential artifacts.<sup>76</sup> The model was then solvated in a simple water box at pH of 7.4 which was treated with NaCl counter ions to balance the charge. Periodic boundary conditions were enabled, and the hydrogen bonding network of the model was optimized by automatic sampling different tautomer/protomer states using Protonate3D.<sup>77</sup> Protonate3D is employed to calculate optimal protonation states, including titration, rotamer and "flips" using a large-scale combinatorial search.<sup>78</sup> A localized energy minimization was run on the solvated system using the MOE function QuickPrep followed by a short global minimization to equilibrate the system for further modeling. After structural preparation, solvation and energy optimization using MOE, the ring-opening C10-GABA bound AiiA\_Co molecular model is referred to as the C10-GABA-prod\_AiiA\_Co model (Figure 57-Step1).

Upon completion of system equilibration, product atom coordinates were used to model the tetrahedral transition state mimetic expected with the cyclobutanone-catalytic hydroxyl bound structure. This model was referred to as the C10-CB-TS\_AiiA\_Co model and reflects the moment just after nucleophilic attack by the activated hydroxyl group at the ring strained cyclobutanone which forms the tetrahedral transition state mimetic structure. The double bond of the C10-GABA carbonyl, proximal to the metal center, were converted to a single bond the bond between the  $\gamma$  carbon and carbonyl carbon of the C10-GABA derivative was reformed using the Builder utility in MOE. The results of these modeling transformations are the creation of a distorted four membered cyclobutanone ring in the hypothesized tetrahedral transition state mimetic inhibitor state. (Figure 57-Step2).

The hydrogen bonding network of the model was then systematically optimized. Charge adjustment of the tetrahedral atoms were applied to the formal catalytic hydroxyl/water atoms and the oxygen associated with the ketone carbonyl resulting in a neutral and negative charge respectively. This was followed by hydrogen bond network optimization of the important active site residues critical for catalysis and transition state mimetic stabilization. These residues were manually adjusted so that active site formal charges kept the overall net charge of the system balanced throughout the process and conservation of matter was strictly adhered too. In total, these minor, but critical system adjustments most heavily effected the ionization states and hydrogen bonding motifs of the Asp108 side chain, considered to be the general acid-base during catalysis, and the atoms associated with the ketone oxygen atoms and catalytic water/hydroxyl group atoms.

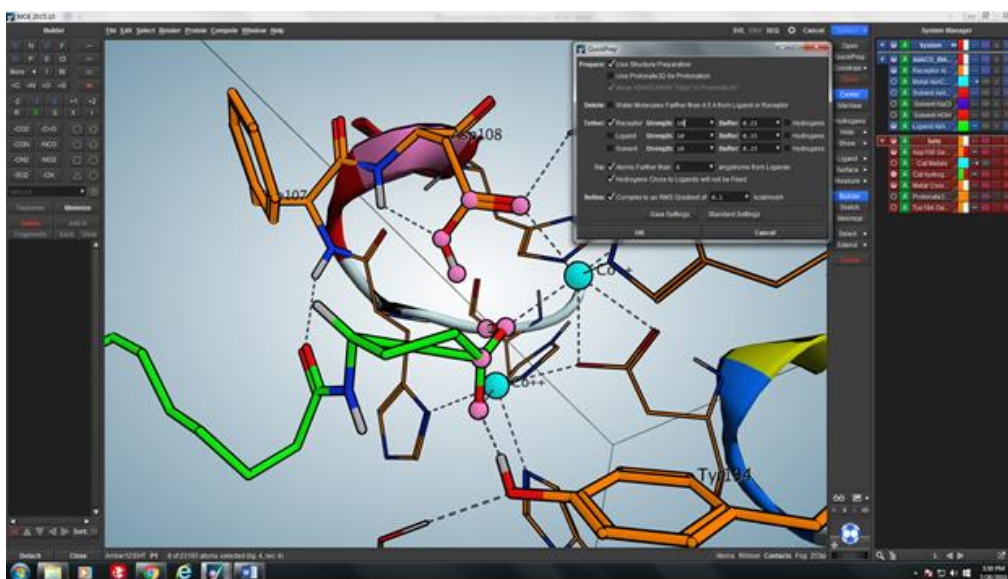


Figure 58. Distorted cyclobutanone transition state mimetic before minimization.

At this stage in the protocol, a localized minimization was conducted to normalize the bond distances/angles of the cyclobutanone ring and tetrahedral atom center to reasonable values as well as balance the net charges of ligand/receptor system (Figure 57-Step3). Following preparation of the *in silico* generated substrate transition state intermediate model, a relatively

short 1.0 ns molecular dynamics equilibration was performed using an NPA algorithm with a Amber12:EHT force field. The MD experiment was initiated with parameters as followed: initial heating from 0K to 300 K over 100 ps followed by equilibration for 100 ps at 300 K, followed by a 700 ps production run, and finally a 100 ps cooling from 300K to 0 K (Figure 57-Step4).

After completion of the dynamics equilibration run, three major changes were observed in the transition state mimetic bound model. The hydrogen bond network strengthened, as indicated by swelling hydrogen bond and VDW contact-cylinder representations, an increase in atom distance of the two catalytic Cobalt atoms from 3.67 Å to 4.09 Å was observed, and the C10 alkyl chain relaxed slightly (Figure 59). This relaxation can be explained by an overall relaxation of crystal packing effects in the model system.

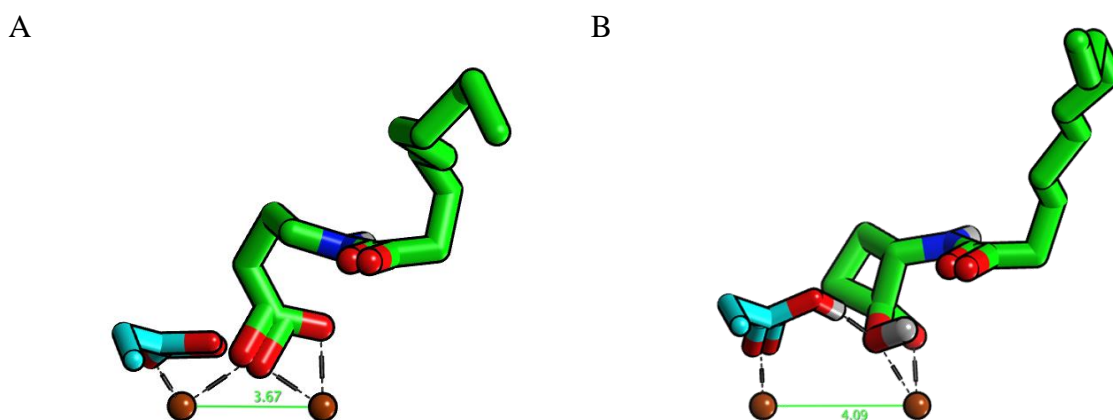


Figure 59. Molecular geometry differences of the active site resulting from transformations in steps 4 to 5 of the PBTSM protocol.

Step 5 in the PBTSM protocol used the final transition state mimetic model from the previous steps to estimate the atomic coordinates of the catalytic hydroxyl group and C10 cyclobutanone ligand bound to the metal center of AiiA. This following model was referred to as the C10-CB\_OH\_AiiA\_Co model and reflected the moment just after deprotonation of the

catalytic water by general acid-base Asp108 but just before nucleophilic attack by the activated hydroxyl group at the cyclobutanone carbonyl to relieve ring strain. MOE's Builder utility was again utilized to first remove the bond between the tetrahedral carbon center and the oxygen closest to Asp108 followed by a ionization state adjustment of the newly formed catalytic water/hydroxide oxygen to a negative ( $\text{O}^- \text{-C---X---OH}$  to  $\text{O}^- \text{-C}^- \text{-OH}$ ). Thus, the catalytic hydroxyl group, coordinated to the metallo-center, was modeled into the system in the approximate area observed in other known dinuclear metalloenzymes. Next, a double bond was reestablished between the tetrahedral carbon center and the anionic oxygen of the tetrahedral ( $\text{O}^- \text{-C}^- \text{ to O=C}$ ) to reform the cyclobutanone carbonyl. Finally, a local minimization with constraints was initiated to correct for distorted molecular bond angles and distances resulting from the Builder manipulations (Figure 57-Step5).

After the *in silico* generated cyclobutanone and catalytic hydroxide model was prepared, a second 1.0 ns molecular dynamics equilibration was performed using an NPA algorithm with a Amber12:EHT force field. The MD experiment was initiated with parameters as followed: initial system heating from 0K to 300 K over 100 ps followed by an equilibration stage at 300 K over 100 ps before an 800 ps production run at constant temperature. The dynamics experiment was concluded with a final 100 ps cooling stage from 300 K to 0 K (Figure 57-Step6).

After completion of the dynamics equilibration run, changes at the metal center were observed in the model. The negatively charged catalytic hydroxyl group forms a strong interaction with both cobalt ions leading to a decrease in distance between the cobalt atoms from 4.09 Å to 3.63 Å. The C10 alkyl chain again was seen to further relax as seen in Figure 60.



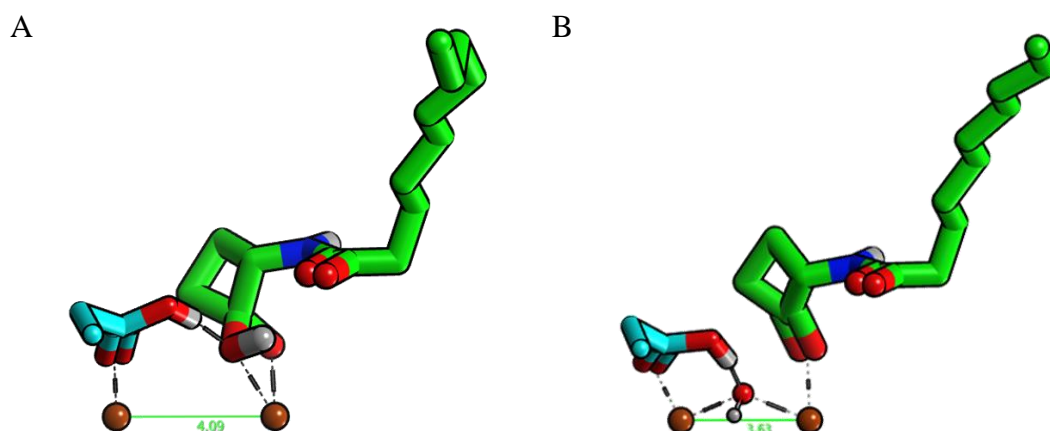


Figure 60. Molecular geometry differences of the active site resulting from transformations in steps 4 to 5 of the PBTSM protocol.

The last step in the PBTSM protocol was a continuation of the previously generated model which was used to estimate the atomic coordinates of the C10 cyclobutanone and catalytic water group bound to the metal center of AiiA. This last model was referred to as the the C10CB-TS\_AiiA\_Co-refined model and reflected the moment just after ligand complexation to the Cobalt metal site but just before activation of the catalytic water by Asp108 deprotonation. The final model was generated using Protonate3D followed by QuickPrep to reoptimize the hydrogen bonding network and perform a localized energy minimization before a final global energy minimization was applied to the model (Figure 57-Step7). The final steps in the PBTSM protocol results in deprotonation of the neutralized carboxylic acid side chain of Asp108 along with a simultaneous protonation of the catalytic hydroxyl group to form the catalytic water as depicted in Figure 61.

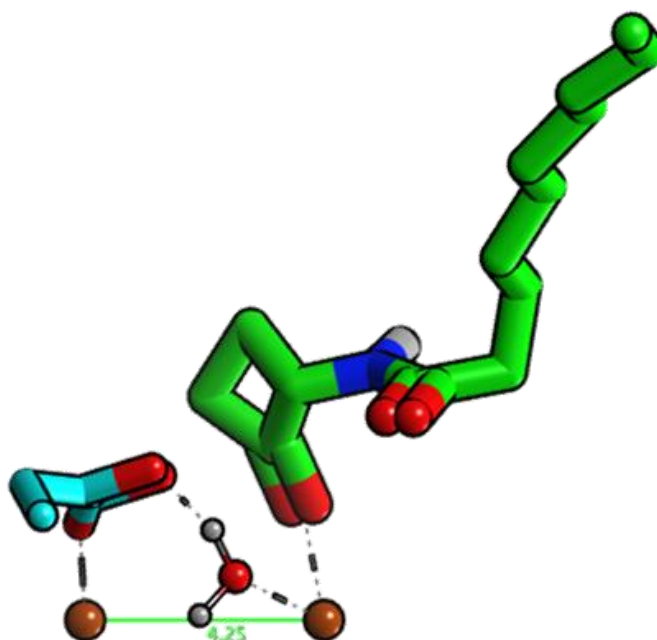


Figure 61. Final ligand binding geometry generated through PBTSM protocol.

## Results and Discussion

### Design of substrate analogs.

We previously found that the reactive  $\alpha$ -amido cyclobutanone moiety could form a tetrahedral intermediate species through covalent bond formation at the reactive serine residue as seen in the crystal structure of a serine hydrolase from *Francisella tularensis* complexed as a serine-bound hemiketal with N-Cyclobutanone sulfonamide inhibitor (PDB ID: 4F21).<sup>186</sup> We hypothesized that the extreme bond angles of the labile cyclobutanone moiety would translate into increase reactivity with the metal center of Quorum Quenching AiiA Metallo- $\gamma$ -lactonase through a similar tetrahedral species after reacting with the metal bound catalytic water/hydroxyl group. The reactive cyclobutanone warhead properties would be paired with modulation of the hydrocarbon tail to achieve interaction with the phenylalanine hydrophobic clamp to lock the ligand in place in the binding pocket.<sup>60</sup> Preliminary co-crystallization results with the C6  $\alpha$ -amido cyclobutanone derivative yielded X-ray structures that possessed limited electron density

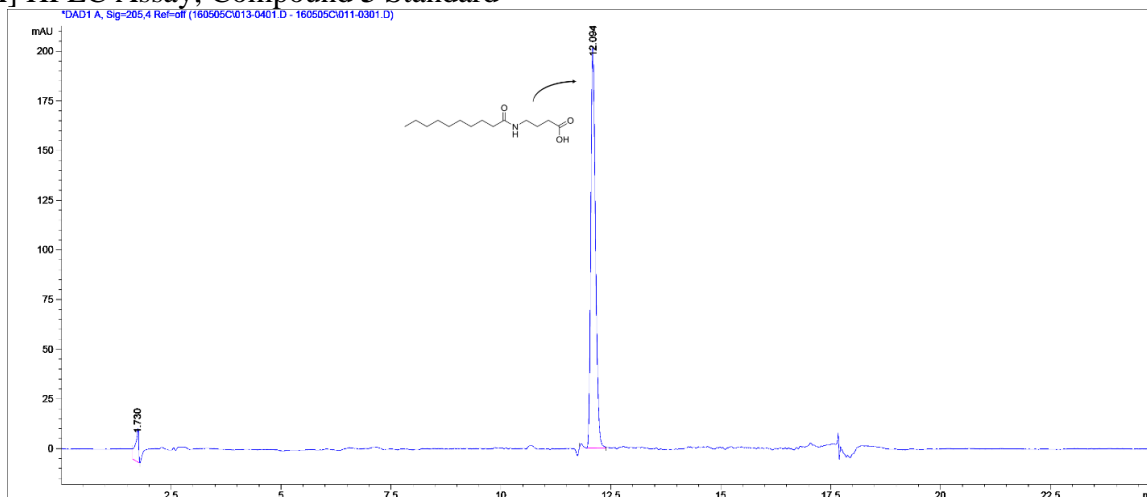
at the metal center but undefined density where the hydrocarbon tail would be expected. Co-crystallization results with the C10  $\alpha$ -amido cyclobutanone show well-defined electron density of the hydrocarbon tail sandwiched in a hydrophobic pocket region formed by the side chains of Thr67, Phe64, Phe68, Phe107 and Met136 as well as a disordered backbone loop made with the residues Glu136, Try137 and Met138. However, the existence of the ring-opened product bound in the active site of AiiA-Co begged the question of whether 4-decanamidebutanoic acid (3) was produced enzymatically, through radical induced side reactions initiated during crystallographic data collection, or a combination of both.

### Ring-opened Analog Formation Via Enzyme-mediated Mechanism.

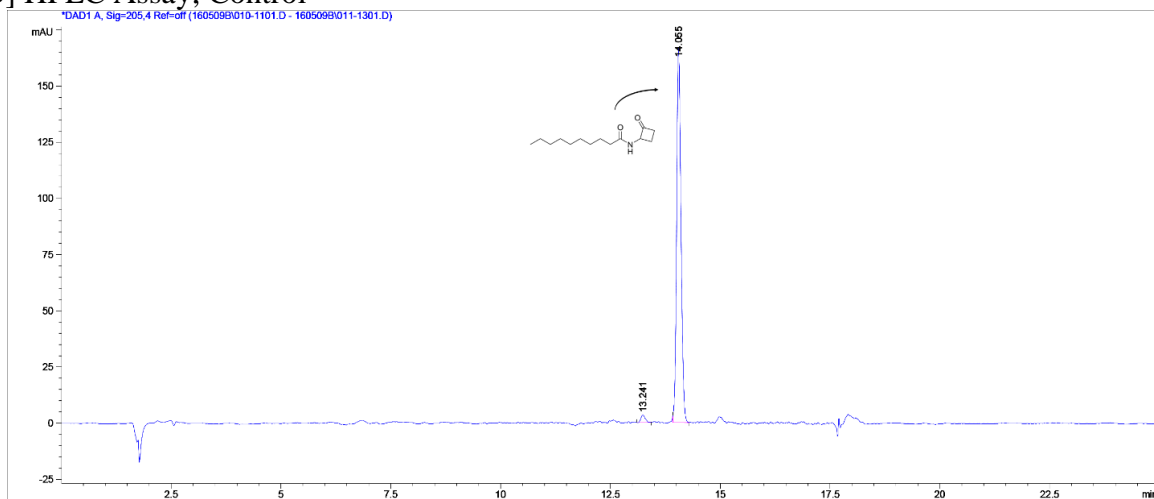
Analysis of the discontinuous enzyme assay with our cyclobutanone analog after exposure to AiiA-Cobalt did not give rise to any detectable ring-opened by-product as indicated by the HPLC results in Table 15 below.

Table 15. HPLC Results of discontinuous enzyme assay with cyclobutanone **2** exposure to AiiA\_Co. A) Standard HPLC of GABA analog **3**. B) Control HPLC of cyclobutanone **2** in Buffer only. C) HPLC Assay with 2.0 mM cyclobutanone **2** + 0.05 mM AiiA\_Co in Buffer incubated over 2 hours, D) HPLC Assay with 2.0 mM cyclobutanone **2** + 0.01 mM AiiA\_Co in Buffer incubated over 2 hours, E) HPLC Assay with 2.0 mM cyclobutanone **2** + 0.05 mM AiiA\_Co in Buffer incubated over 2.5 d.

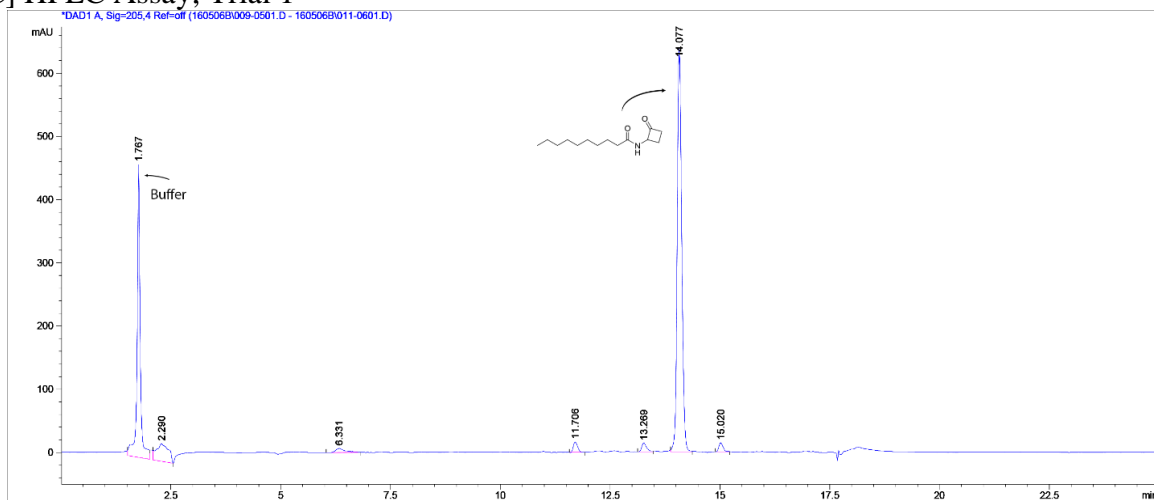
#### [A] HPLC Assay; Compound **3** Standard



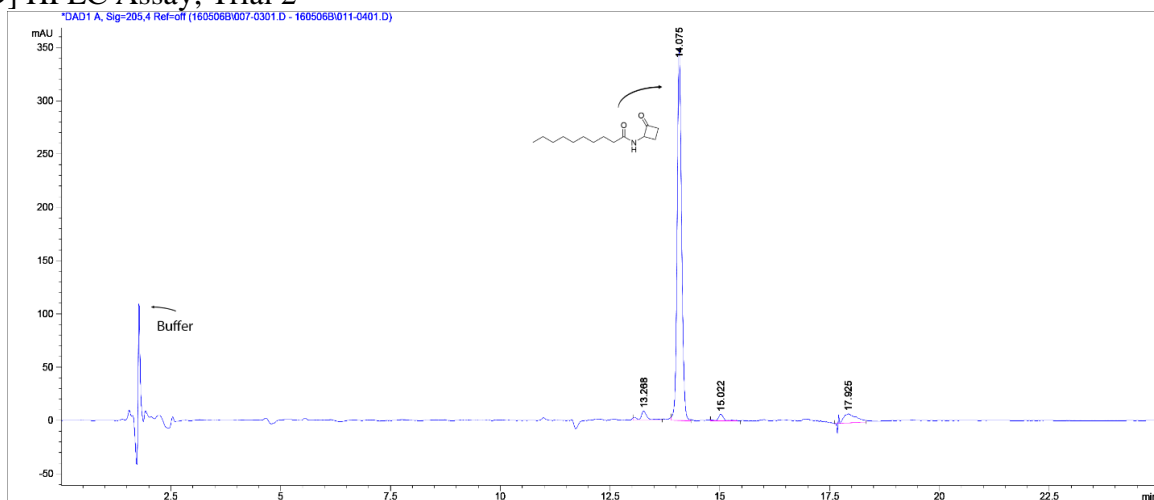
## [B] HPLC Assay; Control

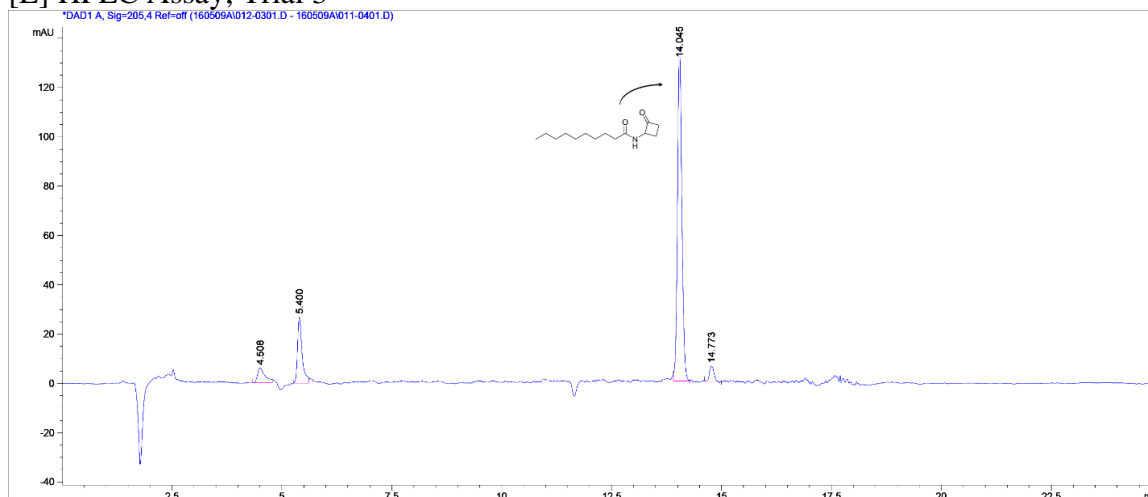


## [C] HPLC Assay; Trial 1



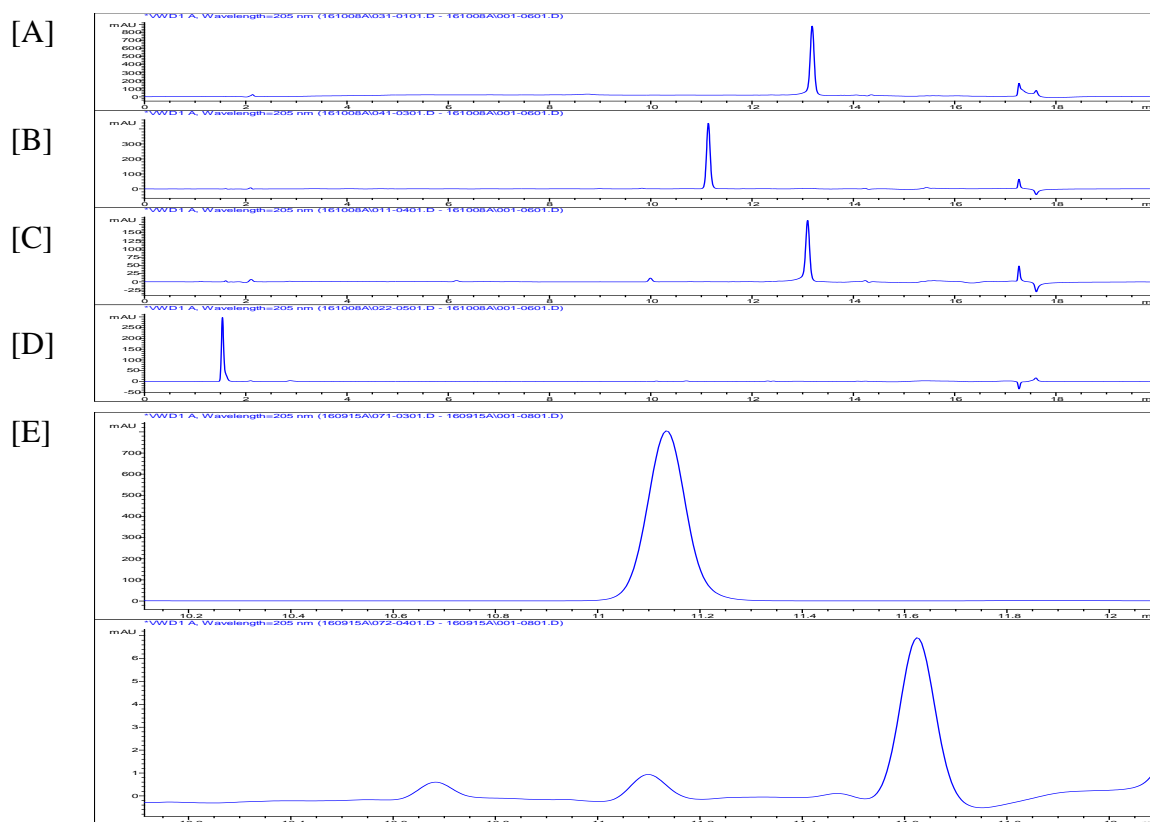
## [D] HPLC Assay; Trial 2



**[E] HPLC Assay; Trial 3****Ring-opened Analog Formation Via Radical-mediated Mechanism.**

The results of the chemically induced ring-opening experiments were inconclusive. Incubation of the cyclobutanone with AIBN showed no production of the ring opened C10-GABA product at 2 hrs and 8 hrs sampling by HPLC analysis (Table 16C). Fenton-like reaction conditions by the addition of  $\text{FeCl}_2$  to the  $\text{H}_2\text{O}_2$  were shown to lead to decomposition of **2** with no observable formation of **3** by HPLC (Table 16D). Incubation with  $\text{H}_2\text{O}_2$  only showed evidence of **3** in small amounts, observable by HPLC, when the cyclobutanone **2** was subjected to high concentration of 30 %  $\text{H}_2\text{O}_2$  (Table 16E). However, we were unable to reproduce this result and without LC-MS capabilities we could not confirm if this very minor byproduct corresponds to the C10-GABA.

Table 16. HPLC Analysis of radical-mediated cyclobutanone ring opening under various conditions.<sup>a</sup>



<sup>a</sup> A) Standard of N-(2-oxocyclobutyl)decanamide (**2**), B) Standard of 4-decanamidebutanoic acid (**3**), C) AIBN mediated reaction at 2 hours, D) H<sub>2</sub>O<sub>2</sub>-mediated reaction at 2 hours with low concentration H<sub>2</sub>O<sub>2</sub>. E) Zoom in comparison view of Control spectrum **3** (Top) and H<sub>2</sub>O<sub>2</sub>-mediated reaction at 30 % H<sub>2</sub>O<sub>2</sub> concentration (bottom).

### Product-Based Transition-State Modeling Analysis.

The X-ray co-crystal structure containing the ring-opened C10-GABA analog was used to model the intact C10 cyclobutanone and tetrahedral transition state mimetic bound to the metal center in an effort to understand substrate recognition and critical enzyme mechanistic machinery. We have employed the *in silico* modeling technique that we refer to as “Product-Based Transition State Modeling” (PBTSM) to model the hypothetical cyclobutanone and the catalytic water/hydroxide bound to AiiA\_Co models respectively as well as the cyclobutanone

tetrahedral transition state mimetic bound AiiA\_Co model. This technique, described in Figure 57 above, employed the ring-opened C10-GABA analog-bound co-crystal structure as a starting point to generate these models in reverse chronology back through the substrate tetrahedral intermediate and further back through two distinct cyclobutanone / catalytic water-hydroxide binding modes.

The atomic coordinates of the structurally prepared model of the C10-GABA bound AiiA\_Co crystal structure, C10-GABA-prod\_AiiA\_Co were used to generate three additional AiiA molecular models of cyclobutanone inhibitor species at key stages along the enzyme's hypothetical catalytic trajectory, which include the C10-CB\_HOH\_AiiA\_Co cyclobutanone inhibitor bound with inactivated catalytic water model, C10-CB\_OH\_AiiA\_Co cyclobutanone inhibitor bound with activated catalytic hydroxide model, and the C10-CB-TS\_AiiA\_Co transition state mimetic bound model after nucleophilic attack at the cyclobutanone carbonyl by the catalytic hydroxide.

Analysis of the binding interaction reveals how the TS mimetic may be stabilized in the active site before X-ray radiation opening of the cyclobutanone ring. Figure 62 shows the tetrahedral transition state mimetic carbonyl oxygen (-O) makes H-bond interaction between the side chain of Try194 and Co2.2 while the catalytic hydroxyl oxygen forms interactions with both cobalt ions as well as the protonated general acid base Asp108. As discussed in Chapter 2, the propensity for a dinuclear metalloenzyme to utilize both an organic H-bond donor and inorganic species to form a pseudo-oxianion hole to achieve polarization of the carbonyl suggested a common mechanistic feature among dinuclear metalloenzymes.

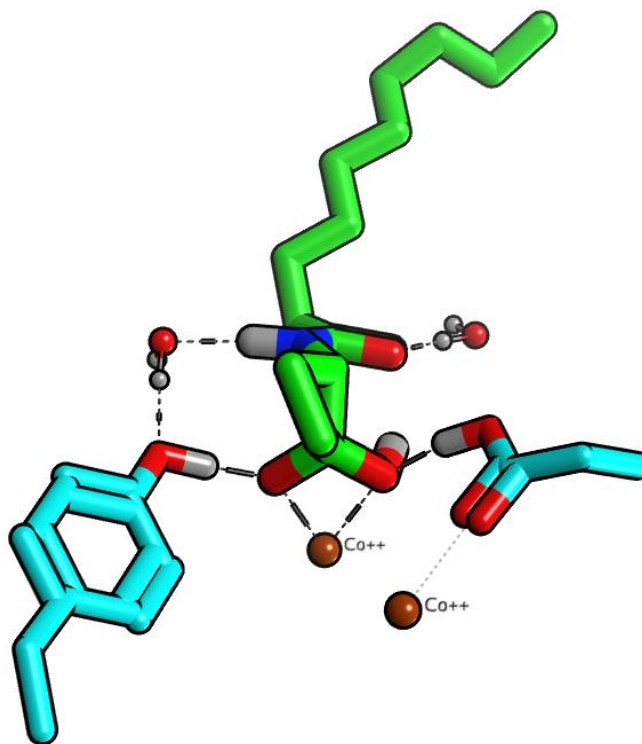


Figure 62. Transition state mimetic stabilization by cobalt, Tyr194 and Asp108.

Additionally, this modeling analysis suggests that the C10 compound **2** forms a water bridge between its amide NH and Tyr194 as well as the amide O between Phe107 backbone NH & Glu136 backbone CO. These crystallographic waters were well defined in the X-ray structures.

The free energy of binding was calculated for the four models using the Generalized Born Volume Integral Weighed Surface Area (GBVI/WSA)  $\Delta G$  method using MOE as previously described in Chapter 2. Binding Affinity found for all four molecular models in the PBTSM series were calculated and reported in Table 17.



Table 17. GBVI/WSA  $\Delta G$  Binding Affinity Calculations for PBTSM-Generated AiiA Structures.

| Model ID              | GBVI/WSA $\Delta G$ |
|-----------------------|---------------------|
| C10-CB_HOH_AiiA_Co    | -7.29 kcal/mol      |
| C10-CB_OH_AiiA_Co     | -6.67 kcal/mol      |
| C10-CB-TS_AiiA_Co     | -11.05 kcal/mol     |
| C10-GABA-prod_AiiA_Co | -11.60 kcal/mol     |

The binding affinity calculations shows an exothermic reaction profile with a clear downhill trend from bound cyclobutanone to the observed crystallographic product.

### Conclusion

The employment of small molecule peptidomimetic derivatives to mimic peptide conformational ensembles is critical in drug discovery toward the development of new pharmaceuticals. The results disclosed above suggest formation of the hypothesized transition-state mimetic occurs but is destroyed upon exposure to high intensity X-ray irradiation during data collection. This would suggest that the cyclobutanone moiety can be utilized as a warhead in targeting alternative di-metalloproteins metal centers for future studies. Ligand hydrocarbon tail access to the hydrophobic phenylalanine clamp binding site favored chain lengths of 10 carbon versus 6 carbons for optimum interaction for the ligand at the metal center. We have contemplated that more potent inhibitors could be synthesized with less flexible side chains.

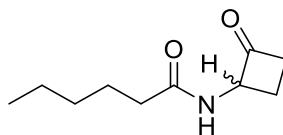
These results seem to suggest that ligand access to the hydrophobic phenylalanine clamp binding site is favored for optimum binding to the active site, and the  $\alpha$ -amido cyclobutanone moiety has the potential utility as a transition-state mimetic warhead in targeting alternative di-metalloproteins metal center in the future. Thus, targeted inhibitors utilizing cyclobutanone derivatives could provide a rapid entry into inhibitors of other metalloenzymes enzyme for

treatment of human disease including bacterial infection. Therefore, the cyclobutanone functional group possesses the potential as a general molecular warhead for target di-nuclear metalloenzyme inhibition.

### Chapter Acknowledgements

I am very grateful to Dali Liu, Ph.D. and Romilla Mascarenhas, Ph.D. for obtaining and solving the AiiA co-crystal structures, and to Maxwell Moore for synthesizing the hexanamide cyclobutanone. I would also like to thank Bogi Nocek, Ph.D. for hosting our X-ray exposure experiments at Argonne.

### Experimental Section

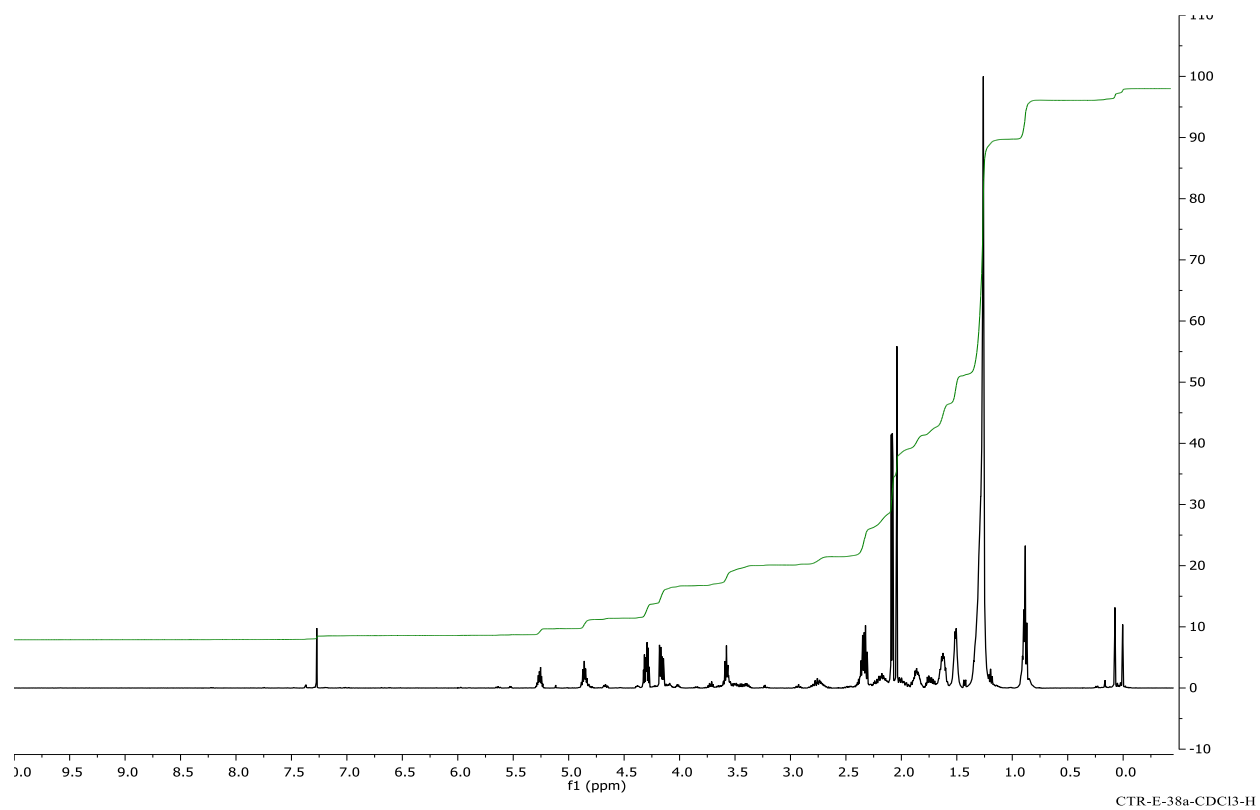


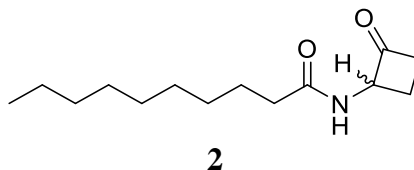
**1**

**Synthesis of N-(2-oxocyclobutyl)hexanamide (1).** To a 10 mL round bottom flask fitted with a condenser was added hexanamide (100 mg, 0.868 mmol), 1,2-bis(trimethylsilyloxy)cyclobutene (242  $\mu$ L, 0.955 mmol), dry THF (2.0 mL) and 1M HCl-ether (2.0 mL) at rt. The reaction mixture was agitated with magnetic stirring under inert argon atmosphere and heated under reflux at 55  $^{\circ}$ C for 3 hrs after which time HPLC and TLC ( $R_f$  = 0.2 at 4:6 ethylacetate-petroleum ether) with PMA staining indicated consumption of hexanamide starting material. Once the reaction was complete the solution was concentrated to dryness at 1 atm using an 80  $^{\circ}$ C heat bath. The resulting crude syrup was dissolved in ether which was purified by passing through a 4 g silica gel flash cartridge, using PMA stain to monitor for desired product. The product was eluted from the column with ether-petroleum ether (1:1) mobile phase to afford the title cyclobutanone **1** (11.8 mg, 72%) as a clear oil.  $^1\text{H}$  NMR (500 MHz,  $\text{CDCl}_3$ ):  $\delta$  5.26 (tdd,  $J$  = 10.1, 5.9, 4.3 Hz, 1H), 4.93 – 4.79 (m, 2H), 4.30 (dq,  $J$  = 11.7, 4.5 Hz, 2H), 4.16 (ddd,  $J$  = 11.9, 5.9, 2.4 Hz, 2H),

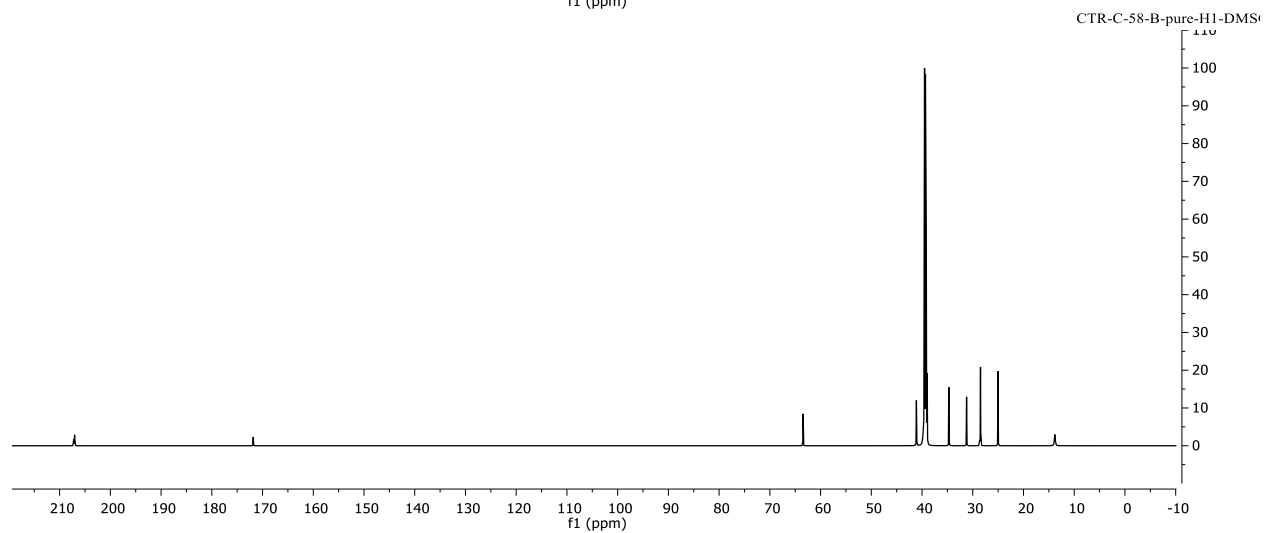
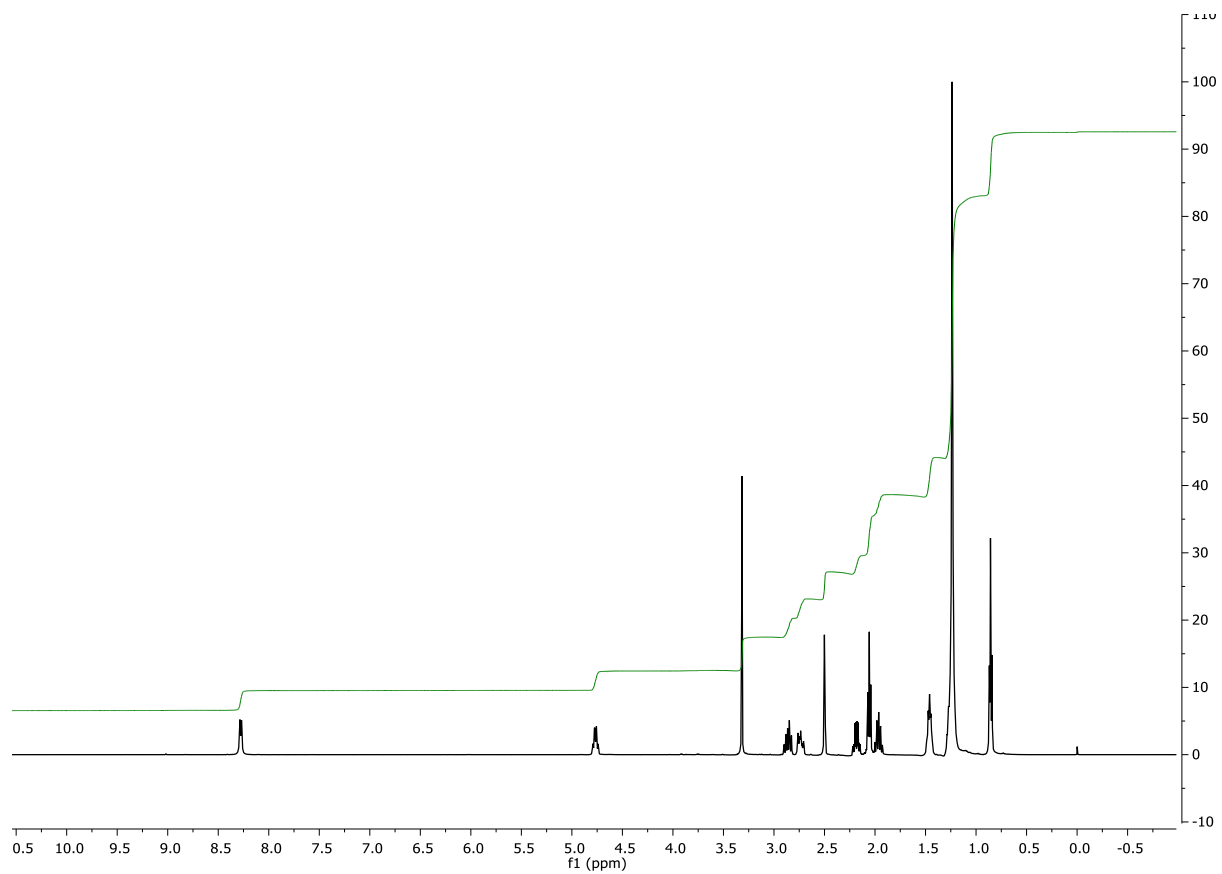
3.62 – 3.54 (m, 1H), 2.85 – 2.64 (m, 1H), 2.41 – 2.28 (m, 4H), 2.25 – 2.13 (m, 1H), 2.10 – 2.07 (m, 6H), 2.04 (s, 5H), 1.86 (dtt, J = 13.5, 6.4, 4.3 Hz, 4H), 1.62 (dq, J = 11.3, 7.1 Hz, 7H), 1.51 (q, J = 6.3 Hz, 10H), 0.97 – 0.83 (m, 3H).

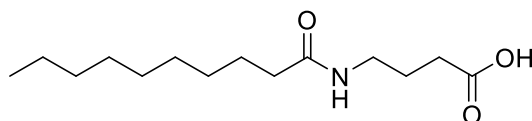
HPLC purity = Found to be 98 % pure at 220 nm.



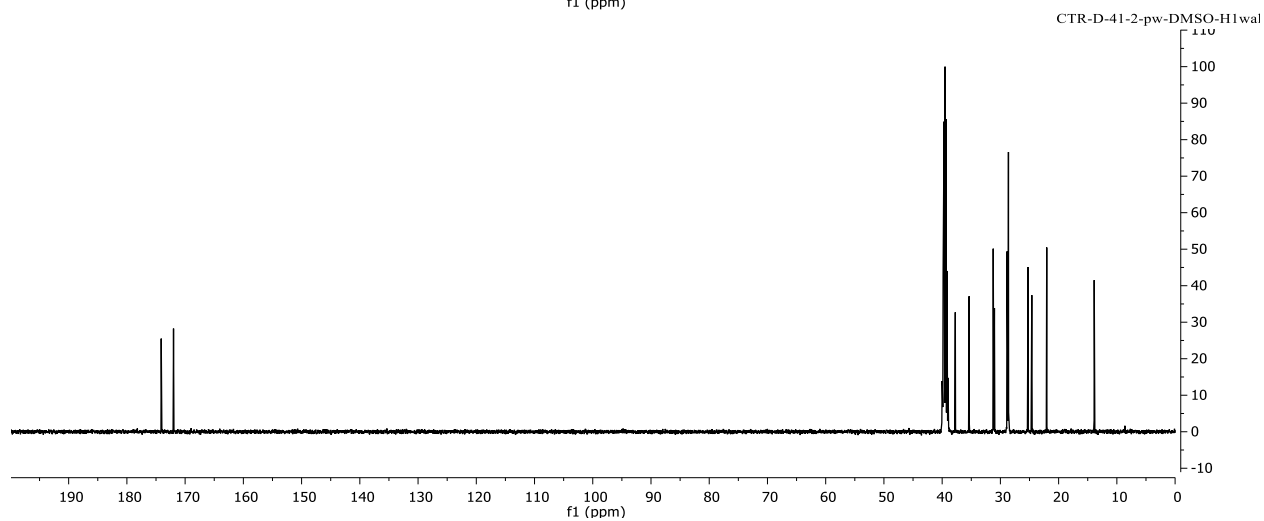
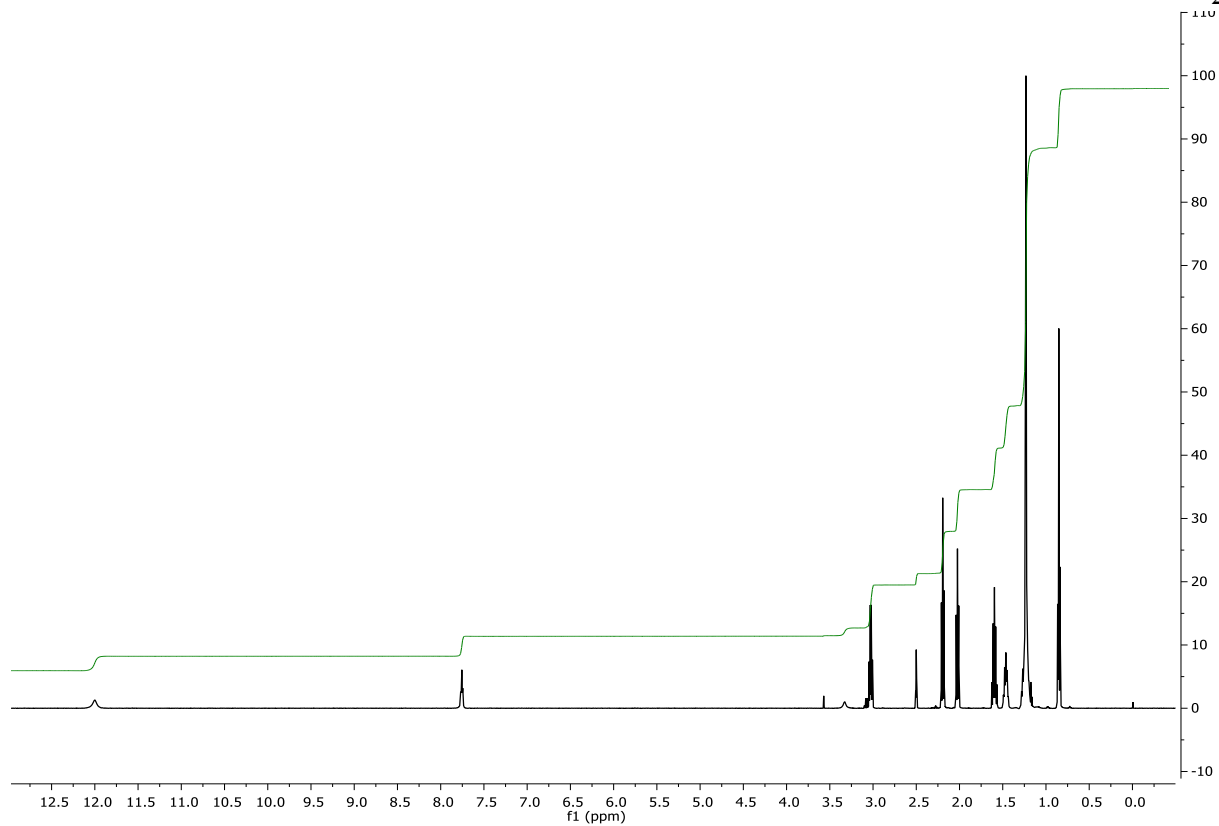
**2**

**Synthesis of N-(2-oxocyclobutyl)decanamide (2).** To a 10 mL round bottom flask fitted with a condenser was added decanamide (200 mg, 1.168 mmol), 1,2-bis(trimethylsilyloxy)cyclobutene (326  $\mu$ L, 1.284 mmol), dry THF (2.7 mL) and 1M HCl-ether (2.7 mL) at rt. The reaction mixture was agitated with magnetic stirring under inert argon atmosphere and heated under reflux at 55  $^{\circ}$ C for 3 hrs after which time HPLC and TLC ( $R_f$  = 0.07 at 1:1 ether-petroleum ether) with PMA staining indicated consumption of decanamide starting material. Once the reaction was complete the solution was concentrated to dryness at 1 atm using an 80  $^{\circ}$ C heat bath. The resulting crude syrup was dissolved in ether and was purified by passing through a 4 g silica gel flash cartridge, using PMA stain to monitor for desired product. The product was eluted from the column with ether-petroleum ether (1:1) mobile phase to afford the title cyclobutanone **2** (152.6 mg, 55 %) as a white crystalline solid.  $^1\text{H}$  NMR (500 MHz,  $d_6$ -DMSO):  $\delta$  8.28 (d,  $J$  = 7.5 Hz, 1H), 4.77 (m, 1H), 3.32 (s, 2H), 2.87 (m, 1H), 2.84 (m, 1H), 2.18 (ddd,  $J$ =20, 10.5, 4.5Hz, 1H), 2.06 (t,  $J$  = 7.3 Hz, 2H), 1.96 (m, 1H), 1.46 (m,  $J$  = 7 Hz, 2H), 1.24 (bs, 12H), 0.85 (j,  $J$  = 6 Hz, 3H).  $^{13}\text{C}$  NMR (500 MHz,  $d_6$ -DMSO):  $\delta$  207.02, 171.82, 63.47, 41.13, 34.34, 31.24, 28.85, 28.61, 28.49, 25.05, 22.07, 18.33, 13.90. HPLC purity = Found to be 98 % pure at 220 nm.  $^{13}\text{C}$  NMR (500 MHz,  $d_6$ -DMSO):  $\delta$  207.2, 207.1, 171.8, 41.1, 39.7, 39.5, 39.3, 39.2, 39.0, 34.7, 28.5, 25.0, 13.9, 13.8.



**3**

**Synthesis of 4-decanamideobutanoic acid (3).**  $\gamma$ -Aminobutyric and trimethylamine was suspended in dry methanol in a 4 g dram vial. The reaction mixture was cooled to 0 °C over 5 min before decanoyl chloride was added to the vial in 5 portions of 38  $\mu$ L over 5 min while under continuous inert gas stream. The reaction was sealed and stirred for an additional 1 h at 0 °C before being allowed to warm to room temperature overnight upon which HPLC indicated consumption of starting material. The reaction mixture was concentrated to dryness before being taken up in 10 mL of DI H<sub>2</sub>O and 10 mL of 1M HCl. The product was extracted with 3x with 10 mL chloroform which were combined and dried over sodium sulfate followed by filtration and concentration to dryness under reduced pressure.<sup>190</sup> The resulting white product was left to dry overnight under high vacuum to afford the title compound **3** (226 mg, 88 %) of a white crystalline solid. HPLC of crude product shows 98 % pure without purification. <sup>1</sup>H NMR (500 MHz, DMSO-d<sub>6</sub>):  $\delta$  12.00 (bs, 1H), 7.76 (t, J = 5.4 Hz, 1H, H-N), 3.34 (bs, solvent, H<sub>2</sub>O), 3.03 (t, J = 12.8, 6.8 Hz, 2H), 2.5 (m, solvent, DMSO), 2.19 (t, J = 7.5 Hz, 2H), 2.02 (t, J = 7.5 Hz, 2H), 1.59 (quin, J = 7.2 Hz, 2H), 1.46 (quin, J = 7.3 Hz, 2H), 1.29-1.18 (m, 12H), 0.85 (t, J = 6 Hz, 3H). <sup>13</sup>C NMR (500 MHz, DMSO-d<sub>6</sub>):  $\delta$  174.1, 172.0, 37.8, 35.4, 31.2, 31.0, 28.9, 28.7, 28.6, 25.3, 24.6, 22.1, 13.9.



## CHAPTER SIX

### GCN-5-RELATED N-ACETYLTRANSFERASE (GNAT) BISUBSTRATE INHIBITORS AND INSIGHT INTO KINETIC AND CHEMICAL MECHANISM

#### **Abstract**

The Gcn5-related N-acetyltransferase (GNAT) PA4794 from *Pseudomonas aeruginosa* has been recently shown to specifically acetylate the C-terminal lysine residue of peptides, although its native function remains unknown. As with many bacterial GNATs, their functions have not yet been determined, which is further hampered by the lack of crystal structures of these proteins with bound acceptor substrates. As part of our ongoing studies to functionally annotate GNATs with unknown functions, we are using PA4794 as a model system for exploring efficient formation of bisubstrate complexes to enhance our success rate in obtaining co-crystal structures of GNATs with ligands bound in their acceptor sites. We have now synthesized and tested substrate analogs of the previously identified N-phenylacetyl glycine lysine (NPAcGK) enabling two separate three-dimensional structures of PA4794 with NPAcGK analog-derived bisubstrates formed through direct reaction with CoA—the first through direct alkylation with a reactive substrate, and the second through X-ray induced radical-mediated process. We also performed docking and molecular dynamics simulations of the reverse reaction pathway from the NPAcGK product back to formation of the tetrahedral intermediate/transition state to complement our structural work.



This allowed us to explore the key protein-ligand interactions within the active site of PA4794 and guide mutant synthesis and kinetics to determine the role of key residues in the active site.

### Introduction

The three-dimensional structures of proteins with ligands bound in their active sites are valuable tools because they provide a framework for determining residues available for binding substrates or products over the course of an enzymatic reaction.<sup>194</sup> In the present age where new sequencing information greatly exceeds the experimental functional annotation of genes, an additional advantage to liganded structures is that the mode of ligand binding in active sites yields important information that can be used to more accurately predict protein function. In collaboration with the Kuhn laboratories of San Francisco State University (SFSU), one of the aims of our research is to improve the structural and functional characterization of bacterial proteins belonging to the Gcn5-related *N*-acetyltransferase (GNAT) superfamily. These proteins use an activated acyl-donor (typically acetyl-coenzyme A (AcCoA)) to transfer an acyl group to an acceptor substrate. The identity of the acceptor substrate can range from small molecules such as polyamines, antibiotics, or arylalkylamines to peptides and proteins.<sup>195-197</sup> Although many proteins belonging to this family have been investigated, most of its members remain uncharacterized with respect to substrates or function.

GNATs have two adjacent but distinct substrate-binding sites: **(1)** the acyl donor substrate binding site, and **(2)** the acceptor substrate binding site. Many GNATs have yielded X-ray structures with AcCoA/CoA bound,<sup>198</sup> but it is less common to have ligands bound in the acceptor substrate binding site. Furthermore, the acyl donor site is highly conserved, making protein-CoA binding interactions in a newly-sequenced GNAT easier to predict, but the acceptor substrate binding site, which is responsible for specificity, is quite diverse among GNATs.

Currently, there are hundreds of structures of GNATs in the Protein Data Bank (PDB); however, many of these do not have acceptor ligands bound in their active sites. Therefore, if the function of the protein is unknown, it is extremely difficult to predict what possible ligands could potentially bind, and even if the ligand is known, it is still not trivial to predict the binding mode of ligands in this site. Obtaining structures of GNATs with bound acceptor substrates is therefore crucial for understanding these enzymes, but has proven to be challenging, as even if the function of the protein is known or potential acceptor substrates have been identified the enzymes often may not bind the ligand in the crystal. Therefore, new approaches and tools are needed to efficiently yield structures with acceptor ligands bound in order to successfully observe and analyze binding modes of substrates.

One strategy for obtaining liganded structures has been to crystallize proteins in the presence of bisubstrate inhibitors.<sup>199, 200</sup> Bisubstrate inhibitors have also been employed in medicinal chemistry in the design of more potent inhibitors, notably in the area of kinases with both ATP and substrate binding pockets.<sup>201</sup> The affinity of the enzyme for the bisubstrate is typically significantly greater than that of the substrate alone; therefore, it is expected that the enzyme will more efficiently bind the ligand in the crystal, which would enable an increase in the number of liganded structures of those enzymes. Several GNAT structures have been determined in the presence of bisubstrates, but they typically involve synthesis and isolation of the full bisubstrate prior to crystallization.<sup>195-197, 202, 203</sup> We propose a different approach for obtaining structures of GNATs with bisubstrate inhibitors bound, where we synthesize the analogs of the potential substrates and have the enzyme catalyze the formation of the bisubstrate in the presence of CoA. The advantages to this approach are: (1) the synthesis and purification procedures for acceptor ligands as opposed to full bisubstrates are simpler, (2) it reduces the

quantity of costly CoA needed for formation of the bisubstrate, (3) many different acceptor ligands can be tested using the same crystals, and (4) this approach can be used regardless of the size of the substrate to be bound. This final advantage is important because the donor and acceptor substrate binding sites of many GNATs are connected by a narrow tunnel, which would not allow a fully formed large bisubstrate analog to thread through the active site. Allowing each substrate to enter its respective binding site separately facilitates formation of a bisubstrate even with a large or bulky acceptor substrate during crystal soaks or co-crystallization.

Crystal structures containing substrate, products, or intermediate-bound enzymes can be extremely valuable tools for understanding the enzyme catalytic mechanisms; however, in many cases it is not possible to capture and obtain a structure of an enzyme in a ligand bound form due to factors such as rapid reaction and release of the products. Therefore, efficient methods for obtaining crystal structures of GNATs with acceptor ligands bound are desirable. In our previous work, we used a broad-substrate screening assay as a method to identify acceptor substrates for an uncharacterized PA4794 GNAT enzyme from *Pseudomonas aeruginosa*<sup>204</sup>. Kuhn found that PA4794 acetylates the dipeptide N-phenylacetyl glycine lysine (NPAcGK) and determined the structure of the ternary complex with CoA and acetylated NPAcGK (PDB ID: 4L8A) as depicted in Figure 63.<sup>205</sup>

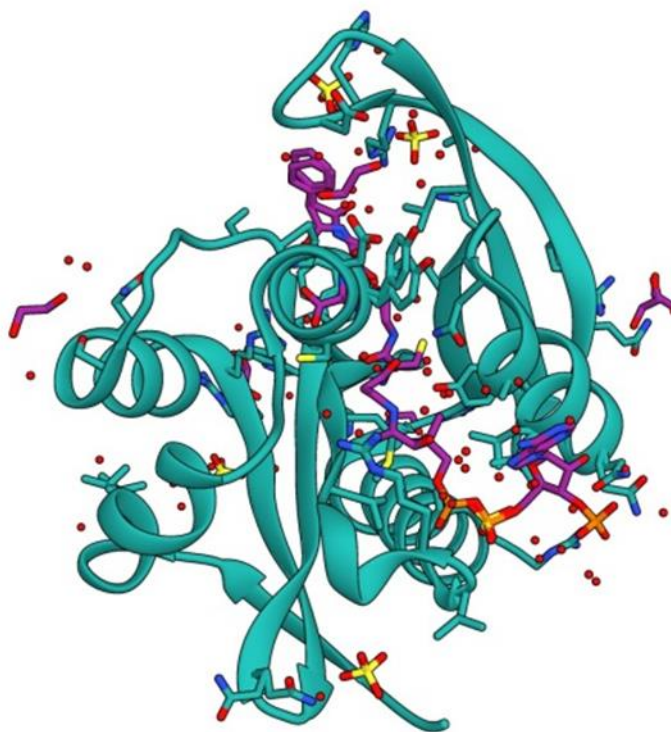


Figure 63. Gen5-related N-Acetyltransferase (4L8A).

Here, we have used the PA4794 enzyme as a model enzyme from the GNAT family to develop a streamlined procedure for obtaining liganded crystal structures of GNATs. We believe our approach is widely applicable across all members of the GNAT superfamily and will advance the knowledge of modes of ligand binding in the acceptor site that will ideally lead to more accurate computational methods of functional prediction or drug design. Furthermore, substrates armed with alkylating agents can serve as covalent inhibitors with therapeutic application, especially given the recent (re)acceptance of covalent inhibitors as drugs<sup>206</sup> for example as applied to protein kinases.<sup>207</sup>

Herein we describe two separate three-dimensional structures of PA4794 with NPACGK analog-derived bisubstrates formed in the active site through reaction with CoA, the first through direct alkylation with a reactive substrate, and then provide evidence that the second bisubstrate

was formed through X-ray induced radical-mediated addition to the alkene moiety of the substrate analog. While a covalent interaction, particularly with an active site residue of an enzyme, can trap an inhibitor in a higher energy conformation, we propose that the two different structures reflect most of the key substrate-active site and product-active site interactions, respectively, which is supported by molecular modeling that shows similar binding interactions with the NPACGK-derived acceptor molecules as in the covalently-bound bisubstrate. In addition, molecular dynamics were employed from the NPACGK product to simulate the reaction pathway in reverse back to the tetrahedral intermediate/transition state and to explore the key interactions with the active site. The key active site residues identified through the bound bisubstrate structures and through molecular dynamics analysis were then interrogated through the preparation and activity of synthesized mutants.

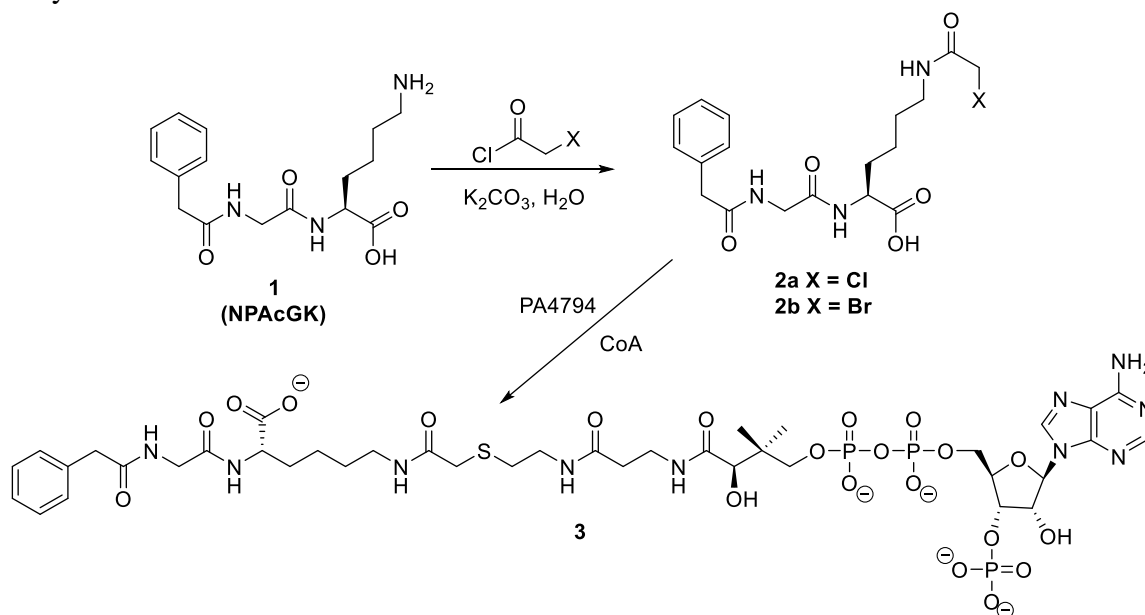
## Results

### Design of substrate analogs.

Majorek and Kuhn previously found that PA4794 acetylates the  $\epsilon$ -amino group of NPACGK and prefers to acetylate a C-terminal lysine residue of peptides<sup>205</sup>, yet its native function remains unknown. We chose this enzyme as a model system for exploring formation of bisubstrates in GNATs because it is small and readily crystallizes, which makes it an ideal protein to study mechanisms of ligand binding. To begin, we analyzed the 3D structure of the ternary complex of PA4794 and its interactions with CoA and acetylated NPACGK (NPACGAcK) peptide (PDB ID: 4L8A) and designed and synthesized reactive analogs of the acceptor substrate that would react with CoA to form bisubstrates in the protein crystal. We reasoned that electrophilic moieties installed near the  $\epsilon$ -amino group of the acceptor substrate should be capable of alkylating the thiol of free CoA to produce a bisubstrate in the active site of

the protein. To mimic the acetyl group transferred from CoA to the acceptor but with a reactive moiety, we installed an  $\alpha$ -haloacetyl group on the  $\epsilon$ -nitrogen of the lysine. The  $\alpha$ -haloacetyl moiety has been utilized extensively as a group to alkylate active site residues in proteins<sup>208</sup>, and in a similar approach, Hwang incorporated an  $\alpha$ -haloacetyl moiety as a replacement for the acetyl moiety of AcCoA, which was able to react with active site residues of acetyltransferases that use AcCoA<sup>209</sup>. Our approach for synthesizing haloacetyl substrates is summarized in Scheme 13 and was accomplished by reacting NPACGK with chloroacetyl chloride or bromoacetyl chloride to obtain compounds **2a** and **2b**, respectively. The PA4794 enzyme-mediated formation of bisubstrate **3** occurred in the presence of CoA and these compounds in the active site.

Scheme 13. Synthesis of  $\alpha$ -haloacetyl derivatives of NPACGK **2a** (X = Cl) and **2b** (X = Br) and enzyme-mediated formation of bisubstrate **3**.

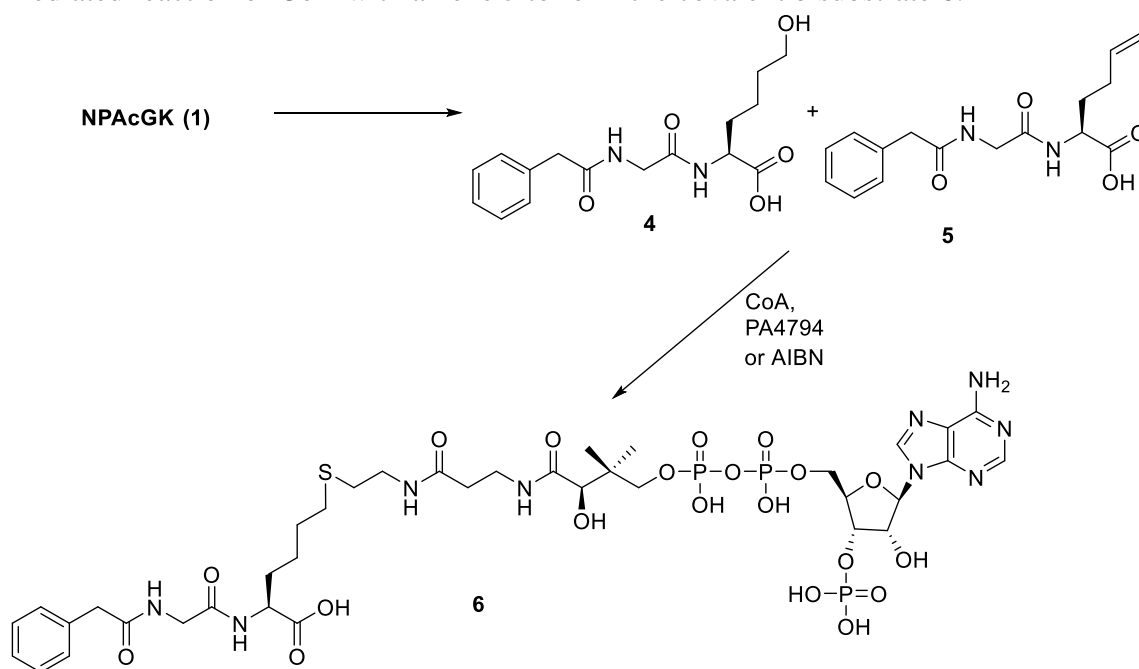


#### PA4794 does not O-acetylate the alcohol substrate analog.

Some GNATs are capable of both *N*- or *O*-acylating substrates<sup>210-212</sup> and we were curious if the PA4794 enzyme could *O*-acetylate NPACGK if the  $\epsilon$ -amino group was replaced with an alcohol. Our strategy for synthesizing the alcohol **4** (Scheme 14) was to convert the  $\epsilon$ -amino

group to the transient diazonium salt with aqueous nitrous acid<sup>213</sup> and ultimately with sodium nitroprusside<sup>214</sup>. As a by-product, the alkene **5** (Scheme 14) was produced via elimination, and the mixture of **4** and **5** were inseparable by normal-phase chromatography or by small molecule crystallization in our hands. Nonetheless, we expected the alcohol **4**, as a direct analog of NPAcGK, to serve as a potential acceptor molecule if PA4794 was indeed capable of O-acylation, whereas the alkene **5** was expected to be unreactive. Therefore, we proceeded with the **4/5** mixture for testing as a potential substrate and for co-crystallization/soaking experiments given the bioisosteric nature of the hydroxyl for amino substitution. We found the PA4794 enzyme was not active toward the **4/5** alcohol/alkene mixture during our kinetic assays and concluded that the enzyme was therefore specific for *N*-acetylation of this molecule.

Scheme 14. Formation of the alcohol/alkene mixture (**4** and **5**) from NPAcGK, and radical-mediated reaction of CoA with alkene **5** to form the covalent bisubstrate **6**.



**Bisubstrate formation in crystals via an enzyme-mediated mechanism.**

Crystals of the PA4794 protein were grown and soaked them with CoA, followed by soaking with the **2a** and **2b** chloroacetyl and bromoacetyl analogs and screened crystals for ligand binding. We found both analogs reacted with CoA to form bisubstrates **3** (Scheme 13, Figure 66B) and exhibited identical binding modes in the structures. The bisubstrates were formed via an enzyme-mediated mechanism whereby the enzyme active site placed the compounds in close proximity for the S<sub>N</sub>2 displacement of the halide by the thiol of CoA.

**Bisubstrate formation in crystals via a radical-mediated mechanism.**

When we soaked crystals of PA4794 with CoA and the alcohol/alkene mixture (**4/5**), our assumption was that the alcohol would bind preferentially in the active site of the enzyme, given the alcohol's ability to H-bond donate and accept, and the comparable steric volume to the amine substrate. We were surprised to observe formation of bisubstrate **6** in the structure (Scheme 14, Figure 66A). This was curious because both alcohol and alkene were expected to be chemically unreactive. To determine the mechanism of bisubstrate formation between the alcohol/alkene analog and CoA, we performed a series of tests to determine if it was produced enzymatically from the alcohol **4** or alkene **5**. Treatment of the **4/5** mixture with the PA4794 enzyme and CoA did not give rise to any detectable bisubstrate **6** by HPLC. However, it is known that a thiol can add to an alkene under free radical conditions,<sup>215</sup> which could have been initiated during X-ray data collection, so we tested whether or not the **4/5** mixture could produce a bisubstrate in the presence of a source of radicals. Treatment of **4/5** and CoA with AIBN at 65 °C for 2 hours showed complete consumption of the alkene **5** from the mixture and corresponding reduction in the concentration of CoA (Figure 64).



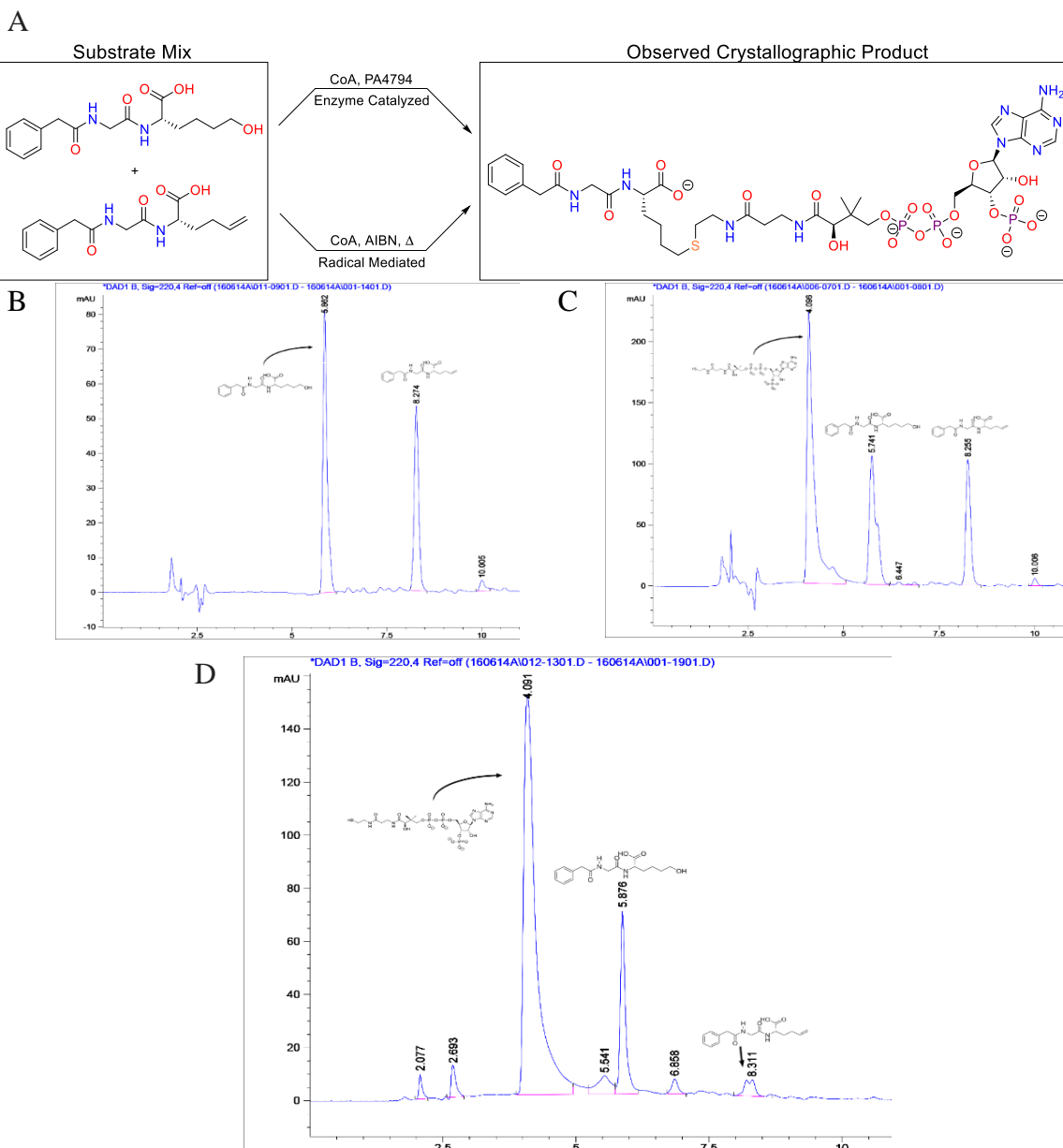


Figure 64. Experimental HPLC Assay Data. A) Discontinuous assay design to determine source of C-S bond formation. Assay result HPLC Chromatogram for B) Control: Mix + Buffer, C) Trial 1: HSCoA + Mix + Buffer, D) Trial 2: HSCoA + Mix + AIBN + Buffer.

There was no detectable effect on the concentration of alcohol **6**, and the production of a new polar peak close in retention time to CoA was shown to be bisubstrate **6** (Figure 65) by mass spectrometry ( $M^-$  obs 1070.2). As a result, the formation of the bisubstrate **6** in the crystal structure is likely due to a radical-mediated mechanism from radiation during data collection.

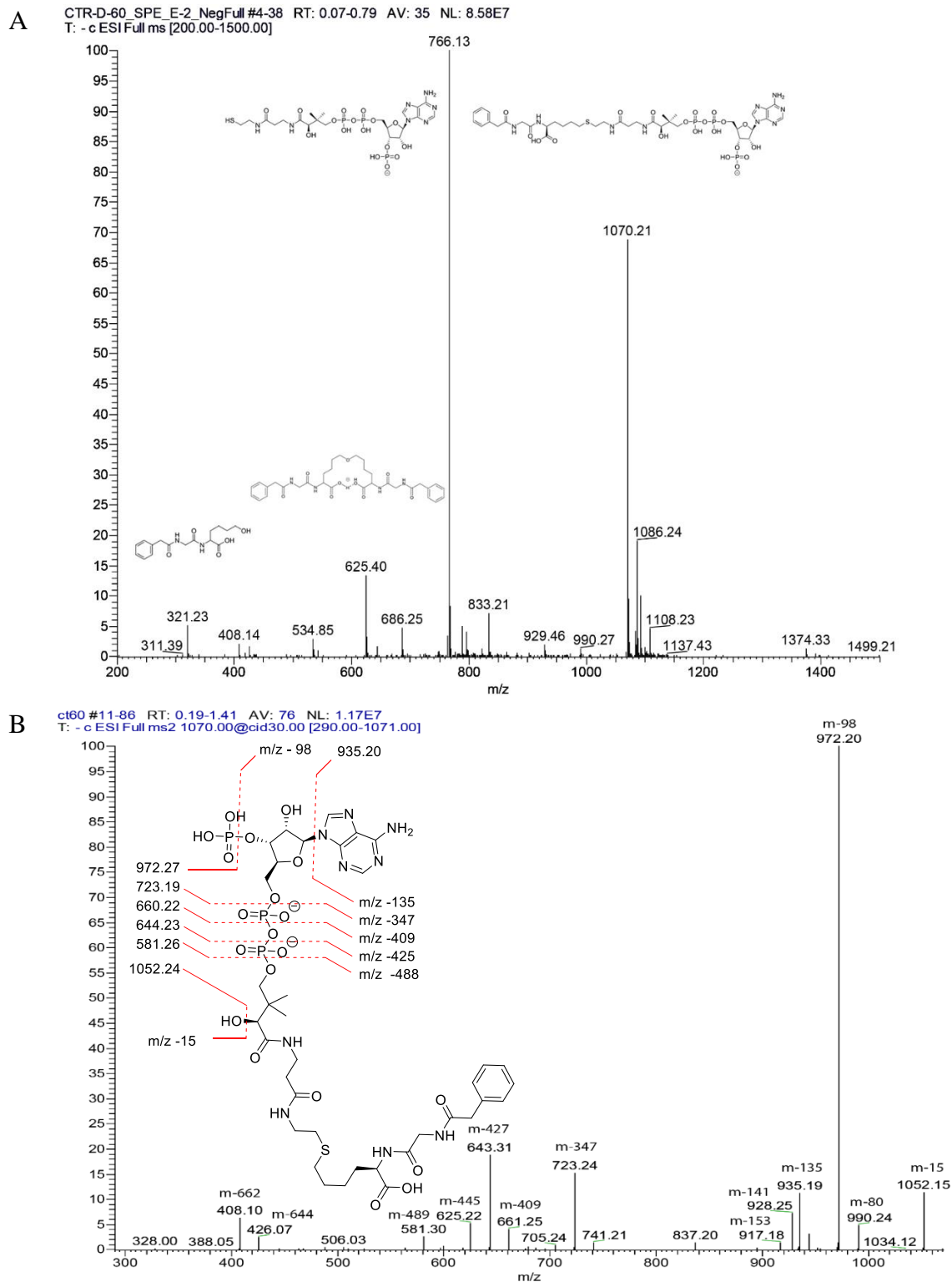


Figure 65. A) MS and B) MS-MS Fragmentation Analysis of Trial 2 After Solid Phase Extraction (SPE) Preparation.

**Two substrate analog binding modes reveal functionally important interactions.**

The bisubstrate analogs formed in the present study through either an enzyme catalyzed or radical mediated mechanism occupy both the AcCoA and acceptor substrate binding sites and enable exploration of key interactions in both pockets. The bisubstrate **3** and **6** CoA moieties are bound in similar conformations and through similar interactions as those of previously determined PA4794 structures (PDB IDs pending, Figure 66A-B). Bisubstrate **6** binding is similar to that of the acylated substrate observed in the ternary complex (PDB ID: 4L8A) structure with NPAcGAcK (Figure 66C). In particular, the most critical charge-charge interactions of the C-terminal carboxyl group of NPAcGAcK occur with Arg49 and the main chain nitrogen of Asn80 as well as several water-mediated interactions. The phenylacetyl moiety lies against a hydrophobic patch composed of residues Phe118, Phe27 and Pro31. The moiety corresponding to the C-terminal lysine side chain of the bisubstrate **6** is shorter by four compared to the acetylated lysine side chain of the product NPAcGAcK (Figure 66B). The bisubstrate compound **3** (Figure 66A) in which the reactive moiety is longer, exhibits a different binding mode compared to the acylated product shown in Figure 66C, but this can be attributed to the longer-atom chain connecting the lysine mimetic to CoA. The modified acetyl-lysine moiety in bisubstrate **3** is extended and is not as distorted as in the ternary complex structure. Specifically, this is due to a movement of the C-terminal carboxyl group of the peptide that now interacts with more surface exposed Arg141 instead of Arg49 (Figure 66A). Arg141 is located closer to the binding pocket opening than Arg49 and allows a more extended conformation of the substrate analog moiety, which is slightly less buried inside of the protein as compared to bisubstrate **6** (Figure 66B). In this case, additional interactions are observed between the  $\epsilon$ -amino group and the acetyl oxygen of the haloacetyl substrate analog derivative and the main chain oxygen of

Ser116 and main chain nitrogens of Asn80 and Met81. The two distinct conformations of the two bisubstrate analog moieties also induce significantly different conformations of Tyr68.

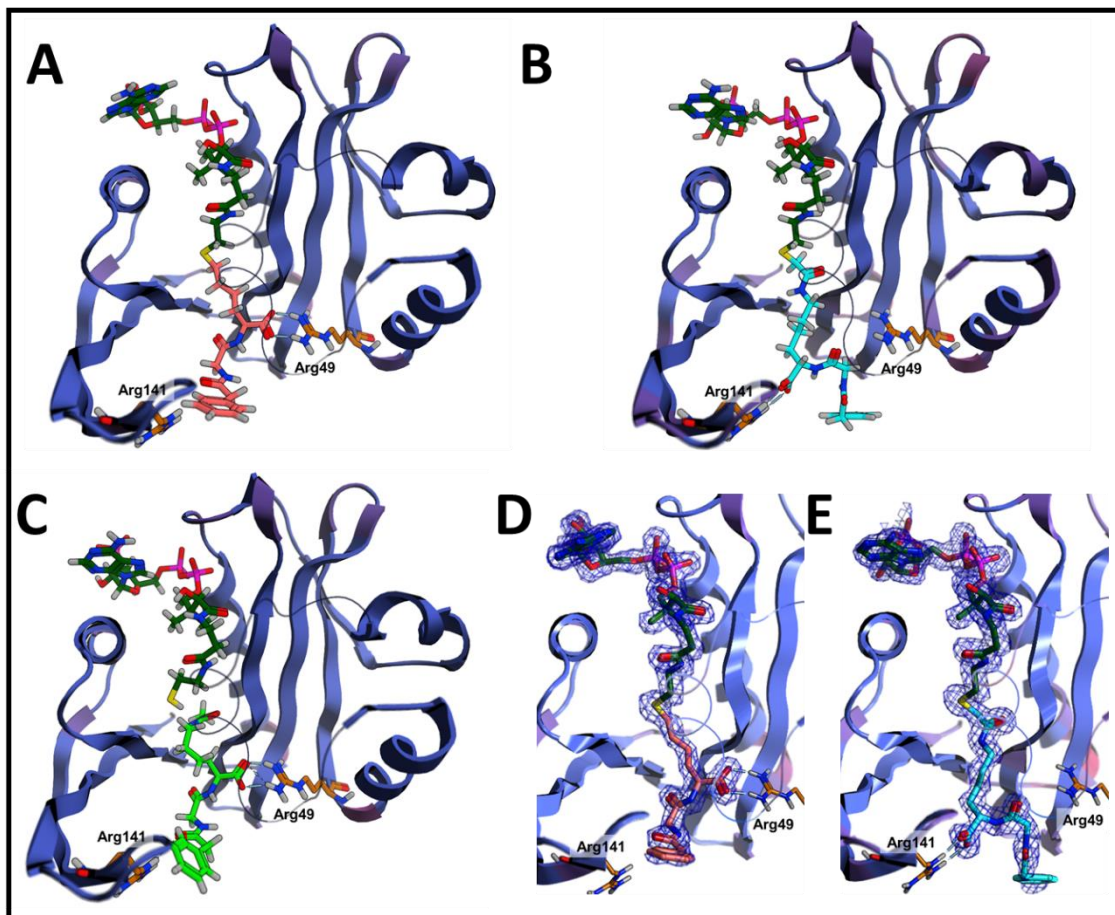


Figure 66. Comparison of binding products and bisubstrate **3** and **6** analogs. PA4794 is shown in orange atoms with B-Factor ribbon diagram. Residues 19-37 are shown as wire-ribbons for clarity. Ligand atoms represented as followed: CoA; dark green, NPAcGK from PDB ID:4L8A; light green, inhibitor atoms attributed to bisubstrate **3** and **6**; cyan & salmon respectively. (A) PA4794 in complex with bisubstrate analog **6** synthesized from CoA and alcohol/alkene mixture 4/5 determined at 1.2 Å. (B) PA4794 in complex with bisubstrate analog **3** synthesized in the active site from CoA and compound **2a** determined at 1.4 Å. (C) Ternary complex structure of PA4794 with the bound reaction products CoA and N $\epsilon$ -acetylated NPAcGAcK. (D) 2Fo-Fc electron density map of the bound bisubstrate analog **6** ( $\sigma=1.0$ ) (E) 2Fo-Fc electron density map of the bound bisubstrate analog **3** ( $\sigma=1.0$ ).

### Importance of Arg49 and Arg141 residues of PA4794.

The binding mode of the bisubstrates revealed two arginine residues (Arg49 and Arg141) that are implicated as playing a potentially important role in binding substrate and/or product. To

elucidate whether these two residues were critical for activity, our collaborators in the Kuhn Lab constructed alanine and glutamine mutants and compared their kinetic activity to the wild-type enzyme (Figure 67). The polyhistidine tag could not be completely removed from all mutants; therefore, the kinetic activity of all mutants and wild-type proteins were screened in the presence of the tag for this experiment. The R49Q mutant was previously determined to display reduced PA4794 catalytic activity, but included it here since the tag was not present previously.<sup>205</sup> All five mutants (R49A, R49Q, R141A, R141Q, and R49QR141Q) showed a significant decrease in activity (between 3.5- and 23-fold decrease) compared to the wild-type enzyme, with the most severe decrease seen for the double mutant. Replacing the more surface-exposed arginine Arg141 with glutamine exhibited diminished activity compared to the wild-type protein, but its replacement with alanine showed a greater decrease in activity. Arg49 mutations also led to decreased activity relative to wild-type, but the glutamine and alanine mutants showed opposite effects compared to the Arg141 mutants: the R49A retained greater activity relative to R49Q. Regardless, it is clear that both of these residues are important for binding peptide, and at least one needs to be present for catalysis to occur.

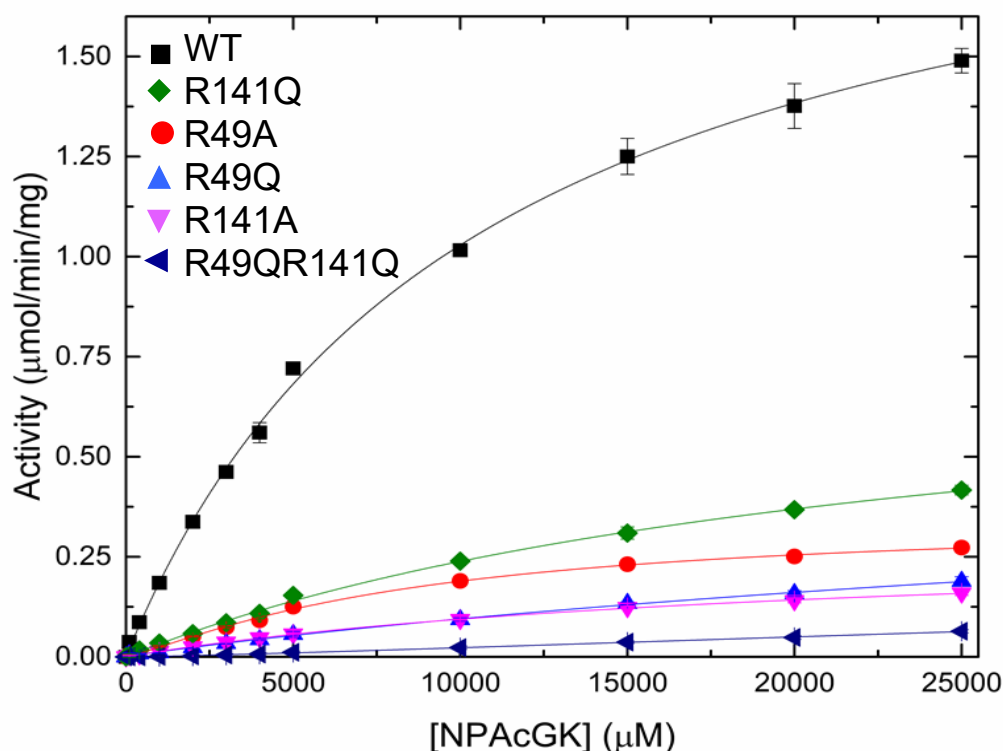


Figure 67. Substrate saturation curves for wild-type and Arg49 and Arg141 mutants. Steady-state enzyme kinetic experiments were performed by holding AcCoA concentration constant at 0.5 mM and varying NPAcGK peptide concentration. Standard deviations for all proteins are shown. See Experimental procedures for details.

### Product-Based Transition-State Modeling Approach.

To complement our enzyme kinetics results and elucidate potential roles of residues during catalysis, the *in silico* modeling method we refer to as “Product-Based Transition-State Modeling” (PBTSM) (See Experimental Procedures for details) was used to elucidate hypothetical substrate and tetrahedral intermediate binding modes for PA4794. This method proceeds in reverse chronological reaction order beginning with reaction products and progressing back through the tetrahedral intermediate toward the original substrates. The process is summarized in Figure 68. Crystallographic data of enzymatic reaction products (PDB ID: 4L8A) or bisubstrate **3** were used as a starting point to systematically backtrack through the

catalytic intermediate steps to computationally guide the placement of atoms that would occur during formation of the tetrahedral intermediate and substrate binding.

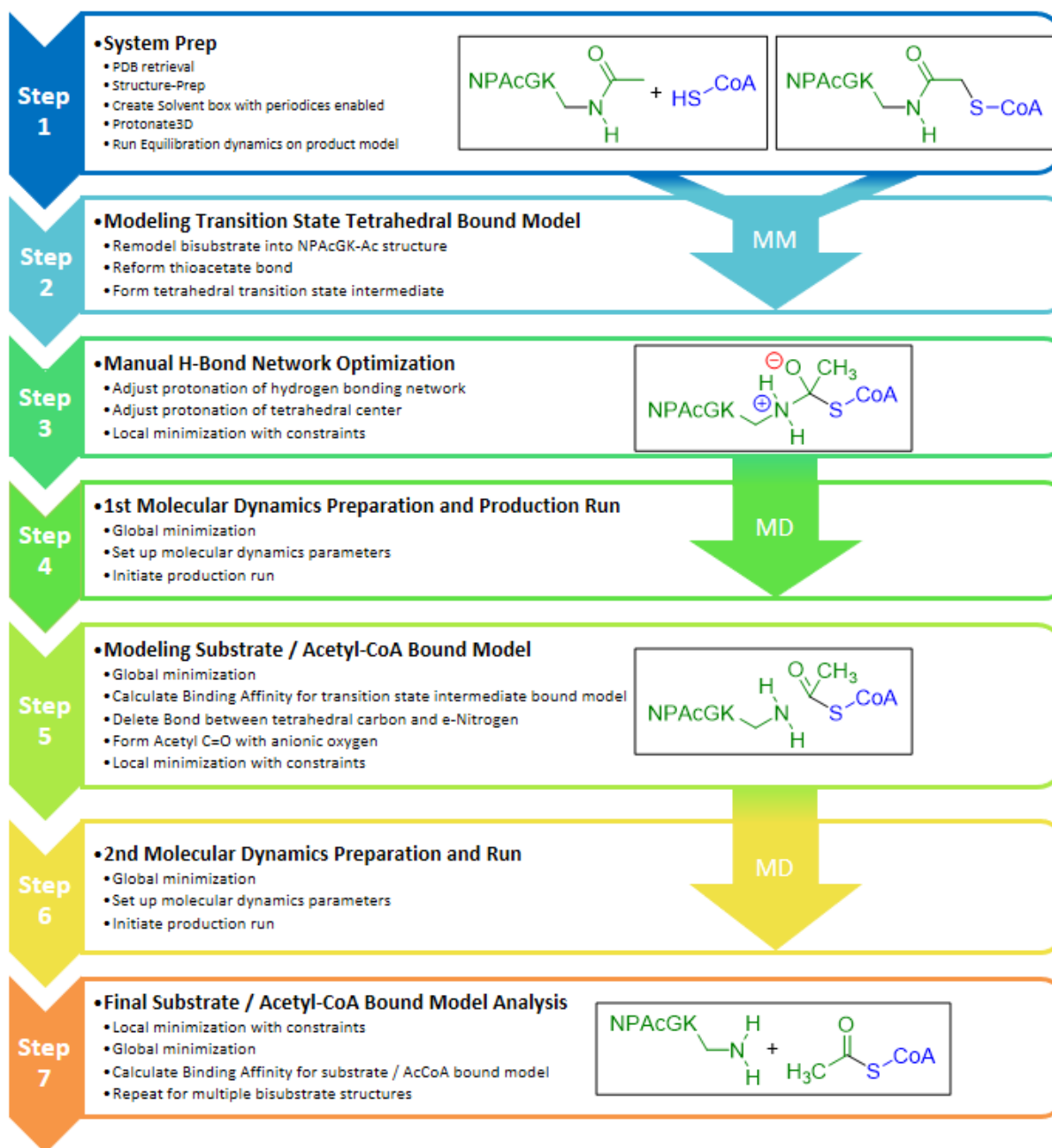


Figure 68. Product-Based Transition-State Modeling (PBTSM). Protocol for systematic remodeling of tetrahedral intermediate and substrate binding modes from product or bisubstrate bound crystal structures. Molecular Minimization (MM) and Molecular Dynamics (MD) stages in the protocol are shown.

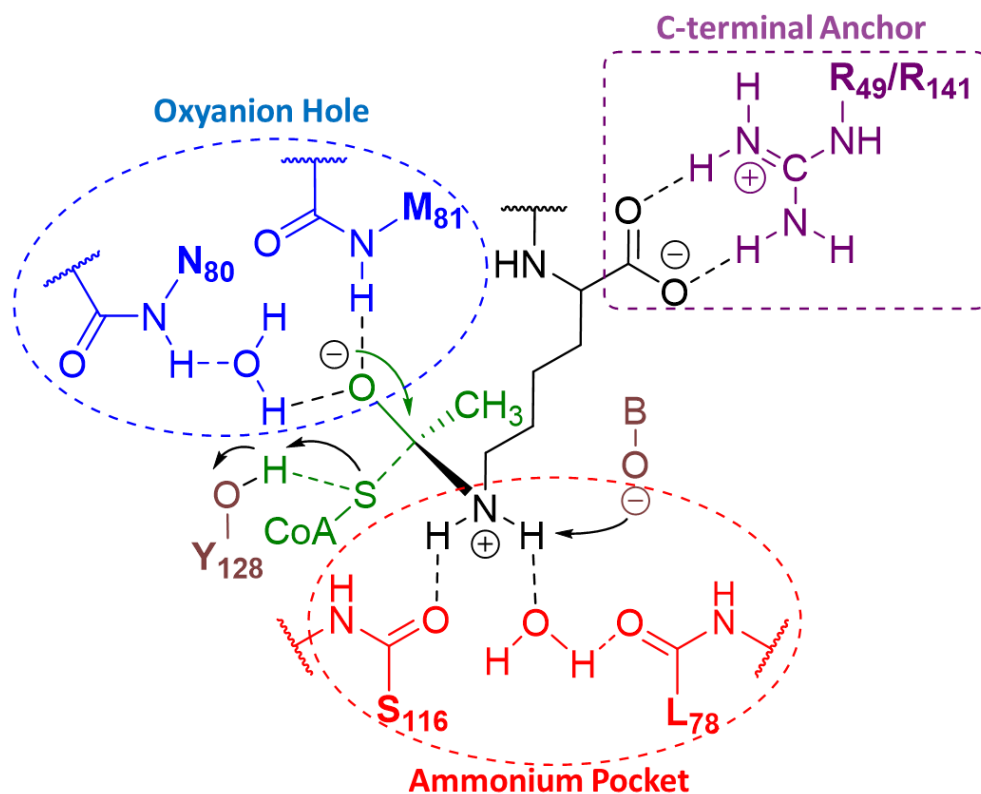
**Active site regions important along the reaction trajectory.**

Using bisubstrate bound crystal structures and PBTSM, we identified a set of important regions of the active site that may help stabilize tetrahedral intermediate formation for the catalytic reaction to proceed. For instance, we identified a potential oxyanion hole composed of the backbone amide hydrogen of Met81, the alpha carbon hydrogen of Cys29, and the backbone amide hydrogen of Asn80 through a water molecule that could stabilize the negatively charged oxygen of the tetrahedral intermediate (Figure 69A, blue circle). The water observed in the crystal structure is present at a nearly identical site as the one observed using the PBTSM protocol, which suggests it plays an important role in the acetyl transfer mechanism when the system is solvated. We also observed that H-bonds were formed directly through two backbone carbonyl oxygens of Ser116 and Leu78 or indirectly through a water molecule to stabilize the nucleophilic approach of the  $\epsilon$ -amino group of NPACGK during formation of the tetrahedral intermediate (Figure 69A, red circle). Two important arginine residues stabilize the C-terminal carboxyl group of the NPACGK substrate (Figure 69A, purple square). Placement of the carbonyl oxygen atom into the oxyanion hole allowed for the accompanying elements involved in formation of the tetrahedral transition state intermediate leading to acetyl transfer to be recognized. A shallow hydrophobic pocket containing Leu78, Ile115, Tyr128 and Met81 residues was also observed to accommodate the methyl of the acetyl group. Finally, the model indicates that the sulfur of CoA forms a stabilizing H-bond interaction with Tyr128 and an ordered water molecule. This catalytic tyrosine has been predicted to play a role as a general acid capable of reprotonating CoA after transfer of the acetyl group to the acceptor substrate has occurred.<sup>205</sup> This ordered water makes further interactions with the backbone carbonyl of Tyr28,

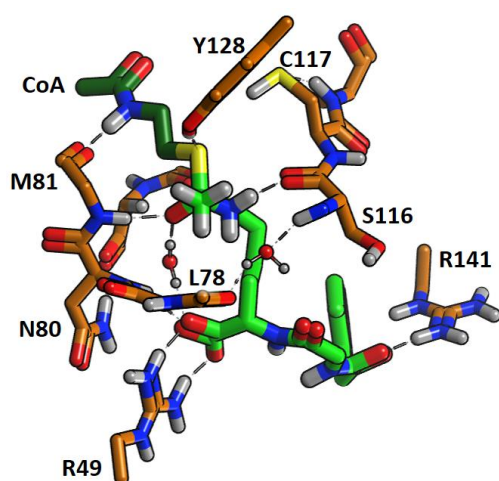


while H-bond donation varies between the backbone amide of Phe118 and the side chain amide of Ans121. The PBTSM generated transition state models are shown in Figure 69B and 69C.

A



B



C

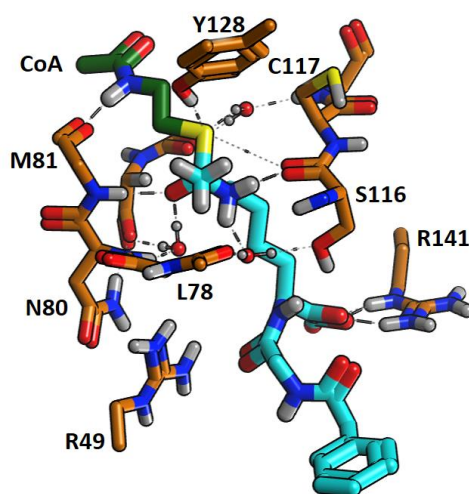


Figure 69. Product-Based Transition-State Modeling Analysis. A) Schematic diagram of tetrahedral transition state intermediate indicating major regions of substrate-enzyme interactions in the active site, including substrate C-terminal carboxylate stabilizing interactions (black square), oxyanion hole (blue circle), and stabilizing interactions for substrate amine approach (red circle). PBTSM generated transition state models are shown in panels B and C. B)

Transition state model based on PA4794 co-crystal structure with products bound (PDB ID: 4L8A) shown in light green. C) Transition state model based on PA4794 structure in complex with bisubstrate **3** shown in cyan. The CoA moiety of the tetrahedral intermediate is shown in dark green and protein side chains are in orange. Amino groups are in dark blue, oxygens in red, sulfurs in yellow, and waters as red and white spheres.

### **Kinetic mechanism of PA4794 toward NPACGK.**

GNAT enzymes typically use either a direct transfer mechanism whereby both substrates bind to the enzyme simultaneously and the acetyl group from AcCoA is transferred directly to the substrate, or they use a ping-pong or double-displacement mechanism with an indirect transfer of the acetyl group via an acetyl-enzyme intermediate. In the latter mechanism, AcCoA binds first and transfers the acetyl group to a residue in the enzyme active site and then CoA leaves and acceptor substrate binds and the acetyl group is transferred from the enzyme to the acceptor substrate. Since our PBTSM modeling experiments predicted a tetrahedral intermediate, which is indicative of a direct transfer mechanism, we performed enzyme kinetic assays and performed kinetic model testing to experimentally determine which kinetic mechanism was preferred for PA4794. Similar to other GNATs, Filippova and Kuhn found the PA4794 protein indeed uses a bisubstrate steady-state kinetic<sup>216, 217</sup> which infers an overall direct transfer of the acetyl group to the acceptor substrate through a transition state intermediate. Thus, our *in vitro* and *in silico* results are compatible.

### **Overall PA4794 reaction sequence.**

Based on our combined results, we propose the sequence of substrate approach, acetyl transfer and final product release in PA4794 occurs as follows. Our kinetic mechanism results indicate there is no specific order for binding AcCoA or NPACGK, thus the substrates may approach the active site in a random order. When the NPACGK substrate binds, its C-terminal carboxylate interacts with Arg141 (located near the binding pocket opening) or ARG49 (located

closer to the catalytic center), and the lysine moiety approaches the catalytic site as a neutral species, having been deprotonated by bulk solvent or an unidentified basic residue near the active site.<sup>205</sup> The nucleophilic  $\epsilon$ -amino group of NPAcGK is guided into the correct conformation by residues that stabilize the incipient positive ammonium species while the acetyl oxygen takes its place in the oxyanion hole. Immediately following formation of the tetrahedral intermediate, the bond between the carbonyl carbon and the sulfur breaks while the negative charge on sulfur is stabilized and ultimately protonated by Tyr128. Protonation may come from bulk solvent or from deprotonation of positively charged ammonium species. The acetylated NPAcGKAc product and CoA would leave the active site and the catalytic cycle would continue. The proposed PA4794 chemical mechanism for acetyltransfer is shown in Figure 70.

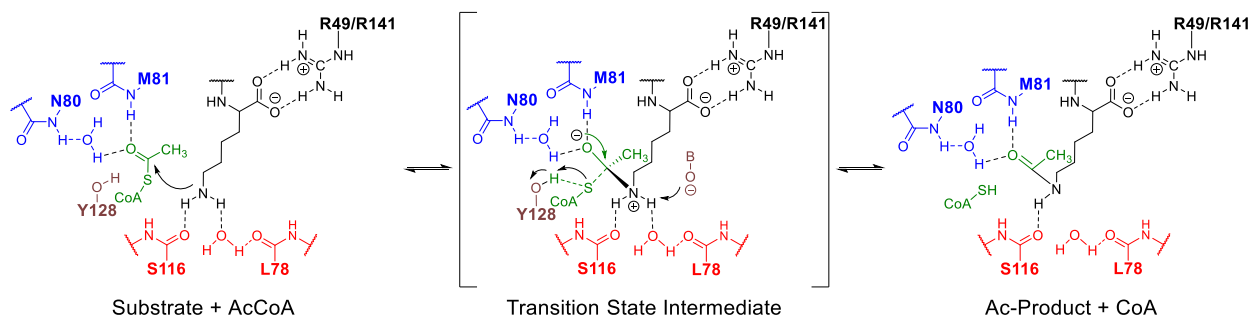


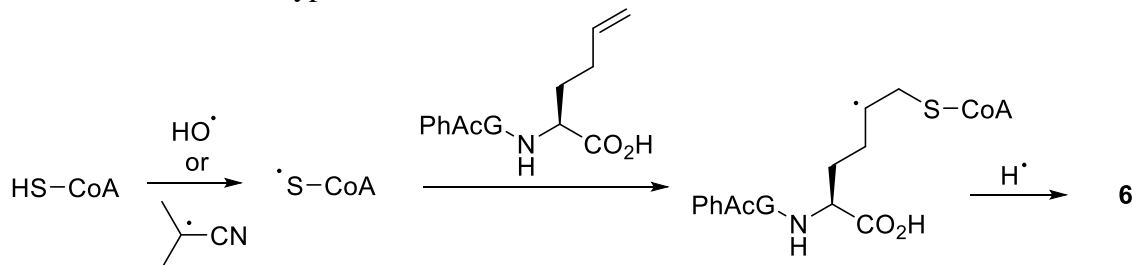
Figure 70. Proposed chemical mechanism for PA4794 acetyl transfer.

## Discussion

We have designed two types of tools that utilize different mechanisms to form bound bisubstrates in GNAT protein crystals: 1) chloroacetyl/bromoacetyl derivatives of an acceptor substrate using an enzyme-mediated mechanism and 2) addition of a thiol to an alkene derivative of acceptor substrate via a radical-mediated mechanism. We chose to use the PA4794 protein of unknown native function from *P. aeruginosa* as a model system to test our bisubstrate tools since its crystallization is highly reproducible, with fast growth of crystals that typically give high

resolution structural data. Upon soaking crystals of PA4794 with the chloroacetyl derivative of PhAcGK **2a** in the presence of CoA followed by structure determination, we observed that the protein enzymatically formed a covalent bisubstrate (Figure 66B) occupying both AcCoA and acceptor substrate sites. Incubation of PA4794 crystal with bromoacetyl substrate **2b** yielded an identical bisubstrate-bound complex. Thus, either organic halide can be used to produce the same enzyme-mediated bisubstrate binding mode.

The formation of bisubstrate **6** was unexpected, but can be attributed to radiation-induced free-radical-mediated addition of the thiol to the alkene moiety of **5**. We hypothesized that bisubstrate **6** was not produced enzymatically, but rather through exposure to free radicals produced by X-ray irradiation during data collection (Scheme 14). X-Ray induced chemical modification of specific moieties is well documented, and sulfur-containing residues are particularly susceptible.<sup>218</sup> Scheme 14 presents a mechanistic hypothesis for the formation of bisubstrate **6** in the active site mediated by hydroxyl radicals produced from the interaction of radiation with ubiquitous water molecules in and around the active site. H-atom abstraction from CoA by a hydroxyl radical would yield the thiol radical which could rapidly add to the carbon-carbon double bond of alkene **5** yielding a secondary radical, which can abstract a hydrogen atom from water or a nearby residue to obtain bisubstrate **6**. The same overall mechanism is expected in the AIBN-mediated process with H-atom abstraction from CoA by the isobutyronitrile radical produced from loss of nitrogen from AIBN.

Scheme 15. Mechanistic hypothesis for the formation of bisubstrate **6** from CoA and alkene **5**.

The radical-mediated addition of the thiol moiety of CoA has not been previously employed to prepare S-alkylated derivatives of CoA, and as demonstrated, this method may be used to prepare bisubstrates of acyltransfer enzymes that employ CoA. There are several reports of the conjugate Michael addition of the thiol moiety of CoA to enones<sup>219-221</sup> but 1,4-addition requires an activating group, typically a carbonyl.

The results of the enzyme-mediated and radical-mediated bisubstrates combined with PBTSM and enzyme kinetics studies provided new information regarding key residues that are important for PA4794 substrate binding and tetrahedral intermediate interactions. The two different binding modes of both types of bisubstrates revealed two arginine residues that could interact with the carboxylate of the NPACGK substrate: ARG49 and Arg141. The alkyl side chain of the C-terminal lysine of the substrate is less distorted in the bisubstrate **3** structure compared to bisubstrate **6** and ternary complex (PDB ID: 4L8A) structures due to its interaction with Arg141 compared to ARG49. The carboxylate of bisubstrate **3** interacts in this manner because the bisubstrate is formed by attacking the alpha-CH<sub>2</sub> of the chloroacetyl group rather than the acyl C=O carbon for formation of bisubstrate **6**, which provides an extra methylene and lengthens the molecule. In absence of the complex structure with bisubstrate **3**, we would not have identified Arg141 as a potentially important residue for ligand binding. It appears that either arginine residue can be present for catalysis to occur, albeit to a lesser extent, but turnover

is dramatically decreased when both are not present. Since the native substrate of this enzyme is not yet known, these results provide new information about the architecture of the active site that is critical for catalysis.

Our study has expanded the tools for forming bisubstrates for GNAT structure determination and can be applied to other acyltransferases, which indicates broad applicability across enzyme families and types of acceptor substrates. In particular, our serendipitous radical-mediated approach for producing bisubstrates could improve the quantity of acyltransferase crystal structures obtained in complex with specific ligands. Since PA4794 is specific for acylating a C-terminal lysine residue, we consider it a model system for identifying the best chemical approaches for studying and designing specific inhibitors for other lysine acetyltransferases, such as histone acetyltransferases.

### **Conclusions**

We have documented two methods of obtaining bisubstrate-CoA molecules in the active site of our model GNAT, one through traditional chemical processes through a substitution reaction of the thiol-CoA with an alpha-acetyl halide, and one through an interesting new route, creating the bound bisubstrate molecule using an X-ray radical catalyzed mechanism to form the Lig-C-S-CoA bond. The new bisubstrates in combination with our prior studies and the PBTSM method have shed light on the theoretical substrate binding mode and identification of importance of two arginine residues that can accommodate the same tetrahedral intermediate stabilizing residues found in the active site of the protein, and expanded upon the existing crystallographic strategies for improving ligand bound GNAT structures. We have used this data to guide mutation studies and *in silico* modeling studies to answer questions regarding mechanism of acetyl transfer in the native enzyme.

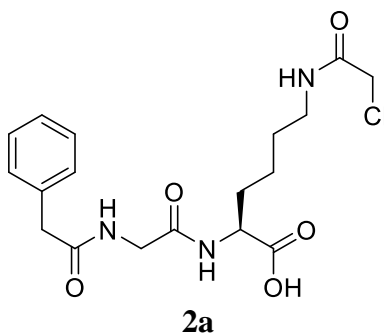
## Experimental Section

### Materials.

All solvents were distilled prior to use, and all reagents were used without further purification unless otherwise noted. All synthetic reactions were conducted under a nitrogen atmosphere. Silica gel 60 Å, 40–75 µm (200 × 400 mesh), was used for column chromatography. Aluminum-backed silica gel 200 µm plates were used for TLC. <sup>1</sup>H NMR spectra were obtained using either a 300 MHz spectrometer or a 500 MHz spectrometer with trimethylsilane (TMS) as the internal standard. <sup>13</sup>C NMR spectra were obtained using a 75 MHz spectrometer or a 125 MHz spectrometer. HRMS spectra were measured on a TOF instrument by electrospray ionization (ESI). Acetyl coenzyme A (AcCoA) and coenzyme A (CoA) trilithium salts and N-phenylacetyllysine (NPAcGK) were purchased from Sigma-Aldrich. All other reagents for biochemical assays were purchased at the highest quality available.

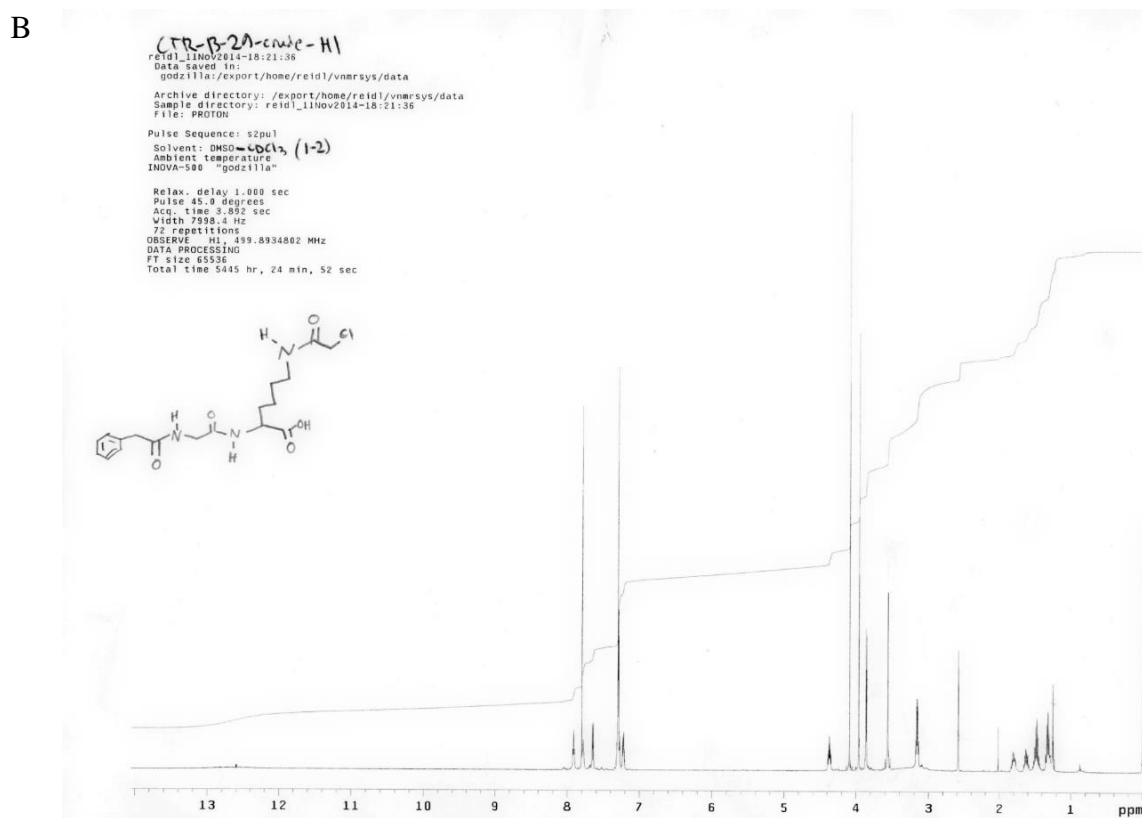
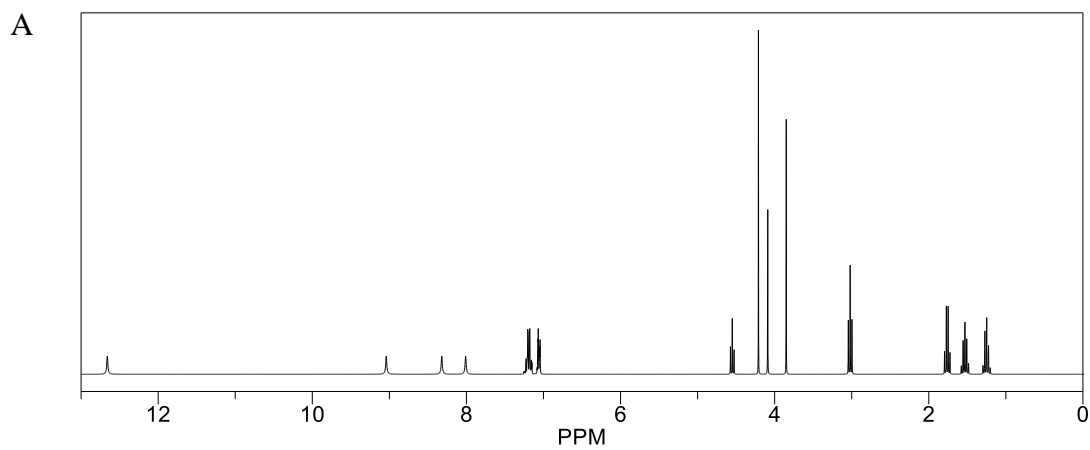
### Chemistry.

NPAcGK (**1**) was reacted with chloroacetyl chloride, and also with bromoacetyl bromide, affording electrophilic derivatives **2a** and **2b**, respectively (Scheme 13). As detailed below, **2a** and **2b** both yielded the same bisubstrate **3** in the active site of PA4794. We employed a classic nitrous acid conversion of the primary ε-amine of the lysine moiety of NPAcGK to obtain a mixture of the alcohol **4** and alkene **5**, produced by reaction with water, or by elimination, respectively (Scheme 14). We found that the diazonium reaction utilizing sodium nitroprusside<sup>214</sup> was milder and higher yielding than the traditional sodium nitrite and hydrochloric acid. The mixture of **4** and **5** proved to be inseparable with normal-phase chromatography, nevertheless this provided the mixture to test as a potential substrate for the enzyme, as well as providing material for cocrystallization.

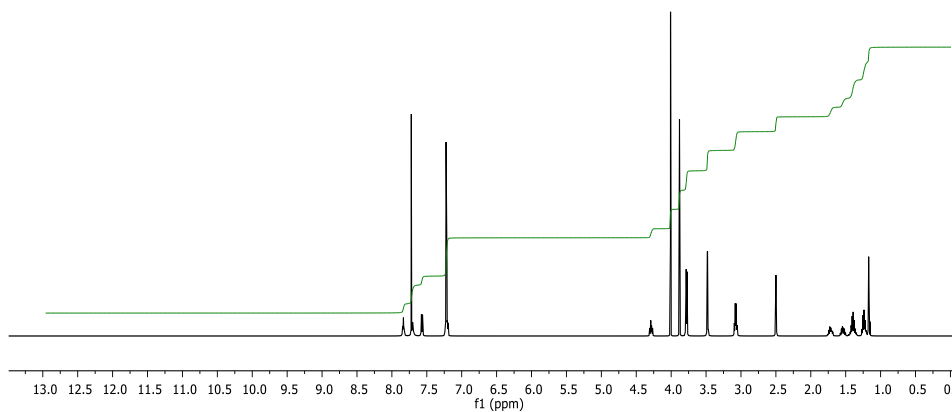


**Synthesis of N6-(2-chloroacetyl)-N2-((2-phenylacetyl)glycyl)-L-lysine (2a).**  $K_2CO_3$  (46.0 mg, 0.33 mmol) was added to a solution of NPAcGK **1** (53.0 mg, 0.165 mmol) in deionized water (0.55 mL). The reaction mixture was then cooled in an ice bath and chloroacetyl chloride (19.8  $\mu$ L, 28.0 mg, 0.248 mmol) was added under nitrogen slowly over several minutes via micro syringe, and the reaction was allowed to warm to RT over 4 hours. The pH of the reaction was adjusted to 4 by adding 4N HCl before liquid/liquid extraction with three portions of ethyl acetate to recover the desired product. The combined organic fractions were washed with brine and dried over magnesium sulfate before being concentrated under reduced pressure to afford the desired chloroacetyl derivative **2a** as a colorless glass (34 mg, 52 %):  $^1H$  NMR (500 MHz, 1:3  $CDCl_3$  +  $d_6$ -DMSO):  $\delta$  12.7 (bs, 1H), 7.91 (t,  $J=5.5$  Hz, 1H), 7.78 (t,  $J=5.0$ , 1H), 7.65 (d,  $J=8$  Hz, 1H), 7.32-7.21 (m, 5H), 4.37 (dt,  $J=8.5, 5.5$  Hz, 1H), 3.96 (s, 2H), 3.86 (d,  $J=5.5$  Hz, 2H), 3.56 (d,  $J=2$  Hz, 2H), 3.16 (q,  $J=6.5$  Hz, 2H), 1.84-1.77 (m, 1H), 1.62 (m, 1H), 1.47 (n,  $J=7$  Hz, 2H), 1.32 (m, 2H); HRMS (MH) $^+$  calc for  $C_{18}H_{25}ClN_3O_5$ , 398.1483; found, 398.1477.





C



D

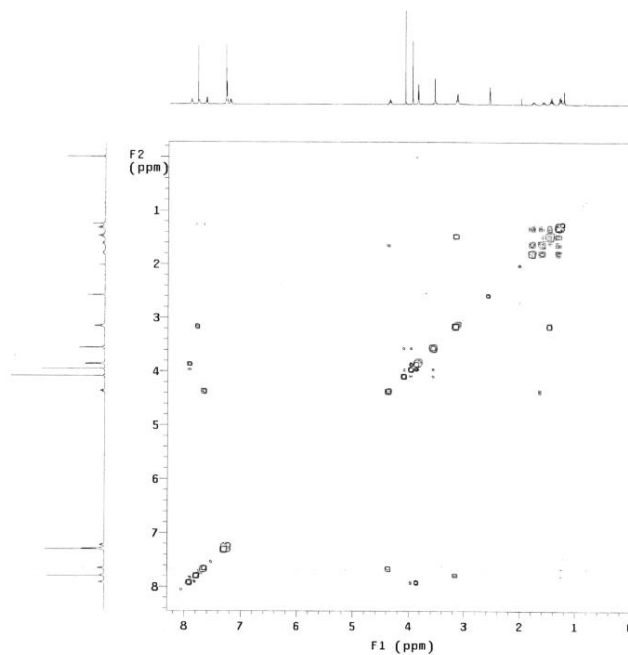
```

reid1_11Nov2014-17:24:27
Data saved to:
godzilla:/export/home/reid1/vnmrSYS/data
Archive directory: /export/home/reid1/vnmrSYS/data
Sample directory: reid1_11Nov2014-17:24:27
File: CDSY

Pulse Sequence: CDSY
Solvent: DMSO
Ambient temperature
INOVA-500 "godzilla"

Relax. delay 1.000 sec
Acq. time 0.128 sec
Width 7998.4 Hz
ZD Width 7998.4 Hz
2 repetitions
128 increments
OBSERVE F1, 499.8534882 MHz
DATA PROCESSING
Sf. size 2048 x 2048
F1 DATA PROCESSING
Sf. size 2048 x 2048
FT size 2048 x 2048
Total time 5 min, 29 sec

```



E

| Best     | Formula            | Score            | Mass       | Mass (MFG)    | Diff (ppm)      | Diff (abs. ppm)    | Diff (mDa)        | ID Source          | Score (MFG)               |
|----------|--------------------|------------------|------------|---------------|-----------------|--------------------|-------------------|--------------------|---------------------------|
| ✓        | C18 H24 Cl N3 O5   | 97.99            | 397.1398   | 397.1404      | 1.61            | 1.61               | 0.64              | MFG                | 97.99                     |
| Species  | Ion Formula        | m/z              | Height     | Score (MFG) * | Score (MFG, MS) | Score (MFG, MS/MS) | Score (MFG, mass) | Score (MFG, abund) | Score (MFG, iso. spacing) |
| □        | (M+H) <sup>+</sup> | C18 H25 Cl N3 O5 | 398.1477   | 1730524.1     | 97.99           | 97.99              | 97.74             | 99.37              | 96.83                     |
| m/z      | m/z (Calc)         | Diff (ppm)       | Diff (mDa) | Height        | Height (Calc)   | Height %           | Height % (Calc)   | Height Sum %       | Height Sum% (Calc)        |
| 398.147  | 398.1477           | 1.71             | 0.7        | 1730593.6     | 1744058.1       | 100                | 100               | 60.4               | 60.8                      |
| 399.1507 | 399.1508           | 0.13             | 0.1        | 368798.2      | 366989.9        | 21.3               | 21                | 12.9               | 12.8                      |
| 400.1457 | 400.1455           | -0.39            | -0.2       | 609662.1      | 612684.6        | 35.2               | 35.1              | 21.3               | 21.4                      |
| 401.148  | 401.1482           | 0.7              | 0.3        | 115070.5      | 123512.9        | 6.6                | 7.1               | 4                  | 4.3                       |
| 402.1541 | 402.1505           | -8.94            | -3.6       | 28906.1       | 18043.2         | 1.7                | 1                 | 1                  | 0.6                       |
| 403.1594 | 403.153            | -15.87           | -6.4       | 5258.3        | 1991.8          | 0.3                | 0.1               | 0.2                | 0.1                       |
| 404.1537 | 404.1554           | 4.21             | 1.7        | 9172.1        | 180.3           | 0.5                | 0                 | 0.3                | 0                         |

Spectrum Identification Results: + Scan (0.191-0.240 min) Sub (CTR-B-29. D (2a))

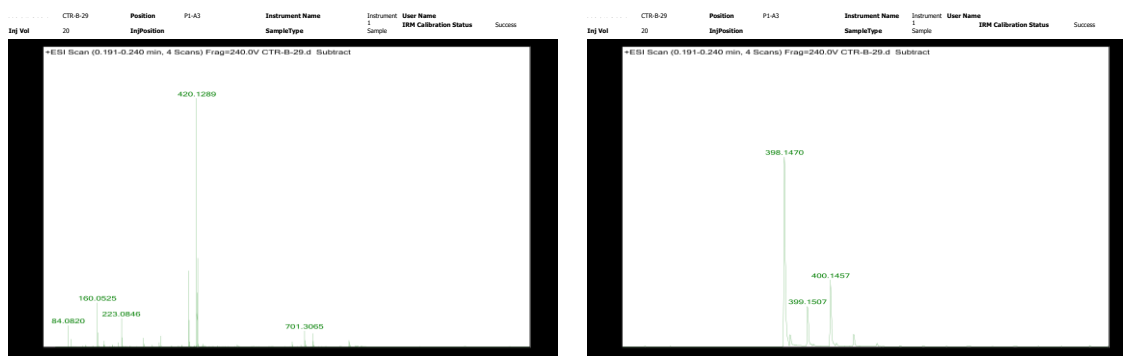
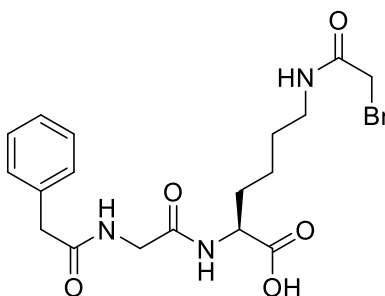
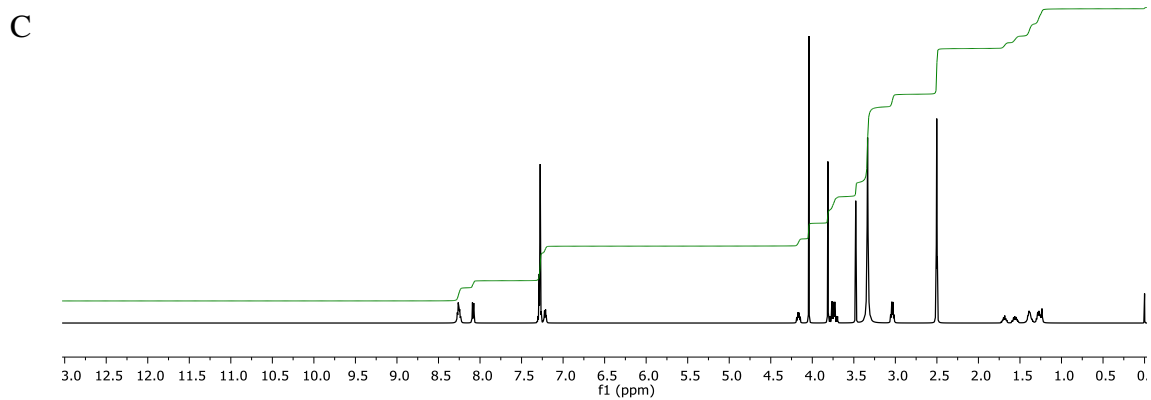
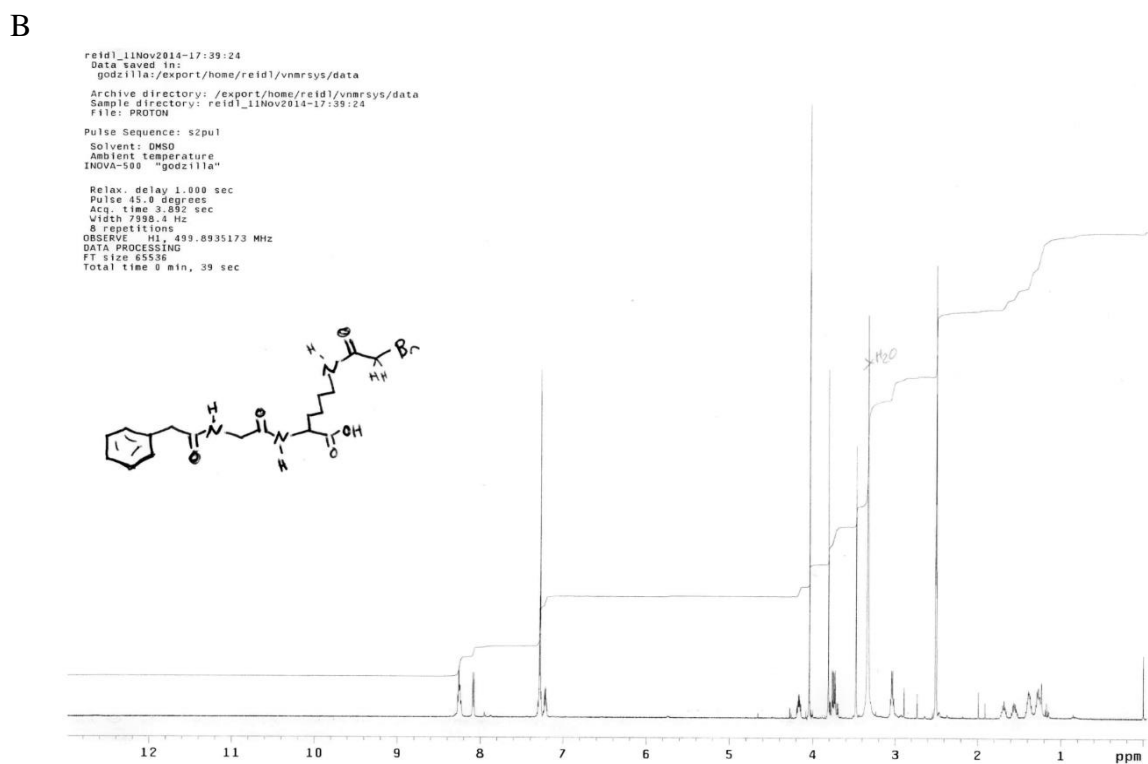
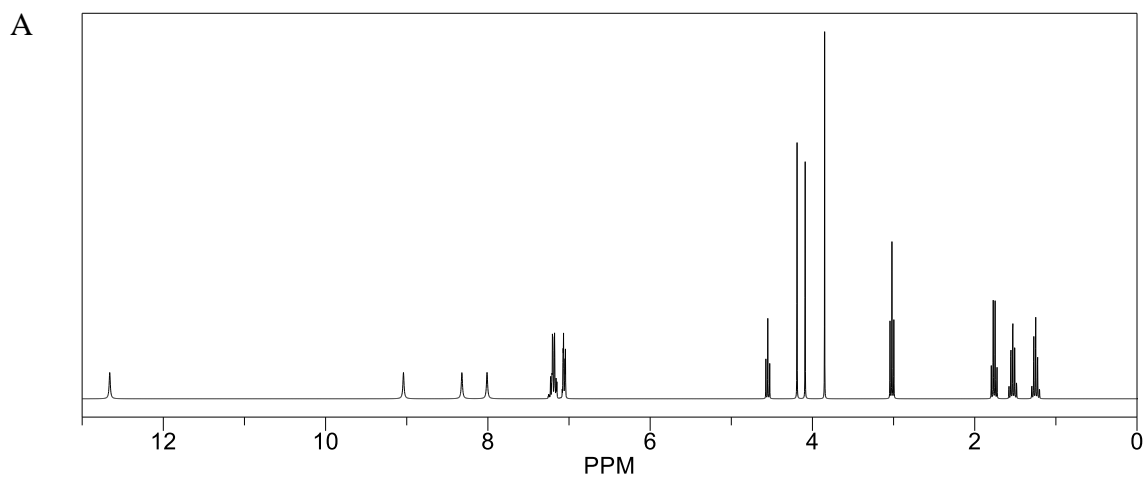


Figure 71.: Spectral data for N6-(2-chloroacetyl)-N2-((2-phenylacetyl)glycyl)-L-lysine (**2a**). A) predicted  $^1\text{H}$  NMR, B) unprocessed  $^1\text{H}$  NMR, C) Mnova-processed  $^1\text{H}$  NMR, D) & COSY NMR, E) HRMS.



**2b**

**Synthesis of N6-(2-bromoacetyl)-N2-((2-phenylacetyl)glycyl)-L-lysine (**2b**).** In a manner analogous to **2a**, bromoacetyl derivative **2b** was prepared as a colorless glass (34 mg, 16 %):  $^1\text{H}$  NMR (500 MHz,  $d_6$ -DMSO):  $\delta$  13.03 (bs, 1H), 8.27-8.23 (m, 2H), 8.08 (d,  $J=8\text{Hz}$ , 1H), 7.31-7.19 (m, 5H), 4.17 (dt,  $J=8.5, 5\text{Hz}$ , 1H), 3.81 (s, 2H), 3.76 (dd,  $J=29, 5.5\text{Hz}$ , 1H), 3.73 (dd,  $J=29, 6\text{Hz}$ , 1H), 3.48 (s, 2H), 3.04 (q,  $J=6\text{Hz}$ , 2H), 1.69 (m, 1H), 1.56 (m, 1H), 1.41-1.24 (m, 4H).



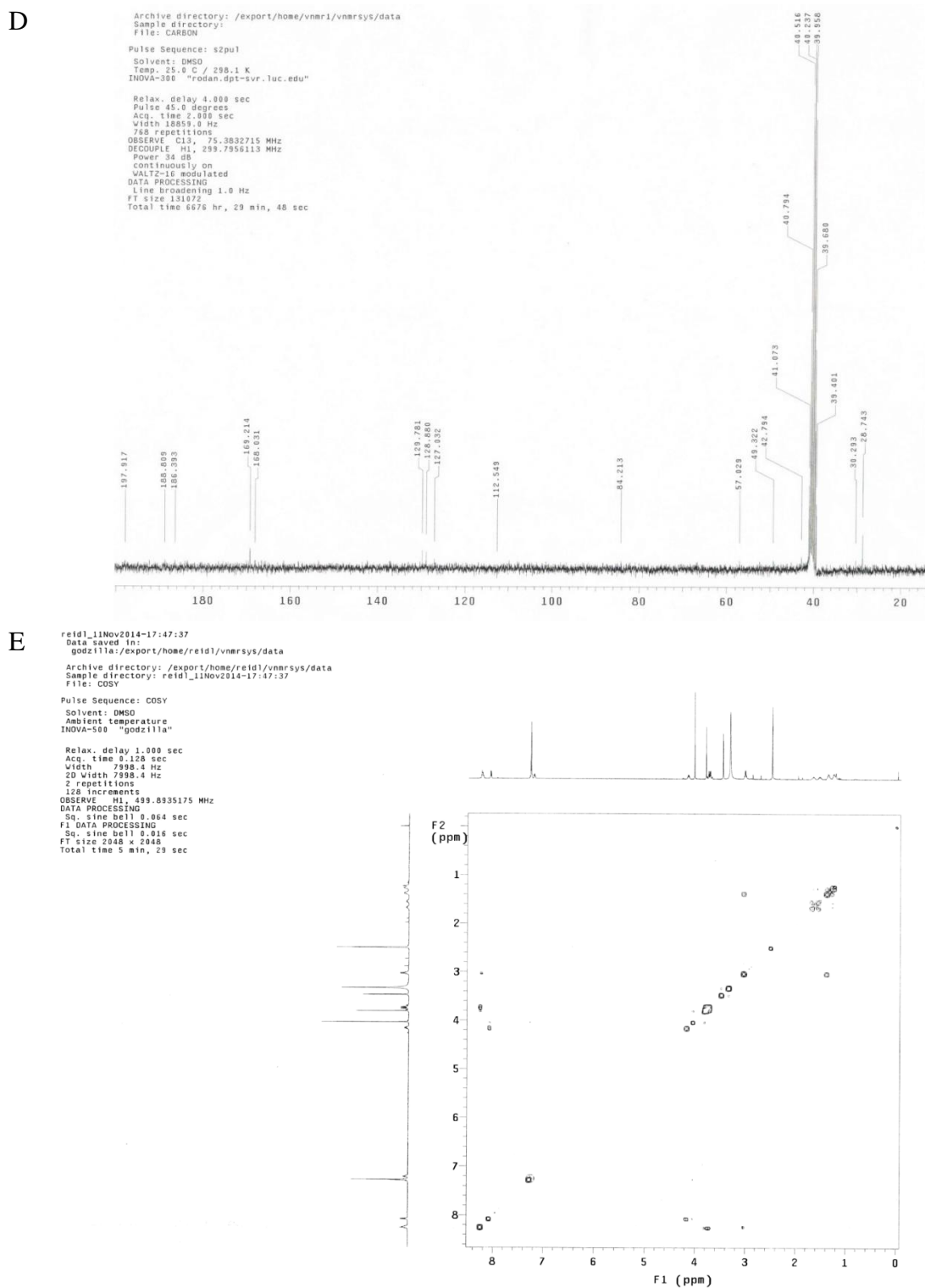
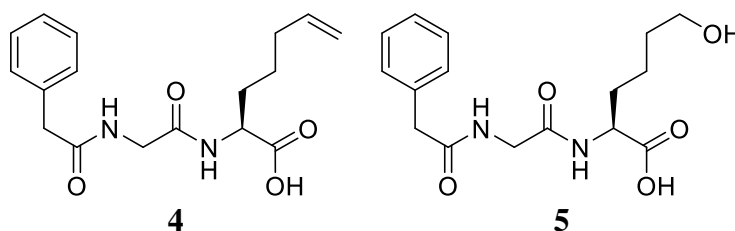


Figure 72. Spectral data for N6-(2-chloroacetyl)-N2-((2-phenylacetyl)glycyl)-L-lysine (**2a**). A) predicted  $^1\text{H}$  NMR, B) unprocessed  $^1\text{H}$  NMR, C) Mnova-processed  $^1\text{H}$  NMR, D)  $^{13}\text{C}$  NMR, E) COSY NMR.

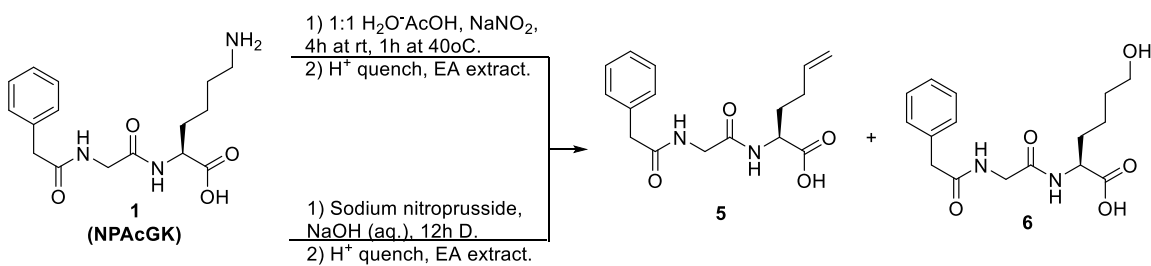


**Synthesis of (S)-6-hydroxy-2-(2-(2-phenylacetamido)acetamido)hexanoic acid (4) and (S)-2-(2-(2-phenylacetamido)acetamido)hex-5-enoic acid (5).** The NPACGK analogs **4/5** were

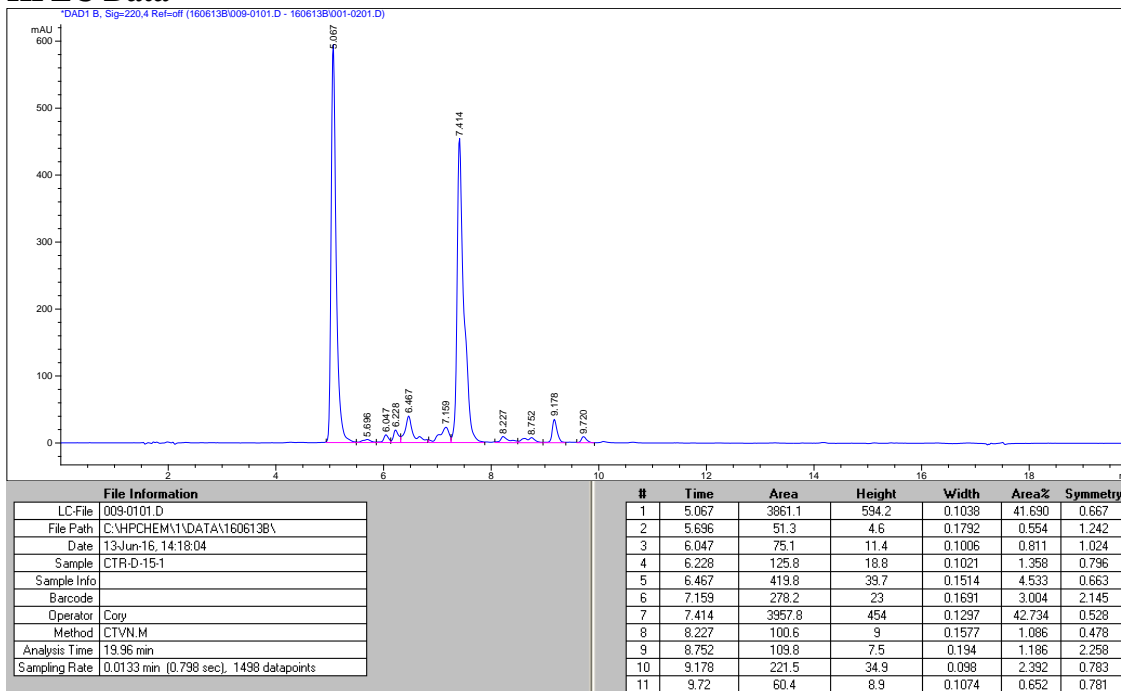
made according to scheme 16 below. NPACGK (**1**) (100 mg, 0.312 mmol) was dissolved in nano-pure H<sub>2</sub>O (4 mL) followed by 4 N NaOH (60 μL). The mixture was then heated overnight at 60 °C. Sodium nitroprusside (115.1 mg, 0.386 mmol) was added to a separate vial and dissolved in H<sub>2</sub>O (200 μL) with gentle heating. The nitroprusside was then added to the NPACGK basic solution slowly with alternating 30 μL portions of nitroprusside followed by 30 μL of 4 N NaOH over 35 min, total volume equaling 150 μL iron catalyst and 170 μL NaOH. The sample was then allowed to stir at 60 °C overnight. The pH of the reaction was adjusted to 4 by adding 4 N HCl before liquid/liquid extraction with three portions of ethyl acetate to recover the desired product. The combined organic fractions were washed with brine and dried over magnesium sulfate before being concentrated under reduced pressure to afford the desired alkene/alcohol product mixture **4/5** as a colorless oil (30.1 mg, 30%). RP LC-MS analysis on a Surveyor Liquid Chromatography system equipped with a Symmetry Shield RP18 column (5.0 μm, 100 Å) and coupled to an LCQ Advantage Mass Spectrum System (Elution with a 5 % CH<sub>3</sub>CN (0.1 v/v TFA)-H<sub>2</sub>O [A]/ 100 % CH<sub>3</sub>CN (0.1 v/v TFA) [B] at 1 mL/min flow rate and T<sub>total</sub> = 20 min. Solvent gradient of T<sub>0 min</sub> = 90 % A / 10 % B to T<sub>15 min</sub> = 10 % A / 90 % B until gradient switch at T<sub>15.1 min</sub> back to 90 % A / 10 % B until T<sub>20 min</sub>) was performed. The alcohol **4** retention time was 5.067 min (MS m/z calc for C<sub>16</sub>H<sub>22</sub>N<sub>2</sub>O<sub>5</sub> obs 322 and alkene **5** retention time

was 7.414 min (MS m/z calc for C<sub>16</sub>H<sub>20</sub>N<sub>2</sub>O<sub>4</sub> 304, obs 304). The product mixture was used without further purification.

Scheme 16. Synthesis of (S)-6-hydroxy-2-(2-(2-phenylacetamido)acetamido)hexanoic acid (**4**) and (S)-2-(2-(2-phenylacetamido)acetamido)hex-5-enoic acid (**5**).



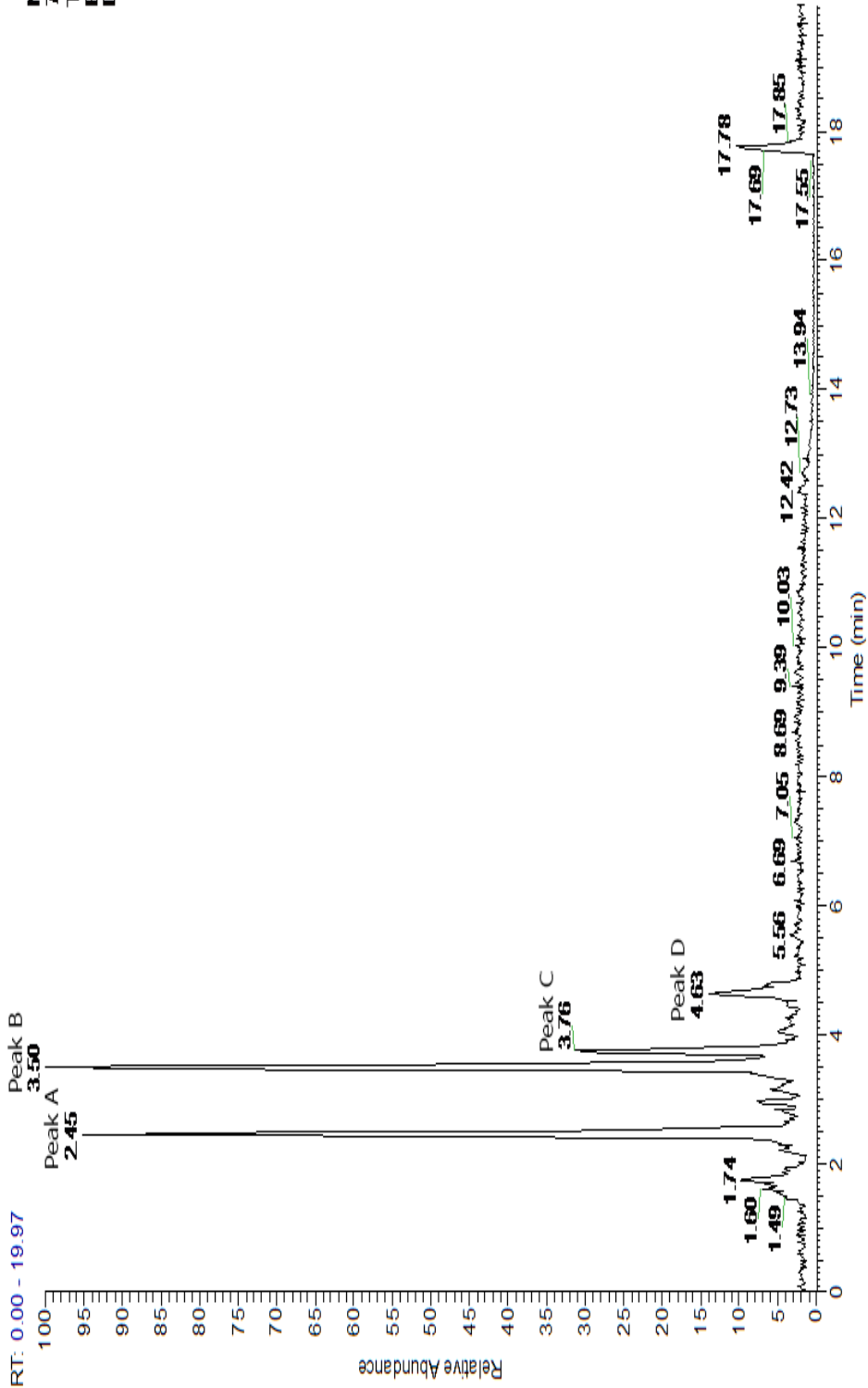
### HPLC Data



# LC-MS Data

RT: 0.00 - 19.97

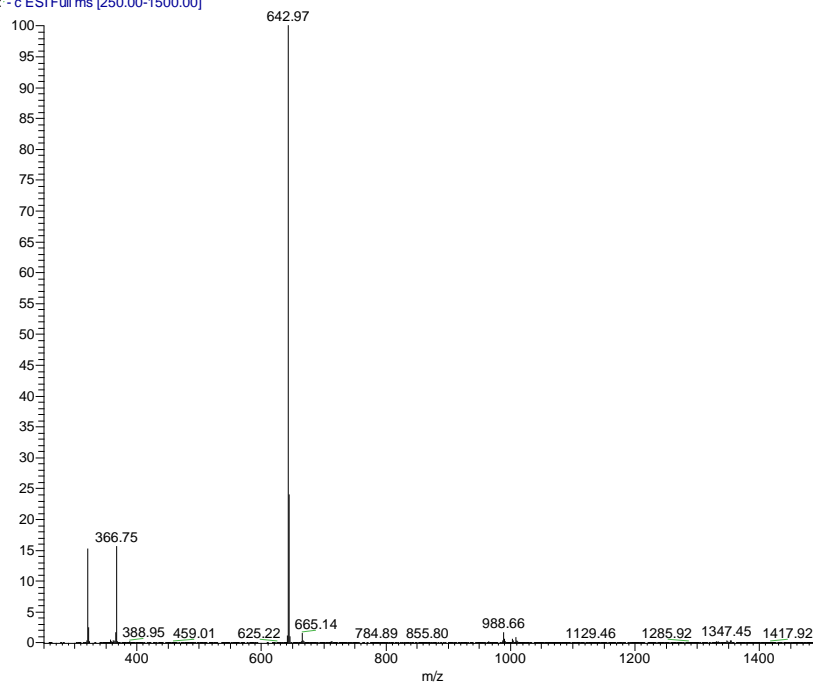
NL:  
7.66E8  
TIC MS  
BG CTR  
D-15-1-pw





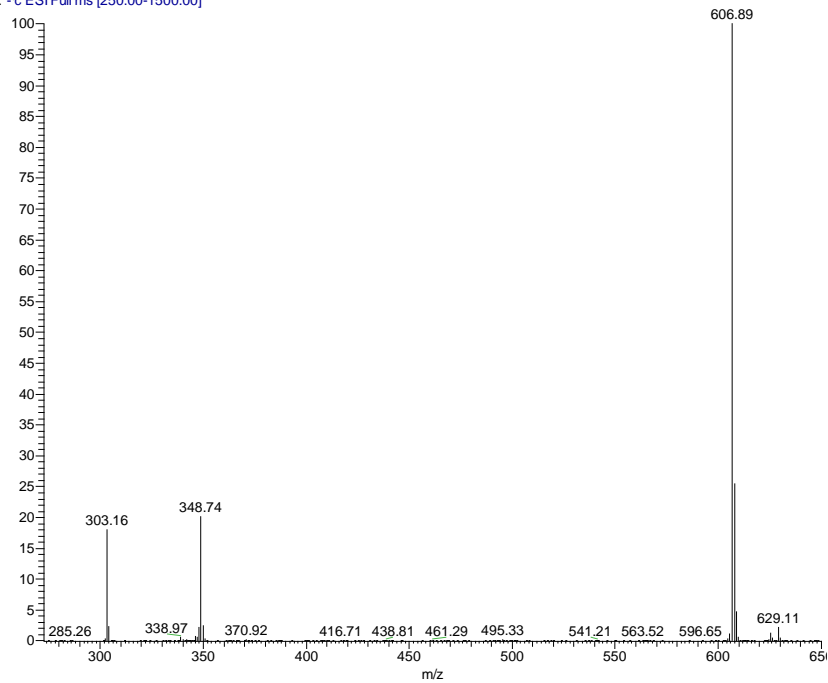
**Peak  
A**  
RT=2.45  
m  
Alcohol

BG\_CTR-D-15-1-pw#125-132 RT: 2.37-2.49 AV: 8 NL: 2.03E8  
T: -c ESI Full ms [250.00-1500.00]



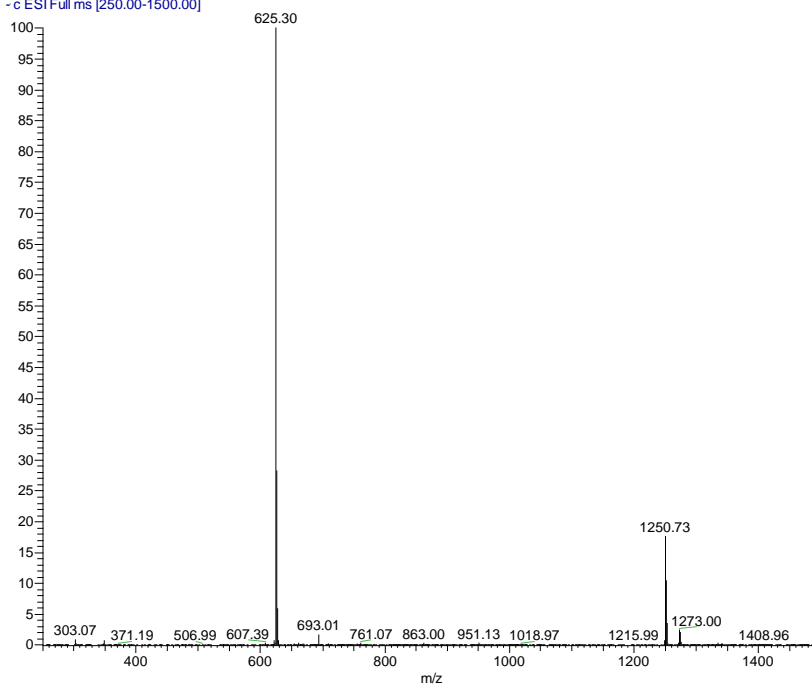
**Peak  
B**  
RT=3.50  
m  
Alkene

BG\_CTR-D-15-1-pw#182-190 RT: 3.41-3.55 AV: 9 NL: 2.00E8  
T: -c ESI Full ms [250.00-1500.00]



**Peak  
C**

BG\_CTR-D-15-1-pw #197-204 RT: 3.67-3.79 AV: 8 NL: 8.37E7  
T: -c ESI Full ms [250.00-1500.00]

**Peak  
D**

BG\_CTR-D-15-1-pw #247-256 RT: 4.60-4.76 AV: 10 NL: 2.27E7  
T: -c ESI Full ms [250.00-1500.00]

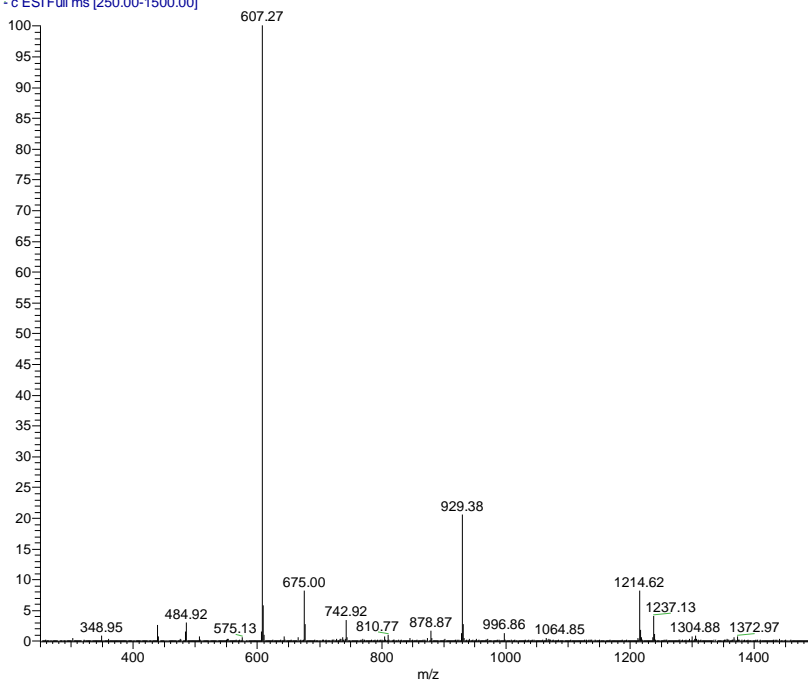
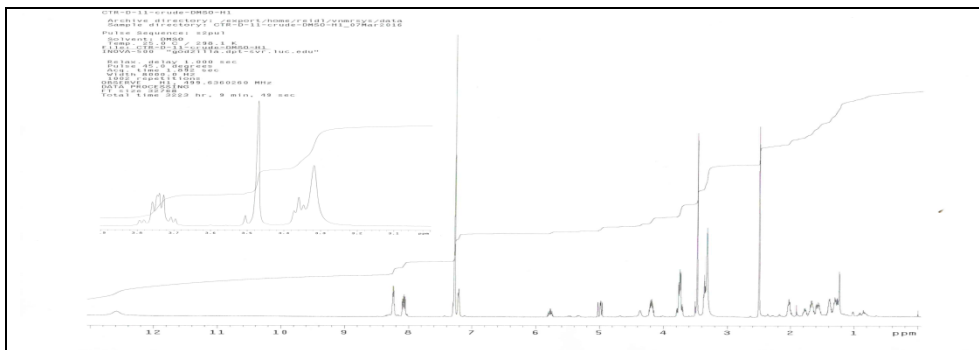
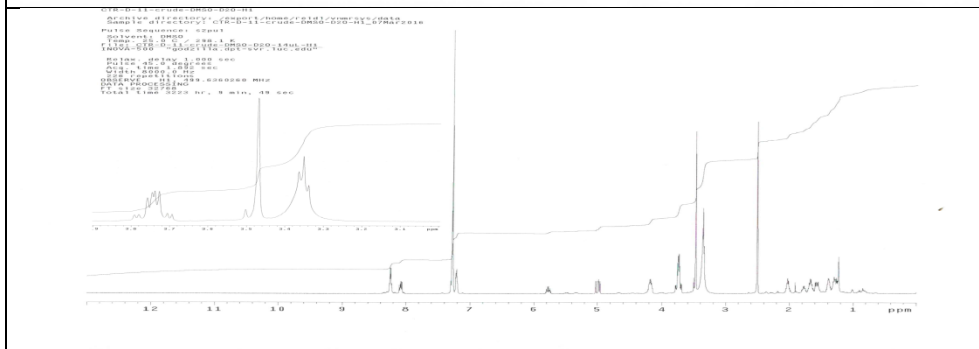


Figure 73. HPLC and LC-MS Data for 4 & 5 Sample Mixture.

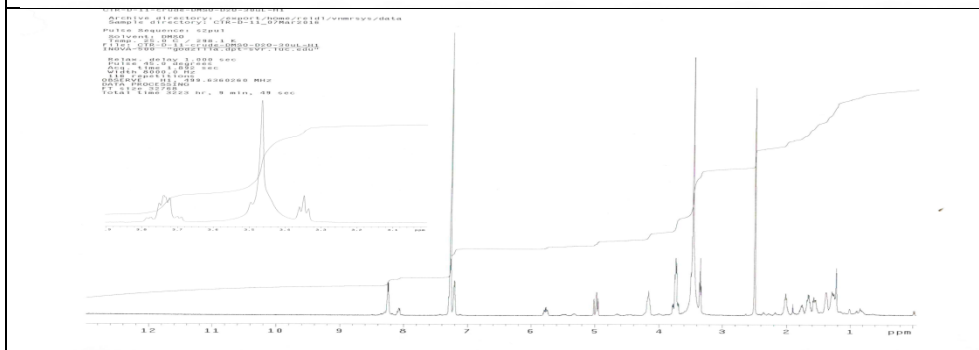
$^1\text{H}$  NMR:  
7.5 mg  
4/5 in  
750  $\mu\text{L}$   
DMSO



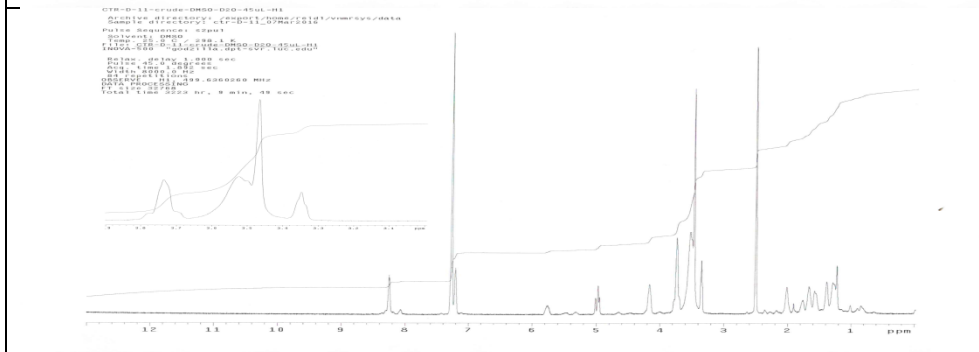
$^1\text{H}$  NMR:  
7.5 mg  
4/5 in  
750  $\mu\text{L}$   
DMSO +  
14  $\mu\text{L}$   
D2O



$^1\text{H}$  NMR:  
7.5 mg  
4/5 in  
750  $\mu\text{L}$   
DMSO +  
30  $\mu\text{L}$   
D2O



$^1\text{H}$  NMR:  
7.5 mg  
4/5 in  
750  $\mu\text{L}$   
DMSO +  
45  $\mu\text{L}$   
D2O



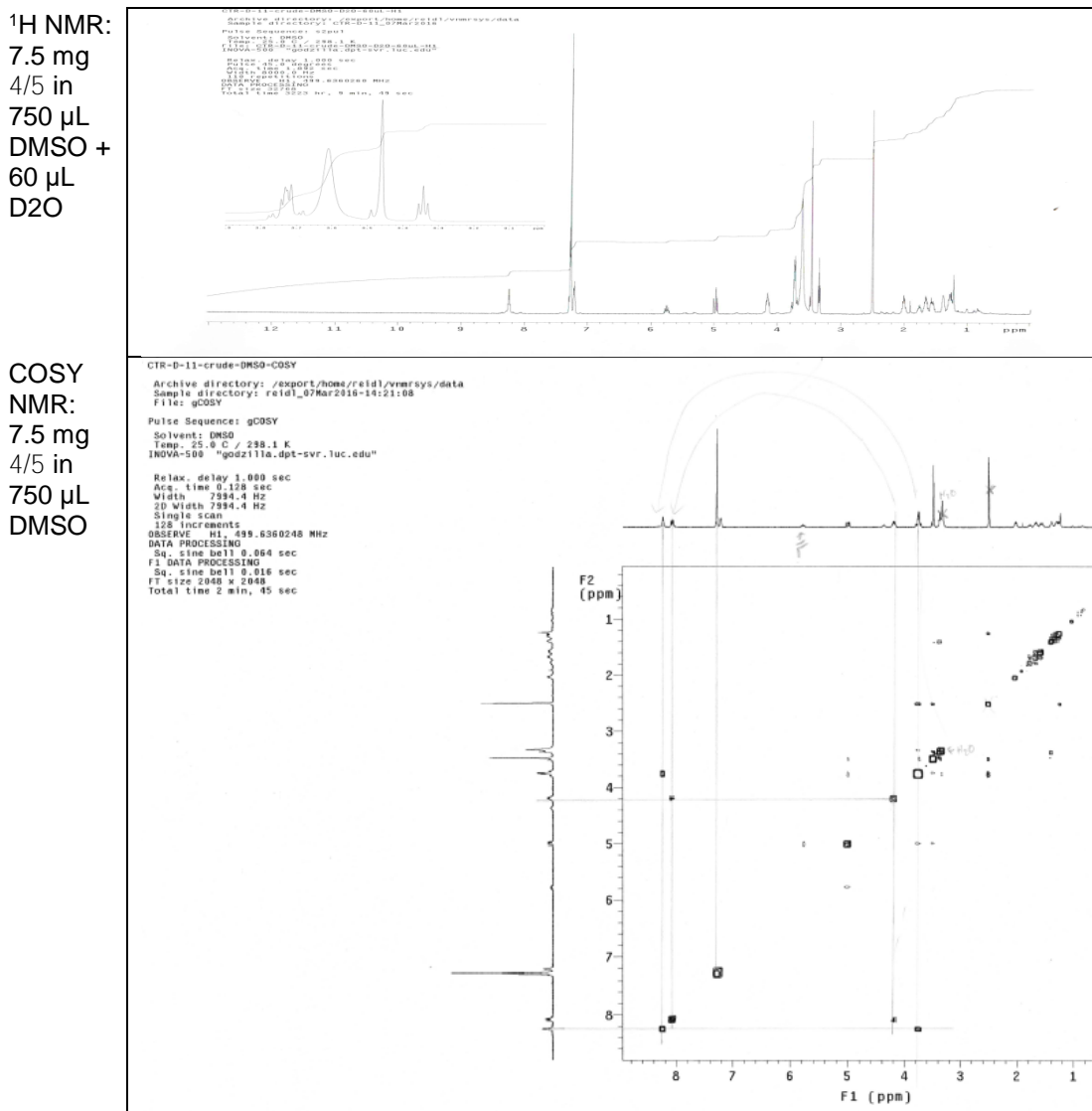


Figure 74. NMR Trituration Experiment on **4/5** Product Mixture.

**Determination of kinetic mechanism.** The most compatible model for the WT PA4794 kinetic mechanism was determined as described previously<sup>216</sup> where a series of four NPACGK substrate saturation curves at set concentrations of AcCoA (0.1, 0.25, 0.5, 1 mM) were produced using cleaved 2.1 μM WT protein while varying NPACGK concentrations from 0-25 mM.

**Substrate analog test.** To determine if the PA4794 enzyme could acetylate the NPACGK alcohol analog, we performed the following assay using the **4/5** mixture since the two compounds could not be separated from each other. A 50 mM stock of the **4/5** mixture was

prepared by dissolving the compounds in 50mM Bicine pH 9.0 buffer. Substrate saturation curves were produced in triplicate using reactions (50  $\mu$ L volume) containing 50 mM Bicine pH 9.0 buffer, 0.5 mM AcCoA, and varying concentrations of the **4/5** alcohol/alkene mixture (from 0-25 mM). The reactions were initiated with 5.1  $\mu$ M WT cleaved enzyme and were processed as described previously<sup>205</sup>.

### **Enzyme-mediated formation of bisubstrate with alkene.**

To determine if the bisubstrate formation was enzyme-mediated, we prepared a 25 mM stock solution of the **4/5** mixture in 50 mM Bicine pH 9.0. Reactions (50  $\mu$ L) contained 50 mM Bicine pH 9.0, 5 mM CoA, and 10 mM **4/5** mixture, and were initiated using either 1.1 or 11  $\mu$ M cleaved WT enzyme and incubated at RT for 19 hrs. Control reactions included: 1) no enzyme, 2) no enzyme and no **4/5** mixture, 3) and no enzyme, no **4/5** mixture, and no CoA. The next day 150  $\mu$ L of MeOH was added to each sample, centrifuged for 5 min at 21,000 x g, and transferred to an HPLC vial for analysis. No precipitate was observed.

### **HPLC analysis of enzyme-mediated formation of bisubstrate with alkene.**

To analyze possible PA4794 enzyme-mediated formation of the bisubstrate, high-performance liquid chromatography (HPLC) analysis was performed according to a previously described HPLC method<sup>193</sup> with the following modifications. Samples were analyzed on a Hewlett Packard 1050 series HPLC system with diode array detector (DAD) set to monitor 205 nm using a Regis Little Champ II ODS guard column coupled to a SymmetryShield RP18, 3.3  $\mu$ m, 100A column. Filtered samples were loaded into standard size VWR autosampler HPLC vials fitted with 300 $\mu$ L conical glass inserts. Samples were eluted on a 5% acetonitrile (0.1% v/v TFA)-H<sub>2</sub>O [A]/ 5% acetonitrile (0.1% v/v TFA) [B] at 1 mL/min flow rate. A solvent gradient from 90% A / 10% B at time 0 to 10% A / 90% B at time 15 min was used. At time 15.1 min the

gradient was switched to 90% A / 10% B for a re-equilibration period until the end of the method at time 25 min. Samples were additionally analyzed on a Surveyor Liquid Chromatography system equipped with a SymmetryShield RP18, 5.0  $\mu\text{m}$ , 100A column and a UV-Vis unit set to monitor absorbance between 200-275 nm. The LC system was coupled to an LCQ Advantage Mass Spectrometer System monitoring both positive and negative modes under full scan.

#### **HPLC analysis of radical-mediated AIBN formation of bisubstrate with alkene.**

The radical-mediated AIBN reaction was used to test for formation of the bisubstrate with the **4/5** mixture in the presence of coenzyme A. A sample of the **4/5** mixture (2.2 mg,  $\sim 6.8$   $\mu\text{mol}$ ) was dissolved in HPLC grade methanol (35  $\mu\text{l}$ ) followed by addition of AIBN (300 mg, 0.34  $\mu\text{mol}$ ) and CoA (5.3 mg, 6.8  $\mu\text{mol}$ ). The reaction was stirred at 60°C over four hours and then diluted with 2.0 mL of methanol. HPLC analysis was performed as described above.

#### **AIBN mediated bisubstrate sample purification & LC MS/MS analysis.**

Solid-phase extraction (SPE) was performed using an AASP Vac-Elut Model AI 6000 vacuum manifold from Analytichem International and was regulated to maintain a flowrate of 3-5 mL/min. The desalting procedure was performed using a 200 mg Oasis HLB resin (Waters) extraction cartridge loaded with a 3 mg sample of concentrated bisubstrate as follows: The SPE cartridge was conditioned with 1 mL acetonitrile followed by 1 mL of 0.1M triethylammonium acetate buffer (TEAA) at pH 7. The crude sample was dissolved in 500  $\mu\text{L}$  0.1 M TEAA and loaded onto the SPE cartridge. The cartridge was washed with 2 x 5 mL of 0.1 M TEAA followed by 5 mL DI H<sub>2</sub>O to remove salts from the sample. The sample was recovered using three consecutive 500  $\mu\text{L}$  elutions of 70% acetonitrile-H<sub>2</sub>O. The purified analyte was then analyzed with direct inject mass spectroscopy on a LCQ Advantage Mass Spectrometer System monitoring negative mode under full scan. Mass calc. for C<sub>37</sub>H<sub>56</sub>N<sub>9</sub>O<sub>2</sub>P<sub>3</sub>S 1071.26, found

1070.21. A MS<sup>2</sup> fragmentation ion spectrum was also obtained for the ion peak at 1070 with a 30% fragmentation power.<sup>222</sup>

### **Protein Crystallization.**

PA4794 protein crystals were grown by Karolina Majorek using vapor diffusion and hanging drop setups. The crystallization drops were a 1  $\mu$ l : 1  $\mu$ l mixture of protein solution at 9 mg/mL and the precipitant composed of 2 M ammonium sulfate and 100 mM Bis-Tris pH 6.5. To obtain structures of the PA4794 protein in the presence of bisubstrates, apo-form crystals were soaked first with 5mM CoA, followed by adding 10 mM of the N6-(2-chloroacetyl)-N2-((2-phenylacetyl)glycyl)-L-lysine **2a** or mixture of (S)-6-hydroxy-2-(2-(2-phenylacetamido)acetamido)hexanoic acid (**4**) and (S)-2-(2-(2-phenylacetamido)acetamido)hex-5-enoic acid (**5**). Prior to data collection, each crystal was transferred to a solution containing a 2:1 mixture of precipitant solution and ethylene glycol and immediately cryo-cooled in liquid nitrogen. Tracking and analysis of the experiments were performed with the LabDB and XtalDB data management system.

### **Data collection, structure determination and refinement.**

Data collection was performed at the 21-ID-G beam line of the Life Sciences Collaborative Access Team at the Advanced Photon Source (APS). Data were collected at a temperature of 100 K and processed with HKL-2000<sup>223</sup>. The PA4794 structure (PDB ID: 4L8A) was used as a model to solve the structure of PA4794 in complex with bisubstrates by molecular replacement (MR) using HKL-3000<sup>224</sup> coupled with MOLREP<sup>225</sup>. Refinement was performed using HKL-3000<sup>226,227, 228</sup> and selected programs from the CCP4 package (Collaborative Computational Project, 1994). The atom B-factors were refined using anisotropic refinement. Structure validation was performed using MOLPROBITY<sup>229</sup> and ADIT<sup>230</sup>. Structures of PA4794

in complex with two bisubstrates were determined: (A) (3R,20S)-1-(((((((2R,3S,4R,5R)-5-(6-amino-9H-purin-9-yl)-4-hydroxy-3-(phosphonoxy)tetrahydrofuran-2-yl)methoxy)(hydroxy)phosphoryl)oxy)(hydroxy)phosphoryl)oxy)-3-hydroxy-2,2-dimethyl-4,8,14-trioxo-20-(2-(2-phenylacetamido)acetamido)-12-thia-5,9,15-triazahenicosan-21-oic acid (**3**) and (B) (2R)-5-((2-(3-((2R)-4-(((((((2R,3S,4R,5R)-5-(6-amino-9H-purin-9-yl)-4-hydroxy-3-(phosphonoxy)tetrahydrofuran-2-yl)methoxy)(hydroxy)phosphoryl)oxy)(hydroxy)phosphoryl)oxy)-2-hydroxy-3,3-dimethylbutanamido)propanamido)ethyl)thio)-2-(2-(2-phenylacetamido)acetamido)pentanoic acid (**6**). The coordinates, structure factors, and intensities were deposited in the PDB (PDB ID: TBD).

### ***In Silico Modeling.***

Modeling and molecular dynamics simulations were performed using Chemical Computing Group's M.O.E. (Molecular Operating Environment).<sup>76</sup> To understand the critical components of the PA4794 acetyl transfer reaction mechanism, the crystal structure of the PA4794 ternary complex (PDB ID: 4L8A) and the bisubstrate co-crystal structure obtained from soaking chloroacetyl derivative **2a** and CoA (PDB ID: TBD) were used to model the tetrahedral intermediate expected to be generated during the acetyl transfer reaction of AcCoA (donor) and NPAcGK (acceptor). Two separate models were prepared as starting points using MOE's utility Structure-Prep.<sup>76</sup> First, the products of the enzymatic reaction were modeled based on the conformation of bisubstrate **3** in the crystal structure using MOE's utility 3D Builder by first removing the bond between the bisubstrate sulfur of CoA and the acetyl methyl carbon of NPAcGAcK. This left NPAcGK-εNHAc and HSCoA ligands bound to the active site of the model. The 4L8A structure<sup>205</sup> already possessed these two products so no remodeling of the



second model was necessary. Next, the models were solvated in a simple water box at pH of 7.4 and treated with NaCl counter ions. Periodic boundary conditions were enabled, and the hydrogen bonding network of the model was optimized by automatic sampling of different tautomer/protomer states using Protonate3D<sup>102</sup>. Atoms were then optimized with a short, localized molecular minimization (MM) using the MOE utility QuickPrep with receptor atom tether constraint strength set to 10 and atoms further than 8 Å from the ligand fixed. Refinement proceeded until a RMS Gradient of 0.1 kcal/mol/Å was reached. Molecular Dynamics parameters were set to globally minimize the protein, ligand and solvent atoms of the models. To minimize variables during in the simulation, the atoms involved in H-bonding between the beta-alanine to beta-cysteamine amide bond were tethered to maintain the occupancy of the CoA in the active site during the annealing process. Simulated annealing was then performed on the product bound models. Molecular dynamics experiments were performed using a NPA algorithm with a Amber12:EHT force field, an initial warming from 0-311 K over 100 ps with equilibration at 311 K over 100 ps, and a 200 ps production stage at constant temperature followed by a 100 ps cooling stage from 300-0 K.

The two equilibrated and optimized NPAcGK-εNAc + HS-CoA product models were then remodeled to produce tetrahedral intermediate models. Another local minimization using QuickPrep was performed to correct the distorted atomic bonds resulting from manual ligand modification. Molecular dynamics simulations were performed to optimize the residue interactions responsible for stabilizing the tetrahedral intermediate. A second simulated annealing simulation was performed as described above except a 700 ps production stage at constant temperature followed by a 100 ps cooling stage from 300-0 K was used. Binding affinities for the molecular dynamics results were calculated based on tetrahedral intermediates.

Similar modeling was performed using the MOE 3D Build utility to systematically transform the tetrahedral intermediates for each model into corresponding substrate NPAcGK + AcCoA models. The bond between N6 and the carbon of the acetyl was deleted and the double bond of the carbonyl was reestablished, and the carbonyl oxygen and the nitrogen atoms were given a neutral charge. Then, a third and final molecular dynamics simulation was performed to validate the model using the same parameters as described above except with a 200 ps equilibration stage and 700 ps production stage at constant temperature and a 100 ps cooling stage from 300-0 K. The differences in binding modes between the two respective models for products, tetrahedral intermediates and substrates were compared to determine the likely residues critical for acetyl transfer and the most reasonable substrate approach to the active site.

### **Chapter Acknowledgements**

I am grateful to Wladek Minor, Ph.D. and Karolina A. Majorek, Ph.D. for obtaining and solving the bisubstrate crystal structures, and Misty Kuhn, Ph.D. and member of her lab for making PA4794 site-directed mutants and running the kinetic assays for this project.

I would like to thank Yasmine Payne, for assisting with running the nitroprusside diazo reactions, and Paul Chiarelli, Ph.D. for showing me how to run the LC-MS and perform the solid phase extraction technique.

APPENDIX A  
MOLECULAR SYSTEM FILE HANDLING GUIDE

The molecular model and molecular dynamics files are saved with the format: ‘ligand name’\_(additional identifier)-‘receptor name and/or pdb code’\_(conformation identifier)-(system refinement state). An example would be: Penicillin\_TS-NDM1\_4RAW-sol-min-md, which indicates the model contains a transition state intermediate of penicillin bound to the NDM1 structure, pdb code 4RAW, and which has been solvated and minimized followed by a molecular dynamics production run. MOE will by default save every file in lower case so dashes and underscores are used to communicate relating information and breaks in component train. Underscores denote entries that are related while dashes indicate a break in relation. This is a semi-cryptic method for saving, but very helpful for keeping track of in silico experiments in a large library of rapidly generated files. It is recommended that refined and finished model systems be saved often. Errors in experimental setup will happen often and it is easier to start from a stable system when solutions cannot be found. It is also good to start from a common starting point when performing variations of experiments on identical systems.

APPENDIX B  
HIGH PERFORMANCE LIQUID CHROMATOGRAPHY  
ANALYTICAL METHODS

**Method CTV1.**

Samples were analyzed on a Hewlett Packard 1050 series HPLC system with diode array detector (DAD) monitoring wave lengths of 205 nm, 220 nm, 245 nm and 275 nm coupled with a Zorbax SB-CN, 5.0  $\mu\text{m}$ , 100  $\text{\AA}$  column. Filtered samples were loaded into standard size VWR autosampler HPLC vials, injected, and eluted using 5 % acetonitrile (0.1 % v/v TFA)-H<sub>2</sub>O [A] & 5 % acetonitrile (0.1 % v/v TFA) [B] at 1 mL/min flow rate. Solvents eluted with gradient from 90 % A / 10 % B at time 0 to 10 % A / 90 % B at time 15 min was used. At time 15.1 min the gradient was switched to 90 % A / 10% B for a re-equilibration period until the end of the method at time 20 min.

**Method CB254.**

Samples were analyzed on a Hewlett Packard 1100 series HPLC system with Photo Diode Array (PDA) detector monitoring 245 nm wavelength coupled with a SymmetryShield RP18, 5.0  $\mu\text{m}$ , 100  $\text{\AA}$  column. Filtered samples were loaded into standard size VWR autosampler HPLC vials, injected, and eluted using 5 % acetonitrile (0.1 % v/v TFA)-H<sub>2</sub>O [A] & 5 % acetonitrile (0.1 % v/v TFA) [B] at 1 mL/min flow rate. Solvents eluted with gradient from 90 % A / 10 % B at time 0 to 10 % A / 90 % B at time 15 min was used. At time 15.1 min the gradient was switched to 90 % A / 10% B for a re-equilibration period until the end of the method at time 20 min.

## REFERENCES

1. Szpunar, J. Advances in analytical methodology for bioinorganic speciation analysis: metallomics, metalloproteomics and heteroatom-tagged proteomics and metabolomics. *Analyst (Cambridge, U. K.)* **2005**, *130*, 442-465.
2. Krezel, A. Metal Ions in Life Sciences, Vol. 12: Metallomics and the Cell edited by Lucia Banci. *ChemBioChem* **2014**, *15*, 473-474.
3. Kendrew, J. C.; Dickerson, R. E.; Strandberg, B. E.; Hart, R. G.; Davies, D. R.; Phillips, D. C.; Shore, V. C. Structure of Myoglobin: A Three-Dimensional Fourier Synthesis at 2 angstroms Resolution. *Nature* **1960**, *185*, 422-427.
4. Dupont, C. L.; Butcher, A.; Valas, R. E.; Bourne, P. E.; Caetano-Anolles, G. History of biological metal utilization inferred through phylogenomic analysis of protein structures. *Proc. Natl. Acad. Sci. U. S. A.* **2010**, *107*, 10567-10572, S10567/1-S10567/23.
5. Zhou, L.; Bosscher, M.; Zhang, C.; Zhang, L.; Zhang, W.; Li, C. J.; Liu, J.; Jensen, M. P.; Lai, L.; He, C. A protein engineered to bind uranyl selectively and with femtomolar affinity. *Nat Chem* **2014**, *6*, 236-241.
6. Wegner, S.; Boyaci, H.; Chen, H.; Jensen, M.; He, C. Engineering A Uranyl-Specific Binding Protein from NikR. *Angewandte Chemie International Edition* **2009**, *48*, 2339-2341.
7. Changela, A.; Chen, K.; Xue, Y.; Holschen, J.; Outten, C. E.; O'Halloran, T. V.; Mondragón, A. Molecular Basis of Metal-Ion Selectivity and Zeptomolar Sensitivity by CueR. *Science* **2003**, *301*, 1383.
8. Valdez, C. E.; Smith, Q. A.; Nechay, M. R.; Alexandrova, A. N. Mysteries of Metals in Metalloenzymes. *Acc. Chem. Res.* **2014**, *47*, 3110-3117.
9. Que, E. L.; Bleher, R.; Duncan, F. E.; Kong, B. Y.; Gleber, S. C.; Vogt, S.; Chen, S.; Garwin, S. A.; Bayer, A. R.; Dravid, V.; Woodruff, T. K.; O'Halloran, T. V. Quantitative mapping of zinc fluxes in the mammalian egg reveals the origin of fertilization-induced zinc sparks. *Nature chemistry* **2014**, *7*, 130-139.
10. Paulsen, I. T.; Saier, M. H., Jr. A novel family of ubiquitous heavy metal ion transport proteins. *J. Membr. Biol.* **1997**, *156*, 99-103.
11. Hall, J. L. Cellular mechanisms for heavy metal detoxification and tolerance. *J. Exp. Bot.* **2002**, *53*, 1-11.

12. Ucisik, M. N.; Chakravorty, D. K.; Merz, K. M. Models for the Metal Transfer Complex of the N-Terminal Region of CusB and CusF. *Biochemistry* **2015**, *54*, 4226-4235.
13. Handing, K. B.; Shabalin, I. G.; Kassar, O.; Khazaipoul, S.; Blindauer, C. A.; Stewart, A. J.; Chruszcz, M.; Minor, W. Circulatory zinc transport is controlled by distinct interdomain sites on mammalian albumins. *Chem. Sci.* **2016**, *7*, 6635-6648.
14. Uda, N. R.; Upert, G.; Angelici, G.; Nicolet, S.; Schmidt, T.; Schwede, T.; Creus, M. Zinc-selective inhibition of the promiscuous bacterial amide-hydrolase DapE: implications of metal heterogeneity for evolution and antibiotic drug design. *Metallomics* **2014**, *6*, 88-95.
15. Broder, D. H.; Miller, C. G. DapE can function as an aspartyl peptidase in the presence of Mn<sup>2+</sup>. *J Bacteriol* **2003**, *185*, 4748-4754.
16. Kim, Y.; Tesar, C.; Mire, J.; Jedrzejczak, R.; Binkowski, A.; Babnigg, G.; Sacchettini, J.; Joachimiak, A. Structure of apo- and mono-metalated forms of NDM-1 - a highly potent carbapenem-hydrolyzing metallo- $\hat{\text{I}}^2$ -lactamase. *PLoS One* **2011**, *6*, e24621.
17. Yang, H.; Aitha, M.; Marts, A. R.; Hetrick, A.; Bennett, B.; Crowder, M. W.; Tierney, D. L. Spectroscopic and mechanistic studies of heterodimetallic forms of metallo- $\hat{\text{I}}^2$ -lactamase NDM-1. *J. Am. Chem. Soc.* **2014**, *136*, 7273-7285.
18. Rydzik, A. M.; Brem, J.; van Berkel, S. S.; Pfeffer, I.; Makena, A.; Claridge, T. D. W.; Schofield, C. J. Monitoring conformational changes in the NDM-1 metallo- $\hat{\text{I}}^2$ -lactamase by 19F NMR spectroscopy. *Angew. Chem., Int. Ed.* **2014**, *53*, 3129-3133.
19. Paphitou, N. I. Antimicrobial resistance: action to combat the rising microbial challenges. *Int. J. Antimicrob. Agents* **2013**, *42*, S25-S28.
20. Aitha, M.; Marts, A. R.; Bergstrom, A.; Moeller, A. J.; Moritz, L.; Turner, L.; Nix, J. C.; Bonomo, R. A.; Page, R. C.; Tierney, D. L.; Crowder, M. W. Biochemical, Mechanistic, and Spectroscopic Characterization of Metallo- $\hat{\text{I}}^2$ -lactamase VIM-2. *Biochemistry* **2014**, *53*, 7321-7331.
21. Anonymous *Antibiotic resistance threats in the United States, 2013.* **2013**, 1.
22. Spellberg, B. Antibiotic Resistance: Promoting Critically Needed Antibiotic Research and Development and Appropriate Use ("Stewardship") of these Precious Drugs . **2010**, .
23. Fair, R. J.; Tor, Y. Antibiotics and bacterial resistance in the 21st century. *Perspect Medicin Chem* **2014**, *6*, 25-64.
24. Gillner, D. M.; Becker, D. P.; Holz, R. C. Lysine biosynthesis in bacteria: a metallodesuccinylase as a potential antimicrobial target. *JBIC, J. Biol. Inorg. Chem.* **2013**, *18*, 155-163.



25. Born, T. L.; Zheng, R.; Blanchard, J. S. Hydrolysis of N-succinyl-L,L-diaminopimelic acid by the *Haemophilus influenzae* dapE-encoded desuccinylase: Metal activation, solvent isotope effects, and kinetic mechanism. *Biochemistry (N. Y.)* **1998**, *37*, 10478-10487.
26. Born, T. L.; Blanchard, J. S. Structure/function studies on enzymes in the diaminopimelate pathway of bacterial cell wall biosynthesis. *Curr. Opin. Chem. Biol.* **1999**, *3*, 607-613.
27. Girodeau, J. M.; Agouridas, C.; Masson, M.; Pineau, R.; Le Goffic, F. The lysine pathway as a target for a new genera of synthetic antibacterial antibiotics? *J. Med. Chem.* **1986**, *29*, 1023-1030.
28. Scapin, G.; Blanchard, J. S. Enzymology of bacterial lysine biosynthesis. *Adv. Enzymol. Relat. Areas Mol. Biol.* **1998**, *72*, 279-324.
29. Pavelka, M. S., Jr.; Jacobs, W. R., Jr Biosynthesis of diaminopimelate, the precursor of lysine and a component of peptidoglycan, is an essential function of *Mycobacterium smegmatis*. *J. Bacteriol.* **1996**, *178*, 6496-6507.
30. Grosdidier, A.; Zoete, V.; Michielin, O. SwissDock, a protein-small molecule docking web service based on EADock DSS. *Nucleic Acids Res.* **2011**, *39*, W270-W277.
31. Fischbach, M. A.; Walsh, C. T. Antibiotics for Emerging Pathogens. *Science (Washington, DC, U. S.)* **2009**, *325*, 1089-1093.
32. Rolain, J. M.; Parola, P.; Cornaglia, G. New Delhi metallo-beta-lactamase (NDM-1): towards a new pandemia?. *Clinical Microbiology and Infection* **2010**, *16*, 1699-1701.
33. Zhang, H. M.; Hao, Q. Crystal structure of NDM-1 reveals a common  $\beta$ -lactam hydrolysis mechanism. *Faseb J.* **2011**, *25*, 2574-2582, 10.1096/fj.11-184036.
34. Fiett, J.; Baraniak, A.; Izdebski, R.; Sitkiewicz, I.; Zabicka, D.; Meler, A.; Filczak, K.; Hryniewicz, W.; Gniadkowski, M. The first NDM metallo- $\beta$ -lactamase-producing Enterobacteriaceae isolate in Poland: evolution of IncFII-type plasmids carrying the blaNDM-1 gene. *Antimicrob. Agents Chemother.* **2014**, *58*, 1203-1207, 6.
35. Rao, Z.; Yang, C.; Lou, Z.; Xiao, Y.; Wang, J.; Wang, T.; Liu, W.; Xia, Q. Patent Application Country: Application: CN; CN; Priority Application Country: CN Patent CN103191091, 2013.
36. Rao, Z.; Yang, C.; Chen, Y.; Bai, C.; Guo, Y.; Xu, Y.; Xia, Q.; Wang, T.; Li, N.; Xu, F. Patent Application Country: Application: CN; CN; Priority Application Country: CN Patent CN103156833, 2013.
37. Rao, Z.; Chen, Y.; Yang, C.; Lou, Z.; Yin, Z.; Xu, Y.; Li, N.; Bai, C.; Xia, Q.; Xie, N.; Zhou, H. Patent Application Country: Application: CN; CN; Priority Application Country: CN Patent CN103156832, 2013.

38. Rao, Z.; Yang, C.; Chen, Y.; Guo, Y.; Bai, C.; Xu, Y.; Xia, Q.; Wang, T.; Li, N.; Xu, F. Patent Application Country: Application: CN; CN; Priority Application Country: CN Patent CN103156834, 2013.
39. Claiborne, T. L.; Cohen, S.; Amaro, R.; Fast, W. L. In *In Design of New Delhi metallo- $\hat{\text{I}}^2$ -lactamase I inhibitors using a synthetic and computational approach*. 2014; pp MEDI-389.
40. Thomas, P.; Zheng, M.; Wu, S.; Guo, H.; Liu, D.; Xu, D.; Fast, W. Characterization of Purified New Delhi Metallo- $\beta$ -lactamase-1. *Biochemistry* **2011**, *50*, 10102-10113.
41. Treon, M.; Yang, H.; Crowder, M. W. In *In Inhibition studies on metallo- $\hat{\text{I}}^2$ -lactamase NDM-1*. 2014; pp CHED-443.
42. Yuan, Q.; He, L.; Ke, H. A potential substrate binding conformation of  $\hat{\text{I}}^2$ -lactams and insight into the broad spectrum of NDM-1 activity. *Antimicrob. Agents Chemother.* **2012**, *56*, 5157-5163.
43. Zhu, K.; Lu, J.; Liang, Z.; Kong, X.; Ye, F.; Jin, L.; Geng, H.; Chen, Y.; Zheng, M.; Jiang, H.; Li, J.; Luo, C. A quantum mechanics/molecular mechanics study on the hydrolysis mechanism of New Delhi metallo- $\hat{\text{I}}^2$ -lactamase-1. *J. Comput. -Aided Mol. Des.* **2013**, *27*, 247-256.
44. Poffenberger, A. R.; Zhou, N.; Yu, S.; Crowder, M. W.; Sutton, L. D. In *In Alteration of metallo-carbapenemase mechanisms upon removal of a single substrate atom*. 2014; pp MWRM-160.
45. Shi, Y.; Lu, M.; Ou, Y.; Wang, X. Patent Application Country: Application: CN; CN; Priority Application Country: CN Patent CN103951680, 2014.
46. Klingler, F.; Wichelhaus, T. A.; Frank, D.; Cuesta-Bernal, J.; El-Delik, J.; Mueller, H. F.; Sjuts, H.; Goettig, S.; Koenigs, A.; Pos, K. M.; Pogoryelov, D.; Proschak, E. Approved Drugs Containing Thiols as Inhibitors of Metallo- $\hat{\text{I}}^2$ -lactamases: Strategy To Combat Multidrug-Resistant Bacteria. *J. Med. Chem.* **2015**, *58*, 3626-3630.
47. Chen, J.; Chen, H.; Zhu, T.; Zhou, D.; Zhang, F.; Lao, X.; Zheng, H. Asp120Asn mutation impairs the catalytic activity of NDM-1 metallo- $\hat{\text{I}}^2$ -lactamase: experimental and computational study. *Phys. Chem. Chem. Phys.* **2014**, *16*, 6709-6716.
48. van Berkel, S. S.; Brem, J.; Rydzik, A. M.; Salimraj, R.; Cain, R.; Verma, A.; Owens, R. J.; Fishwick, C. W. G.; Spencer, J.; Schofield, C. J. Assay Platform for Clinically Relevant Metallo- $\hat{\text{I}}^2$ -lactamases. *J. Med. Chem.* **2013**, *56*, 6945-6953.
49. Ye, H.; Zhou, Y.; Huang, G.; Yin, J. Bioinformatic analysis of New Delhi metallo-beta-lactamase 1. *Xinan Guofang Yiyao* **2012**, *22*, 1161-1163.
50. Gonzalez, M. M.; Kosmopoulou, M.; Mojica, M. F.; Castillo, V.; Hinchliffe, P.; Pettinati, I.; Brem, J.; Schofield, C. J.; Mahler, G.; Bonomo, R. A.; Llarrull, L. I.; Spencer, J.; Vila,

- A. J. Bisthiazolidines: A Substrate-Mimicking Scaffold as an Inhibitor of the NDM-1 Carbapenemase. *ACS Infect. Dis.* **2015**, *1*, 544-554.
51. Wang, S.; Chiu, S.; Lin, Y.; Tsai, Y.; Mu, J. Carbapenem resistant Enterobacteriaceae carrying New Delhi metallo- $\beta$ -lactamase gene (NDM-1) in Taiwan. *Diagn. Microbiol. Infect. Dis.* **2013**, *76*, 248-249.
  52. Thomas, P. W.; Fast, W. In *In Covalent inactivation of the non-covalent New Delhi metallo- $\beta$ -lactamase-1 mechanism*. 2013; pp SWRM-549.
  53. Thomas, P. W.; Cammarata, M.; Brodbelt, J. S.; Fast, W. Covalent Inhibition of New Delhi Metallo- $\beta$ -Lactamase-1 (NDM-1) by Cefaclor. *ChemBioChem* **2014**, *15*, 2541-2548.
  54. Sutton, L. D.; Yang, H.; Young, H.; Yu, S.; Crowder, M. W. In *In Dependence of transition-state structure upon electronic properties of cephalosporins*. 2014; pp MWRM-77.
  55. Li, T.; Wang, X.; Fu, S.; Li, C.; Chen, S.; Cai, J.; Huang, T.; Fu, H. New Delhi metallo  $\beta$ -lactamase 1 found in two strains of E. coli in Hainan. *Linchuang Jianyan Zazhi (Nanjing, China)* **2013**, *31*, 872-874.
  56. Liu, D.; Lepore, B. W.; Petsko, G. A.; Thomas, P. W.; Stone, E. M.; Fast, W.; Ringe, D. Three-dimensional structure of the quorum-quenching N-acyl homoserine lactone hydrolase from *Bacillus thuringiensis*. *Proc. Natl. Acad. Sci. U. S. A.* **2005**, *102*, 11882-11887.
  57. Liao, R.; Yu, J.; Himo, F. Reaction Mechanism of the Dinuclear Zinc Enzyme N-Acyl-L-homoserine Lactone Hydrolase: A Quantum Chemical Study. *Inorg. Chem.* **2009**, *48*, 1442-1448.
  58. Ben-David, M.; Wieczorek, G.; Elias, M.; Silman, I.; Sussman, J. L.; Tawfik, D. S. Catalytic Metal Ion Rearrangements Underline Promiscuity and Evolvability of a Metalloenzyme. *J. Mol. Biol.* **2013**, *425*, 1028-1038.
  59. Dong, Y.; Zhang, L. Quorum sensing and quorum-quenching enzymes. *J. Microbiol. (Seoul, Repub. Korea)* **2005**, *43*, 101-109.
  60. Mascarenhas, R.; Thomas, P. W.; Wu, C.; Nocek, B. P.; Hoang, Q. Q.; Liu, D.; Fast, W. Structural and Biochemical Characterization of AidC, a Quorum-Quenching Lactonase with Atypical Selectivity. *Biochemistry* **2015**, *54*, 4342-4353.
  61. Hutton, C. A.; Perugini, M. A.; Gerrard, J. A. Inhibition of lysine biosynthesis: An evolving antibiotic strategy. *Mol. BioSyst.* **2007**, *3*, 458-465.
  62. Karita, M.; Etterbeek, M. L.; Forsyth, M. H.; Tummuru, M. K. R.; Blaser, M. J. Characterization of *Helicobacter pylori* dapE and construction of a conditionally lethal dapE mutant. *Infect. Immun.* **1997**, *65*, 4158-4164.

63. Nocek, B. P.; Gillner, D. M.; Fan, Y.; Holz, R. C.; Joachimiak, A. Structural Basis for Catalysis by the Mono- and Dimetalated Forms of the dapE-Encoded N-succinyl-L,L-Diaminopimelic Acid Desuccinylase. *J. Mol. Biol.* **2010**, *397*, 617-626.
64. Rowsell, S.; Pauptit, R. A.; Tucker, A. D.; Blow, D. M.; Brick, P. Crystal structure of carboxypeptidase G2, a bacterial enzyme with applications in cancer therapy. *Structure (London)* **1997**, *5*, 337-347.
65. Desmarais, W.; Bienvenue, D. L.; Bzymek, K. P.; Petsko, G. A.; Ringe, D.; Holz, R. C. The high-resolution structures of the neutral and the low pH crystals of aminopeptidase from *Aeromonas proteolytica*. *JBIC, J. Biol. Inorg. Chem.* **2006**, *11*, 398-408.
66. Bienvenue, D. L.; Gilner, D. M.; Davis, R. S.; Bennett, B.; Holz, R. C. Substrate Specificity, Metal Binding Properties, and Spectroscopic Characterization of the DapE-Encoded N-Succinyl-L,L-Diaminopimelic Acid Desuccinylase from *Haemophilus influenzae*. *Biochemistry* **2003**, *42*, 10756-10763.
67. Coper, N. J.; Bienvenue, D. L.; Shokes, J. E.; Gilner, D. M.; Tsukamoto, T.; Scott, R. A.; Holz, R. C. The dapE-encoded N-Succinyl-L,L-Diaminopimelic Acid Desuccinylase from *Haemophilus influenzae* is a Dinuclear Metallohydrolase. *J. Am. Chem. Soc.* **2003**, *125*, 14654-14655.
68. Davis, R.; Bienvenue, D.; Swierczek, S. I.; Gilner, D. M.; Rajagopal, L.; Bennett, B.; Holz, R. C. Kinetic and spectroscopic characterization of the E134A- and E134D-altered dapE-encoded N-succinyl-L,L-diaminopimelic acid desuccinylase from *Haemophilus influenzae*. *JBIC, J. Biol. Inorg. Chem.* **2006**, *11*, 206-216.
69. Ye, Q.; Xie, S.; Ma, Z.; Huang, M.; Hanzlik, R. P. Structural basis of catalysis by monometalated methionine aminopeptidase. *Proc. Natl. Acad. Sci. U. S. A.* **2006**, *103*, 9470-9475.
70. Copik, A. J.; Swierczek, S. I.; Lowther, W. T.; D'souza, V. M.; Matthews, B. W.; Holz, R. C. Kinetic and Spectroscopic Characterization of the H178A Methionyl Aminopeptidase from *Escherichia coli*. *Biochemistry* **2003**, *42*, 6283-6292.
71. Holz, R. C. The aminopeptidase from *Aeromonas proteolytica*: structure and mechanism of co-catalytic metal centers involved in peptide hydrolysis. *Coord. Chem. Rev.* **2002**, *232*, 5-26.
72. Nocek, B.; Starus, A.; Makowska-Grzyska, M.; Gutierrez, B.; Sanchez, S.; Jedrzejczak, R.; Mack, J. C.; Olsen, K. W.; Joachimiak, A.; Holz, R. C. The dimerization domain in DapE enzymes is required for catalysis. *PLoS One* **2014**, *9*, e93593/1-e93593/11, 11.
73. Dutta, D.; Mishra, S. The structural and energetic aspects of substrate binding and the mechanism of action of the DapE-encoded N-succinyl-L,L-diaminopimelic acid desuccinylase (DapE) investigated using a hybrid QM/MM method. *Phys. Chem. Chem. Phys.* **2014**, *16*, 26348-26358.

74. Starus, A.; Nocek, B.; Bennett, B.; Larrabee, J. A.; Shaw, D. L.; Sae-Lee, W.; Russo, M. T.; Gillner, D. M.; Makowska-Grzyska, M.; Joachimiak, A.; Holz, R. C. Inhibition of the dapE-Encoded N-Succinyl-L,L-diaminopimelic Acid Desuccinylase from *Neisseria meningitidis* by L-Captopril. *Biochemistry* **2015**, *54*, 4834-4844.
75. Dutta, D.; Mishra, S. Structural and mechanistic insight into substrate binding from the conformational dynamics in apo and substrate-bound DapE enzyme. *Phys Chem Chem Phys* **2016**, *18*, 1671-1680.
76. Molecular Operating Environment (MOE), 2013.08; Chemical Computing Group Inc., 1010 Sherbooke St. West, Suite #910, Montreal, QC, Canada, H3A 2R7, 2016, .
77. Labute, P. The generalized Born/volume integral implicit solvent model: estimation of the free energy of hydration using London dispersion instead of atomic surface area. *J. Comput. Chem.* **2008**, *29*, 1693-1698.
78. Shoichet, B. K. Virtual screening of chemical libraries. *Nature* **2004**, *432*, 862-865.
79. Agarwal, R.; Burley, S. K.; Swaminathan, S. Structural Analysis of a Ternary Complex of Allantoate Amidohydrolase from *Escherichia coli* Reveals its Mechanics. *J. Mol. Biol.* **2007**, *368*, 450-463.
80. Botelho, T. O.; Guevara, T.; Marrero, A.; Arede, P.; Fluxa, V. S.; Reymond, J.; Oliveira, D. C.; Gomis-Rueth, F. Structural and Functional Analyses Reveal That *Staphylococcus aureus* Antibiotic Resistance Factor HmrA Is a Zinc-dependent Endopeptidase. *J. Biol. Chem.* **2011**, *286*, 25697-25709.
81. Dobritsch, D.; Gojkovic, Z.; Andersen, B.; Piskur, J. Crystallization and preliminary x-ray analysis of  $\beta^2$ -alanine synthase from the yeast *Saccharomyces kluyveri*. *Acta Crystallogr. , Sect. D: Biol. Crystallogr.* **2003**, *D59*, 1267-1269.
82. Na $\tilde{A}$  m, M.; Bhat, S.; Rankin, K. N.; Dennis, S.; Chowdhury, S. F.; Siddiqi, I.; Drabik, P.; Sulea, T.; Bayly, C. I.; Jakalian, A.; Purisima, E. O. Solvated Interaction Energy (SIE) for Scoring Protein $\hat{A}$ Ligand Binding Affinities. 1. Exploring the Parameter Space. *J. Chem. Inf. Model.* **2007**, *47*, 122-133.
83. Galli, C. L.; Sensi, C.; Fumagalli, A.; Parravicini, C.; Marinovich, M.; Eberini, I. A Computational Approach to Evaluate the Androgenic Affinity of Iprodione, Procymidone, Vinclozolin and Their Metabolites. *PLOS ONE* **2014**, *9*, e104822.
84. Simon, L.; Goodman, J. M. Enzyme catalysis by hydrogen bonds: The balance between transition state binding and substrate binding in oxyanion holes. *J. Org. Chem.* **2010**, *75*, 1831-1840.
85. Tang, A. W.; Kong, X.; Terskikh, V.; Wu, G. Solid-State  $^{17}O$  NMR of Unstable Acyl-Enzyme Intermediates: A Direct Probe of Hydrogen Bonding Interactions in the Oxyanion Hole of Serine Proteases. *J Phys Chem B* **2016**, *120*, 11142-11150.

86. Aitha, M.; Moller, A. J.; Sahu, I. D.; Horitani, M.; Tierney, D. L.; Crowder, M. W. Investigating the position of the hairpin loop in New Delhi metallo- $\beta$ -lactamase, NDM-1, during catalysis and inhibitor binding. *J. Inorg. Biochem.* **2016**, *156*, 35-39.
87. Tripathi, R.; Nair, N. N. Mechanism of Meropenem Hydrolysis by New Delhi Metallo  $\beta$ -Lactamase. *ACS Catal.* **2015**, *5*, 2577-2586.
88. Kim, Y.; Cunningham, M. A.; Mire, J.; Tesar, C.; Sacchettini, J.; Joachimiak, A. NDM-1, the ultimate promiscuous enzyme: substrate recognition and catalytic mechanism. *Faseb J.* **2013**, *27*, 1917-1927, 10.1096/fj.12-224014.
89. Chiou, J.; Leung, T. Y.; Chen, S. Molecular mechanisms of substrate recognition and specificity of New Delhi metallo- $\beta$ -lactamase. *Antimicrob. Agents Chemother.* **2014**, *58*, 5372-5378, 8.
90. Feng, H.; Ding, J.; Zhu, D.; Liu, X.; Xu, X.; Zhang, Y.; Zang, S.; Wang, D.; Liu, W. Structural and Mechanistic Insights into NDM-1 Catalyzed Hydrolysis of Cephalosporins. *J. Am. Chem. Soc.* **2014**, *136*, 14694-14697.
91. Klevens, R. M.; Morrison, M. A.; Nadle, J.; Petit, S.; Gershman, K.; Ray, S.; Harrison, L. H.; Lynfield, R.; Dumyati, G.; Townes, J. M.; Craig, A. S.; Zell, E. R.; Fosheim, G. E.; McDougal, L. K.; Carey, R. B.; Fridkin, S. K. Invasive methicillin-resistant staphylococcus aureus infections in the united states. *JAMA, J. Am. Med. Assoc.* **2007**, *298*, 1763-1771.
92. Howe, R. A.; Bowker, K. E.; Walsh, T. R.; Feest, T. G.; MacGowan, A. P. Vancomycin-resistant Staphylococcus aureus. *Lancet* **1998**, *351*, 602.
93. Gillner, D.; Armoush, N.; Holz, R. C.; Becker, D. P. Inhibitors of bacterial N-succinyl-L,L-diaminopimelic acid desuccinylase (DapE) and demonstration of in vitro antimicrobial activity. *Bioorg. Med. Chem. Lett.* **2009**, *19*, 6350-6352.
94. Mandal, R. S.; Das, S. In silico approach towards identification of potential inhibitors of Helicobacter pylori DapE. *J. Biomol. Struct. Dyn.* **2015**, *33*, 1460-1473.
95. Lin, Y.; Myhrman, R.; Schrag, M. L.; Gelb, M. H. Bacterial N-succinyl-L-diaminopimelic acid desuccinylase. Purification, partial characterization and substrate specificity. *J. Biol. Chem.* **1988**, *263*, 1622-1627.
96. Bienvenue, D. L.; Gilner, D. M.; Davis, R. S.; Bennett, B.; Holz, R. C. Substrate specificity, metal binding properties, and spectroscopic characterization of the DapE-encoded N-succinyl-L,L-diaminopimelic acid desuccinylase from Haemophilus influenzae. *Biochemistry* **2003**, *42*, 10756-10763.
97. Kindler, S. H.; Gilvarg, C. N-Succinyl-L- $\alpha$ , $\beta$ -diaminopimelic acid deacylase. *J. Biol. Chem.* **1960**, *235*, 3532-3535.

98. Nocek, B. Unpublished results: X-ray crystal structure of DapE from *H. influenzae* with bound products of L,L-SDAP hydrolysis. , .
99. McGregor, W. C.; Swierczek, S. I.; Bennett, B.; Holz, R. C. Characterization of the catalytically active Mn(II)-loaded argE-encoded N-acetyl-L-ornithine deacetylase from *Escherichia coli*. *JBIC, J. Biol. Inorg. Chem.* **2007**, *12*, 603-613.
100. Friedman, M. Applications of the Ninhydrin Reaction for Analysis of Amino Acids, Peptides, and Proteins to Agricultural and Biomedical Sciences. *J. Agric. Food Chem.* **2004**, *52*, 385-406.
101. Uda, N. R.; Creus, M. Selectivity of inhibition of N-succinyl-L,L-diaminopimelic acid desuccinylase in bacteria: the product of DapE-gene is not the target of L-captopril antimicrobial activity. *Bioinorg. Chem. Appl.* **2011**, 306465, 6.
102. Labute, P. The generalized Born/volume integral implicit solvent model: Estimation of the free energy of hydration using London dispersion instead of atomic surface area. *Journal of Computational Chemistry* **2008**, *29*, 1693-1698.
103. Shoichet, B. K. Virtual screening of chemical libraries. *Nature* **2004**, *432*, 862-865.
104. de Tejada, G. M.; Heinbockel, L.; Ferrer-Espada, R.; Heine, H.; Alexander, C.; BÃ¡rcena-Varela, S.; Goldmann, T.; Correa, W.; WiesmÃ¼ller, K.; Gisch, N.; SÃ¡nchez-GÃ³mez, S.; Fukuoka, S.; SchÃ¼holz, T.; Gutschmann, T.; Brandenburg, K. Lipoproteins/peptides are sepsis-inducing toxins from bacteria that can be neutralized by synthetic anti-endotoxin peptides. *Scientific Reports* **2015**, *5*, 14292.
105. Humann, J.; Lenz, L. L. Bacterial peptidoglycan degrading enzymes and their impact on host muropeptide detection. *Journal of innate immunity* **2009**, *1*, 88-97.
106. Yang, H.; Aitha, M.; Marts, A. R.; Hetrick, A.; Bennett, B.; Crowder, M. W.; Tierney, D. L. Spectroscopic and mechanistic studies of heterodimetallic forms of metallo-Î²-lactamase NDM-1. *J. Am. Chem. Soc.* **2014**, *136*, 7273-7285.
107. Karsisiotis, A. I.; Damblon, C. F.; Roberts, G. C. K. A variety of roles for versatile zinc in metallo-small beta]-lactamases. *Metallomics* **2014**, *6*, 1181-1197.
108. Rahman, M.; Shukla, S. K.; Prasad, K. N.; Ovejero, C. M.; Pati, B. K.; Tripathi, A.; Singh, A.; Srivastava, A. K.; Gonzalez-Zorn, B. Prevalence and molecular characterisation of New Delhi metallo-Î²-lactamases NDM-1, NDM-5, NDM-6 and NDM-7 in multidrug-resistant Enterobacteriaceae from India. *Int. J. Antimicrob. Agents* **2014**, *44*, 30-37.
109. Pereira, P. S.; Borghi, M.; Albano, R. M.; Lopes Jonathan, C. O.; Silveira, M. C.; Marques, E. A.; Oliveira Jane, C. R.; Asensi, M. D.; Carvalho-Assef Ana, P. D. Coproduction of NDM-1 and KPC-2 in *Enterobacter hormaechei* from Brazil. *Microb Drug Resist* **2014**, .

110. Sun, Y.; Liu, Q.; Chen, S.; Song, Y.; Liu, J.; Guo, X.; Zhu, L.; Ji, X.; Xu, L.; Zhou, W.; Qian, J.; Feng, S. Characterization and plasmid elimination of NDM-1-producing *Acinetobacter calcoaceticus* from China. *PLoS One* **2014**, *9*, e106555/1-e106555/6, 6.
111. Farzana, R.; Shamsuzzaman, S. M.; Mamun, K. Z. Isolation and molecular characterization of New Delhi metallo-beta-lactamase-1 producing superbug in Bangladesh. *J. Infect. Dev. Countries* **2013**, *7*, 161-168.
112. Chaudhary, M.; Payasi, A. Molecular characterization and antimicrobial susceptibility study of *Acinetobacter baumannii* clinical isolates from Middle East, African and Indian patients. *J. Proteomics Bioinf.* **2012**, *5*, 265-269.
113. Castanheira, M.; Farrell, S. E.; Krause, K. M.; Jones, R. N.; Sader, H. S. Contemporary diversity of  $\hat{\text{P}}^2$ -lactamases among Enterobacteriaceae in the nine U.S. census regions and ceftazidime-avibactam activity tested against isolates producing the most prevalent  $\hat{\text{P}}^2$ -lactamase groups. *Antimicrob. Agents Chemother.* **2014**, *58*, 833-838, 7.
114. Hasan, B.; Perveen, K.; Olsen, B.; Zahra, R. Emergence of carbapenem-resistant *Acinetobacter baumannii* in hospitals in Pakistan. *J. Med. Microbiol.* **2014**, *63*, 50-55.
115. Hudson, C. M.; Bent, Z. W.; Meagher, R. J.; Williams, K. P. Resistance determinants and mobile genetic elements of an NDM-1-encoding *Klebsiella pneumoniae* strain. *PLoS One* **2014**, *9*, e99209/1-e99209/14, 14.
116. Jovicic, B.; Lepsanovic, Z.; Begovic, J.; Filipic, B.; Kojic, M. Two copies of blaNDM-1 gene are present in NDM-1 producing *Pseudomonas aeruginosa* isolates from Serbia. *Antonie van Leeuwenhoek* **2014**, *105*, 613-618.
117. Li, B.; Xu, X.; Zhao, Z.; Wang, M.; Cao, Y. High prevalence of metallo- $\hat{\text{P}}^2$ -lactamase among carbapenem-resistant *Klebsiella pneumoniae* in a teaching hospital in China. *Can. J. Microbiol.* **2014**, *60*, 691-695.
118. Olaitan, A. O.; Diene, S. M.; Gupta, S. K.; Adler, A.; Assous, M. V.; Rolain, J. Genome analysis of NDM-1 producing *Morganella morganii* clinical isolate. *Expert Rev. Anti-Infect. Ther.* **2014**, *12*, 1297-1305.
119. Pillonetto, M.; Arend, L.; Vespero, E.; Pelisson, M.; Chagas, T.; Carvalho-Assef, A.; Asensi, M. First Report of NDM-1-Producing *Acinetobacter baumannii* Sequence Type 25 in Brazil. *Antimicrob. Agents Chemother.* **2014**, *58*, 7592-7594.
120. Rubin, J. E.; Peirano, G.; Peer, A. K.; Govind, C. N.; Pitout, J. D. D. NDM-1-producing Enterobacteriaceae from South Africa: moving towards endemicity?. *Diagn. Microbiol. Infect. Dis.* **2014**, *79*, 378-380.
121. Sartor, A. L.; Razb, M. W.; Abbasi, S. A.; Day, K. M.; Perry, J. D.; Paterson, D. L.; Sidjabat, H. E. Molecular epidemiology of NDM-1-producing Enterobacteriaceae and



- Acinetobacter baumannii isolates from Pakistan. *Antimicrob. Agents Chemother.* **2014**, *58*, 5589-5593, 6.
122. Tada, T.; Miyoshi-Akiyama, T.; Shimada, K.; Kirikae, T. Biochemical analysis of metallo- $\beta$ -lactamase NDM-3 from a multidrug-resistant Escherichia coli strain isolated in Japan. *Antimicrob. Agents Chemother.* **2014**, *58*, 3538-3540, 4.
  123. Voulgari, E.; Gartzonika, C.; Vrioni, G.; Politi, L.; Priavali, E.; Levidiotou-Stefanou, S.; Tsakris, A. The Balkan region: NDM-1-producing Klebsiella pneumoniae ST11 clonal strain causing outbreaks in Greece. *J. Antimicrob. Chemother.* **2014**, *69*, 2091-2097.
  124. Zafer, M. M.; Amin, M.; El Mahallawy, H.; Ashour, M. S. E.; Al Agamy, M. First report of NDM-1-producing Pseudomonas aeruginosa in Egypt. *Int. J. Infect. Dis.* **2014**, *29*, 80-81.
  125. Abouddihaj, B.; El Otmani, F.; El Yaagoubi Fouzia, L.; Mustapha, T.; Khalid, Z.; Mohammed, T. First report of a Klebsiella pneumoniae strain coproducing NDM-1, VIM-1 and OXA-48 carbapenemases isolated in Morocco. *Apmis* **2013**, *121*, 675-677.
  126. Barantsevich, E. P.; Churkina, I. V.; Barantsevich, N. E.; Pelkonen, J.; Schlyakhto, E. V.; Woodford, N. Emergence of Klebsiella pneumoniae producing NDM-1 carbapenemase in Saint Petersburg, Russia. *J. Antimicrob. Chemother.* **2013**, *68*, 1204-1206.
  127. Barrios, H.; Garza-Ramos, U.; Reyna-Flores, F.; Sanchez-Perez, A.; Rojas-Moreno, T.; Garza-Gonzalez, E.; Llaca-Diaz, J. M.; Camacho-Ortiz, A.; Guzman-Lopez, S.; Silva-Sanchez, J. Isolation of carbapenem-resistant NDM-1-positive Providencia rettgeri in Mexico. *J. Antimicrob. Chemother.* **2013**, *68*, 1934-1936.
  128. Fischer, J.; Schmoger, S.; Jahn, S.; Helmuth, R.; Guerra, B. NDM-1 carbapenemase-producing Salmonella enterica subsp. enterica serovar Corvallis isolated from a wild bird in Germany. *J. Antimicrob. Chemother.* **2013**, *68*, 2954-2956.
  129. Hidalgo, L.; Hopkins, K. L.; Gutierrez, B.; Ovejero, C. M.; Shukla, S.; Douthwaite, S.; Prasad, K. N.; Woodford, N.; Gonzalez-Zorn, B. Association of the novel aminoglycoside resistance determinant RmtF with NDM carbapenemase in Enterobacteriaceae isolated in India and the UK. *J. Antimicrob. Chemother.* **2013**, *68*, 1543-1550.
  130. Janvier, F.; Jeannot, K.; Tesse, S.; Robert-Nicoud, M.; Delacour, H.; Rapp, C.; Merens, A. Molecular characterization of blaNDM-1 in a sequence type 235 Pseudomonas aeruginosa isolate from France. *Antimicrob. Agents Chemother.* **2013**, *57*, 3408-3411.
  131. Kim, S. Y.; Shin, J.; Shin, S. Y.; Ko, K. S. Characteristics of carbapenem-resistant Enterobacteriaceae isolates from Korea. *Diagn. Microbiol. Infect. Dis.* **2013**, *76*, 486-490.
  132. Oteo, J.; Saez, D.; Bautista, V.; Fernandez-Romero, S.; Hernandez-Molina, J. M.; Perez-Vazquez, M.; Aracil, B.; Campos, J. Carbapenemase-producing Enterobacteriaceae in Spain in 2012. *Antimicrob. Agents Chemother.* **2013**, *57*, 6344-6347.

133. Revathi, G.; Siu, L. K.; Lu, P.; Huang, L. First report of NDM-1-producing *Acinetobacter baumannii* in East Africa. *Int. J. Infect. Dis.* **2013**, *17*, e1255-e1258.
134. Samuelsen, O.; Naseer, U.; Karah, N.; Lindemann, P. C.; Kanestrom, A.; Leegaard, T. M.; Sundsfjord, A. Identification of Enterobacteriaceae isolates with OXA-48 and coproduction of OXA-181 and NDM-1 in Norway. *J. Antimicrob. Chemother.* **2013**, *68*, 1682-1685.
135. Shahcheraghi, F.; Nobari, S.; Ghezalgeh, F. R.; Nasiri, S.; Owlia, P.; Nikbin, V. S.; Fooladi, A. A. I. First report of New Delhi metallo-beta-lactamase-1-producing *Klebsiella pneumoniae* in Iran. *Microb. Drug Resist. (New Rochelle, NY, U. S. )* **2013**, *19*, 30-36.
136. Shaheen, B. W.; Nayak, R.; Boothe, D. M. Emergence of a New Delhi metallo- $\beta$ -lactamase (NDM-1)-encoding gene in clinical *Escherichia coli* isolates recovered from companion animals in the United States. *Antimicrob. Agents Chemother.* **2013**, *57*, 2902-2903.
137. Shibl, A.; Al-Agamy, M.; Memish, Z.; Senok, A.; Khader, S. A.; Assiri, A. The emergence of OXA-48- and NDM-1-positive *Klebsiella pneumoniae* in Riyadh, Saudi Arabia. *Int. J. Infect. Dis.* **2013**, *17*, e1130-e1133.
138. Sonnevend, A.; Al Baloushi, A.; Ghazawi, A.; Hashmey, R.; Girgis, S.; Hamadeh, M. B.; Al Haj, M.; Pal, T. Emergence and spread of NDM-1 producer Enterobacteriaceae with contribution of IncX3 plasmids in the United Arab Emirates. *J. Med. Microbiol.* **2013**, *62*, 1044-1050.
139. Tada, T.; Miyoshi-Akiyama, T.; Dahal, R. K.; Sah, M. K.; Ohara, H.; Kirikae, T.; Pokhrel, B. M. NDM-8 metallo- $\beta$ -lactamase in a multidrug-resistant *Escherichia coli* strain isolated in Nepal. *Antimicrob. Agents Chemother.* **2013**, *57*, 2394-2396.
140. Bogaerts, P.; Rezende de Castro, R.; Roisin, S.; Deplano, A.; Huang, T.; Hallin, M.; Denis, O.; Glupczynski, Y. Emergence of NDM-1-producing *Acinetobacter baumannii* in Belgium. *J. Antimicrob. Chemother.* **2012**, *67*, 1552-1553.
141. Giske, C. G.; Froeding, I.; Hasan, C. M.; Turlej-Rogacka, A.; Toleman, M.; Livermore, D.; Woodford, N.; Walsh, T. R. Diverse sequence types of *Klebsiella pneumoniae* contribute to the dissemination of blaNDM-1 in India, Sweden, and the United Kingdom. *Antimicrob. Agents Chemother.* **2012**, *56*, 2735-2738.
142. Halaby, T.; Reuland, A. E.; Al Naiemi, N.; Potron, A.; Savelkoul, P. H. M.; Vandembroucke-Grauls, C. M. J. E.; Nordmann, P. A case of New Delhi metallo- $\beta$ -lactamase 1 (NDM-1)-producing *Klebsiella pneumoniae* with putative secondary transmission from the Balkan region in the Netherlands. *Antimicrob. Agents Chemother.* **2012**, *56*, 2790-2791.
143. Ho, P.; Li, Z.; Lai, E. L.; Chiu, S. S.; Cheng, V. C. C. Emergence of NDM-1-producing Enterobacteriaceae in China. *J. Antimicrob. Chemother.* **2012**, *67*, 1553-1555.

144. Krizova, L.; Bonnin, R. A.; Nordmann, P.; Nemeč, A.; Poirel, L. Characterization of a multidrug-resistant *Acinetobacter baumannii* strain carrying the blaNDM-1 and blaOXA-23 carbapenemase genes from the Czech Republic. *J. Antimicrob. Chemother.* **2012**, *67*, 1550-1552.
145. Mazzariol, A.; Bosnjak, Z.; Ballarini, P.; Budimir, A.; Bedenic, B.; Kalenic, S.; Cornaglia, G. NDM-1-producing *Klebsiella pneumoniae*, Croatia. *Emerging Infect. Dis.* **2012**, *18*, 532-534.
146. Poirel, L.; Ozdamar, M.; Ocampo-Sosa, A. A.; Turkoglu, S.; Ozer, U. G.; Nordmann, P. NDM-1-producing *Klebsiella pneumoniae* now in Turkey. *Antimicrob. Agents Chemother.* **2012**, *56*, 2784-2785.
147. Williamson, D. A.; Sidjabat, H. E.; Freeman, J. T.; Roberts, S. A.; Silvey, A.; Woodhouse, R.; Mowat, E.; Dyet, K.; Paterson, D. L.; Blackmore, T.; Burns, A.; Heffernan, H. Identification and molecular characterization of New Delhi metallo- $\beta$ -lactamase-1 (NDM-1)- and NDM-6-producing Enterobacteriaceae from New Zealand hospitals. *Int. J. Antimicrob. Agents* **2012**, *39*, 529-533.
148. Fallah, F.; Taherpour, A.; Vala, M. H.; Hashemi, A. Global spread of New Delhi metallo-beta-lactamase-1 (NDM-1). *Iran. J. Clin. Infect. Dis.* **2011**, *6*, 171-177.
149. Mandal, R. S.; Das, S. In silico approach towards identification of potential inhibitors of *Helicobacter pylori* DapE. *J. Biomol Struct Dyn* **2015**, *33*, 1460-1473.
150. Uda, N. R.; Creus, M. Selectivity of Inhibition of N-Succinyl-L,L-Diaminopimelic Acid Desuccinylase in Bacteria: The product of dapE-gene Is Not the Target of L-Captopril Antimicrobial Activity. *Bioinorg Chem Appl* **2011**, *2011*, 306465.
151. Yang, H.; Aitha, M.; Hetrick, A. M.; Richmond, T. K.; Tierney, D. L.; Crowder, M. W. Mechanistic and Spectroscopic Studies of Metallo- $\beta$ -lactamase NDM-1. *Biochemistry* **2012**, *51*, 3839-3847.
152. Liu, D.; Zhao, G.; Xiang, L. Diverse Strategies for the Synthesis of the Indoline Scaffold. *Eur. J. Org. Chem.* **2010**, 3975-3984.
153. Borrer, A. L.; Chinoporos, E.; Filosa, M. P.; Herchen, S. R.; Petersen, C. P.; Stern, C. A.; Onan, K. D. Regioselectivity of electrophilic aromatic substitution: syntheses of 6- and 7-sulfamoylindolines and -indoles. *J. Org. Chem.* **1988**, *53*, 2047-2052.
154. Wu, Y.; Sun, L.; He, H.; Chen, J.; Starrett, J. E.; Dextraze, P.; Daris, J.; Boissard, C. G.; Pieschl, R. L.; Gribkoff, V. K.; Natale, J.; Knox, R. J.; Harden, D. G.; Thompson, M. W.; Fitzpatrick, W.; Weaver, D.; Wu, D.; Gao, Q.; Dworetzky, S. I. Synthesis and KCNQ2 opener activity of N-(1-benzo[1,3]dioxol-5-yl)-ethyl, N-[1-(2,3-dihydro-benzofuran-5-yl)-ethyl], and N-[1-(2,3-dihydro-1H-indol-5-yl)-ethyl] acrylamides. *Bioorg. Med. Chem. Lett.* **2004**, *14*, 4533-4537.

155. Wang, L.; Woods, K. W.; Li, Q.; Barr, K. J.; McCroskey, R. W.; Hannick, S. M.; Gherke, L.; Credo, R. B.; Hui, Y.; Marsh, K.; Warner, R.; Lee, J. Y.; Zielinski-Mozng, N.; Frost, D.; Rosenberg, S. H.; Sham, H. L. Potent, Orally Active Heterocycle-Based Combretastatin A-4 Analogues: Synthesis, Structure-Activity Relationship, Pharmacokinetics, and In Vivo Antitumor Activity Evaluation. *J. Med. Chem.* **2002**, *45*, 1697-1711.
156. Ikan, R.; Fatal, Y. Synthesis in indole series. Chloromethylation and chlorosulfonation of 1-acetyl-5-bromoindoline. *J. Chem. Eng. Data* **1971**, *16*, 125-126.
157. Gutmann, B.; Cantillo, D.; Kappe, C. O. Continuous-Flow Technology-A Tool for the Safe Manufacturing of Active Pharmaceutical Ingredients. *Angew. Chem., Int. Ed.* **2015**, *54*, 6688-6728.
158. Pelleter, J.; Renaud, F. Facile, Fast and Safe Process Development of Nitration and Bromination Reactions Using Continuous Flow Reactors. *Org. Process Res. Dev.* **2009**, *13*, 698-705.
159. Shalygina, E. E.; Kobylinskii, D. V.; Ivanovskii, S. A.; Balakin, K. V.; Dorogov, M. V.; Toporova, T. A. Synthesis and properties of 1-acylindolinesulfonamides. *Izv. Vyssh. Uchebn. Zaved., Khim. Khim. Tekhnol.* **2004**, *47*, 91-96.
160. Morkūnaitė, V.; Baranauskienė, L.; Zubrienė, A.; Kairys, V.; Ivanova, J.; Trapencieris, P.; Matulis, D. Saccharin Sulfonamides as Inhibitors of Carbonic Anhydrases I, II, VII, XII, and XIII. *BioMed Research International* **2014**, *2014*, 9.
161. Liu, H.; Wan, N.; Huan, M.; Jia, Y.; Yuan, X.; Zhou, S.; Zhang, B. Enhanced water-soluble derivative of PC407 as a novel potential COX-2 inhibitor injectable formulation. *Bioorg. Med. Chem. Lett.* **2014**, *24*, 4794-4797.
162. Hanaya, K.; Suetsugu, M.; Saijo, S.; Yamato, I.; Aoki, S. Potent inhibition of dinuclear zinc(II) peptidase, an aminopeptidase from *Aeromonas proteolytica*, by 8-quinolinol derivatives: inhibitor design based on Zn<sup>2+</sup> fluorophores, kinetic, and X-ray crystallographic study. *JBIC, J. Biol. Inorg. Chem.* **2012**, *17*, 517-529.
163. Goddard-Borger, E.; Stick, R. V. An Efficient, Inexpensive, and Shelf-Stable Diazotransfer Reagent: Imidazole-1-sulfonyl Azide Hydrochloride. *Org. Lett.* **2007**, *9*, 3797-3800.
164. Kim, S. H.; Park, S. H.; Choi, J. H.; Chang, S. Sulfonyl and Phosphoryl Azides: Going Further Beyond the Click Realm of Alkyl and Aryl Azides. *Chem. - Asian J.* **2011**, *6*, 2618-2634.
165. Yoo, E. J.; Ahlquist, M.; Bae, I.; Sharpless, B. K.; Fokin, V. V.; Chang, S. Mechanistic Studies on the Cu-Catalyzed Three-Component Reactions of Sulfonyl Azides, 1-Alkynes and Amines, Alcohols, or Water: Dichotomy via a Common Pathway. *The Journal of Organic Chemistry* **2008**, *73*, 5520-5528.

166. Kim, J.; Lee, S. Y.; Lee, J.; Do, Y.; Chang, S. Synthetic Utility of Ammonium Salts in a Cu-Catalyzed Three-Component Reaction as a Facile Coupling Partner. *J. Org. Chem.* **2008**, *73*, 9454-9457.
167. Namitharan, K.; Pitchumani, K. Copper(I)-catalyzed [3+2] cycloaddition/ring-opening rearrangement/[4+2] cycloaddition/aromatization cascade. An unprecedented chemo- and stereoselective three-component coupling of sulfonyl azide, alkyne and N-arylidene-pyridin-2-amine to pyrido[1,2-a]pyrimidin-4-imine. *Adv. Synth. Catal.* **2013**, *355*, 93-98.
168. Bock, V. D.; Hiemstra, H.; van Maarseveen, J. H. Cu(I)-catalyzed alkyne-azide click cycloadditions from a mechanistic and synthetic perspective. *Eur. J. Org. Chem.* **2005**, 51-68.
169. Hein, J. E.; Fokin, V. V. Copper-catalyzed azide-alkyne cycloaddition (CuAAC) and beyond: new reactivity of copper(i) acetylides. *Chem. Soc. Rev.* **2010**, *39*, 1302-1315.
170. Kappe, C. O.; Van, d. E. Click chemistry under non-classical reaction conditions. *Chem. Soc. Rev.* **2010**, *39*, 1280-1290.
171. Kolb, H. C.; Sharpless, K. B. The growing impact of click chemistry on drug discovery. *Drug Discovery Today* **2003**, *8*, 1128-1137.
172. Bock, V. D.; Hiemstra, H.; van Maarseveen, J. H. Cu(I)-catalyzed alkyne-azide click cycloadditions from a mechanistic and synthetic perspective. *Eur. J. Org. Chem.* **2005**, 51-68.
173. Song, W.; Lei, M.; Shen, Y.; Cai, S.; Lu, W.; Lu, P.; Wang, Y. Copper-Catalyzed Four-Component Reaction of Baylis-Hillman Adducts with Alkynes, Sulfonyl Azides and Alcohols. *Adv. Synth. Catal.* **2010**, *352*, 2432-2436.
174. Husmann, R.; Na, Y. S.; Bolm, C.; Chang, S. Copper-catalyzed one-pot synthesis of  $\beta$ -functionalized imidates. *Chem. Commun. (Cambridge, U. K.)* **2010**, *46*, 5494-5496.
175. Cho, S. H.; Yoo, E. J.; Bae, I.; Chang, S. Copper-Catalyzed Hydrative Amide Synthesis with Terminal Alkyne, Sulfonyl Azide, and Water. *J. Am. Chem. Soc.* **2005**, *127*, 16046-16047.
176. Bae, I.; Han, H.; Chang, S. Highly Efficient One-Pot Synthesis of N-Sulfonylamidines by Cu-Catalyzed Three-Component Coupling of Sulfonyl Azide, Alkyne, and Amine. *J. Am. Chem. Soc.* **2005**, *127*, 2038-2039.
177. Yoo, E. J.; Bae, I.; Cho, S. H.; Han, H.; Chang, S. A Facile Access to N-Sulfonylimidates and Their Synthetic Utility for the Transformation to Amidines and Amides. *Org. Lett.* **2006**, *8*, 1347-1350.
178. Kawai, K.; Nagata, N. Metal-ligand interactions: An analysis of zinc binding groups using the Protein Data Bank. *Eur. J. Med. Chem.* **2012**, *51*, 271-276.

179. Jacobsen, F. E.; Lewis, J. A.; Cohen, S. M. The design of inhibitors for medically relevant metalloproteins. *ChemMedChem* **2007**, *2*, 152-171.
180. Bai, X.; Li, Y.; Gu, H.; Hua, Z. Selective colorimetric sensing of Co<sup>2+</sup> and Cu<sup>2+</sup> using 1-(2-pyridylazo)-2-naphthol derivative immobilized polyvinyl alcohol microspheres. *RSC Adv.* **2015**, *5*, 77217-77226.
181. Hu, Y.; Xiang, J. S.; DiGrandi, M. J.; Du, X.; Ipek, M.; Laakso, L. M.; Li, J.; Li, W.; Rush, T. S.; Schmid, J.; Skotnicki, J. S.; Tam, S.; Thomason, J. R.; Wang, Q.; Levin, J. I. Potent, selective, and orally bioavailable matrix metalloproteinase-13 inhibitors for the treatment of osteoarthritis. *Bioorg. Med. Chem.* **2005**, *13*, 6629-6644.
182. Phillips, D.; Sonnenberg, J.; Arai, A. C.; Vaswani, R.; Krutzik, P. O.; Kleisli, T.; Kessler, M.; Granger, R.; Lynch, G.; Chamberlin, A. R. 5'-Alkyl-benzothiadiazides: A New Subgroup of AMPA Receptor Modulators with Improved Affinity. *Bioorg. Med. Chem.* **2002**, *10*, 1229-1248.
183. Johnson, J. W.; Gretes, M.; Goodfellow, V. J.; Marrone, L.; Heynen, M. L.; Strynadka, N. C. J.; Dmitrienko, G. I. Cyclobutanone analogues of  $\beta$ -lactams revisited: Insights into conformational requirements for inhibition of serine- and metallo- $\beta$ -lactamases. *J. Am. Chem. Soc.* **2010**, *132*, 2558-2560.
184. Lall, M. S.; Ramtohol, Y. K.; James, M. N. G.; Vederas, J. C. Serine and Threonine  $\beta$ -Lactones: A New Class of Hepatitis A Virus 3C Cysteine Proteinase Inhibitors. *J. Org. Chem.* **2002**, *67*, 1536-1547.
185. Paetzel, M.; Danel, F.; de Castro, L.; Mosimann, S. C.; Page, M. G. P.; Strynadka, N. C. J. Crystal structure of the class D beta]-lactamase OXA-10. *Nat Struct Mol Biol* **2000**, *7*, 918-925.
186. Filippova, E. V.; Weston, L. A.; Kuhn, M. L.; Geissler, B.; Gehring, A. M.; Armoush, N.; Adkins, C. T.; Minasov, G.; Dubrovskaya, I.; Shuvalova, L.; Winsor, J. R.; Lavis, L. D.; Satchell, K. J. F.; Becker, D. P.; Anderson, W. F.; Johnson, R. J. Large Scale Structural Rearrangement of a Serine Hydrolase from Francisella tularensis Facilitates Catalysis. *J. Biol. Chem.* **2013**, *288*, 10522-10535.
187. Liu, C. F.; Liu, D.; Momb, J.; Thomas, P. W.; Lajoie, A.; Petsko, G. A.; Fast, W.; Ringe, D. A Phenylalanine Clamp Controls Substrate Specificity in the Quorum-Quenching Metallo- $\beta$ -lactonase from Bacillus thuringiensis. *Biochemistry* **2013**, *52*, 1603-1610.
188. Liao, R.; Yu, J.; Himo, F. Reaction Mechanism of the Dinuclear Zinc Enzyme N-Acyl-L-homoserine Lactone Hydrolase: A Quantum Chemical Study. *Inorg. Chem.* **2009**, *48*, 1442-1448.
189. Armoush, N.; Syal, P.; Becker, D. P. Synthesis of substituted 2-aminocyclobutanones. *Synth. Commun.; Synthetic Communications* **2008**, *38*, 1679-1687.

190. Riva, E.; Wilkening, I.; Gazzola, S.; Li, W. M. A.; Smith, L.; Leadlay, P. F.; Tosin, M. Chemical Probes for the Functionalization of Polyketide Intermediates. *Angew. Chem., Int. Ed.* **2014**, *53*, 11944-11949.
191. Armoush, N.; Syal, P.; Becker, D. P. Synthesis of substituted 2-aminocyclobutanones. *Synth. Commun.* **2008**, *38*, 1679-1687.
192. Fiasella, A.; Nuzzi, A.; Summa, M.; Armirotti, A.; Tarozzo, G.; Tarzia, G.; Mor, M.; Bertozzi, F.; Bandiera, T.; Piomelli, D. 3-Aminoazetid-2-one Derivatives as N-Acylethanolamine Acid Amidase (NAAA) Inhibitors Suitable for Systemic Administration. *ChemMedChem* **2014**, *9*, 1602-1614.
193. Wang, W.; Morohoshi, T.; Ikenoya, M.; Someya, N.; Ikeda, T. AiiM, a novel class of N-acylhomoserine lactonase from the leaf-associated bacterium *Microbacterium testaceum*. *Appl. Environ. Microbiol.* **2010**, *76*, 2524-2530.
194. Fetrow, J. S.; Siew, N.; Di Gennaro, J. A.; Martinez-Yamout, M.; Dyson, H. J.; Skolnick, J. Genomic-scale comparison of sequence- and structure-based methods of function prediction: does structure provide additional insight?. *Protein Sci.* **2001**, *10*, 1005-1014.
195. Vetting, M. W.; de Carvalho, Luiz Pedro S.; Yu, M.; Hegde, S. S.; Magnet, S.; Roderick, S. L.; Blanchard, J. S. Structure and functions of the GNAT superfamily of acetyltransferases. *Arch. Biochem. Biophys.* **2005**, *433*, 212-226.
196. Yu, M.; Sorio de Carvalho, L. P.; Sun, G.; Blanchard, J. S. Activity-Based Substrate Profiling for Gcn5-Related N-Acetyltransferases: The Use of Chloroacetyl-Coenzyme A To Identify Protein Substrates. *J. Am. Chem. Soc.* **2006**, *128*, 15356-15357.
197. Vetting, M. W.; Magnet, S.; Nieves, E.; Roderick, S. L.; Blanchard, J. S. A Bacterial Acetyltransferase Capable of Regioselective N-Acetylation of Antibiotics and Histones. *Chem. Biol.* **2004**, *11*, 565-573.
198. Salah Ud-Din Abu, I. M.; Tikhomirova, A.; Roujeinikova, A.; Roujeinikova, A. Structure and Functional Diversity of GCN5-Related N-Acetyltransferases (GNAT). *Int J Mol Sci* **2016**, *17*,.
199. Gao, F.; Yan, X.; Baettig, O. M.; Berghuis, A. M.; Auclair, K. Regio- and Chemoselective 6'-N-Derivatization of Aminoglycosides: Bisubstrate Inhibitors as Probes To Study Aminoglycoside 6'-N-Acetyltransferases. *Angewandte Chemie* **2005**, *117*, 7019-7022.
200. Poux, A. N.; Cebrat, M.; Kim, C. M.; Cole, P. A.; Marmorstein, R. Structure of the GCN5 histone acetyltransferase bound to a bisubstrate inhibitor. *Proc. Natl. Acad. Sci. U. S. A.* **2002**, *99*, 14065-14070.
201. Lavogina, D.; Enkvist, E.; Uri, A. Bisubstrate Inhibitors of Protein Kinases: from Principle to Practical Applications. *ChemMedChem* **2010**, *5*, 23-34.

202. Cole, P. A. Chemical probes for histone-modifying enzymes. *Nat Chem Biol* **2008**, *4*, 590-597.
203. Pegg, A. E. Spermidine/spermine-*N*<sup>1</sup>-acetyltransferase: a key metabolic regulator. *Am. J. Physiol. Endocrinol. Metab.* **2008**, *294*, E995-E1010.
204. Kuhn, M. L.; Majorek, K. A.; Minor, W.; Anderson, W. F. Broad-substrate screen as a tool to identify substrates for bacterial Gcn5-related N-acetyltransferases with unknown substrate specificity. *Protein Science* **2013**, *22*, 222-230.
205. Majorek, K. A.; Kuhn, M. L.; Chruszcz, M.; Anderson, W. F.; Minor, W. Structural, Functional, and Inhibition Studies of a Gcn5-related N-Acetyltransferase (GNAT) Superfamily Protein PA4794. *J. Biol. Chem.* **2013**, *288*, 30223-30235.
206. Singh, J.; Petter, R. C.; Baillie, T. A.; Whitty, A. The resurgence of covalent drugs. *Nat. Rev. Drug Discovery* **2011**, *10*, 307-317.
207. Liu, Q.; Sabnis, Y.; Zhao, Z.; Zhang, T.; Buhrlage, S. J.; Jones, L. H.; Gray, N. S. Developing Irreversible Inhibitors of the Protein Kinase Cysteine. *Chem. Biol. (Oxford, U. K. )* **2013**, *20*, 146-159.
208. Joest, C.; Nitsche, C.; Scholz, T.; Roux, L.; Klein, C. D. Promiscuity and Selectivity in Covalent Enzyme Inhibition: A Systematic Study of Electrophilic Fragments. *J. Med. Chem.* **2014**, *57*, 7590-7599.
209. Hwang, Y.; Thompson, P. R.; Wang, L.; Jiang, L.; Kelleher, N. L.; Cole, P. A. A selective chemical probe for coenzyme A-requiring enzymes. *Angew. Chem., Int. Ed.* **2007**, *46*, 7621-7624.
210. Hamano, Y.; Hoshino, Y.; Nakamori, S.; Takagi, H. Overexpression and Characterization of an Aminoglycoside 6'-N-Acetyltransferase with Broad Specificity from an  $\epsilon$ -Poly-l-lysine Producer, *Streptomyces albus* IFO14147. *The Journal of Biochemistry* **2004**, *136*, 517-524.
211. Vetting, M. W.; Hegde, S. S.; Javid-Majd, F.; Blanchard, J. S.; Roderick, S. L. Aminoglycoside 2prime]-N-acetyltransferase from *Mycobacterium tuberculosis* in complex with coenzyme A and aminoglycoside substrates. *Nat Struct Mol Biol* **2002**, *9*, 653-658.
212. Lau, E. Y.; Felton, J. S.; Lightstone, F. C. Insights into the o-acetylation reaction of hydroxylated heterocyclic amines by human arylamine N-acetyltransferases: a computational study. *Chem. Res. Toxicol.* **2006**, *19*, 1182-1190.
213. Liu, Y.; Zhang, W.; Sayre, L. M. An alternative total synthesis of pentosidine. *J. Heterocycl. Chem.* **2011**, *48*, 426-433.
214. McGarvey, G. J.; Kimura, M. Sodium nitroprusside-mediated substitution of oxygen for nitrogen at saturated carbon centers. *J. Org. Chem.* **1986**, *51*, 3913-3915.



215. Hoyle, C. E.; Bowman, C. N. Thiol-Ene Click Chemistry. *Angew. Chem., Int. Ed.* **2010**, *49*, 1540-1573.
216. Filippova, E. V.; Kuhn, M. L.; Osipiuk, J.; Kiryukhina, O.; Joachimiak, A.; Ballicora, M. A.; Anderson, W. F. A Novel Polyamine Allosteric Site of SpeG from *Vibrio cholerae* Is Revealed by Its Dodecameric Structure. *J. Mol. Biol.* **2015**, *427*, 1316-1334.
217. Majorek, K. A.; Osinski, T.; Tran, D. T.; Revilla, A.; Anderson, W. F.; Minor, W.; Kuhn, M. L. Insight into the 3D structure and substrate specificity of previously uncharacterized GNAT superfamily acetyltransferases from pathogenic bacteria. *Biochimica et Biophysica Acta (BBA) - Proteins and Proteomics* **2017**, *1865*, 55-64.
218. Burmeister, W. P. Structural changes in a cryo-cooled protein crystal owing to radiation damage. *Acta Crystallogr D Biol Crystallogr* **2000**, *56*, 328-341.
219. Makowski, K.; Mera, P.; Paredes, D.; Herrero, L.; Ariza, X.; Asins, G.; Hegardt, F. G.; Garcia, J.; Serra, D. Differential Pharmacologic Properties of the Two C75 Enantiomers: (+)-C75 Is a Strong Anorectic Drug; (-)-C75 Has Antitumor Activity. *Chirality* **2013**, *25*, 281-287.
220. Li, X.; Liu, N.; Zhang, H.; Knudson, S. E.; Li, H.; Lai, C.; Simmerling, C.; Slayden, R. A.; Tonge, P. J. CoA Adducts of 4-Oxo-4-phenylbut-2-enates: Inhibitors of MenB from the *M. tuberculosis* Menaquinone Biosynthesis Pathway. *ACS Med. Chem. Lett.* **2011**, *2*, 818-823.
221. Leggans, E. K.; Akey, D. L.; Smith, J. L.; Fecik, R. A. A general scheme for synthesis of substrate-based polyketide labels for acyl carrier proteins. *Bioorg. Med. Chem. Lett.* **2010**, *20*, 5939-5942.
222. Gilar, M.; Belenky, A.; Wang, B. H. High-throughput biopolymer desalting by solid-phase extraction prior to mass spectrometric analysis. *J. Chromatogr. A* **2001**, *921*, 3-13.
223. Otwinowski, Z.; Minor, W.; W Jr, C. C. Processing of X-ray diffraction data collected in oscillation mode. **1997**, .
224. Minor, W.; Cymborowski, M.; Otwinowski, Z.; Chruszcz, M. HKL-3000: the integration of data reduction and structure solution—from diffraction images to an initial model in minutes. *Acta Crystallographica Section D: Biological Crystallography* **2006**, *62*, 859-866.
225. Vagin, A.; Teplyakov, A. Molecular replacement with MOLREP. *Acta Crystallographica Section D: Biological Crystallography* **2009**, *66*, 22-25.
226. Murshudov, G. N.; Skubák, P.; Lebedev, A. A.; Pannu, N. S.; Steiner, R. A.; Nicholls, R. A.; Winn, M. D.; Long, F.; Vagin, A. A. REFMAC5 for the refinement of macromolecular crystal structures. *Acta Crystallographica Section D: Biological Crystallography* **2011**, *67*, 355-367.

227. Emsley, P.; Lohkamp, B.; Scott, W. G.; Cowtan, K. Features and development of Coot. *Acta Crystallographica Section D: Biological Crystallography* **2010**, *66*, 486-501.
228. Emsley, P.; Cowtan, K. Coot: model-building tools for molecular graphics. *Acta Crystallographica Section D: Biological Crystallography* **2004**, *60*, 2126-2132.
229. Davis, I. W.; Leaver-Fay, A.; Chen, V. B.; Block, J. N.; Kapral, G. J.; Wang, X.; Murray, L. W.; Arendall, W. B., 3rd; Snoeyink, J.; Richardson, J. S.; Richardson, D. C. MolProbity: all-atom contacts and structure validation for proteins and nucleic acids. *Nucleic Acids Res* **2007**, *35*, W375-83.
230. Yang, H.; Guranovic, V.; Dutta, S.; Feng, Z.; Berman, H. M.; Westbrook, J. D. Automated and accurate deposition of structures solved by X-ray diffraction to the Protein Data Bank. *Acta Crystallogr. , Sect. D: Biol. Crystallogr.* **2004**, *D60*, 1833-1839.

## VITA

Cory T. Reidl attended Quincy University in Quincy Illinois, where he was a student-athlete. His hard work culminated in a Bachelor of Science, cum laude honors, in Chemistry, pre-professional concentration, with a Biology minor, in May 2011.

Reidl began his Ph.D. program at Loyola University Chicago in August 2011 under the guidance of Daniel P. Becker, Ph. D. During his graduate studies, he was a capable and dedicated Organic Laboratory teaching assistant. Throughout this time, he was an active member of the football coaching staff for Loyola's intercollegiate club football team where he developed valuable leadership skills that served him well during his other academic and mentoring endeavors.

Reidl was the Denkewalter Symposium poster presentation winner in September 2015. In early 2016, he was awarded the Arthur J. Schmitt Dissertation Fellowship for the 2016-2017 academic year. This gave him the opportunity and time to hone his undergraduate research mentoring activities, develop a "Computers in Medicinal Chemistry" teaching mini-course (earning him an invitation to give an oral presentation at the 2016 ACS national meeting in DC) and provide the opportunity to helm a weekly departmental Molecular Operating Environment (MOE) workshop as forum to discuss the various in silico computational projects around the department. In addition, he served three years as a judge at the Chicago Area Undergraduate Research Symposium.

A doctoral degree in Medicinal and Synthetic Chemistry will be conferred upon

Reidl in May 2017. He has been invited to teach the Organic Chemistry B summer section at Loyola University before continuing his post-graduate career in the Pharmaceutical industry in the greater Chicago area.